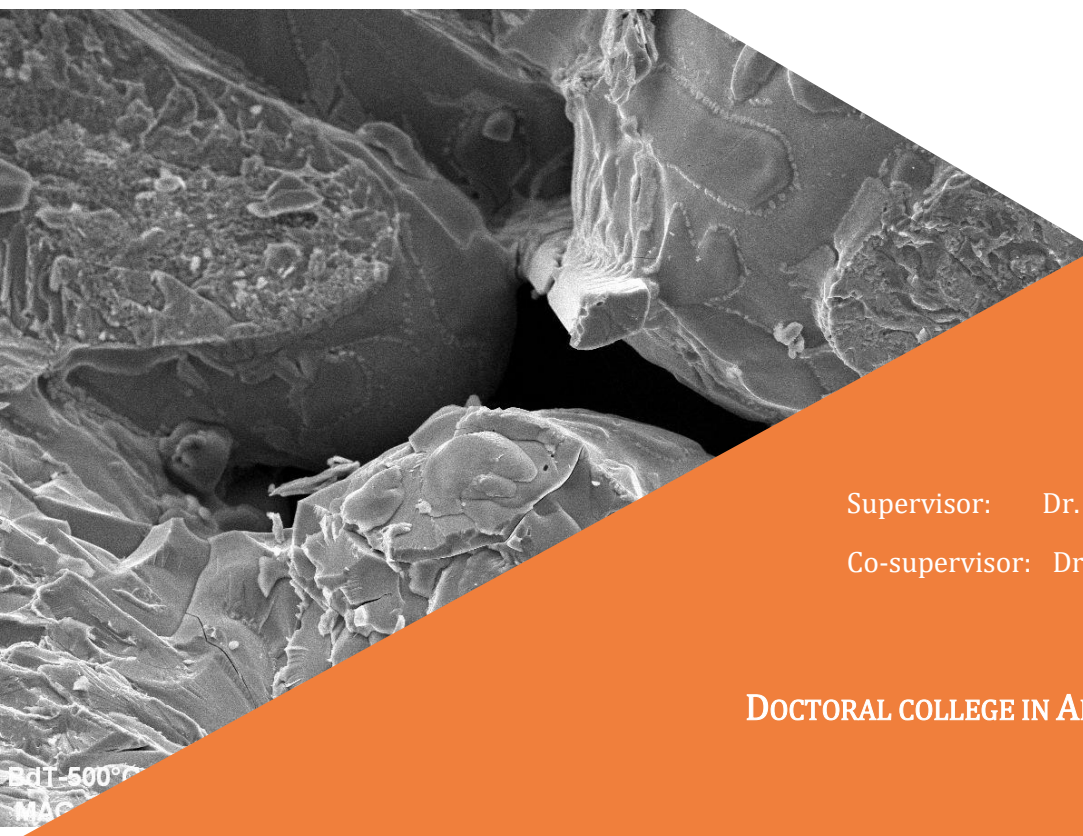# Étude des liens Procédés–Microstructures–Propriétés pour des Alliages hors équilibre (Aciers à outils et Ti6Al4V)

A thesis submitted in partial fulfillment of the requirements
for the degree of Doctor of Philosophy (Phd) in Engineering Science

by

Jérôme Tchoufang TCHUINDJANG

Supervisor: Dr. Anne MERTENS

Co-supervisor: Dr. Anne Marie HABRAKEN

DOCTORAL COLLEGE IN AEROSPACE AND MECHANICS

DECEMBER 2020

Étude des liens Procédés–Microstructures–Propriétés pour les Alliages hors équilibre (Aciers à outils et Ti6Al4V)

A thesis submitted in partial fulfillment of the requirements
for the degree of Doctor of Philosophy (Phd) in Engineering Science

by

Jérôme Tchoufang TCHUINDJANG

Supervisor: Dr. Anne MERTENS

Co-supervisor: Dr. Anne Marie HABRAKEN

DOCTORAL COLLEGE IN AEROSPACE AND MECHANICS

DECEMBER 2020

Study of the Processes–Microstructures–Properties correlations for Alloys under non-equilibrium conditions (High Speed Steels and Ti6Al4V)

A thesis submitted in partial fulfillment of the requirements
for the degree of Doctor of Philosophy (Phd) in Engineering Science

by

Jérôme Tchoufang TCHUINDJANG

Supervisor: Dr. Anne MERTENS

Co-supervisor: Dr. Anne Marie HABRAKEN

DOCTORAL COLLEGE IN AEROSPACE AND MECHANICS

DECEMBER 2020

Table des matières

Remerciements

On y est !

Effectivement, cette exclamation peut valoir pour le temps estival inhabituel qu'il fait ce jour, au moment où je boucle cet ouvrage ! Il aurait pu être celui d'une vie, mais heureusement, la mienne en comporte bien d'autres volets que le professionnel. Mais oui, on y est, parce que le mémoire est rédigé et bouclé ce jour.

Mais encore, on y est aussi parce que cette échéance sans cesse repoussée, est enfin atteinte, du moins pour la partie concernant la rédaction. Le reste semble-t-il devrait être une formalité, surtout que le temps, pas celui du jour, est devenu très incertain, crise sanitaire oblige.

On y est, oui, et on y est arrivé !

Mais à quoi donc ?

A concrétiser ce que plusieurs ont toujours considéré comme une formalité, au point justement que l'obtenir ne semblait plus une obligation, une exigence à soi imposée.

Voilà c'est fait en tout cas, le bébé est né, après une gestation sans nulle autre pareille.

C'est donc ici l'occasion de remercier à juste titre, différentes personnes, pour avoir contribué chacune à sa façon, à ce que ceci se réalise.

Je commencerais par Jacqueline LECOMTE-BECKERS, qui m'a engagé dans ce service dont je suis encore membre, dès mon diplôme d'Ingénieur en main. C'était en 1998. Aujourd'hui pensionnée, elle a indubitablement marqué les esprits, et le mien en particulier. Ma façon d'être un chercheur qui trouve de temps en temps, et qui répond parfois aux attentes des autres, est sa marque de fabrique. Elle a été ma responsable de service, chef de projet, promotrice de DEA, et collègue attentive et attentionnée pour tous. L'ouvrage que je dépose ce jour, avait été impulsé par elle.

Je remercie les industriels d'hier (ceux du Groupe AKERS, dont les matériaux ont été utilisés pour un de chapitres de la thèse), et d'aujourd'hui, notamment Marichal Ketin, autre grand pourvoyeur des matières que j'ai étudiées, et notamment Mario SINNAEVE, et Jean-Pierre BREYER. J'ai une pensée profonde pour ce dernier, qui a une santé fragile depuis un moment. Je nourris la même pensée pour le Professeur TERZIEV, qui fut associé un temps à des travaux avec le service.

Je remercie Greg, qui en sa qualité de président du département motivé, avait pris le relais de Jacqueline, pour assurer la coordination de ce même projet. C'est lui qui a fixé le format final, même s'il n'est pas resté promoteur officiel de la thèse. Merci pour ton parler direct.

Je remercie enfin deux dames, oui, qui s'y sont mises ensemble, pour bousculer celui qui était un peu dans sa zone de confort, à conseiller sans avoir le grade dit-on ! Ce sera chose faite dorénavant. Je remercie donc Anne Marie et Anne, ma nouvelle cheffe d'unité. Leur tandem de choc, est aussi à l'image de la collaboration nouvelle et fructueuse déjà existante du temps de Jacqueline, mais désormais plus que jamais renforcée, entre numériciens et métallurgistes. La fabrication additive a posé le ciment de cette collaboration, et l'ouvrage que je produis aujourd'hui, en est l'illustration. J'espère que nous poursuivrons avec encore plus de gloire scientifique, dans les publications bien sûr !

Je vais aussi remercier tous mes collègues de service, plus ou moins anciens, même si je garde (après Rosine), le flambeau de doyen désormais. Rosine, Sylvie, Hakan, Olivier, Tommaso, Jocelyn, et Enrico, je

profite ici pour vous dire combien il est plaisant de bosser ensemble, même si le contexte actuel a un peu cassé la convivialité qui nous habite souvent. Notez aussi que les échanges que nous avons, autant pour les cas d'expertise que pour les sujets de recherche, sont toujours très fructueux, car le challenge de la confrontation des idées aide à comprendre ensemble, ce que parfois on ne parvient pas à faire seul !

Les amis sont aussi dans mes pensées, en ce moment, car plusieurs d'entre eux, ont souvent demandé à quand le grand moment.

En réalité je l'avais pensé autrement, mais je me réjouis vraiment d'avoir bouclé le sujet aujourd'hui. Je pourrais toujours écrire d'autres choses demain, avec moins de pression.

Et je finirai par ce qui représente le fondement, la fondation, le repère et le refuge, quand on est en proie au doute… C'est aussi ce qui représente les premiers témoins des bons et des mauvais moments. La famille, puisque c'est d'elle qu'il s'agit. Dans mon cas, elle est grande, ou plutôt elle a continué à s'agrandir, ce qui en soit est une grâce. J'ai cependant une pensée émue pour un de ces piliers, le baobab, Doc comme on l'appelait qui rentrera dans l'histoire comme le premier des médecins à être terrassé par ce virus qui continue à sévir. C'était au mois d'Avril de cette année, au Cameroun.

Mais je sais pouvoir compter aussi et surtout sur tous les autres, frères, sœurs, parents, aussi bien utérins, que les autres rentrés dans le cercle, par alliance. La solidarité qui s'est renouvelée autrement dans ce contexte sanitaire est à encourager et à perpétrer. Je remercie une fois encore mes parents qui m'ont encouragé tout le temps, et mes frères et sœurs.

Je bouclerai la boucle par ma tribu, le petit cercle qui est dans mon quotidien. Malika, Kamau et Nura, vous êtes chacun une source de vie qui pousse à avancer, avec le souhait de vous voir vous réaliser. Vous m'avez fait comprendre que parent c'est un métier à temps plein.

A Danielle, ma meilleure moitié, bijou de naissance, je voudrais te remercier pour ta présence, ton soutien et ton engagement au quotidien, dans ma vie, dans notre vie.

. RÉSUMÉ

Le travail présenté dans cet ouvrage est le fruit d'une approche pluridisciplinaire, étudiant des phénomènes métallurgiques tels que la solidification ou les transformations en phases solide, en conditions hors équilibre. Cette étude vise à comprendre les microstructures, afin d'une part d'établir un lien avec le comportement des alliages du système Fe-Cr-C-X soumis à des sollicitations sévères (Partie A), et d'autre part à déterminer la nature et l'évolution des phases dans un alliage Ti6Al4V élaboré par fabrication additive (Partie B).

Pour la Partie A, l'étude de la solidification et des transformations en phase solide permet notamment la mise en évidence d'un effet de sursaturation qui influence les mécanismes d'endommagement. Les alliages de la Partie A sont des aciers à outils ou des fontes alliées, issus de deux procédés d'élaboration. Le premier procédé est mixte (coulée conventionnelle au four électrique, suivie d'une métallurgie secondaire par refusion d'électrode consommable (ESR), avant un traitement thermomécanique (forgeage)). Le second mode d'élaboration est la coulée centrifuge verticale. Au niveau de la microstructure, toutes les phases des alliages Fe-C sont considérées, depuis la ferrite δ jusqu'à la perlite qui se forment en conditions d'équilibre, jusqu'aux phases hors équilibre telles que la bainite et la martensite, qui sont obtenues après traitements thermiques spécifiques. La caractérisation des phases est réalisée en utilisant différents outils et techniques d'analyse, notamment la microscopie optique, la microscopie électronique à balayage (associée à l'EDX et à l'EBSD), la dilatométrie, l'analyse thermique différentielle, les duretés, etc. En outre on accorde une attention particulière à une phase rarement étudiée, à savoir la troostite, en la différenciant de la perlite avec laquelle on la confond parfois. Cette phase est induite par la sursaturation. Outre la troostite, on décrit plusieurs phénomènes découlant de la sursaturation, notamment la précipitation en phase solide de carbures au sein d'une matrice.

Les propriétés des matières sont étudiées notamment après l'élaboration de traitements thermiques optimisés au sens de l'homogénéisation de la microstructure et de la dureté.

La partie B étudie la solidification et les transformations en phase solide dans un alliage Ti6Al4V produit par fusion laser de poudres projetées sur un substrat. Dans cette partie, on part de la description du dispositif de fabrication jusqu'à la caractérisation macroscopique des dépôts obtenus en considérant des stratégies de fabrication distinctes. Un modèle grossier de description du procédé est d'abord esquissé, pour établir un refroidissement équivalent. Ensuite on montre comment l'apport d'un modèle thermique éléments finis validé, permet de connaître l'évolution de la température en tout point du dépôt. Cette information est exploitée pour interpréter l'évolution de la microstructure via un palier isotherme et un refroidissement final, dans un échantillon homogène. L'utilisation de la même approche sur un dépôt hétérogène permet d'obtenir des histoires thermiques plus complexes. C'est l'analyse de ces histoires thermiques qui permet de développer un concept nouveau : les blocs de temps et de transformations de phases ou Time – Phase Transformations – Blocks en abrégé TTB. Cette approche permet de découper en séquences l'ensemble de l'histoire thermique, chaque séquence étant en lien avec des mécanismes de transformations de phases bien identifiés. En outre, le concept TTB propose une description qui tient compte de toutes les étapes de la fabrication additive, en ce compris les périodes de chauffage rapides et le refroidissement final.

Cette thèse applique l'approche à rebours (appelée aussi analyse inverse), où l'on part de la fin pour remonter à la source, suite à une problématique soulevée dans les conditions de service. L'analyse du problème permet d'établir des corrélations entre des phénomènes qu'on n'aurait pas forcément liés initialement.

La thèse fait la synthèse de 8 articles, dont 5 pour la Partie A et 3 pour la Partie B. Chacun des articles donne lieu à un chapitre où on rappelle le contexte de l'étude, et surtout on apporte des résultats complémentaires et inédits, dont le contenu a été jugé essentiel à la compréhension globale de la thématique.

Cette étude réalisée sur deux familles d'alliages distinctes montre que le domaine hors équilibre reste encore un vaste champ exploratoire. Ceci s'applique tout particulièrement au phénomène de sursaturation qui conduit à la formation de phases dites métastables. De telles phases sursaturées peuvent déjà être générées avec des procédés de coulée classique, et elles le sont davantage quand on considère la fabrication additive.

Les corrélations microstructure-propriétés finales constituent la contribution principale majeure de ce manuscrit pour la Partie A. Elles proposent un lien au sens du paradigme de la science des matériaux, et donne par exemple une explication pour l'endommagement d'une pièce de fonderie pendant sa phase d'élaboration. L'autre contribution majeure développée dans la Partie B est l'élaboration d'un concept métallurgique nouveau, le TTB. Ce concept se destine à servir d'une part comme outil de base à la compréhension des mécanismes de transformations en phase solide, et d'autre part au développement de modèles cinétiques adaptés pour les procédés de fabrication additive, qui sont fortement hors équilibre.

Mots-clés : *Aciers à outils, Sursaturation, Solidification, Transformations de phases, Troostite, Caractérisation microstructurale, Propriétés mécaniques, ATD, Dilatométrie, Ti6Al4V, DED, Modèle thermique, Modèle métallurgique descriptif*

• ABSTRACT

The work presented in PhD thesis is the result of a multidisciplinary approach, studying metallurgical phenomena such as solidification or transformations in solid phases under non-equilibrium conditions. The purpose of the study is twofold and divided into two parts A and B. In Part A, the work aims to understand the microstructures in order to establish a link with the behavior of alloys belonging to complex Fe-Cr-CX system that undergo severe stresses on the one hand. In Part B, the work helps to determine the nature and the evolution of phases in a Ti6Al4V alloy that produced by additive manufacturing.

Within Part A, both the solidification and subsequent solid phase transformations help enhancing the supersaturation effect which later influences the damage mechanisms. Studied materials are made of tool steels and high alloyed cast irons, which come from two manufacturing processes. The first one is a conventional casting in an electric arc furnace (EAF), followed by secondary metallurgy under Electro Slag remelting (ESR) prior to forging. The second one is vertical spin casting. Almost all the phases that exist within the Fe-C system are considered, starting from the high temperature δ ferrite up to pearlite, which are often formed under equilibrium conditions, including non-equilibrium hardened phases such as bainite and martensite that are obtained after specific heat treatments. The characterization of theses phases is achieved while using different techniques and tools such as light microscope, scanning electron microscope associated with EDS, EBDS, dilatometry, differential thermal analysis (DTA), hardness, etc. In addition, special attention is paid to troostite that has been little studied to date, and which is often considered as a fine pearlite. Alike troostite that originated from supersaturation, several phenomena including carbides precipitating in the solid state are also considered.

Mechanical properties of materials are also studied, especially after elaborating optimized heat treatments that help achieving structural homogeneity and adequate hardness.

Part B is devoted to solidification and solid phase transformations in a Ti6Al4V alloy produced by Directed Energy Deposition (DED). The description of the manufacturing device and the macroscopic characterization of DED deposits obtained from different building strategies are achieved. A rough metallurgical model is set that accounts for the whole deposition process, the sketch being ascribed to a single equivalent cooling stage. Adding a 3D thermal finite element model that is validated makes it possible to simulate the evolution of the temperature at any point of the deposit. This information is used to interpret the evolution of the microstructure via a pseudo-isothermal annealing followed by final cooling stage, while considering a homogeneous sample. Using the same approach on a heterogeneous deposit allows for more complex thermal histories, thus justifying the development of a new concept, the so-called Time- phase Transformation – Block hereafter referred to as TTB concept. This approach allows the entire thermal history to be broken down into sequences, each sequence being linked to well-identified phase transformation mechanisms. In addition, the TTB concept offers a description that takes into account all stages of additive manufacturing, including rapid changes in temperature either during heating or cooling stages.

The PhD thesis is the synthesis of 8 articles, of which 5 made Part A and 3 Part B. Each of the articles gives rise to a chapter where the framework of the study is recalled while bringing complementary and unpublished results. As such the overall content of a chapter helps better understanding of the topic.

This study carried out on two distinct families of alloys shows that the non-equilibrium domain still remains a large field of investigation. This is particularly the case of supersaturation that leads to the formation of metastable phases. The supersaturated phases which already exist with conventional processes will be even more numerous if additive manufacturing processes are considered.

The microstructure-properties correlations constitute the major contribution of this work, which provide a link to the materials science paradigm and give for example an explanation for the damage of a cast part during its development phase. The other major contribution developed in Part B is the development of a new metallurgical tool, the so-called TTB concept. TTB concept may serve as a basic tool for understanding the mechanisms of solid phase transformations. Moreover, it may help to develop kinetic models that are more adapted to additive manufacturing processes.

Keywords: *High Speed Steels, Supersaturation, Solidification, Solid state transformations, Troostite, Microstructure characterization, Mechanical properties, DTA, Dilatometry, Ti6Al4V, DED Thermal modeling, Descriptive metallurgical model*

. INTRODUCTION GÉNÉRALE

.. Evolution de la Science des Matériaux

La science des matériaux est un sujet pluridisciplinaire. C'est en combinant les disciplines qu'on parvient à une meilleure compréhension des phénomènes de type physique, chimique, électrique, électronique, métallurgique et mécanique qui se produisent au sein des matériaux. Outre ce caractère pluridisciplinaire, il existe un effet d'échelle quand le matériau est soumis à des contraintes diverses (thermique, mécanique, physico-chimique, etc.) séparées ou combinées. On parle du niveau macroscopique, mésoscopique, microscopique ou nanoscopique selon les dimensions des paramètres de la structure pris en compte (taille et orientation de grains, phases de la matrice, précipités, défauts cristallins) susceptibles d'influencer les propriétés du matériau (*Figure O-1*)
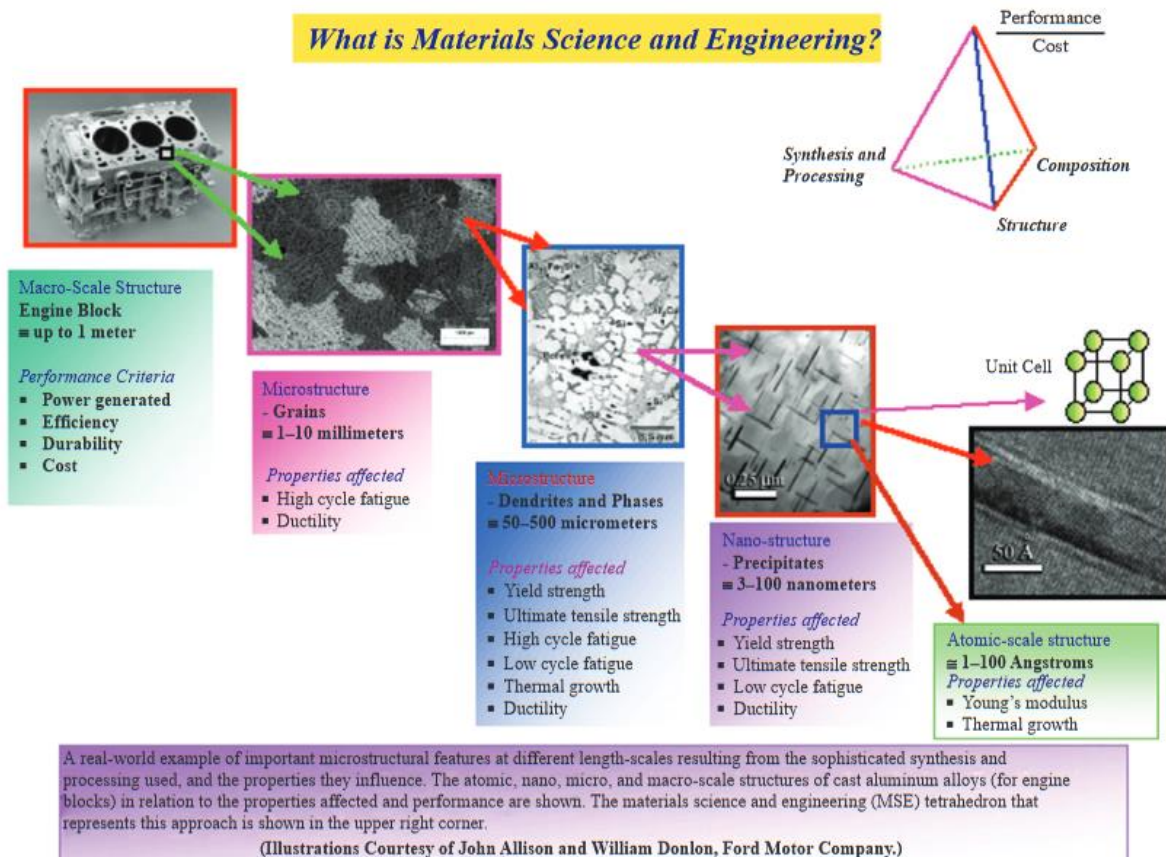
Figure O-1 : Illustration de l'approche pluridisciplinaire et multi-échelles de la science des matériaux (Askeland et al., 2010)

L'échelle macroscopique permet d'expliquer grossièrement un phénomène observé, tandis qu'on doit approfondir l'analyse à plus petite échelle si on veut comprendre les dispersions autour du comportement moyen. Cependant, la compréhension n'est possible que si des compétences croisées existent, qui permettent alors d'établir des corrélations entre les propriétés observées dans les différents domaines. C'est ce paradigme de la science des matériaux qui est généralement illustré par un tétraèdre comportant une discipline en chacun de ses quatre sommets (**FigureO-2**). A l'origine, ce tétraèdre était un triangle (**Figure O-3**) aux sommets duquel se trouvaient les procédés, la structure et les propriétés (DeHoff, 1999; Mageto, 2003). En ajoutant les Performances comme 4e sommet (**Figure O-4**), la pyramide est née (D. E. Burkes et al., 2008; Nicholas et al., 2014). Des extensions de la forme pyramidale ont été faites (**Figure O-5**), notamment en inscrivant en son centre un point dit de convergence, illustré soit par la Caractérisation

soit par la Modélisation, pour montrer combien chacun de ses deux volets représentent le caractère multidisciplinaire de la science des matériaux.
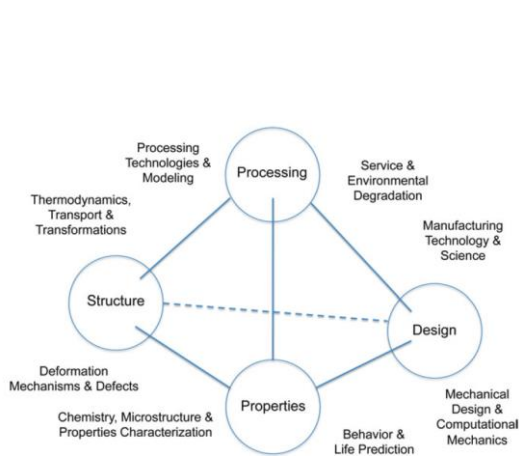
Figure O-2 : Tétraèdre définissant les quatre disciplines de la science des matériaux, et leurs interactions (Dimiduk, 2011)
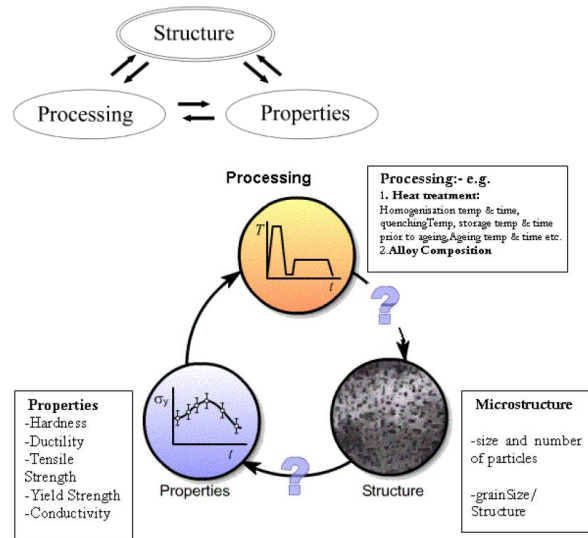
Figure O-3 : Le paradigme de la science des matériaux avec les corrélations entre structure, procédés et propriétés, adapté de (DeHoff, 1999; Mageto, 2003)

Un 5ᵉ point apparait pour former un octaèdre. Il s'agit le plus souvent de l'Environnement (**Figure O-5**), discipline désormais très populaire notamment avec la problématique du recyclage (Kimura, 2017).

Figure O-4 : Tétraèdre de la Science des matériaux indiquant le rôle central de la caractérisation et de la modélisation dans l'interaction entre les différents domaines (D. E. Burkes et al., 2008; Nicholas et al., 2014)
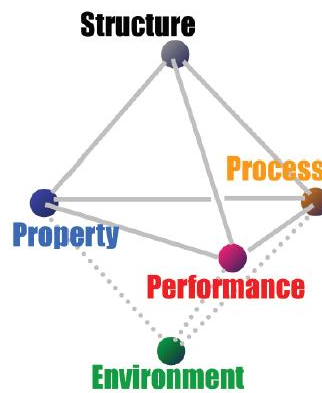
Figure O-5 : Octaèdre de la science des matériaux (Kimura, 2017)

Une spécificité peut encore être mentionnée à ce stade, qui concerne la distinction entre la caractérisation conventionnelle des propriétés, et l'étude du comportement. Dans le premier cas, on peut considérer un état fixé et figé, obtenu au terme d'un essai mécanique, d'un traitement thermique, ou d'un traitement thermomécanique. La caractérisation se focalise alors sur l'état final, sans nécessairement décrire la manière avec laquelle on parvient à cet état.

.. La sursaturation

Si par contre on cherche à comprendre comment s'amorce et se propage l'endommagement, alors il est indispensable de mettre ensemble tous les paramètres susceptibles d'influencer le mécanisme à chacun des stades de son évolution. C'est cette approche qui requiert une expertise poussée associée à une connaissance approfondie de chacun des phénomènes mis en œuvre dans le mécanisme global, en tenant compte de l'échelle où s'opère l'interaction.

C'est le cas du comportement statique d'une éprouvette rompue en traction issue d'un matériau de type acier à outils et contenant à la fois des inclusions et des carbures. Ces derniers, de taille et d'origine diverses, sont en lien avec l'élaboration du matériau et ses post traitements thermomécaniques. La compréhension de l'endommagement statique va par exemple exiger la prise en compte à l'échelle nanoscopique de l'effet de durcissement des carbures tertiaires très fins. Ces derniers ont précipité dans la martensite lors du revenu et ancrent les dislocations du fait de leur relation de cohérence avec la matrice. Cependant, dans le même temps, les carbures secondaires précipités dans l'austénite primaire après la solidification, sont semi-cohérents avec la martensite (phase secondaire issue de la transformation de l'austénite). Ils vont améliorer la résistance tout en constituant des sites d'initiation de micro-vides avant coalescence (rupture ductile). Enfin, en considérant les carbures primaires formés pendant la solidification, (facettés, non-cohérents avec la matrice et fragiles), on aura plutôt un effet d'entaille néfaste, de type concentration de contraintes, qui va rapidement conduire à leur fissuration.

De la même manière, les inclusions pourront impacter le comportement suivant leur nature (malléables ou non-malléables présentant une interface plus ou moins discontinue avec la matrice), leur distribution et leur géométrie. Enfin, la matrice elle-même peut présenter un comportement qui changera avec sa nature (martensite plus dure et moins ductile que bainite) et son état de sursaturation. On parle de sursaturation lors du dépassement de la limite de solubilité en conditions d'équilibre pour les éléments interstitiels ou de substitution. Il convient de préciser que la notion de sursaturation a jusqu'ici été très peu considérée, notamment parce que les procédés de fabrication (coulée et traitements thermomécaniques ultérieurs), étaient approximés en conditions proches de l'équilibre. Cette hypothèse est satisfaisante tant que la diffusion des éléments est possible lors du procédé. Ce sont les procédés de fabrication additive qui remettent en question cette approche. Les chercheurs doivent de plus en plus tenir compte de la sursaturation avec en corollaire l'existence de phases ayant des compositions très éloignées de l'équilibre. L'influence de la sursaturation autant comme marqueur local des concentrations en éléments qui contrôlent les transformations en phase solide, que comme expression de la surfusion et induite par des vitesses de refroidissements rapides qui limitent les ségrégations, a fait l'objet d'une lecture plénière de l'auteur, lors d'un congrès associant des fabricants de cylindres (Tchuindjang et al., 2017).

Cette sursaturation est un des fils conducteurs de cette thèse, car on montre que le phénomène existait déjà avec des procédés de coulée conventionnels. En l'occurrence, on va décrire plusieurs phénomènes découlant de la sursaturation, et notamment la précipitation en phase solide de carbures au sein d'une matrice. Une phase observée dans plusieurs alliages de la thèse illustre ce phénomène : la troostite présente dans les nuances d'aciers HSS (High Speed Steel) analysés dans 4 des 5 articles de la Partie A de cette thèse.

.. Le choix de l'échelle de l'analyse

La prise en compte de l'échelle renvoie aussi aux outils d'analyse considérés. Il existe des techniques de caractérisation et des méthodes de détermination des propriétés associées à chacune des échelles d'analyse. La microscopie optique sert notamment pour caractériser la structure à une échelle variant du macroscopique au microscopique. La microscopie électronique à balayage permet de réduire l'échelle de

caractérisation tout en diversifiant la nature des analyses via les différents types de détecteurs qui lui sont associés. Enfin, si on considère la microscopie électronique en transmission, on peut descendre jusqu'au niveau nanoscopique.

… Echelle macroscopique

En général, le passage d'une échelle plus grossière à une autre plus fine se justifie par le désir de mieux comprendre, ce qui a préalablement été simplifié. C'est par exemple le cas, avec un essai mécanique tel que la traction jusqu'à rupture d'une éprouvette, qui donne comme résultat macroscopique une limite élastique, une contrainte de rupture, et un allongement à la rupture. Ce résultat mécanique peut être corrélé à une caractérisation macroscopique, telle la taille des grains ou la dureté. Ces deux propriétés macroscopiques sont d'ailleurs souvent reprises par une loi de type Hall-Petch.

Cependant, un même matériau pourra présenter une dureté différente selon sa microstructure pour une même taille de grain. On s'intéressera alors à la nature et la proportion des phases en présence dans le matériau. Par exemple, les phases se forment lors des traitements thermiques ou thermomécaniques, après la coulée qui a elle-même été réalisée via un procédé spécifique. La coulée d'un lingot fixe une structure de solidification macroscopique: la taille, l'orientation des grains, mais aussi les ségrégations chimiques et métallurgiques. Quand elles sont de type majeur, donc à l'échelle du lingot (entre le cœur et la peau par exemple), les ségrégations sont difficiles à modifier par un traitement ultérieur. Par contre si elles sont mineures, soit à l'échelle des grains ou des dendrites (cœur et joints), alors une homogénéisation peut se faire via des traitements thermiques ou thermomécaniques ultérieurs. Le forgeage, par exemple, est souvent utilisé pour activer la recristallisation, et donc promouvoir un affinage du grain qui au départ de la coulée, est grossier. Il peut aussi améliorer la compacité des pièces, qui dans l'état brut de coulée peuvent présenter des défauts de structure, notamment des retassures ou des porosités. Affiner le grain améliore les propriétés mécaniques, quand l'objectif est de relever la résistance statique par contre cela détériore les propriétés de fluage. Notons à ce sujet, les aubes de turbine pour lesquelles on produit parfois un mono-grain.

En résumé, on peut dire que l'analyse à l'échelle macroscopique porte sur les grains (taille et orientation), les ségrégations majeures, et les défauts de structure (retassures). La macrostructure se définit par l'identification de la ou des phases principales dans le matériau issues de la solidification comme les carbures eutectiques dans les aciers. Pour les applications requérant une bonne tenue à l'usure et à l'abrasion, on recherchera des compositions d'alliage favorisant la formation de carbures de solidification très durs, désignés ici par carbures primaires (voir l'Article #5).

… Echelle microscopique

En changeant d'échelle pour descendre au niveau microscopique, on s'intéresse à la proportion des phases, à leur distribution dans le matériau. Pour l'acier, on cherchera à avoir des phases douces pour faciliter l'usinage et des phases plus dures pour améliorer la résistance en service. On cherchera aussi à précipiter des carbures secondaires dans la matrice martensitique pour améliorer sa ténacité tout en préservant sa dureté. Si par contre, on recherche une bonne tenue à la corrosion, on évitera d'avoir des précipités dans la matrice, car ceux-ci peuvent la sensibiliser en créant des micro-piles où la corrosion sera amorcée. L'échelle microscopique fait donc intervenir les phases, et les transformations entre elles, à l'état solide, phases qui sont qualifiées de secondaires. Les analyses à l'échelle microscopique permettent d'expliquer les différences de comportement ou de propriétés macroscopiques, en tenant compte de la microstructure donnée par la nature et la distribution des phases.

… Echelle nanoscopique

Toutefois, quand on désire comprendre des mécanismes très complexes qui caractérisent le comportement des matériaux, on doit souvent descendre à l'échelle nanoscopique. A ce niveau d'analyse

où on s'intéresse aux interfaces entre phases, aux propriétés intrinsèques ductiles ou fragiles de chaque phase, y compris les plus fines d'entre elles, aux interactions entre les défauts cristallins et les phases, notamment les dislocations, etc. L'échelle nanoscopique fait donc intervenir des phases dites tertiaires, qui sont issues de la transformation ou de la décomposition de phases secondaires. C'est notamment le cas avec les carbures tertiaires nanoscopiques qui précipitent dans la martensite (phase secondaire), elle-même issue de la transformation en phase solide de l'austénite formée lors de la solidification (phase primaire). L'influence de la nature des phases et de leur interface avec la matrice sera notamment abordée dans l'Article #1 pour expliquer le comportement statique et dynamique d'aciers à outils forgés. Si des dislocations en mouvement s'ancrent sur des carbures tertiaires cohérents avec la matrice, elles améliorent la résistance mécanique, mais elles peuvent aussi s'empiler sur une phase fragile tel un carbure primaire au joint de grain et induire sa fissuration comme détaillé dans l'Article #5. Le rôle des dislocations sera aussi évoqué dans l'Article #8 traitant des conditions de recristallisation en cours de traitements thermiques.

.. Approche à rebours

Cette thèse applique l'approche à rebours (appelée aussi analyse inverse), où l'on part de la fin pour remonter à la source, suite à une problématique soulevée dans les conditions de service. L'analyse du problème permet d'établir des corrélations entre des phénomènes qu'on n'aurait pas forcément liés initialement.

L'approche à rebours est couramment utilisée dans le cadre d'expertises pour poser le diagnostic sur la nature de l'endommagement observé sur une pièce. En présence de ruptures ou corrosions dans des conditions environnementales complexes et variables, difficiles à reproduire en laboratoire, c'est l'unique stratégie possible. La liste des travaux reprise dans l'Annexe 2 et l'Annexe 3, montre la diversité des sujets traités par l'auteur de cette thèse.

L'analyse inverse est utilisée dans ce travail, comme illustré par l'ordre des articles abordés en première partie. Dans un sens inversé, on remonte la filière du laminage. L'Article #1 traite de cylindres pour laminage à froid, et donc de tôles fines. Ces tôles proviennent elles-mêmes du laminage à chaud pour lequel plusieurs étapes existent, à savoir le dégrossissage appliqué à la brame ou au lingot (tôles fortes), suivi par le laminage de finition. L'Article #2 traite des cylindres des dernières cages finisseuses du train à larges bandes, quand l'Article #3 aborde les cylindres des premières cages finisseuses. Enfin les articles #4 et #5 analysent les cylindres des cages dégrossisseuses.

La **Figure O-6** rappelle les opérations de laminage faisant suite au procédé de coulée continue.
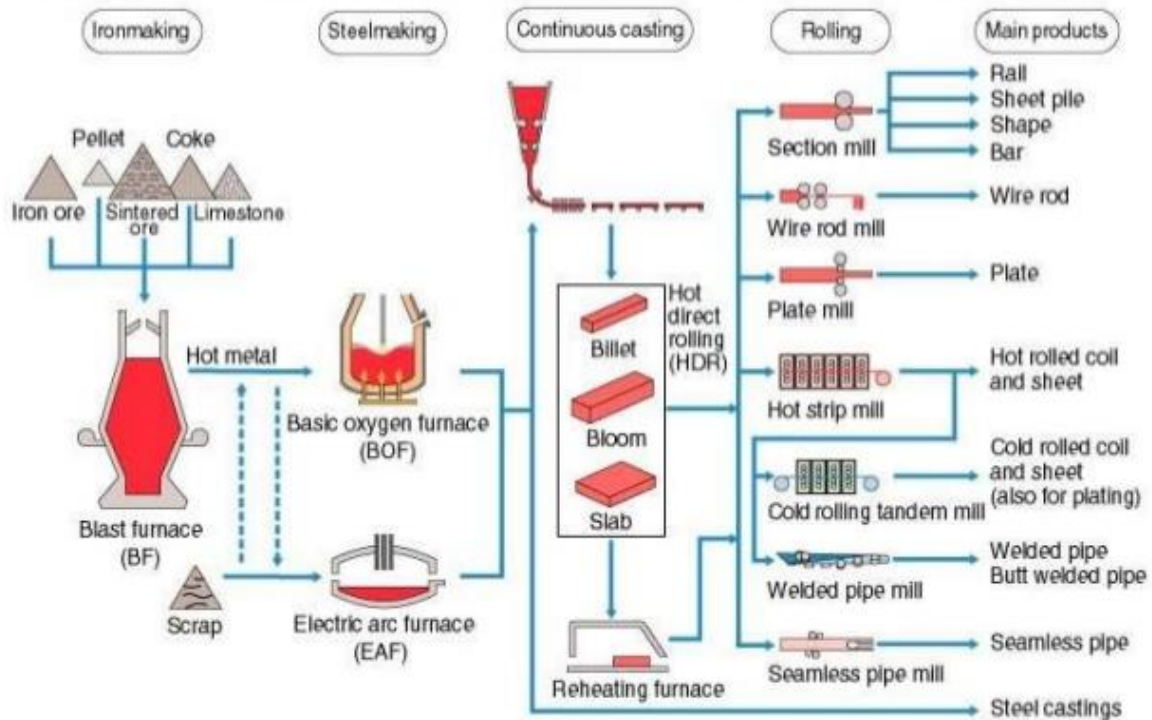
***Figure O-6** : Fabrication des produits longs en acier (from Engineering Materials II (MEng 2122)*

La fabrication additive constitue une rupture technologique majeure et un autre exemple d'application de la méthode à rebours. C'est un champ de recherches très vaste puisque différents procédés sont possibles en fonction de la nature de la source de chaleur assurant la fusion de la matière (faisceau laser ou électronique, torche plasma, etc.) et de la nature du matériau à fondre (poudre, filament). En outre, les gradients thermiques très élevés entrainent la genèse de matériaux éloignés des domaines d'équilibre souvent considérés pour prédire la nature des phases en présence et leurs transformations éventuelles. De plus, des approches hybrides existent désormais, combinant un procédé de fabrication additive avec un autre procédé plus classique, afin d'optimiser les propriétés. C'est notamment le cas avec les traitements thermomécaniques après fabrication additive, pour affiner et densifier la structure. L'explication finale des propriétés du matériau nécessite l'analyse de sa genèse et procède souvent par méthode inverse.

.. **Contexte de la thèse**

Le travail présenté dans cet ouvrage est principalement le fruit d'une approche pluridisciplinaire. On s'appuie sur l'étude et la compréhension de phénomènes métallurgiques tels que la solidification ou les transformations en phases solide, pour faire un lien avec le comportement d'alliages soumis à des sollicitations sévères d'une part et d'autre part comprendre la genèse des phases en fabrication additive par pulvérisation de poudre refondues au laser.

Ce travail est le fruit de plusieurs collaborations qui sortent du cadre de la métallurgie. C'est notamment le cas avec la mise au point d'essais mécaniques (Articles #1, #4 et #5), ou le développement de modèles d'endommagement (Article #5), ou thermique (Articles #7 et #8).Cependant, les corrélations entre le comportement observé et la microstructure a toujours constitué une contribution personnelle. Ce type d'approche est aussi présent dans les travaux cités dans l'Annexe 3, non décrits dans le cadre de cet ouvrage.

.. Contenu de la thèse

L'ouvrage se décompose en deux grandes parties. La première est focalisée sur les alliages du système complexe Fe-C-Cr-X correspondant à des aciers à outils ou à des fontes alliées, et la seconde partie est consacrée à l'alliage Ti6Al4V élaboré par fabrication additive.

Cette répartition permet aussi de fixer les grandes lignes du travail effectué.

Pour la Partie A, il s'agit de l'étude de la solidification et des transformations en phase solide d'alliages ferreux avec mise en évidence de l'effet de la sursaturation sur le mécanisme d'endommagement. Pour chaque article on conserve l'étude des 3 thématiques du **Tableau O-1** suivant :

Solidification	Solid State Transformations	Mechanical properties and related damage mechanisms

Tableau O-1: Liste des thématiques de base considérées dans les articles de la Partie A

Ce tableau est dès lors repris dans chacun des chapitres dédiés aux articles, et il constitue le fil rouge de cette partie.

Les alliages étudiés dans cette partie sont issus de deux procédés d'élaboration. Le premier procédé est mixte, avec une coulée conventionnelle au four électrique suivie ou pas d'une métallurgie secondaire par refusion d'électrode consommable (ESR), avant le forgeage final qui assure à la fois la compacité des pièces et la réduction des carbures primaires éventuels (Article #1). Le second mode d'élaboration est la coulée centrifuge verticale réalisée en deux temps, d'abord pour le métal d'enveloppe puis pour le métal de cœur. Seul le métal d'enveloppe est étudié ici (Articles #2 à 5). Au niveau de la microstructure, toutes les phases des alliages Fe-C sont considérées, depuis la ferrite et la perlite souvent formées en conditions d'équilibre, jusqu'à la bainite et la martensite obtenues après traitements thermiques spécifiques. Les traitements thermiques pour plupart mis au point en conditions de laboratoire constituent une étape essentielle pour obtenir les propriétés requises, y compris l'homogénéisation des lots de matières différents. Les corrélations microstructure-propriétés finales constituent la contribution principale majeure de ce manuscrit. Elles proposent un le lien au sens du paradigme de la science des matériaux, et donne par exemple une explication pour le bris d'un cylindre de laminoir pendant sa phase d'élaboration (Article #5).

Les **Figures O-7 à O-10** montrent l'évolution des grades utilisés dans les cylindres de laminoir, ainsi que leur localisation dans un train à bandes à chaud.

Figure O-7 : Evolution de l'utilisation des grades de cylindres sur les trains à larges bandes à chaud (1950 - 2003)
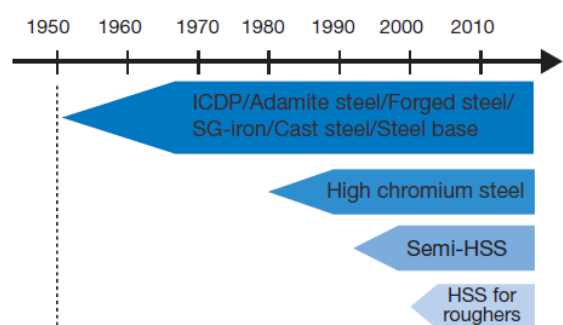
Figure O-8 : Historique de l'évolution de l'utilisation des cylindres dans les cages dégrossisseuses pour laminoirs à chaud (1950-2015)
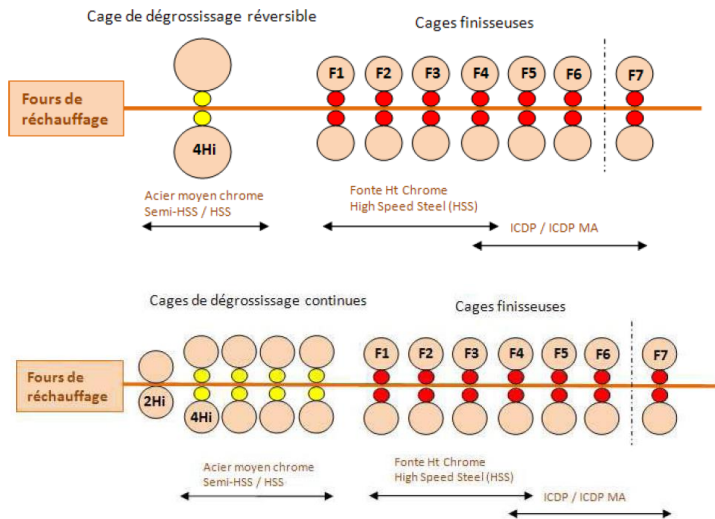
Figure O-9 *: Trains de laminoir à bandes semi-continu(en haut) et continu (en bas)*
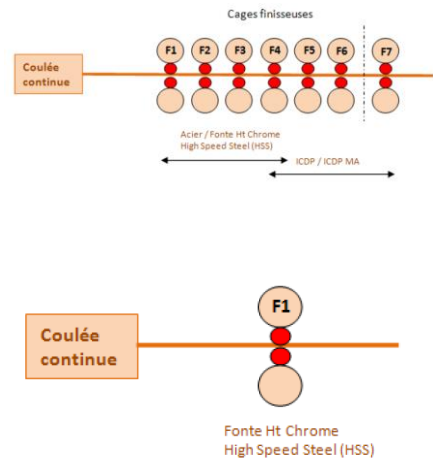
Figure O-10 *: Trains compacts de type CSP ou Mini-mill (en haut) et pour coulée en bandes minces (Direct Strip Casting, en bas)*

La partie B étudie la solidification et les transformations en phase solide dans un alliage Ti6Al4V produit par fabrication additive, en partant de sa caractérisation macroscopique pour arriver à un concept susceptible d'aider à développer de nouveaux modèles thermocinétiques. Dans cette partie, on part de la description du dispositif de fabrication jusqu'à la caractérisation macroscopique des dépôts obtenus en considérant des stratégies de fabrication distinctes (article #6). Un modèle grossier de description du procédé est esquissé. Il établit un refroidissement unique équivalent, pour tout le procédé de fabrication.

L'Article #7 décrit un modèle thermique éléments finis validé, qui permet de connaitre l'évolution de la température en tout point du dépôt. Cette information est exploitée pour interpréter l'évolution de la microstructure via un palier isotherme et un refroidissement final.

Enfin, l'Article #8 considère un dépôt présentant une microstructure hétérogène. Le modèle thermique éléments finis précédent est appliqué. L'analyse des histoires thermiques particulièrement complexes de plusieurs points d'intérêt a permis de développer un concept nouveau : le TTB (Time-Temperature-Bloc).Cette approche permet de découper en séquences l'ensemble de l'histoire thermique. Chaque séquence est en lien avec des mécanismes de transformations de phases bien identifiés. Le concept de TTB propose une description qui tient compte de toutes les étapes de la fabrication additive, en ce compris les périodes de chauffage rapides et le refroidissement final.

La **Figure O-11** ci-après fait la synthèse de l'approche développée dans la partie B.
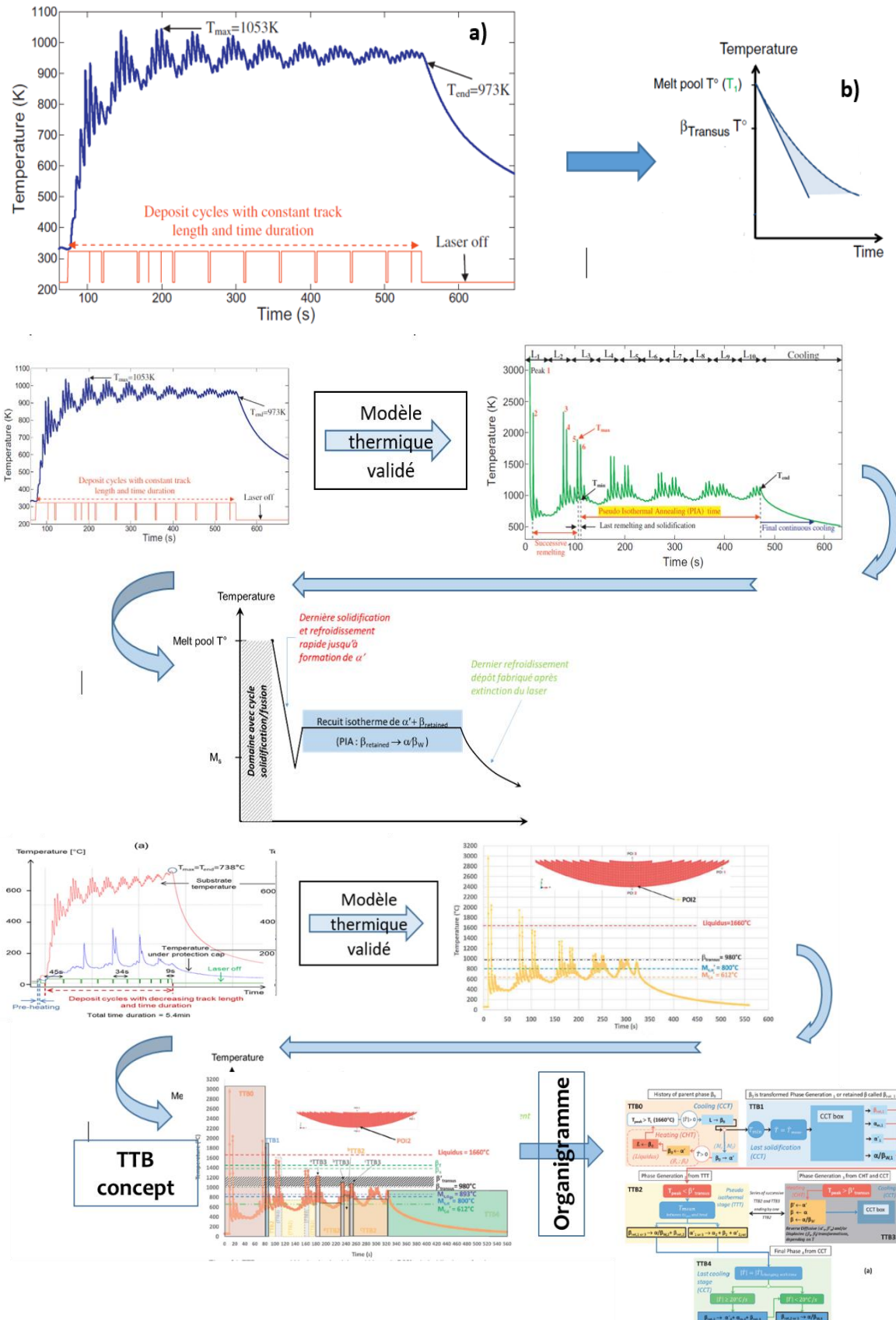
Figure O-11 : *Méthode d'étude mise en œuvre dans la partie B, avec approche à rebours pour Article #6 (haut), analyse pluridisciplinaire pour Article #7 (milieu), et approche à rebours associée à analyse pluridisciplinaire pour Article #8 (bas)*

.. Organisation de la thèse

A la suite de l'introduction générale se trouvent les présentations spécifiques de chacun des 8 articles constituant la recherche doctorale. Chaque présentation d'article constitue un chapitre où on rappelle le contexte de l'étude, et surtout on apporte des résultats complémentaires et inédits, dont le contenu a été jugé essentiel à la compréhension globale de la thématique.

Après les présentations d'articles, l'ouvrage comporte une conclusion générale, et des perspectives qui correspondent aux domaines d'études explorés à l'heure actuelle, puis des annexes

En synthèse, la thèse s'organise comme suit :

- **Une introduction générale**
- Le corps de la thèse qui est scindé en deux parties, dont :
  - La Partie A sur les alliages Fe-Cr-C-X, élaborée en 5 chapitres :
    - **Chapitre 1** : Présentation et compléments d'étude sur l'Article #1
    - **Chapitre 2** : Présentation et compléments d'étude sur l'Article #2
    - **Chapitre 3** : Présentation et compléments d'étude sur l'Article #3
    - **Chapitre 4** : Présentation et compléments d'étude sur l'Article #4
    - **Chapitre 5** : Présentation et compléments d'étude sur l'Article #5
  - La Partie B sur le Ti6Al4V comportant 3 chapitres :
    - **Chapitre 6** : Présentation et compléments d'étude sur l'Article #6
    - **Chapitre 7** : Présentation et compléments d'étude sur l'Article #7
    - **Chapitre 8** : Présentation et compléments d'étude sur l'Article #8
- **Une conclusion générale**
- **Des perspectives**
- Des annexes réparties comme suit :
  - **Annexe 1** contenant le texte intégral des articles de référence pour la thèse de doctorat de l'auteur
  - **Annexe 2** comportant la liste des publications de l'auteur, limitée aux articles parus dans des revues scientifiques
  - **Annexe 3** constituant un court CV de l'auteur où sont présentées les thématiques d'études faites en tant chercheur pour des demandes externes en rupture, corrosion et autres avis scientifiques

La littérature additionnelle éventuelle qui est utilisée pour un chapitre se retrouve à la fin de celui-ci.

On rappelle dans le **Tableau O-2** suivant, une nomenclature utile pour les différentes désignations des alliages de la Partie A, qui sont repris sous des noms différents dans plusieurs articles.

Nature ou type	Désignations	Références (Chapitre, Article)
Aciers à outils forgés, de type semi-HSS	MGx (x = 1 à 4)	Chapitre 1 et Article #1
Fonte alliée de type ICDP	HACIx (x = 1 à 2)	Chapitre 2 et Article #2
Aciers à outils coulés par centrifugation	HSS y (y = A ou B)	Chapitre 3 et Article #3
Aciers à outils coulés par centrifugation	Semi-HSS x (x = 1 à 3)	Chapitre 4 et Article #4
Acier à outils coulé par centrifugation	HCS	Article #4
	HCCS	Chapitre 5 et Article #5

Tableau O-2: Rappel de la nature des alliages et de leurs désignations dans les références

.. Références

Askeland, D.R., Fulay, P.P., Battacharya, D.K., 2010. Essentials of Materials Science & Engineering, Second Edition, SI. ed. Cengage Learning.

D. E. Burkes, D. M. Wachs, D. D. Keiser, J. Gan, F. J. Rice, R. Prabhakaran, B. D. Miller, M. A. Okuniewski, 2008. Fresh Fuel Characterization of U-Mo Alloys. United States.

DeHoff, R.T., 1999. Engineering of microstructures. Materials Research 2, 111–126.

Dimiduk, D.M., 2011. Microstructure–Property–Design Relationships in the Simulation Era: An Introduction, in: Ghosh, S., Dimiduk, D. (Eds.), Computational Methods for Microstructure-Property Relationships. Springer US, Boston, MA, pp. 1–29. https://doi.org/10.1007/978-1-4419-0643-4_1

Kimura, M., 2017. Recent Investigations of Structural Materials Using Synchrotron Radiation. Synchrotron Radiation News 30, 23–28. https://doi.org/10.1080/08940886.2017.1316127

Mageto, M.J., 2003. Tem study of microstructure in relation to hardness and ductility in Al-Mg-Si (6xxx) alloys.

Nicholas, J.D., Qi, Y., Bishop, S.R., Mukherjee, P.P., 2014. Introduction to Mechano-Electro-Chemical Coupling in Energy Related Materials and Devices. J. Electrochem. Soc. 161, Y11. https://doi.org/10.1149/2.0231411jes

Tchuindjang, J.T., Sinnaeve, M., Lecomte-Beckers, J., 2017. Effects of High Solidification Rates on Segregations and Solid Phase Transformations in High Speed Steels, in: Proccedgings of ABRASION 2017 Conference. Presented at the ABRASION 2017 - The 6th International Conference on Abrasion Wear Resistant Alloyed White Cast Iron for Rolling and Pulverizing Mills, Osaka (Japan).

I. CHAPITRE 1 : PRÉSENTATION ET COMPLÉMENTS D'ÉTUDE SUR L'ARTICLE #1

I.1. Introduction

Cet article établit l'influence des carbures et des inclusions sur le comportement mécanique pour un chargement statique (traction) ou dynamique (fatigue). Une hiérarchisation des « précipités » est suggérée, en lien avec leur nature (carbure ou inclusion), le type d'interface avec la matrice (continue ou discontinue, mouillabilité, cohérence), leurs propriétés (cisaillables ou non), leur taille et leur localisation (intérieur ou bord). L'influence des carbures et des inclusions se situe à une échelle microscopique. Un autre paramètre est aussi pris en compte à une échelle plus macroscopique. Il s'agit du fibrage hérité de la mise à forme à chaud, en comparant le comportement en long à celui en travers.

Ci-après des résultats obtenus ultérieurement sur les mêmes matières sont décrits. Ils apportent un complément d'informations en lien avec les trois grands thèmes de la première partie de la thèse, rappelés dans le tableau ci-dessous. Il s'agit de la solidification, des transformations en phase solide, et des corrélations microstructure-propriétés. Le tableau ci-dessous mentionne les points existants (vert) et les points additionnels (rouge).

On rappelle par ailleurs que les bases du travail publié dans cet article sont contenues dans ouvrage qui fixait déjà un état de synthèse scientifique (Tchuindjang, 2004). Ledit travail a été élaboré à la suite de deux projets de recherche successifs[1].

Solidification	Solid State Transformations	Mechanical properties and related damage mechanisms
• Enhancement of eutectic carbides and restoration of solidification sequence (reverse analysis) DTA during reheating stage up to complete remelting	• Determination of critical points for austenitization (DTA heating stage) • Enhancement of Troostite occurrence through DTA tests and existence of a critical cooling rate + supersaturation effect (I10CR8DV = MAT R, to be compared to alloys that did not exhibit the same transformation = I8CR5S + I6Cr= MAT) • Martensite start points from same DTA curves as compared to prediction from linear formulations • Optimization of Heat Treatment (including preliminary annealing) to achieve maximum hardness during quenching (maximum amount or martensite)	• Influence of carbides and inclusions contents on damage mechanisms under both static and dynamic stresses • Enhancement of notch effect on impact toughness

Tableau I.1-1: Thématiques présentes dans l'article (vert), et compléments décrits ci-après (rouge)

La nomenclature établie dans l'article reprend l'essentiel des abréviations utilisées.

I.2. Résultats complémentaires

I.2.1. Solidification

En réalisant des essais d'analyse thermique différentielle ou ATD (méthode présentée aux Articles #2, #3 et #4), on peut restaurer la séquence de solidification qui s'était produite dans la matière livrée, par une

---

[1] Convention RW 9713651 : Relation entre le schéma inclusionnaire et les propriétés mécaniques sur des aciers fortement alliés (1998 – 2001)

Convention RW 114877 : Effet des inclusions et des carbures dans des aciers et fontes fortement alliés, soumis à des sollicitations mécaniques sévères (2002 – 2004)

étude des courbes obtenues au chauffage (**Figure I-1**). L'étude peut se faire sur les courbes brutes, mais en cas de pics complexes, on peut lever les indéterminations en utilisant la dérivée première du signal, méthode publiée récemment (Maurizi Enrici et al., 2020).

On peut ainsi confirmer la présence de carbures eutectiques dans 3 nuances (MG1, MG3 et MG4), et leur absence dans MG2. Le pic relatif aux carbures eutectiques est similaire sur MG1 et MG3, tandis que celui observé sur MG4 se produit à plus haute température. Tous les matières ont un péritectique inverse et finissent donc leur fusion par la ferrite delta (δ).
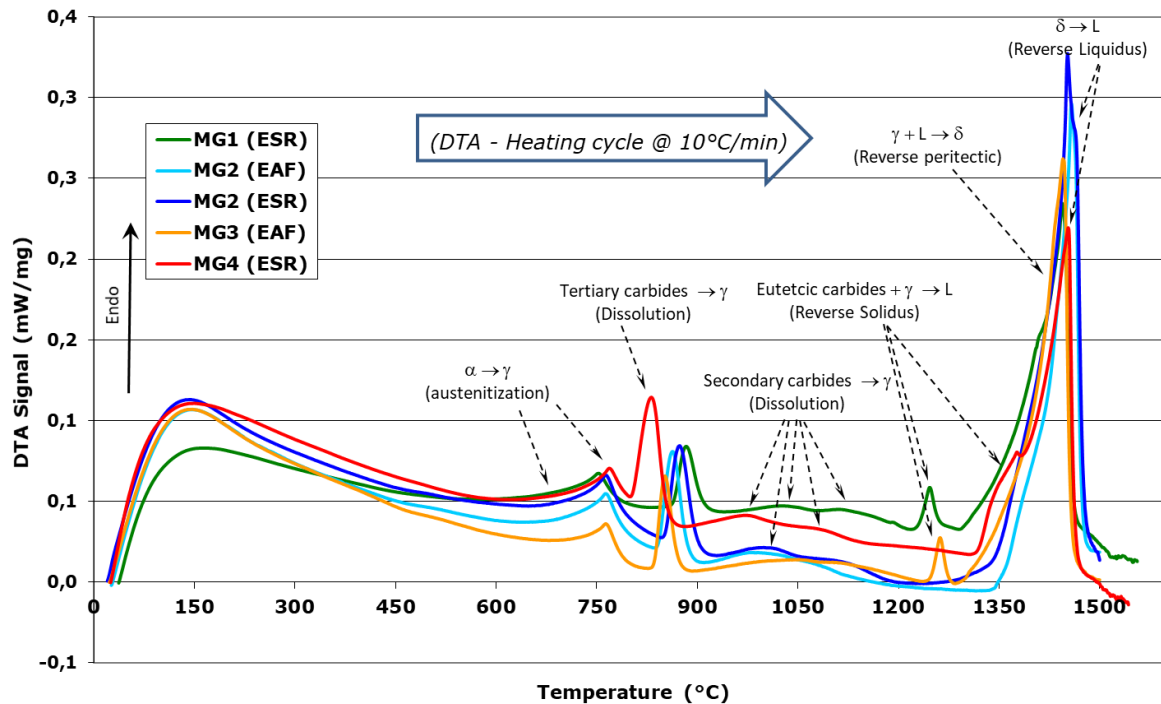
Figure I-1 : *Thermogrammes ATD des matières MGx (état brut de livraison) avec vitesse de balayage constante de 10°C/min au chauffage jusqu'à fusion complète, et identification directe des pics*

En considérant les mêmes matières lors du refroidissement ATD (**Figure I-2**), on obtient un liquidus (premier solide = δ) similaire sur les deux nuances de MG2, qui est plus élevé que le liquidus obtenu sur les autres 3 matières (MG1, MG3 et MG4). Ce résultat est en accord avec l'influence de la teneur en C sur la formation de δ (diminution de la température avec l'augmentation de la teneur en C). La température du péritectique semble plus variable, probablement en lien avec composition mais aussi la taille des dendrites de δ. En outre le solidus est donné par la fin du péritectique pour MG2, et par une température plus basse correspondant à la formation de carbures eutectiques, pour les trois autres matières (MG1, MG3 et MG4). La position de l'eutectique est similaire pour les 3 nuances, ce qui suggère un carbure de même nature, avec cependant une amplitude très faible pour le pic observé sur MG4, en lien avec la plus faible proportion de carbures formée. En outre on peut noter la finesse du pic relatif au péritectique, qui est en lien avec le caractère figé de la composition chimique des germes de la phase concernée, à savoir l'austénite (γ).

Partie A – Article #1 – Fractography survey on high cycle fatigue failure: Crack origin characterisation and correlations between mechanical tests and microstructure in Fe-C-Cr-Mo-X alloys. Tchuindjang & Lecomte-Beckers. IJF 29 (2007), pp. 713-728

13
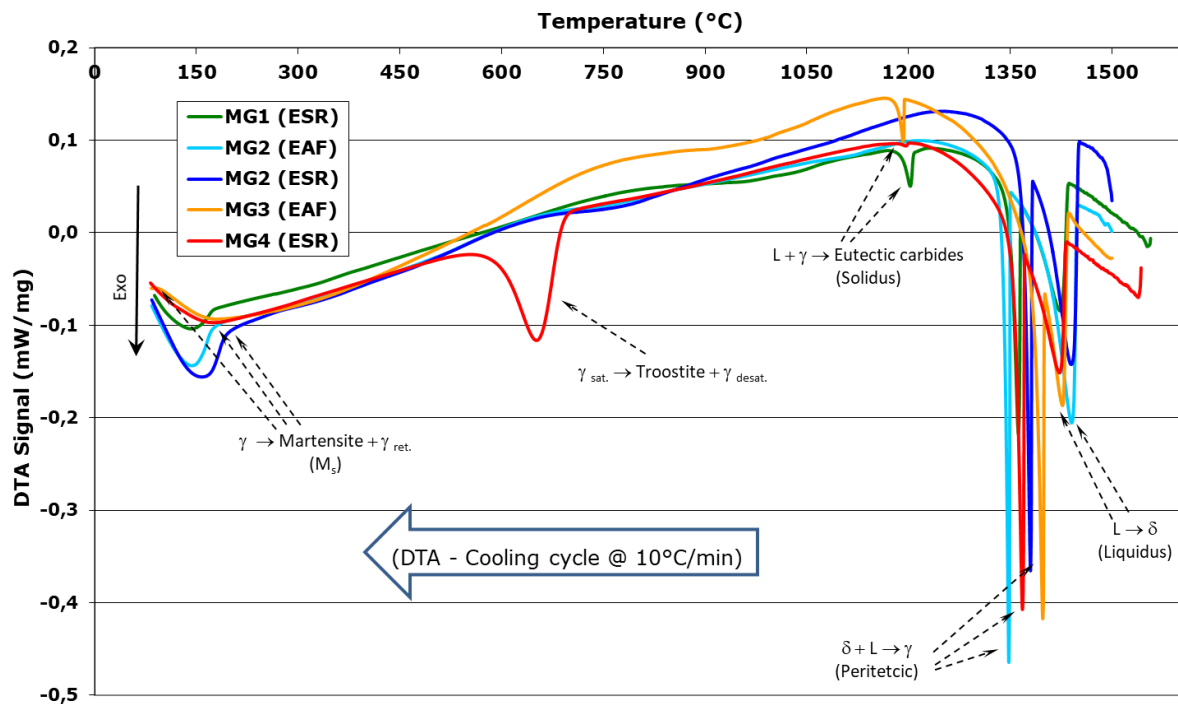
Figure I-2 : *Thermogrammes ATD des matières MGx avec vitesse de balayage constante de 10°C/min au refroidissement jusqu'à l'ambiante, et identification directe des pics*

I.2.2. **Transformations en phase solide**

I.2.2.i. *Troostite*

L'observation des cycles ATD au refroidissement (**Figure I-3**) montre un pic autour des 700°C, uniquement pour MG4. Ce pic correspond à la phase troostite, qui est étudiée plus en détail dans l'Article #3. On notera que cette même phase a été observée lors d'un cycle ATD réalisé à plus grandes vitesses (10 et 20°C/min), avec une proportion apparente qui augmente avec la vitesse du refroidissement (**Figure I-3**). Dans le même temps, la proportion apparente de carbures eutectiques diminue quand on augmente la vitesse de refroidissement dans l'intervalle de solidification. Et comme déjà mentionné avant, le liquidus reste invariant. Toutefois, pour une vitesse réduite à 2°C/min, un pic reste présent dans la même région, mais c'est la phase perlitique qui est formée. On rappelle qu'à l'origine, c'est bien la perlite qui est présente dans l'état brut livré. La troostite est due à un phénomène de sursaturation combinant un effet de composition avec un effet de vitesse (voir Article #3). On en déduit que le refroidissement lors de l'élaboration des différentes nuances de MG1, s'est produit à une vitesse relativement faible, autorisant la formation d'une phase d'équilibre perlitique et pas de troostite.

I.2.2.ii. *Martensite*

Celle-ci est aussi observée dans les échantillons ATD en fin de refroidissement, et se marque par un pic caractéristique sur la courbe ATD (**Figure I-2**). Le pic marque surtout le début de la transformation martensitique (M_s), la fin de la transformation (M_f) étant souvent située en-dessous de l'ambiante (voir plus de détails avec Articles #2, 3 et 5). Il n'y a pas de martensite dans la nuance MG4 quand la troostite est présente.
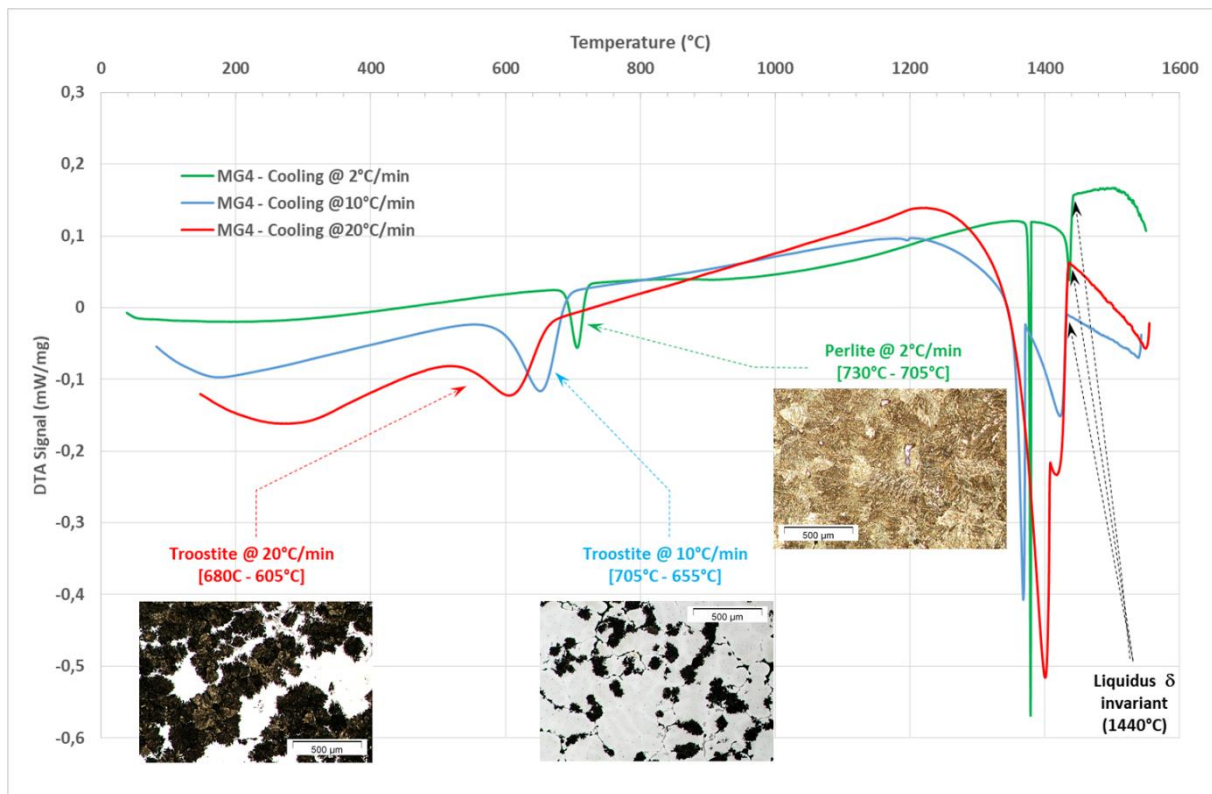
Figure I-3 : *Thermogrammes ATD de MG4 montrant influence de la vitesse de refroidissement sur les transformations en phase solide (perlite à 2°C/min et troostite à 10 et 20°C/min) et micrographies associées; liquidus est invariant*

I.2.3. **Optimisation des traitements thermiques**

En considérant un état de livraison très variable en fonction de l'origine des matières, la caractérisation préliminaire a montré que les états de départs n'étaient pas conformes à la structure dite normalisée qui est requise pour chaque matière. Cette structure correspond à celle recherchée dans le métal de cœur pour assurer ductilité et résilience en service (**Tableau I-2**). L'état normalisé facilite aussi les opérations d'usinage. Des traitements thermiques ont été réalisés de manière à produire l'état normalisé (**Tableau I-2**) avant d'effectuer un second traitement thermique dit de qualité, en vue de produire la microstructure finale requise pour la surface de travail du cylindre.

La normalisation est une étape essentielle dans les matières issues de la coulée en lingots et/ou produites par un traitement thermomécanique car elle permet d'homogénéiser la microstructure en gommant les ségrégations mineures en particulier. En outre cette étape est indispensable si on a des matériaux d'origines diverses, pour produire un état défini. Pour les différentes matières, l'état normalisé est mentionné au (**Tableau I-3**) avec le traitement élaboré pour y arriver (TTN), en considérant une structure finale homogène sur des blocs ayant des poids compris entre 5 et 16 kg. La température de normalisation est systématiquement située au-dessus de celle de dissolution des carbures dits tertiaires (**Figure I-1**). Il s'agit des carbures très fins précipités dans une phase secondaire, notamment la martensite, qui passent ensuite en solution dans l'austénite nouvellement formée (Song et al., 2016). La distinction entre les carbures primaires, secondaires ou tertiaires est abordée dans l'article #5 (Tchuindjang et al., 2015).

Le traitement thermique dit de qualité (TTQ) a été réalisé en poursuivant un objectif, celui de la maximisation de la dureté après chacune des deux étapes que sont la trempe et le revenu. Pour la trempe consistant en une austénitisation suivie d'un refroidissement rapide dans l'huile, la température puis le temps de maintien ont été établis pour obtenir dans le brut de trempe, la dureté maximale correspondant aussi à un niveau minimal pour l'austénite résiduelle. La prise en compte des courbes ATD permet de

Partie A – Article #1 – Fractography survey on high cycle fatigue failure: Crack origin characterisation and correlations between mechanical tests and microstructure in Fe-C-Cr-Mo-X alloys. Tchuindjang & Lecomte-Beckers. IJF 29 (2007), pp. 713-728

15

constater que la température choisie pour MG1 est située en-dessous de l'intervalle de dissolution des carbures secondaires, tandis que pour les autres matières, cette température suppose une dissolution partielle ou complète de ces carbures. On peut en déduire que dans le cas de MG1, le taux de carbone en solution dans la matrice austénitique chauffée à 950°C est suffisant pour produire un maximum de martensite très dure à l'ambiante. En effet, au-dessus de cette température on dissout les carbures secondaires en enrichissant la matrice, ce qui augmente l'austénite résiduelle à l'ambiante, avec possibilité de coalescence du grain (Ceschini et al., 2013; Zhou et al., 2018).

Dénomination (Mode de coulée)	Microstructure (état de livraison) (Duretés)	Etat de Conformité (Structure Normalisée recherchée)
MG1 (ESR et EAF)	Homogène (Perlite globulaire) (200 à 230 HV)	NON (Perlite Lamellaire)
MG2 (ESR et EAF)	Mixte et Hétérogène (Perlitique et bainitique) (250 à 310 HV)	NON (Perlite Globulaire)
MG3 (EAF)	Bainite Revenue (300 HV)	NON (Perlite Globulaire)
MG4 (ESR et EAF)	Bainite Revenue (320 et 250 HV, ESR et EAF)	NON (Perlite Globulaire)

Tableau I-2 : Caractérisation microstructurale de l'état de livraison des matières étudiées, et rappel de la microstructure recherchée

Dans les cas des autres matières, la température d'austénitisation plus élevée s'est justifiée, pour maximiser la dureté et le taux de martensite, en dissolvant cependant tout ou partie des carbures secondaires.

Le revenu réalisé sous forme de cycles a permis de déstabiliser toute l'austénite résiduelle. Il a relevé la dureté, notamment en se situant juste au-dessus du pic de durcissement secondaire, qui représente la température pour laquelle on forme la plus grande quantité de carbures « tertiaires » dans la matrice. Cette dernière reste martensitique, sans être désaturée. Les pièces de références pour le TTQ étaient des éprouvettes ébauchées, ayant les dimensions des échantillons pour les tests mécaniques, avec une surépaisseur de 500 µm.

Matières	TTN	Microstructure et HV30	TTQ	Microstructure et HV30
MAG1 (ESR et EAF)	900°C/6h/RC (RC ~12°C/min)	Perlite fine Lamellaire (~240 HV)	950°C/20'/H 100°C/4h/Air (*2)	Martensite « relaxée » (~820 HV)
MG2 (ESR et EAF)	1000°C/4h/RC (RC~15°C/h)	Perlite fine globulaire (~190 HV)	1055°C/5'/H 500°C/2h/Air (*2)	Martensite revenue et CS (~740 HV)
MG3 (EAF)	1020°C/4h/RC (RC~10°C/h)	Perlite fine globulaire (~190 HV)	1100°C/10'/H 500°C/3h/Air (* 3)	Martensite Revenue et CS (~700 HV)
MG4 (ESR et EAF)	1050°C/4h/RC (RC~10°C/h)	Perlite fine globulaire (~200 HV)	1120°C/10'/H 515, 500 et 485°C/3h/Air	Martensite Revenue et CS (~800 HV)

Tableau I-3 : Traitements thermiques élaborés pour réaliser le TTN et le TTQ, et rappel des microstructures et des duretés moyennes obtenues

Partie A – Article #1 – Fractography survey on high cycle fatigue failure: Crack origin characterisation and correlations between mechanical tests and microstructure in Fe-C-Cr-Mo-X alloys. Tchuindjang & Lecomte-Beckers. IJF 29 (2007), pp. 713-728

16

I.2.4. **Compléments sur les propriétés mécaniques : résilience**

La résilience est uniquement présentée pour MG1 et MG2. Deux géométries d'éprouvettes ont été testées, la première avec entaille en U (pour forcer l'effet d'entaille extrinsèque), et la seconde avec une section carrée (éprouvette dite prismatique, la section de résistance plus large permettant de vérifier l'effet d'entaille intrinsèque, dû au contenu inclusionnaire). Les essais de résilience ont été effectués dans l'état normalisé, et les résultats sont illustrés à la **Figure I-4.**

La résilience sur les éprouvettes pleines (prismatiques) est relativement élevée quel que soit le sens du prélèvement (comprise entre 100 et 350 J), sauf pour un cas où elle chute à 50 J (MG1 (ET)). Ce résultat correspond à la matière contenant les inclusions les plus grosses. Le mode de rupture associé aux niveaux de résilience les plus élevées est majoritairement ductile (Ceschini et al., 2013; Jia et al., 2017; Parsons and Edmonds, 1987; Zhang et al., 2011).

Pour la matière MG1, le procédé avec le laitier a apporté une résilience plus élevée par rapport au laitier b. Pour un même laitier, on est systématiquement meilleur en L qu'en T. Cette observation est attendue vu que le forgeage augmente la taille et la nocivité des inclusions suivant T. L'ESR b constitue une exception en lien avec un contenu inclusionnaire déjà plus faible en T qu'en L. Dans le cas du laitier a, l'efficacité évolutive en cours de procédé ESR justifie aussi la meilleure résilience en tête de lingot (fin du procédé) qu'au pied (début). L'influence de la proportion des inclusions se marque aussi indirectement à travers le taux de corroyage. En effet, plus il est élevé, plus la proportion relative d'inclusions augmente, ce qui tendra à diminuer la tenue à l'impact. C'est probablement pourquoi MG1 (B) présente l'énergie maximale absorbée à l'impact (Ceschini et al., 2013; Zhou et al., 2018).
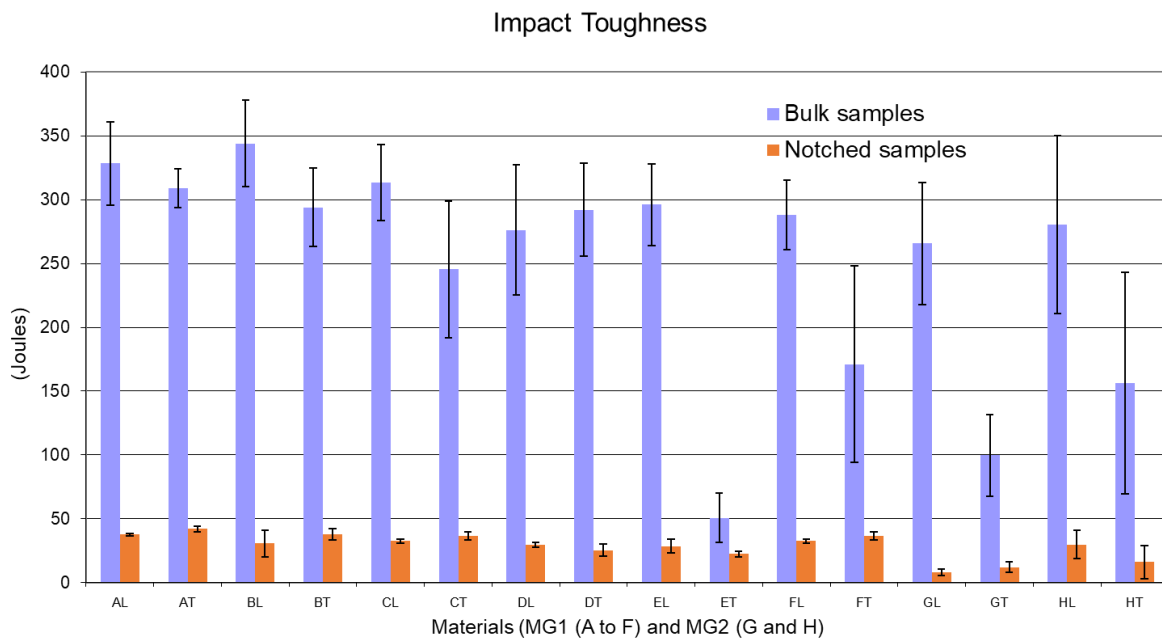
Figure I-4 : Résilience mesurée sur des échantillons massifs ou entaillés

L'écart entre les propriétés en L et en T est moins élevé en ESR qu'en EAF, le cas de MG1 (E(T)) étant singulier (rupture presque fragile !!), en lien avec l'efficacité du laitier ESR pour réduire la quantité et la taille des inclusions. En outre la différentiel L et T est davantage marqué sur MG2 que sur MG1, alors que le volume et la taille des inclusions sont plus faibles dans la première matière[2]. Cette différence est probablement due à la microstructure, qui est perlitique globulaire dans MG2 et moins dure (190HV), au

---

[2] Voir Table 3 dans l'Article #1, sur la quantification des inclusions

Partie A – Article #1 – Fractography survey on high cycle fatigue failure: Crack origin characterisation and correlations between mechanical tests and microstructure in Fe-C-Cr-Mo-X alloys. Tchuindjang & Lecomte-Beckers. IJF 29 (2007), pp. 713-728

17

contraire de la perlite lamellaire dans MG1 plus dure (240 HV). A contenu inclusionnaire équivalent et non « fragilisant », la dureté de la perlite améliorera donc la valeur de l'énergie absorbée à l'impact (Jia et al (2017), Hong et al. (2018)).

On observe une meilleure tenue à l'impact pour MG1 en comparaison avec MG2, un résultat qu'on peut aussi lier au niveau de dureté plus élevé dans la première matière (240HV) que dans la seconde (190HV). Le caractère lamellaire de la perlite ne semble donc pas constituer un problème, au contraire de la morphologie allongée des inclusions. Le facteur le plus critique pour la résilience est donc la taille des inclusions, leur proportion intervenant seulement en second lieu.

Le cas de MG2 confirme le lien entre le taux inclusionnaire et la tenue à l'impact, car le comportement est meilleur pour EAF (moins chargé en inclusions) que pour ESR[3].

Avec les éprouvettes entaillées en U, toutes les matières présentent des valeurs similaires, comprises en moyenne entre 25 et 40 J, ce qui correspond aux valeurs de la littérature (Hong et al., 2018). Le mode de rupture qui est associé à de tels niveaux d'énergie à l'impact est majoritairement fragile. On observe aussi une inversion du comportement, avec une tenue légèrement améliorée suivant le sens T que dans le sens L, ce qui est entièrement justifié si on considère que dans le sens L, on est davantage susceptible de mettre à nu une inclusion que dans le sens T (SK Nath and Uttam Das, 1970).

La taille des grains et/ou l'effet de la température d'austénitisation, qui sont parfois réputées influencer le mode de rupture n'ont pas été évaluées ici (Ceschini et al., 2013; Kumar et al., 2010).

1.3. Conclusions

- On a montré comment la technique de l'ATD permet d'établir la séquence de solidification d'un ensemble d'alliages par méthode inverse. On a notamment mis en évidence la présence de carbures eutectiques. Ces informations à fixer les températures critiques où on dissout les éventuels carbures de type secondaires ou tertiaires.
- Le cycle de refroidissement en ATD a aussi permis de comparer la structure finale avec celle d'un état industriel brut (de coulée ou forgé).
- Pour mettre en évidence les conditions de formation d'une phase hors-équilibre telle que la troostite, on a établi un lien avec la vitesse du refroidissement qui doit être suffisamment élevée.
- On a établi l'influence néfaste des inclusions, via un effet d'entaille intrinsèque sur les propriétés mécaniques en statique, en dynamique et au choc. Cette influence est définie suivant la nature, la taille, la quantité et la répartition des inclusions.
- Quand ils sont présents, les carbures de solidification souvent massifs, peuvent aussi influencer les propriétés mécaniques. Cependant, cette influence est moindre comparée à celle des inclusions.
- En présence d'une entaille, le comportement à l'impact devient similaire, quel que soit la matière, avec une rupture fragile, et cela définit un effet d'entaille dit extrinsèque.

---

[3] Voir Table 3 dans l'Article #1, sur la quantification des inclusions.

I.4. Références

Ceschini, L., Marconi, A., Martini, C., Morri, A., Di Schino, A., 2013. Tensile and impact behaviour of a microalloyed medium carbon steel: Effect of the cooling condition and corresponding microstructure. Materials & Design 45, 171–178. https://doi.org/10.1016/j.matdes.2012.08.063

Hong, Z., Zhang, X., Zhang, C., Wen, Z., Jin, X., Yan, Q., 2018. Achievement of high strength-ductility combination in railway wheel steel with thin pearlite and spherical cementite via composition and undercooling design. Materials Research Express 6, 016546. https://doi.org/10.1088/2053-1591/aae6d7

Jia, N.N., Guo, K., He, Y.M., Wang, Y.H., Peng, J.G., Wang, T.S., 2017. A thermomechanical process to achieve mechanical properties comparable to those of quenched-tempered medium-C steel. Materials Science and Engineering: A 700, 175–182. https://doi.org/10.1016/j.msea.2017.06.011

Kumar, A.S., Kumar, B.R., Datta, G.L., Ranganath, V.R., 2010. Effect of microstructure and grain size on the fracture toughness of a micro-alloyed steel. Materials Science and Engineering: A 527, 954–960. https://doi.org/10.1016/j.msea.2009.09.027

Maurizi Enrici, T., Mertens, A., Sinnaeve, M., Tchuindjang, J.T., 2020. Elucidation of the solidification sequence of a complex graphitic HSS alloy under a combined approach of DTA and EBSD analyses. J Therm Anal Calorim 141, 1075–1089. https://doi.org/10.1007/s10973-019-09093-9

Parsons, S.A., Edmonds, D.V., 1987. Microstructure and mechanical properties of medium-carbon ferrite–pearlite steel microalloyed with vanadium. Materials Science and Technology 3, 894–904. https://doi.org/10.1179/mst.1987.3.11.894

SK Nath, Uttam Das, 1970. Effect of Microstructure and Notches on the Fracture Toughness of Medium Carbon Steel. JNAME 3. https://doi.org/10.3329/jname.v3i1.925

Song, X.Y., Zhang, X.J., Fu, L.C., Yang, H.B., Yang, K., Zhu, L., 2016. Evaluation of microstructure and mechanical properties of 50Cr5NiMoV steel for forged backup roll. Materials Science and Engineering: A 677, 465–473. https://doi.org/10.1016/j.msea.2016.09.079

Tchuindjang, J.T., 2004. Effet des inclusions et des carbures sur les propriétés mécaniques dans des alliages Fe-Cr-C-X : application à la rupture en fatigue (Diplôme d'Etudes Approfondies en Sciences Appliquées). Université de Liège, Liège, Belgique.

Tchuindjang, J.T., Torres, I.N., Flores, P., Habraken, A.M., Lecomte-Beckers, J., 2015. Phase Transformations and Crack Initiation in a High-Chromium Cast Steel Under Hot Compression Tests. J. of Materi Eng and Perform 24, 2025–2041. https://doi.org/10.1007/s11665-015-1464-7

Zhang, C., Liu, Y., Zhou, L., 2011. Transformation Conditions - Microstructures - Mechanical Properties Relationship in 0.60%C Hypoeutectoid Steel. steel research international 82, 1207–1212. https://doi.org/10.1002/srin.201100075

Zhou, L., Tang, G., Ma, X., Wang, L., Zhang, X., 2018. Relationship between microstructure and mechanical properties of M50 ultra-high strength steel via quenching-partitioning-tempering process. Materials Characterization 146, 258–266. https://doi.org/10.1016/j.matchar.2018.10.009

II. CHAPITRE 2 : PRÉSENTATION ET COMPLÉMENTS D'ÉTUDE SUR L'ARTICLE #2

II.1. Introduction

Cet article met en évidence l'effet d'éléments d'alliage fortement carburigènes sur la structure de solidification et sur les transformations en phases solide dans des fontes à graphite lamellaire. La nuance de base ne contient pas les éléments d'alliage additionnels tandis qu'un grade modifié contient une certaine proportion de Nb, Ti et V, qui sont des éléments susceptibles de former des carbures très durs. L'étude consiste à comparer les deux nuances dans un état dit de service (brut de coulée industrielle suivi d'un double revenu), et dans un autre état remis en solution (trempé sans revenu) par Analyse Thermique Différentielle. Les corrélations sont complétées au moyen d'analyses métallographiques et quantitatives, sur les carbures. On identifie la séquence de solidification ainsi que l'influence de la vitesse de solidification sur la nature, la taille et la distribution des phases (carbures et graphite). On établit aussi la stabilité relative de l'austénite enrichie en éléments d'alliage après remise en solution, et on identifie enfin différents types de martensite en lien avec leurs compositions chimiques. Ces observations sont utiles pour comprendre les paramètres influençant la microstructure des pièces brutes de fabrication, dans la perspective de corréler celle-ci aux propriétés en cours de service, notamment pour des applications où la tenue à l'usure et à la corrosion est recherchée.

II.2. Bref rappel sur le contexte

Les pièces d'origine ayant servi à l'étude sont des cylindres bimétalliques obtenus par coulée centrifuge verticale. Ces pièces représentent des cylindres de laminoir à chaud, utilisés dans les dernières cages du train de bandes finisseuses. Concernant le procédé d'élaboration, c'est d'abord le métal d'enveloppe qui est coulé dans un moule jusqu'à solidification, ensuite on coule le métal de cœur en produisant une bonne jonction métallurgique. L'enveloppe se compose d'un des alliages étudiés, tandis que le cœur est obtenu à partir d'une fonte classique ferritique et perlitique, à graphite nodulaire.

Les échantillons soumis à l'étude sont essentiellement prélevés dans le métal d'enveloppe, sous forme de barreaux. Les sections étudiées sont orientées perpendiculairement à l'axe de symétrie du cylindre. La zone d'intérêt pour le prélèvement des éprouvettes ayant servi aux analyses diverses (thermiques, métallographiques) et à la caractérisation des propriétés mécaniques sont prélevées endéans une profondeur de 40 mm environ, entièrement comprise dans le métal d'enveloppe. Le contexte général de ce travail est donné dans un projet de recherche appliqué[4].

Dans ce qui suit, on propose de rajouter des résultats obtenus sur les mêmes matières mais qui ne sont pas explicitement mentionnés dans l'article, parce qu'ils apportent un complément d'informations en lien avec les trois grands thèmes de la première partie de la thèse, et qui sont rappelés dans ci-après (**Tableau II-1**). Il s'agit de la solidification, des transformations en phase solide, et des corrélations microstructure-propriétés, avec mention des points existants (vert) et des points additionnels (rouge).

---

[4] Convention RW 114877 : Effet des inclusions et des carbures dans des aciers et fontes fortement alliés, soumis à des sollicitations mécaniques sévères (2002 – 2004)

Partie A – Article #2 – Structural Investigations of Solidification and Heat Treatments Influence on High Alloyed Cast Irons Grades with Nb-V-Ti additions. J. Lecomte-Beckers & J. Tchoufang Tchuindjang. DDF 289-292 (2009), pp. 77-86

20

Solidification	Solid State Transformations	Mechanical properties and related damage mechanisms
• Solidification sequence from DTA tests	• Martensitic transformations (two types (plate or lath), depending on the location and the composition)	• Enhancement of intrinsic notch effect during tensile test (with or without notched samples) • Enhancement of hardening behavior under compression tests (UTS 5 times higher in compression compared to tensile)

Tableau II.21 : Thématiques présentes dans l'article (vert), et compléments décrits ci-après (rouge)

Glossaire *(avec abréviations utilisées dans l'Article)*

(Nb, V)C'	Eutectic or chinese script MC carbide	Carbures secondaires (précipités et dissous en phase solide)
α'	Martensite (lath or plate-like)	Martensite (issue de la transformation sans diffusion de l'austénite au refroidissement)
C_A	Type A lamellar Graphite	Graphite lamellaire de type A (suivant norme ISO 945 - 1975)
C_D	Type D lamellar Graphite	
DTA	Differential Thermal Analysis	Analyse Thermique Différentielle
γ	Austenite	Austénite (phase cellulaire, premier solide formé à la coulée, définissant le liquidus)
HACI	High Alloyed Cast Iron	Fonte alliée
HACIi	HACI1 (conventional ICDP grade) or HACI2 (ICDP containing Nb/V/Ti)	
HSM	Hot Strip Mill	Laminoir à trains à bandes à chaud
IC1i	Sample number i, cut out of HACI1	
IC2i	Sample number i, cut out of HACI1	
ICDP	Indefinite Chill Double Poured	Fonte à Trempe Indéfinie
Li	Liquid (melt)	Métal liquide (indice « i » en lien avec moment d'apparition de la phase dans la séquence de solidification/fusion)
M_3C	Cementite	Cémentite (carbure eutectique définissant le solidus ou fin de solidification)
M_4C_3	V-rich fine secondary carbides	Carbures secondaires (précipités et dissous en phase solide)
MC	Carbide MC	Carbure MC
M_s	Martensite start point	Point de début de transformation martensitique, au refroidissement
NbC	Angular and primary Nb-rich MC carbide	
RA	Retained Austenite	Austénite résiduelle

Errata : Les figures 1a, 1b, 2a et 2b illustrant les thermogrammes ATD dans l'article #2 comportent toute la même erreur, sur le sens des pics indiquant le caractère endothermique ou exothermique des réactions. Les flèches doivent être inversées sur chaque figure !

Partie A – Article #2 – Structural Investigations of Solidification and Heat Treatments Influence on High Alloyed Cast Irons Grades with Nb-V-Ti additions. J. Lecomte-Beckers & J. Tchoufang Tchuindjang. DDF 289-292 (2009), pp. 77-86

21

II.3. Résultats complémentaires

II.3.1. Solidification

Les thermogrammes obtenus en ATD sont relativement simples à interpréter. La séquence proposée est pertinente, puisqu'elle tient compte de la microstructure dans l'état initial Brut de Coulée après Revenu (BCR) qui est rappelée ci-dessous. En effet, les NbC primaires se forment avant le graphite, et selon leur densité et leur taille, ils peuvent ségréger dans le liquide vers la peau du cylindre, sous l'effet de la force centrifuge (voir figures ci-dessous, montrant la microstructure à différentes profondeurs de l'enveloppe). Leur relative mobilité dans le liquide résiduel en cours de solidification pendant la coulée centrifuge, fait que certains peuvent être piégés dans un nid de graphite formé ultérieurement (fin de solidification, de type eutectique). Par contre les carbures les plus denses, dont les plus enrichis en Nb, vont ségréger près de la surface de l'enveloppe du cylindre bimétallique (Voir **Figure II-1 à Figure II-4**).

Figure II.3.1: *NbC I massif et anguleux (Rose) et Graphite lamellaire en agrégats (HACl2 ; profondeur de 0 à 10 mm dans le métal d'enveloppe (poli-miroir, état BCR)*
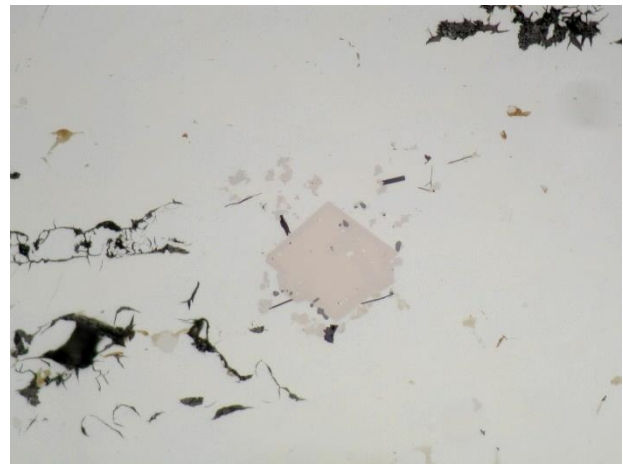
Figure II.3.1: *NbC I massif et anguleux, Agrégat de NbC II globulaire (Rose), Graphite et inclusions (Alumine) ; profondeur de 10 à 20 mm dans le métal d'enveloppe (poli-miroir, état BCR)*
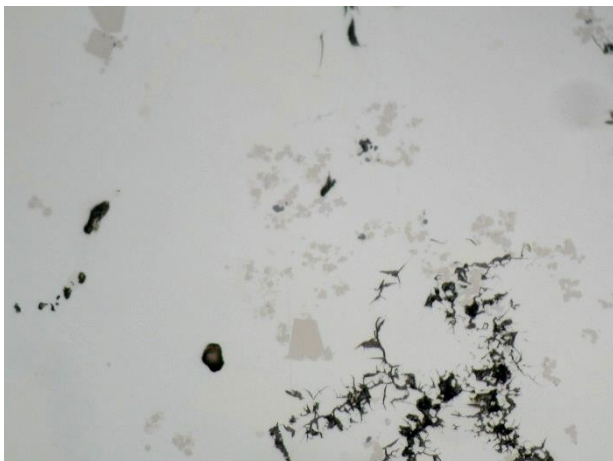
Figure II.3.1: *Agrégat de NbC (I et II, Rose) et Graphite Lamellaire (Noir) - (IC21 ; profondeur de 30 à 40 mm de profondeur dans le métal d'enveloppe (poli-miroir, état BCR)*
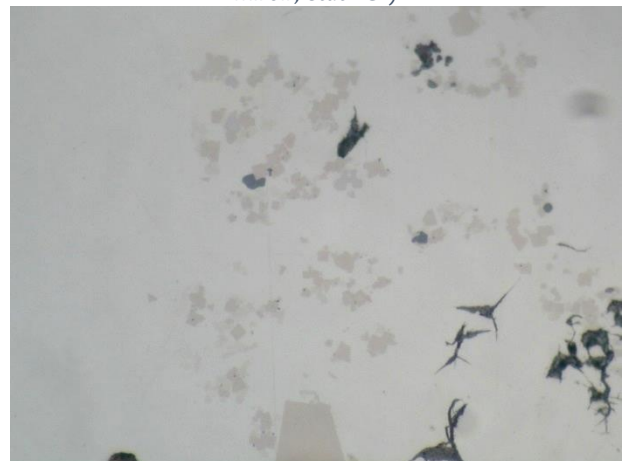
Figure II.3.1: *Agrégat de NbC II Globulaires (Rose), TiC (Globules Gris) et NbC I ; profondeur de 40 à 50 mm dans le métal d'enveloppe (poli-miroir, état BCR)*

Les différences observées entre les microstructures après ATD (voir figures dans l'article) et celles du BCR (**Figures II-1 à Figure II-4**) se marquent surtout pour la macrostructure (taille de grains plus élevée en ATD comparée au BCR), et la taille et la morphologie de certaines phases notamment les carbures NbC et le

graphite. Les NbC massifs et anguleux sont présents dans les deux conditions (BCR et après ATD), avec toutefois une taille plus massive dans le BCR (jusqu'à 50 μm de longueur, **Figure II-5**). Les NbC en écriture chinoise sont surtout observés après ATD, tandis qu'on voit des carbures plus fins en agrégats globulaires dans le BCR.
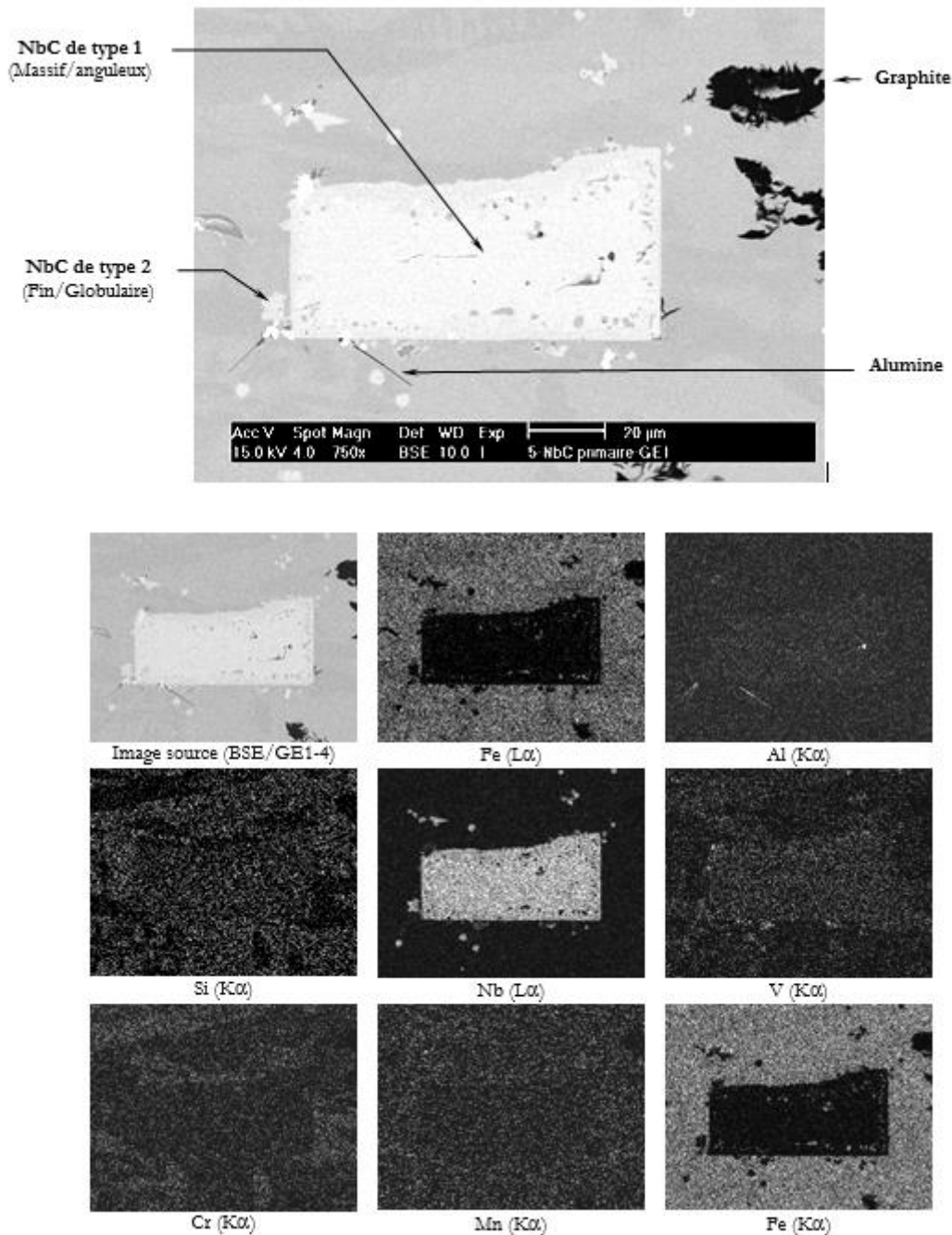
Figure II.3.1: *Caractérisation par MEB et cartographie EDX d'un carbure massif et anguleux de type NbCI, et des carbures globulaires fins de type (Nb,V)C', (aussi illustrés à la Fig. II-1), montrant l'enrichissement exclusif en Nb du premier, tandis que les seconds contiennent Nb associés à V – (état BCR)*

Le graphite a une morphologie majoritairement lamellaire dans le BCR, même si quelques nodules peuvent être observés. Le graphite est entièrement lamellaire après ATD, et il se situe de manière très précise, dans les espacements interdendritiques. Ces différences sont directement induites par la vitesse du refroidissement lors de la solidification, celle-ci se faisant avec un gradient thermique plus élevé lors

Partie A – Article #2 – Structural Investigations of Solidification and Heat Treatments Influence on High Alloyed Cast Irons Grades with Nb-V-Ti additions. J. Lecomte-Beckers & J. Tchoufang Tchuindjang. DDF 289-292 (2009), pp. 77-86

23

de la coulée centrifuge qu'avec l'ATD[5]. Toutefois l'approche principale de l'étude est le recours à une analyse inverse par ATD au chauffage jusqu'à fusion complète, pour reconstituer la séquence de solidification effective survenue pendant la coulée centrifuge. Ensuite, la seconde partie de l'essai ATD réalisé à une vitesse de refroidissement contrôlée plus faible que la vitesse réelle du procédé de coulée, permet de déterminer de manière précise une séquence de solidification en condition proche de l'équilibre, qui reste intéressante pour comprendre et mettre en évidence l'effet de la vitesse sur la microstructure.

Le caractère relativement simple de la séquence de solidification réelle, en lien avec le nombre relativement limité de phases en présence et l'absence de transformation à haute température, permet de se limiter à l'interprétation directe des thermogrammes, sans avoir besoin de recourir à la technique plus élaborée de la dérivée première du signal ATD (Maurizi Enrici et al., 2020). Cette possibilité d'interprétation directe signifie le plus souvent que l'effet de sursaturation est limité.

II.3.2. Transformations en phase solide

L'essentiel est déjà mentionné dans l'article #2, que ce soit pour la présence de martensites distinctes en fin de refroidissement après solidification, ou sur la stabilité relative de l'austénite résiduelle après remise en solution et trempe, pour les deux nuances avec ou sans rajout d'éléments de transition. Toutefois, on peut mentionner le fait que la dureté moyenne est quasiment du même ordre de grandeur dans les deux nuances.

II.3.3. Propriétés mécaniques et corrélations

Les propriétés mécaniques concernent la tenue à la traction et le comportement en compression, avec un rappel des valeurs de duretés. Les dimensions des éprouvettes de traction sont illustrées à la **Figure II-6**. Pour les essais avec entaille, on a usiné sur ces mêmes éprouvettes une rainure en U située au milieu du fût (profondeur de 1 mm pour un rayon de courbure à fond d'entaille de 0.5 mm). Les éprouvettes de compression sont données par des cylindres de 16 mm de hauteur pour 10 mm de diamètre. Deux profondeurs sont considérées pour les prélèvements d'éprouvettes dans le métal d'enveloppe, à savoir 20 et 40 mm, et l'échantillonnage pour chaque essai et pour chaque matériau est composé de 10 éprouvettes.

Une seule coulée est considérée pour HACI1, tandis qu'on a prélevé des échantillons sur deux coulées distinctes de l'alliage modifié, qui sont notées HACI2_1 et HACI2_2.
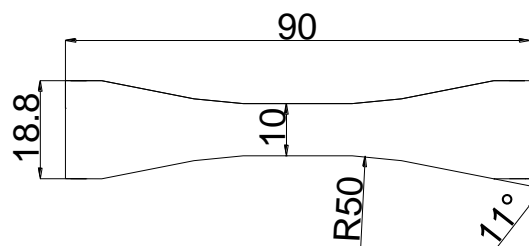
Figure II.3.3 : *Aperçu des dimensions de l'éprouvette de traction (sans entaille)*

Les résultats de l'analyse quantitative des phases, des essais mécaniques et de duretés Vickers sont rappelés dans le **Tableau II-2**. Les mesures de duretés correspondent à la filiation en croix sur 5 points

---

[5] Voir note sur la simulation de la vitesse de refroidissement dans l'enveloppe d'un cylindre au chapitre V (§ V.3.2.i)

Partie A – Article #2 – Structural Investigations of Solidification and Heat Treatments Influence on High Alloyed Cast Irons Grades with Nb-V-Ti additions. J. Lecomte-Beckers & J. Tchoufang Tchuindjang. DDF 289-292 (2009), pp. 77-86

24

espacés d'un centimètre. La rupture en traction survient de manière fragile, quasiment sans déformation plastique. Pour les éprouvettes entaillées, la rupture est parfois survenue en dehors de l'encoche.

Les valeurs moyennes obtenues en traction et en compression sur les deux nuances sont illustrées à la **Figure II-7.** L'alliage conventionnel (HACI1) a une résistance supérieure à l'alliage amélioré (HACI2) en traction, le comportement s'inversant pour la compression.

Alliages	Phases				Charges de rupture (UTS)			Duretés (HV30)
	Martensite (%)	Cémentite (%)	Graphite (%)	MC (%)	Rm Traction (MPa)	Rm Traction avec entaille (MPa)	σmax Compression (MPa)	
HACI1	57.5 ± 3.9	39.4 ± 4.3	2.9 ± 0.7	-	439 ± 19	408 ± 32	2077 ± 62	626 ± 26
HACI2_1	62.8 ± 3.6	33.0 ± 3.5	2.9 ± 0.4	1.3 ± 0.3	433 ± 20	317 ± 40	2163 ± 71	692 ± 24
HACI2_2	64.6 ± 5.2	31.0 ± 5.4	3.3 ± 0.3	1.3 ± 0.2	374 ± 19			682 ± 33

Tableau II.3.3 : Résultats d'analyse quantificative, des essais mécaniques et duretés Vickers sur éprouvettes issues d'alliages HACI1 et HACI2 dans l'état BCR

Dans le cas de la traction, il existe un effet d'entaille intrinsèque, notamment induit par le graphite lamellaire, puis en second lieu, par la présence de NbC de forme anguleuse. La dureté induite par la martensite n'influence pas le résultat en traction. La fragilisation intrinsèque se marque davantage en présence des carbures NbC, quand on considère des éprouvettes entaillées, car la réduction de la résistance mécanique est plus significative sur la nuance améliorée que sur la nuance normale. Par ailleurs en tenant compte des remarques faites précédemment, la plus faible proportion de martensite associée à une dureté légèrement plus faible sur la nuance entaillée testée, ne va pas nécessairement compter dans le comportement final en traction.

Dans le cas de la compression, la nuance améliorée présente un résultat meilleur que la nuance normale. En outre la charge de rupture en compression est près de 4 fois supérieure à celle obtenue en traction, comme cela est bien établi aussi dans la littérature. La contribution positive des éléments d'alliage se marque donc nettement en compression, à travers la dureté de la matrice notamment, et l'absence de l'effet d'entaille observé en traction.

Partie A – Article #2 – Structural Investigations of Solidification and Heat Treatments Influence on High Alloyed Cast Irons Grades with Nb-V-Ti additions. J. Lecomte-Beckers & J. Tchoufang Tchuindjang. DDF 289-292 (2009), pp. 77-86

25
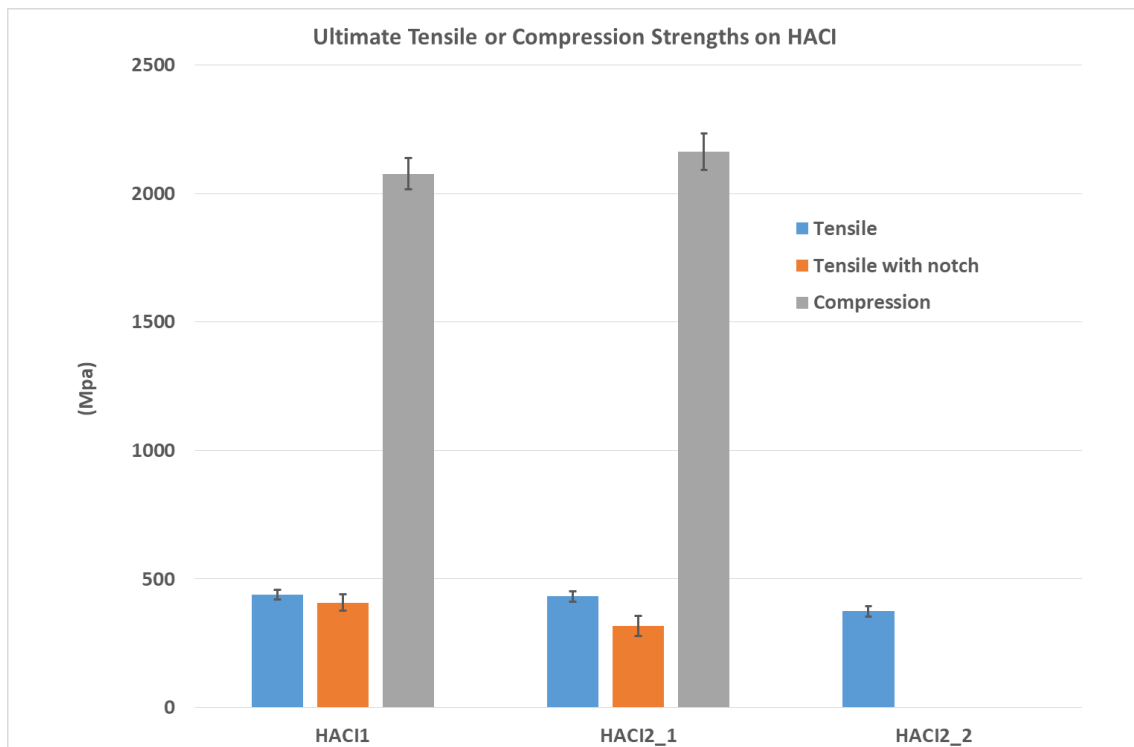
Figure II.3.3: Valeurs des résistances moyennes en traction (avec et sans entaille) et en compression sur éprouvettes issues d'alliages HACI1 et HACI2 dans l'état BCR

II.4. Conclusions

- On a montré l'apport de l'ATD pour d'une part rétablir la séquence de solidification d'un ensemble d'alliages par méthode inverse, notamment en mettant en évidence la présence de carbures eutectiques, et pour d'autre part aider à fixer les températures critiques où on dissout les éventuels carbures de type secondaires ou tertiaires.

- Le cycle de refroidissement en ATD a aussi permis de comparer la structure finale avec celle d'un état industriel brut (de coulée ou forgé), pour mettre en évidence l'effet de la vitesse sur la taille, la proportion et la distribution des phases en particulier, celles-ci étant relativement similaire pour les deux types de conditions. Les analyses complémentaires focalisées sur les propriétés mécaniques statiques en traction ont permis de mettre en évidence l'effet d'entaille intrinsèque dans ce type d'alliage, qui est principalement induit par la présence du graphite lamellaire. Cet effet est accentué en présence de carbures primaires NbC, dont la forme est anguleuse.

- A l'inverse, le comportement de ces matériaux en compression est plutôt bon, avec une résistance 4 à 5 fois plus élevée que le niveau atteint en traction, l'effet d'entaille ne se marquant plus. Les matériaux restent cependant fragiles avec peu de ductilité, à cause de la présence en grande quantité d'un carbure eutectique tel que la cémentite, qui est uniformément réparti en volume. L'ajout d'éléments de transition améliore la résistance en compression, en même temps que la dureté.

II.5. Références

Maurizi Enrici, T., Mertens, A., Sinnaeve, M., Tchuindjang, J.T., 2020. Elucidation of the solidification sequence of a complex graphitic HSS alloy under a combined approach of DTA and EBSD analyses. J Therm Anal Calorim 141, 1075–1089. https://doi.org/10.1007/s10973-019-09093-9

Partie A – Article #2 – Structural Investigations of Solidification and Heat Treatments Influence on High Alloyed Cast Irons Grades with Nb-V-Ti additions. J. Lecomte-Beckers & J. Tchoufang Tchuindjang. DDF 289-292 (2009), pp. 77-86

26

III. CHAPITRE 3 : PRÉSENTATION ET COMPLÉMENTS D'ÉTUDE SUR L'ARTICLE #3

III.1. Introduction

Cet article compare deux alliages de type acier de coupe rapide (HSS) dénommés ci-après HSS A et HSS B qui sont notamment utilisés comme métal d'enveloppe pour des cylindres bimétalliques dans les premières cages finisseuses d'un train à bandes à chaud (laminoir).

Les compositions chimiques des deux alliages sont proches, avec essentiellement une modification concernant leur W_{eq} (2Mo +W), à travers le binôme W et Mo. En pratique, on augmente W_{eq} en passant de HSS A vers HSS B, et on cherche à comprendre pourquoi les microstructures des pièces coulées industriellement, sont différentes des échantillons observés après certaines mesures au laboratoire MMS. La différence est focalisée sur la présence inattendue d'une phase de type « perlitique », dans le grade HSS B qui présente pourtant un potentiel de durcissement plus élevé que HSS A.

Des simulations thermodynamiques à l'équilibre ainsi que des essais expérimentaux en Analyse Thermique Différentielle ou ATD (« Differential Thermal Analysis » ou DTA en anglais) pour les conditions hors équilibre sont réalisés, afin d'établir et de comparer la séquence de solidification des deux alliages. La différence de microstructure entre les deux états coulés (industriel et DTA) conduit à intercaler dans le refroidissement continu après solidification par DTA, des paliers isothermes qui permettent de former la phase recherchée à l'état solide.

Des résultats additionnels à ceux de l'article sont proposés dans cette introduction. D'une part, l'influence de N sur la germination des VC primaires est démontrée, ainsi que la modification des transformations ultérieures en phase solide (relèvement du point Ms, et/ou formation de bainite au lieu de martensite). D'autre part, la formation de Troostite est mise en évidence. Cette phase se différencie de la perlite, par un mécanisme spécifique de création et des variations de composition.

III.2. Bref rappel sur le contexte

Les pièces d'origine ayant servi à l'étude sont des cylindres bimétalliques obtenus par coulée centrifuge verticale. Ces pièces représentent des cylindres de laminoir à chaud, utilisés dans les premières cages du train de bandes finisseuses. Lors du procédé d'élaboration, le métal d'enveloppe est coulé en premier dans un moule et se solidifie, ensuite on coule le métal de cœur en produisant une bonne jonction métallurgique. L'enveloppe se compose d'un des alliages étudiés, tandis que le cœur est obtenu à partir d'une fonte classique ferritique et perlitique, à graphite nodulaire.

Les échantillons soumis à l'étude sont essentiellement prélevés dans le métal d'enveloppe, sous forme de barreaux. Les sections étudiées sont orientées perpendiculairement à l'axe de symétrie du cylindre. La zone d'intérêt pour le prélèvement des éprouvettes ayant servi aux analyses diverses (thermiques, métallographiques) et à la caractérisation des propriétés mécaniques est localisée à une profondeur de 60 mm environ. Elle est entièrement comprise dans le métal d'enveloppe.

Ci-après, des résultats obtenus sur les mêmes matières, non mentionnés dans l'article, sont présentés car ils apportent un complément d'informations en lien avec les trois grands thèmes de la première partie de la thèse (**Tableau III.2**). Il s'agit de la solidification, des transformations en phase solide, et des corrélations microstructure-propriétés. Ce tableau mentionne les points existants dans l'article en vert et les points additionnels en rouge. Rappelons aussi que la phase principale étudiée dans l'article n'est pas la perlite, mais bien la Troostite.

Partie A – Article #3 – Study of the origin of the unexpected pearlite during the cooling stage of two cast high-speed steels. J. Lecomte-Beckers & J. Tchoufang Tchuindjang. SSP 172-174 (2011), pp. 803-808

27

Solidification	Solid State Transformations	Mechanical properties and related damage mechanisms
• Solidification sequence from DTA tests	• Troostite formation under Heat treatment route (HSS B alloy)	• Microstructure influencing mechanical behavior during compression tests
• Enhancement of primary carbides (MC, due to high N content) influence on solidification sequence and solid state transformation, including martensite HSS B	• Enhancement of Intergranular Troostite occurrence from supersaturated eutectic austenite • Supersaturation influencing in-situ M_2C carbides transformation HSS B	

Tableau III.2 : Thématiques présentes dans l'article (vert), et compléments décrits ci-après (rouge)

III.3. Résultats complémentaires

III.3.1. Solidification – Influence de l'azote sur la microstructure de coulée

Les thermogrammes obtenus en DTA sont relativement simples à interpréter. On présente ci-après les micrographies (**Figure III-1** et **Figure III-2**) donnant les microstructures obtenues après solidification par DTA, pour les deux alliages étudiés. Les thermogrammes correspondant aux cycles DTA sont eux déjà repris dans l'article, avec les séquences de solidification et de transformations en phase solide pour les pics principaux.
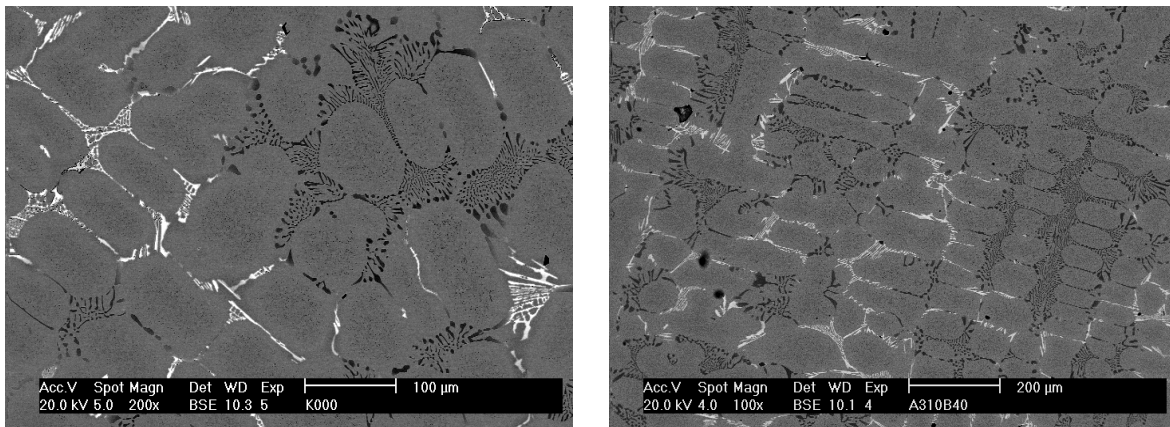
Figure III-1 : Vue générale après DTA (5°C/min) montrant la distribution des carbures eutectiques suivant des régions interdendritiques distinctes, et formant un réseau continu (M_2C clairs et MC foncés) – HSS A (à gauche), et HSS B (à droite)
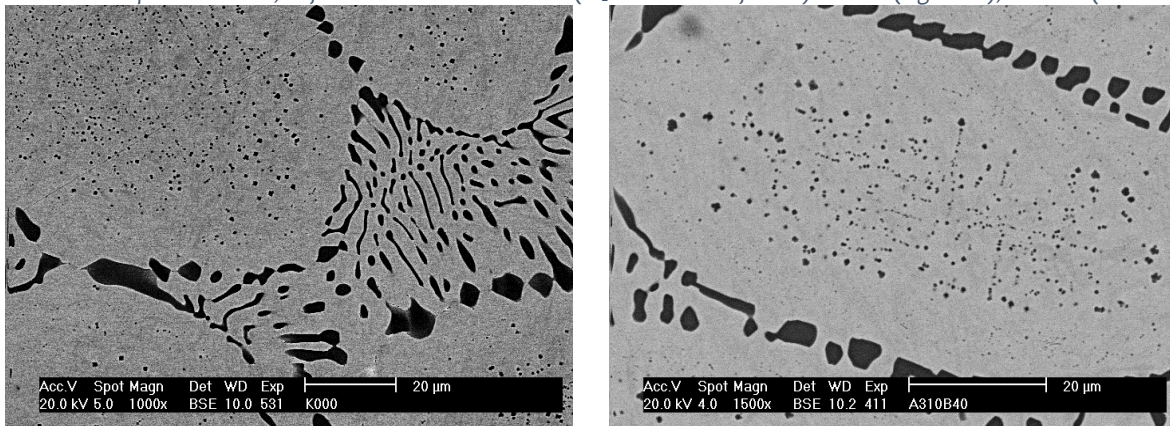
Figure III-2 : Zoom montrant la présence de carbures fins précipités dans le grain à l'état solide, de type MC, avec carbures de solidification MC aux joints de grains, et existence d'une région sans précipité près des joints de grains – HSS A à gauche et HSS B à droite

Partie A – Article #3 – Study of the origin of the unexpected pearlite during the cooling stage of two cast high-speed steels. J. Lecomte-Beckers & J. Tchoufang Tchuindjang. SSP 172-174 (2011), pp. 803-808

28

Dans cette introduction à l'Article # 3, une singularité découverte ultérieurement[6] porte sur l'influence de l'azote sur la microstructure de l'alliage HSS B en particulier.

La figure ci-dessous montre le résultat des simulations thermodynamiques suivant le modèle de Scheil-Gulliver (S-G).
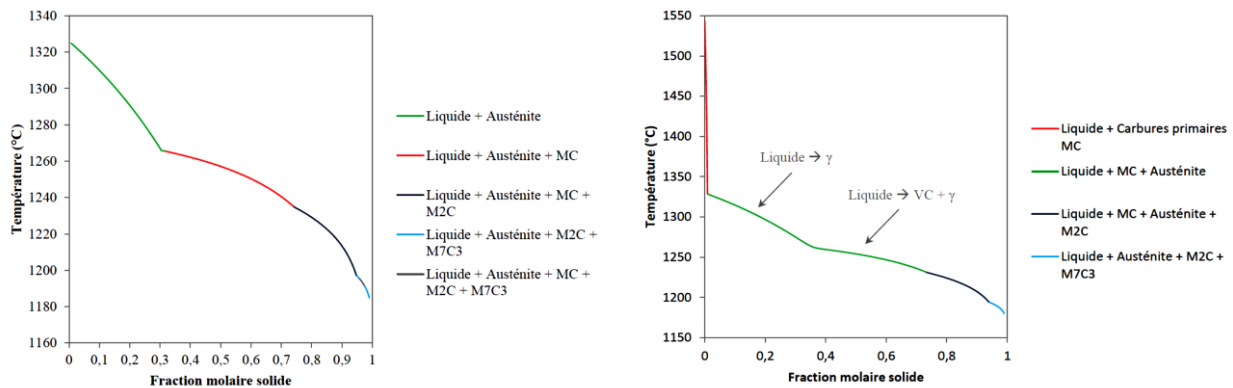
Figure III-3 : Simulation thermodynamique de la séquence de solidification par module Scheil-Gulliver montrant l'évolution de la fraction molaire pour l'alliage HSS B sans azote (à gauche) et avec azote (à droite)

Pour rappel, le modèle S-G dit de pseudo-équilibre autorise un gradient de composition dans la phase solide en croissance, en modifiant la condition de réversibilité totale des transformations en conditions d'équilibre. En général, on y inclut la rétrodiffusion de l'élément interstitiel. Les hypothèses principales qui fixent ce modèle sont les suivantes :

- homogénéité du métal liquide dont la composition évolue en cours de transformation ;
- équilibre à l'interface entre le liquide et le solide, avec une même composition chimique ;
- pas de diffusion dans la phase solide.

Le modèle S-G prédit la formation de carbures primaires MC comme 1er solide.

Les carbures primaires ont été observés pour diverses localisations dans l'enveloppe de la nuance HSS B dans l'état brut de coulée (analyse sur la profondeur) mais pas dans la nuance HSS A (**Figure III-4** et **Figure III-5**). Ces carbures massifs ont ensuite aussi été observés dans certains échantillons solidifiés par ATD (**Figure III-6**).

Figure III-4 : Microstructure de la nuance HSS A issue de la coulée centrifuge, après attaque profonde (dissolution de la matrice) montrant un réseau continu de carbures aux joints de grains, sans carbures massifs MC

Figure III-5 : Microstructure de la nuance HSS B issue de la coulée centrifuge, après attaque profonde (dissolution de la matrice) montrant un réseau continu de carbures aux joints de grains et des carbures massifs primaires MC localisés de manière aléatoire (dans les grains et aux joints de grains)
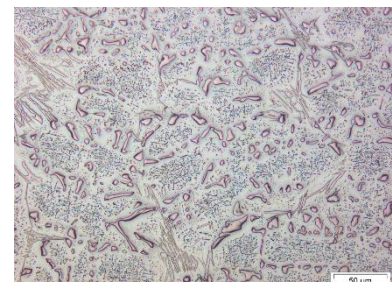
Figure III-6 : Microstructure de la nuance HSS B après solidification ATD, polissage à l'OPS et Contraste par Interférométrie différentielle montrant la présence de carbures massifs MC (primaires) dans et aux joints de grains

---

[6] Convention RW 6148 sur le développement de technologies et de matériaux innovants pour la fabrication de cylindres de travail à chaud

Les essais DTA réalisés sur la nuance HSS B dopée en azote ont produit des courbes semblables à celles de l'alliage de base, qui contenait moitié moins d'azote (voir Article #3). Des essais additionnels réalisés sur l'alliage de base à partir d'une carotte prélevée plus en profondeur, ont permis d'avoir des courbes DTA distinctes. L'une est similaire à la courbe initiale et les deux autres montrant une séquence similaire à celle prédite par le modèle S-G, avec des carbures MC comme premier solide (**Figure III-7**). En pratique, l'échantillon présentant une solidification selon un schéma avec des MC comme 1er solide contient déjà ces carbures dans l'état brut de coulée (**Figure III-8).**

On en a déduit que la présence d'azote, même en quantité modérée, favorise la germination des carbures primaires (**Figure III-9)**. Cependant, ceux-ci, à cause de leur plus faible densité que le métal liquide, vont ségréger vers l'intérieur du cylindre, pendant la coulée centrifuge. Ce mouvement dit de flottaison va s'opposer à celui dit de décantation qui a été observé dans les fontes ICDP (Article # 2), avec des carbures NbC plus denses que le métal liquide rejetés vers la surface.

Le caractère relativement simple de la séquence de solidification réelle, en lien avec le nombre réduit de phases en présence et l'absence de transformation à haute température, permet de se limiter à l'interprétation directe des thermogrammes. Il est inutile de recourir à la technique plus élaborée de la dérivée première du signal DTA (Maurizi Enrici et al., 2020). Cette possibilité d'interprétation directe signifie le plus souvent que l'effet de sursaturation est limité.

Toutefois, on note que l'ajout d'azote ne conduit pas à une modification systématique du schéma de solidification. En effet, bien que la présence de cet élément induise une germination plus marquée des MC riches en V (comme déjà établi dans l'article # 2 avec les NbC dans les fontes ICDP), on note en pratique que le schéma de solidification varie de manière aléatoire suivant les échantillons DTA.

On conclut donc que lors de la coulée d'un cylindre HSS B, l'azote va favoriser la germination de carbures MC de type primaire. Ceux-ci sont cependant susceptibles de ségréger, étant donné leur densité plus faible que celle du métal encore liquide.
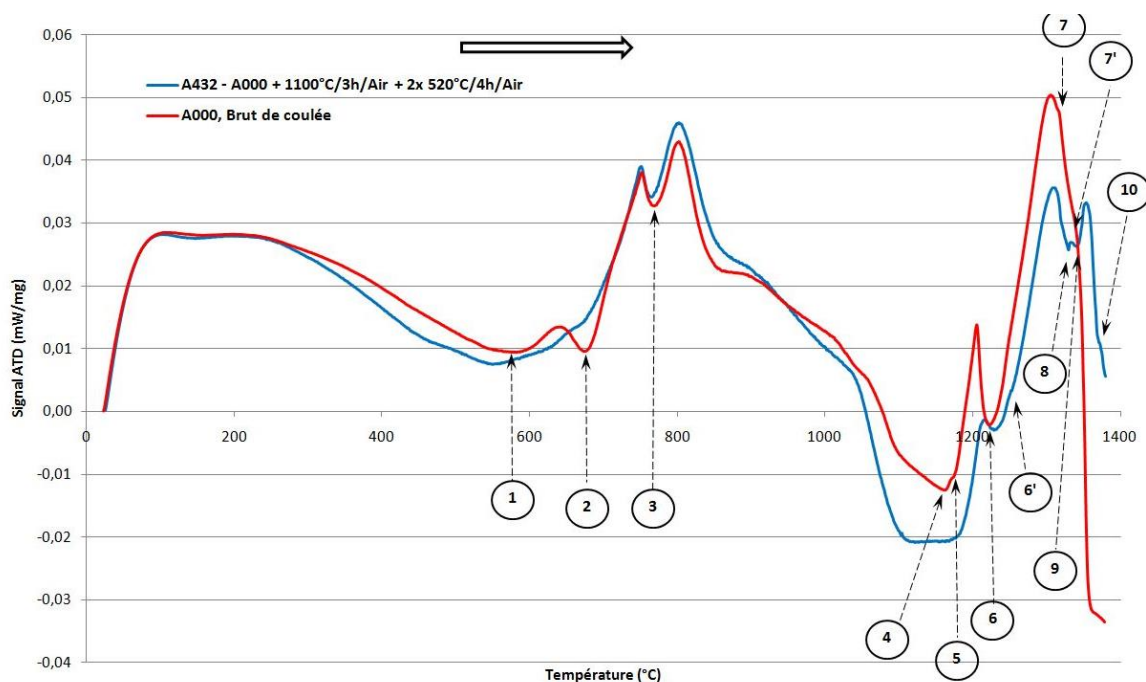
Figure III-7 : Mise en évidence de la présence de Troostite dans le brut de coulée (pic 1 sur A000) et de carbures primaires MC dans un échantillon (A432) situé plus en profondeur de l'enveloppe (pics 9 et 10 de fusion des carbures MC) ; la présence des carbures primaires est en relation avec les ségrégations d'origine

Partie A – Article #3 – Study of the origin of the unexpected pearlite during the cooling stage of two cast high-speed steels. J. Lecomte-Beckers & J. Tchoufang Tchuindjang. SSP 172-174 (2011), pp. 803-808

30

Figure III-8 : Mise en évidence de l'effet de la précipitation de carbures primaires (MC) sur le schéma de solidification et les transformations ultérieures en phase solide, lors du refroidissement continu (5°C/min). Les carbures primaires MC (1er solide) se forment dans les échantillons qui en contenaient déjà avant l'essai ATD (A000 comme HSS B brut de coulée, comme brut de coulée, et Axxx comme échantillons de HSS B traités thermiquement)

Figure III-9 : Séquence de solidification et transformations en phases solides dans un alliage de type HSS B dopé en N; séquence similaire à celle de l'alliage normal, traduisant l'existence de ségrégations majeures dans la pièce coulée (ici, absence de carbures primaires, avec austénite comme 1er solide)

Partie A – Article #3 – Study of the origin of the unexpected pearlite during the cooling stage of two cast high-speed steels. J. Lecomte-Beckers & J. Tchoufang Tchuindjang. SSP 172-174 (2011), pp. 803-808

31

III.3.2. **Transformations en phase solide**

III.3.2.i. Troostite

a. Identification dans le HSS B

Il s'agit de la phase douce observée dans l'HSS B (**Figure III-10 et III-11**). Initialement désignée comme une perlite fine, on a modifié son nom parce qu'il s'agit d'une phase différente, comme on le montre ci-après. En effet, la caractérisation de cette phase au SEM par EBSD et EDX, indique qu'il s'agit d'un agrégat de carbures de type $M_{23}C_6$, riches en chrome (**Figure III-12 à Figure III-14**). En outre, on notera l'aspect quasi-lamellaire de la troostite, quand on l'observe après polissage à l'OPS. Le même type d'analyse réalisé autour de la troostite a permis de caractériser aussi les autres phases (matrice, carbures eutectiques, fins carbures secondaires **Figure III-15** à **Figure III-18**).
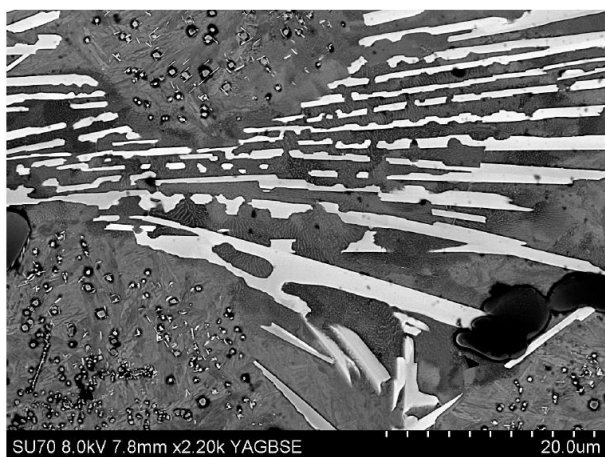
Figure III-10 : Vue générale d'une zone intergranulaire avec carbures de solidification de type MC globulaire (noir) et M_2C aciculaire (blanc), avec présence de fins carbures secondaires dans les grains – Préparation OPS
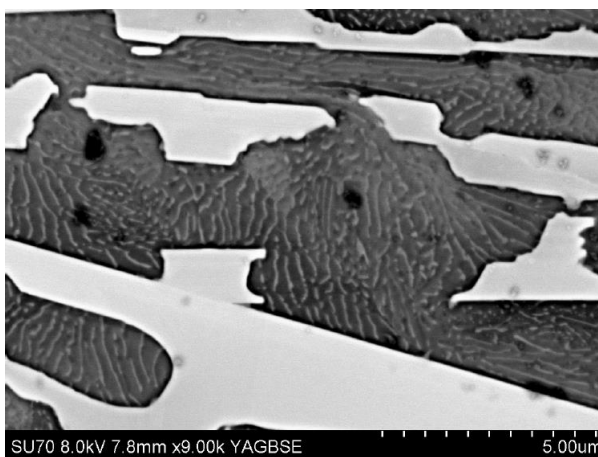
Figure III-11 : Zoom sur la troostite avec sa morphologie quasi-lamellaire, localisée dans l'espacement entre les lamelles du carbure M_2C, traduisant transformation de l'austénite eutectique associée au carbure eutectique M_2C (blanc)
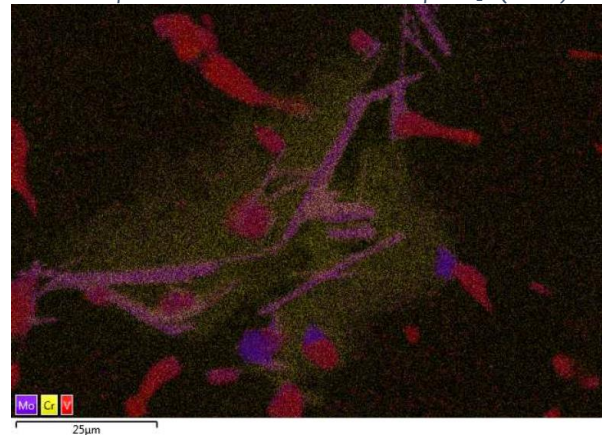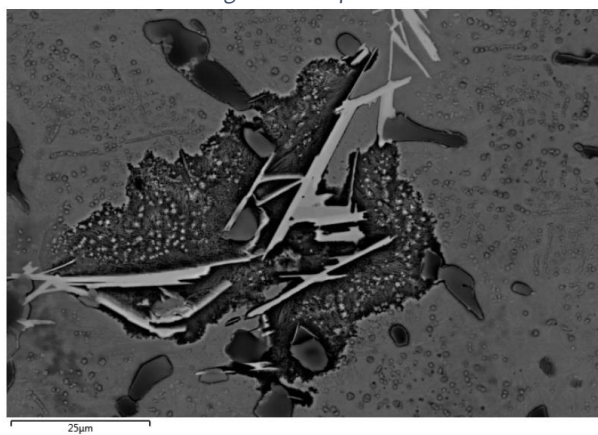
Figure III-12 : Vue générale d'une zone intergranulaire avec carbures de solidification et troostite (préparation OPS, à gauche), et cartographie EDX indiquant la distribution chimique des éléments Fe, Cr et V (à droite) - enrichissement de la troostite en Cr

Partie A – Article #3 – Study of the origin of the unexpected pearlite during the cooling stage of two cast high-speed steels. J. Lecomte-Beckers & J. Tchoufang Tchuindjang. SSP 172-174 (2011), pp. 803-808

32

Structure	Système cristallin	Groupe de Laue	Groupe d'espace	Paramètres de maille					
				a [nm]	b [nm]	c [nm]	α [°]	β [°]	γ [°]
Fe-α	Cubique m3m (bcc)	11	129	0.2866	0.2866	0.2866	90	90	90

Element	C	Al	Si	V	Cr	Fe	Ni	Mo	Total
At%	13.84	0.85	1.26	1.43	6.19	72.24	0.64	3.55	100.00
Wt%	3.30	0.46	0.70	1.45	6.40	80.18	0.75	6.77	100.00

Figure III-13 : *Cliché EBSD, paramètres de maille et composition chimique de la matrice martensitique dans le grain près de la troostite*

Structure	Système cristallin	Groupe de Laue	Groupe d'espace	Paramètres de maille					
				a [nm]	b [nm]	c [nm]	α [°]	β [°]	γ [°]
Fe-α	Cubique m3m (bcc)	11	129	0.2866	0.2866	0.2866	90	90	90

Elément	C	Al	Si	V	Cr	Fe	Ni	Mo	Total
%At	29.15	0.26	0.88	1.33	14.24	49.01	0.66	4.47	100.00
%Wt	7.97	0.16	0.56	1.54	16.85	62.28	0.88	9.76	100.00

Figure III-14 : *Cliché EBSD, paramètres de maille et composition chimique du carbure $M_{23}C_6$ composant la troostite*
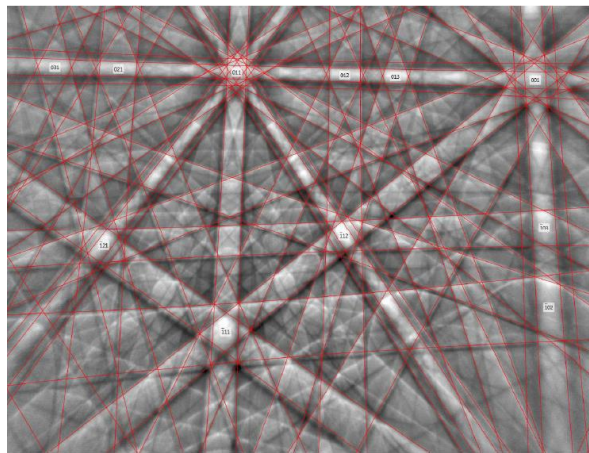
Structure	Système cristallin	Groupe de Laue	Groupe d'espace	Paramètres de maille					
				a [nm]	b [nm]	c [nm]	α [°]	β [°]	γ [°]
VC	Cubique m3m (FCC)	11	225	0.430	0.430	0.430	90	90	90

Element	C	Al	V	Cr	Fe	Mo	Total
At%	45.67	0.44	37.32	3.45	2.09	11.03	100.00
Wt%	14.38	0.31	49.82	4.70	3.06	27.72	100.00

Figure III-15 : *Cliché EBSD, paramètre de maille et composition chimique du carbure MC riche en V, localisé dans l'espace intergranulaire*
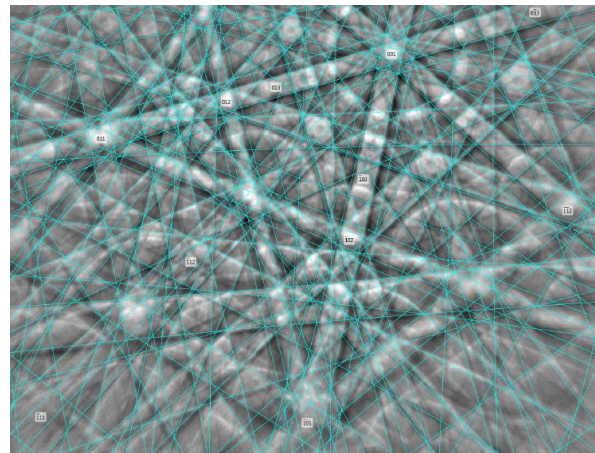
Structure	Système cristallin	Groupe de Laue	Groupe d'espace	Paramètres de maille					
				a [nm]	b [nm]	c [nm]	α [°]	β [°]	γ [°]
Mo2C	Trigonal -3m	7	162	0.5190	0.5190	0.4724	90	90	120

Element	C	Al	V	Cr	Fe	Mo	Total
At%	39.48	0.61	12.56	11.88	7.18	28.28	100.00
Wt%	9.75	0.34	13.16	12.70	8.24	55.80	100.00

Figure III-16 : *Cliché EBSD, paramètre de maille et composition chimique du carbure M_2C riche en Mo, localisé dans l'espace intergranulaire*

Partie A – Article #3 – Study of the origin of the unexpected pearlite during the cooling stage of two cast high-speed steels. J. Lecomte-Beckers & J. Tchoufang Tchuindjang. SSP 172-174 (2011), pp. 803-808

33
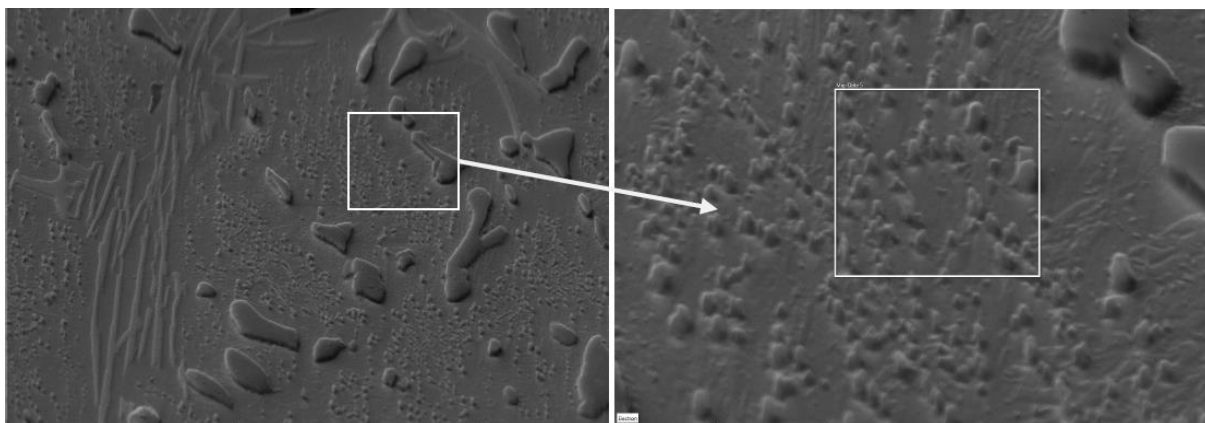
Figure III-17 : Autre région d'analyse de l'HSS B avec présence de carbures secondaires dans la matrice – Vue générale à gauche et zoom sur une zone avec carbures (à droite) – Préparation OPS
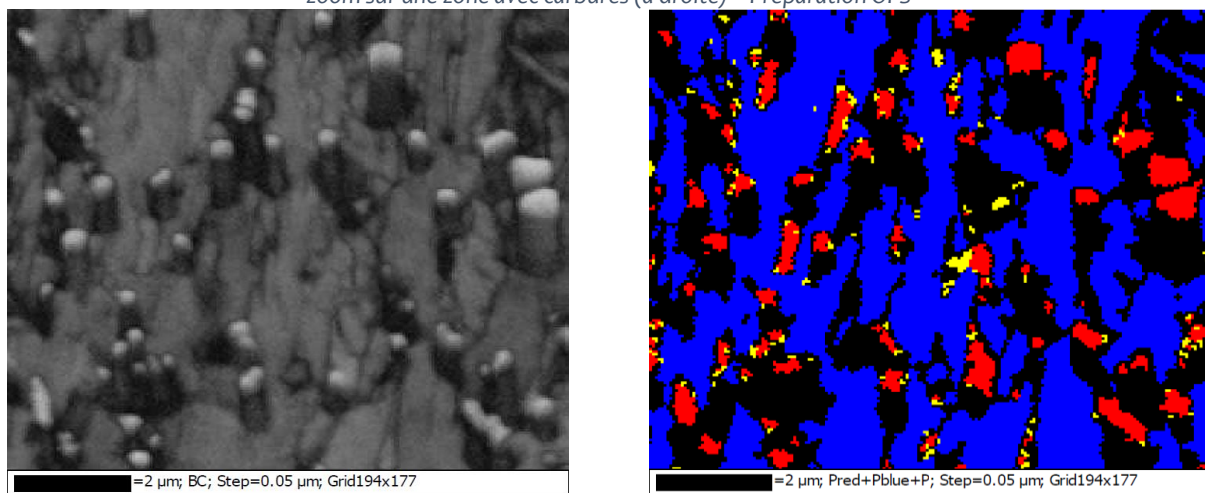
Figure III-18 : Cliché EBSD en contraste de bandes (à gauche) et cartographie des phases identifiées (à droite), illustrant la matrice martensitique (bleu), et les fins carbures mixtes de type VC (rouge) et Mo_2C (jaune)

b. Mécanisme de formation de la troostite

La singularité observée sur la composition de la troostite a conduit à rechercher le mécanisme responsable de sa formation, pour faire une distinction nette avec la perlite.

La caractérisation de cette phase au MEB par EBSD et EDX, montre qu'il s'agit d'un agrégat de carbures de type $M_{23}C_6$, riches en chrome. Ces carbures forment un réseau quasi-lamellaire. Ces caractéristiques sont propres à une réaction définie comme une précipitation discontinue cellulaire ou DCP (Discontinuous Cellular Precipitation). La DCP peut aussi être décrite comme la décomposition d'une solution solide sursaturée en une matrice désaturée et un précipité (phase cellulaire) de part et d'autre d'un joint de grain en mouvement (Findik, 1998). Dans cette désignation, le caractère discontinu est relatif au paramètre de maille de la phase-mère (matrice) qui change de manière discontinue au passage du front de réaction (**Figure III-19**) (Hornbogen, 1972; Knutsen et al., 2004; Manna, 1998; Srinivas and Kutumbarao, 2004). Celui-ci est donné par le joint de grain en migration, avec à l'arrière du front la précipitation de cellules lamellaires. La particularité de la DCP est son caractère autocatalytique, c'est-à-dire une aptitude à déplacer ou à reproduire les défauts cristallins sur le front de réaction. Ce phénomène accélère la germination et la croissance des produits de réaction, correspondant souvent à des phases d'équilibre.

Plusieurs types de troostite peuvent exister, en fonction du nombre et de la nature des phases impliquées au début et à la fin de la réaction. Notons qu'il y a toujours une phase-mère sursaturée qui désature après la réaction (**Figure III-20**). On peut donc définir pour la transformation martensitique, un mécanisme idoine de type troostitique.

Partie A – Article #3 – Study of the origin of the unexpected pearlite during the cooling stage of two cast high-speed steels. J. Lecomte-Beckers & J. Tchoufang Tchuindjang. SSP 172-174 (2011), pp. 803-808

34

Figure III-19: Changement discontinu du paramètre de maille du molybdène dans un alliage Fe-20Mo vieilli à 600°C (Hornbogen, 1972)

Figure III-20: Différents types de DCP observées dans les alliages métalliques, avec α' correspondant à la phase-mère sursaturée (Findik, 1998)

c. Exemples de phases troostitiques (désignation et nature)

La Troostite a souvent été observée dans différents alliages, mais sans qu'on ne lui accorde un intérêt particulier, en la confondant le plus souvent avec la perlite dans le cas des aciers. Diverses appellations ont déjà été évoquées, telles que « nodular bainite » (Reynolds et al., 1990b, 1990a; Spanos et al., 1990), « spiky nodules » (Kolmskog and Borgenstam, 2011), « fine pearlite » en lien avec une transformation incomplète (Efremenko et al., 2013; Hwang et al., 1998; Inthidech et al., 2012), «fanlike or acicular structure » (Kolmskog and Borgenstam, 2011), « dark-etching constituent » (Hackenberg and Shiflet, 1998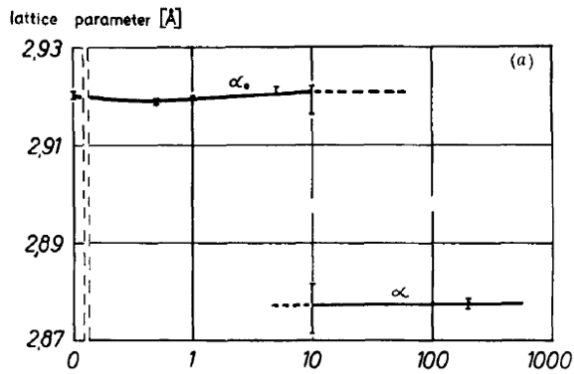), « fibrous carbides » (Berry and Honeycombe, 1970; Bhadeshia and Honeycombe, 2006; Shiflet and Aaronson, 1990), « cellular structure » (Movchan et al., 1980), « grain boundary allotriomorphs » (Shiflet and Aaronson, 1990), ''delta-pearlite'' formée par un mur discontinu (discontinuous wall) de carbures M_6C après une transformation péritectoïde (De Mello et al., 1985; Nurbanasari et al., 2014), etc.

Au niveau des phases constituant les différentes troostites, il y a les carbures de type $M_{23}C_6$ riches en Cr, mais aussi les carbures M_2C ou M_6C riches en Mo. Ces carbures peuvent être seuls en très fines lamelles adjacentes, ou parfois associés à une autre phase matricielle, telle que la ferrite ou l'austénite. Certains travaux ont conduit à dire que les réactions troostitiques sont des réactions de types eutectoïdiques, qui peuvent se produire avec deux ou trois composants. Dans le premier cas avec deux composants, il s'agirait d'une précipitation de M_6C au départ d'une phase sursaturée austénitique, tandis que dans le second cas à trois composants, l'austénite initiale produirait de la ferrite avec le carbure $M_{23}C_6$ (Hackenberg and Shiflet, 1998).

Il existe aussi des troostites formées à partir de nitrures comme phase quasi-lamellaire principale, notamment les Cr_2N, dans les aciers inoxydables.

d. Différenciation entre troostite et perlite

La perlite est le produit d'une réaction eutectoïde à trois composants, la première phase étant une solution solide avec une composition invariante. L'organigramme ci-dessous donnant la classification des différentes transformations de phases permet de distinguer la Perlite de la Troostite (DCP). A ces critères, on peut ajouter le fait que, quand les conditions thermodynamiques sont réunies pour former la Perlite, la réaction est complète, sur l'ensemble du grain initial. A l'inverse, la Troostite se caractérise systématiquement par une limitation de son étendue dans le grain de départ. Ce résultat a déjà été mis en évidence dans un des alliages présentés dans l'Article # 1. La réaction s'arrête quand la force motrice est annulée, c'est-à-dire quand la concentration relative de l'élément interstitiel diminue pour s'équilibrer de part et d'autre du front de réaction. C'est probablement ce qui justifie le contour en dents de scie de la nouvelle phase au sein du grain initial.
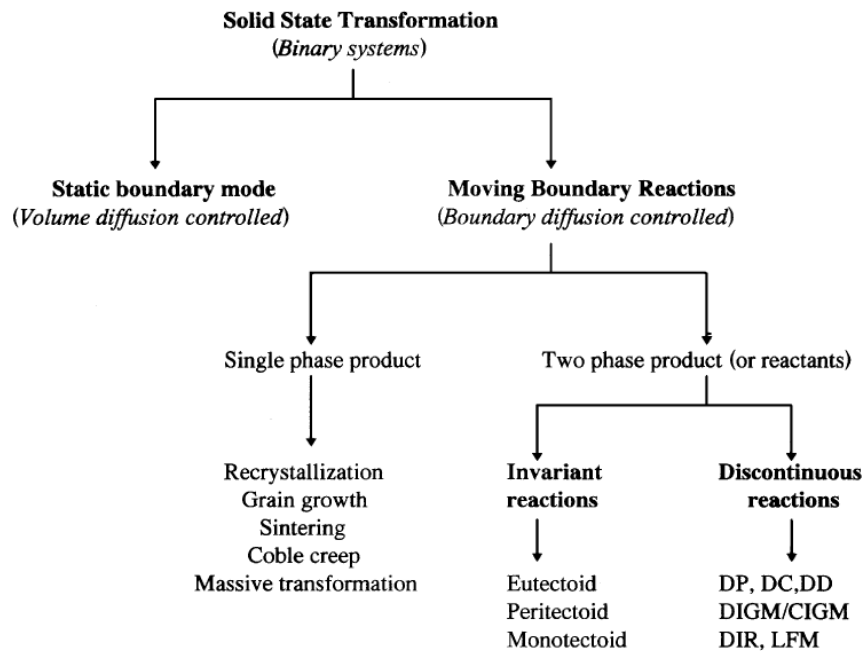
Partie A – Article #3 – Study of the origin of the unexpected pearlite during the cooling stage of two cast high-speed steels. J. Lecomte-Beckers & J. Tchoufang Tchuindjang. SSP 172-174 (2011), pp. 803-808

35

Solid State Transformation
(*Binary systems*)

Static boundary mode
(*Volume diffusion controlled*)

Moving Boundary Reactions
(*Boundary diffusion controlled*)

Single phase product

Two phase product (or reactants)

Recrystallization
Grain growth
Sintering
Coble creep
Massive transformation

Invariant reactions

Discontinuous reactions

Eutectoid
Peritectoid
Monotectoid

DP, DC,DD
DIGM/CIGM
DIR, LFM

Figure III-21: Classification des réactions en phase solide avec migration du joint de grain (Manna, 1998)

III.3.2.ii. Transformation-décomposition en phase solide de carbures M_2C

En lien avec la présence de la troostite, on peut proposer un mécanisme pour la transformation ou décomposition de carbures de solidification, en cours de recuit. Le moteur de cette transformation est la sursaturation, dont le marquage a été signalé précédemment par la présence de la troostite. Ici, on fait l'hypothèse que c'est l'état de sursaturation local qui justifie les réactions observées ultérieurement, sur les carbures. On pose donc une condition pour la décomposition des M_2C, celle de la sursaturation locale, soit sur le carbure de référence seul, soit sur le carbure et la matrice avoisinante.

Dans le cas du HSS B, la sursaturation est d'abord symbolisée par la présence à température ambiante de troostite intergranulaire (**Figure III-22**). Une fois celle-ci dissoute au chauffage, il y a activation de la déstabilisation du carbure adjacent qui était lui-même sursaturé, à travers la diffusion vers l'interface entre le carbure et la matrice, de plusieurs éléments. V et Mo quittent le carbure pour l'interface, tandis que C part de la matrice environnante pour migrer vers l'interface. Le résultat est la formation de nouveaux carbures à l'interface, illustrant un **phénomène dit de bourgeonnement**. Ailleurs, là où la sursaturation n'existe pas, il n'y a pas de décomposition des carbures M_2C (Tchuindjang et al., 2011). Ce même phénomène de décomposition a aussi été observé dans une étude plus récente faite sur un alliage de type HSS graphitique, en produisant toutefois des produits de décomposition différents, et en considérant uniquement la sursaturation pour le carbure initial M_2C (Maurizi Enrici et al., 2020). La même approche de décomposition à partir du carbure sursaturé M_2C, sans avoir nécessairement de sursaturation de la matrice avoisinante, a aussi été observée sur un alliage de type semi-HSS, après des traitements thermiques similaires à ceux réalisés sur l'HSS B (**Figure III-23** et Tchuindjang et al., 2011). Ces travaux ont montré que le carbure initial M_2C est préservé, en changeant toutefois sa composition chimique. Ce résultat se distingue des cas où on arrive à la fusion partielle du carbure eutectique M_2C, quand les températures sont proches ou équivalentes au solidus (au-dessus de 1150°C). En effet, le carbure M_2C initial est alors totalement transformé en un nouveau carbure M_6C qui peut plus ou moins coalescer suivant la durée plus ou moins longue du maintien à température (Fredriksson et al., 1979; Hashimoto et al., 2004; Kang and Lee, 2016; Lee et al., 1998).

Partie A – Article #3 – Study of the origin of the unexpected pearlite during the cooling stage of two cast high-speed steels. J. Lecomte-Beckers & J. Tchoufang Tchuindjang. SSP 172-174 (2011), pp. 803-808

36
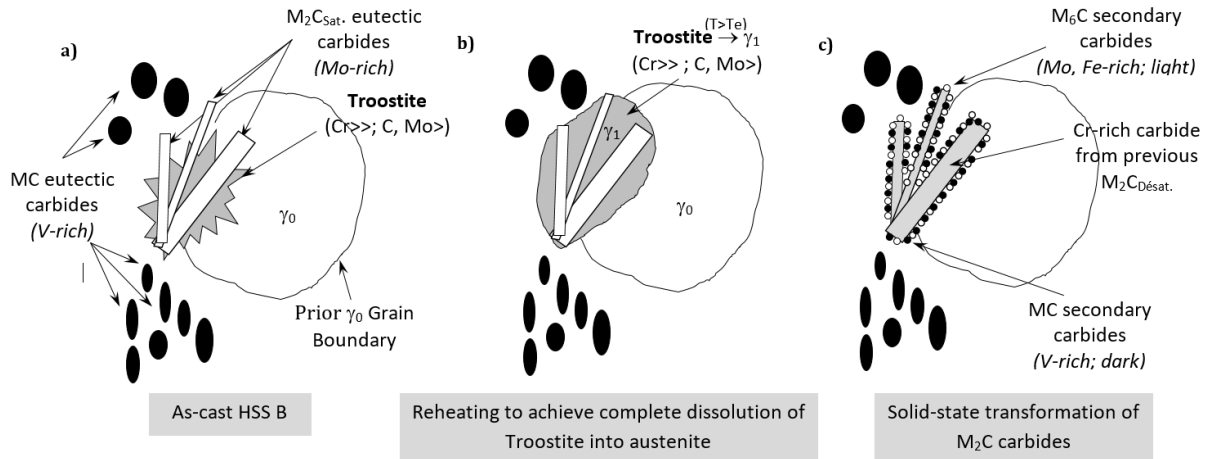
Figure III-22: *a) HSS B dans l'état brut de coulée avec troostite intergranulaire, et séquence des transformations en phase solide – b) dissolution de la troostite lors du chauffage jusqu'à l'austénitisation – c) Transformation in-situ des carbures M₂C sursaturés, réagissant avec l'austénite eutectique sursaturée, avec effet de bourgeonnement à l'interface (adapté de (Tchuindjang et al., 2011))*

$M_2C_{sat.} + \gamma_{1, Eutectique, Sat.} \rightarrow M_2C_{Désat.} + \gamma_{1, Eutectique, Désat.} + MC + M_6C$	(Tchuindjang et al., 2011)
$M_2C_{sat} + \gamma \rightarrow M_2C_{desat} + M_6C + Graphite$	(Maurizi Enrici et al., 2020)
$M_2C + \gamma\text{-}Fe \rightarrow M_6C + M_7C_3 + MC$	(Hashimoto et al., 2004)
$M_2C + \gamma \rightarrow M_6C + MC + \alpha + C$	(Fredriksson et al., 1979)
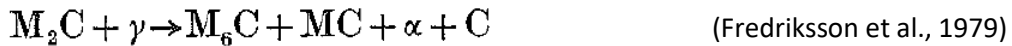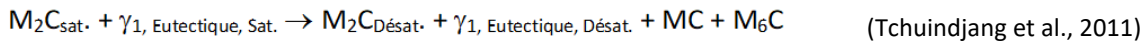
Tableau III-2 : *Différentes séquences de décomposition en phase solide des carbures M₂C sous l'effet de la température, avec (Maurizi Enrici et al., 2020; Tchuindjang et al., 2011) ou sans (Fredriksson et al., 1979; Hashimoto et al., 2004; Kang and Lee, 2016; Lee et al., 1998; Zhou et al., 2012) hypothèse de sursaturation du carbure initial*
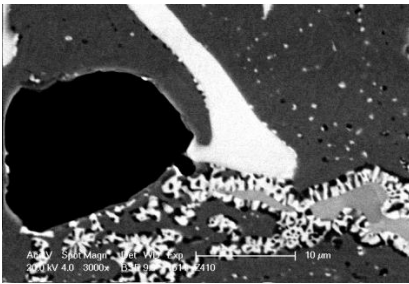
Figure III-23: *Décomposition (bourgeonnement) de M₂C dans un semi-HSS après austénitisation de 20' à 1100°C, produisant des MC et des M6C (Tchuindjang et al., 2011)*
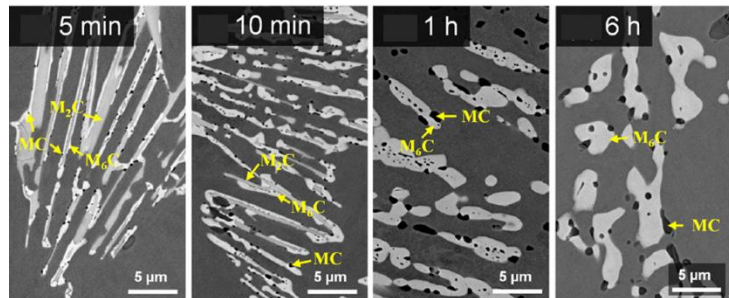
Figure III-24: *Transformation complète du carbure initial M₆C à 1150°C en M₆C et MC, avec coalescence des M₆C sous l'effet de la durée du maintien à température (Kang and Lee, 2016)*

Partie A – Article #3 – Study of the origin of the unexpected pearlite during the cooling stage of two cast high-speed steels. J. Lecomte-Beckers & J. Tchoufang Tchuindjang. SSP 172-174 (2011), pp. 803-808

37

III.4. Conclusions

L'analyse comparée de deux aciers à outils, HSS A et HSS B, de compositions chimiques proches mais distinctes a permis de mettre en évidence différents phénomènes qui sont résumés comme suit.

- Le HSS B a tendance à former comme premier solide, des carbures MC riches en V. Leur germination est favorisée par la présence d'azote. Ces carbures ont tendance à ségréger vers l'axe lors de la coulée centrifuge verticale, du fait de leur densité plus faible que le liquide.
- La troostite est présente dans le HSS B en conditions brut de coulée. Sa caractérisation montre qu'elle se compose de carbures $M_{23}C_6$.
- Le troostite est une phase distincte de la perlite, qui outre sa composition différente, répond aussi à un mécanisme de formation spécifique, de type DCP (précipitation discontinue cellulaire). La force motrice de la transformation est donnée par la sursaturation de l'élément interstitiel, le carbone.
- La sursaturation évoquée avec la troostite dans les HSS B peut être associée à une autre sursaturation du carbure M_2C riche en Mo qui lui est proche, pour justifier le phénomène de décomposition de ce carbure qui a lieu sous l'effet de la température. La décomposition est similaire à un phénomène dit de bourgeonnement, avec précipitation de carbures nouveaux à l'interface du carbure initial.

Dans l'Article #4 ci-après, les schémas de solidification présentés ici seront à nouveau analysés avec un focus sur les conditions à l'équilibre et hors d'équilibre pour divers alliages Une condition nécessaire pour l'apparition de la Troostite sera mise en évidence. Enfin on abordera les transformations de phases lors de la trempe (bainite et martensite) et les performances des cylindres obtenues.

III.5. Références

Berry, F.G., Honeycombe, R.W.K., 1970. The isothermal decomposition of austenite in Fe– Mo– C alloys. Metallurgical transactions 1, 3279–3286.

Bhadeshia, H.K.D.H., Honeycombe, S.R., 2006. 4 - The Effects of Alloying Elements on Iron-Carbon Alloys, in: Bhadeshia, H.K.D.H., Honeycombe, S.R. (Eds.), Steels (Third Edition). Butterworth-Heinemann, Oxford, pp. 71–93. https://doi.org/10.1016/B978-075068084-4/50006-6

De Mello, J.D.B., Hamar-Thibault, S., Durand-Charre, M., 1985. Eutectoid transformations and precipitation in high carbon tool steels. J Mater Sci 20, 3453–3461. https://doi.org/10.1007/BF01113752

Efremenko, V., Shimizu, K., Chabak, Y., 2013. Effect of destabilizing heat treatment on solid-state phase transformation in high-chromium cast irons. Metallurgical and Materials Transactions A 44, 5434–5446.

Findik, F., 1998. Discontinuous (cellular) precipitation. Journal of materials science letters 17, 79–83.

Fredriksson, H., Hillert, M., Nica, M., 1979. The decomposition of the M 2 C carbide in high speed steel. Scandinavian Journal of Metallurgy 8, 115–122.

Hackenberg, R.E., Shiflet, G.J., 1998. Transitions in carbide morphology in a ternary Fe-CW steel. Metallurgical and Materials Transactions A 29, 2087–2100.

Hashimoto, M., Kubo, O., Matsubara, Y., 2004. Analysis of Carbides in Multi-component White Cast Iron for Hot Rolling Mill Rolls. ISIJ International 44, 372–380. https://doi.org/10.2355/isijinternational.44.372

Hornbogen, E., 1972. Systematics of the cellular precipitation reactions. Metallurgical and Materials Transactions B 3, 2717–2727.

Hwang, K.C., Lee, S., Lee, H.C., 1998. Effects of alloying elements on microstructure and fracture properties of cast high speed steel rolls: Part I: Microstructural analysis. Materials Science and Engineering: A 254, 282–295.

Inthidech, S., Sricharoenchai, P., Matsubara, Y., 2012. Effect of molybdenum content on subcritical heat treatment behaviour of hypoeutectic 16 and 26 wt-% chromium cast irons. International Journal of Cast Metals Research 25, 257–263. https://doi.org/10.1179/1743133612Y.0000000009

Kang, M., Lee, Y.-K., 2016. The Effects of Austenitizing Conditions on the Microstructure and Wear Resistance of a Centrifugally Cast High-Speed Steel Roll. Metall Mater Trans A 47, 3365–3374. https://doi.org/10.1007/s11661-016-3536-1

Partie A – Article #3 – Study of the origin of the unexpected pearlite during the cooling stage of two cast high-speed steels. J. Lecomte-Beckers & J. Tchoufang Tchuindjang. SSP 172-174 (2011), pp. 803-808

38

Knutsen, R.D., Lang, C.I., Basson, J.A., 2004. Discontinuous cellular precipitation in a Cr–Mn–N steel with niobium and vanadium additions. Acta Materialia 52, 2407–2417. https://doi.org/10.1016/j.actamat.2004.01.031

Kolmskog, P., Borgenstam, A., 2011. Eutectoid transformations in 4.12 mass Pct Cr 0.88 mass Pct C steel. Metallurgical and Materials Transactions A 42, 3941–3951.

Lee, E.-S., Park, W.-J., Jung, J.Y., Ahn, S., 1998. Solidification microstructure and M2C carbide decomposition in a spray-formed high-speed steel. Metall Mater Trans A 29, 1395–1404. https://doi.org/10.1007/s11661-998-0354-0

Manna, I., 1998. Grain Boundary Migration in Solid State Discontinuous Reactions. Interface Science 6, 113–131. https://doi.org/10.1023/A:1008672705642

Maurizi Enrici, T., Mertens, A., Sinnaeve, M., Tchuindjang, J.T., 2020. Elucidation of the solidification sequence of a complex graphitic HSS alloy under a combined approach of DTA and EBSD analyses. J Therm Anal Calorim 141, 1075–1089. https://doi.org/10.1007/s10973-019-09093-9

Movchan, V.L., Pedan, L.G., Voronkina, L.A., 1980. Formation of cellular structures in carburized high-speed steels. Metal Science and Heat Treatment 22, 188–191.

Nurbanasari, M., Tsakiropoulos, P., Palmiere, E.J., 2014. On the Solidification of a H23 Tool Steel. Trans Indian Inst Met 67, 935–944. https://doi.org/10.1007/s12666-014-0420-9

Reynolds, W.T., Li, F.Z., Shui, C.K., Aaronson, H.I., 1990a. The incomplete transformation phenomenon in Fe-C-Mo alloys. Metallurgical Transactions A 21, 1433–1463.

Reynolds, W.T., Liu, S.K., Li, F.Z., Hartfield, S., Aaronson, H.I., 1990b. An investigation of the generality of incomplete transformation to bainite in Fe-CX alloys. Metallurgical Transactions A 21, 1479–1491.

Shiflet, G.J., Aaronson, H.I., 1990. Growth and overall transformation kinetics above the bay temperature in Fe-C-Mo alloys. Metallurgical Transactions A 21, 1413–1432.

Spanos, G., Fang, H.S., Sarma, D.S., Aaronson, H.I., 1990. Influence of carbon concentration and reaction temperature upon bainite morphology in Fe-C-2 Pct Mn alloys. Metallurgical Transactions A 21, 1391–1411.

Srinivas, N.C.S., Kutumbarao, V.V., 2004. Growth mechanism for discontinuous precipitation in a multi-component (Fe–Cr–Mn–N) system. Scripta Materialia 51, 1105–1109. https://doi.org/10.1016/j.scriptamat.2004.07.029

Tchuindjang, J.T., Sinnaeve, M., Lecomte-Beckers, J., 2011. Influence of High Temperature Heat Treatment on in situ Transformation of Mo-rich Eutectic Carbides in HSS and Semi-HSS Grades, in: Conference Proceedings of Abrasion 2011. Presented at the Abrasion 2011, 4th Edition - Abrasion Wear Resistant Alloyed White Cast Irons For Rolling And Pulverizing Mills, MMS-ULg, Liege, pp. 61–75.

Zhou, X.F., Fang, F., Jiang, J.Q., Zhu, W.L., Xu, H.X., 2012. Study on decomposition behaviour of M_2C eutectic carbide in high speed steel. Materials Science and Technology 28, 1499–1504. https://doi.org/10.1179/1743284712Y.0000000081

Partie A – Article #3 – Study of the origin of the unexpected pearlite during the cooling stage of two cast high-speed steels. J. Lecomte-Beckers & J. Tchoufang Tchuindjang. SSP 172-174 (2011), pp. 803-808

39

IV. CHAPITRE 4 : PRÉSENTATION ET COMPLÉMENTS D'ÉTUDE SUR L'ARTICLE #4

IV.1. Introduction

Dans cet Article #4, cinq alliages sont caractérisés. Deux sont déjà utilisés dans les cages dégrossisseuses d'un train à bandes à chaud (l'acier à haut chrome et le HSS pour dégrossisseurs) quant aux trois autres, ils sont candidats pour cette même application (les semi-HSS).

Leur caractérisation principale a été faite suivant les pratiques industrielles courantes, à savoir l'évaluation de paramètres spécifiques mais qualitatifs, directement d'après les retours des utilisateurs de laminoirs pendant le service. Bien que de tels paramètres soient relatifs, la pratique reste toujours d'actualité pour la majorité des laminoirs. Le procédé très complexe, qui met en œuvre non seulement les cylindres de travail, mais aussi les cylindres d'appuis et surtout la brame à laminer à chaud, implique un nombre de variables très important, qui rend la modélisation difficile.

L'approche des essais sur site en vue de qualifier une nouvelle nuance de cylindre est donc toujours souvent utilisée, ce qui justifie le contenu de cet article. Les trois nouveaux alliages semi-HSS sont en fait une évolution d'une même nuance en vue de parvenir à un résultat comparable voire meilleur que les solutions existantes.

Ce faisant, on rappelle qu'à la base, une seule nuance (l'ICDP déjà présentée dans l'article #2) était utilisée dans tous les étages des trains à bandes à chaud. Les progrès en R&D ont permis de mettre au point des alliages plus adaptés. Cependant, on n'est pas parvenu à ce jour à élaborer une nuance autre que l'ICDP, pour les dernières cages du train finisseur.

L'article met l'accent sur le semi-HSS, qui est comparé à l'acier à haut chrome élaboré avant lui. Notons que cet acier à haut chrome est plus largement étudié dans l'article #5. Le HSS pour dégrossisseur qui est également présenté de façon succincte, était une nuance encore en cours d'élaboration lors de notre étude. Les coulées expérimentales sont dans ce cas testées chez un lamineur, et c'est seulement à partir des premiers résultats concluants qu'on procède à une analyse plus approfondie de l'alliage. Sa caractérisation est ici donc sommaire.

Dans cet article, on compare la simulation thermodynamique (Thermo-Calc®) à l'essai expérimental (« Differential Thermal Analysis » ou DTA) pour la détermination des schémas de solidification, en mettant en évidence les limitations d'une méthode par rapport à l'autre. Ces deux approches sont aussi comparées au cas réel de la coulée centrifuge, en notant que celle-ci produit un gradient de vitesse plus élevé que la DTA, et aussi une force centrifuge qui tend à compacter la matière en cours de solidification. Cette remarque est importante quand on considère le cas des retassures.

L'article met aussi en avant des performances de cylindres qui ont été obtenues par retour d'exploitation. Il montre l'intérêt grandissant pour les semi-HSS qui présentent des performances prometteuses, en comparaison avec les autres nuances. Les tendances du marché pour les cylindres équipant les cages dégrossisseuses de train à bandes sont ainsi dressées. Pour compléter l'étude, des résultats inédits relatifs aux nuances semi-HSS expérimentales proches du semi-HSS 3 qui est un grade industriel, sont présentés. Les deux nuances expérimentales désignées semi-HSS 1 et semi-HSS 2 ont des compositions chimiques proches du semi-HSS 3, à la différence qu'elles ne contiennent pas de Nb. En outre pour le semi-HSS 3, on a légèrement diminué la teneur en carbone. Ces résultats concernent la mise en évidence de l'effet de composition chimique et du mode de coulée sur :

- la séquence de solidification et les défauts de structure associés,

- les transformations en phase solide, notamment la troostite dans le semi-HSS 2, puis la bainite et la martensite dans le semi-HSS 3, en lien avec la conduite du traitement thermique,

De plus quelques corrélations entre la microstructure et les propriétés mécaniques sont présentées. Le caractère dual de la microstructure du semi-HSS 3 (grade de référence) est rappelé, en justifiant son origine et en mettant en évidence son influence sur diverses propriétés.

IV.2. Bref rappel sur le contexte

Les pièces d'origine ayant servi à l'étude sont des cylindres bimétalliques obtenus par coulée centrifuge verticale. Ces pièces représentent des cylindres de laminoir à chaud, utilisés dans les cages dégrossisseuses du laminoir à chaud. Le procédé d'élaboration qui est propre à la société Marichal Ketin reste la coulée centrifuge verticale, déjà évoquée dans les articles #2 et #3.

Les échantillons sont prélevés dans le métal d'enveloppe, sous forme de barreaux. Les sections étudiées sont orientées perpendiculairement à l'axe de symétrie du cylindre. La zone d'intérêt pour le prélèvement des éprouvettes ayant servi aux analyses diverses (thermiques, métallographiques) et à la caractérisation des propriétés mécaniques se trouve à une profondeur de 40 mm environ, entièrement comprise dans le métal d'enveloppe.

Les résultats principaux de l'article ont été obtenus dans le cadre d'une convention RW coordonnée par l'industriel[7], suivie par un projet de collaboration scientifique avec la Bulgarie[8]. La publication a été rééditée pour faire partie d'un chapitre d'un livre sur les cylindres de laminoir à paraître chez AIST, en y rajoutant à la demande de l'éditeur l'identification et la quantification des carbures de solidification des alliages étudiés.

Dans ce qui suit, on ajoute de nouveaux résultats obtenus sur les mêmes matières. Ils apportent un complément d'informations en lien avec les trois grands thèmes, fil rouge de la première partie de la thèse. Il s'agit de la solidification, des transformations en phase solide, et des corrélations microstructure-propriétés. Le **Tableau IV-1** distingue les points existants (vert) dans l'article et les points additionnels (rouge).

Solidification	Solid State Transformations	Mechanical properties and related damage mechanisms
• Solidification sequence from DTA tests and comparison with thermodynamic simulations • Enhancement of heterogeneities and segregations	• Enhancement of Intragranular troostite occurrence from supersaturation peritectic austenite [semi-HSS 2] within the as-received conditions (under high cooling rates) + DTA (heating mode for reverse transformations; Cooling mode under a cooling rate lower than the critical cooling for troostite formation]) • Desaturation influencing peritectoid precipitation inside remaining delta-ferrite zones (Semi-HSS 3) • Martensitic transformation (Ms) under DTA tests (semi-HSS 1, 2 and 3)	• Hot hardness and rough corrosion behavior • Roll performances (trends) • Dual-like matrix influencing mechanical behavior of semi-HSS 3

Tableau IV.1: Thématiques présentes dans l'article (vert), et thèmes ajoutés pour compléter l'étude (rouge).

---

[7] Convention RW 5359 (2007-2009) : Etude de la dégradation thermochimique des cylindres de travail à chaud
[8] Convention CGRI Wallonie-Bulgarie (2009-2011)

Partie A – Article #4 – Current Developments of Alloyed Steels for Hot Strip Roughing Mills: Characterization of High-Chromium Steel and Semi-High Speed Steels. J. Lecomte-Beckers, M. Sinnaeve & J. Tchoufang Tchuindjang. Iron and Steel Technolgy 2 (2012), pp. 33-40

41

IV.3. Résultats complémentaires

IV.3.1. Solidification et hétérogénéités de structure

IV.3.1.i. Etude en condition hors équilibre par ATD

Les résultats des essais ATD réalisés sur les trois nuances semi-HSS sont rappelés ci-dessous, en illustrant l'entièreté des thermogrammes du refroidissement, jusqu'à la température ambiante (**Figure IV-2**).
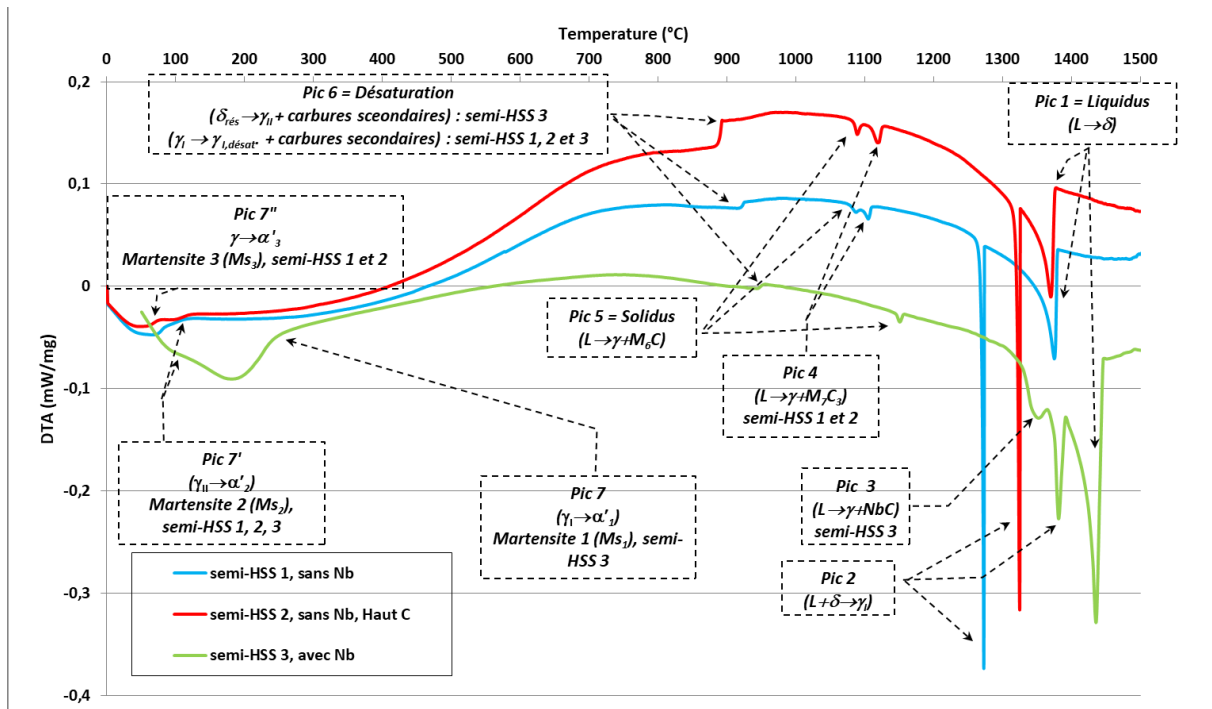

Figure IV-1 : *Solidification et transformations en phases solides après essais DTA (5°C/min) sur semi-HSS 1, 2 et 3 – Effet de Nb sur séquence de solidification (non-terminaison péritectique) et transformations martensitiques*

La séquence de solidification est relativement facile à établir, puisqu'il n'y a que des pics individuels et pas de pics complexes dans le cas des semi-HSS 1 et 2. Le premier solide est δ, puis il y a un péritectique pour former γ au détriment de δ, et enfin deux types de carbures eutectiques se forment, le second M_6C constituant le solidus. L'intervalle et le schéma de solidification sont similaires pour les semi-HSS 1 et 2. Par contre le semi-HSS 3 présente des différences, avec un liquidus plus élevé, mais une séquence distincte aussi. Si le premier solide reste δ suivi par le péritectique, il y a pendant la phase de croissance de γ, précipitation de NbC, puis en fin de solidification, formation de l'eutectique M_2C.

La formation des NbC parallèlement au péritectique bloque cette réaction, en provoquant la présence de δ résiduelle dans la nuance semi-HSS 3. Cette phase subit ensuite transformation péritectoïde, qui correspond à la formation d'austénite associée à la précipitation de carbures secondaires. Cette transformation est aussi connue sous le nom de réaction δ-eutectoïde (De Mello et al., 1985; Nurbanasari et al., 2014; Riedl and Fischmeister, 1990; Zhao et al., 2016). Notons que l'austénite « péritectique » est le siège d'une précipitation de carbures secondaires moins marquée que dans le cas de δ résiduelle, qui correspond à une désaturation. On définit ainsi deux types d'austénite dans le semi-HSS 3, alors qu'on a un seul type dans les semi-HSS 1 et 2. La première austénite dite péritectique (γ_I) résulte de la réaction à trois composants, qui va jusqu'à son terme. On la qualifie d'austénite primaire, car elle se forme à partir de l'état liquide. La transformation péritectique qui survient dans les zones où la ferrite en régression n'est plus en contact avec le liquide conduit à la formation d'un liseré de carbures (comme déjà établi

Partie A – Article #4 – Current Developments of Alloyed Steels for Hot Strip Roughing Mills: Characterization of High-Chromium Steel and Semi-High Speed Steels. J. Lecomte-Beckers, M. Sinnaeve & J. Tchoufang Tchuindjang. Iron and Steel Technolgy 2 (2012), pp. 33-40

42

dans les résultats additionnels de l'Article #1). La seconde austénite dite péritectoïde ou δ-eutectoïde, apparaît en phase solide (γ_{II}), au départ de la ferrite delta résiduelle ($\delta_{rés.}$) non complètement transformée, uniquement dans le cas du semi-HSS 3. On la qualifie d'austénite secondaire. Les rubriques qui suivent apportent des précisions sur ces observations, en mettant en évidence les hétérogénéités chimiques.

Par ailleurs la structure formée en ATD, à une vitesse de refroidissement inférieure à celle de la coulée, va produire une microstructure qui peut être différente de celle de l'enveloppe du cylindre, même si les phases en présence sont du même type. En l'occurrence la structure après ATD sera plus grossière, avec des carbures plus massifs qui pourront se présenter par endroits en réseau continu. En même temps, le caractère statique de la solidification dans le creuset ATD va favoriser la formation de retassures en quantité plus importante que dans le cas industriel (**Figure IV-2**)
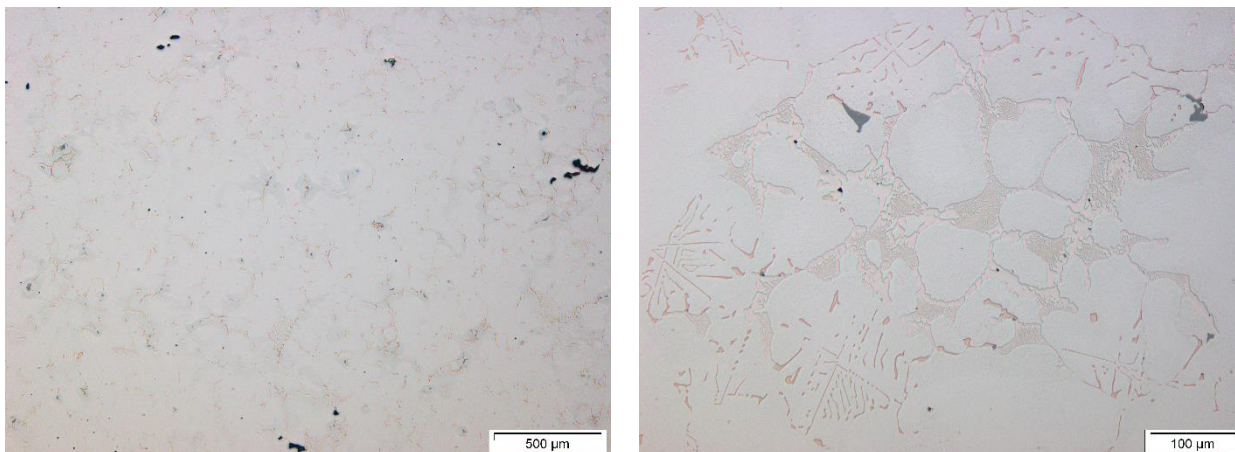

Figure IV-2 : Vue générale de la structure dans le semi-HSS 3 avec présence de retassures (zones noires) et de lobules (bleu clair) à gauche, et zoom sur zone montrant continuité du réseau de carbure eutectiques ayant une forme plus massive que dans le cas de la coulée industrielle (M_2C lamellaires associées à NbC en écriture chinoise) – Poli-miroir (échantillon ATD)

IV.3.1.ii. Analyse des échantillons issus de la coulée centrifuge

En ce qui concerne l'état brut de coulée industrielle (BCI), on observe une structure homogène pour le semi-HSS 1 en particulier, qui a une matrice martensitique dans tous ses grains (**Figure IV-3**). Cependant, tous les joints de grains ne présentent pas de carbures eutectiques ce qui rend leur réseau discontinu. En outre il existe une répartition différenciée des carbures dans les joints suivant chacun des deux types identifiés, à savoir les M_7C_3 riches en Cr, ou les M_2C riches en Mo (**Figure IV-4**).
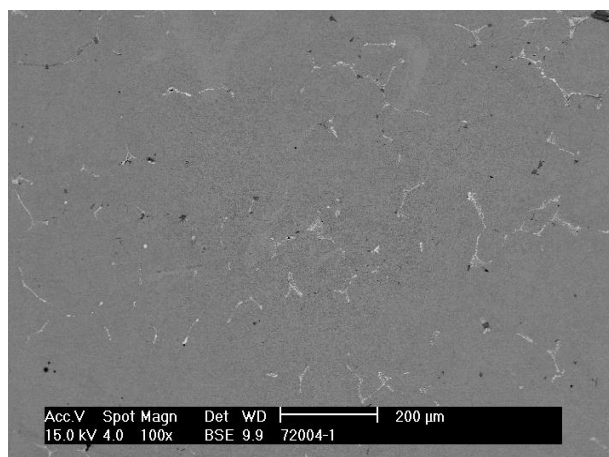
Figure IV-3 : Vue générale de la microstructure homogène dans le semi-HSS 1, avec réseau discontinu de carbures eutectiques aux joints de grains (M_7C_3 gris et M_2C blancs) dans une matrice homogène (échantillon BCI) – Nital
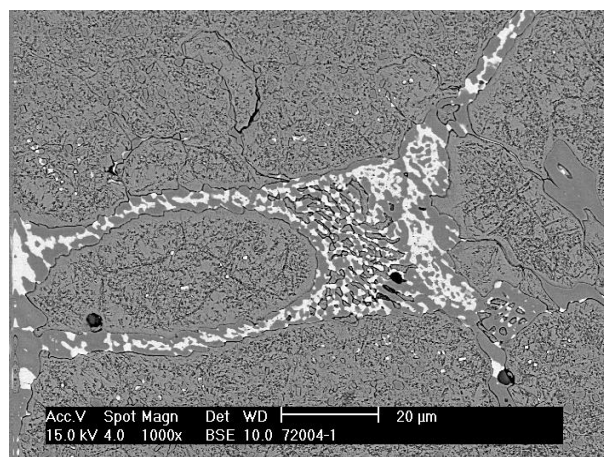
Figure IV-4 : Zoom montrant les carbures riches en Mo (clairs, formés en fin de solidification) à côté des carbures riches en Cr (gris), et matrice martensitique dans semi-HSS 1 homogène (échantillon BCI) – Nital

Partie A – Article #4 – Current Developments of Alloyed Steels for Hot Strip Roughing Mills: Characterization of High-Chromium Steel and Semi-High Speed Steels. J. Lecomte-Beckers, M. Sinnaeve & J. Tchoufang Tchuindjang. Iron and Steel Technolgy 2 (2012), pp. 33-40

43

La structure du semi-HSS 2 est presque similaire à celle du semi-HSS 1, pour la martensite dans les grains, et le duo de carbures eutectiques en réseau discontinu aux joints de grains (**Figure IV-5**). Cependant, la troostite présente à certains sous-joints de grains constitue une hétérogénéité de structure. Les sous-joints considérés se caractérisent par un liseré de carbures. Il a déjà été établi que ce liseré est le marquage de la fin de la transformation péritectique (sans la phase liquide). Cette réaction se marque à la frontière ou la phase-mère δ a régressé au détriment de l'austénite péritectique, et le marquage prend la forme d'un liseré de carbures (**Figure IV-6**). Ce type de carbure localisé dans un sous-joint n'est donc pas un eutectique. La troostite observé dans le semi-HSS 2 est de type granulaire, car elle résulte de la désaturation du grain. L'hétérogénéité évoquée ici se caractérise en particulier par une différence significative de dureté entre la martensite plus dure du grain, et la troostite qui l'est beaucoup moins.
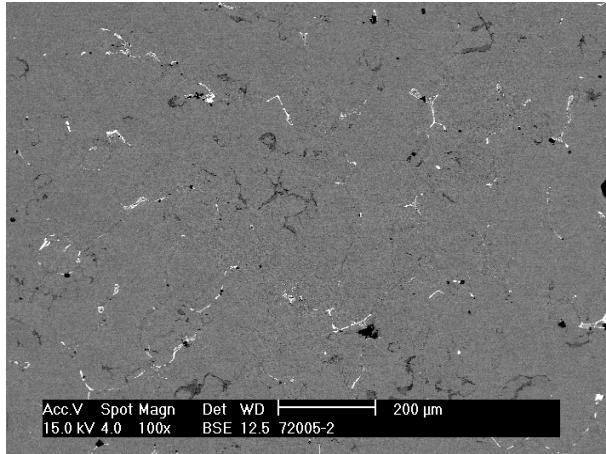
Figure IV-5 : *Vue générale de la microstructure hétérogène à cause de la présence de troostite dans le semi-HSS 2 (échantillon BCI) – Nital*
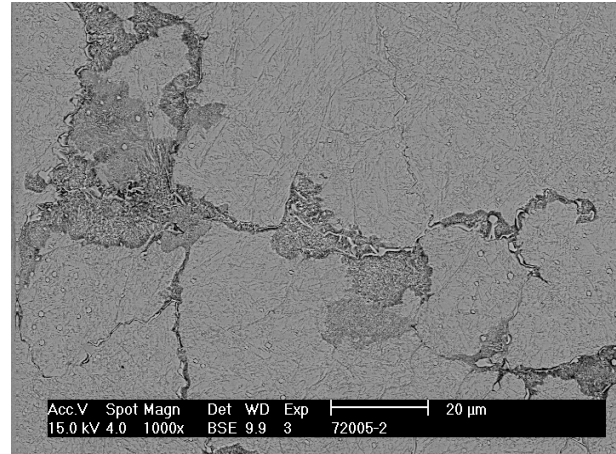
Figure IV-6 : *Zoom montrant région avec troostite granulaire, associée à un liseré de carbures marquant la fin de la transformation péritectique ; martensite en lattes ailleurs dans les grains – Illustration de l'hétérogénéité dans le semi-HSS 2 (échantillon BCI) - Nital*

Pour le semi-HSS 3, il se compose d'une matrice hétérogène, formée par deux austénites d'origine différente, et un réseau discontinu de carbure eutectiques (**Figure IV-7**). Il y a d'abord l'austénite péritectique (majoritaire) qu'on désigne aussi par austénite primaire, et il y a l'austénite péritectoïde (secondaire) qui a la forme de lobules. Les carbures de solidification sont respectivement les NbC et les M_2C (**Figure IV-8**).
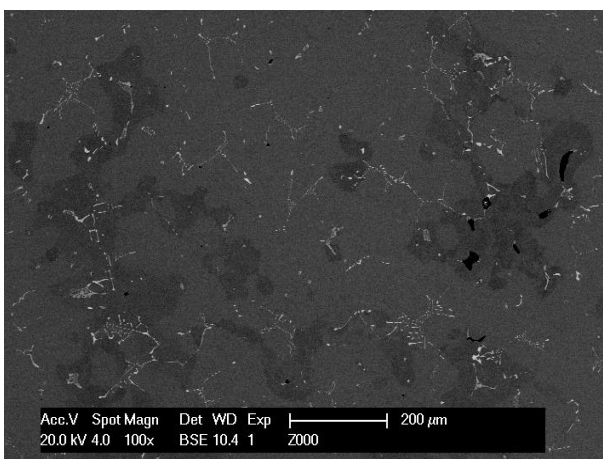
Figure IV-7 : *Vue générale de la microstructure hétérogène sur semi-HSS 3 avec lobules (gris foncé) minoritaires localisés aux sous-joints de grains, et réseau de carbures discontinu (phases claires) aux joints de grains - matrice mixte (duale) – Nital*
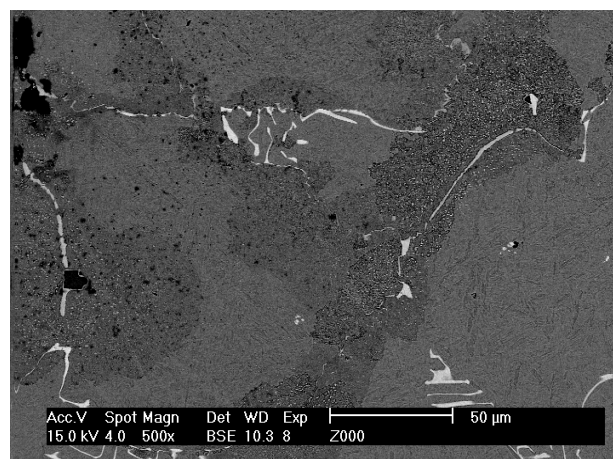
Figure IV-8 : *Zoom sur région avec lobules d'austénite secondaire contenant un liseré de carbures à cœur ; fine précipitation dans les lobules et absence de précipités à l'intérieur des grains adjacents ; carbures eutectiques (NbC et M_2C) plus fins qu'en ATD, par effet de vitesse de refroidissent – Nital*

Partie A – Article #4 – Current Developments of Alloyed Steels for Hot Strip Roughing Mills: Characterization of High-Chromium Steel and Semi-High Speed Steels. J. Lecomte-Beckers, M. Sinnaeve & J. Tchoufang Tchuindjang. Iron and Steel Technolgy 2 (2012), pp. 33-40

44

IV.3.2. **Transformations en phase solide**

IV.3.2.i. Lors du refroidissement après la solidification

Lors du refroidissement qui suit la solidification, les carbures secondaires se forment dans la matrice, à travers un phénomène de désaturation de cette dernière, qui survient à cause de la diminution de la solubilité des éléments dans le réseau qui se contracte sous l'effet de la température. Leur présence est clairement illustrée sur le thermogramme ATD par l'existence du pic n° 6 en escalier avec une rampe dont l'extension traduit la variation de la composition chimique des précipités au cours de la transformation (**Figure IV-3**).

Le cas du semi-HSS 3 est encore différent des deux autres. La différence vaut par la nature des carbures, car la présence des NbC empêche la formation des M_7C_3 probablement parce que le carbone n'est plus disponible. Les M_2C sont toujours présents comme solidus, mais ils se forment à plus haute température que dans les semi-HSS 1 et 2 (**Figure IV-4**), suggérant une composition chimique différente. Et enfin, il y a de nombreux lobules localisés aux sous-joints de grains, là où sont présents les liserés de carbures marquant la fin de la transformation péritectique. Cette phase lobulaire représente une autre austénite die secondaire. Sa composition est différente de l'austénite péritectique qui constitue la phase matricielle majoritaire. La structure du semi-HSS 3 est donc hétérogène.

En synthèse, il existe dont des hétérogénéités dans les semi-HSS 2 et 3, et pas dans le semi-HSS 1 qui est plus homogène. Cette hétérogénéité n'a pas la même origine dans les deux nuances. Pour le semi-HSS 2, l'hétérogénéité est donnée par la troostite présente dans les sous-joints de grains. Il s'agit d'une troostite granulaire, formée à partir d'un sous-joint de grain austénitique, dans une gamme de température proche de 700°C. Pour le semi-HSS 3, l'hétérogénéité est constituée par l'existence de deux phases austénitiques, dont l'une minoritaire, sous forme de lobules, qui se localise aussi aux-sous joints de grains. Ces lobules donnent le contour de $\delta_{rés.}$ non consommée par la réaction péritectique qui se produit à plus haute température, pendant la solidification. La non-terminaison de la réaction est due à la formation concomitante des NbC, qui en consommant le liquide disponible, empêche la réaction péritectique de se poursuivre normalement. Cette hypothèse est corroborée par la présence de nombreuses retassures dans le semi-HSS 3 (**Figure IV-2**). Leur proportion est significativement plus élevée en ATD que pour toutes les autres nuances, y compris les autres semi-HSS. Par contre on peut considérer dans le cas de la coulée centrifuge, que la mobilité du liquide compense sans nécessairement l'éliminer, cette tendance à la formation de retassures.

IV.3.2.ii. Lors des traitements thermiques pour homogénéiser la matrice

On se focalise dans cette partie, sur les transformations qui se produisent lors des traitements thermiques qui ont été réalisés sur le semi-HSS 3 en particulier. Une campagne d'essais similaire à celle déjà présentée dans l'Article #1, avec pour objectif la détermination de l'optimum pour la trempe, au sens de la dureté. On va se limiter à l'analyse sur le traitement optimal, défini pour une température d'austénitisation de 1025°C pendant 20 minutes suivi d'un refroidissement à l'air calme (échantillon 210). On propose de considérer en plus le cas du traitement thermique réalisé à une température plus élevée, proche mais inférieure au solidus, avec un temps de maintien long, pour évaluer la stabilité des hétérogénéités chimiques. Cet autre cas concerne l'échantillon 430, austénitisé à 1100°C pendant 3 h.

Les **Figure IV-9** à **Figure IV-19** illustrent la distribution des éléments dans les différentes phases présentes dans le semi-HSS 3, pour mettre en évidence les phénomènes éventuels d'homogénéisation par diffusion d'éléments. Les analyses ont été faites au moyen d'un MEB par électrons Auger. Le **Tableau IV-2** rappelle les zones d'intérêt choisies.

Partie A – Article #4 – Current Developments of Alloyed Steels for Hot Strip Roughing Mills: Characterization of High-Chromium Steel and Semi-High Speed Steels. J. Lecomte-Beckers, M. Sinnaeve & J. Tchoufang Tchuindjang. Iron and Steel Technolgy 2 (2012), pp. 33-40

45

Zone 1 (matrice)	Zone 2 (matrice)	Zone 3 (carbure au joint de grain)	Zone 4 (carbure)	Zone 5 (carbure)	Zone 6 (liseré de carbures au sous-joint de grain)
γ_I	γ_{II}	M_2C	NbC massif	NbC en écriture chinoise	M_2C

Tableau IV-2: *Zones d'intérêt pour les analyses MEB-Auger sur phases caractéristiques d'échantillons de semi-HSS 3 après traitements thermiques.*
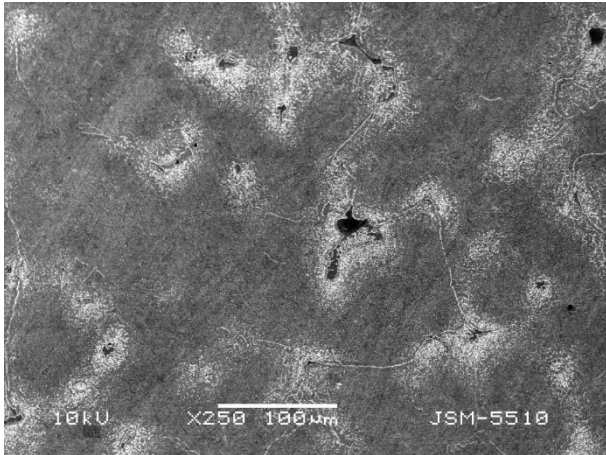
Figure IV-9 : *Vue générale de la zone d'analyse sur l'échantillon 210 illustrant régions lobulaires résiduelles (zones claires, avec fine précipitation de carbures ilustrant la désaturation), matrice gris clair, et liseré de sous-joints de grains ; NbC non contrastés (MEB-SE, Nital)*
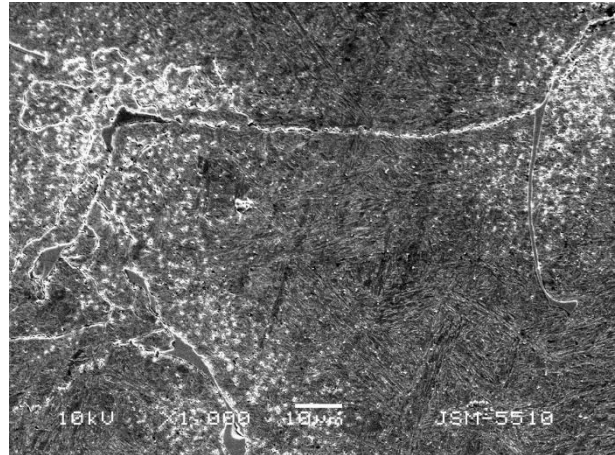
Figure IV-10 : *Zoom sur un agrégat de carbures eutectiques M_2C à un joint de grains avec précipitation secondaire autour, et mise en évidence du liseré fin (sous-joint) et de la matrice martensitique en lattes (échantillon 210, MEB-Nital)*
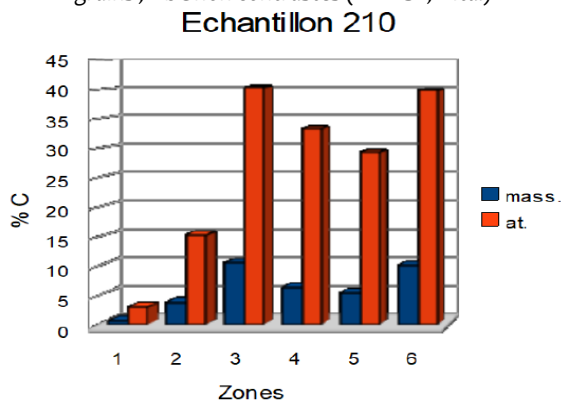
Figure IV-11 : *γ_{II} (zone 2) plus riche en C que γ_I (zone 1), par effet de fine précipitation secondaire, illustrant l'hétérogénéité au sein de la matrice ; C majoritaire dans tous les carbures (zones 3 à 6)*
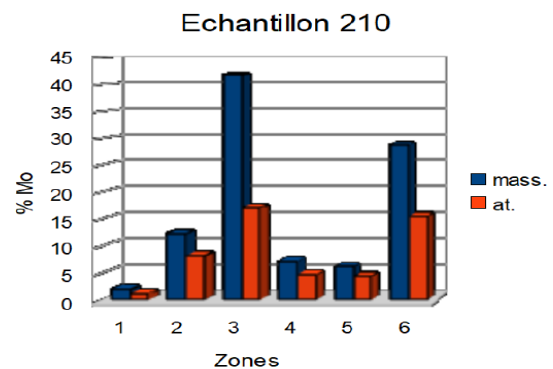
Figure IV-12 : *γ_{II} (zone 2) plus riche en Mo que γ_I (zone 1) par présence carbures secondaires, avec confirmation de l'hétérogénéité chimique au sein de la matrice ; Mo élément majoritaire dans le carbure M_2C (zone 3), et sur le liseré au sous-joint (zone 6)*
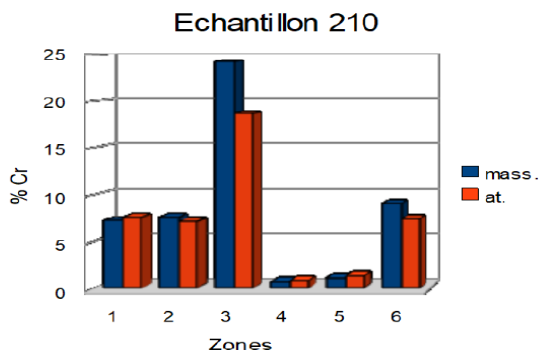
Figure IV-13 : *Distribution de Cr dans les différentes phases de l'échantillon 210*
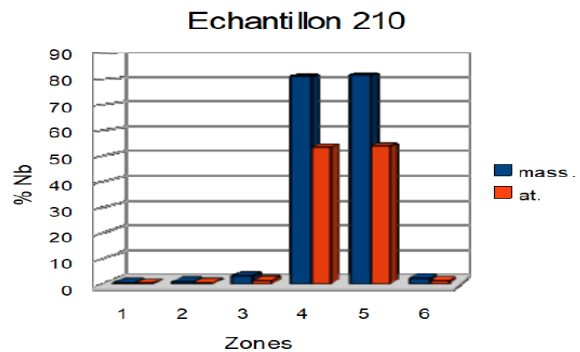
Figure IV-14 : *Distribution de Nb dans les différentes phases de l'échantillon 210*

Partie A – Article #4 – Current Developments of Alloyed Steels for Hot Strip Roughing Mills: Characterization of High-Chromium Steel and Semi-High Speed Steels. J. Lecomte-Beckers, M. Sinnaeve & J. Tchoufang Tchuindjang. Iron and Steel Technolgy 2 (2012), pp. 33-40

46

On peut faire les observations suivantes concernant l'échantillon 210 (**Figure IV-9 à Figure IV-14**).

- Le carbone (C) est davantage présent dans δ (premier solide, zone 2) que dans γ péritectique (zone 1), avec un ratio trois fois plus élevé (**Figure IV-11**). Cependant, la stabilité du carbone dans δ diminue fortement lors du refroidissement, ce qui justifie la forte désaturation (précipitation) observée en ATD et sur les micrographies, lors de la transformation péritectoïde (pic 6, **Figure IV-1**). Le carbone est aussi l'élément principal fixé par tous les carbures (**Figure IV-11**)

- Mo se dissout davantage dans δ que dans γ (3 fois plus environ), est présent dans le M_2C pour une quantité équivalente à celle du liseré de carbures, et en moindre proportion dans le NbC (**Figure IV-12**).

- Cr est l'élément qui se distribue le mieux entre toutes les phases (**Figure IV-13**). Il est présent en proportions équivalentes (et presque similaires à la teneur initiale) dans les grains de δ (zone 2) ou ceux de γ (zone 1), est fixé préférentiellement dans les carbures M_2C aux joints de grains (zone 3) en quantité équivalente au Mo. Sa teneur est un peu inférieure à celle de Mo dans le liseré (sous-joint de grains, zone 6). C'est dans le NbC que sa proportion est la plus faible, même si elle n'est pas nulle.

- Nb est uniquement fixé dans les carbures NbC, et ne se retrouve quasiment pas dans le carbures M_2C, et encore moins dans la matrice (**Figure IV-14**).

- En corollaire, Nb reste dans le liquide jusqu'au moment de la précipitation de NbC. En effet, Nb ne rentre pas en solution dans les grains du premier solide formé δ, puisqu'on ne le retrouve pas dans la phase γ_2 (zone 2) qui est le produit de la transformation de δ résiduelle (lobules), en phase solide. Nb ne rentre pas non plus dans les nouveaux grains de γ_1 (zone 1) issus de la réaction péritectique, pendant la solidification.

Le traitement thermique fait sur l'échantillon 430 n'altère que très peu de phases. En l'occurrence, il y a re-dissolution quasi complète des carbures secondaires de l'austénite péritectoïde (zone 2), avec doublement de la teneur en carbone par rapport au traitement à 1025°C (**Figure IV-17**). Celle-ci en contenait davantage que l'austénite péritectique (zone 1) dont la teneur en carbone augmente aussi, mais en moindre proportion. Le carbure NbC est insensible au traitement thermique, car sa composition ne change pas (**Figure IV-17 à IV-20**) en comparaison avec les conditions de l'échantillon 210. Par contre le carbure M_2C s'enrichit davantage en Mo (**Figure IV-18**), en perdant notamment du Cr (**Figure IV-19**). Il est possible que cette modification de composition de M_2C s'accompagne d'une décomposition, comme cela a déjà été établi ailleurs.

Le chrome est l'élément qui se distribue le mieux entre les diverses phases de la matrice et des carbures. Le molybdène a aussi une tendance à se répartir dans toutes les phases, avec cependant une préférence pour δ dans les grains, et pour les carbures M_2C lors de la solidification. Le niobium est un élément de ségrégation absolu, qui reste dans le liquide pour se fixer presque exclusivement au carbone, au moment de former le carbure NbC. Ce faisant, son non-partitionnement est responsable de l'interruption de la réaction péritectique par défaut de liquide, avec conséquence double. La première concerne la formation de nombreuses retassures, et le seconde l'existence de deux phases matricielles différentes, qui ne peuvent être homogénéisées par traitement thermique

Partie A – Article #4 – Current Developments of Alloyed Steels for Hot Strip Roughing Mills: Characterization of High-Chromium Steel and Semi-High Speed Steels. J. Lecomte-Beckers, M. Sinnaeve & J. Tchoufang Tchuindjang. Iron and Steel Technolgy 2 (2012), pp. 33-40

47
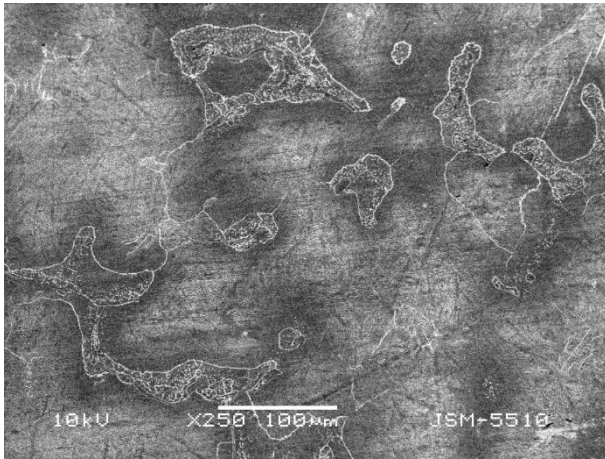
Figure IV-15 : *Vue générale de la zone d'analyse sur échantillon 430 illustrant régions globulaires avec contours marqués par le triatement thermique ; contraste plus clair suggérant présence d'austénite résiduelle dans la matrice ; NbC non contrastés (MEB-SE, Nital)*
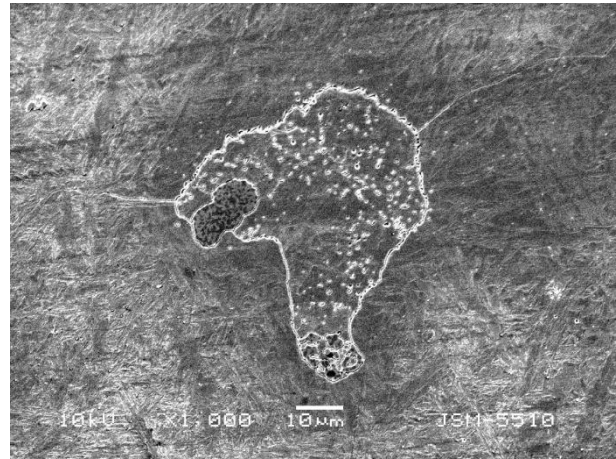
Figure IV-16 : *Zoom sur globule illustrant forte diminution des carbures secondaires par effet de dissolution au traitement thermique et début de transformation des carbures M$_2$C (échantillon 430)*
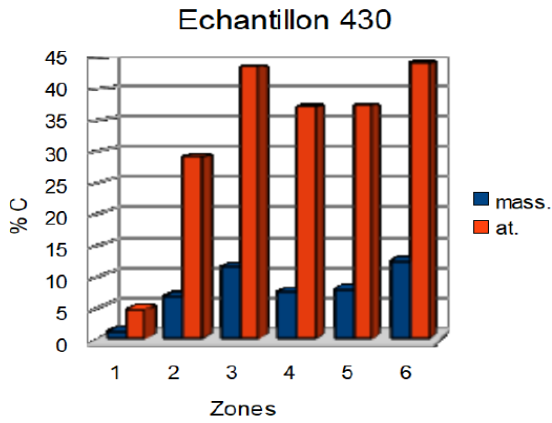
Figure IV-17 : *γ_{II} (zone 2) encore plus riche en C que γ_I (zone 1) par effet de dissolution des carbures secondaires (en comparaison avec 210)*
C majoritaire dans tous les carbures
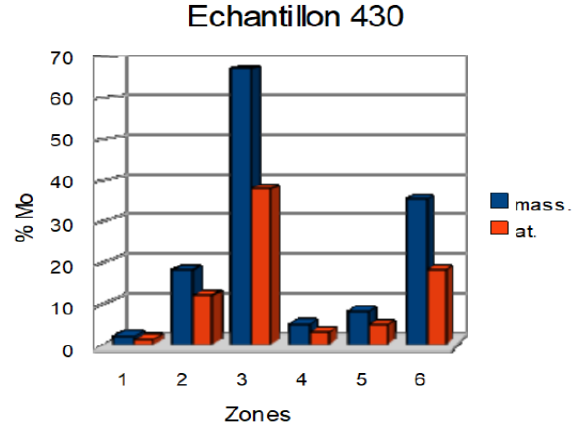
Figure IV-18 : *γ_{II} (zone 2) davantage enrichie en Mo que γ_I (zone 1) par effet de dissolution de carbures secondaires Mo élément majoritaire du carbure M$_2$C, et du liseré (idem à 210)*
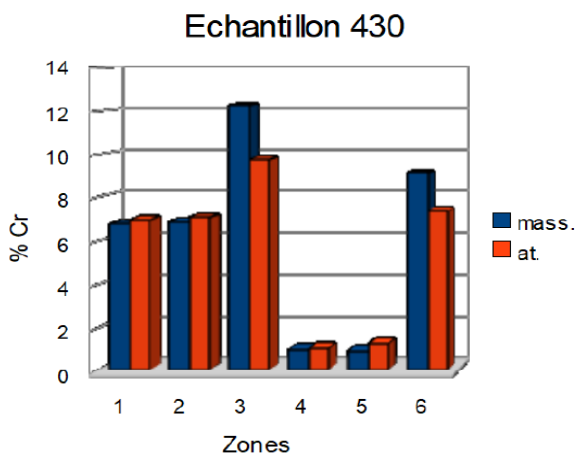
Figure IV-19 : *Distribution de Cr dans les différentes phases de l'échantillon 430*
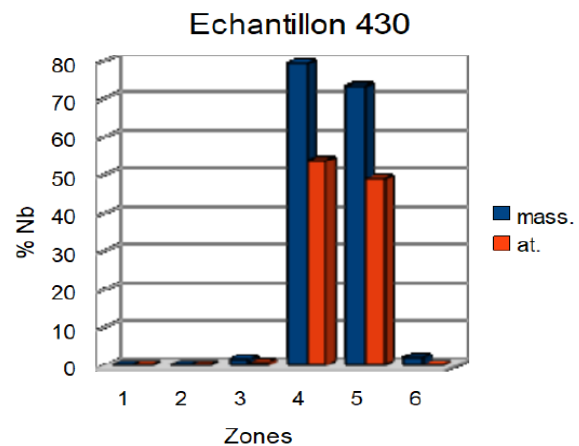
Figure IV-20 : *Distribution de Nb dans les différentes phases de l'échantillon 430*

Partie A – Article #4 – Current Developments of Alloyed Steels for Hot Strip Roughing Mills: Characterization of High-Chromium Steel and Semi-High Speed Steels. J. Lecomte-Beckers, M. Sinnaeve & J. Tchoufang Tchuindjang. Iron and Steel Technolgy 2 (2012), pp. 33-40

48

IV.3.2.iii. Cas de la troostite dans le semi-HSS 2

La troostite a uniquement été observée dans le semi-HSS 2 issu de la coulée industrielle par centrifugation verticale (**Figure IV-5 et IV-6**). Les vitesses maximales de refroidissement réalisables en ATD ne suffisent pas pour la former. Ce résultat est similaire à celui déjà mentionné pour le HSS B de l'Article # 3. En outre le semi-HSS 3 qui contient des NbC qui fixent une quantité plus importante de carbone que les deux autres semi-HSS qui n'en contiennent pas. Le semi-HSS 3 ne peut donc pas former de troostite. Par contre il peut former de la perlite, phase d'équilibre, moyennant un traitement thermique adapté (**Figure IV-21**). Ceci confirme une fois encore la condition de sursaturation au joint de grain ou dans le grain, qui est indispensable pour former la troostite.
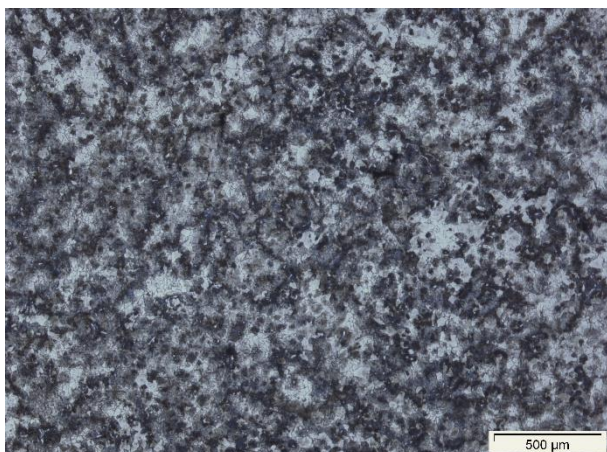
Figure IV-21 : *Perlite dans le semi-HSS 3 après austénitisation de 1025°C/1h, puis maintien isotherme de 24h à 700°C (Nital) –* **Dureté moyenne 224 ± 29 HV$_{30}$**
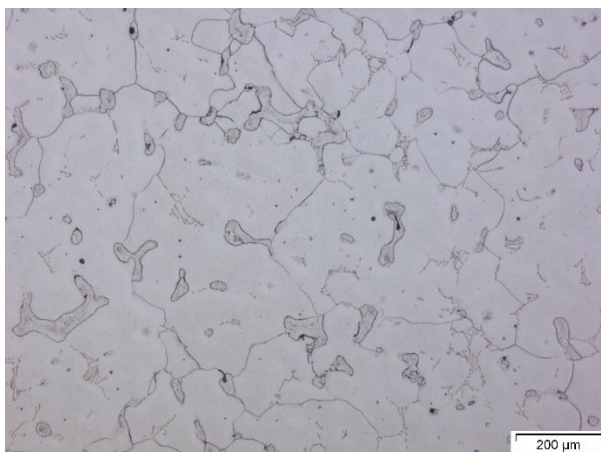
Figure IV-22 : *Austénite résiduelle stabilisée dans le semi-HSS 3 après austénitisation de 1025°C/1h, puis maintien isotherme de 24h à 600°C (Villela) – Les lobules d'austénite secondaire attaque peu marquante de la structure, traduisant présence importante d'austénite résiduelle* **Dureté moyenne 690 ± 59 HV$_{30}$**

IV.3.3. **Corrélations microstructure et propriétés mécaniques**

IV.3.3.i. Contexte et préparation préliminaire

Des essais de compressions ont été réalisés sur l'état traité et optimisé pour l'alliage semi-HSS 3. Cet état a été obtenu après une austénitisation de 20 minutes à 1025°C, suivie d'une trempe cryogénique pour produire un état entièrement martensitique (780 HV$_{30}$ de moyenne en dureté Vickers).

L'allure des cycles thermiques et thermomécaniques est illustrée à la *Figure IV-23*.

L'objectif est de déterminer le comportement mécanique des phases simples (martensite, austénite), dans la perspective de l'implémentation d'un modèle d'endommagement. Ce travail spécifique a fait l'objet d'une thèse déjà publiée (Neira Torres, 2015).

On rappelle que le même type de tests est proposé dans l'Article #5 qui suit, pour l'acier à haut chrome.

IV.3.3.ii. Résultats et discussions sur les essais de compressions

Les courbes contraintes-déformations sont données à la *Figure IV-24.*

La microstructure du semi-HSS 3 soumis à un cycle thermique similaire à celui réalisé pour les essais mécaniques, mais sans appliquer de contraintes, donne une matrice majoritairement bainitique. Après compression à 700°C, on obtient à nouveau une structure bainitique, mais une certaine quantité d'austénite est présente dans la microstructure (*Figure IV-25*). Les régions qui contiennent encore de l'austénite non transformée semblent être localisée la phase dite secondaire, en forme de lobules. Les

Partie A – Article #4 – Current Developments of Alloyed Steels for Hot Strip Roughing Mills: Characterization of High-Chromium Steel and Semi-High Speed Steels. J. Lecomte-Beckers, M. Sinnaeve & J. Tchoufang Tchuindjang. Iron and Steel Technolgy 2 (2012), pp. 33-40

49

mécanismes par lesquels la contrainte mécanique peut inhiber la transformation plutôt que la favoriser, sont largement expliqués et discutés dans l'Article #5.
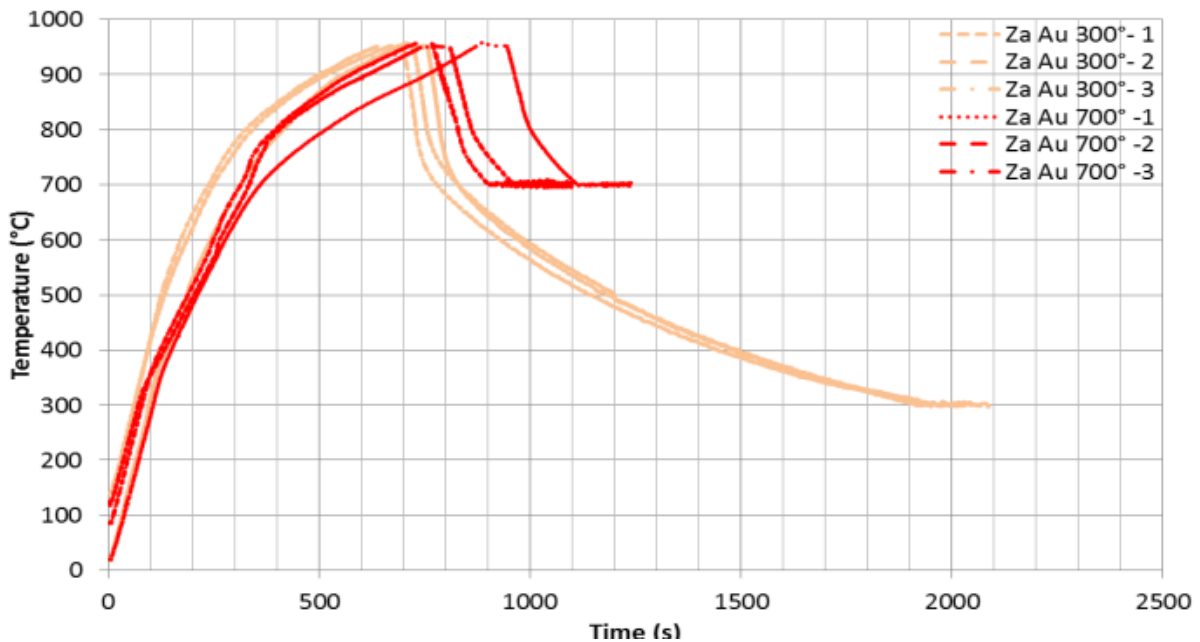
Figure IV-23 : *Allure des cycles thermiques (chauffage/refroidissement) avant essais de compression*
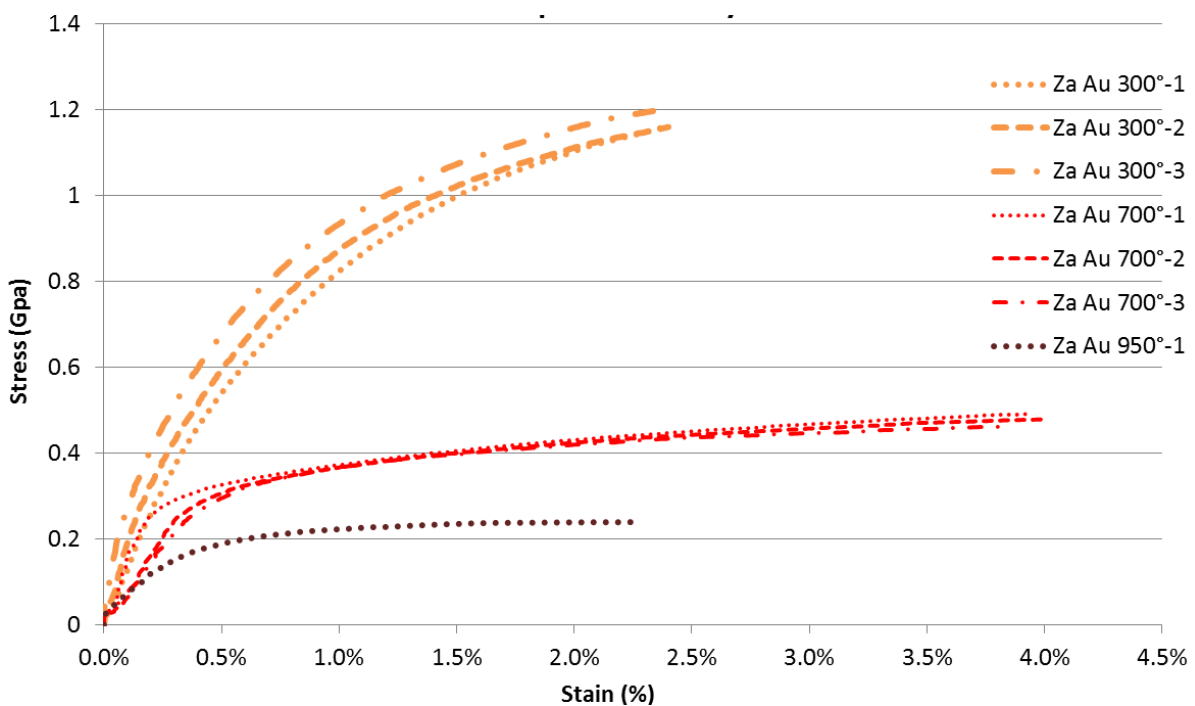
Figure IV-24 : *Courbes contraintes-déformations obtenues sur semi-HSS 3 en partant d'une structure austénitique refroidie avant essai*

Les essais de compression faits sur l'austénite refroidie à plus basse température (300°C) donnent à la fois un durcissement plus important (***Figure IV-24***) et un aspect final différent (***Figure IV-26).*** Cet état semble justifier par la transformation complète des deux austénites, probablement en martensite et en bainite.

La présence de bainite aussi bien lors du refroidissement continu dans le four, qu'après essais de compression à 700°C, confirme la difficulté à former la perlite en refroidissement continu dans le semi-

Partie A – Article #4 – Current Developments of Alloyed Steels for Hot Strip Roughing Mills: Characterization of High-Chromium Steel and Semi-High Speed Steels. J. Lecomte-Beckers, M. Sinnaeve & J. Tchoufang Tchuindjang. Iron and Steel Technolgy 2 (2012), pp. 33-40

50

HSS3. Par ailleurs la bainite qui apparaît à 700°C est certes activée par la contrainte, mais elle peut aussi se former préférentiellement dans une seule des deux phases austénitiques, à savoir celle contenant le moindre carbone. Dans le même temps, la transformation bainitique amorcée sous contrainte à 700°C, ne va pas nécessairement être complète. A contrario, le même phénomène peut se produire lors de l'essai à 300°C, avec toutefois une finalisation des transformations en bainite/martensite.

Figure IV-25 : *Microstructure du semi-HSS 3 après essai de compression de l'austénite à 700°C, illustrant matrice bainitique, avec possible plages d'austénite résiduelle (austénite secondaire en lobules)*
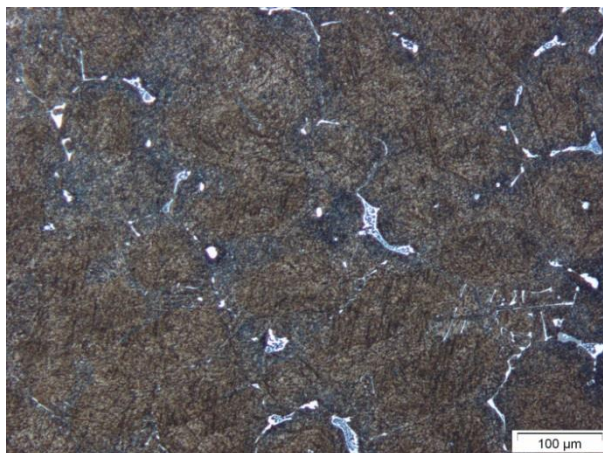
Figure IV-26 : *Microstructure du semi-HSS 3 après essai de compression de l'austénite à 300°C, suggérant transformation complète de la matrice en bainite et surtout en martensite, ce qui justifie l'écrouissage observé expérimentalement*

IV.4. Conclusions

Dans cet article, on caractérise la microstructure de solidification et après transformation en phase solide d'alliages déjà utilisés dans les cages dégrossisseuses d'un train à bandes à chaud (l'acier à haut chrome et le HSS pour dégrossisseurs) et de nouveaux aciers semi-HSS développés pour cette même application, dont l'alliage semi-Hss 3 considéré comme une référence.

Les performances sur laminoir sont comparées, avec un avantage relatif pour le semi-HSS.

Les analyses complémentaires, présentées ci-dessus, mettent en évidence et expliquent le caractère dual de la matrice dans le semi-HSS 3, qui est constituée de deux austénites d'origine et de composition chimique différentes. Ce sont les carbures NbC qui provoquent ces phénomènes tout en générant des retassures du fait de l'interruption de la réaction péritectique.

Il existe donc des effets de ségrégation hérités de la solidification, qui perdurent à l'état solide, et qui ne sont pas modifiées par les traitements thermiques ultérieurs. Ces ségrégations influencent le comportement mécanique de l'alliage. Cependant, il a aussi été établi que seul le retour à l'état liquide peut permettre de restituer une certaine homogénéité, s'il y avait besoin.

On a aussi insisté sur l'influence des éléments d'alliage dans la séquence de solidification, et dans leur distribution chimique, celle-ci influençant fortement la microstructure finale, en comparant les différentes nuances semi-HSS entre elles. La troostite observée dans un des alliages semi-HSS est de type granulaire, et elle résulte d'un phénomène de sursaturation comme cela a déjà été établi précédemment (Article #3). Le comportement mécanique en compression est présenté vu l'impact de la mécanique sur les changements de phases, cependant son analyse est succincte car ceci fera l'objet de l'Article #5.

Partie A – Article #4 – Current Developments of Alloyed Steels for Hot Strip Roughing Mills: Characterization of High-Chromium Steel and Semi-High Speed Steels. J. Lecomte-Beckers, M. Sinnaeve & J. Tchoufang Tchuindjang. Iron and Steel Technolgy 2 (2012), pp. 33-40

51

IV.5. Références

De Mello, J.D.B., Hamar-Thibault, S., Durand-Charre, M., 1985. Eutectoid transformations and precipitation in high carbon tool steels. J Mater Sci 20, 3453–3461. https://doi.org/10.1007/BF01113752

Neira Torres, I., 2015. Modelling of cooling and heat treatment of bimetallic rolling mill rolls. Université de Liège, Liège, Belgique.

Nurbanasari, M., Tsakiropoulos, P., Palmiere, E.J., 2014. On the Solidification of a H23 Tool Steel. Trans Indian Inst Met 67, 935–944. https://doi.org/10.1007/s12666-014-0420-9

Riedl, R., Fischmeister, H.F., 1990. Dendrite arm climb by temperature gradient zone melting during solidification of a high-speed tool steel. Metall Mater Trans A 21, 264–266. https://doi.org/10.1007/BF02656446

Zhao, S.-L., Fan, J.-F., Zhang, J.-Y., Chou, K.-C., Le, H.-R., 2016. High speed steel produced by spray forming. Adv. Manuf. 4, 115–122. https://doi.org/10.1007/s40436-016-0137-6

Partie A – Article #4 – Current Developments of Alloyed Steels for Hot Strip Roughing Mills: Characterization of High-Chromium Steel and Semi-High Speed Steels. J. Lecomte-Beckers, M. Sinnaeve & J. Tchoufang Tchuindjang. Iron and Steel Technolgy 2 (2012), pp. 33-40

52

V. CHAPITRE 5 : PRÉSENTATION ET COMPLÉMENTS D'ÉTUDE SUR L'ARTICLE #5

V.1. Introduction

Cet article traite du travail mené autour d'un modèle d'endommagement multiphasé pour une pièce complexe, à savoir un cylindre bimétallique obtenu par coulée centrifuge. Le métal d'enveloppe est composé d'un acier à haut chrome tandis que le métal de cœur est constitué d'une fonte grise à graphite sphéroïdal. L'implémentation de tels modèles d'endommagement néglige souvent le calcul de la cinétique de transformation sachant que le suivi de chaque phase exigera la détermination de lois de comportement pour chacune . Dans le cas présent, on doit caractériser expérimentalement chaque phase prise séparément, pour produire les paramètres d'entrée du modèle à valider. L'existence de plusieurs phases impose est prise en compte par une loi des mélanges, qui associe la loi de comportement intrinsèque de chacune des phases au prorata de sa proportion dans l'alliage réel.

Seul le matériau d'enveloppe est étudié. En outre, l'article se focalise sur une seule phase : l'austénite. Un essai de compression est réalisé à deux températures distinctes obtenues en refroidissant l'échantillon initialement à l'état d'austénite.

L'originalité de l'article se trouve dans son approche focalisée sur la compréhension des phénomènes métallurgiques qui s'opèrent lors de l'endommagement. Partant de propriétés macroscopiques, telles que la courbe contrainte -déformation plastique, on se propose de descendre jusqu'à une dimension nanoscopique, pour expliquer les différents phénomènes métallurgiques en jeu. Ces derniers sont reliés à la microstructure de l'alliage, en incluant autant les paramètres directement identifiables tels que les carbures de solidification aux joints de grains, les carbures secondaires ou la nature de la matrice dans les grains, que – plus indirectement – les carbures tertiaires nanoscopiques ou les dislocations.

Cette approche apportant des outils de compréhension des mécanismes à différentes échelles, a valu à l'article d'être sélectionné et mis en avant par l'éditeur du journal où il a été publié.[9]

L'analyse de la **solidification** compare les prédictions thermodynamiques et la réalité de la coulée industrielle. La technique expérimentale de l'Analyse thermique différentielle (ATD) permet de faire le lien entre les deux approches. Cette comparaison sert de base pour la première mise en évidence du phénomène de sursaturation.

On aborde aussi les transformations en phase solide, notamment pour mettre en évidence les conditions de la **formation de la troostite** présente dans le brut de coulée industriel, mais difficile à reproduire au laboratoire. On expose aussi les moyens de la caractériser expérimentalement, via des techniques d'analyse telle que la dilatométrie et l'ATD. Une approche de traitement thermique hybride est présentée. Elle montre comment il est possible d'obtenir la **bainite** qui a uniquement été observée via le dispositif de chauffage et de test en compression, mais pas dans l'alliage initial, ni après les traitements thermiques d'optimisation. La technique de l'ATD sert pour former la bainite, tandis que l'EBSD est utilisée pour sa caractérisation.

Les conditions pour la formation de la **martensite** sont aussi présentées, et le **comportement mécanique** de cette phase est discuté, en s'appuyant comme dans l'article, sur des essais de compression à différentes températures. On montre notamment via la dilatométrie et des trempes cryogéniques, comment on peut former et caractériser la martensite et ses points critiques.

---

[9] L'article a été retenu parmi 5 publications de JMEPEG parus au cours de toute l'année 2015, sur des critères de qualité de compréhension et d'excellence. Cette sélection rend l'article libre d'accès.

Partie A – Article #5 – Phase Transformations and Crack Initiation in a High-Chromium Cast Steel Under Hot Compression Tests. . Tchoufang Tchuindjang, I. Neira Torres, P. Flores, A. M. Habraken & J. Lecomte-Beckers. J. of Materi Eng and Perform 24 (2015), pp. 2025-2041

53

Enfin, on montre l'effet de la microstructure sur le comportement de l'alliage en **traction**. Et en revenant sur le **phénomène de sursaturation** avec une fragilisation observée expérimentalement dans la matière, on propose une interprétation métallurgique du **phénomène de bris de cylindre**, dont l'étude a justifié l'élaboration des modèles d'endommagement déjà présentés dans le travail d'Ingrid NEIRA (Neira Torres, 2015).

V.2. Bref rappel sur le contexte

Les pièces étudiées sont des cylindres bimétalliques obtenus par coulée centrifuge verticale. Ces pièces représentent des cylindres de laminoir à chaud, utilisés dans les cages dégrossisseuses. Le procédé d'élaboration qui est propre à la société Marichal Ketin reste la coulée centrifuge verticale, déjà évoquée dans les articles #2 et #3.

Les échantillons sont prélevés dans le métal d'enveloppe, sous forme de barreaux. Les sections étudiées sont orientées perpendiculairement à l'axe de symétrie du cylindre. La zone d'intérêt pour le prélèvement des éprouvettes ayant servi aux analyses diverses (thermiques, métallographiques) et à la caractérisation des propriétés mécaniques est localisée à une profondeur de 40 mm environ, entièrement comprise dans le métal d'enveloppe.

Les résultats principaux de l'article ont été obtenus dans le cadre du projet SOUBIRO, associé à la thèse de doctorat (Neira Torres, 2015).

Dans ce qui suit, on ajouter des résultats obtenus sur les mêmes matières et qui apportent un complément d'informations en lien avec les trois grands thèmes de la première partie de la thèse. Il s'agit de la solidification, des transformations en phase solide, et des corrélations microstructure-propriétés. Le **Tableau V-1** mentionne les points additionnels (en rouge).

Solidification	Solid State Transformations	Mechanical properties and related damage mechanisms
• Solidification sequence from DTA[10] tests and comparison with thermodynamic simulations and spin casting	• Enhancement of Intragranular troostite occurrence from supersaturation peritectic austenite within the as-received conditions (under high cooling rates) + both DTA and dilatometry characterization • Enhancement of conditions for bainite occurrence with validation under DTA test • Martensitic transformation (Ms) under DTA and dilatometry tests, and determination of critical points including cryogenic test	• Orowan mechanism influencing High compression strength • Internal embrittlement enhancement Intergranular cracking under tensile tests

Tableau V-1: Rappel des thématiques ajoutées pour compléter l'étude

---

[10] Differential Thermal Analysis (DTA), notée suivant l'abréviation française ATD dans la suite du texte

Partie A – Article #5 – Phase Transformations and Crack Initiation in a High-Chromium Cast Steel Under Hot Compression Tests. . Tchoufang Tchuindjang, I. Neira Torres, P. Flores, A. M. Habraken & J. Lecomte-Beckers. J. of Materi Eng and Perform 24 (2015), pp. 2025-2041

54

V.3. Résultats complémentaires

V.3.1. Solidification et hétérogénéités de structure

V.3.1.i. Simulations en conditions d'équilibre et de pseudo-équilibre

Une séquence de solidification simulée par Thermo-Calc ® via le modèle de Scheil-Gulliver (SG) a été établie (**Figure V-1**). Elle considère des conditions de pseudo-équilibre, que l'on compare avec des conditions d'équilibre pur (**Figure V-2**). Cette simulation donne comme premier solide l'austénite γ (FFC_A1#1), et comme dernier eutectique le carbure M_6C. Les températures de formation de ces deux phases constituent respectivement le liquidus (1395°C) et le solidus (1195C°) théoriques du HCCS. On peut noter que le solidus obtenu en conditions d'équilibre pur, soit 1240°C, est encore plus haut que celui donné par le modèle SG. La séquence de solidification en conditions d'équilibre est aussi plus courte et moins élaborée qu'avec le modèle SG.
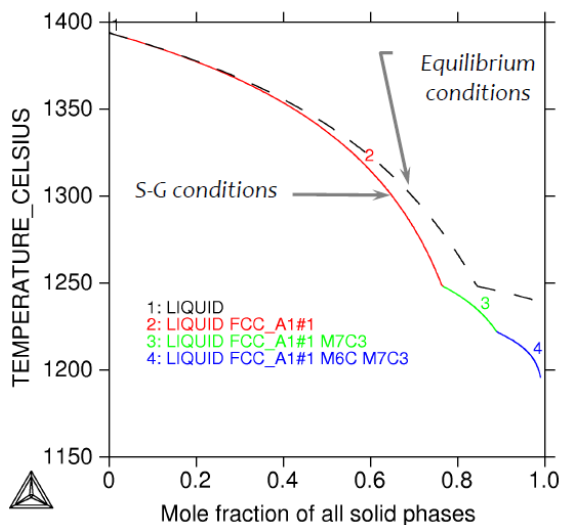

Figure V-1 : *Séquence et intervalle de solidification de l'alliage HCCS d'après modèle de Scheil-Gulliver, et comparaison avec conditions d'équilibre (1er solide = γ)*
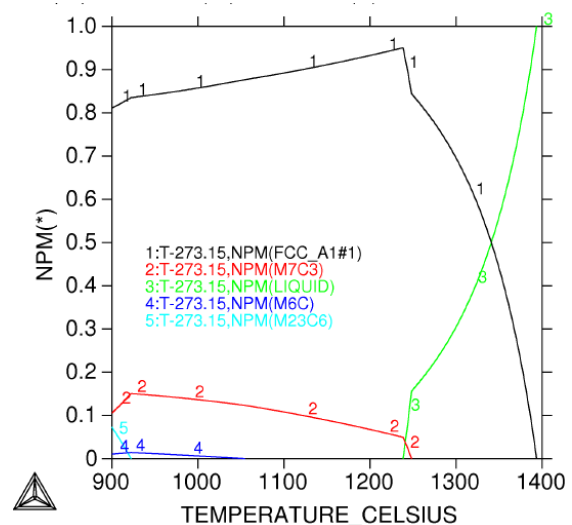
Figure V-2 : *Evolution de la proportion des phases depuis le liquide jusque 900°C en conditions d'équilibre pur pour HCCS*

V.3.1.ii. Essais ATD, en conditions hors équilibre

Les différents thermogrammes obtenus en ATD sont donnés à la **Figure V-3**. La comparaison des conditions de pseudo-équilibre avec les résultats expérimentaux obtenus par ATD révèle des différences notables. En effet, l'ATD montre que le 1er solide est la ferrite δ, et la réaction péritectique produisant l'austénite γ se produit juste après la formation de cette ferrite δ, en réduisant considérablement la période de croissance de cette dernière. Les deux pics relatifs à la formation des deux phases sont en effet rapprochés en ATD. Le liquidus prédit par la simulation (**Figure V-1**) reste cependant proche de celui observé expérimentalement. Ce résultat est attribué au fait que le mode de solidification est de type hétérogène, et donc peu tributaire de la surfusion. Par contre le solidus en ATD est plus bas, à 1145°C.

Le liquidus observé en ATD n'est pas influencé par la vitesse de refroidissement (**Figure V-3**). Par contre, la taille des grains diminue quand on augmente la vitesse de solidification (refroidissement). Cet effet est illustré par des essais ATD réalisés en refroidissement continu à deux vitesses (20°C/min et 5°C/min). Il y a effectivement une augmentation de la taille des grains quand on diminue la vitesse de solidification de 20°C/min (**Figure V-4**) à 5°C/min (**Figure V-5**). Comme déjà illustré avec les compléments de l'Article #1, le liquidus sur les thermogrammes ATD ne change pour ces deux vitesses.
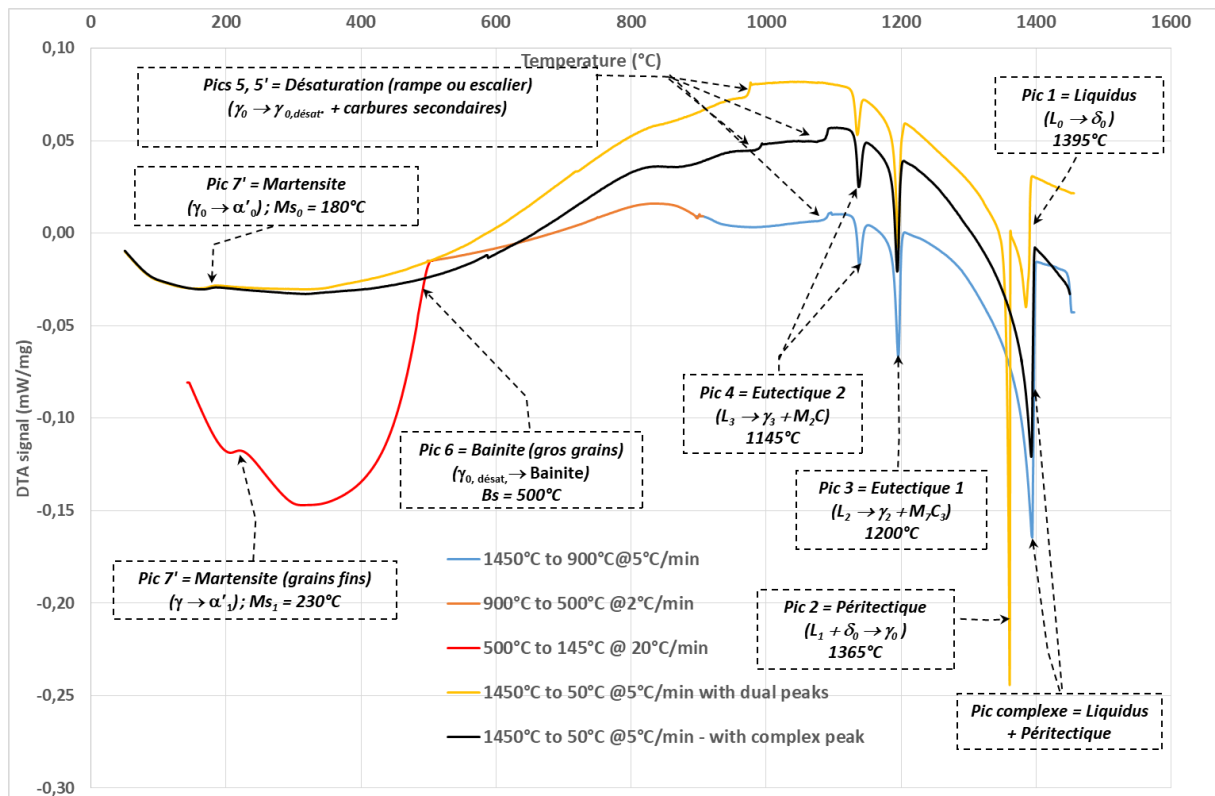
Figure V-3 : *Séquence de solidification et transformations subséquentes en phase solide, à refroidissement constant (formationde martensite) ou variable (pour la formation de bainite) surAcier Haut Chrome: Pic double en début de solidification (ferrite δcomme premier solide immédiatement suivi du péritectique) pour grain cellulaire, carbures eutectiques intercellulaire (M₇C₃ et M₂C), escaliers pour précipitation secondaire intracellulaire (première désaturation dans le grain austénitique), et transformation en phase solide de la matrice cellulaire (martensite, ou bainite si refroidissement variable, avec existence d'austénite résiduelle non transformée)*
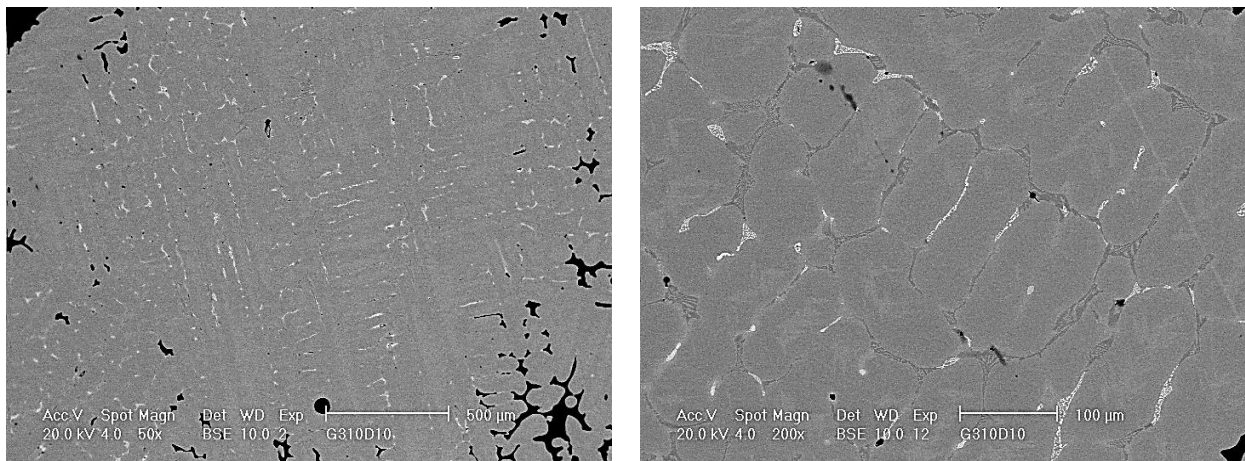
Figure V-4 : *Vue générale (à gauche) et vue zoomée (droite) de la microstructure du HCCS après solidification par ATD avec une vitesse de refroidissement constante de 20°C/min ; carbures eutectiques aux joints de grains et présence de martensite (lattes claires) dans les grains encore composés d'austénite résiduelle (SEM- BSE)*

Partie A – Article #5 – Phase Transformations and Crack Initiation in a High-Chromium Cast Steel Under Hot Compression Tests. . Tchoufang Tchuindjang, I. Neira Torres, P. Flores, A. M. Habraken & J. Lecomte-Beckers. J. of Materi Eng and Perform 24 (2015), pp. 2025-2041

56

Figure V-5 : Vue générale (à gauche) et vue zoomée (droite) de la microstructure du HCCS après solidification par ATD avec une vitesse de refroidissement constante de 5°C/min ; carbures eutectiques aux joints de grains, avec taille de grains plus grossière qu'avec refroidissement à 20°C/min (SEM- BSE)
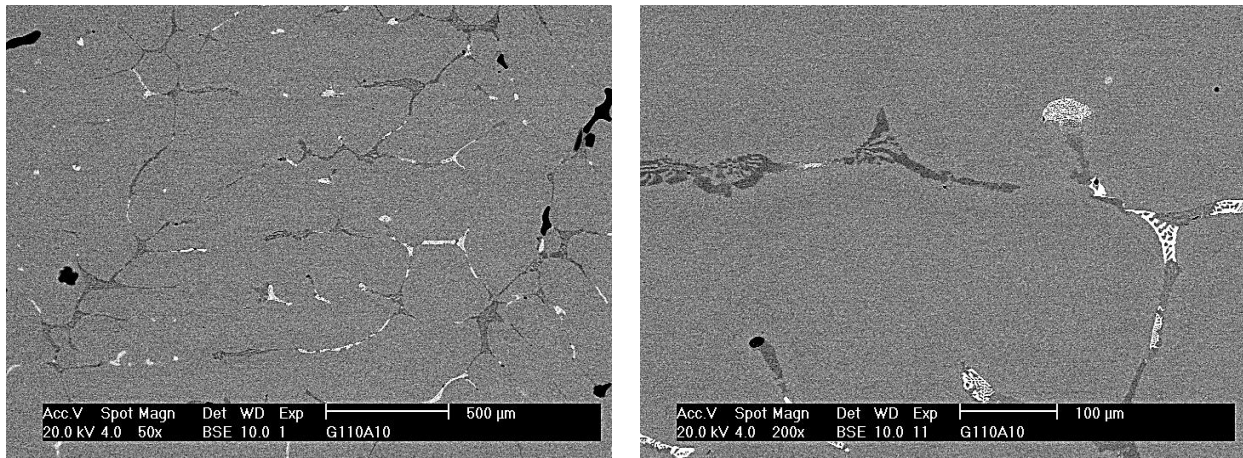
V.3.1.iii. Brut de coulée industrielle

La microstructure du brut de coulée industrielle est donnée aux **Figure V-6** et **Figure V-7**. Outre la martensite et l'austénite résiduelle majoritaires, il existe de la troostite dans certains grains. Les carbures eutectiques de deux types sont situés aux joints de grains.

La comparaison entre échantillons ATD solidifiés aux deux vitesses de 20°C/min et 5°C/min et l'état brut de coulée industrielle montre que ce dernier a une taille de grains encore plus petite (**Figure V-6**). Ce résultat découle de la vitesse de refroidissement lors de la coulée centrifuge, qui est légèrement supérieure à 200°C/min pour les couches superficielles de l'enveloppe en HCCS (**Figure V-9**) qui ont été considérées pour l'étude.

Le péritectique se marque davantage dans le brut de coulée centrifuge que dans les échantillons ATD. Ce marquage est illustré par les fins carbures en liseré formant un sous-joint distinct du joint cellulaire où se trouvent les carbures eutectiques (**Figure V-7**). Il correspond à la transformation péritectique, qui est la fin de la réaction eutectique, et qui se produit dans les zones où il n'y a plus de liquide sans participation de la phase liquide, tel que mentionné pour le semi-HSS de l'Article #4. Il s'agit d'une réaction en phase solide avec une phase-mère unique, soit la ferrite δ résiduelle en régression, et deux produits de réactions : l'austénite γ et des carbures dits secondaires, qui forment un liseré.
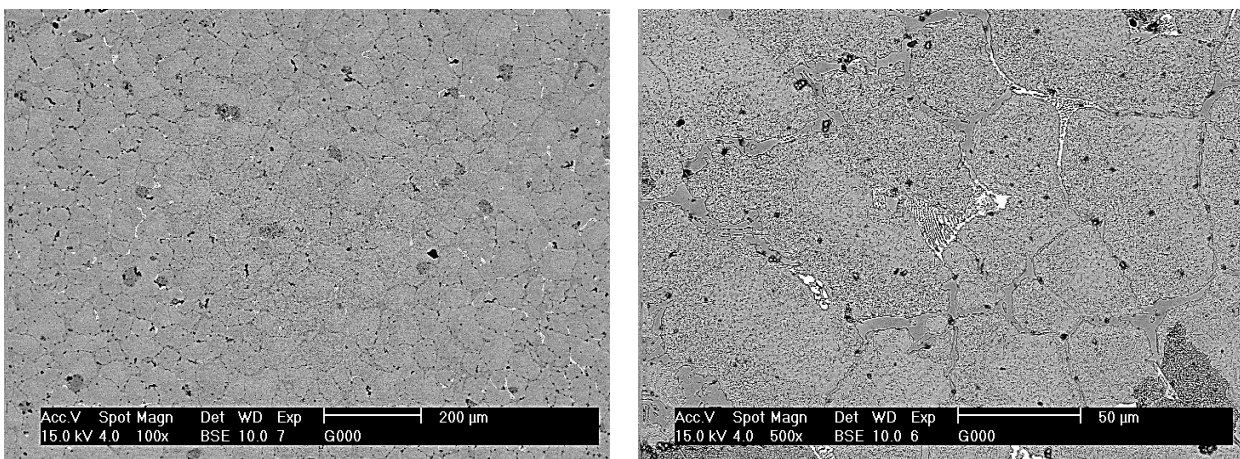
Figure V-6 : Vue générale (à gauche) et vue zoomée (droite) de la microstructure du HCCS brut de coulée industrielle (près de la surface de l'enveloppe), faite de martensite et d'austénite résiduelle, carbures eutectiques aux joints de grains, et présence de troostite intragranulaire (phase gris foncé) dans certains grains ; la taille des grains est plus fine qu'en ATD (SEM- BSE)

Partie A – Article #5 – Phase Transformations and Crack Initiation in a High-Chromium Cast Steel Under Hot Compression Tests. . Tchoufang Tchuindjang, I. Neira Torres, P. Flores, A. M. Habraken & J. Lecomte-Beckers. J. of Materi Eng and Perform 24 (2015), pp. 2025-2041

57

Figure V-7 : *Aperçu d'une zone avec des nodules de troostite intragranulaire (à gauche, mode SE du SEM) illustrant la présence du liseré de carbures secondaires formant un sous-joint de grain caractéristique du marquage de la fin de la transformation péritectique dans le matériau brut de coulée centrifuge ; Contraste chimique (à droite mode BSE), indiquant les carbures eutectiques M_7C_3 (gris) et M_2C (blanc)*

V.3.2. **Transformations en phase solide**

V.3.2.i. Formation de troostite par recuit isotherme en coulée centrifuge

La troostite est présente dans l'état brut de coulée du métal d'enveloppe du cylindre HCCS obtenu par coulée centrifuge verticale, avec une proportion apparente diminue avec la profondeur (**Figure V-8**). Sa présence est révélatrice de phénomènes de sursaturation survenus lors de la solidification (voir l'introduction ci-dessus et l'Article #3).
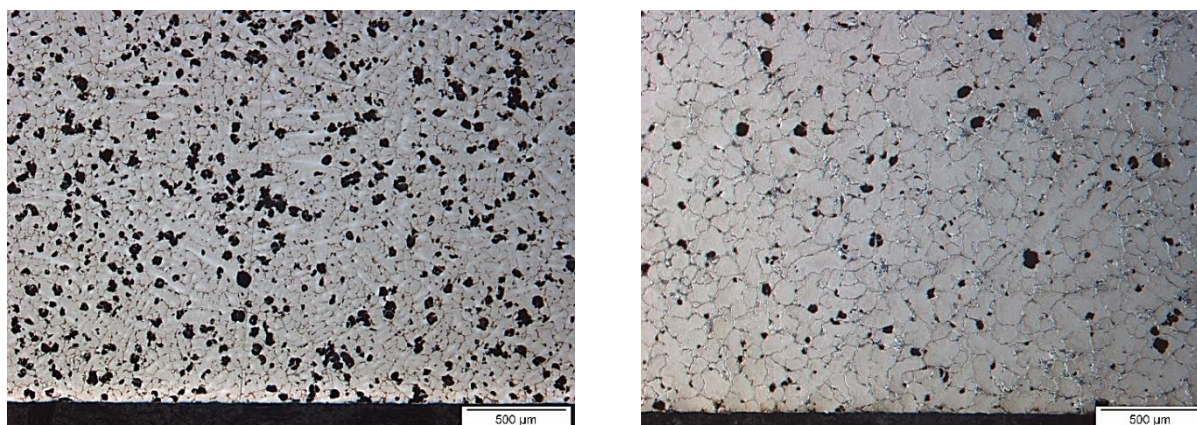
Figure V-8 : *Aperçu de l'évolution de la taille du grain entre la surface de l'enveloppe (à gauche) et une région plus profon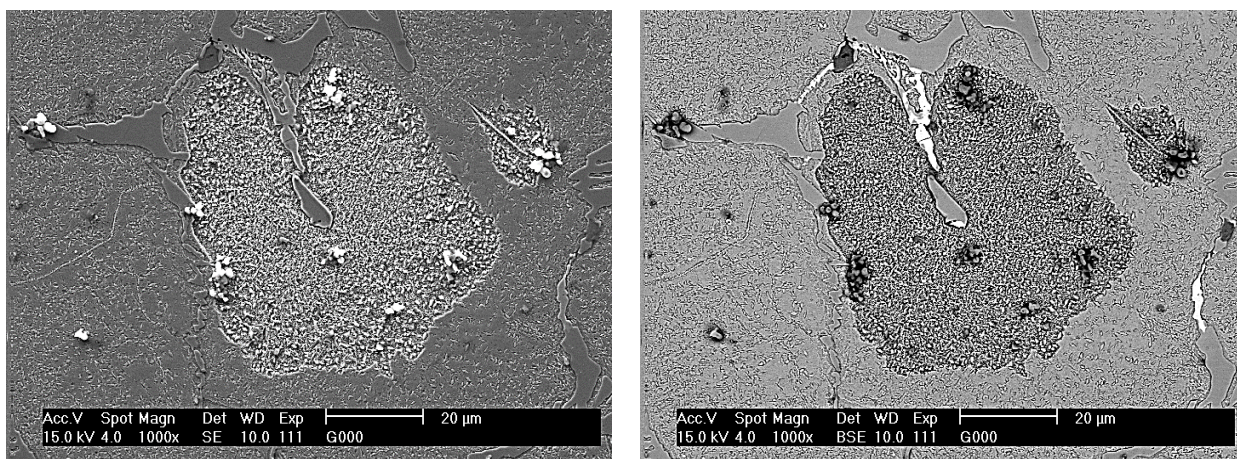de (à droite) dans un barreau d'acier à Haut Chrome à l'état brut de coulée (matrice composée d'austénite résiduelle et de martensite, avec quelques plages de troostite). La proportion de troostite diminue aussi avec la profondeur (Nital) – Dureté moyenne 224 ± 29 HV30*

Le profil d'évolution de la température dans l'enveloppe a été obtenu à l'aide d'une simulation EF faite via le logiciel Experto ViewCast® développé par Sirris (**Figure V-9**). Les points de calibration avec thermocouples sont placés dans les couches du moule.

A partir de la simulation thermique, il apparaît que la vitesse moyenne de refroidissement à la surface de la table (enveloppe du cylindre de travail) est d'environ 216°C/min, quand on la calcule dans l'intervalle de solidification (**Figure V-9**). Cette vitesse diminue fortement avec la profondeur de l'enveloppe, pour atteindre 20°C/min à mi-profondeur. En outre, il existe une discontinuité de la vitesse de refroidissement dans le métal d'enveloppe, qui survient au moment où on coule le métal de cœur et qui correspond à une augmentation de température suivie d'un refroidissement. Le métal d'enveloppe subit donc dans les couches superficielles en particulier, un recuit de type pseudo-

Partie A – Article #5 – Phase Transformations and Crack Initiation in a High-Chromium Cast Steel Under Hot Compression Tests. . Tchoufang Tchuindjang, I. Neira Torres, P. Flores, A. M. Habraken & J. Lecomte-Beckers. J. of Materi Eng and Perform 24 (2015), pp. 2025-2041

58

isotherme, dont la durée et la température[11] sont plus importantes que pour les couches plus profondes.

Les différences de vitesses suivant la profondeur d'enveloppe justifient les variations dans la taille du grain. L'ordre de grandeur de la vitesse obtenue à mi-profondeur correspond au maximum réalisable en ATD, soit 20°C/min. Près de la surface de l'enveloppe, la vitesse de solidification est suffisamment élevée pour qu'on considère que les grains plus petits présenteront un effet de sursaturation. Le recuit pseudo isotherme dans ces zones sera donc de nature à favoriser la formation de la troostite.
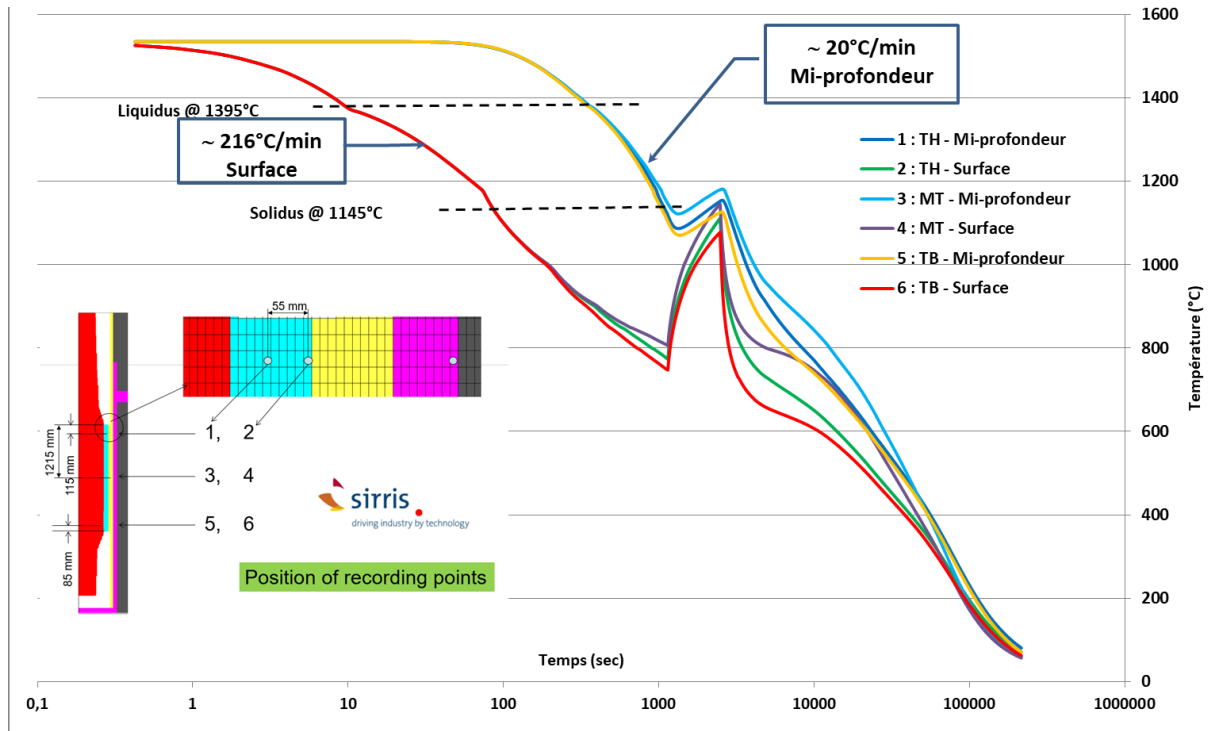

Figure V-9 : Evolution de la température dans le métal d'enveloppe pendant le refroidissement d'un cylindre de type HCCS lors d'une coulée centrifuge (métal de cœur coulé après le métal d'enveloppe) déterminée par simulation EF avec Experto ViewCast ® (Sirris); estimation des vitesses moyennes de refroidissement lors du passage dans l'intervalle de solidification

V.3.2.ii. Détermination des points de transformation martensitique

La martensite peut être formée dans l'alliage HCCS après un refroidissement à l'air calme, après homogénéisation de la matrice. Conformément à l'approche déjà présentée dans les articles précédents sur l'optimisation du traitement thermique (au sens de la dureté), c'est 1025°C qui a été retenu comme température pour HCCS. La trempe à l'air calme donne une dureté moyenne de 805 ± 9 HV30 tandis que celle réalisée dans l'azote liquide produit une dureté plus élevée de 820 ± 5 HV30. La trempe cryogénique est utilisée pour être sûr de terminer la transformation martensitique, comme cela est discuté ci-après.

Une analyse dilatométrique a permis de mettre en évidence l'existence de points de début de transformation martensitique distincts, qui ont été respectivement attribués aux grains d'austénite pour le premier, et aux zones sans précipités (appelées PFZ) situées près des joints de grains pour le second (**Figure V-10**). L'augmentation de la température d'austénitisation conduit à un abaissement des points M_s, lié à un changement de la composition chimique des phases-mères. On note en effet une augmentation de la teneur en carbone par effet de dissolution des fins carbures.

---

[11] L'estimation faite sur les courbes simulées donne les caractéristiques suivantes de la discontinuité de température sur TB (6) : 32'' passées pour monter de 750°C à 1067°C avant de redescendre à nouveau à 750°C. Au point 4, on remonte de 811°C à 1144°C avant de redescendre à nouveau à 804°C en 58''.

Partie A – Article #5 – Phase Transformations and Crack Initiation in a High-Chromium Cast Steel Under Hot Compression Tests. . Tchoufang Tchuindjang, I. Neira Torres, P. Flores, A. M. Habraken & J. Lecomte-Beckers. J. of Materi Eng and Perform 24 (2015), pp. 2025-2041
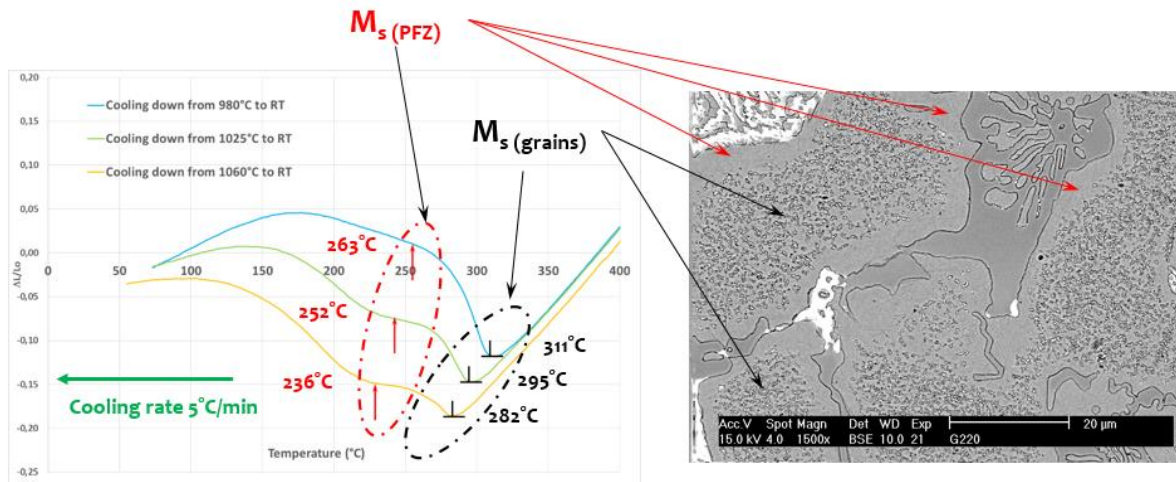
59

Figure V-10 : *Détermination du point de début de transformation martensitique (M$_S$) à partir de différentes températures d'austénitisation par analyse dilatométrique sur HCCS – (à droite) vue de la microstructure d'un HCCS après austénitisation à 1025°C et refroidissement à l'air, montrant les carbures secondaires dans les grains, l'existence de zones sans précipités (Precipitation Free Zone ou PFZ) près des joints de grains, ces deux zones définissant des points M$_s$ distincts*

Un essai de trempe cryogénique avec suivi de température à cœur de l'éprouvette-test a permis de déterminer en plus du point M$_s$, le point M$_f$ qui caractérise la fin de la transformation martensitique (**Figure V-11**). On note que la microstructure obtenue après la trempe cryogénique est caractérisée par une précipitation massive de fins carbures dits tertiaires dans la matrice martensitique sursaturée (**Figure V-12**), phénomène qui survient quand on passe sous le point M$_f$, et qui se poursuit quand on remonte à la température ambiante (Gill et al., 2011).
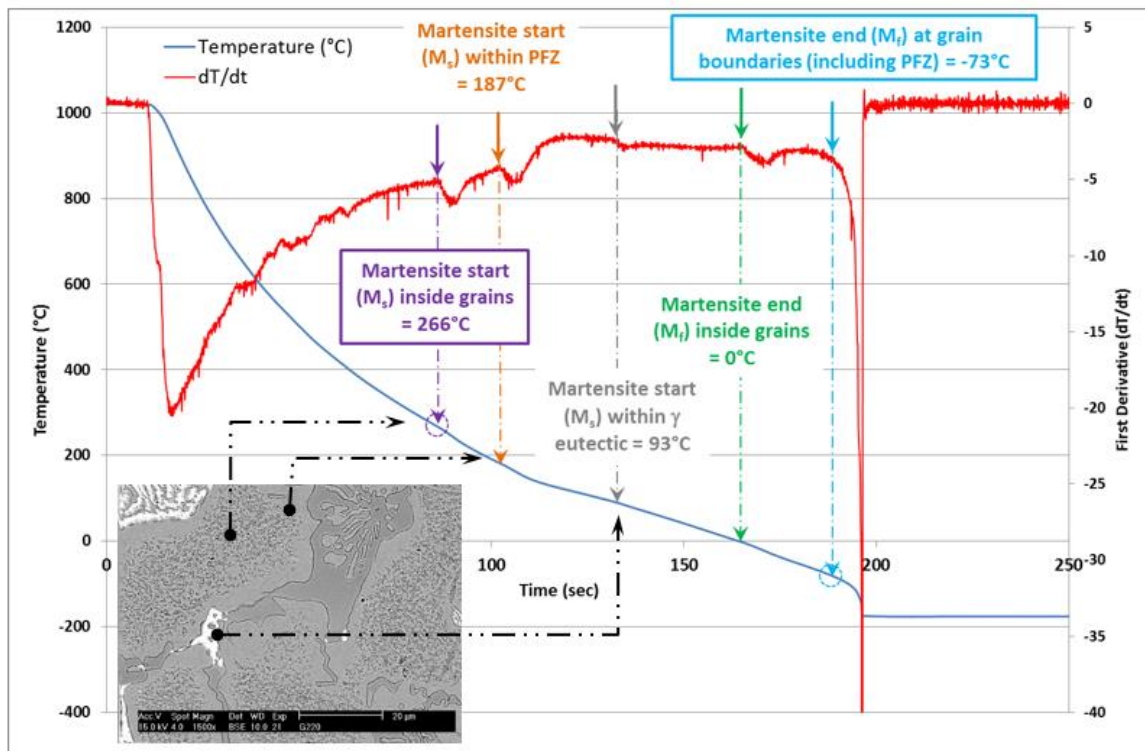
Figure V-11 : *Points critiques de début et de fin de transformation martensitique, dans les grains et aux joints de grains (PFZ) pour HCCS austénitisé à 1025°C et trempé dans l'azote liquide*

Partie A – Article #5 – Phase Transformations and Crack Initiation in a High-Chromium Cast Steel Under Hot Compression Tests. . Tchoufang Tchuindjang, I. Neira Torres, P. Flores, A. M. Habraken & J. Lecomte-Beckers. J. of Materi Eng and Perform 24 (2015), pp. 2025-2041

60

V.3.3. **Corrélations microstructures- propriétés mécaniques, en lien avec la sursaturation**

V.3.3.i. Compressions sur un échantillon en état martensitique

Des essais de compressions à différentes température, ont été réalisés sur des échantillons trempés dans l'azote liquide, pour caractériser la martensite en vue d'élaborer le modèle d'endommagement (Neira Torres, 2015). Les résultats obtenus avant rupture et pour de faibles niveaux de déformation sont donnés à la **Figure V-12**. La présence de carbures fins en forte proportion dans la matrice martensitique justifie le niveau de contrainte élevé, en accord avec le mécanisme d'Orowan (Ghasemi-Nanesa and Jahazi, 2014).

Figure V-12 : *Courbes σ-ε en compression sur HCCS martensitique après trempe cryogénique et aperçu de la microstructure contenant une proportion importante de fins carbures tertiaires*

V.3.3.ii. Fragilisation aux joints de grains lors du traitement thermique

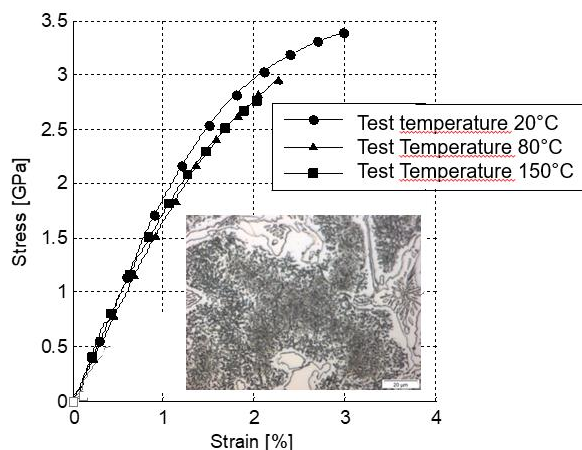On a observé sur trois éprouvettes de contrôle prélevées dans des barreaux traités thermiquement[12], des fissures en réseau continu (**Figure V-13, Figure V-14**). Le cas de l'échantillon traité à 1025°C/60' puis refroidi à l'air est présenté. Le réseau de fissures est apparu sur la section après polissage.
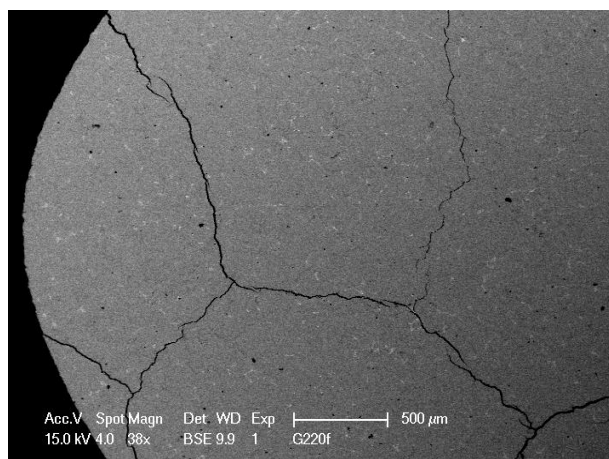
Figure V-13 : *Vue générale du réseau de fissures sur la section polie d'un échantillon HCCS après traitement thermique (1025°C/60 sec /Air) (MEB-BSE)*
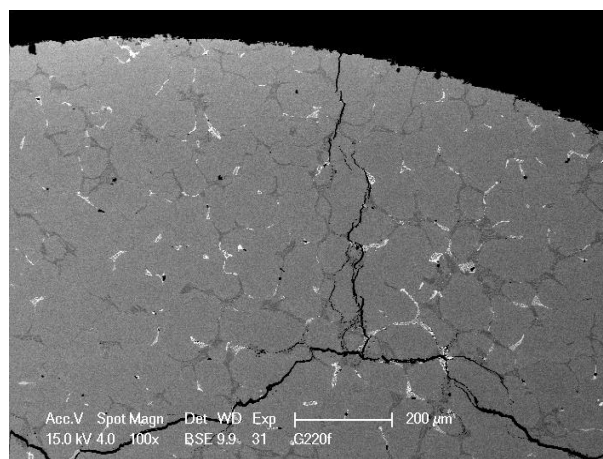
Figure V-14 : *Autre zone de l'échantillon HCCS présentant des fissures. Les carbures eutectiques sont clairement visibles avec leur contraste différent de la matrice, soit les M_2C (blancs) et les M_7C_3 (gris foncé)*

---

[12] Les éprouvettes ont été prélevées à la même profondeur des barreaux (1 cm de la surface), et elles ont un diamètre de 10 mm. Il s'agit des barreaux de la taille de ceux présentés dans l'article, qui ont subi les traitements suivants : 980°C/20'/Air, 980°C/6'/Air, 1025°C/60'/Air et 1060°C/180'/Air.

Partie A – Article #5 – Phase Transformations and Crack Initiation in a High-Chromium Cast Steel Under Hot Compression Tests. . Tchoufang Tchuindjang, I. Neira Torres, P. Flores, A. M. Habraken & J. Lecomte-Beckers. J. of Materi Eng and Perform 24 (2015), pp. 2025-2041

61

Le réseau de fissures se répartit en suivant les joints de grains, qui peuvent correspondre aux grains primaires d'austénite. Ceux-ci sont en effet plus grands que les cellules marquées chacune par des carbures eutectiques sur leur contour (**Figure V-14**). L'observation des ramifications des fissures montre que celles-ci prennent naissance sur et dans le voisinage direct des carbures M7C3, en formant des micro-vides disjoints, qui coalescent ensuite, pour produire une fissure (**Figure V-15** à **Figure V-17**).
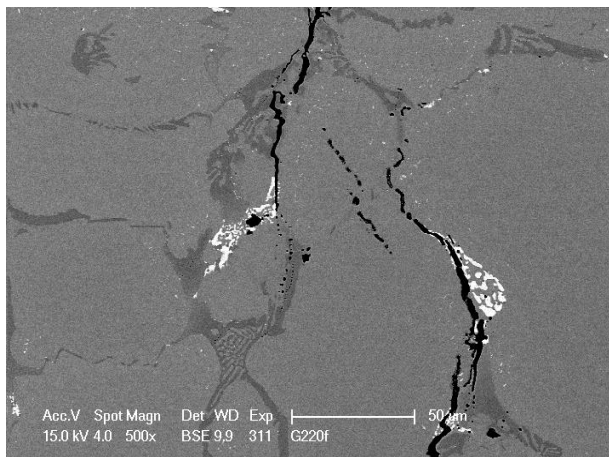
Figure V-15 : Aperçu d'une région avec ramification de fissures (propagation) alignées suivant le réseau de carbures
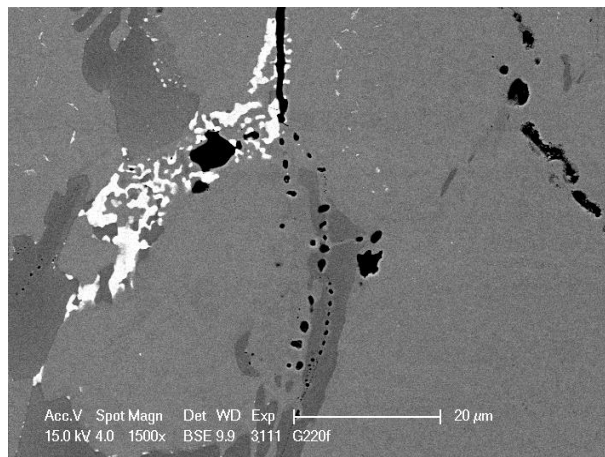
Figure V-16 : Zoom sur la fissure montrant clairement la présence de cavités dans le carbure (M_7C_3), qui préfigurent la propagation de la fissure
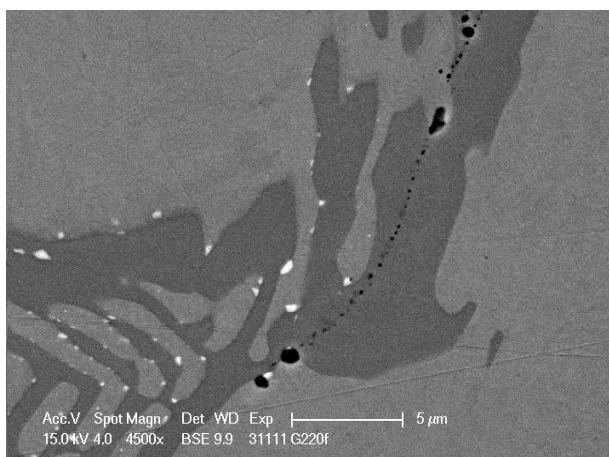
Figure V-17 : Autre zone avec cavités dans carbure M_7C_3 (à gauche) et zoom montrant existence de cavités sur le carbure lui-même, et à proximité du carbure (à droite)
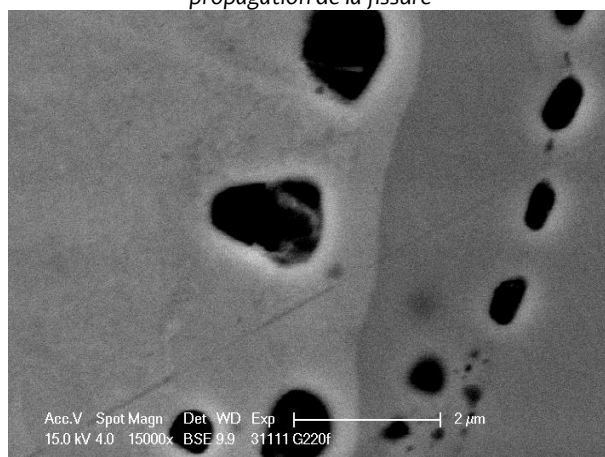
La présence des fissures observées dans l'alliage HCCS répond à au moins deux des quatre critères repris par Briant et Banerji dans leur revue générale sur les fissures intergranulaires dans les aciers (Briant and Banerji, 1978). Ces critères sont les suivants :

- La présence de phases secondaires aux joints de grains ;
- L'impact des traitements thermiques causant les ségrégations d'impuretés aux joints de grains sans toutefois provoquer de précipitation observable ;
- L'action de l'environnement ;
- La combinaison des contraintes (locales et externes) avec la haute température.

En plus de ces critères généraux sur la fissuration intergranulaire, certains phénomènes spécifiques sont susceptibles de conduire à un endommagement similaire. Il s'agit notamment de la fissuration au réchauffage surtout dans les joints soudés (« Intergranular Reheat Cracking ») (Briant and Banerji, 1978; Chauvy and Pillot, 2010; Dhooge and Vinckier, 1987; Fan et al., 2019; Gotoh, 1993), de la fissuration dans le

puits de ductilité (« Ductility Dip Cracking ») (Noecker and Dupont, 2009; Ramirez and Lippold, 2004), de la fragilisation ou revenu (« Temper Embrittlement ») (Mulford et al., 1976; Takayama et al., 1980; Viswanathan, 1971), des ségrégations d'impuretés aux joints de grains (Olson et al., 1983), et enfin de la cavitation au fluage (George et al., 1987).

Dans le cas du HCCS, on rappelle qu'il contient des carbures aux joints de grains. En outre, son état de sursaturation qui induit déjà la formation de troostite, est aussi susceptible de générer des contraintes résiduelles internes. Pour les impuretés éventuelles, le phosphore et le soufre sont réputés ségréger aux joints de grains, le phosphore pouvant rester libre puisque le soufre se fixe à Mn pour former des inclusions (sulfures MnS) qui sont présentes dans le HCCS.

On en déduit donc que l'alliage HCCS peut être le siège d'un endommagement pendant une période de chauffage, un phénomène en lien avec son état de sursaturation. Cet endommagement peut provoquer une fissuration intergranulaire comme celle qui a été observée expérimentalement, après traitement thermique.

V.3.3.iii. Tractions sur le brut de trempe

Des essais de tractions ont été réalisés sur des éprouvettes HCCS dans l'état brut de trempe, à température ambiante (**Figure V-18**), à 150°C, à 300°C et à 500°C (**Figure V-19**). Le faciès de rupture est de type fragile intergranulaire. Ce n'est qu'à 500°C qu'on observe quelques zones ductiles, très minoritaires.

Figure V-18 : *Vue générale et vues zoomées illustrant la rupture intergranulaire sur l'éprouvette HCCS trempée et testée en traction à température ambiante*

Partie A – Article #5 – « Phase Transformations and Crack Initiation in a High-Chromium Cast Steel Under Hot Compression Tests. . Tchoufang Tchuindjang, I. Neira Torres, P. Flores, A. M. Habraken & J. Lecomte-Beckers. J. of Materi Eng and Perform 24 (2015), pp. 2025-2041
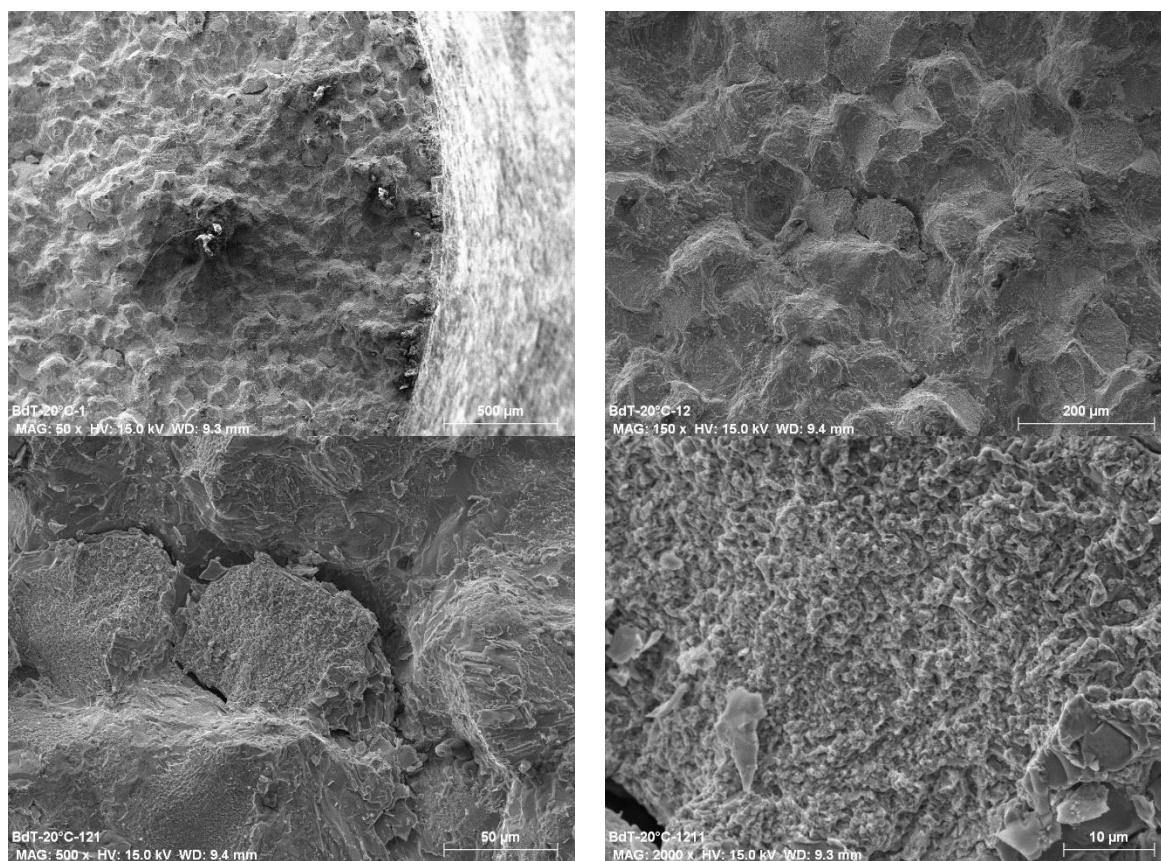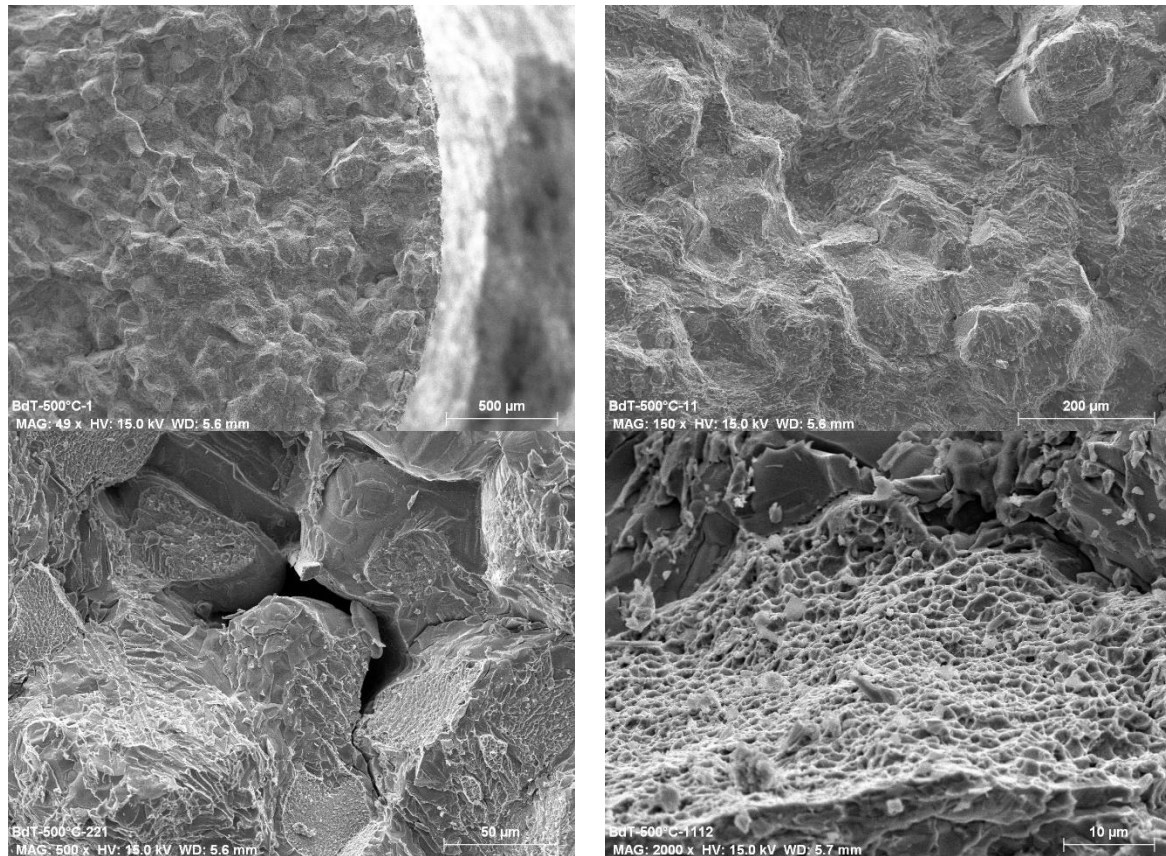
63

Figure V-19 : *Vue générale et vues zoomées illustrant la rupture intergranulaire sur l'éprouvette HCCS trempée et testée en traction à 500°C*

V.3.3.iv. Complément à l'analyse par éléments finis du bris du cylindre bimétallique HCCS-Fonte grise nodulaire

Les constatations précédentes apportent des éléments complémentaires à l'analyse macroscopique faite par (Torres et al., 2015), en appliquant un modèle d'endommagement au refroidissement après coulée du cylindre (ou PCC) suivi par le traitement thermique (revenu à 500°C ou THT). La simulation avait prédit une rupture dans le métal de cœur pendant le refroidissement après coulée (Post Casting Cooling ou PCC), suivie par une propagation de la fissure dans l'enveloppe durant le THT, la propagation étant arrêtée près de la surface par les régions où les contraintes sont en compression.

En tenant compte des observations sur la sursaturation intrinsèque du HCCS, qui se marque dans les grains et qui n'est pas totalement supprimée à la température ambiante, on note que le matériau possède aussi des joints de grains primaires fragilisés, toujours en lien avec le phénomène de sursaturation.

V.4. Conclusions

Dans l'Article #5, on caractérise les mécanismes d'endommagement en relation avec la microstructure. Les paramètres qui influencent l'initiation de la rupture sont ainsi mis en évidence. L'analyse est à la fois multi-échelle et pluridisciplinaire, de sorte que les corrélations établies sont relativement extensives.

Un complément d'informations est apporté dans le texte introductif, qui met en avant un autre aspect du matériau HCCS qui est responsable à la fois de ses propriétés améliorées suivant certains types d'essais, mais aussi de sa fragilisation interne intrinsèque vis-à-vis d'autres aspects. Il s'agit de la sursaturation qui est illustrée par la troostite.

Partie A – Article #5 – Phase Transformations and Crack Initiation in a High-Chromium Cast Steel Under Hot Compression Tests. . Tchoufang Tchuindjang, I. Neira Torres, P. Flores, A. M. Habraken & J. Lecomte-Beckers. J. of Materi Eng and Perform 24 (2015), pp. 2025-2041

64

V.5. Références

Briant, C.L., Banerji, S.K., 1978. Intergranularfailure in steel: the role of grain-boundary composition. International Metals Reviews 23, 164–199. https://doi.org/10.1179/imtr.1978.23.1.164

Chauvy, C., Pillot, S., 2010. Prevention of Weld Metal Reheat Cracking During Cr-Mo-V Heavy Reactors Fabrication. Presented at the ASME 2009 Pressure Vessels and Piping Conference, American Society of Mechanical Engineers Digital Collection, pp. 243–251. https://doi.org/10.1115/PVP2009-78144

Dhooge, A., Vinckier, A., 1987. Reheat cracking—A review of recent studies. International Journal of Pressure Vessels and Piping 27, 239–269. https://doi.org/10.1016/0308-0161(87)90012-3

Fan, Z.D., Zhang, Z.B., Ma, Y.C., Ma, J.M., Niu, K., Liu, C.X., 2019. Mechanism of intergranular reheating crack in butt-welded joint of 12Cr1MoV tube served for 40,000 hours. Materials at High Temperatures 36, 430–436. https://doi.org/10.1080/09603409.2019.1601803

George, E.P., Li, P.L., Pope, D.P., 1987. Creep cavitation in iron—I. Sulfides and carbides as nucleation sites. Acta Metallurgica 35, 2471–2486. https://doi.org/10.1016/0001-6160(87)90144-1

Ghasemi-Nanesa, H., Jahazi, M., 2014. Simultaneous enhancement of strength and ductility in cryogenically treated AISI D2 tool steel. Materials Science and Engineering: A 598, 413–419. https://doi.org/10.1016/j.msea.2014.01.065

Gill, S., Singh, J., Singh, R., Singh, H., 2011. Metallurgical principles of cryogenically treated tool steels-a review on the current state of science. International Journal of Advanced Manufacturing Technology 54, 59–82. https://doi.org/10.1007/s00170-010-2935-5

Gotoh, A., 1993. Reheat cracking - the mechanism and countermeasures. Welding International 7, 266–268. https://doi.org/10.1080/09507119309548387

Mulford, R.A., McMahon, C.J., Pope, D.P., Feng, H.C., 1976. Temper embrittlement of Ni-Cr Steels by phosphorus. Metallurgical Transactions A 7, 1183–1195. https://doi.org/10.1007/BF02656602

Neira Torres, I., 2015. Modelling of cooling and heat treatment of bimetallic rolling mill rolls. Université de Liège, Liège, Belgique.

Noecker, F.F., Dupont, J.N., 2009. Metallurgical Investigation into Ductility Dip Cracking in Ni-Based Alloys: Part II. Welding Journal 88, 62s–77s.

Olson, G.B., Anctil, A.A., Desisto, T.S., Kula, E.B., 1983. Anisotropie embrittlement in high-hardness ESR 4340 steel forgings. Metallurgical Transactions A 14, 1661–1669. https://doi.org/10.1007/BF02654394

Ramirez, A.J., Lippold, J.C., 2004. High temperature behavior of Ni-base weld metal: Part II – Insight into the mechanism for ductility dip cracking. Materials Science and Engineering: A 380, 245–258. https://doi.org/10.1016/j.msea.2004.03.075

Takayama, S., Ogura, T., Fu, S.-C., McMahon, C.J., 1980. The calculation of transition temperature changes in steels due to temper embrittlement. Metallurgical Transactions A 11, 1513–1530. https://doi.org/10.1007/BF02654515

Torres, I.N., Gilles, G., Tchuindjang, J.T., Flores, P., Lecomte-Beckers, J., Habraken, A.M., 2015. FE modeling of the cooling and tempering steps of bimetallic rolling mill rolls. International Journal of Material Forming 3, 287–305. https://doi.org/10.1007/s12289-015-1277-0

Viswanathan, R., 1971. Temper embrittlement in a Ni-Cr steel containing phosphorus as impurity. Metallurgical Transactions 2, 809–815. https://doi.org/10.1007/BF02662740

Partie A – Article #5 – Phase Transformations and Crack Initiation in a High-Chromium Cast Steel Under Hot Compression Tests. . Tchoufang Tchuindjang, I. Neira Torres, P. Flores, A. M. Habraken & J. Lecomte-Beckers. J. of Materi Eng and Perform 24 (2015), pp. 2025-2041

65

VI. CHAPITRE 6 : PRÉSENTATION ET COMPLÉMENTS D'ÉTUDE L'ARTICLE #6

VI.1. Introduction

Le Ti6Al4V est le plus connu et le plus répandu des alliages de titane de type alpha-beta, qui a initialement été développé pour l'aéronautique et le spatial. Il représente 50% de la production mondiale d'alliages de titane, et 80% du volume de tous les alliages de titane utilisés en aéronautique. L'autre domaine d'utilisation du Ti6Al4V est la médecine, notamment pour les prothèses, avec environ 3% du volume global. Cependant, il a été établi que l'aluminium et le vanadium, relâchés par l'alliage, sont toxiques pour l'organisme humain, ce qui restreint son usage dans ce domaine.

L'intérêt principal de cet alliage réside dans ses propriétés mécaniques, thermophysiques et physicochimiques, en comparaison avec d'autres métaux. Son module de Young est environ deux fois moins élevé que celui des aciers, pour une résistance mécanique comparable. La présence en solution solide d'éléments d'alliage augmente sa résistivité électrique, tandis que sa capacité à former rapidement en surface un oxyde protecteur, lui procure une bonne résistance à la corrosion.

L'article suivant (#6) présente un dispositif pour déposer par un procédé de fabrication additive, des couches d'alliage Ti6Al4V sur un substrat issu du même matériau, mais obtenu par un procédé classique de coulée et son post-traitement de mise à forme à chaud.

La géométrie du dépôt est choisie de façon à simuler un phénomène de réparation. Les paramètres de fabrication sont sélectionnés pour évaluer en même temps l'effet de l'énergie incidente (« incident energy » - IE, selon deux niveaux : haut (HIE) et bas (LIE)) et de la stratégie de construction (soit une longueur de cordon constante (« Constant Track Length » ou CTL) ou décroissante (« Decreasing Track Length ou DTL)), sur l'homogénéité du dépôt. En outre les paramètres de fabrication considérés ont déjà optimisés pour produire un dépôt sain, c'est-à-dire sans défauts internes, telles que les porosités.

L'homogénéité est considérée ici d'un point de vue macroscopique, notamment via la dureté mesurée sur le dépôt brut de fabrication. Ce résultat d'homogénéité est pris en compte pour produire des éprouvettes de traction, qui permettent d'évaluer la bonne qualité de la liaison entre dépôt et substrat.

De plus, on réalise aussi une caractérisation grossière (en optique) et affinée (au microscope électronique à balayage) de la microstructure, aussi bien dans les dépôts que dans la principale Zone Affectée Thermiquement (« Heat Affected Zone » ou HAZ), c'est-à-dire celle qui se forme entre le substrat et le dépôt.

L'étude se termine par une description très simplifiée de la relation entre les microstructures observées et un refroidissement « équivalent » (vitesse moyenne variable cohérente avec une microstructure représentative de chaque dépôt). L'hypothèse forte d'une homogénéité de chacun des trois cas étudiés est faite pour estimer cette vitesse moyenne. Les articles #7 et #8 viendront lever cette hypothèse.

VI.2. Bref rappel sur le contexte

Les échantillons analysés proviennent d'un programme de recherche (BLISK ou Bladed Disk), de la convention RW 6247[13], dont l'objectif était l'étude de faisabilité de composants réparés soit par soudage en friction linéaire, soit par rechargement en fabrication additive par fusion de poudre au laser. Dans le cadre de ce projet, l'unité MMS s'est focalisée sur les aspects métallurgiques des composants produits de manière à garantir dès le départ leur qualité et ainsi optimiser les paramètres de fabrication. Le MMS

---

[13] Coordination assurée par Techspace Aero, de 2010 à 2013.

a aussi réalisé la caractérisation mécanique et thermophysique des composants, puis les corrélations microstructures – propriétés mécaniques (traction et fatigue) ont été établies, en vérifiant la bonne tenue des pièces soudées ou rechargées, et notamment les zones de la liaison métallurgique avec le substrat. Dans ce qui suit, on se focalise uniquement sur les pièces issues de la fabrication additive.

Le tableau 6.1 rappelle les thématiques principales considérées pour toute l'étude de l'alliage Ti6Al4V (partie B de la thèse, article #,#7,#8). Ces thématiques au nombre de trois constituent un fil conducteur structurant le travail. Elles sont libellées comme suit :

- Caractérisation métallographique et propriétés mécaniques
- Description microstructurale et transformations en phases solides
- Modélisation thermique et prédiction de la microstructure via des modèles de la cinétique des changements de phase.

Pour chaque thématique (**Tableau VI-1**), on explicite en vert le travail développé dans l'Article #6, quand la couleur rouge introduit les nouveaux résultats présentés dans cette introduction.

Characterization at a macro scale (Macrostructure and mechanical properties)	Characterization at a micro scale (Microstructure determination and Description and/or Highlighting of solid phase transformations)	Modeling (Thermal model and predictive approaches for kinetic models implementation)
• Macrostructure characterization leading to the enhancement of the homogeneity as influenced by IE and building strategies, and related hardness maps (3 samples, 2 strategies (CTL and DTL), and two IE (HIE-CTL+DTL, and LIE-DTL) • Mechanical properties of the material constituted of assembly of the subtrate + deposit under static load (tensile) (HIE-CTL samples) exhibiting an homogeneous structure • Fatigue tests on the deposit (HIE-CTL samples)	• Macro HAZ characterization (bounding zone with the substrate) • Final microstructure identification within the three samples as related to thinner and thicker zones	• Rough descriptive model for macrostructure and microstructure based on a single stage with an equivalent cooling rate exhibiting more or less variations with position

Tableau VI-1 : Thématiques présentes dans l'article (vert), et compléments décrits ci-après (rouge)

VI.3. Résultats principaux

VI.3.1. Caractérisation macroscopique

La caractérisation macroscopique concerne d'une part la santé métallurgique interne, et d'autre part la taille des grains. Les paramètres de procédé qui ont été choisi ont permis d'obtenir des échantillons denses, c'est-à-dire exempts de porosités internes.

La macrostructure est observée après attaque spécifique, et montre d'une part des grains colonnaires grossiers à croissance épitaxiale pour les énergies incidentes élevées, et des grains colonnaires plus fins et en zigzag pour les énergies incidentes plus faibles. La macrostructure est essentiellement influencée par les paramètres du procédé, *tandis que la stratégie de fabrication (Constant Track Length CTL ou Decrease Track Length DTL) n'a que peu d'influence.*

La dureté Vickers obtenue sous une charge de 10 kg donne une cartographie relativement homogène pour les deux configurations CTL sous faible et forte énergies incidentes, les duretés moyennes correspondantes étant respectivement de 368 et 333 HV$_{10}$. Par contre l'hétérogénéité est très marquée pour la configuration DTL, où les zones fines sont systématiquement plus dures (357 HV$_{10}$ en moyenne)

que les zones épaisses (330 HV$_{10}$ en moyenne) du dépôt, l'épaisseur étant reliée à la profondeur déposée dans la cuvette initiale.

VI.3.2. **Caractérisation microstructurale**

La microstructure est influencée à la fois par la stratégie de fabrication et les paramètres de procédé. La microstructure la plus homogène est celle observée sur la configuration CTL sous faible énergie incidente (LIE). La matrice est martensitique à fines lattes, et sa dureté moyenne de 368 ± 8 HV$_{10}$ est la plus élevée obtenue sur l'ensemble des configurations. On observe aussi une martensite α' à lattes plus épaisses dans les régions fines de la configuration DTL, qui présente cependant une dureté un peu moins élevée (en moyenne 357 HV$_{10}$). La différence de dureté peut être rattachée tant à l'épaisseur des lattes qu'à la taille initiale du grain β primaire, ou à la vitesse du refroidissement lors de la transformation de phase. Ces aspects sont discutés dans l'Article #8 présenté plus loin dans cette même partie de la thèse. La différence avec le substrat (320 HV$_{10}$) est cependant assez significative.

La configuration CTL sous énergie incidente élevée (HIE) produit une microstructure homogène, qui est majoritairement formée de structure de Widmanstätten (α/β_W). La dureté moyenne est d'environ 330 HV$_{10}$, et l'écart avec le substrat est donc minimal (10 HV de différence). Remarquons que le même type de microstructure est observé dans la partie épaisse de l'échantillon de la configuration DTL sous HIE, avec un niveau de dureté similaire.

VI.3.3. **Propriétés mécaniques en traction**

Les essais de traction ont été réalisés sur deux lots de 8 et 10 éprouvettes respectivement, chaque lot correspondant à une séquence de fabrication à partir d'un lot défini de poudres. Les paramètres de fabrication sont les mêmes pour les deux lots, et ils correspondent à la configuration CTL sous HIE. On n'a pas observé de différences de composition chimique ni de microstructure entre les deux lots.

Lors de l'essai de traction, on place un extensomètre centré sur le dépôt de l'éprouvette, de longueur 30 mm, qui quantifie la déformation dans le dépôt. Un capteur externe est placé au niveau des têtes de l'éprouvette pour mesurer son allongement global. En pratique, l'allongement global correspond à celui dans la zone utile auquel on ajoute l'allongement parasite des têtes de l'éprouvette.

Les courbes finales montrent une variation d'endommagement marquée par un escalier, qui traduit l'entrée en plasticité dans une zone localisée de la pièce « substrat + dépôt ». La zone plastifiée en premier soit celle qui présente la limite élastique la moins élevée, est en fait le métal de base où se produit la rupture. L'attaque réalisée sur des éprouvettes rompues en traction met en évidence la région du dépôt et celle du substrat d'origine, et confirme bien la localisation systématique du plan moyen de rupture dans le métal de base, loin de la HAZ.

Partie B – Article #6 – Laser cladding as repair technology for Ti–6Al–4V alloy: Influence of building strategy on microstructure and hardness. H. Paydas, A. Mertens, R. Carrus, J. Lecomte-Beckers, & J. Tchoufang Tchuindjang. Mater. & Des. 85 (2015), pp.497-510
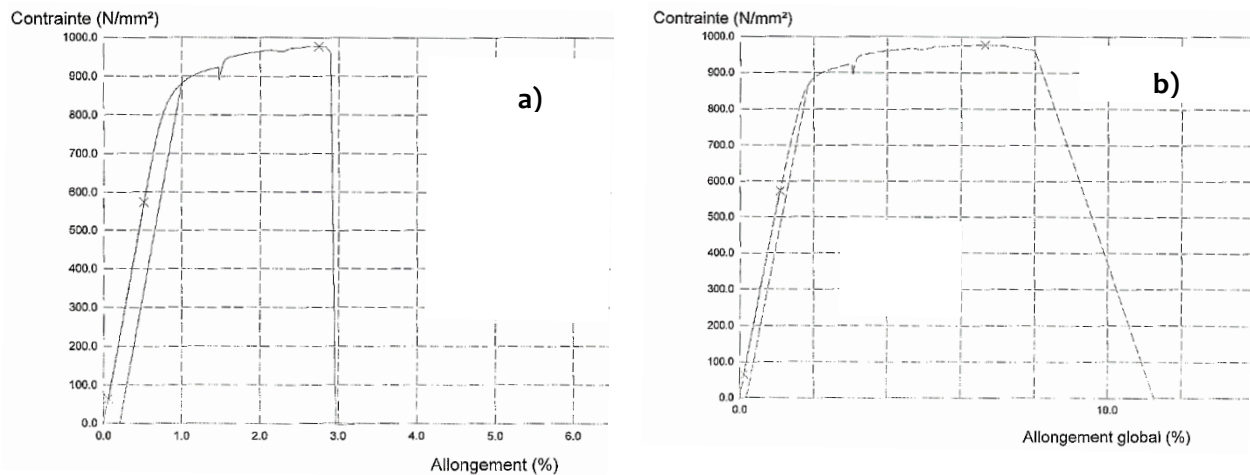
68

Figure VI-1 : *Courbes contraintes-déformations montrant l'allongement au centre du dépôt (a), d'après une mesure de l'extensomètre de 30 mm centrée sur le dépôt, et l'allongement global (b) sur les deux parties de l'éprouvette ADD195-4 lors d'un essai de traction jusqu'à rupture*
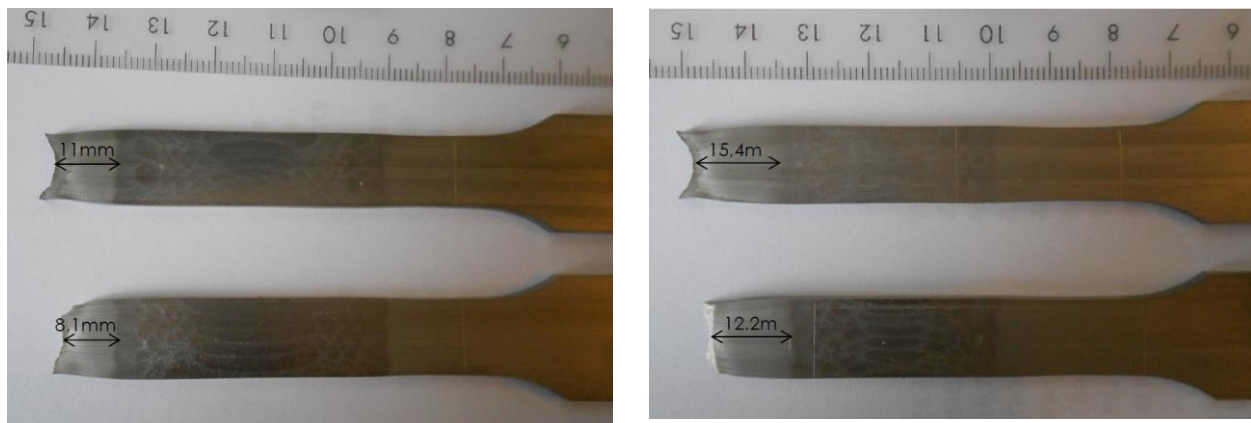
Figure VI-2 : *Aperçu de la région rompue située dans le métal de base sur deux éprouvettes issues du lot 1, après essais de traction (les deux côtés des éprouvettes se situent respectivement à gauche et à droite de l'image, avec éprouvette ADD195-4 en haut, et ADD 195-8 en bas)*

VI.4. Résultats complémentaires en dynamique (essais de fatigue)

Des essais de fatigue ont été réalisés sur des éprouvettes issues de la configuration HIE-CTL, produisant une microstructure homogène dans le dépôt. Cette même configuration a fourni les résultats de traction statique.

Les essais de fatigue se font de sorte que la zone utile corresponde entièrement à une matière déposée en fabrication additive. La plupart du temps, on casse dans la zone utile, c'est-à-dire dans le dépôt dont la microstructure est réputée homogène, et constituée de martensite décomposée. En outre la rupture démarre de la surface de l'éprouvette, sauf quand un défaut interne existe, tel qu'une porosité (**Tableau VI-2**).

Partie B – Article #6 – Laser cladding as repair technology for Ti–6Al–4V alloy: Influence of building strategy on microstructure and hardness. H. Paydas, A. Mertens, R. Carrus, J. Lecomte-Beckers, & J. Tchoufang Tchuindjang. Mater. & Des. 85 (2015), pp.497-510

69

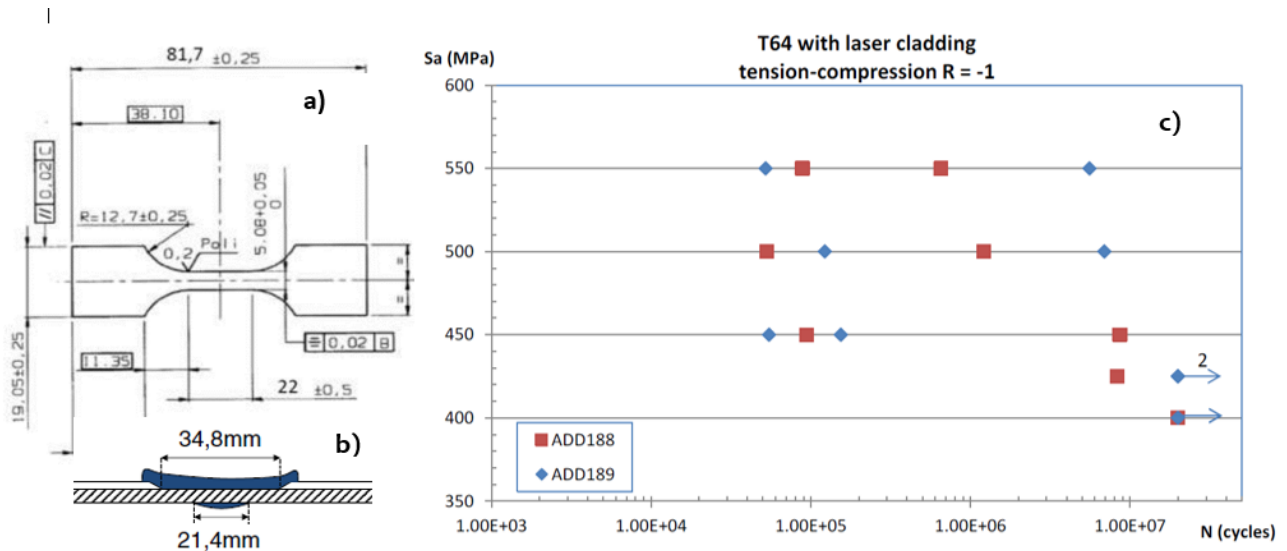**Figure VI-3** : *a) dimensions normalisées de l'éprouvette de fatigue et b) aperçu de la zone de prélèvement dans l'échantillon fabriqué par dépôt laser de façon à ce que la région du dépôt corresponde à la zone utile (fût de l'éprouvette de fatigue) ; c) résultats des essais de fatigue en sollicitations alternées sur 17 éprouvettes (dont 4 non rompues après 2.10⁷ cycles), avec 5 niveaux de charge (550, 500, 450, 425 et 400 MPa), indiquant une limite d'endurance d'environ 400 MPa, pour le dépôt (4 éprouvettes non rompues-)*

Bien que la limite d'endurance n'ait pu être déterminée avec précision, on note que le niveau de la contrainte maximale à 10^7 cycles, soit 400 MPa, reste largement en-dessous des niveaux généralement obtenus que ce soit sur les structures bimodales classiques où on est entre 460 MPa et 700 Mpa (Crupi et al., 2017; Janeček et al., 2015; Saitova et al., 2009; Zuo et al., 2008), ou pour les structures de type Widmanstätten (α/β_W) où la résistance en fatigue peut varier entre 475 Mpa et 550 Mpa (Crupi et al., 2017; Saitova et al., 2009; Zuo et al., 2008). On note cependant que la structure bimodale présentera toujours un résultat supérieur à celui de la structure $\alpha\beta_W$ pour la tenue en fatigue (Saitova et al., 2009). En outre si cette résistance est significativement améliorée avec l'affinage du grain (Saitova et al., 2009), la présence de défauts va considérablement la dégrader (Prabhu et al., 2015). Le comportement des pièces issues de la fabrication additive est plus variable et fortement dispersé, car influencé par différents paramètres, notamment le type de procédé, la direction de fabrication, les post-traitements, les défauts, etc. (Fatemi et al., 2019; Günther et al., 2017; Prabhu et al., 2015; Sterling et al., 2016; Vayssette et al., 2019; Walker et al., 2017). Les valeurs de résistance en fatigue pour les pièces AM peuvent ainsi varier de 600 jusqu'à 100 Mpa pour le minimum, et parfois le frittage est requis pour supprimer la porosité résiduelle qui reste critique en fatigue.

Le résultat trouvé reste donc logique, si on tient compte de la macrostructure (grains colonnaires grossiers perpendiculaires à la direction de la sollicitation), de la possible existence de porosités même en faible proportion, et aussi de la nature de la microstructure dans les pièces rechargées. En effet, la microstructure dans la zone utile est mixte (martensite faiblement décomposée associée à la structure $\alpha\beta_W$) dont la genèse sera discutée dans l'Article #7 suivant (voir la microstructure du POI2). Dans ce cas, c'est surtout la phase β située entre les lamelles de α dans la structure $\alpha\beta_W$ qui apporte la réserve de ductilité. En effet, les lattes résiduelles de α' non dissoutes, ne vont pas présenter de phase β aux joints de lattes, car le phénomène de décomposition n'est pas achevé (température équivalente de maintien de 670°C en POI2, avec seulement un peu plus de 6 minutes de temps de maintien équivalent). La décomposition de la martensite démarre souvent à partir de 680 °C, et pour des temps de maintien de l'ordre de plusieurs dizaines de minutes (Cao et al., 2018; Wu et al., 2016; Xu et al., 2017; Zafari et al., 2019).

Partie B – Article #6 – Laser cladding as repair technology for Ti–6Al–4V alloy: Influence of building strategy on microstructure and hardness. H. Paydas, A. Mertens, R. Carrus, J. Lecomte-Beckers, & J. Tchoufang Tchuindjang. Mater. & Des. 85 (2015), pp.497-510

70

En définitive, le résultat obtenu ici correspond déjà à la moyenne supérieure observée dans la littérature sur l'alliage Ti6Al4V issu de la fabrication additive, si on considère des conditions d'essais en fatigue similaires (sollicitation alternée en traction et compression, fréquence, etc.). Cependant, l'écart encore significatif qui existe avec le même alliage produit par le procédé classique doit être réduit, notamment en augmentant la réserve de ductilité de la matrice dans le dépôt.

reference	S_a (MPa)	N (cycles)	state	location
ADD188-13	-	-	-	-
ADD188-7	450	8654672	R	effective zone
ADD189-4	450	54927	R	radius beginning
ADD188-8	450	94560	R	radius beginning
ADD189-9	450	154560	R	radius beginning
ADD188-6	400	2.00E+07	NR	-
ADD189-2	400	2.00E+07	NR	-
ADD189-5	425	2.00E+07	NR	-
ADD188-9	425	8278489	R	effective zone
ADD188-11	500	53300	R	effective zone
ADD189-7	500	122700	R	radius beginning
ADD188-12	500	1211600	R	effective zone
ADD189-8	500	6899700	R	radius beginning
ADD189-1	550	52200	R	effective zone
ADD188-10	550	654700	R	effective zone
ADD189-6	550	5570100	R	effective zone
ADD188-5	550	88900	R	effective zone
ADD189-3	425	2.00E+07	NR	-

b)
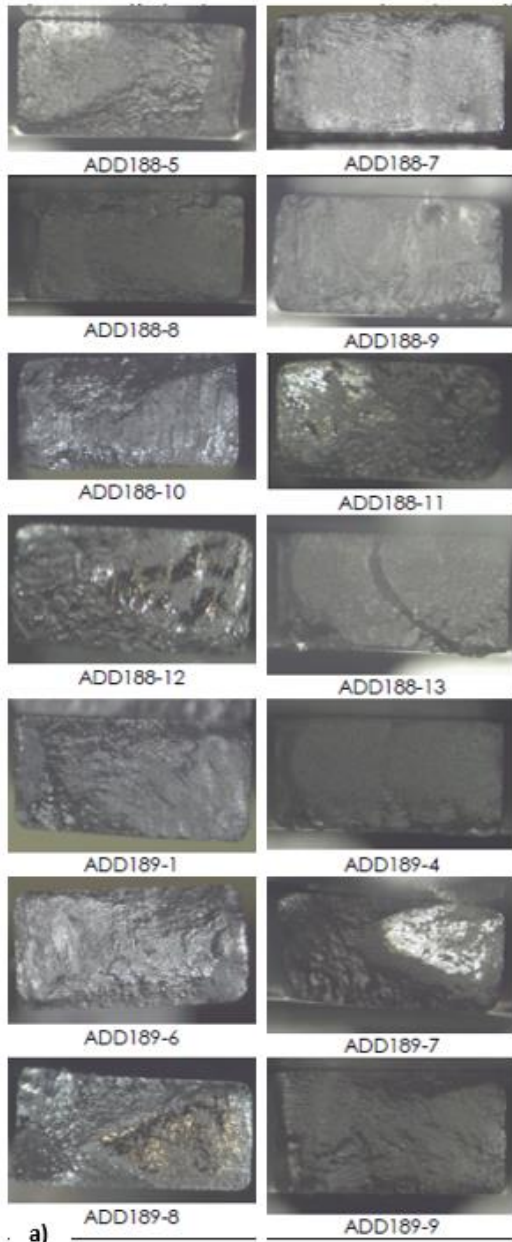
Tableau VI-2 : *a) Faciès de rupture macroscopique (loupe binoculaire) des éprouvettes rompues en fatigue (à gauche) ; b) Rappels du code éprouvette, du niveau de charge maximale, de la durée de vie à rupture éventuelle, et de la localisation du plan de rupture (zone tuile (effective zone) ou congé de raccordement (radius beginning) sur les 18 éprouvettes issues de deux lots équivalents, produits avec les mêmes paramètres de procédé*

Partie B – Article #6 – Laser cladding as repair technology for Ti–6Al–4V alloy: Influence of building strategy on microstructure and hardness. H. Paydas, A. Mertens, R. Carrus, J. Lecomte-Beckers, & J. Tchoufang Tchuindjang. Mater. & Des. 85 (2015), pp.497-510

71

VI.5. Conclusions

On a caractérisé la macrostructure de pièces issues de la fabrication additive obtenues suivant des stratégies de dépôt qui permettent d'obtenir des structures plus ou moins homogènes, l'homogénéité étant évaluée principalement à partir de la dureté dans cet Article #6.

La pièce homogène (HIE-CTL) a été caractérisée d'un point de vue mécanique, en statique et en dynamique, et les résultats montrent que la liaison entre le dépôt et le substrat n'est pas une région de fragilisation préférentielle des pièces. En effet, la rupture est systématiquement survenue dans le métal de base en statique. Pour les essais cycliques réalisés sur le dépôt, la limite d'endurance en fatigue ultra-longue est dans le minimum de la fourchette observée pour le Ti6Al4V obtenu par des procédés différents. Cette observation résulte de la plus faible ductilité intrinsèque du matériau brut de fabrication.

Concernant la caractérisation du procédé de fabrication en lien avec les microstructures finales obtenues, un premier modèle grossier est établi basé sur un refroidissement final équivalent. Les variations face à cette moyenne produisent les dispersions qui impactent l'homogénéité de la structure. Pour le refroidissement, on adopte une température équivalente pour le bain de fusion, qui reste indéterminée, mais dont la valeur augmente avec la puissance initiale du laser. L'homogénéité de la microstructure est évaluée de manière grossière via la dureté, et au niveau microscopique via la nature des phases en présence. Au final, le modèle descriptif est très simplifié, puisqu'il ne tient pas compte de tous les événements thermiques susceptibles de se produire dans le dépôt en cours de fabrication. A ce stade, différents paramètres restent inconnus : la température équivalente du bain de fusion et la vitesse moyenne du refroidissement, ainsi que son degré de variation éventuel. Par ailleurs, aucun lien n'est établi entre le relevé de température dans le substrat et l'évolution éventuelle de la température dans le dépôt.

La **Figure VI-4** montre l'approximation faite pour parvenir à une description équivalente de la microstructure finale dans le dépôt.
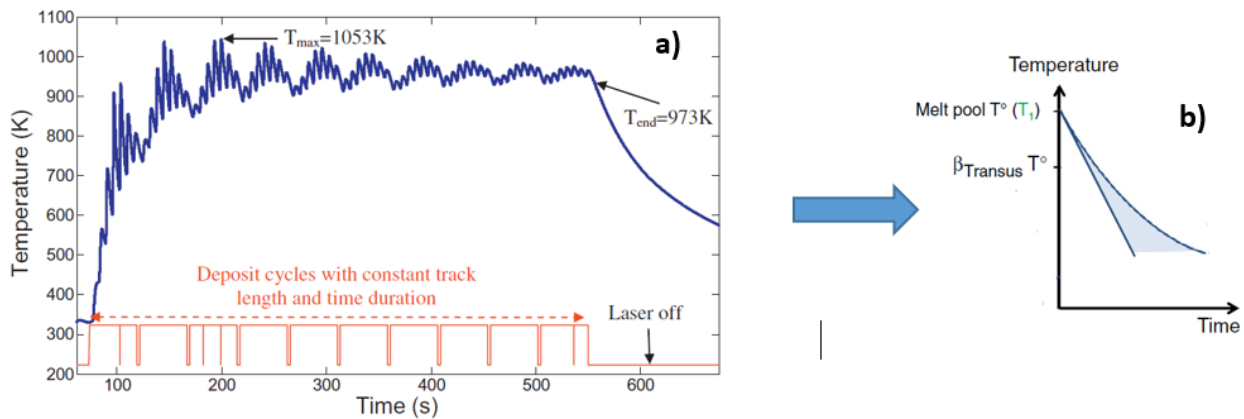

Figure VI-4 *: a) Relevé des températures enregistrées dans le substrat en cours de fabrication du dépôt (stratégie HIE-CTL) jusqu'à refroidissement final après extinction de la source laser; b)* ***Esquisse du modèle métallurgique équivalent,*** *pour déterminer la nature de la microstructure finale dans le dépôt. En fonction d'un refroidissement équivalent depuis la température indicative du bain de fusion, les vitesses et leur dispersion fixent l'hétérogénéité de la microstructure*

Toutefois, cette approche très simpliste est remise en question dans les Articles #7 et #8, où on va prendre en compte l'histoire thermique prédite, pour reconstituer l'évolution de la microstructure en cours de fabrication.

VI.6. Références

Cao, S., Chu, R., Zhou, X., Yang, K., Jia, Q., Lim, C.V.S., Huang, A., Wu, X., 2018. Role of martensite decomposition in tensile properties of selective laser melted Ti-6Al-4V. Journal of Alloys and Compounds 744, 357–363. https://doi.org/10.1016/j.jallcom.2018.02.111

Crupi, V., Epasto, G., Guglielmino, E., Squillace, A., 2017. Influence of microstructure [alpha+beta and beta] on very high cycle fatigue behaviour of Ti-6Al-4V alloy. International Journal of Fatigue 95, 64–75. https://doi.org/10.1016/j.ijfatigue.2016.10.002

Fatemi, A., Molaei, R., Simsiriwong, J., Sanaei, N., Pegues, J., Torries, B., Phan, N., Shamsaei, N., 2019. Fatigue behaviour of additive manufactured materials: An overview of some recent experimental studies on Ti-6Al-4V considering various processing and loading direction effects. Fatigue & Fracture of Engineering Materials & Structures 42, 991–1009. https://doi.org/10.1111/ffe.13000

Günther, J., Krewerth, D., Lippmann, T., Leuders, S., Tröster, T., Weidner, A., Biermann, H., Niendorf, T., 2017. Fatigue life of additively manufactured Ti–6Al–4V in the very high cycle fatigue regime. International Journal of Fatigue, Fatigue and Fracture Behavior of Additive Manufactured Parts 94, 236–245. https://doi.org/10.1016/j.ijfatigue.2016.05.018

Janeček, M., Nový, F., Harcuba, P., Stráský, J., Trško, L., Mhaede, M., Wagner, L., 2015. The Very High Cycle Fatigue Behaviour of Ti-6Al-4V Alloy. Acta Phys. Pol. A 128, 497–503. https://doi.org/10.12693/APhysPolA.128.497

Prabhu, A.W., Vincent, T., Chaudhary, A., Zhang, W., Babu, S.S., 2015. Effect of microstructure and defects on fatigue behaviour of directed energy deposited Ti–6Al–4V. Science and Technology of Welding and Joining 20, 659–669. https://doi.org/10.1179/1362171815Y.0000000050

Saitova, L.R., Höppel, H.W., Göken, M., Semenova, I.P., Valiev, R.Z., 2009. Cyclic deformation behavior and fatigue lives of ultrafine-grained Ti-6AL-4V ELI alloy for medical use. International Journal of Fatigue 31, 322–331. https://doi.org/10.1016/j.ijfatigue.2008.08.007

Sterling, A.J., Torries, B., Shamsaei, N., Thompson, S.M., Seely, D.W., 2016. Fatigue behavior and failure mechanisms of direct laser deposited Ti–6Al–4V. Materials Science and Engineering: A 655, 100–112. https://doi.org/10.1016/j.msea.2015.12.026

Vayssette, B., Saintier, N., Brugger, C., El May, M., Pessard, E., 2019. Numerical modelling of surface roughness effect on the fatigue behavior of Ti-6Al-4V obtained by additive manufacturing. International Journal of Fatigue 123, 180–195. https://doi.org/10.1016/j.ijfatigue.2019.02.014

Walker, K.F., Liu, Q., Brandt, M., 2017. Evaluation of fatigue crack propagation behaviour in Ti-6Al-4V manufactured by selective laser melting. International Journal of Fatigue 104, 302–308. https://doi.org/10.1016/j.ijfatigue.2017.07.014

Wu, S.Q., Lu, Y.J., Gan, Y.L., Huang, T.T., Zhao, C.Q., Lin, J.J., Guo, S., Lin, J.X., 2016. Microstructural evolution and microhardness of a selective-laser-melted Ti–6Al–4V alloy after post heat treatments. Journal of Alloys and Compounds 672, 643–652. https://doi.org/10.1016/j.jallcom.2016.02.183

Xu, W., Lui, E.W., Pateras, A., Qian, M., Brandt, M., 2017. In situ tailoring microstructure in additively manufactured Ti-6Al-4V for superior mechanical performance. Acta Materialia 125, 390–400. https://doi.org/10.1016/j.actamat.2016.12.027

Zafari, A., Barati, M.R., Xia, K., 2019. Controlling martensitic decomposition during selective laser melting to achieve best ductility in high strength Ti-6Al-4V. Materials Science and Engineering: A 744, 445–455. https://doi.org/10.1016/j.msea.2018.12.047

Zuo, J.H., Wang, Z.G., Han, E.H., 2008. Effect of microstructure on ultra-high cycle fatigue behavior of Ti–6Al–4V. Materials Science and Engineering: A 473, 147–152. https://doi.org/10.1016/j.msea.2007.04.062

VII. CHAPITRE 7 : PRÉSENTATION ET COMPLÉMENTS D'ÉTUDE SUR L'ARTICLE #7

VII.1. Introduction

L'Article #7 dédié à la fabrication additive fait suite au précédent article présenté dans cet ouvrage (Article #6). En particulier, on y développe un modèle thermique éléments finis 3D à partir de l'histoire de température enregistrée dans le substrat, et des propriétés thermophysiques déterminées expérimentalement pour des dépôts réalisés en Ti6Al4V. Ce modèle est validé en se basant sur les dimensions de la zone refondue et de la zone affectée thermiquement (HAZ) situées dans la zone de liaison entre le substrat et le dépôt.

Ce modèle permet de déterminer des histoires thermiques simulées au sein du dépôt (tâches réalisées par l'équipe MSM). En partant de ces simulations, je propose d'interpréter les transformations de phases, en tenant compte des variations de températures et de leur effet sur les points critiques de transformations de phases. L'identification et la validation du modèle thermique sont donc réalisées en 2 étapes. Le modèle est tout d'abord calibré en considérant les dimensions de la HAZ et de la zone de dilution dans la liaison substrat-dépôt, ainsi que l'histoire thermique. Puis a posteriori, il est validé en établissant les corrélations des histoires de température prédites avec les microstructures observées.

VII.2. Bref rappel sur le contexte

Un seul échantillon est considéré dans cette étude, et il s'agit du dépôt réalisé avec une énergie incidente élevée et une stratégie de fabrication et une longueur de cordon constante (HIE-CTL), déjà présenté à l'article #6, pour lequel la macrostructure a été identifiée comme homogène, notamment par la cartographie de la dureté Vickers. Le dépôt provient du programme de recherche (BLISK ou Bladed Disk), de la convention RW 6247[14], dont l'objectif était l'étude de faisabilité de composants réparés soit par soudage en friction linéaire, soit par rechargement en fabrication additive par fusion de poudre au laser. Les propriétés thermophysiques déterminées expérimentalement dans le cadre du projet pour le dépôt et pour le substrat, sont utilisées ici pour établir le modèle thermique.

Le tableau 7.1 reprend les thématiques principales et rappelle le fil conducteur structurant le travail pour les trois articles de cette partie de la thèse.

La partie numérique a été réalisée par le premier auteur de l'article (H-S TRAN), qui fait partie de l'équipe MSM dirigée par A. M. HABRAKEN. Il s'agit d'un travail de collaboration pour lequel les paramètres d'entrée ont été fournis par le service MMS (propriétés thermophysiques notamment, mesurées expérimentalement). La validation du modèle, tenant compte de l'effet du gradient thermique sur les transformations de phase, a été apportée par mes soins. Le champ thermique a été calculé par le logiciel EF propre au Département ArGenCo, Lagamine®. Les détails ici seront donc limités aux principes généraux.

Le travail développé pour chaque thématique est rappelé dans le **Tableau VII-1** qui suit.

Characterization at a macro-scale	Characterization at a micro-scale (Microstructure determination and Description and/or Highlighting of solid phase transformations)	Modeling (Thermal model and predictive approaches for kinetic models implementation)
• Homogeneous macrostructure (CTL configuration @HIE) with the definition of three Points of interest (POIs)	• Solid state phase transformation, under pseudo TTT	• Thermal model implementation and validation • Simulated thermal curves leading to rough microstructure description (three POIs) with enhancement of pseudo –TTT and solid state phases transformations

Tableau VII.2 : Rappel des thématiques présentes dans l'article

---

Partie B – Article #7 – 3D thermal finite element analysis of laser cladding processed Ti-6Al-4V part with microstructural correlations. H-S Tran, J. Tchoufang Tchuindjang. H. Paydas, A. Mertens, R. T. Jardin, L. Duchêne, R. Carrus, J. Lecomte-Beckers & A. M. Habraken. Mater. & Des. 128 (2017), pp.130-142

74

VII.3. Résultats principaux

VII.3.1. Développement et implémentation du modèle thermique et influence sur la solidification

La connaissance du code maison Lagrangien Lagamine® permet d'avoir un contrôle total des modèles thermiques et mécaniques, ainsi que des types et des méthodes d'activation des éléments. Le maillage, les conditions aux limites initiales, le flux thermique, de même que l'analyse de sensibilité ne sont pas abordés ici, étant donné que ces notions font appel à des compétences spécifiques de numéricien.

Par contre, on rappelle que la validation du modèle thermique s'est faite en reproduisant l'allure du cyclage thermique des courbes de référence enregistrées par les thermocouples placés dans le substrat, après le dépôt de 7 couches et après le dépôt final de 10 couches dans la pièce.

Le modèle validé permet de reconstituer la géométrie 3D du bain de fusion en cours de fabrication à chaque étape de la simulation, en considérant toutes les températures supérieures ou égales au liquidus. On notera ici que ce premier contrôle impose de considérer uniquement le liquidus, car le solidus est influencé par la vitesse de chauffage, avec pour les grandes vitesses, une approximation d'égalité avec le liquidus. Le modèle thermique permet de déterminer les vitesses élevées atteintes lors des cycles avec fusion successive en différents points du dépôt. On peut ainsi atteindre localement une vitesse maximale de 12.000K/sec au chauffage, et de près de 465 K/sec au refroidissement depuis le liquide.

De la même manière, le contrôle pour la validation des dimensions de la HAZ entre le substrat et le dépôt suggère aussi un décalage vers le haut des températures critiques de transformation en phase solide avec la vitesse de chauffage. C'est notamment le cas pour le passage dans le domaine de la phase β, soit T_{DISS} ou $\alpha_{transus}$ comme début de transformation de α en β, et pour le $\beta_{transus}$.

VII.3.2. Transformations en phase solide dans le dépôt en cours de fabrication – description et validation

Les histoires thermiques simulées permettent de suivre l'évolution de la température en des points d'intérêts (POIs). Les trois POIs choisis présentent à peu près la même évolution de température qui traduit l'homogénéité de celle-ci dans le dépôt en cours de fabrication.

En se focalisant sur ce qui se passe après la dernière solidification, on note la formation de martensite α'. Le premier point de discussion porte alors sur la pertinence des conditions d'occurrence de cette transformation, en termes de vitesses et de points critiques pour le début de la réaction (M_s) : ce point sera étudié en détail dans l'Article #8.

Avec la martensite formée, l'exploitation des courbes simulées permet de proposer une approximation de recuit isotherme, à une température de maintien où α' ne subit pas de nouvelle transformation, et où la portion de la phase-mère encore présente à côté de la martensite, soit $\beta_{retained}$ peut par contre subir une transformation isotherme et diffusive, conduisant à la structure dite de Widmanstätten (α/β_W).

L'analyse descriptive ci-dessus, faite à partir des histoires thermiques simulées est ensuite validée par l'analyse micrographique des zones considérées sur le dépôt (coupes). C'est ainsi qu'on met en évidence à l'échelle microscopique, l'existence d'une structure mixte $\alpha' + \alpha/\beta_W$ dans la matrice, structure qui semble être présente partout dans le dépôt, en produisant alors une homogénéité macroscopique que reflète la dureté du même ordre de grandeur partout.

Partie B – Article #7 – 3D thermal finite element analysis of laser cladding processed Ti-6Al-4V part with microstructural correlations. H-S Tran, J. Tchoufang Tchuindjang. H. Paydas, A. Mertens, R. T. Jardin, L. Duchêne, R. Carrus, J. Lecomte-Beckers & A. M. Habraken. Mater. & Des. 128 (2017), pp.130-142

75

VII.4.   Conclusions et perspectives

On a établi un modèle EF 3D thermique validé qui permet de prédire l'histoire thermique en tout point du dépôt en cours de fabrication additive. La validation consiste autant dans la restitution du cycle thermique enregistré au niveau du substrat en cours de procédé, que dans les dimensions de la zone de dilution et de la HAZ associée à la jonction entre le substrat et le dépôt.

Le modèle thermique 3D validé fournit la géométrie du bain de fusion dans le dépôt en cours de fabrication.

La configuration HIE-CTL est homogène à l'échelle macroscopique (dureté), avec une matrice mixte de type $\alpha' + \alpha\beta_W$. Ces aspects sont aussi expliqués par l'analyse des courbes thermiques simulées. C'est ainsi qu'on établit l'approximation du recuit isotherme à plus ou moins basse température de la martensite en tout point du dépôt déjà solidifié, période pendant laquelle la phase-mère résiduelle ($\beta_{retained}$) se transforme en structure $\alpha\beta_W$.

La **Figure VII-1** montre de quelle manière l'approximation est faite pour définir une période de recuit isotherme (PIA) expliquant la microstructure finale dans le dépôt.
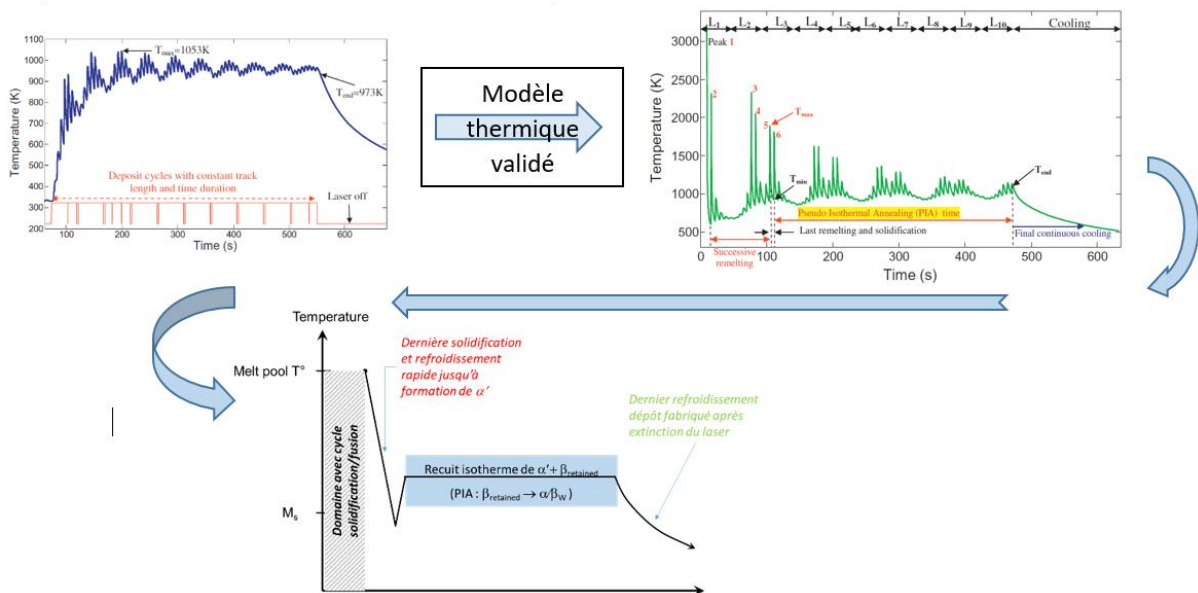

*Figure VII-1 : Passage du relevé des températures enregistrées dans le substrat en cours de fabrication du dépôt (stratégie HIE-CTL) aux histoires thermiques simulées en plusieurs points du dépôt via **l'utilisation du modèle thermique validé**, avant **l'approximation du procédé par un recuit isotherme** (PIA) suivie d'un **refroidissement final libre**. Les phases en présence ($\alpha' + \beta_{retained}$) au début de l'isotherme sont données par le refroidissement rapide lors du dernier pic de solidification en un point, après un cycle de plusieurs fusions en ce même point.*

Cette approche simplifiée, est remise en question dans l'article suivant #8. Ce dernier prend en compte tous les événements thermiques pour établir un lien avec les phénomènes métallurgiques associés, que ce soit lors de la solidification ou en particulier, pour les transformations en phase solide au cours de la fabrication du dépôt.

Partie B – Article #7 – 3D thermal finite element analysis of laser cladding processed Ti-6Al-4V part with microstructural correlations. H-S Tran, J. Tchoufang Tchuindjang. H. Paydas, A. Mertens, R. T. Jardin, L. Duchêne, R. Carrus, J. Lecomte-Beckers & A. M. Habraken. Mater. & Des. 128 (2017), pp.130-142

76

VIII. CHAPITRE 8 : PRÉSENTATION ET COMPLÉMENTS D'ÉTUDE SUR L'ARTICLE #8

VIII.1. Introduction

Cet article boucle la série après les deux premiers dédiés respectivement à la fabrication et la caractérisation macroscopique de dépôts par pulvérisation de poudre fondue au laser (« Directed Energy Deposition » ou DED), ainsi qu'à l'utilisation d'un modèle thermique validé pour décrire l'évolution de la microstructure au sein d'un dépôt qui présente une macrostructure homogène.

Pour rappel, on a jusqu'ici considéré des approches simplifiées pour décrire la microstructure finale observée dans un dépôt issu d'un procédé DED. La première approche considérant des dépôts obtenus par des stratégies de fabrication différentes a suggéré un refroidissement équivalent depuis la température du bain de fusion, les variations locales (dans le volume du dépôt, centre d'une couche ou bord, bas ou haut du dépôt, …) dans la vitesse du refroidissement étant susceptibles d'induire l'hétérogénéité dans la microstructure.

L'introduction d'un modèle EF permettant de simuler les histoires thermiques en tout point du dépôt a montré que cette première approximation n'était pas adaptée. En effet, on a établi l'existence de cycles thermiques avec des gradients élevés au chauffage et au refroidissement, gradients qui étaient susceptibles de décaler les points de transformation. Toutefois l'exploitation du modèle thermique s'était limité à un dépôt homogène, qui présentait quasiment la même microstructure partout, microstructure pour laquelle une approximation de type recuit isotherme a permis de valider l'ensemble du dépôt.

Dans cet article #8, on va considérer le cas plus complexe du dépôt obtenu avec une stratégie de fabrication qui génère une accumulation de chaleur localisée dans le centre de la cuvette, les bords étant refroidis très rapidement. Il s'agit de l'échantillon HIE-DTL (énergie incidente élevée, longueur de cordon décroissante), qui présente des hétérogénéités à toutes les échelles, tant macroscopique (dureté Vickers) que microscopique (matrice).

Après avoir considéré les cas simples, l'étude de ce cas complexe a permis de définir un nouveau concept, celui dit des blocs de temps et de transformations de phase ou Time-phase-Transformation-Block (TTB). Ce concept s'avère nécessaire non seulement à la compréhension des transformations en phase solide, mais il est aussi indispensable pour implémenter les modèles cinétiques adaptés pour la fabrication additive en général.

L'article a nécessité un double état de l'art pour d'une part, rechercher la littérature existante sur la prédiction de l'évolution des transformations de phases en cours de fabrication additive, peu importe le type de procédé, et d'autre part, pour comprendre pourquoi les modèles cinétiques de transformation de phases existants ne fonctionnent pas quand on les utilise avec les procédés AM, notamment quand on peut former des phases complexes ou multiples.

Cet article fait donc un état de l'art sur les procédés AM et le type de structures attendues, avec une focalisation sur leur caractérisation via les mesures de duretés. De plus il apporte une revue sur les modèles thermocinétiques en indexant les conditions dans lesquels ils ont été conçus, ces conditions fournissant des indications précieuses sur les paramètres à modifier ou à adapter si on veut les appliquer aux procédés AM. La critique pour des modèles connus à ce jour concerne majoritairement la non-prise en compte des effets de vitesses, pour certains lors du refroidissement, mais pour tous les cas lors du chauffage. Ces effets se marquent en particulier par un déplacement des points de transformations qui peut être très significatif, alors que le plus souvent ces points ont été considérés comme des valeurs fixes.

De plus, la revue de la littérature permet de rappeler les mécanismes de transformations en phase solide, avec ou sans diffusion, en insistant sur les conditions qui favorisent l'un ou l'autre mécanisme, la vitesse étant une fois encore un paramètre important.

VIII.2. Bref rappel sur le contexte

Un seul échantillon est considéré dans cette étude, et il s'agit du dépôt HIE-DTL, déjà présenté à l'article #6, pour lequel à la fois la macrostructure (dureté Vickers) et la microstructure ont été identifiées comme hétérogènes. Le dépôt provient du programme de recherche (BLISK ou Bladed Disk), de la convention RW 6247[15], dont l'objectif était l'étude de faisabilité de composants réparés soit par soudage en friction linéaire soit par rechargement en fabrication additive par fusion de poudre au laser. Les propriétés thermophysiques déjà déterminées dans le cadre du projet, sont utilisées ici pour établir le modèle thermique.

Le **Tableau VIII-1** rappelle le fil conducteur structurant le travail pour les trois articles de cette partie de la thèse.

La caractérisation microstructurale porte sur trois points d'intérêt choisis parce qu'ils correspondent aux extrema et à la valeur médiane de la dureté. Les microstructures en ces points sont elles aussi différentes. Les transformations de phases à l'état solide sont passés en revue, pour préciser non seulement les mécanismes (diffusif ou displacif) mais aussi les conditions pour les réaliser (vitesse, points critiques de transformations, etc.).

La partie numérique est assurée par l'équipe du service MS²F dirigée par A. M. HABRAKEN, ce qui permet de restituer les histoires thermiques en chacun des trois points d'intérêt choisi. A partir des histoires thermiques, on propose un concept nouveau qui permet de décrire qualitativement l'évolution de la microstructure en cours de fabrication additive.

Characterization at a macro scale	Characterization at a micro scale (Microstructure determination and Description and/or Highlighting of solid phase transformations)	Modeling (Thermal model and predictive approaches for kinetic models implementation)
• Heterogeneous macrostructure (DTL configuration @HIE) with the definition of three points of interest (POIs)	• Solid state phase transformations, under either CHT, CCT and TTT conditions	• Thermal model implementation and validation • Simulated thermal curves leading to accurate microstructure description (three POIs) • Qualitative description of solidification and subsequent solid phase transformation mechanisms

Tableau VIII.2 : Rappel des thématiques présentes dans l'article

VIII.3. Résultats principaux

VIII.3.1. Modèle thermique EF et observation relative à la solidification

L'approche est similaire à celle déjà présentée dans l'article #7, avec cependant une différence dans le positionnement du thermocouple, et aussi une différence dans la géométrie du dépôt à cause de la stratégie DTL (longueur de cordon décroissante), ce qui nécessite un nouveau maillage.

---

[15] Coordination assurée par Techspace Aero, de 2010 à 2013.

Partie B – Article #8 – A New Concept for Modeling Phase Transformations inTi6Al4V alloy manufactured by Directed Energy Deposition. J. Tchoufang Tchuindjang. H. Paydas, H-S Tran, R. Carrus, L. Duchêne, A. Mertens, &. A. M. Habraken. To be submitted.

78

La validation du modèle thermique s'est faite en reproduisant l'allure du cyclage thermique des courbes de référence enregistrées par les thermocouples placés dans le substrat, après le dépôt final de 10 couches dans la pièce.

Le modèle validé permet de reconstituer la géométrie 3D du bain de fusion en cours de fabrication à chaque étape de la simulation, en considérant toutes les températures supérieures ou égales au liquidus.

La prédiction et l'observation expérimentale des dimensions de la zone affectée thermiquement (« Heat Affected Zone » ou HAZ) principale, entre le substrat et le dépôt, suggère un décalage vers le haut des températures critiques de transformation en phase solide avec la vitesse de chauffage, et notamment le passage dans le domaine de la phase β, soit T_{DISS} ou $\alpha_{transus}$ comme début de transformation de α en β, et $\beta_{transus}$.

VIII.3.2. Etat de l'art sur les transformations de phases, les microstructures et les modèles cinétiques

La revue approfondie de la littérature a permis de mettre en évidence les mécanismes existants dans l'alliage Ti6Al4V, notamment de type displacif ou diffusif, et ce en considérant aussi bien le chauffage que le refroidissement. Cette mise en évidence n'a jamais été présentée telle quelle à ce jour, cela a nécessité de croiser de nombreux travaux dont les objectifs étaient très variés.

La même approche sur les microstructures existantes pour l'alliage étudié, et notamment les valeurs de duretés, a également présenté un intérêt majeur. Notre travail démontre que ce paramètre seul ne peut être pris en compte pour distinguer les phases en présence dans l'alliage.

La revue sur les modèles cinétiques a enfin permis de démontrer les limites des approches constantes quant aux procédés de fabrication additive. Ces limites sont autant liées aux conditions expérimentales initiales utilisées pour déterminer les paramètres identifiant les modèles, qu'à une compréhension insuffisante des mécanismes de transformation.

La thèse de Master d'Elena Esteva (Esteva Fàbrega, 2018) « Microstructure prediction of Ti6Al4V Processed by Laser Cladding » a permis de montrer l'inadéquation des approches de simulation du style de « Crespo » (Crespo and Vilar, 2010), qui appliquent les modèles phénoménologiques classiques à la fabrication additive. Ces modèles, outre le problème du paramétrage, prennent mal en compte les effets spécifiques qui peuvent survenir au chauffage. Notons aussi que ces modèles considèrent le plus souvent des points critiques de transformations fixes, y compris pour les réactions avec diffusion sous variations rapides de la température.

VIII.3.3. Transformations en phase solide dans le dépôt en cours de fabrication – introduction du concept de TTB

Les histoires thermiques simulées permettent de suivre l'évolution de la température en des points d'intérêts (POIs). Les trois POIs choisis présentent des histoires thermiques différentes, en lien avec la stratégie de fabrication et leur localisation dans le dépôt.

On considère en premier le cas du POI2, qui représente le point avec l'histoire thermique la plus complexe. Il se situe dans le fond de la cuvette, là où l'accumulation de chaleur est la plus significative. En partant de la revue de la littérature sur les transformations de phase, on dispose des outils pour comprendre ce qui se produit même en présence de gradients de température élevés. C'est ainsi qu'on parvient à fixer les conditions pour chaque type de transformation de phase, en incluant le cas du chauffage trop souvent ignoré.

Partie B – Article #8 – A New Concept for Modeling Phase Transformations inTi6Al4V alloy manufactured by Directed Energy Deposition. J. Tchoufang Tchuindjang. H. Paydas, H-S Tran, R. Carrus, L. Duchêne, A. Mertens, &. A. M. Habraken. To be submitted.

79

Via un essai de remise en solution réalisé en laboratoire, les conditions pour avoir la transformation en phase β solide, avec recristallisation dans cette phase ont été vérifiées. Cette expérience supplémentaire est indispensable pour mettre en évidence l'absence de ce type de réaction pendant le procédé de fabrication.

Le concept de TTB est défini. Il s'applique à des blocs temps caractéristiques des domaines où au moins une transformation de phase spécifique peut se produire.

Plus simple, le cas de POI1 découle aisément du cas POI2. Il correspond à l'absence d'accumulation de chaleur, ce qui limite les interactions avec les couches antérieures.

Le cas du POI3, situé au somment du dépôt, présente une singularité facilement identifiable via l'analyse basée sur le concept de TTB. En effet, on met en évidence la possibilité de changer de mécanisme de transformation de phase au cours d'un même refroidissement, et ce à cause du changement de la vitesse de refroidissement qui diminue pour devenir inférieure à la vitesse critique pour la transformation martensitique.

L'analyse descriptive ci-dessus, faite à partir des histoires thermiques simulées est validée par l'analyse micrographique des zones considérées sur le dépôt (coupes). C'est ainsi qu'on met en évidence à l'échelle microscopique, l'existence de toutes les structures distinctes observées pour les 3 POIs. Le lien avec leurs duretés respectives explique comment des microstructures constituées de phases variées, ayant plus ou moins subies des transformations, peuvent produire des duretés similaires, en étant toutefois très différentes.

La **Figure VIII-1** montre de quelle manière on procède pour élaborer l'organigramme final, qui tient compte des mécanismes des transformations de phases, en s'appuyant sur les blocs de type TTB.
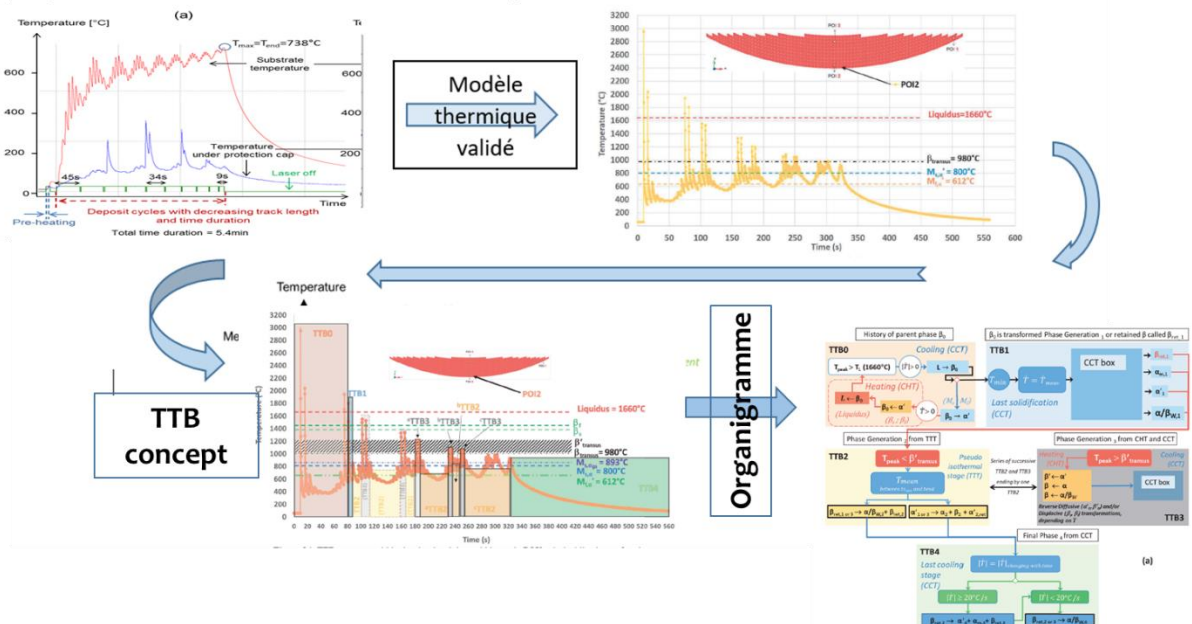

*Figure VIII-1 : Passage du relevé des températures enregistrées dans le substrat en cours de fabrication du dépôt (stratégie HIE-CDTL) aux histoires thermiques simulées en plusieurs points du dépôt via **l'utilisation du modèle thermique validé**, avant **l'élaboration du concept TTB**, qui permet de générer **un organigramme** qui tient compte des **mécanismes de transformations de phases** dans chaque bloc, en considérant les CHT, TTT et CCT*

Partie B – Article #8 – A New Concept for Modeling Phase Transformations inTi6Al4V alloy manufactured by Directed Energy Deposition. J. Tchoufang Tchuindjang. H. Paydas, H-S Tran, R. Carrus, L. Duchêne, A. Mertens, &. A. M. Habraken. To be submitted.

80

VIII.4.   Conclusions et perspectives

On a établi un concept nouveau, nécessaire pour comprendre les transformations de phases et qui peut servir de base pour l'implémentation de modèles cinétiques corrigés pour s'adapter aux cinétiques présentes en fabrication additive.

La prise en compte du concept de TTB permet enfin de considérer toutes les étapes du cycle thermique, en expliquant pour chacune d'elle, tous les mécanismes possibles en lien avec les transformations de phases.

Au niveau des perspectives, outre l'implémentation de modèles cinétiques modifiés, à partir de plans expérimentaux adaptés (déjà en cours, avec dilatométrie rapide), on suit aussi la piste de la nano-indentation pour aider à différencier les phases à une échelle plus fine, au contraire des duretés Vickers.

VIII.5.   Références

Crespo, A., Vilar, R., 2010. Finite element analysis of the rapid manufacturing of Ti–6Al–4V parts by laser powder deposition. Scripta Materialia 63, 140–143. https://doi.org/10.1016/j.scriptamat.2010.03.036

Esteva Fàbrega, E., 2018. Master thesis: Microstructure prediction of Ti6Al4V processed by Laser Cladding. 25/07/2018 109.

IX. CONCLUSION GÉNÉRALE

IX.1. Rappel du contexte

Les cylindres de laminoir à froid ou à chaud sont destinés à une application où les contraintes en service sont très complexes. Le procédé de laminage est en lui-même difficile à simuler, à cause de la nécessité de prendre en compte à la fois le comportement du cylindre mais aussi celui du matériau laminé et de l'environnement du laminage (température, lubrification, contraintes physico-chimiques, mécaniques, thermiques, etc.). En pratique, les fabricants de cylindres ont développé différentes classes d'alliages afin d'obtenir les propriétés principales liées à chaque étage du train de laminoir. Les modifications d'alliages candidats s'opèrent relativement lentement, car il faut d'une part que les performances effectives lors du laminage soient améliorées par rapport aux alliages déjà existants, et d'autre part, que les coûts d'élaboration restent comparables. Les nouveaux alliages doivent de plus confirmer leur fiabilité en cours d'opération, et leur comportement en cas d'incident.

C'est ce qui explique qu'un alliage tel que l'ICDP reste à ce jour la référence dans les dernières cages finisseuses des trains à bandes à chaud. Les autres étages ont connu des modifications majeures, mais les alliages utilisés tels que les HSS, semi-HSS ou HCS peuvent encore être optimisés. A cette fin, l'approche de la science de matériaux permet d'établir des corrélations procédés - microstructures – propriétés qui peuvent guider des évolutions futures, exploitant notamment des phases formées hors d'équilibre, dont certaines restent encore mal connues.

Dans le même temps, le Ti6Al4V est d'un usage très répandu en aéronautique et aérospatiale. Cependant la qualification actuelle de ce matériau est liée à une routine d'élaboration bien éprouvée, telle que la coulée en lingot suivie de la mise à forme à chaud. Or l'usage de procédés de fabrication additive génère des microstructures complexes, qu'il convient de bien connaître afin de les adapter soit aux domaines d'application existants, soit à de nouveaux domaines.

IX.2. Apports de la thèse

On a montré dans la première partie de cet ouvrage comment en partant d'une macrostructure (mode de solidification et une taille de grains) imposée par un procédé de fabrication, on peut obtenir différentes microstructures qui vont influencer les propriétés mécaniques. On peut alors, à partir d'une caractérisation multi-échelle et pluridisciplinaire, identifier les paramètres métallurgiques qui sont les plus pertinents pour expliquer les phénomènes d'endommagement observés dans le matériau. L'établissement de corrélations micro-macro apparaît comme un outil indispensable à la compréhension du comportement des matériaux. Ces liens sont des plus utiles pour développer – de façon critique et raisonnée - les modèles numériques prédictifs (lois de comportement, modèle d'endommagement…) à implémenter pour que disposer d'outils calculant les propriétés finales suite au mode de fabrication.

On a aussi montré dans la première partie de la thèse, à travers le développement de routines de traitements thermiques optimisés du point de vue métallurgique, dans quelles mesures ceux-ci pouvaient aider à homogénéiser une structure héritée d'un procédé d'élaboration. En l'occurrence, il est apparu que les ségrégations même mineures, qui apparaissent lors de la coulée conventionnelle ne sont pas nécessairement faciles à gommer par des traitements thermiques. Si le forgeage a montré qu'on pouvait plus facilement réduire l'échelle critique de la structure de solidification, en facilitant l'homogénéisation et la densification du matériau, la pièce massive brute de coulée s'avère plus difficile à homogénéiser par traitement thermique, même en se rapprochant du point critique qu'est le solidus. Ce faisant, cette situation démontre que seule une nouvelle fusion peut permettre de parvenir à un métal homogène, comme on l'a réalisé en ATD sur des échantillons de petite taille. A grande échelle, cela reste un défi majeur, qui représente aussi un coût non négligeable. En général, on procède par une métallurgie dite

secondaire pour effectuer une nouvelle mise à nuance, en profitant aussi pour essayer de rendre la matière plus propre du point de vue du contenu inclusionnaire, un autre aspect qui est critique pour les propriétés mécaniques, comme cela a aussi pu être établi dans cette thèse. Mais cette réflexion sur la taille du volume critique admissible pour une nouvelle fusion qui permette à la fois d'affiner la structure de solidification en la maintenant propre au niveau inclusionnaire, établit naturellement le pont vers la fabrication additive, qui est abordée dans la seconde partie de l'ouvrage. En effet, les procédés d'impression 3D pour les métaux ont ceci en commun que c'est la taille réduite du bain de fusion, en comparaison avec la poche de coulée massive pour la fonderie classique, qui fait toute la différence, y compris pour les gradients thermiques élevés qui sont atteints.

Dans la seconde partie de l'ouvrage consacré naturellement à la fabrication additive, on a montré à partir d'une analyse multi-échelles couplant la caractérisation expérimentale et la modélisation thermique par éléments finis, les liens entre les propriétés mécaniques finales issue d'une microstructure fine et sa genèse. La prédiction de l'évolution de la microstructure pendant la fabrication additive s'appuie sur une description des mécanismes des transformations en phase solide. Cette démarche apparaît indispensable pour définir et calibrer les modèles cinétiques adaptés à la fabrication additive. Cette connaissance est un pré requis essentiel pour optimiser les paramètres de fabrication visant une propriété finale, associée à une microstructure bien contrôlée.

Au final, on note en travaillant sur deux familles d'alliages différentes, que la métallurgie reste un domaine particulier, où l'avancement des connaissances reste fortement tributaire de l'évolution historique d'un matériau donné, de son élaboration et de ses applications. Pour les aciers et fontes, le schéma de solidification, de même que les transformations en phase solide, peuvent déboucher sur des structures complexes, dont la plupart ont souvent été bien étudiées. Par contre dans le cas du Ti6Al4V uniquement constitué de deux phases à l'équilibre, d'importantes lacunes subsistent dans nos connaissances, notamment en ce qui concerne la transformation martensitique, ou la précipitation en phase solide dans l'intervalle intercritique. De telles lacunes résultent souvent des types de microstructure communément générés par les procédés classiques.

En réalité, pour la plupart des alliages, le domaine hors équilibre reste encore un vaste champ exploratoire. Ceci s'applique tout particulièrement au phénomène de sursaturation qui conduit à la formation de phases dites métastables. Cette thèse a montré que certains procédés de coulée classique conduisent déjà à la formation de phases sursaturées telles que la troostite qui précipite pendant la coulée centrifuge. La fabrication additive est par excellence le procédé où le phénomène de sursaturation est le plus courant. Là où les conditions d'équilibre supposent un nombre limité de phases, ayant des compositions chimiques faciles à prédire, le domaine hors équilibre peut déboucher sur une multitude de phases métastables, dont certaines pourraient avoir des propriétés intéressantes, ouvrant la voie à de nouvelles applications.

X. PERSPECTIVES

Les perspectives peuvent être abordées suivant deux angles de vue. Le premier concerne la continuité sur les thématiques mises en évidence dans ce travail. Le second angle est plus prospectif, avec une volonté de reconsidérer le triptyque de la science des matériaux.

Les expertises au service de l'industrie offrent toujours l'occasion de croiser différentes disciplines pour répondre à des questions sur l'endommagement mécanique ou physico-chimique de pièces diverses, souvent soumises à des contraintes sévères et complexes[16]. L'approche de l'analyse multi-échelle comme outil de compréhension est donc toujours très utile à ce sujet, avec un intérêt pour différents alliages métalliques.

La sursaturation dans le cas des aciers et fontes alliées est apparue comme le piégeage d'un atome interstitiel dans une matrice δ ou γ, à haute température et sous un effet de vitesse, qui est plus ou moins facilité par la structure de la maille élémentaire, notamment sa distorsion par la présence de binôme d'atomes en substitution[17]. Ce piégeage conduit avec le refroidissement, à une désaturation marquée par la libération de l'atome interstitiel, qui se recombine avec d'autres pour former des carbures. La désaturation peut survenir plusieurs fois au sein de la même matrice, en fonction de la température, en lien avec la limite de solubilité de l'atome interstitiel. C'est notamment ce qui a été observé pour le grain austénitique du HCCS, dans lequel on observe en premier lieu la précipitation des carbures secondaires juste après la solidification, en refroidissement continu autour des 1000°C Une seconde désaturation donne lieu, ultérieurement, à la formation de la troostite granulaire, lors d'un pseudo-recuit autour de 700°C[18].

La sursaturation est aussi présente dans la martensite, comme phénomène intrinsèque lié à l'absence de diffusion lors de la transformation à partir de la phase-mère, sous une vitesse de refroidissement supérieure à une valeur critique. Ce constat est autant valable pour les aciers et fontes alliées[19], que pour l'alliage Ti6Al4V[20], respectivement au départ de la phase γ ou de la phase β. Dans le cas de la martensite, la désaturation prend la forme d'une précipitation de carbures pour les aciers, et d'une décomposition pour le Ti6Al4V. Ces phénomènes peuvent survenir lors de traitements thermiques bien élaborés, ou en cours de fabrication. Les microstructures qui en résultent peuvent présenter des propriétés améliorées, comparativement aux structures brutes de coulée ou de fabrication additive. On a montré que le choix de la routine d'élaboration nécessitait aussi une bonne connaissance des propriétés des phases dans l'état brut de coulée/fabrication, et après traitements thermiques.

Dans cette thèse, la sursaturation est apparue comme un état favorisant une multitude de phase dites métastables, qui sont distinctes des phases d'équilibre, et qui induisent des propriétés spécifiques. Le domaine hors équilibre qui est la référence en fabrication additive, apparaît donc comme un champ nouveau pour étudier la nature et les propriétés de ces « nouvelles » phases ; ainsi que leurs applications.

En considérant donc la sursaturation comme un paramètre à part entière, et en ayant connaissance des mécanismes qui pilotent l'endommagement, on peut décider de fixer d'abord la microstructure qui conviendra à une application donnée, avant de déterminer ensuite la méthode d'élaboration qu'il faudra suivre pour produire ladite microstructure. Il s'agit de l'approche du dimensionnement d'alliages (Bian et al., 2018; Cui et al., 2008; Imayev et al., 2007; Kang et al., 2009), appelée aussi l'ingénierie des

---

[16] Voir Note sur les compétences en expertises (Annexes)

[17] Voir Articles #1, #3 et #4

[18] Voir Article #5

[19] Voir Articles #1, #2, #4 et #5

[20] Voir Articles #7 et #8

microstructures. Ce dernier concept intègre la variation de l'échelle d'analyse comme paramètre clé (DeHoff, 1999; Ledermueller et al., 2018). Donc, au lieu de subir les contraintes d'un procédé d'élaboration pour ensuite essayer par des post-traitements de produire les propriétés les plus favorables à ce procédé, on pourrait plutôt définir les caractéristiques métallurgiques les plus adéquates, pour trouver à rebours, la séquence de fabrication. Ce concept est désormais assez répandu dans différents alliages métalliques (Bian et al., 2018; Cui et al., 2008; Imayev et al., 2007; Kang et al., 2009). Les possibilités offertes par la fabrication additive devraient permettre d'étendre ce concept.

Les collaborations scientifiques et l'essor de la fabrication additive ouvrent aussi un champ d'investigation idéal pour développer l'approche croisée. Ce domaine concerne des travaux en cours, sur de l'aluminium fabriqué par SLM[21] et par WAAM[22], des composites inox renforcés par des carbures et des aciers à outils produits par DED[23], du titane produit par DED, SLM et EBM[24]. Les travaux en question font pour la plupart l'objet de thèses de doctorat menées en tutelle ou cotutelle au sein du service MMS. Comme chercheur sénior, j'ai une implication majeure dans l'encadrement des plus jeunes doctorants, notamment pour les aspects de caractérisation et de corrélations micro-macro. En outre de nombreuses collaborations sont menées avec l'unité MS²F, pour le volet numérique.

Plus précisément, suivant les domaines du triptyque que sont les procédés, la caractérisation de microstructure et les propriétés, voici les pistes poursuivies…

X.1. Procédés

- Sur la solidification qui intervient dans les procédés, le constat de l'inadéquation entre les simulations thermodynamiques et les analyses en conditions hors équilibre faites en DTA, sont une piste à suivre, qui a déjà été discuté avec Thermo-Calc®. Il s'agit notamment de prévoir des essais pour parvenir à prédire correctement le premier solide dans les aciers, et aussi d'améliorer la prédiction des carbures de solidification, en particulier le carbure M_2C.

- Sur les transformations en phase solide, le champ d'investigation concerne autant la troostite que la martensite ou la bainite. Pour la troostite, sa présence dans l'espace intergranulaire a aussi été observée dans un alliage HSS obtenu par DED (A11), ce qui rappelle la nécessité de continuer à l'étudier[25]. Pour la martensite, il s'agit surtout de mieux l'étudier dans le cadre du l'alliage Ti6Al4V, et notamment de déterminer ses points critiques de transformation M_s et M_f. L'approche croisée entre DTA et dilatométrie qui a montré des résultats intéressants pour les aciers, sera utilisée dans ce cadre. Dans le cas de la bainite, sa caractérisation par mesures thermophysiques est aussi en cours, notamment pour la distinguer de la martensite.

X.2. Caractérisation de la microstructure

- Au niveau de la caractérisation microstructurale des phases, la microscopie électronique à balayage, en association avec diverses techniques connexes, restera une approche de choix. Suivant la méthode déjà établie sur un HSS et sur un acier inoxydable renforcé par des carbures et fabriqué par DED, la caractérisation de phases métastables combinera EBSD, EDX, et éventuellement DTA pour déterminer la température critique des phases concernées (Maurizi Enrici et al., 2020).

---

[21] PhD J. Delahaye (en cours)

[22] Projets IAWATHA (InnovAtion en Wallonie par les TecHnologies Additives) et LongLifeAM

[23] PhD T. Maurici-Enrizi (en cours)

[24] Projet IAWATHA (en cours)

[25] Projet RECYLCLAD (2011 – 2016) - Fabrication de CYLindres bimétalliques par REchargement Laser (Laser cladding) d'aciers à outils optimisés sur axes REutilisables

- Sur l'identification et la quantification des phases, la technique de la nanoindentation qui n'a pas été présentée dans cette étude, a déjà fait l'objet de travaux notamment sur les composites inox renforcés par des carbures[26], et sur le Ti6Al4V (Tchuindjang et al., 2019). Cette technique présente l'avantage de couvrir une échelle allant de quelques microns (donc la taille des grains en AM) à quelques nanomètres, cette dernière dimension permettant d'approcher les interfaces de phases (joints de lattes pour la martensite, ou fins précipités et matrices). La technique paraît aussi prometteuse pour une approche quantitative, via la réalisation de macro-grilles d'indentation, à partir du moment où on peut déterminer les propriétés des phases (dureté et module de Young) à faible échelle[27]. Les analyses en cours sur un HSS produit par DED sont prometteuses[28]. La technique est aussi intéressante pour la caractérisation à l'échelle locale, notamment pour identifier les zones affectées thermiquement dans les dépôts issus de la fabrication additive, comme cela a déjà été effectué pour l'alliage AlSi10Mg produit par fusion sélective au laser (Selective laser melting ou SLM) (Delahaye et al., 2019; Mertens et al., 2020).

X.3. Propriétés

- Concernant les propriétés, l'usure à température ambiante et à chaud fait désormais partie des domaines phares de l'unité. Outre la caractérisation d'alliages conventionnels, il y a celle d'alliages issus de la fabrication additive qui est réalisée régulièrement, avec des résultats intéressants (Hashemi et al., 2017). L'objectif n'est pas de reproduire les conditions de service des pièces dans leurs applications spécifiques, mais de mettre en évidence des mécanismes d'endommagement dont la compréhension est très utile pour développer des méthodes prédictives. Une fois encore, les modèles thermomécaniques seront développés en collaboration avec les numériciens.

X.4. Modélisation

- Le modèle thermique présenté dans cette étude concernant l'alliage Ti6Al4V, a déjà été développé et validé à 2D pour l'acier HSS M4 produit par DED (Jardin et al., 2019). L'alliage composite 316L renforcé par des carbures WC a aussi fait l'objet d'une simulation 2D par l'équipe MS²F, qui permet de restituer l'histoire thermique en tout point du dépôt DED (Fetni et al., 2020).
- L'extension au modèle thermique 3D du HSS M4 produit par DED, ainsi que sa modélisation thermomécanique qui inclut les transformations de phases et les contraintes, fait déjà l'objet d'une autre thèse menée au sein du service MS²F[29]. Une telle extension est aussi envisagée pour les composites DED en inox renforcés par des carbures.
- Au niveau des modèles cinétiques, le concept TTB élaboré à partir du procédé DED sur Ti6Al4V fixe la base pour la prédiction des phases finales[30]. Ce travail se fera en collaboration avec les équipes de numériciens.

X.5. Références

Bian, J., Lu, H.Z., Wang, W.J., Guo, A.M., 2018. Alloying Design and Process Strategy for High Performance 1800 MPa Press Hardening Steel, in: Advanced High Strength Steel and Press Hardening. WORLD SCIENTIFIC, pp. 3–13. https://doi.org/10.1142/9789813277984_0001

Cui, X.-H., Shan, J., Yang, Z.-R., Wei, M.-X., Wang, S.-Q., Dong, C., 2008. Alloying Design for High Wear-Resistant Cast Hot-Forging Die Steels. Journal of Iron and Steel Research, International 15, 67–72. https://doi.org/10.1016/S1006-706X(08)60146-6

---

[26] PhD T. Maurici Enrizi

[27] Projet IAWATHA

[28] Projet IAWATHA

[29] PhD R. Jardin

[30] Voir Article #8

DeHoff, R.T., 1999. Engineering of microstructures. Materials Research 2, 111–126. https://doi.org/10.1590/S1516-14391999000300002

Delahaye, J., Tchuindjang, J.T., Lecomte-Beckers, J., Rigo, O., Habraken, A.M., Mertens, A., 2019. Influence of Si precipitates on fracture mechanisms of AlSi10Mg parts processed by Selective Laser Melting. Acta Materialia 175, 160–170. https://doi.org/10.1016/j.actamat.2019.06.013

Enrici, T.M., Dedry, O., Boschini, F., Tchuindjang, J.T., Mertens, A., 2020. Microstructural and Thermal Characterization of 316L + WC Composite Coatings Obtained by Laser Cladding. Advanced Engineering Materials n/a, 2000291. https://doi.org/10.1002/adem.202000291

Fetni, S., Enrici, T.M., Niccolini, T., Tran, S.H., Dedry, O., Jardin, R., Duchêne, L., Mertens, A., Habraken, A.M., 2020. 2D thermal finite element analysis of laser cladding of 316L+WC Composite coatings. Procedia Manufacturing, 18th International Conference on Metal Forming 2020 50, 86–92. https://doi.org/10.1016/j.promfg.2020.08.016

Hashemi, N., Mertens, A., Montrieux, H.-M., Tchuindjang, J.T., Dedry, O., Carrus, R., Lecomte-Beckers, J., 2017. Oxidative wear behaviour of laser clad High Speed Steel thick deposits: Influence of sliding speed, carbide type and morphology. Surface and Coatings Technology 315, 519–529. https://doi.org/10.1016/j.surfcoat.2017.02.071

Imayev, R.M., Imayev, V.M., Oehring, M., Appel, F., 2007. Alloy design concepts for refined gamma titanium aluminide based alloys. Intermetallics 15, 451–460. https://doi.org/10.1016/j.intermet.2006.05.003

Jardin, R.T., Tchoufang Tchuindjang, J., Duchêne, L., Tran, H.-S., Hashemi, N., Carrus, R., Mertens, A., Habraken, A.M., 2019. Thermal histories and microstructures in Direct Energy Deposition of a High Speed Steel thick deposit. Materials Letters 236, 42–45. https://doi.org/10.1016/j.matlet.2018.09.157

Kang, N., Na, H.S., Kim, S.J., Kang, C.Y., 2009. Alloy design of Zn–Al–Cu solder for ultra high temperatures. Journal of Alloys and Compounds 467, 246–250. https://doi.org/10.1016/j.jallcom.2007.12.048

Ledermueller, C., Li, H., Primig, S., 2018. Engineering Hierarchical Microstructures via Advanced Thermo-Mechanical Processing of a Modern HSLA Steel. Metall Mater Trans A 49, 6337–6350. https://doi.org/10.1007/s11661-018-4934-3

Maurizi Enrici, T., Mertens, A., Sinnaeve, M., Tchuindjang, J.T., 2020. Elucidation of the solidification sequence of a complex graphitic HSS alloy under a combined approach of DTA and EBSD analyses. J Therm Anal Calorim 141, 1075–1089. https://doi.org/10.1007/s10973-019-09093-9

Mertens, A., Delahaye, J., Dedry, O., Vertruyen, B., Tchuindjang, J.T., Habraken, A.M., 2020. Microstructure and Properties of SLM AlSi10Mg: Understanding the Influence of the Local Thermal History. Procedia Manufacturing, 23rd International Conference on Material Forming 47, 1089–1095. https://doi.org/10.1016/j.promfg.2020.04.121

Tchuindjang, J.T., Paydas, H., Maurizi-Enrici, T., Carrus, R., Mertens, A., 2019. Micro-mechanical properties of the alpha' martensite phase occurring in a Ti-6Al-4V alloy after various processing routes, including Laser Metal Deposition. Presented at the The 14th World Conference on Titanium.

- ## ANNEXE 1 : ARTICLES DE RÉFÉRENCE POUR LA THÈSE

  - ## .. Article #1

Fractography survey on high cycle fatigue failure: Crack origin characterisation and correlations between mechanical tests and microstructure in Fe–C–Cr–Mo–X alloys

Jérôme Tchoufang Tchuindjang *, Jacqueline Lecomte-Beckers

Université de Liège (ULg), Département, Aérospatiale & Mécanique, Service de Métallurgie et Science des Matériaux,
Unité, Matériaux Métalliques Spéciaux IMGC, Bât. B52-1, Chemin des chevreuils, 4000 Liège, Belgium

Abstract

Raw materials were cast from different specific processes in order to produce cleaner steels with a reduced amount of inclusions. Studied materials that are HSS hardened alloys belonging to the Fe–Cr–C–X system were shared out in four groups depending on the tempering temperature and the presence of secondary and primary carbides. Both inclusions and carbides were roughly assessed by means of Image Analysis.

Forging was done on all studied materials with different reduction ratios in order to highlight the texture influence on mechanical properties.

High cycle fatigue tests were made using the boundary method to allow a quick evaluation of results.

Fractographic analyses carried out on broken samples led to the definition of four failure modes depending on the nature and the location of the point from which the crack was initiated in one hand, and the roughness of striations in the propagating area over and around the initiation point. Internal and surface crack initiation points were found, the latter being more harmful than the first ones. Though oxides appeared to be more detrimental than other inclusions, primary carbides were also found to be both crack initiation candidates and crack propagation enhancers.

Various parameters likely to influence high cycle fatigue failures were finally defined, the most significant one dealing with the nature and location of embedded precipitates and the forging reduction ratio.

© 2006 Elsevier Ltd. All rights reserved.

Keywords: Tool steels; High cycle fatigue; Forging; Inclusions; Carbides; Boundary method; Fractography; Crack initiation; Soakness

1. Introduction

Complex Fe–C–Cr–Mo–X systems, where X consists of V and/or W elements, are custom alloys for tool steels or high speed steels (HSS) as they exhibit excellent hardness and good wear resistance at higher temperatures [1]. The final microstructure is directly influenced not only by the solidification rates at the time of casting, but also by the later heat or thermo mechanical treatments.

Fe–C–Cr–Mo–X alloys can thus contain in their hardened matrix desired precipitates such as carbides, and also more or less exogenous and endogenous inclusions, depending on the way casting process was performed [1–4].

Inclusions are present in all commercial materials as a result of deoxidising additions, impurities or entrained exogenous material. Inclusions are common sites for fatigue crack nucleation and are known to be particularly deleterious in high strength steel [5].

Considerable studies have been done on weakening the influence of inclusions on fatigue behaviour, especially on its nature and size features [6–9]. Reducing inclusions size leads to increased fatigue behaviour [7–9] and a methodology

* Corresponding author. Tel.: +32 4 366 91 62; fax: +32 4 366 91 13.
URL: http://www.ulg.ac.be/metaux (J. Tchoufang Tchuindjang).

Nomenclature

A–S	studied material main coding
A_L–S_L	raw material (A–S) in a longitudinal direction
A_T–S_T	raw material (A–S) in a transversal direction
AED	average equivalent diameter of a precipitate (from Image Analysis)
BM	boundary method, for quick evaluation of transition range in fatigue tests
BSE	backscattered electron in SEM analysis
CIH	crack initiation halo
D	distance between the two levels of alternating load in boundary method
EAF	electrical arc furnace, as conventional casting
EDX	energy dispersive by X-rays
ESR	electro slag remelting (casting process)
FCI	failure crack initiation
FM1–FM4	failure mode 1 to failure mode 4
FRR	forging reduction ratio
GCF	giga cycle fatigue
HCF	high cycle fatigue
HSS	high speed steel
HV30	Vickers hardness with a 30 kg load
ICIP	internal crack initiation point
$K\alpha$ ($L\alpha$)	element spectrum line linked to electron orbital energy in EDX Analysis
L_1 (L_2)	Level 1 (Level 2) as probabilistic load near the range of transition in BM
LCF	low cycle fatigue
M_xC_y	carbide formulation with C for carbon and M for metallic element
MCIP	multiple crack initiation point
MED	maximum equivalent diameter of a precipitate (from Image Analysis)
MG1–MG4	material group 1 to material group 4, as a distribution related to the presence of secondary and primary carbides
n	Number of tested specimens per level while using BM
N_g	defined greater number of cycles to failure
ODA	optically dark area
P_F	probability of fatigue failure while using BM
r	number of broken specimens after HCF test while using BM
R_P	ultimate tensile strength (UTS)
S_a	alternating load for fatigue tests
SCIP	surface crack initiation point
SE	secondary electron in SEM analysis
SEM	scanning electron microscopy
$S_{FL,1}$ ($S_{FL,2}$)	alternating load related to Level 1 (Level 2) while using BM
UTS	ultimate tensile strength (R_P)

had been proposed to define the maximum defect size allowable in a casting component.

Fatigue crack initiation (FCI) usually occurs on the specimen surface in low cycle fatigue (LCF). However, there are more and more data which show that fatigue cracks initiate from the specimen subsurface when the cyclic lives are higher (or at a lower stress level). Furthermore, another study led to the hypothesis that the cause of fatigue failure in the surperlong life regime was due to the mechanical fatigue threshold for a small crack emanating from a non-metallic inclusion which was reduced by an environmental effect associated with hydrogen trapped at non-metallic inclusions (ODA concept) [6,8,10–12].

While subsurface crack initiation behaviour has been clearly detected in many materials under any testing conditions, the mechanism has not been fully understood [10].

Thus, studies dealing with features other than either inclusions or internal defects to explain fatigue failure are rare. In fact, carbides contrary to inclusions are expected in tool steels and their volume fraction is nearly controlled in order to yield the defined microstructure which could achieve the desired metallurgical properties [13]. Thus, the question of how carbides could influence fatigue behaviour remains of concern.

High cycle fatigue (HCF) tests are performed to focus on every weakening feature that could have an influence on fatigue behaviour, in the field of endurance life over 10^7 cycles. Therefore, using HCF tests could allow highlighting of carbides influence in extreme conditions together with inclusion effects.

As fatigue tests are known to enhance possible crack initiation points (geometry defects and stress concentration) [14,15], HCF tests could set an overall harmfulness gradation between inclusions and carbides while focussing on any harmful point that is a crack initiation candidate.

It is well known that the more a precipitate is weakened, the more the fatigue failure will be initiated early on this point [6,7,11,16]. And once the crack starts, there are other metallurgical features which support its propagation [6,7,11]. Then again, such a study could enhance carbides effect on propagation stage of fatigue failure.

In this work, four groups of Fe–C–Cr–Mo–X system were studied with respect to tensile and fatigue, the former distribution depending on whether fully martensitic matrix contained primary eutectic carbides or not.

These materials were of cleaner steel since a reduced inclusions amount was set through appropriate processes.

In fact, inclusions found were of very small size (below 50 μm), and they were often rare.

Inclusions elongation and high temperature malleability on carbides were also studied towards various forging reduction ratios, to allow investigations on texture influence on mechanical properties while comparing samples cut from a direction parallel to the forging axis and between samples perpendicular to the mentioned direction.

An attempt in precipitates assessment was made towards Image Analysis in order to correlate size and volume fraction of inclusions and carbides to fatigue behaviour.

Fractography was used to identify crack origin and to characterise the propagation area of the failure over and around the initiating stage on samples which undergo HCF.

2. Experimental procedures

2.1. Material and specimen preparation

2.1.1. Material origin and processing

Studied materials are hot worked bars of Fe–C–Cr–Mo–X type. Ingots to be hot worked came from conventional casting with EAF or ESR processes, both processes leading to cleaner materials [9].

After forging, full annealing was performed before quenching and tempering.

Hot working led to a forging reduction which can vary on a single ingot, and also from an ingot to another, in order to investigate the deformation behaviour of inclusions and carbides.

Average chemical compositions are given in Table 1 with the corresponding forging reduction ratio. Materials can be divided up by four groups related to their major alloying elements ratios that yield Materials Group1 (MG1) for A–F, MG 2 for G and H, MG3 for S, and MG4 for Q and R.

MG1 comprised of minor features both for EAF and ESR processes, which were, respectively, performed with (E) or without (F) any inert gas protection on the casting

stream, and with a more powerful slag on D than the one used on A, B and C.

Other ESR materials of MG2, MG3 and MG4 were obtained with a slag similar to the one used on A, B and C, while related EAF materials of the same groups were obtained with a protected casting stream.

2.1.2. Heat treatment sequence and machining

Heat treatments were carried out aiming at one goal: achieve a similar microstructure on each group of materials despite the casting process and the thermomechanical history involved [5].

Heat treatments were done on two stages. Full annealing was performed at once on blocks coming from rolled/forged ingots, as a preliminary heat treatment was necessary to gum heterogeneities on blocks, and it led to a pearlitic matrix. Cylinders were then cut out from the normalised blocks and turned into rough samples to be hardened, with an oil quenching followed by a three times tempering to yield a fully tempered martensitic matrix with fine and spread secondary carbides precipitation, as the tempering was performed just above the possible secondary hardening peak especially for MG2, MG3 and MG4. A stress relaxed tempering was done on MG1 which exhibited no second hardening peak as the related temperature was very low.

2.2. Testing procedure

As HCF involved a long regime before failure, it is quite important to use both experimental procedures that are time saving and methods that could allow quick evaluation of results while using a limited amount of samples. Higher frequencies are favourite ways to achieve ultra long life regimes (as fatigue properties are independent of frequency) [8], but the number of samples to be tested is still of concern in order to get statistical and significant results.

There are many existing test methods and data reduction techniques for statistical properties of fatigue strength at a specific fatigue life, but few of them have been validated by experiment and simulation. Validation by simulation

Table 1
Average chemical composition (% weight, with balance of Fe) and FRR of studied materials

Material groups	Codes	Casting process	C (wt%)	Cr (wt%)	Mo (wt%)	Si (wt%)	V (wt%)	Forging reduction ratios (FRR) (%)
MG1	A	ESR	0.85–0.95	4.85–5.00	0.10–0.20	0.70–0.90	<0.05	82
	B							50
	C							82
	D							82
	E	EAF						86
	F							86
MG2	G	ESR	0.60–0.65	5.00–5.30	1.00–1.30	1.00–1.10	0.20–0.50	82
	H	EAF						80
MG3	S	EAF	0.80	9.40	1.05	0.45	0.30	89
MG4	Q	EAF	0.85–0.95	7.20–7.50	1.40–1.55	0.85–1.05	1.25–1.30	83
	R	ESR						82

is preferable because high cycle fatigue tests are usually very subjective, not repeatable, and time consuming [17,18]. Furthermore, safe evaluation of fatigue data in the range of finite endurance was done, to compare probabilities and transformation functions in order to suggest a method with safety-factors that enable important correction on fatigue values in respect to sampling [19].

The Boundary method appears to be an interesting technique to assess fatigue tests, especially for a given fatigue life. The related accuracy is thus linked to trials performed at a given level [17–19].

2.2.1. Tensile and fatigue tests

Fatigue and tensile specimens were the same ones according to their geometry (Fig. 1), and the loading direction was axial.

Tensile tests were performed prior to fatigue tests, in order to set a static reference. In fact, it had been shown that fatigue limit and R_P had a one-to-one correspondence [20].

Fatigue tests were performed at room temperature on a AMSLER Vibrophore. The operating frequency was 200 Hz with a minimum tensile stress set at 70 MPa and a load ratio between 0.07 and 0.2, depending on the previous ultimate tensile strength obtained on every single material. Fatigue tests were performed to failure or to the maximum life of 10^7 cycles.

Fatigue tests were performed at room temperature on a AMSLER Vibrophore.

2.2.2. The boundary method [21]

The boundary method uses only two levels (namely L_1 and L_2) and tries to place them near the lower and upper borders of the range of transition, which is just above the infinite-endurance range. Practical comparative studies and theoretical ones have proved the suitability of the method which leads to conservative values as smaller deviations are combined with low fatigue endurance limit values. Furthermore, it is assumed that the distribution in the range of transition is symmetric. Therefore, this method leads to a quick evaluating diagram given by a straight line where arithmetic probability of failure is set as a function of alternating load on a log scale. This curve allows the determination of failure probabilities by simple linear extrapolation.

The boundary technique starts by testing one randomly chosen specimen at any level of alternating load. Tests are
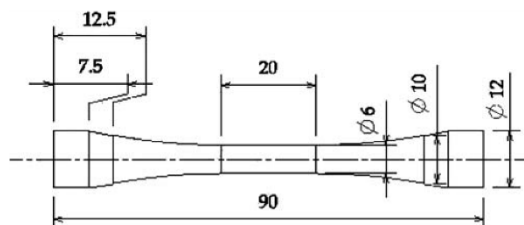
done until the defined endurance life of 10^7 cycles is reached (N_g). If no fracture happens before this limit, next specimens are tested at higher levels raised stepwise until the opposite event happens, that is fracture before 10^7 cycles.

The stress level with the first opposite event becomes the first fully tested level, with the defined amount of specimens that set the accuracy of the method. If the first tested specimen fractures before N_g, the next ones are to be tested stepwise until the opposite event happens: no fracture.

For the second level of alternating load, the distance D is estimated by Eqs. (1) and (2), where S_a is the alternating load (difference between maximum and minimum stress) of the first tested level and d is a parameter related to specimen geometry:

$$D = (1 - r/n) \cdot d \cdot S_a \quad \text{if } r \leqslant 0.5\,n \tag{1}$$

$$D = (-r/n) \cdot d \cdot S_a \quad \text{if } r \geqslant 0.5n \tag{2}$$

For a given level of load, the probability of fracture P_F (percentage) is calculated by the following Eqs. (3) and (4), which had been defined by theoretical studies and some comparative investigations:

$$P_F = 100 \cdot (3r - 1)/(3n + 1) \tag{3}$$

$$P_F(r = 0) = 0.5 \cdot P_F(r = 1) = 100/(3n + 1) \tag{4}$$

2.2.3. SEM/EDX investigation, optical identification and Image Analysis

Nature of inclusions and carbides present on the rough samples was determined by means of SEM prior to optical identification [3,4]. Both SE and BSE detectors allowed, respectively, phase–matrix interface characterisation and complexity of the involved phase. EDX mapping made it possible to get qualitative identification of different phases, especially ratios between elements, while Optical microscopy allowed macroscopic characterisation of inclusions and carbides (colour, shape, etc.) prior to their quantification towards Image Analysis.

2.2.4. Metallographic characterisation

The mean value of the Vickers hardness (HV30) was measured as a 5-points cross on a transversal polished section of every failed tensile sample in order to control heat treatment.

2.2.5. Fractography analysis

The three most common fracture mechanisms in metals and alloys are ductile fracture, cleavage and intergranular fracture [20]. Many studies also focused on fatigue failures modes and fracture mechanisms related to fracture surface examination, which is also known as Fractography analysis [7,11]. Such a method was used in the present study to characterise failure mode of broken samples.

This type of analysis makes it possible to observe and characterise the fracture topography. In the case of fatigue failure the aim was the determination of the location and

Fig. 1. Samples geometry for tensile and fatigue tests (mm).

the nature of crack initiation as well as failure mode through the characterisation of crack propagation. This was done towards metallographic examination and SEM investigation on broken samples.

3. Results

3.1. Heat treatments and metallographic characterisation

Hardening had been done in such a way that bulk hardness of martensite in the as-quenched conditions was max-imal for every single material. Tempering was then performed to yield the final microstructure [5]. Heat treatments performed on each material are given in Table 2 together with macro hardness, and related microstructures are illustrated in Fig. 2 here after.

At the end of heat treatment, MG1 was fully martensitic (Fig. 2a), MG2 (Fig. 2b) had a great secondary hardening effect, while MG3 and MG4 exhibited a fully martensitic matrix with both secondary and primary carbides (Fig. 2c and d). Eutectic carbides were not expected in MG1 and MG2.

Table 2
Heat treatments achieved on studied materials

Material group	Hardening	Bulk hardness (HV 30)
MG1 (ESR and EAF)	950 °C/20 min austenitising, oil quenching Double tempering at 100 °C (stress relaxation)	820
MG2 (ESR and EAF)	1055 °C/5 min austenitising, oil quenching Double tempering at 500 °C	740
MG3 (EAF)	1100 °C/10 min austenitising, oil quenching Triple tempering at 500 °C	720
MG4 (ESR and EAF)	1120 °C/15 min austenitising, oil quenching Triple tempering at 515, 500 and 485 °C	790
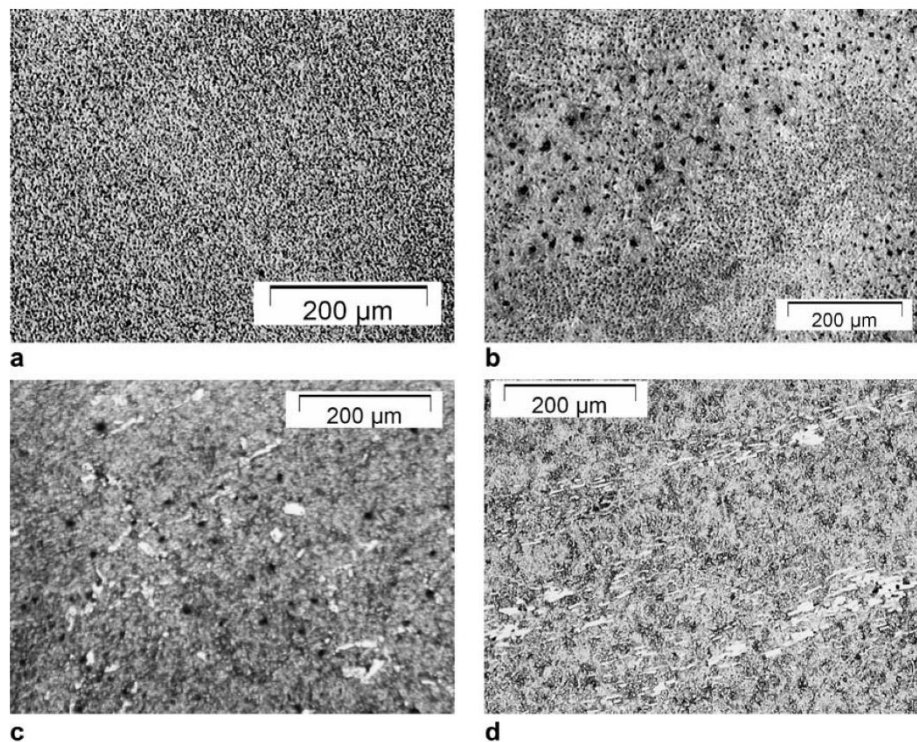
Fig. 2. Microstructures after heat treatments (quenching and tempering): (a) relaxed Martensite with fine secondary carbides (MG1); (b) tempered Martensite with finely dispersed secondary carbides (MG2); (c) tempered Martensite with both secondary and eutectic carbides (MG3); and (d) tempered martensite with secondary carbides and quasi continuous network of eutectic carbides (MG4).

For MG1, all the carbon content of the raw material is dissolved in the matrix as there are no eutectic carbides. Otherwise tempering on MG1 was done at a low temperature in order to destabilise retained austenite and stress relaxed former martensite. So it appeared to be a significant increase in bulk hardness while comparing MG1 to other material groups as the carbon content of the MG1 martensite is the higher one. In fact, MG3 and MG4 exhibit a microstructure with important network of massive carbides which are C-rich, thus decreasing the carbon content of the matrix.

The double stress relaxing heat treatment performed on MG1 enhanced bulk hardness of the former quenched matrix as the temperature involved is low to avoid significant tempering of martensite but also high enough to destabilise retained austenite.

3.2. Characterisation and quick assessment of inclusions and carbides

3.2.1. Inclusions and carbides characterisation

Only small TiN and oxides inclusions were founded in MG1 and MG2 ESR type, while related EAF type exhibited bigger inclusions of the same nature with sulphides ones in addition (Fig. 3).

Comparison between longitudinal samples and transversal ones showed a relative malleability of certain inclusions (sulphides), as they appeared to be particularly elongated in sections parallel to the forging axis (same as sample axis).

Furthermore, ESR materials were cleaner than EAF ones.

Both MC (V-rich) and M_7C_3 (Cr-rich) eutectic carbides were found in MG3 and MG4, with fine dispersed secondary carbides of $M_{23}C_6$ type (V-rich). Inclusions of MG3 and MG4 were similar to those of the previous material groups, namely TiN, oxides and sulphides.

3.2.2. Image Analysis on inclusions and carbides

Digital images from the as-polished conditions were obtained towards optical microscopy using a 12-bit Peltier cooled CCD camera with a maximum resolution of 1280 by 1024 squared-pixels [2].

Only precipitates visible in the as-polished conditions towards optical microscopy were quantified by the means of Image Analysis. Moreover, a threshold value of 3.87 μm was set as the minimum of the precipitates equivalent diameter prior to assessment procedure to allow accurate distinction between precipitates themselves.

An assessment of inclusions and carbides was partially done as not all the batch of specimens was concerned. In fact, only longitudinal directions of MG1 were investigated in addition to the transversal direction of the so-called A material of the same group, in order to allow further comparison related to forging process.

A complete assessment was done on inclusions of MG2 and MG4, and MCs carbides of MG4. Eutectic M_7C_3 carbides were not quantified as they exhibit a weak contrast within the lattice in the as-polished conditions while fine secondary carbides were either invisible in the as-polished conditions or smaller than the defined threshold value.
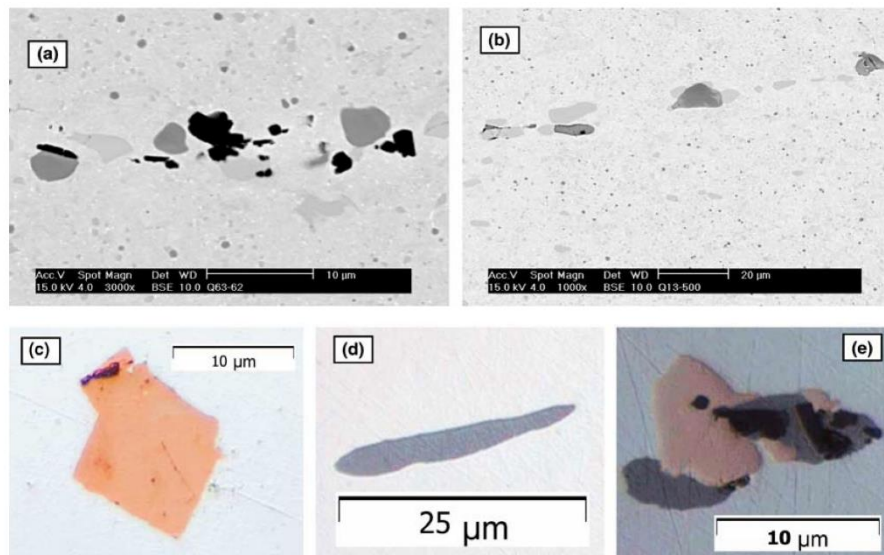

Fig. 3. Inclusions characterisation: (a, b) cluster of inclusions (dark oxides, grey sulphides) associated with carbides (SEM on Q_L and Q_T); (c) angular TiN (B_L); (d) elongated MnS (E_T); and (e) complex TiN, MnS, oxide (F_L).

Furthermore, the overall area considered for the quantification accounted for approximately 30% of the polished cross-section of each sample.

No quantification was made on MG3 samples.

Some quantification results are given in Table 3, namely volume fraction, average and maximum equivalent diameters per material group. Volume fraction involved two-dimensional investigation performed on the polished section perpendicular to the axis of any specimen that had been broken after tensile test.

Largest inclusions were founded in MG1, especially on E_T (transversal direction of E, and maximum of MED).

D_L (MG1) and H_L (MG2) inclusions volume fractions were almost as weak as A_L (MG1) one which was the smaller one.

Inclusions of MG4 seemed to be the smaller ones with respect to AED parameter, but these inclusions were always entrapped in massive carbides which were twice larger than them. Then MG4 exhibited the bigger AED in bulk, when taking into account both carbides and inclusions, while MG2 appeared to be the material with the smaller AED in bulk.

Overall precipitates of volume fraction was maximum for MG4 samples.

Table 3
Results of inclusions and carbides 2-D assessment

Material group	Materials and related direction compared to forging axis	Inclusions volume fraction (%)	Inclusions AED (μm)	Inclusions MED (μm)	MCs carbides volume fraction (%)	MCs carbides AED (μm)	MCs carbides MED (μm)
MG1	A_L	0.016	4.44	14.37	–	–	–
	A_T	0.020	4.76	19.69	–	–	–
	B_L	0.038	5.39	15.65	–	–	–
	B_T	–	–	–	–	–	–
	C_L	0.033	4.65	15.08	–	–	–
	C_T	–	–	–	–	–	–
	D_L	0.018	–	–	–	–	–
	D_T	–	–	–	–	–	–
	E_L	0.052	6.80	30.23	–	–	–
	E_T	–	–	–	–	–	–
	F_L	0.056	5.05	22.64	–	–	–
	F_T	–	–	–	–	–	–
MG2	G_L	0.034	3.99	16.37	–	–	–
	G_T	0.035	3.56	18.35	–	–	–
	H_L	0.017	4.57	14.49	–	–	–
	H_T	0.021	4.33	14.04	–	–	–
MG4	Q_L	0.045	3.54	13.10	0.316	7.93	20.21
	Q_T	0.081	3.76	18.05	0.348	9.01	24.92
	R_L	0.038	3.23	12.59	0.266	6.96	19.25
	R_T	0.036	3.85	17.31	0.266	8.99	27.95
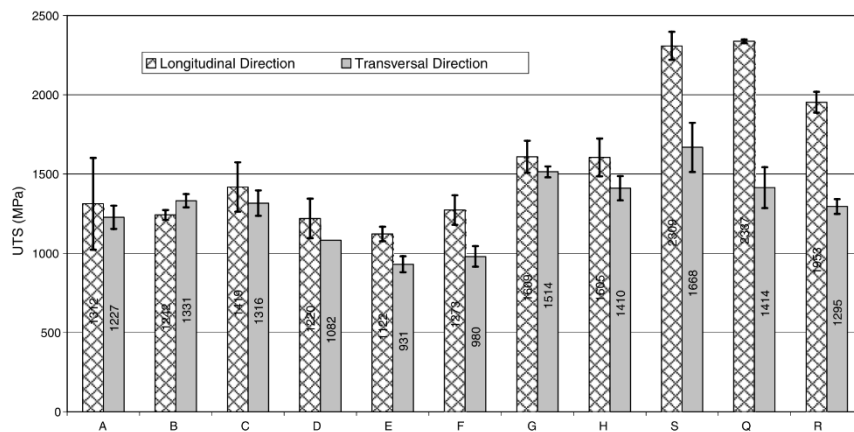
Fig. 4. Ultimate tensile strength (MPa) for longitudinal and transversal directions of MG1 to MG4.

3.3. Tensile test results

Tensile test results are given in Fig. 4, where UTS is considered instead of yield strength as all the studied materials appeared to be very brittle.

Longitudinal tensile behaviour seems to be better than the transversal one, except for B (MG1, ESR casting), which exhibits the lower FRR. It seems that there is a leverage phenomenon with the existence of a cross value, where longitudinal direction becomes better than the transversal one, while considering UTS.

The maximum of R_P (or UTS) was achieved on R_L (MG4, ESR casting), that is the material with the higher content of primary carbides while considering longitudinal samples, which had their principal axis parallel to the forging axis. The minimum of UTS had been obtained on E_T (MG1, EAF casting) which is the material with the highest amount of inclusions.

3.4. Fatigue test results

Evaluation of fatigue tests had been done according to the boundary method (Section 2.2.2).

As the starting level is a private recommendation, it was set to 33% of the UTS obtained from previous unidirectional tensile test. Then the boundary method was performed leading to the two wanted levels with their related probability of failure (see Table 4). The defined number of specimen per level (n) was set to 5.

The maximum of endurance limit at 10^7 cycles was achieved on A_L while the minimum had been realised on Q_T.

Longitudinal direction seems to present a better fatigue behaviour than the transversal one, except for B, as it had already been the case for static tensile load.

3.5. Fractography analysis

3.5.1. Failure modes (FM) definition

Observations carried out on various fracture topographies had allowed the definition of four failure modes (FM) according to whether there is or not a visible point of initiation and according to striation orientation towards the propagation area of the failure (Fig. 5). The four types of failure named FM1, FM2, FM3 and FM4 could be described as follows:

- *FM1* (Fig. 5a), with a smooth halo around the Internal crack initiating point (ICIP) and a fanlike propagation zone beyond the ICIP, with related fine striations spreading away.
- *FM2* (Fig. 5b, c), with a light and smoother halo around the ICIP and a propagation area with deeper and parallel striations.
- *FM3* (Fig. 5d), with a hardly visible origin and rough and complex marks in the propagation area involving multiple crack initiation points (MCIP).

Table 4
Fatigue test results and sampling

Materials and related direction compared to forging axis	$S_{FL,1}$ (MPa) Level 1	Related P_F at L1 (%)	$S_{FL,2}$ (MPa) Level 2	Related P_F at L2 (%)	Number of samples
A_L	909.1	84.6	839.2	26.3	15
A_T	629.4	68.7	524.5	14.3	16
B_L	699.3	63.6	629.4	20.0	13
B_T	769.2	70.2	629.4	6.2	15
C_L	874.1	68.7	769.2	26.3	12
C_T	769.2	68.7	594.4	6.2	14
D_L	699.3	50	629.4	12.5	16
D_T	629.4	50	559.4	6.2	16
E_L	629.4	50	559.4	12.5	11
E_T	419.6	50	367.1	6.2	15
F_L	699.3	68.7	594.4	6.2	14
F_T	489.5	50	419.6	7.7	14
G_L	692.0	87.5	629.1	84.6	13
G_T	629.1	57.9	553.6	6.3	12
H_L	754.7	50	660.4	7.7	12
H_T	628.9	84.6	503.1	12.5	12
Q_L	345.0	87.5	301.0	12.5	12
Q_T	230.0	87.5	186.0	6.3	15
R_L	336.0	50.0	301.0	12.5	11
R_T	336.0	87.5	301.0	31.3	12
S_L	672.3	89.0	636.9	6.0	11
S_T	566.2	88.0	452.9	6.0	10

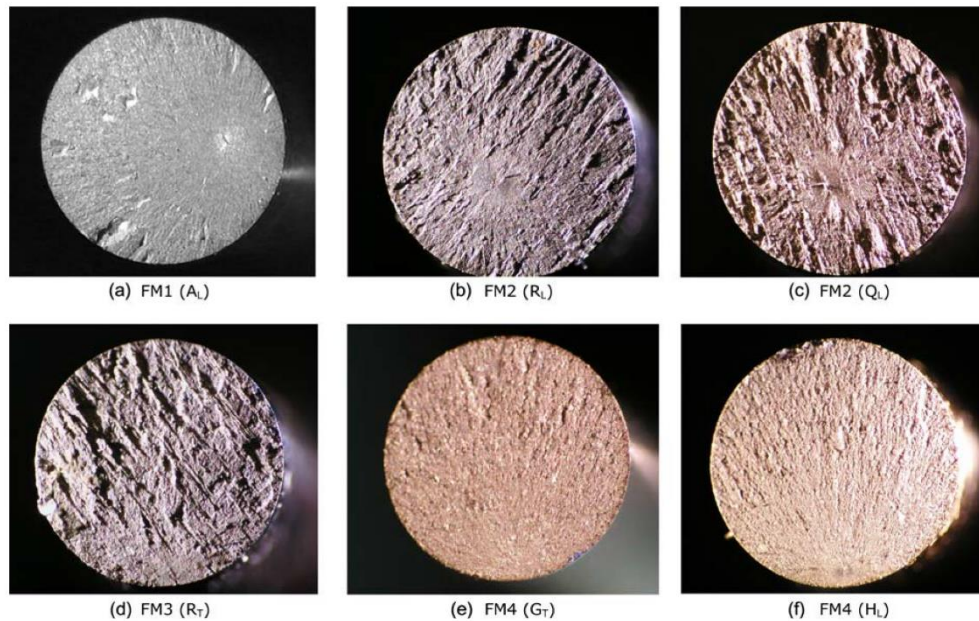Fig. 5. Different failure modes (FM) obtained after HCF tests.

Table 5
HCF failure modes characterisation on studied materials

Failure modes	FM1	FM2	FM3	FM4
Failure origin	ICIP in a halo	ICIP in a halo	MCIP	None or SCIP
Crack propagating area	Smoother fanlike striations	Rougher and almost parallel striations	Rougher and complex striations	Smoother striations
Materials	A, B, C, E, F (MG1) Q, R (MG4)	Q, R (MG4)	S (MG3) Q, R (MG4)	D (MG1) G, H (MG2) S (MG3)
Related casting processes	ESR, EAF (MG1) ESR, EAF (MG4)	ESR, EAF (MG4)	EAF (MG3) ESR, EAF (MG4)	ESR (MG1) ESR, EAF (MG2) EAF (MG3)
Sampling direction	L and T (MG1) L (MG4)	T (MG4)	T (MG3) T (MG4)	L and T (MG1) L and T (MG2) L (MG3)

- *FM4* (Fig. 5e, f), with a smooth section and origin-less area, involving a surface crack initiation point (SCIP) with the major stage of the failure being achieved by crack propagation.

Table 5 gives the FM distribution of studied materials in relation with casting process and cutting out directions.

3.5.2. Nature of ICIP and related scale halo
There are halos on broken sections that are related to ICIP nature (Fig. 6).

Figs. 7–10 show results of EDX analyses done on various ICIP. In Fig. 7, there is a major rate of aluminium and oxygen corresponding to an alumina inclusion, while in Fig. 8 the inclusion involved is a complex oxide/TiN. The first ICIP (alumina type) appears to be a cluster with no soakness within the matrix, contrary to the latter ICIP of TiN type. In fact, facetted surface of the mentioned TiN involved fracture upon external loading. Therefore, alumina which had no cohesion interface with the matrix seem to be pulled out very easily while TiN will be broken because of a slight adhesion within the lattice.

3.5.3. Final fractography analysis results
Both internal crack initiating points (ICIP) and surface crack initiating points (SCIP) were founded, the first ones being prevalent.
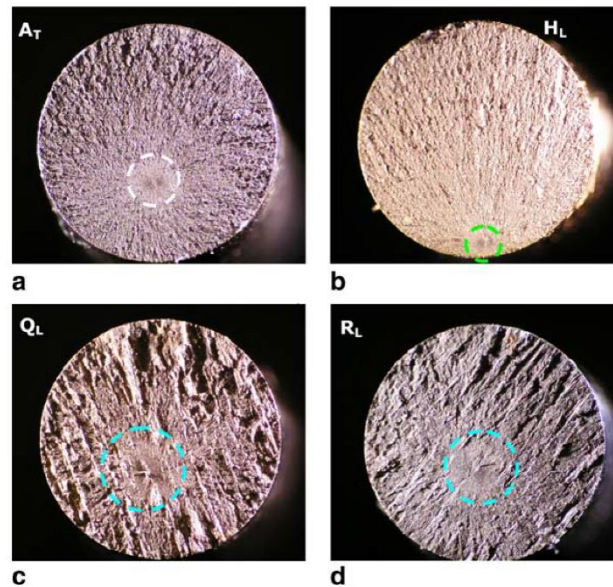
Fig. 6. (a–d) Halo diameter related to the nature of ICIP: (a, b) inclusion as ICIP, with a related reduced halo diameter at the crack origin; (c, d) carbide as ICIP, with a more extended area for crack initiation halo (CIH).
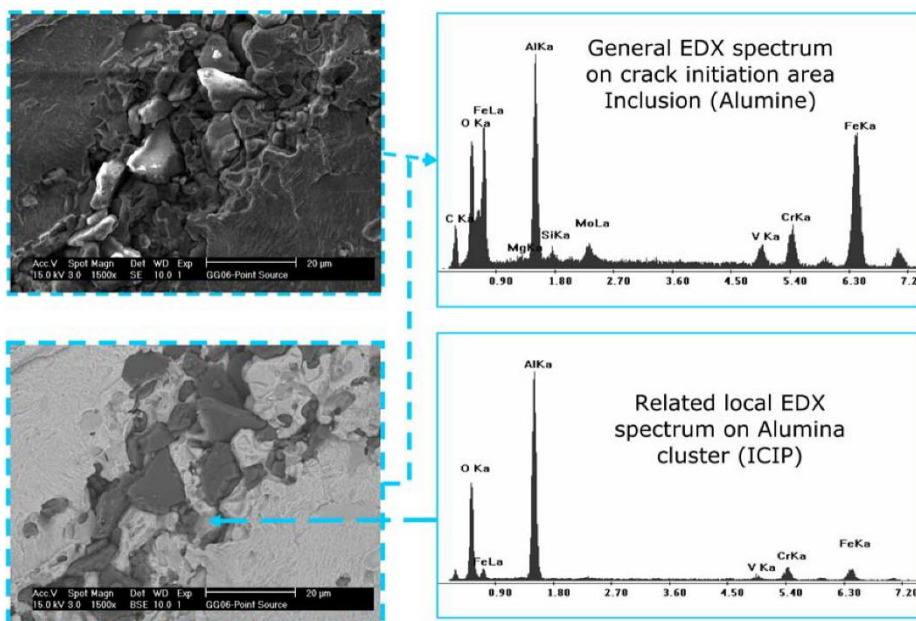
Fig. 7. Lack of soakness for an alumina cluster ICIP (Q_T, FM1).

While considering transversal direction and materials with primary carbides, ICIP appeared to become multiple crack initiating points (MCIP) as crack could be initiated on several points simultaneously.

Studied materials exhibited four types of failure namely failure modes FM1, FM2, FM3 and FM4 which could be distinguished according to the existence and the location of a crack origin and according to the roughness of the pos-

(a) ICIP near the surface

(b) Smoother CIH over and around ICIP

(c) Angular facetted inclusion (TiN) as ICIP

(d) General EDX spectrum on 8c
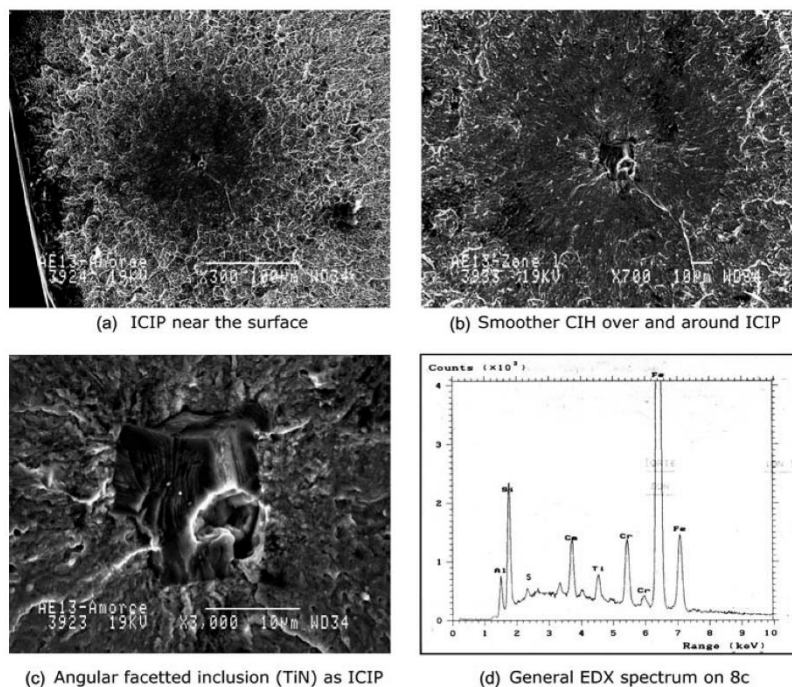
Fig. 8. Complex oxide/TiN inclusion as ICIP and related smoother CIH (B_L – MG1) The centre hole probably gives the previous location of a pulled out oxide (Si, Al): (a) ICIP near the surface; (b) smoother CIH over and around ICIP; (c) angular facetted inclusion (TiN) as ICIP; and (d) general EDX spectrum on c.

sible propagation area beyond the smoother halo that represented crack initiation.

FM1 consists of an ICIP with a related fine halo which characterised the crack initiation and a smooth fanlike area around and over the halo that was crack propagation stage.

FM2 consists of a CIH around an ICIP, but contrary to FM1, propagation area is characterised by rougher and quasi parallel striations, involving texture directions of mixed carbides and inclusions clusters.

FM3 is related to MCIP, with a sharper failure section.

FM1 turns into FM4 when the crack was initiated on the surface sample. FM4 also involved materials without primary carbides.

Oxides were most harmful because of their weak soakness inside the matrix. Angular nitrides had a better soakness than oxides, but it remains lower than that of carbides (primary or secondary ones).

The association of an oxide with a more soaker precipitate reduced the harmfulness of oxide while increasing the pulling out of the carbide.

There seems to be a critical size for the ICIP while considering HSS–HCF. However, a given precipitate with a size lower than the critical threshold could be a SCIP when located near the surface, which leads to a surface initiation crack. Moreover, a harmless precipitate in HCF mode can become weak in giga cycle fatigue (GCF).

The precipitate location is also important. In fact, the ICIP ability is firstly influenced by its size and then by its soakness when it is located in the bulk. And when the precipitate is on the surface, it can yield a notch with a related detrimental stress concentration effect.

Moreover, it seems that secondary carbides improve resistance to crack propagation resistance, owing to the fact that their homogeneous distribution inhibits the possible defects of second-order (dislocations, grain boundary, etc.).

4. Discussion

While considering tensile tests, UTS of the longitudinal direction is always higher than transversal direction one, except for B, where there is a so-called leverage effect related to FRR (Fig. 4 and Table 1).

The gap between longitudinal and transversal directions is more important on MG3 and MG4 than it is on MG1 and MG2. This could be the link to the presence of inclusions and carbides more than the bulk hardness effect of the material. In fact, MG1 exhibit the smaller UTS with the maximum of the bulk hardness, while there are only inclusions as precipitates in the matrix. At the same time, MG3 and MG4 which contain both inclusions and eutectic carbides present a better tensile behaviour with bigger UTS.
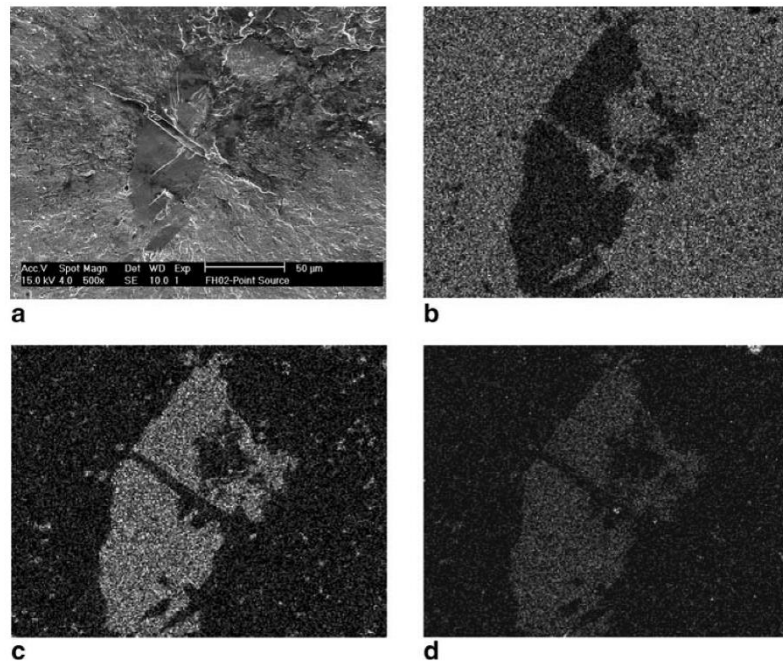
Fig. 9. (a–d) ICIP (M$_7$C$_3$,Cr-rich) and related EDX Map – embedded matrix inside the transversal crack involving carbide failure during forging: (a) cracked carbide as ICIP and related smoother surrounding halo (FM2 – R$_T$); (b) Fe (Kα) distribution over the matrix (EDX Map); (c) Cr (Kα) distribution on M$_7$C$_3$ carbide; and (d) V (Lα) distribution on M$_7$C$_3$ carbide.

Inclusions embedded into carbides seem to be less detrimental for tensile tests as it is the case for MG3 and MG4.

Thus, inclusions appear to be very harmful for UTS especially when they are isolated and big in size (E and F), or even when they are small in size but of oxide types (D). In fact MG1 exhibit UTS almost two times smaller than those of MG3 or MG4.

Furthermore, differences in longitudinal and transversal behaviour arise as long as precipitates (inclusions and even carbides) within the matrix are textured from one direction to another which is much the case in MG3 and MG4 than it is in MG1 and MG2. However, the presence of eutectic carbides appears to yield to tensile behaviour enhancement especially when weakening inclusions are entrapped in these massive carbides (MG3 and MG4).

Failure which starts in an "internal" point (ICIP) produces a halo whose extent varies according to the nature of the ICIP. This failure mode leads to a fish-eye like appearance. There could be a relationship between the crack initiation halo (CIH) ray and the nature of the precipitate that initiated the failure. In fact, related smooth areas for ICIP originating from inclusions (Fig. 6a, b) are less extended than those originating from carbides (Fig. 6c, d).

Moreover, it seems that in the case of FM1, most of fatigue cycles before failure occur during initiation stage of the failure. The ray of the CIH could then be proportional to the number of cycles carried out before the final cycle appear.

Hence, one can also correlate the ray of the CIH with the nature of crack origin. In fact, widest CIH seem to be those which result from the "internal fracture" of a massive eutectic carbide. When micro cracks appeared within the interface between carbides and embedded inclusions, the ring was smaller.

In the case of a crack initiated from an elongated oxides cluster, the related ring had an elliptic shape with a lengthening in the principal direction of the inclusion cluster.

Inclusions as far as eutectic carbides are considered constitute preferential sites of crack initiation in HCF failure, especially in MG3 and MG4 materials. On the one hand, alumina, nitride or complex alumina/nitride/sulphide inclusions were found to be very harmful, as they were ICIP for materials MG1, 3 and 4. And on the other hand, carbides were found to be ICIP in materials MG3 and MG4.

Carbide as ICIP candidate could exhibit itself one or more internal cracks prior to overall failure crack initiation of the specimen since it is isolated (Figs. 9 and 10) or associated with oxides (Fig. 11). Hence, eutectic carbides appeared to be good ICIP candidates as they broke themselves through internal cracks likely to initiate HCF failure (Figs. 9 and 10).
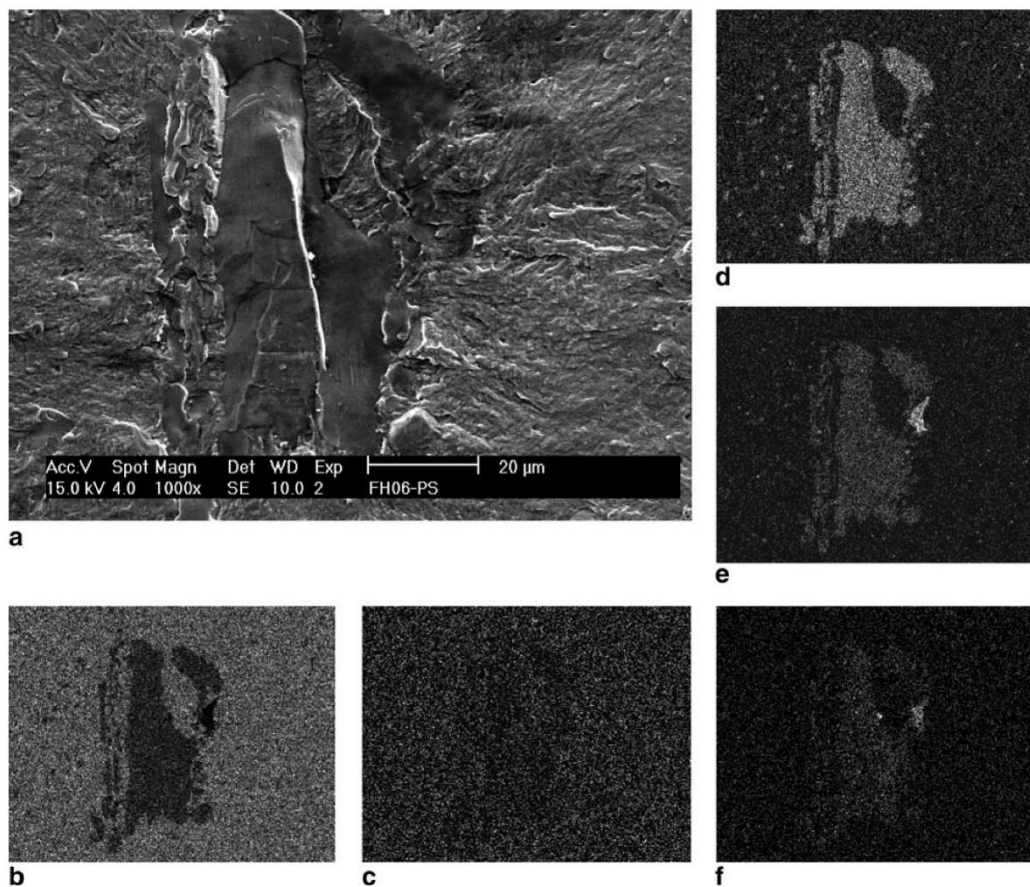
Fig. 10. (a–f) Typical facets on a complex carbide (M_7C_3/MC), respectively, originated from previous hot working (left and alongside, with embedded matrix) and latter HCF test (carbide centre), and leading to an ICIP – related EDX Map (b–f): (a) cracked complex carbide as ICIP and related smoother surrounding halo (FM2 – R_T); (b) Fe ($K\alpha$) distribution over the matrix (No Fe in M_7C_3 carbide); (c) Si ($K\alpha$) distribution (mainly inside the matrix); (d) Cr ($K\alpha$) distribution on M_7C_3 carbide; (e) V ($K\alpha$) distribution on both MC and M_7C_3 carbides; and (f) ($L\alpha$) distribution on MC carbide.

Furthermore, internal cracks on a carbide could be enhanced by the presence of embedded inclusions that weakened the surrounding carbide as the interface with the latter is non-cohesive. Carbide–inclusion boundaries then become preferential zones for micro cracks appearance, prior to the formation of an actual ICIP (Fig. 11).

Eutectic primary carbides are both ICIP candidates and propagating crack enhancers, especially when they form a cluster aligned in a direction perpendicular to that of the external load in fatigue.

Secondary carbides are not ICIP candidates, and it is quite possible that these finely spread precipitates inhibited notch effect in less-eutectic-carbide materials of MG2.

There could be a threshold set as a critical size under which the involved particle will not constitute an ICIP. In other words, reducing size of inclusions (and incidentally of carbides) could improve fatigue resistance, as it had been seen on materials originating from ESR process. In fact, ESR materials exhibit tensile and fatigue strengths higher than those of EAF materials.

It seems to have an antagonistic phenomenon while considering the association between carbides and inclusions. In fact, surrounding carbides tend to reduce the harmfulness effect of inclusions when they are associated to the latter, while embedded inclusions weaken carbides as their non-cohesive interface becomes a preferential site for pulling out or even flaking off prior to important cracking that can yield an ICIP.

Hot working could yield weakening internal cracks in carbides which promoted subsequent ICIP formation on the broken carbide. Carbide cracks inherited from forging could be easily defined by the presence of a matrix in their groove inside the broken carbide (Fig. 9).

726   *J. Tchoufang Tchuindjang, J. Lecomte-Beckers / International Journal of Fatigue 29 (2007) 713–728*
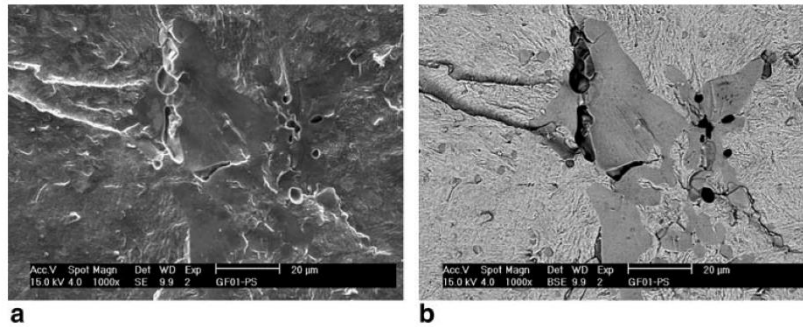
Fig. 11. ICIP on Q_L – failure Mode resulting from internal cracking at interfaces between carbide and sulphides inclusions and from pulling out of oxides previously embedded in the carbide: (a) holes on a carbide ICIP involving previous embedded inclusions (SE detector) and (b) broken M_7C_3 carbide (smooth and grey), sunken embedded sulphide and residual oxides.

There are another type of carbides cracks that are directly caused by HCF tests as they do not exhibit any interstitial matrix groove contrary to carbides broken during forging process (Fig. 10).

Hot working split up fragile particles and at the same time, lengthen malleable particles in a direction normal to that of the external load. Moreover, the increase in the compactness of the matter also leads to a relative increase in the volume density of the particles. Brittle particles could yield an increase of the weakness of the material after hot working as the splitting up arises their number especially near the surface, and thus increases the notch effect.

Hot working also yields internal cracks inside carbides, and thus enhances weakening of the material as the broken carbide becomes a good ICIP candidate.
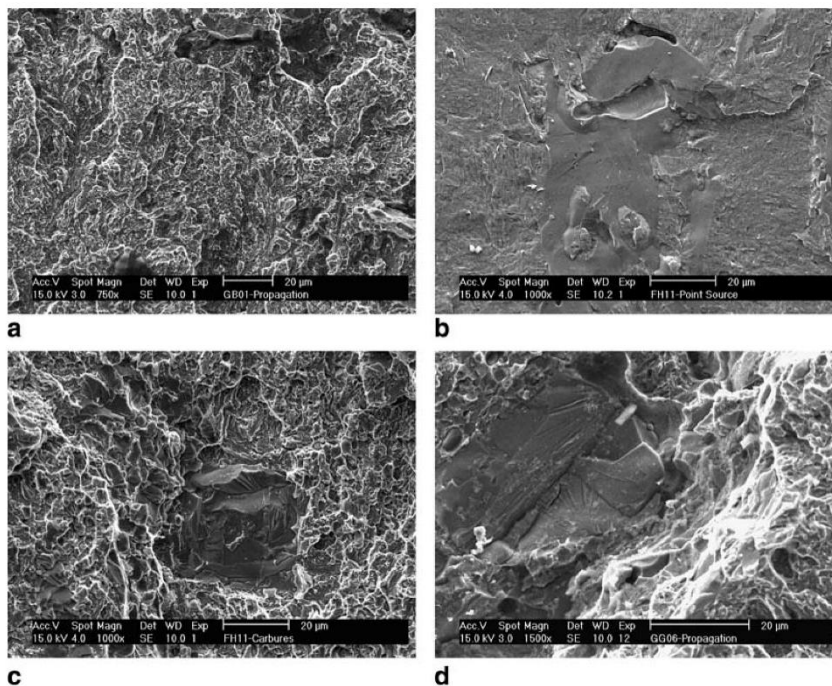
Fig. 12. Roughness differences between CIH and crack propagation area on R_L and R_T: (a) crack propagation zone (FM1 – R_L); (b) smoother area around an ICIP of carbide type, with holes related to pulled out inclusions (FM1 – R_L); (c) facets of a broken carbide and dimples around in the crack propagation area (FM1 – R_L); (d) facets of a broken carbide in the grooved mark of a rough striation (crack propagation zone, FM3 – R_T).

Crack propagation areas are characterised by dimples on a rough surface (Fig. 12a), contrary to the smoother fracture of CIH (Fig. 12b). It is possible to find facetted and flanged broken carbides in crack propagation zone (Fig. 12c, d) for the related material groups containing primary carbides.

The studied materials present four types of failure which could be distinguished according to the existence of a crack origin and according to the aspect of the propagation area beyond the smoother ring that represents crack initiation, when it exists.

It had been shown that *S–N* curves related to surface crack initiation depend on the surface crack propagation threshold as a function of crack length, which is defined by the surface fatigue limit and the fatigue crack propagation threshold for long cracks. The same study had n that *S–N* curves related to an internal initiating crack depend on the type and size of inclusion, the tensile residual stresses around it, the amount of hydrogen in the material, some particular features of the microstructure related with the hydrogen trapping places, and the threshold for pure fatigue crack propagation [6].

In the present work, internal crack which gave place to a CIH led to a propagation stage as slow features promoting crack propagation are less present. Parameters which support crack propagation of fatigue failure were both inclusions and carbides clusters, the later being aligned according to their largest principal direction in the failure plan.

The nature of ICIP could also have a great influence on the so-called moistening effect on lattice. Oxides are well known to be barely soaked in the matrix unlike titanium nitrides or carbides. But compared to eutectic carbides, TiN are more angular and brittle and thus lead to a different behaviour while taking into account a fatigue test.

But it is probably the better "soakness" of TiN which explains that for a given size, an internal crack initiated by a TiN will arise at a higher level of cycle than another one initiated by an oxide, that is less "moistening".

5. Conclusions

Inclusions appeared to be very harmful for tensile behaviour especially when they are isolated and of oxide types. But this weakening effect on UTS is reduced by the entrapment of inclusions in massive eutectic carbides. In addition, the gap between longitudinal and transversal directions while considering tensile behaviour of forging materials could increase with the related overall precipitates texture when comparing the two perpendicular directions.

Studied materials exhibited four types of fatigue failure namely FM1, FM2, FM3 and FM4, which could be distinguished according to the existence and the location of a crack origin and according to the roughness of the possible propagation area beyond the smoother halo that represented crack initiation.

Nature and size of precipitates highly influence HCF behaviour, and so does their inferring soakness in the lattice. In fact, precipitate size characterise its propensity to constitute an ICIP together with its location.

ICIP are mainly inclusions of oxide type, with possible association with nitrides. However, carbides were found to be also ICIP candidates while considering transversal direction that is perpendicular to the rolling axis.

Moreover, eutectic primary carbides are both ICIP candidates and propagating crack enhancers, especially when they form a cluster aligned in a direction perpendicular to that of the external load in fatigue.

Secondary carbides are not ICIP candidates contrary to primary eutectic ones.

FRR leads to a leverage phenomenon with the existence of a cross value, where longitudinal direction becomes better than the transversal one, when considering mechanical properties (fatigue and tensile). Material compactness together with its texture degree, are secondary parameters that influence HCF behaviour, just after precipitates are found in the HSS microstructure.

References

[1] Hwang Keun Chul, Lee Sunghak, Lee Hui Choon. Effect of alloying elements on microstructure and fracture properties of cast high speed steels rolls. Part I: microstructural analysis. Mater Sci Eng 1998;A256:282–95.

[2] De Colnet L, Pirard E, Lecomte-Beckers J, Tchoufang Tchuindjang J, Boeraeve P, Ghfiri R. Quantitative description of MC, M_2C, M_6C and $_7C_3$ in high speed steels rolls. In: Proceedings of the MSMF-3 international conference held in Brno; June 2001. COST ISBN 80 214 1892-3.

[3] J. Tchoufang Tchuindjang, J. Lecomte-Beckers, Inclusions and carbides characterisation in high-speed steels. In: Proceedings of the annual meeting of SBM, RUCA, Antwerp; May 2003.

[4] Tchoufang Tchuindjang J, Lecomte-Beckers J. Use of microscopy for identification of complex carbides in high-speed steels. GIT Imaging Microsc 2005;2:2–3.

[5] Tchoufang Tchuindjang J, Lecomte-Beckers J. Importance of heat treatment procedure in the study and the characterization of impurities in high alloyed steel. In: Proceedings of the international COST517 workshop on cleaner metal for industrial exploitation, Czech Republic; December 1999. p. 45. ED.EUR 19710 ISBN 92 828 8323 X.

[6] Murakami Y, Yokoyama NN, Nagata J. Mechanism of fatigue failure in ultralong life regime. Fatigue Fract Eng Mater Struct 2002;25:735–46.

[7] Wang QY, Bathias C, Kawagoishi N, Chen Q. Effect of inclusion on subsurface crack initiation and gigacycle fatigue strength. Int J Fatigue 2002;24:1269–74.

[8] Furuya Y, Matsuoka S, Abe T, Yamaguchi K. Gigacycle fatigue properties for high-strength low-alloy steel at 100 Hz, 600 Hz and 20 kHz. Scripta Mater 2002;46:157–62.

728   *J. Tchoufang Tchuindjang, J. Lecomte-Beckers / International Journal of Fatigue 29 (2007) 713–728*

[9] Suh Chang-Min, Hwang Byung-Won, Murakami Ri-Ichi. Characteristics of fatigue crack initiation and fatigue strength of nitrided 1Cr–1Mo–0.25V turbine rotor steels. KSME Int J 2002;16(8):1109–16.

[10] Billaudeau T, Nadot Y. Support for an environmental effect on fatigue mechanisms in the long life regime. Int J Fatigue 2004;26:839–47.

[11] Chapetti MD, Tagawa T, Miyata T. Ultra-long cycle fatigue of high-strength carbon steels part I: review and analysis of the mechanism of failure. Mater Sci Eng 2003;A356:227–35.

[12] Murakami Y, Nomoto T, Ueda T, Murakami Y. On the mechanism of fatigue failure in super long life regime ($N > 10^7$ cycles). Part I: influence of hydrogen trapped by inclusions. Fatigue Fract Eng Mater Struct 2000;23:893–902.

[13] Meurling F, Melander A, Tidesten M, Westin L. Influence of carbide and inclusion contents on the fatigue properties of high speed steels and tools steels. Int J Fatigue 2001;23:215–24.

[14] Billaudeau T, Nadot Y, Bezine G. Multiaxial fatigue limit for defective materials: mechanisms and experiments. Acta Mater 2004;52:3911–20.

[15] Nadot Y, Denier V. Fatigue failure of suspension arm: experimental analysis and multiaxial criterion. Eng Fail Anal 2004;11:485–99.

[16] Farfan S, Rubio-Gonzalez C, Cervantes-Hernandez b T, Mesmacque G. High cycle fatigue, low cycle fatigue and failure modes of carburized steel. Int J Fatigue 2004;26:673–8.

[17] Lin Sheng-Kuei, Lee Yung-Li, Lu Ming-Wei. Evaluation of the staircase and the accelerated test methods for fatigue limit distributions. Int J Fatigue 2001;23:75–83.

[18] Jahn Jurgen, Maennig Wolfgang-Werner. Safe evaluation of fatigue data in the range of finite endurance. Int J Fatigue 1997;19(4):335–44.

[19] Sunder R, Porter J, Ashbaugh NE. The effect of stress ratio on fatigue crack growth rate in the absence of closure. Int J Fatigue 1997;19(1):211–21.

[20] Oh Hung-Kuk. Characterization of dynamic fatigue life by the uniaxial tensile test. J Mater Process Technol 1995;54:365–71.

[21] Planning and evaluation of fatigue tests – fatigue and failure, ASM handbook, vol. 19. p. 303–19.

.. Article #2

Structural Investigations of Solidification and Heat Treatments Influence on High Alloyed Cast Irons Grades with Nb-V-Ti additions

Jacqueline Lecomte-Beckers[1, a] and Jérôme Tchoufang Tchuindjang[1,b]

[1]University of Liege, Aerospace & Mechanics Dpt., Metallurgy & Materials Science unit – IMGC, Bât. B52 – Chemin des Chevreuils, 1 – 4000 Liege, Belgium

[a]Jacqueline.Lecomte@ulg.ac.be, [b]J.Tchuindjang@ulg.ac.be

Abstract. Two High Alloyed Cast Irons (HACI) were studied, both belonging to the Fe-C-Cr-Si-X system where X represented a strong carbide forming element. One of these alloys was obtained after adding Nb, V and Ti to the chemical composition of the other alloy.

Raw materials originated from spun cast rolls for hot strip mill were submitted to different heat treatments routes, in order to study the influence of alloying elements on the microstructure.

Both HACI grades contained a mixture of martensite and retained austenite matrix in the as-cast conditions and after quenching.

Differential Thermal Analysis was carried out on the heat treated samples in order to determine the phase transformations occurring during re-melting and subsequent solidification sequence.

Diffusionless transformations leading to various types of martensite were found in the matrix.

Bulky NbC carbides precipitating at the beginning of the solidification process strongly influence the nature and the rate of the subsequent diffusional phase transformations, particularly for HACI grade with Nb, V and Ti additions.

Quantitative metallography was done to determine graphite, NbC carbides, cementite and matrix volume fraction in HACI studied grades.

Introduction

High Alloyed Cast Iron (HACI) also known as Indefinite Chill Cast Irons (ICDP) when used as rolling mill rolls, are cast iron belonging to the Fe-Cr-C-X system, where X is represented by Mo, Nb, V, Ti or W. Such alloying elements are also known as strong carbides forming elements [1-7]. Mechanical properties involved in HACI depend on the chemical composition of the alloy, on its crystallization behavior, and finally on the heat treatments performed subsequently [2, 3, 6-9]. Alloying elements and solidification route set the as-cast HACI microstructure, that is often made of a mixture of primary carbides and free graphite both embedded in the remaining matrix.

Austenite which exists in the microstructure at the end of the solidification process can decompose itself through both diffusional and diffusionless transformations, depending respectively on the cooling rate or the temperature [10]. In HACI diffusional transformation could involve the decomposition of austenite into an eutectoid phase (pearlite or bainite) with the precipitation of secondary carbides, while diffusionless transformation lead to the formation of martensite from previous austenite. Both martensite and bainite are the defined matrix phases that are sought for HACI working rolls in Hot Strip Mill (HSM) process. But retained austenite (RA) is always present in HACI microstructure at the end of casting process, as the result of the incompletion of both diffusional and diffusionless phase transformations.

Then subsequent heat treatments such as tempering with or without a preliminary quenching, are performed at the end of casting procedure in order to allow a fully transformation of RA into an expected and advisable martensite or bainite matrix [1, 2, 8-16].

Because HSM involved wear and hot corrosion resistances, the microstructure advisable for HACI is composed of a mixture of martensite and cementite, with a certain amount of free graphite and other carbides known as eutectic MC or M_7C_3, and fine secondary carbides (M_4C_3 or $M_{23}C_6$), the latter carbides being fully distributed inside the material to improve its hardness [1, 3, 5, 12, 16]. Graphite helps achievement of lubrication during rolling process [5, 14, 17], while MC eutectic carbides are advisable for wear resistance, as they exhibit a higher hardness [1]. Graphite morphology can vary from flaky to spheroidal type depending on several parameters, each type having an influence on subsequent mechanical properties of the cast iron alloy [1, 7, 15, 18]. Indeed rare earth elements and cooling rates were reported to strongly influence the type of graphite that precipitated during the solidification process [5, 19, 20].

Particular attention must be paid if hard MC eutectic carbides that precipitate from diffusional phase transformation are being promoted, as it is not recommended that a high hardness difference exists between the matrix itself and the strengthening carbides widespread distributed within the matrix. Important hardness gradient must be avoided [5, 6]. Hence the purpose is either to enhance bulk hardness of HACI by promoting hard MC carbides precipitation, or to insure that such carbides are small in size and uniformly distributed inside the matrix in order to limit the possible differential degradation of the roll.

Controlling the size of carbides, especially eutectic carbides originated from the liquid at the beginning of the solidification process remains of concern, as many parameters are involved is such a phenomenon. In fact, the chemical composition of the alloy, the casting route and even the subsequent heat treatments can strongly influence the carbides nature, size and distribution inside the matrix [1-6, 20, 21].

In this work, two grades of HACI have been studied, one grade being obtained after adding Nb, V and Ti to the other grade. The stability of RA was enhanced through heat treatments performed on the as-cast samples in order to promote martensite transformation. The study had been focused on the microstructure characterization by the means of DTA, light microscopy, and Image analysis.

Materials and Methods

Studied materials were cut out of the shell part of bimetallic rolls originated from vertical spin casting route. The shell material which is composed of HACI grade represents the barrel whereas the core is formed by a nodular grey cast iron. Only the shell materials are study afterwards.
Average chemical compositions of studied HACI1 and HACI2 materials are given in Table 1. HACI1 represents the "conventional" ICDP grade, whereas HACI2 contains Nb, Ti and V additions. Afterwards samples from HACI1 and HACI2 are respectively called IC1x series and ICI2 series.

Table 1: Average chemical compositions of HACI studied grades, -wt%

	C	Si	Ni	Cr	Mn	Mo	Nb	V	Ti	Fe
HACI1	3.0 – 4.0	1.5 – 1.5	3.5 – 5.0	1.5 – 2.5	0.5 – 1.5	0.2 – 0.8	-	-	-	Bal.
HACI2	3.0 – 4.0	1.5 – 2.5	3.5 – 5.0	1.5 – 2.5	0.5 – 1.5	1.0 – 2.0	1.0 – 2.5	0.5 – 1.5	0.1 – 0.5	Bal.

Experimental methods laid on heat treatments, solidification and phase transformations study, microstructure characterization, and quantitative metallography.

Heat treatments were done on the specimens, prior to sampling for either metallographic analysis or DTA tests. The heat treatment performed after the casting process was a double tempering followed or not by a quenching. The purpose of the thermal treatment was the achievement of a fully martensitic matrix after tempering process and to study the stability of the austenite during quenching. Heat treatment sequences are given in Table 2.

Table 2: *Enhancement of origin and heat treatments routes on studied samples, and related analysis types achieved*

Sample code	Sample Origin	Sample location on the cast roll	Heat treatment sequence	Type of Analysis performed
IC11		Between 20 and 40 mm deep (shell)	As-cast + Double tempering (525°C /24 h x 2)	Quantitative Metallography
IC12	HACI1		As-cast + Double tempering (525°C /24 h x 2) + DTA	DTA Optical microscopy
IC13			IC11 + Quenching (1000°C/1h/Oil) + DTA	DTA Optical microscopy
IC21 **IC22**		Between 15 and 40 mm deep (shell)	As-cast + Double tempering (525°C /24 h x 2)	Quantitative Metallography
IC24	HACI2		As-cast + Double tempering (525°C /24 h x 2) + DTA	DTA Optical microscopy
IC25			IC21 + Quenching (1000°C/1h/Oil) + DTA	DTA Optical microscopy

DTA tests were performed on a Nestchz STA 449 device. The samples were heated and cooled in argon at a rate of 10°C/min for a primary stage that took place entirely in the solid state (up to 1100°C), then a slower heating rate of 5°C/min was used up to the complete melting.
DTA tests were done on heat treated specimens in order to determine the solid state transformation and the re-melting behavior of the studied materials.
Furthermore, DTA allowed the enhancement of the crystallization behavior of studied samples.

Specimens of heat treated materials and re-solidified materials after DTA tests were polished and etched in order to be examined under optical and scanning electron microscope. Indeed both shape and phase compositions were investigated by the means of SEM/EDX analysis.
Optical characterization of specimens was the preliminary stage before the achievement of the carbides volume fractions assessment towards image analysis.

Results

DTA diagrams are illustrated on fig. 1 (heating mode) and fig. 2 (cooling mode). Table 3 and Table 4 give the phase transformations which are respectively related to peaks found during the heating and the cooling modes. Fig.3 and fig.4 illustrate the microstructure of re-solidified samples at the end of DTA route, respectively for IC1x and IC2x series.

Phases transformations during DTA heating mode
From Fig. 1a, quenched specimens of HACI1 grade did not exhibited a range for re-austenitisation during the DTA heating mode (lack of peak 3' on IC13), contrary to the double tempered specimen (occurrence of peak 3' on IC12). Thus RA appeared to be more stable after quenching in IC1x series due to the lowering of the diffusionless martensitic start transformation (Ms point) [12, 13].

At the same time, an endothermic peak (peak 2') was observed during DTA heating mode (Fig. 1a) on both the quenched IC13 sample and the double tempered IC12 sample, before the austenitisation range. This decomposition did not occur in IC2x specimens.

80   **Diffusion in Materials - DIMAT2008**

In IC2x series both double-tempered and quenched specimens exhibited similar peaks while re-heating them, especially phase transformations that took place before austenitisation (peak 1') and at the time of austenitisation (peaks 3' and 4').

Peak 4', that is only present in double tempered IC24 specimen, involved dissolution of fine secondary carbides inside de austenitic matrix. Such carbides were neither found in the as-quenched IC25 sample nor in the IC1 series. Such an observation is consistent with the fact that quenching did not allow fine secondary carbides precipitation contrary to tempering [1].

Above 1000°C, we observed the reactions that involved re-melting sequence, such as reverse eutectic transformations related to direct melting of both NbC carbides (peak 5') or ledeburite (Cementite/austenite eutectic, peak 6'), or up to direct re-melting of graphite (peaks 7' and 8').

Reverse eutectic reaction that involved ledeburite melting (peak 6') appeared to be hardly influence by the previous heat treatments done on the samples for both IC1x and IC2x series. In fact, double tempered specimens such as quenched specimens of IC1x and IC2x series exhibited similar ranges for reverse eutectic reactions.

Furthermore, the lack of secondary carbides in the tempered IC12 suggested that alloying elements involved in secondary hardening process are no longer present inside the as-cast matrix. Indeed, IC1x series did not contain V, which is well-known to improve secondary hardening during tempering heat treatment.

Although Mo is also a great secondary hardening enhancer, we must assume that most of the Mo containing element was already dissolve inside eutectic carbides for IC1x series.

The melting temperature was obtained around 1260°C on IC1x series whereas this temperature was set at 1245°C on IC2 series. Thus Nb, Ti and V additions appeared to lower the melting point of HACI.

Quenching seemed to enhance RA stability on both IC1x and IC2x series, as the related peak 3' involving austenitisation during DTA heating mode exhibited a reduced or zero amplitude, when compared to that of the double tempered specimens.
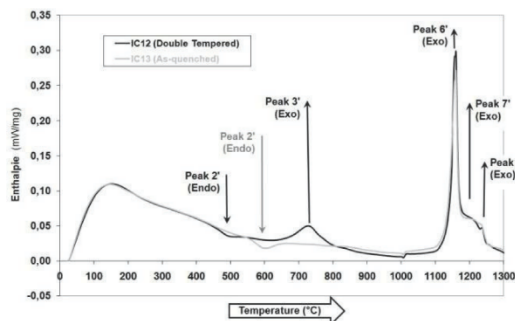
Fig. 1a: *DTA curves on IC12 and IC13 (Heating mode at 10°C from Room T° to 1000°C, then 5°C/min up to complete melting)*
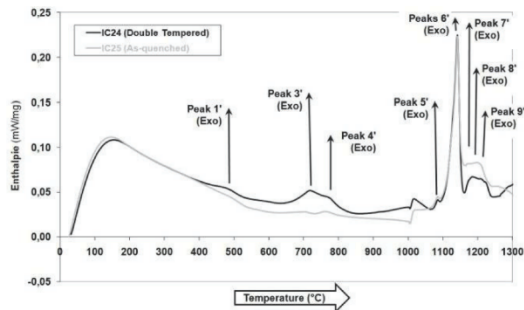
Fig. 1b: *DTA curves on IC24 and IC25 (Heating mode at 10°C from Room T° to 1000°C, then 5°C/min up to complete melting)*

Crystallization behavior towards DTA cooling mode

Solidification sequence as determined during the DTA cooling mode was quite similar for both IC1x and IC2x grades, except for the primary NbC carbides precipitation at the beginning of the solidification process (peak 9), and for the diffusionless martensitic transformations appearing close to the room temperature (peaks 1 and 1bis). Indeed peak 1bis amplitude was lower on IC1x series (fig. 2a) than that of IC2x series (fig 2b).
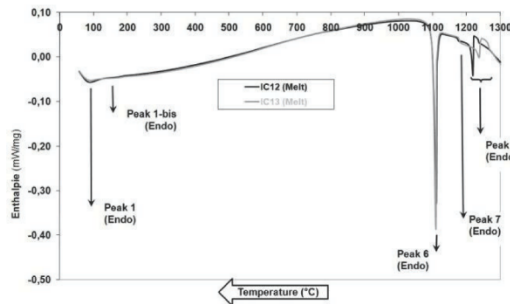
Fig. 2a: *DTA curves on IC12 and IC13 (Cooling mode at 5°C/min, from the melt and down to room T°)*
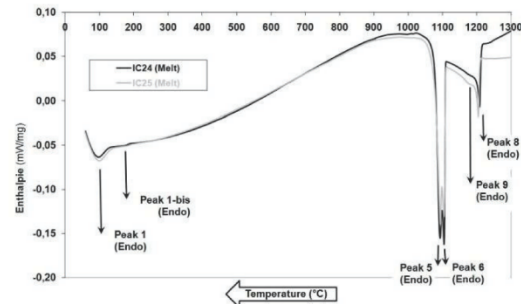
Fig. 2b: *DTA curves on IC24 and IC25 (Cooling mode at 5°C/min, from the melt and down to room T°)*

Peak 1bis that is more clearly enhanced on IC2x series than IC1x series, was reported to be related to a reaction quite similar to that of peak 1, namely martensitic transformation from a retained austenitic phase at the end of the cooling stage of the DTA test. Such a differentiation between peak 1 and peak 1bis suggested that martensitic phases that are linked to these peaks could be of different types.

The DTA cooling mode yields a reduced number of peaks, when compared to the DTA heating mode. Indeed, only 5 and 6 peaks were respectively observed on IC1x and IC2x series at the end of the DTA cooling stage whereas as 8 to 9 peaks were found during the DTA heating stage.

Table 3: *Signification of DTA peaks and related phase transformations, during heating mode on ICx1 series and IC2x series.*

Peaks number	Phase transformation reactions	Phase transformation designations	Peaks occurrence			
			IC12	IC13	IC24	IC25
1'	$\alpha' \rightarrow \gamma_1$	Direct transformation of martensite into austenite	No		Yes	
2'	$\alpha' \rightarrow \alpha'' + \eta$	Decomposition of martensite and fine carbides precipitation	Yes		No	
3'	$\alpha'' \rightarrow \gamma_2$	Reverse eutectoid 1 (tempered martensite transformed into austenite	Yes	No	Yes	
4'	$M_4C_3 + \gamma_{2'} \rightarrow \gamma_3$	Reverse eutectoid 2 (Fine secondary carbides dissolution)	No		Yes	
5'	$(Nb, V)C' + \gamma_4 \rightarrow L_1$	Reverse eutectic 1 (direct melting of eutectic (Nb,V)C)	No		Yes	
6'	$M_3C + \gamma_5 \rightarrow L_2$	Reverse eutectic 2 (direct melting of ledeburite)	Yes		Yes	
7'	$C_A (+ \gamma_6) \rightarrow L_3$	Direct melting of Graphite type A	Yes		Yes	
8'	$C_D + (\gamma_7) \rightarrow L_4$	Direct melting of Graphite type D	Yes		Yes	
9'	$NbC \rightarrow L_5$	Direct melting of primary NbC	No		Yes	

Microstructure characterization

The observation of re-melted samples at the end of DTA cooling tests led to set the sequence of phase precipitations within the cross section of the given sample, since solidification started close to the sample surface and ended in the centre of the sample (see fig. 3a to 3f, for IC1 series and fig. 4a to 4f, for IC2x series).

Indeed, cubic eutectic NbC carbides were found near the surface of IC2x re-solidified samples (fig. 4a, 4f), owing the fact that such carbides precipitated at the beginning of the solidification process.

Another type of eutectic NbC namely Chinese script shaped NbC, was found in the core of the re-melted sample (fig. 4c). Thus, it had been assumed that bulky cubic NbC precipitated first, and Chinese script NbC precipitated latter, the former type being promoting by higher cooling rates occurring near the surface.

Similar observations could be made regarding graphite morphology. Indeed two types of graphite were found in both re-melt IC1 and IC2 series, namely type A and type D, the latter being finer in size than the former (fig. 3a to 3d). Type D graphite appeared to form firstly, as it was located near the surface (fig. 3a, 4a) whereas type A which is flakier, is located deeper inside the re-solidified sample (fig. 3d, 4a, 4c).

Quenching seemed to have less influence on phase transformations in IC2x series than in IC1x series. Alloying elements that are dissolved in IC2x series austenite during quenching tended to inhibit martensite transformation into austenite, during re-heating, as it was the case with IC1x series.

By failing to recover all the peaks related to phase transformations that occurred at the time of the casting process, DTA tests enhance the difficulty which exists when simulations are carried out in order to reproduce the actual solidification route of complex alloys such as HACI. Indeed, the industrial spin casting process involved various cooling rates together with fluid dynamics phenomenon, as the melt is submitted to a significant rotation.

However, certain reactions could be studied and were found to be little influenced by alloying elements additions as ledeburite and graphite exhibited similar ranges on both IC1 and IC2 series.

Table 4: Signification of DTA peaks and related phase transformations, during cooling mode on IC1x and IC2x series.

Peaks number	Phase transformation reactions	Phase transformation designations	Peaks occurrence IC12 IC13	IC24 IC25
9'	$L_1 \rightarrow NbC$	Direct precipitation of tetragonal primary NbC	No	Yes
8'	$L_0 \rightarrow C_D + (\gamma_1)$	Direct precipitation of Graphite type D	Yes	Yes
7'	$L_2 \rightarrow C_A (+ \gamma_2)$	Direct precipitation of Graphite type A	Yes	No
6'	$L_3 \rightarrow M_3C + \gamma_3$	Eutectic 1 (Formation of Ledeburite from the melt)	Yes	Yes
5'	$L_4 \rightarrow (Nb, V)C' + \gamma_4$	Eutectic 2 (precipitation of Chinese script (Nb,V)C)	No	Yes
1bis'	$\gamma_6 \rightarrow \alpha'_2$	Diffusionless Martensitic start transformation (Lath type)	Yes	Yes
1'	$\gamma_5 \rightarrow \alpha'_1$	Diffusionless Martensitic start transformation (Plate type)	Yes	Yes

Phase volumes fractions

Quantification of phases was carried out towards images analysis. Results are given in Table 5.

IC2x series exhibit an improved amount of martensite, when compared to IC1x series, with a related reduced volume fraction of Cementite. Graphite amount remained similar in both grades.
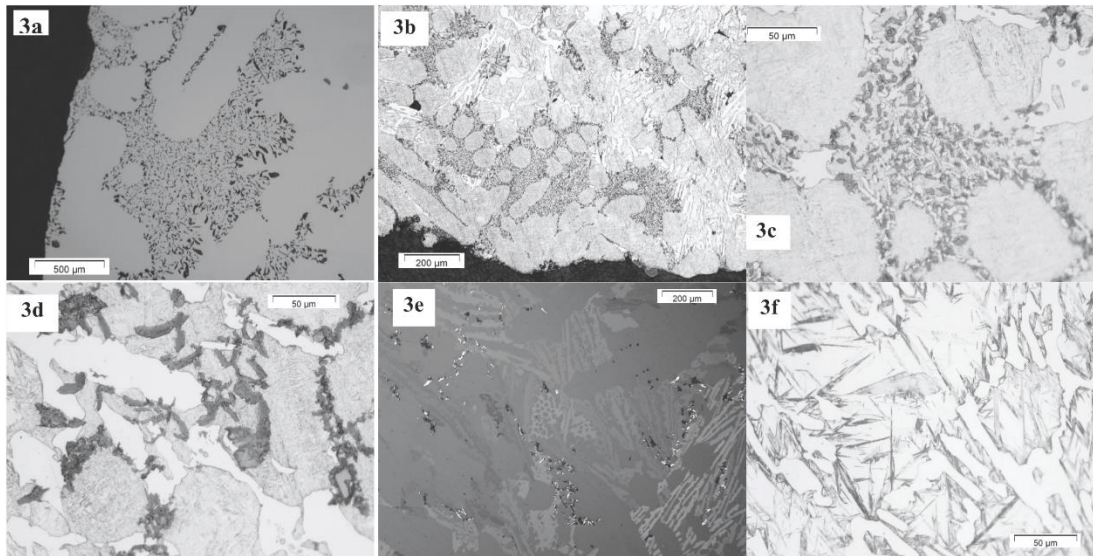
Figure 3: Re-solidified microstructures on IC1 grades, after DTA tests.
3a: Graphite Type D (dark) close to the surface on IC12, in as-polished conditions, with Polarized Light (Crossed Nichols); 3b: Graphite Type D (dark) close to the surface and Cementite (light) on IC12; 3c: Graphite Type D (dark), Cementite (light), and matrix on IC12; 3d: Graphite Type A (dark) with surrounding Cementite (light) and mixed matrix on IC12; 3e: Ledeburite (light to grey) towards Crossed Nichols on IC13, as-polished (polarized light); 3f: Plate Martensite (needles) and retained austenite (light), in the vicinity of Cementite on IC12
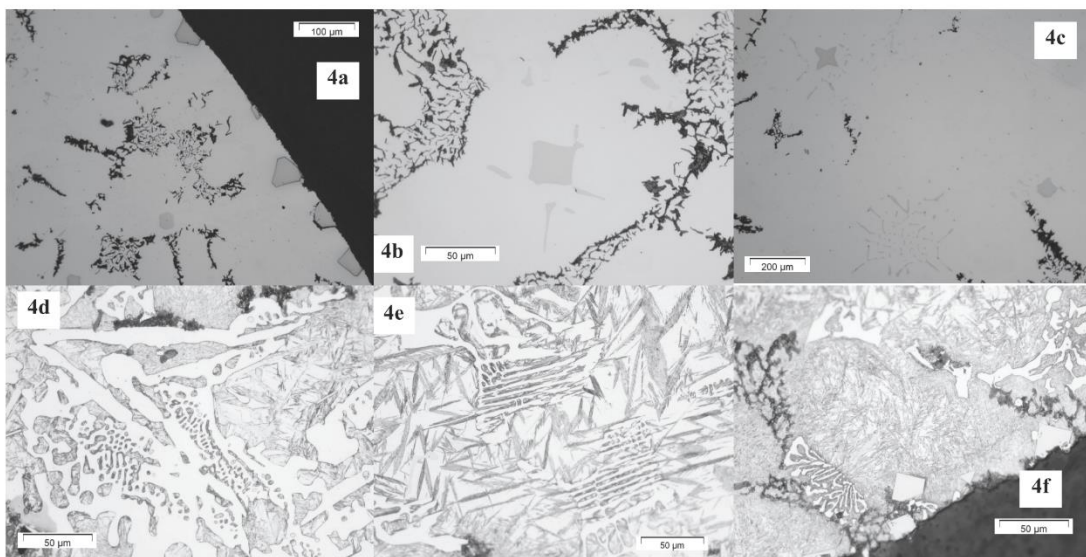
Figure 4: Re-solidified microstructures on IC2 grades, after DTA tests.
4a: Primary tetragonal NbC (light grey) near the surface and Graphite Type D (dark) deep inside the as-polished IC25 sample; 4b: Tetragonal primary NbC surrounded by Graphite Type D in as-polished IC24; 4c: Tetragonal Primary NbC (near the surface) and Chinese Script eutectic (Nb,V)C' inside with free-graphite (dark) inside as-polished IC24; 4d: Ledeburite surrounded by a mixed matrix of martensite and retained austenite on IC24; 4e: Plate Martensite (type 1, larges needles) and retained austenite (light) with surrounding ledeburite on IC24; 4f: Lath martensite (type 2, light and fine needles) near the surface and in the vicinity of both graphite(dark) and NbC primary carbides in IC24

Table 5: *Average volume fraction of various phases found on studied samples (%)*

Samples Phases	IC11	IC21	IC22
NbC	-	0.2 – 1.7	1.0 – 1.5
Graphite	2.3 – 4.2	2.5 – 3.4	3.0 – 3.5
M$_3$C	34 – 45	28 – 38	25 – 40
Martensite	52 – 62	58 – 68	55 – 70

Discussion

Two types of NbC carbides were found on IC2x series. First we observed the tetragonal bulky NbC, often located near the surface of re-solidified samples. Secondly, finer Chinese script NbC carbides were found deep inside the sample, at the end of DTA test.
Then it could be assumed that higher solidification rates promoted tetragonal NbC whereas as lower solidification rates gave rise to finer NbC.
Two types of graphite were also found on both HACI alloys, namely types A and D [17, 18].
The type D seemed to be more numerous than graphite A, on re-melted samples IC2x specimens. Such a higher graphite D content suggested that this type of graphite is promoted by higher solidification rates [4].
Two types of martensite were found in both IC1x and IC2x series, namely conventional plate martensite and additional lath-like martensite [1]. Each type of martensite is being linked to a specific peak at the time of DTA cooling stage. Moreover, lath martensite appeared to be located in the vicinity of either bulky NbC or graphite clusters, whereas plate martensite was found close to ledeburite areas.
The occurrence of a double peak, namely peak 1 and peak 1bis suggested that the two martensitic phases could probably be differentiated through their alloying elements content [1, 23]. Indeed a major differentiation was observed on the morphology of these two martensite phases. The first one located near tetragonal NbC and graphite cluster was finer than the plate-like martensite found in the vicinity of ledeburite.
Nb, V and Ti additions appeared to:
- lower the melting point of HACI grade
- enhance the secondary carbides precipitation at the time of tempering
- promote the formation of a lath martensite in addition to the plate martensite type, the former being located in the vicinity of bulky primary NbC and graphite clusters

The overall phase volume fractions was hardly modified with Nb/Ti/V additions, as there was a slight increase of martensite together with a slight decrease of both cementite and graphite.

Conclusions

Two types of NbC carbides were observed in as-cast IC2x series with Nb, Ti and V additions, whereas no NbC carbides were found in the same time in IC1x grades.
Nb, V and Ti additions appeared to lower the melting point of HACI grade, to enhance the secondary carbides precipitation at the time of tempering, and to promote the formation of a lath martensite in addition to the plate martensite type.
Two types of flaky graphite were found on both IC1 and IC2 grades, namely type A and type D graphite depending on the solidification rate.

Defect and Diffusion Forum Vols. 289-292　　　　　**85**

Two types of martensite were also found in both IC1x and IC2x series, namely plate-like martensite and lath-like martensite, the previous arising with enhanced cooling rates. Both martensite types depend strongly on the local chemical composition of the matrix.

The overall phase volume fractions of all these phases were hardly modified with Nb/Ti/V additions.

Retained austenite found in the quenched IC1x series without Nb, V and Ti additions exhibited an enhanced stability.

Almost all the phase transformations observed in both IC1x and IC2x series are diffusional transformations which are strongly depending on the chemical composition of the matrix and the cooling rate. The austenite to martensite transformation is a diffusionless reaction that depends on the temperature and on the chemical composition of the matrix.

Acknowledgements

References

[1]　M. Durand-Charre: *La microstructure des aciers et des fontes (Genèse et interprétation)* – SIRPE Editeur, Paris, 2003

[2]　J. Tchoufang Tchuindjang and J. Lecomte-Beckers: Inter. Jr. Fat. Vol. 29 (2007), p. 713

[3]　H-Q. Wu, N. Sasaguri, Y. Matsubara: Abrasion 2002, Proceedings, Fukuoka (Japan), p. 167

[4]　T. G. Oakwood, G. M. Goodrich, R. B. Gundlach: AFS Transactions, Vol. 02-031, (2002), p. 1

[5]　T. Nylen: Niobium 2001, Proceedings, Orlando (USA), p. 1063

[6]　Y. Matsubara, N. Sasaguri, K. Shimizu and S. K. Yu: Wear Vol. 250 (2001), p. 502

[7]　Y-H. Shy, C-H. Hsu, S-C. Lee, C-Y. Hou: Mater. Sci. Eng. A Vol. 278 (2000), p. 54

[8]　S.K. Hann and J. D. Gates: Jr. of Mater. Sci. Vol. 32 (1997), p. 1249

[9]　Y. Uematsu, K. Tokaji, T. Horie and K. Nishikagi: Mater. Sci. Eng. A Vol. 471 (2007), p. 15

[10] D. A. Porter and K. E. Easterling: *Phase Transformations in Metals and Alloys* – Second Edtion, Chapman & Hall, 1992

[11] J. Tchoufang Tchuindjang, L. Terziev, M. Sinnaeve, G. Mukadi Kantabilenga, J. Lecomte-Beckers: SBM 2007, Annual Meeting, Proceedings, Liege (Belgium)

[12] H. Liu, J. Wang, H. Yang and B. Shen: Mater. Sci. Eng. A Vol. 478 (2008), p. 324

[13] N. Luzginova, L. Zhao, J. Sietsma: Mater. Sci. Eng. A Vol. 448 (2007), p. 104

[14] G. Zajac and J. Pacyna: Jr. of Mater. Proc. Techno. Vol. 162-163 (2005), p. 442

[15] A. R. Ghaderi, M. Nili Ahmadabadi and H. M. Ghasemi: Wear Vol. 255 (2003), p. 410

[16] L. A. Dobrzanski, A. Zarychta and M. Ligarski: Jr. of Mater. Proc. Techno. Vol. 63 (1997), p. 531

[17] D. D. Double and A. Hellawell: Acta; Metall; Mater. Vol. 43 (1995), p. 2435

[18] G. F. Geier, W. Bauer, B. J. McKay and P. Schumacher: Mater. Sci. Eng. A Vol. 413-414 (2005), p. 339

[19] R. Källbom, K. Hamberg, M. Wessen and L.-E. Björkegren: Mater. Sci. Eng. A Vol. 413-414 (2005), p. 346

[20] K. Edalati, F. Akhlaghi, M. Nili-Ahmadabadi: Jr. of Mater. Proc. Techno. Vol. 160 (2005), p. 183

[21] C. G. Schön and A. Sinatora: Calphad Vol. 22, No 4 (1999), p. 437

[22] J. Lecomte-Beckers and J. Tchoufang Tchuindjang: EMAC 2004, Proceedings, Antwerp (Belgium)

[23] H. K. D. H. Bhadeshia: Metal Science Vol. 17 (1983), p. 151

.. Article #3

Study of the origin of the unexpected pearlite during the cooling stage of two cast high-speed steels

Jérôme TCHOUFANG TCHUINDJANG[1,a] and Jacqueline LECOMTE-BECKERS[1, b]

[1]Metallic Materials Science Unit – Aerospace & Mechanics Department. – University of Liege
IMGC, Bât. B52; 1, Chemin des Chevreuils – 4000 Liège, Belgium
[a]j.tchuindjang@ulg.ac.be, [b]jacqueline.lecomte@ulg.ac.be

Key words: HSS, crystallization behaviour, carbides, phase transformations, pearlite.

Abstract. Two HSS grades (A and B) belonging to the complex system Fe-Cr-C-Si-X, where X is a strong carbide-forming element such as V, Mb or W, were studied. Samples in the as-received conditions came from an industrial spin casting process, with a varying cooling rate during processing. Chemical compositions of both alloys were closed to each other and were chosen to enhance their hardenability and to avoid less resistant phases such as pearlite and ferrite. Differential Thermal Analysis was performed on both alloys, in order to increase their crystallization behaviour. Light microscopy and SEM associated with EDS analyses were done to characterize the microstructure of both alloys in the as-received conditions and after DTA trials.
The matrix of both HSS grades was composed of eutectic carbides, martensite and retained austenite, these phases exhibiting similar chemical compositions in both alloys. Unexpected pearlite was found in the as-cast HSS alloy B without W, this grade containing more Mo, more V and less Cr than the HSS grade A. It appeared from DTA tests that pearlite found in the alloy B arose more from the destabilisation of the Cr-rich retained austenite associated with the plate-like M_2C carbide, than from the matrix itself. In fact, pearlite zones located in the vicinity of M_2C are due to related isothermal solid phase transformations form the previous austenitic eutectic phase that is enriched with Cr and Mo.

Introduction

High Speed Steels alloy (HSS) are alloys belonging to the complex system Fe-C-Si-X, where X is a strong carbide forming element such as Cr, V, Nb, Mo, W, etc [1-8]. HSS alloys contain very hard carbides at grain boundaries with matrix composed of martensite or bainite in order to sustain wear and oxidation resistances in cold or hot conditions as in this the case for rolling mill applications [2, 9]. Carbides usually found in HSS are type MC, M_2C, M_7C_3, M_6C or M_3C both pro-eutectic and eutectic ones, as they precipitate during the solidification process. Their nature mainly varies either with the chemical composition of the alloy or the cooling rate [3-7, 10-13]. The chemical composition and the casting route on HSS alloys influence dendritism and grain size, these features playing a great role on mechanical properties such as strength, wear, toughness and hardness [3-5]. For most of the previous works done on HSS alloys, the study of solidification paths seemed to be the main issue. Thus solid state transformations occurring below the solidification range are generally little or less discussed since HSS contain alloying elements which increase the hardenability of the matrix. Furthermore the expected matrix of HSS alloys in the as-cast conditions is often known to be of martensite or bainite type, with more or less retained austenite, the latter phase being transformed during subsequent heat treatments [4, 10, 14]. Maratray and Ussegliot-Nanot showed that an increase in the Cr/C ratio as well as in the Mo content improved significantly the hardenability of such alloys through the delay in incubation time for pearlitic transformation together with the precipitation of a Cr-rich fine secondary carbide inside the newly destabilised austenite matrix. Such a destabilisation of the prior austenite grain deeply influence the S and C-curves of TTT and CCT diagrams respectively [15].

804   **Solid-Solid Phase Transformations in Inorganic Materials**

This paper lays emphasis on the conditions that promote the occurrence of pearlite in the vicinity of eutectic carbide M_2C during the casting route while the matrix remains unconcerned as its austenitic phase keeps a great and expected hardenability. Such an insight of the so-called abnormal pearlite formation is enhanced by the metallurgical comparison between two HSS grades with similar casting conditions and different but closed chemical compositions.

Raw Materials

The studied alloys come from the shell material of bimetallic composite work rolls used in the rear finishing stands of the Hot Strip Mill. These rolls were obtained by a vertical spin casting process. Samples for subsequent microstructural analyses were cut out near the surface of the shell, from the earlier 25 mm in depth on the shell material.

The average composition of the studied materials is given in Table 1. HSS grade B is free of W, but contains more V, more Mo and less Cr than HSS grade A, the other alloying elements being similar in their amount for both grades.

Table 1: Average chemical composition of HSS materials [% weight]

HSS Grades	Alloying elements								
	C	Si	Mn	Ni	Cr	V	Mo	W	Fe
A	1.6 –	0.3 –	0.7 –	1.0 –	5.0 – 7.0	3.0 – 5.0	3.0 – 5.0	1.0 – 3.0	Bal.
B	2.0	0.6	1.2	1.5	3.0 – 5.0	4.0 – 6.0	5.0 – 7.0	-	

Experimental methods

Thermodynamical simulations were performed while using MTData® software with SGTE data base. MTData simulations assume infinitely slow variations of the temperature with free diffusion of the alloying elements either in the melt or in the solid state.

Differential Thermal Analysis (DTA) was used to help the casting route simulation through the enhancement of phase transformations during remelting and solidification sequence of the studied alloys. DTA tests were obtained on a Netzsch STA 449 device at a constant heating or cooling rates of 5°C/min.

Microstructure characterization was realised through both light microscopy, on an Olympus BX 60M apparatus, and Scanning Electron Microscopy (SEM) together with Energy Dispersive X-rays Spectroscopy (EDS), on a XL-30 FEG ESEM Philips.

Results

Equilibrium and non-equilibrium simulations. Major results obtained from equilibrium diagrams by thermodynamical simulations are given in Table 2. In the equilibrium conditions, the solidification sequence starts with the formation of γ-FCC prior to the formation of eutectic MC carbides for both HSS grades. Carbides other than MC eutectics are also predicted by equilibrium simulations, these carbides been eutectoid ones as they appear in the solid state, late below the solidus. Eutectoid carbides predicted by equilibrium conditions are M_7C_3, M_6C and $M_{23}C_6$ HSS grade A, and only $M_{23}C_6$ type for HSS grade B.

Table 2: Important temperatures obtained from Equilibrium simulations on HSS grades A and B

Phase transformations	HSS grade A	HSS grade B
Liquidus (γ-FCC)	1330°C	1320°C
MC eutectic carbides	1260°C	
Solidus	1200°C	
M_7C_3 eutectoid carbides	1050°C	-
M_6C eutectoid carbides	1050°C	-
$M_{23}C_6$ eutectoid carbides	925°C	925°C
Ferritic transformation start, A_3 (α-BCC)	780°C	790°C
Ferritic transformation end, A_1 (α-BCC)	660°C	660°C

Non-equilibrium conditions obtained from DTA tests are illustrated on figure 1 and table 3 for the cooling mode, with the enhancement of the crystallisation behaviour of both HSS grades. Each peak of the DTA thermogram curve is related to a phase transformation.
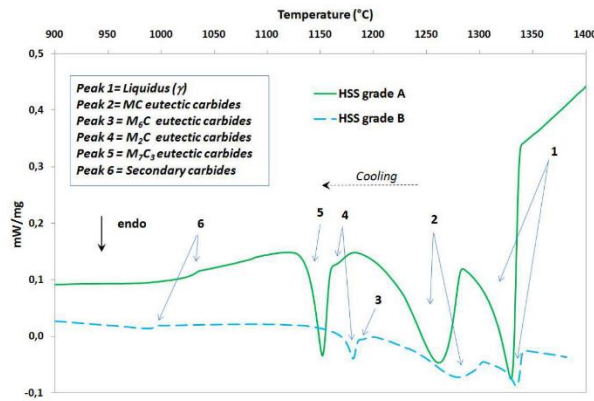
Figure 1: Crystallisation behaviour of HSS grades A and B through DTA cooling mode
(DTA tests performed at 5°C/min for the cooling rate)

The same carbides like those predicted from equilibrium conditions are also present in non-equilibrium conditions, but their designations are different since all of them are eutectic ones, except for $M_{23}C_6$ which remain of eutectoid type. The temperature ranges for the solidification sequence and subsequent phase transformations in the solid state are not similar in equilibrium and non equilibrium conditions, except for the liquidus temperature on both grades.

Table 3: Important temperatures obtained from DTA experiments on HSS grades A and B

Peaks	Phase transformation designations	Peaks occurrence (T°)	
		A grade	B Grade
1 : L $\rightarrow$ γ_0	Solidification start (Liquidus)	Yes (1340°C)	Yes (1340°C)
2 : L $\rightarrow$ γ_1 + MC	Eutectic 1 (precipitation of V-rich carbides)	Yes (1280°C)	Yes (1305°C)
3: L $\rightarrow$ γ_4 + M_6C	Eutectic 4 (precipitation of Mo-rich carbides)	No	Yes (1190°C)
4: L $\rightarrow$ γ_2 + M_2C	Eutectic 2 (precipitation of Mo-rich carbides)	Yes (1175°C)	Yes (1175°C) *Solidus*
5: L $\rightarrow$ γ_3 + M_7C_3	Eutectic 3 (precipitation of Cr-rich carbides)	Yes (1160°C) *Solidus*	No
6 : γ_0 $\rightarrow$ fine secondary carbides (+ γ_5)	Eutectoid 1 (precipitation of fine secondary carbides)	Yes (1030°C)	Yes (985°C)

As-cast microstructures characterisation. Micrographs obtained from the as-cast industrial conditions are given at figures 2 to 5. Optical (fig. 2 and 3) and electron (fig. 4 and 5) micrographs show a quasi continuous network of intercellular eutectic carbides at grain boundaries (GB) with a matrix composed of martensite and retained austenite (RA) for both HSS grades A and B.

3 types of eutectic carbides are present on HSS grade A in the as-cast conditions, namely petal-like V-rich MC, fishbone-like Cr-rich M_7C_3 and acicular or needle-like Mo and W-rich M_2C (fig. 2 and 4). Only MC and M_2C eutectic carbides are present on as-cast HSS grade B (fig. 3 and 5). EDS map (fig. 6b) gives an overview of the elements distribution within the studied phases on HSS grade B. Both morphology and average chemical compositions of carbides found in HSS grades A and B seem to be in good agreement with the results given in previous studies [1-9, 11-15].
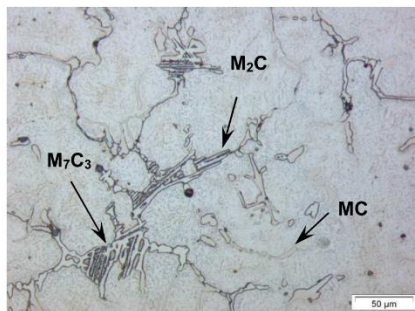
Figure 2: HSS grade A after industrial casting, showing eutectic carbides (light) at GB with a mixed martensite-RA matrix – *Nital etched*
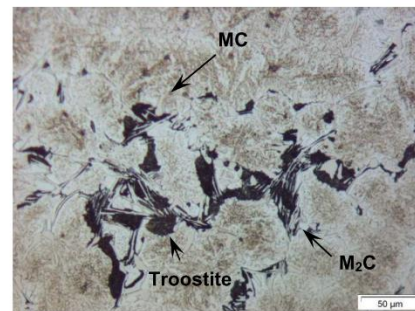
Figure 3: HSS grade B after industrial casting showing eutectic carbides at GB, troostite (dark) in the vicinity of M_2C carbides, and martensite-RA matrix – *Nital etched*
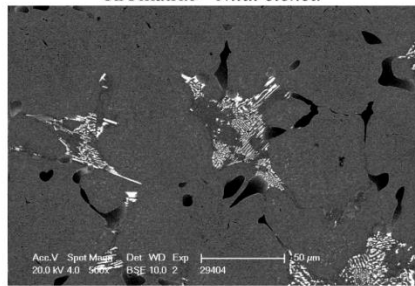
Figure 4: HSS grade A after industrial casting - Petal-like MC carbides (dark) and complex M_7C_3/M_2C carbides (light) in a martensite/RA matrix (grey) – *As polished*
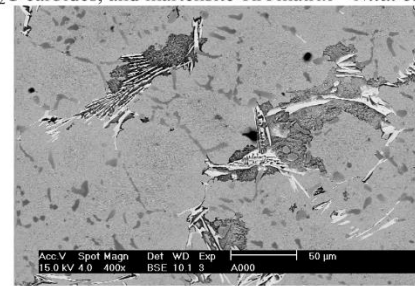
Figure 5: HSS grade B after industrial casting with Petal-like MC carbides (dark), Acicular M_2C carbides (light) with neighbouring troostite (dark grey) in an martensite/RA matrix – *Nital etched*
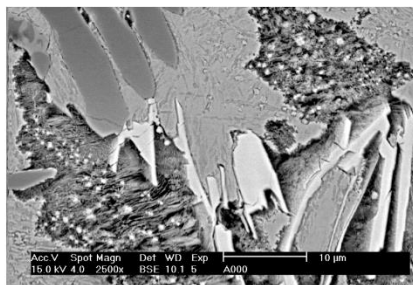
Figure 6a: Microstructure of HSS grade B in as-cast conditions, with the enhancement of the troostite fine lamellar structure located in the vicinity of M_2C carbides; very fine Mo-rich carbides are fully dispersed within the troostite – *Nital etched*
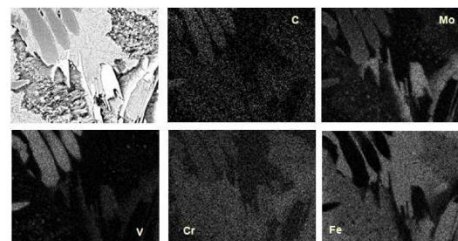
Figure 6b: EDS map related to figure 6a showing the distribution of major elements on MC carbides (V-rich), M_2C carbides (Mo-rich), and troostite (Cr-rich); there are small Mo-rich precipitates within the troostite

Compared to HSS grade A, HSS grade B in the as-cast conditions does not contains Cr-rich M_7C_3 carbides but exhibits an additional phase also known as troostite (fig. 3, 5 and 6a), a very fine pearlite. The troostite found in HSS grade B is Cr-rich and it contains very fine Mo-rich secondary carbides that are fully dispersed within this phase (fig. 6a). Furthermore, this troostite seems to be always located in the vicinity of M_2C eutectic carbides (fig. 3, 5 and 6a).

Discussion

Equilibrium versus Non-Equilibrium. It appears from DTA tests that non-equilibrium conditions lead to a microstructure different from the one predicted by equilibrium thermodynamical simulations. The following statements can be made:

- Only one eutectic carbide (MC) is predicted by equilibrium diagram instead of the three types (MC, M_2C and M_7C_3) found in HSS grade A, or the two types (MC and M_2C) found in HSS grade B;
- Neither the modification in alloying elements nor equilibrium or non-equilibrium conditions do affect the liquidus temperature, which appears similar for both HSS grades (around 1330°C). But there is a shift of the solidus point to lower temperatures when moving from equilibrium conditions to non-equilibrium ones;
- The decrease of the solidus temperature in the non-equilibrium conditions is related to the modification of the M_2C and M_7C_3 carbides types from eutectoid ones in the equilibrium simulations to eutectic ones in the non-equilibrium ones.
- The actual solidus temperature of HSS grade A appears lower than that of the HSS grade B as M_7C_3 eutectic carbides precipitated only in the former HSS grade, and these carbides precipitated after the M_2C type which is present in both HSS grades.

| *a) No IIS* | *b) IIS at 650°C/2h – No Troostite* | *c) IIS at 750°C/2h – No Troostite* |

| *d) IIS at 700°C/2h – **Troostite*** | *e) IIS at 650°C/4h – **Troostite*** | *f) IIS at 700°C/4h – **Troostite*** |
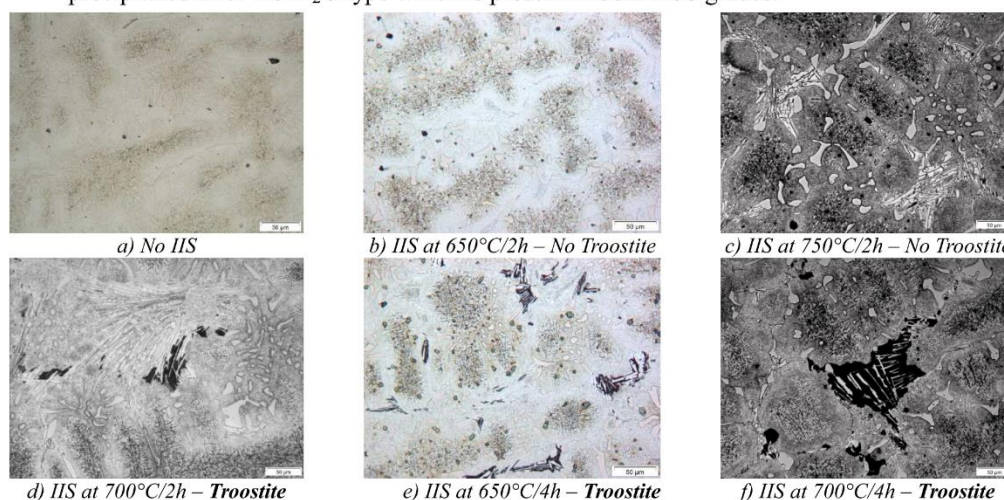
Figure 7 a) to f): Optical micrographs showing the occurrence of troostite in HSS grade B as a function of temperature and holding time when an Isothermal Intermediate Stage (IIS) is set within the continuous cooling sequence of DTA test (cooling rate of 5°C/min) – *Nital etched*

Mixed CCT-TTT conditions for troostite occurrence. As no troostite was found after classical DTA tests performed at a constant cooling rate of 5°C/min on HSS grade B, others trials were made on the same alloy to simulate a complete solidification sequence starting from the melt down to room temperature, either at faster (20 and 10°C/min) or lower cooling rates (2 and 1°C/min). These trials did not allow the formation of pearlite. It is the reason why the constant cooling rate of 5°C/min during DTA tests was change to introduce an Intermediate Isothermal Stage (IIS), this level been intercalated in the overall cooling sequence. The temperature of the IIS was chosen respectively at 800, 750, 700, 650, 600 and 500°C with a holding time of 2 or 4 hours, to allow the interception of a possible pearlitic nose in the unknown isothermal diagram of such an alloy. Major results of tests with ISS are illustrated by the optical micrographs of figure 7.

For a 2 hours holding time on the ISS during the DTA cooling sequence, troostite was found only on the sample with ISS set at 700°C. For a 4 hours holding time on the ISS, the 650°C sample exhibited troostite whereas the 750°C sample did not. Meanwhile, an increase of the holding time form 2 h to 4 h led to an increase of the troostite amount in the 700°C sample.

Whenever troostite occurred, this phase was still located closed to M_2C carbides (fig 7d to 7f), like it had been previously seen in the industrial as-cast HSS grade B samples (fig 3 and 5).

Thus it could be assumed that the "pearlitic nose" for the mixed CCT-TTT conditions is closed to 700°C as the incubation time for troostite occurrence is minimal for this temperature. The real incubation time remains unknown but could be considered lower or equal to 2h.

Furthermore, it is suggested that the enrichment in Cr and Mo of the eutectic austenite associated with M_2C carbides in HSS B during the solidification stage is responsible of the formation of the latter troostite through a pseudo continuous cooling sequence with an ISS. It could also been assumed that fine Mo-rich secondary carbides found in the troostite result from the precipitation of a certain amount of Mo and C previously contained in the parent eutectic austenitic phase associated with M_2C carbide when such a phase undergoes eutectoid transformation. On the same time, the bulk austenitic grain remained untransformed till the martensitic point is reached.

Conclusions

A slight variation in major alloying elements could modify the solidification path, especially the occurrence of eutectic carbides. In fact, three types of eutectic carbides were found in HSS grade A namely V-rich MC, Mo and W-rich M_2C and Cr-rich M_7C_3, these carbides precipitating in the corresponding sequence. HSS grade B with more Mo, more V and less Cr than HSS A, contains only MC and M_2C eutectic carbides.

Equilibrium simulations allow a partial prediction of actual solidification paths, as only the liquidus temperature and the occurrence of MC eutectics carbides were found similar either for equilibrium and non equilibrium simulations in both HSS grades, while the predicted solidus temperature was higher than the actual one obtained from non equilibrium experiments.

The austenite associated with M_2C to form the eutectic phase in HSS grade B contains more Cr and more Mo than that of HSS grade A. As a consequence, this austenite undergoes an eutectoid transformation during the industrial cooling sequence, leading to the formation of troostite in the vicinity of M_2C carbides. In the same time the bulk austenitic grain remains untransformed.

References

[1] T. Okane and T Umeda: Sci. and Tech. of Adv. Mater. 2 (2001), p. 247

[2] Y. Pan, H. Yang, X. Liu and X. Bian: Mater. Letters 58 (2004), p. 1912

[3] C. K. Kim, J. Il Park, S. Lee, Y. C. Kim, N. J. Kim and J. S. Yang: MMT A36 (2005), p. 87

[4] J. Lecomte-Beckers, J. T. Tchuindjang, E. Pirard and J-P. Breyer: Stal' Vol. 2 (2003), p. 88

[5] W. Shizhong, Z. Jinhua, X. Liujie and L. Rui: Mat. and Design 27 2006), p. 58

[6] F. Pan, M. Hirohashi, Y Lu, P. Ding, A. Tang and D. V. Edmonds: MMT A35 (2004), p. 2757

[7] L. A. Dobrzanski, A. Zarychta and M Ligarski: Jrn. of Mater. Proc. Tech. 63 (1997), p. 531

[8]   M. Boccalini and H. Goldenstein: Internat. Mater. Rev. Vol. 46 No.2 (2001), p. 92

[9]   M. Hashimoto, O. Kubo and Y. Matsubara: ISIJ Intern. Vol. 44 No. 2 (2004), p. 372

[10] J. Lecomte-Beckers and J. T. Tchuindjang: Def. and Diff. Forum Vol. 289-292 (2009), p. 77

[11] J. D. B. DeMello, M. Durand-Charre and S. Hamar-Thibault: Met. Tr. 14A (1983), p. 1793

[12] H. F. Fischmeister, R. Riedl and S. Karagöz: Met. Trans. 20A (Oct. 1989), p. 2133

[13] J. Lecomte-Beckers and J. T. Tchuindjang: GIT – Imaging and Microscopy Vol. 2 (2005), p. 2

[14] B. Decaudin, C. Djega-Mariadassou and G. Cizeron: Jrn. of All. and Comp. 226 (1995), p. 208

[15] F. Maratray and R; Usseglio-Nanot: *Facteurs affectant la structure des fontes blanches au chrome et au chrome-molybdène,* edited by Climax Molybdenum S.A., Paris, France

Solid-Solid Phase Transformations in Inorganic Materials
doi:10.4028/www.scientific.net/SSP.172-174

Study of the Origin of the Unexpected Pearlite during the Cooling Stage of Two Cast High-Speed Steels
doi:10.4028/www.scientific.net/SSP.172-174.803

.. Article #4

Feature Article

Current Developments of Alloyed Steels for Hot Strip Roughing Mills: Characterization of High-Chromium Steel and Semi-High Speed Steel

In the early 1980s, a chrome steel work roll grade was developed by European rollmakers and has, since then, been introduced in most roughing stands of hot strip mills (HSMs), as well as into the early finishing stands of compact strip mills. As of 2010, chrome steel grade was still a standard grade in many HSMs over the world, as can be seen in Figure 1.
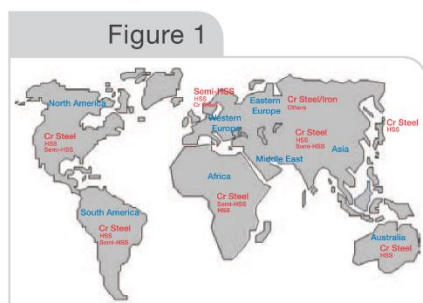
Figure 1

Dominant roughing mill work roll grades in the world.
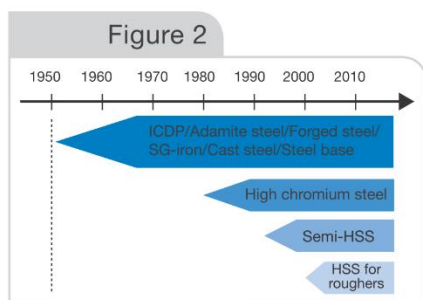
Figure 2

History of HSM roughing mill work roll grades from 1950 to 2010.

The ever-increasing requirements for roughing mills, in terms of cost/performance ratio, including higher throughput, improved product quality and higher safety standards, prompted European rollmakers in the early 1990s to develop a new roll grade for roughing stands, which is known as semi-high-speed steel (semi-HSS). This new grade was considered to be a real revolution in terms of roll performance in nearly all aspects of the required behavior.

Semi-HSS acquired a strong position, especially in Western European HSMs. However, some applications, like stainless and special steel rolling, have shown interest in further developments to overcome some insufficiencies of semi-HSS. A special high-speed steel (HSS) grade for roughing mill application was developed to meet this new challenge in the late 1990s (see the history of work roll development in Figure 2).

Work Roll Grades for Roughing Stands

Chemical Composition —
The typical chemical compositions of the main roughing roll grades used today in hot strip rolling are listed in Table 1. This table indicates the main elements such as carbon, chromium, tungsten equivalent, MC-carbide-forming elements, as well as

Abstract

Two alloys grades for work rolls used in the roughing stand of Hot Strip Mill — high chromium steel (HCS) and semi-high-speed steel (semi-HSS), In this paper, the new semi-high-speed steel grade is studied.

Authors

Jacqueline Lecomte-Beckers
head of metallic materials science unit, aerospace and mechanics department, University of Liège, Liège, Belgium
jacqueline.lecomte@ulg.ac.be

Mario Sinnaeve
director, R&D and quality, Marichal Ketin Belgium, Liège, Belgium
qualitycontrol@mkb.be

T. Jerome Tchuindjang
researcher, MMS unit, University of Liège, Liège, Belgium
j.tchuindjang@ulg.ac.be

This article is available online at AIST.org for 30 days following publication.

AIST.org

Feature Article

the carbide content and hardness range of the different roughing roll grades.

Semi-HSS 1 and semi-HSS 2 are semi-HSS grades with different carbon contents. Both grades contain MC-carbide-forming elements, whereas the semi-HSS 3 shows the highest MC-carbide-forming elements content (V, Ti, Nb, Ta, etc.).

The chrome steel grade microstructure is mainly determined by a matrix of tempered martensite with eutectic carbides of the M_7C_3 and M_6C type. The highly increased hardness of the matrix and of the different carbide types other than cementite have determined a much higher wear resistance and fire crack resistance compared to former standard grades. In the mid-1980s, this roll type became a standard roughing mill work roll grade. The semi-HSS grade is characterized by a matrix of tempered martensite with a strong effect of temper hardening, where special carbides of the M_7C_3, M_6C and MC type are embedded. This structure already offers the typical characteristics of HSS grades like high-temperature strength and hot hardness. The latest-developed HSS grade for roughing stands has increased amounts of MC and M_6C carbides replacing, to a greater extent, the M_7C_3 type carbides. Both semi-HSS and HSS for roughers do not present a continuous carbide network. These last two roll grades are submitted to a long, sophisticated heat treatment, which is responsible for the homogeneous basic structure and contributes to their high performance level.

The type, hardness and amount of these carbides have a strong influence on wear resistance, surface deterioration and oxidation behavior of the different roll types.[1–5]

The present work will be focused on Cr steel and the three semi-HSS work rolls.

Microstructures — Many different roll grades have been used in roughing stands of HSMs since the beginning of hot strip rolling.[6] Only some recent roll grades will be discussed here in further detail. The microstructures of these grades are shown in Figure 3.

Metallurgical Characterization

Thermodynamic Simulations — Thermodynamic simulations were obtained from Thermo-Calc® software (TC). Examples of equilibrium diagrams of Cr steel and semi-HSS 3 are shown in Figures 4a–d. TC simulations assume constant equilibrium conditions, which means a very low cooling rate where ideal diffusion is allowed for all the alloying elements either in the liquid or in the solid state. These figures show the phase volume fraction of stable phases in the studied alloys between 500 and 1,500°C with a 10°C step.

From TC simulations, it appears that the first solid is almost the face-centered cubic austenite, except for the semi-HSS 3 grade, where the first solid to precipitate is the bold-centered cubic delta ferrite. From this statement, a peritectic transformation occurs in the semi-HSS 3 grade during the solidification process (Figure 4d). This peritectic transformation is known to promote a new austenite phase from the decomposition of the previous delta ferrite phase.

As M_7C_3 carbides in both Cr steel and semi-HSS grades 1 and 2 seem to start their precipitation close to or below the solidus temperature, with an increase of their amount with decreasing temperature, these carbides could be assume to be of eutectoid type.

Figure 3
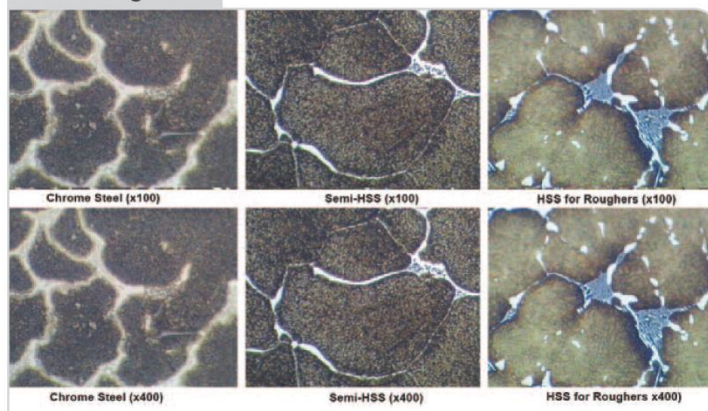
Overview of work roll microstructures for roughing stands.

Table 1

Roughing Mill Roll Grades — Analysis, Carbide Content and Hardness of Working Zone

Roll grade	C, wt. %	Cr, wt. %	W eq. (=W+2Mo) wt. %	MC-carbide-forming elements (wt. %)	Carbide content (wt. %)	Hardness (Shore C)
Cr steel	1.3–1.6	11–13	6–10	< 0.5	10–15	70–80
Semi-HSS 1	0.6–0.9	7–9	4–8	0.5–1.0	< 5	75–85
Semi-HSS 2	0.8–1.1	7–9	4–8	0.5–1.0	< 5	75–85
Semi-HSS 3	0.6–0.9	7–9	4–8	1.0–2.0	< 5	75–85
HSS (roughing)	1.3–1.6	3–6	6–10	4–8	10–15	72–82

Only MC carbides found in semi-HSS 3 through the equilibrium diagram could be considered as truly eutectic, as they precipitated from the liquid.

Thus in equilibrium conditions, semi-HSS grades 1 and 2 did not exhibit eutectic carbides, as M_7C_3 and the latter M_6C precipitated in the solid state.

Furthermore, when the temperature decreases in equilibrium conditions, all of the primary carbides (MC, M_7C_3 and M_6C) transform themselves close to the A1 point (Figures 4a–4d) in a partial or complete reaction, which leads to other types of carbides known as fine secondary carbides, such as $M_{23}C_6$, M_2C and MC.

Solidification Paths — Solidification paths were obtained from differential thermal analysis (DTA) tests. From this technique, a difference in energy is measured between the material to be tested and an inert reference material as a function of temperature, while both samples are submitted to a controlled temperature program. A phase transformation occurring in the studied material appears as an endothermic or an exothermic peak when the DTA cycle goes on.[7]

Figure 5 illustrates the results of DTA tests on the four grades during the cooling cycle, which starts from the melt down to room temperature at 5°C/minute.

The solidification range was obtained while considering the liquidus and the solidus temperatures on the four studied grades. Table 3 gives the results obtained from the comparison between equilibrium (from TC) and non-equilibrium (from DTA) conditions.

SEM-EDS analyses (Figures 6a and b) performed after the DTA tests allow for the identification of the phases present at room temperature, such as the eutectic carbides and the matrix (mixture of martensite and retained austenite). Such a DTA solidification sequence had already been enhanced in previous work.[8–10]

Only the starting points of M_7C_3 and M_6C, which are considered as eutectic carbides in the equilibrium conditions, are illustrated in Table 2. It was observed that the phase transformation range is shorter in the non-equilibrium conditions than that of the equilibrium conditions.

From the comparison between Cr steel and semi-HSS grades, the following observations arise:

Figure 4
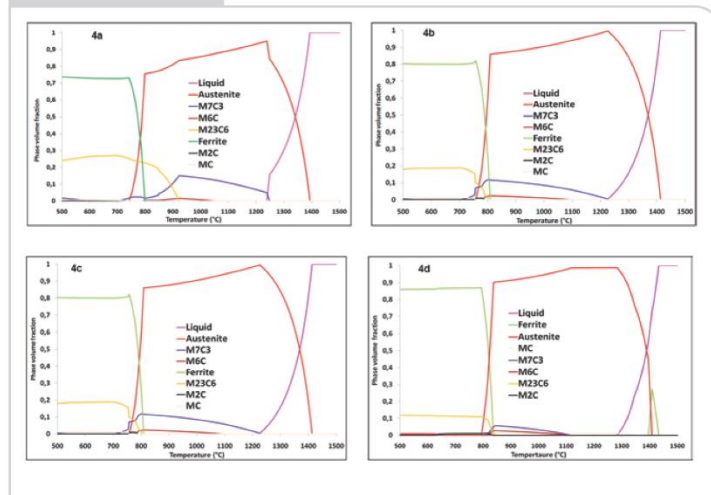
Phase volume fractions with temperature in equilibrium conditions on high-Cr steel (4a) and on semi-HSS 1 (4b). Phase volume fractions with temperature in equilibrium conditions on semi-HSS2 (4c) and on semi-HSS 3 (4d).


Figure 5
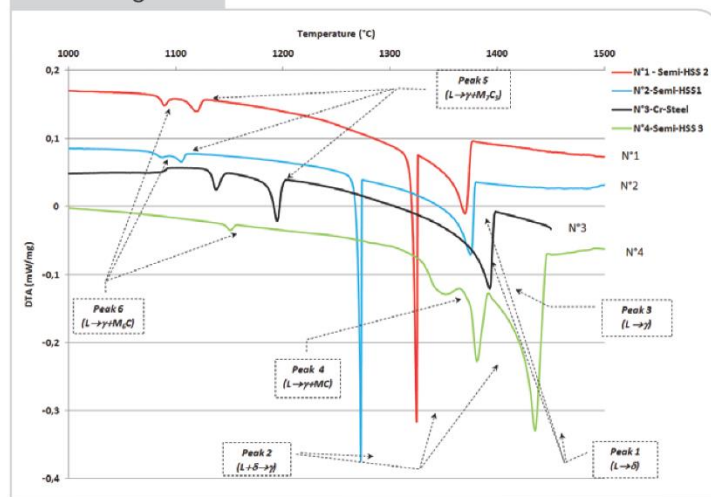
Solidification sequences on the four studied alloys during DTA cooling stage at 5°C/minute.

- The liquidus temperature of semi-HSS grades is always higher than that of the Cr steel, no matter what the conditions are from equilibrium or non-equilibrium.
- The semi-HSS 3 exhibits the higher liquidus temperature in the non-equilibrium conditions (1,428°C).
- The semi-HSS 3 grade contains MC eutectic carbides which precipitate at high temperature (1,353°C); as a consequence, no M_7C_3 are found

Feature Article

Figure 6
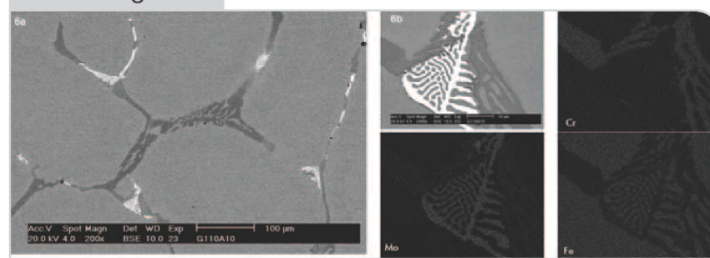
Eutectic carbides network on Cr steel after DTA test: fishbone-like M_7C_3 (grey) and fine-lamellar M_6C (light) (6a); and complex M_7C_3/M_6C eutectic carbide in a Cr steel and related EDS mapping showing major elements of each phase (Cr-rich M_7C_3 and Mo-rich M_6C) (6b).
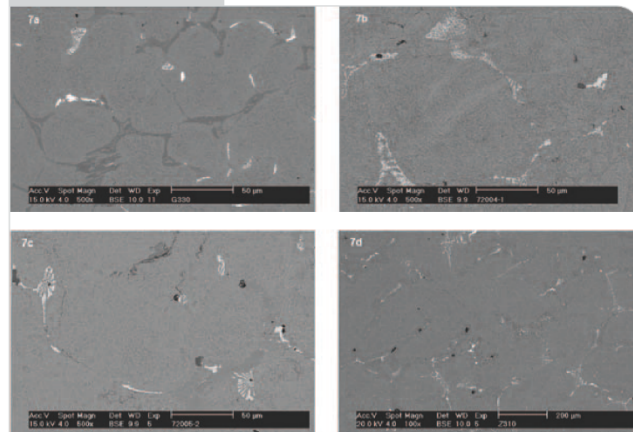
Table 2

Comparison of Phase Transformations Between Equilibrium and Non-Equilibrium Conditions

Phase transformation obtained from the solidification sequence (Peak number)	Grades	Temperature range from DTA (non-equilibrium conditions; cooling at 5°C/minute)	Temperature from TC (equilibrium conditions)
$L \rightarrow \delta$ (start) Peak 1	Semi-HSS 1	1,430°C (Liquidus)	—
	Semi-HSS 2	1,430°C (Liquidus)	—
	Semi-HSS 3	1,443°C (Liquidus)	1,428°C (Liquidus)
$L + \delta \rightarrow \gamma$ (start) Peak 2	Semi-HSS 1	1,337°C	—
	Semi-HSS 2	1,399°C	—
	Semi-HSS 3	1,389°C	1,405°C
$L + \delta \rightarrow \gamma$ (end)	Semi-HSS 1	1,422°C	—
	Semi-HSS 2	1,419°C	—
	Semi-HSS 3	1,384°C	1,395°C
$L \rightarrow \gamma$ (start) Peak 3	Chromium steel	1,394°C (Liquidus)	1,388°C (Liquidus)
	Semi-HSS 1	—	1,429°C (Liquidus)
	Semi-HSS 2	—	1,409°C (Liquidus)
	Semi-HSS 3	—	1,395°C
$L \rightarrow \gamma + MC$ (start) Peak 4	Semi-HSS 3	1,364°C	1,343°C
$L \rightarrow \gamma$ (end)	Chromium steel		1,238°C (Solidus)
	Semi-HSS 1		1,279°C (Solidus)
	Semi-HSS 2		1,228°C (Solidus)
	Semi-HSS 3	1,389°C	1,293°C (Solidus)
$L \rightarrow \gamma + MC$ (end)	Semi-HSS 3	1,353°C	1,117°C
$L \rightarrow \gamma + M7C3$ (start) Peak 5	Chromium steel	1,201°C	1,238°C
	Semi-HSS 1	1,168°C	1,165°C
	Semi-HSS 2	1,176°C	1,228°C
	Semi-HSS 3	—	1,115°C
$L \rightarrow \gamma + M6C$ (start) Peak 6	Chromium steel	1,143°C (Solidus at 1,135°C)*	1,052°C
	Semi-HSS 1	1,145°C (Solidus at 1,144°C)*	1,084°C
	Semi-HSS 2	1,150°C (Solidus at 1,147°C)*	1,089°C
	Semi-HSS 3	1,158°C (Solidus at 1,153°C)*	1,117°C

*End of the eutectic reaction from DTA tests

in this alloy, and M_6C precipitated earlier (1,158°C) when compared to the related eutectic transformations on Cr steel, semi-HSS 1 and semi-HSS 2 grades.

• Eutectic M_7C_3 and M_6C carbides have achieved precipitation at higher and more distinguishable temperatures in Cr steel than their equivalents in semi-HSS grades 1 and 2 in the DTA solidification sequence.

From the comparison between equilibrium and non-equilibrium conditions, the following observations are made:

• Liquidus temperature obtained by DTA is always above that which was obtained from TC simulation.
• The first solid to precipitate in the non-equilibrium conditions is not correctly found by TC simulation, as it was the case of the three semi-HSS grades in which delta-ferrite precipitated first, instead of austenite.
• Eutectic carbides found in non-equilibrium conditions appear only in solid-state transformations in the equilibrium conditions; thus, they must be considered as eutectoid carbides.
• The solidification range is always larger in the non-equilibrium conditions than that found in TC simulation, even if the first solid to form is the same in both conditions (see the case of chromium steel).
• Eutectic carbides obtained from the continuous cooling of the melt are still present at room temperature, unlike the corresponding carbides found in the equilibrium conditions, as the latter disappear with solid-state transformation. In fact, M_7C_3 and M_6C transform themselves respectively into $M_{23}C_6$ and M_2C in the TC simulation.

The differences observed between non-equilibrium and equilibrium simulations could be explained in several ways.

Delta ferrite that appears in the semi-HSS grades during non-equilibrium DTA tests could probably arise from inclusions (sulfides or oxides), as they are known to be delta-ferrite germs and they can promote non-heterogeneous nucleation.[9]

While equilibrium conditions assume a full diffusion of all the alloying elements, there is a segregation phenomenon in the non-equilibrium conditions, especially within the interdendritic space where strong carbide-forming elements, such as Nb, Mo, Cr that are gamma-incompatible, are rejected when the growing dendrite is of the austenite type.

Microstructures Through SEM Analysis — Typical microstructures of studied rolls are shown in Figures 7a–d as obtained from a scanning electron microscope (SEM). The microstructure of all rougher grades in the

Figure 7

High-Cr steel (near the surface of the shell): network of eutectic M_7C_3 (fishbone-like, grey) and M_6C (light) carbides at grain boundaries, in a tempered martensitic matrix (7a). Semi-HSS 1 (close to the scrap diameter): network of eutectic M_7C_3 (grey) and M_6C (light) carbides at grain boundaries, in a tempered martensitic matrix (7b). Semi-HSS 2 (close to the scrap diameter): network of eutectic M_7C_3 (bulk, grey) and M_6C (light) at grain boundaries, in a tempered martensitic matrix (7c). Semi-HSS 3 (near the surface of the shell): network of eutectic MC (Chinese script, light) and M_6C (rod-like, light) carbides at grain boundaries, in a tempered martensitic matrix (7d).

Figure 8
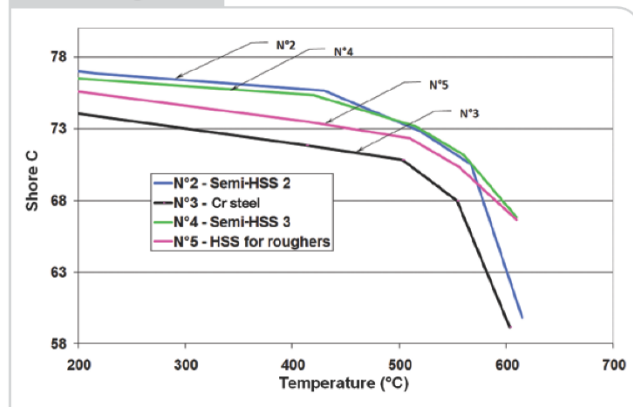
Hot hardness (Shore C) on Semi-HSS grades 2 and 3, Cr steel, and HSS for roughers (as a reference).

service conditions consists of a non-continuous network of eutectic carbides located at grain boundaries, with a tempered martensitic matrix. Such a distribution of carbides is common for HSS grades.[8,10]

Hardness Features — Hot hardness had been determined on three of the four studied grades with regard to HSS for roughers as a reference.

Feature Article

Figure 8 gives the hot hardness behavior of three studied grades and HSS rougher.

Both semi-HSS grades 2 and 3 seem to have similar and flat hot hardness behaviors, except for temperature above 570°C, where hot hardness of semi-HSS grade 3 decreases slowly when that of semi-HSS grade 2 collapses. Such a leveling of the hot hardness above 570°C on semi-HSS 3, which is also observed on HSS for roughers, is probably due to the presence of a higher amount of MC carbides on both compared to semi-HSS grade 2 or Cr steel.

Corrosion Behavior — Some static corrosion tests were performed in a liquid medium on Cr steel and semi-HSS 3 in a laboratory with the following conditions: 60°C; holding time from 4 to 27 hours; [Cl⁻] from 350 to 1,000 ppm and [HOCl⁻] from 0 to 5 ppm. Figure 9 shows the results obtained on the surface of the samples at the end of the corrosion tests. Semi-HSS 3 appears to exhibit a less-corroded surface than Cr steel, as pits found on the previous are smaller than those found on the latter.

Roll Behavior in Service

Layouts of Hot Strip Roughing Mills — In order to obtain a better understanding of the behavior aspects of roughing mill work roll grades, a short description of
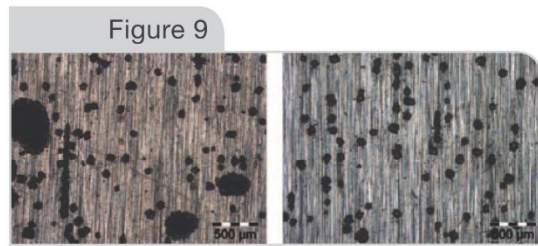
Figure 9

Overview of corrosion pits on Cr steel (left) and semi-HSS 3 (right) surfaces.
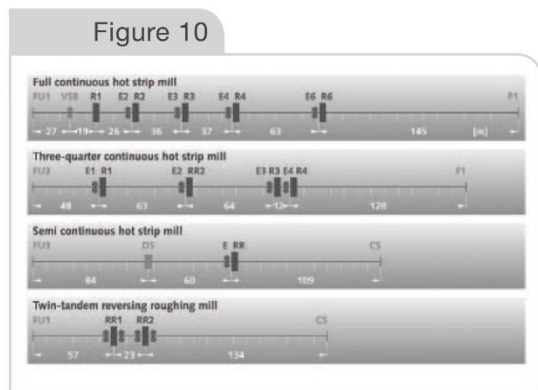
Figure 10

Layouts of hot strip roughing mills.

the different layouts found worldwide will be helpful for the reader (Figure 10).

Many different kinds of roughing mills have been designed over the last 60 years. There are fully continuous HSMs with five to seven roughing stands and additional edgers. This concept was born in the 1960s and was phased out after the first oil crisis of the early 1970s. In this layout, there is only a one-way rolling operation in the roughing mill. The distances between different roughing stands must be adapted to the length of the slab after each stand. Therefore, the whole roughing mill is considerably long.

Another concept is the so-called three-quarter continuous HSM, which includes at least a reversing roughing stand and one or several one-way roughing stands. The length of the roughing mill for this type is quite reduced when compared to the full-continuous mill. The next type, the semi-continuous HSM, includes just one reversing roughing mill combined with a vertical edger or a sizing press. Most of the HSMs built since 2000 are based on this concept. A twin-tandem reversing roughing mill has been realized as well, which combines the advantage of a short roughing mill and a high throughput. On the other hand, this solution asks for a more sophisticated process control. The roughing stands may be built as 2-high or 4-high mills, one-way, reversing, single or tandem configuration.

Situation in European Roughing Mills — A survey made in 25 western European HSMs clearly highlights the dominant position of semi-HSS or HSS roughing mill grades in all types of roughing mills in Europe (Figure 11).

Mill Demands With Respect to Work Roll Properties for Roughing Stands — The interpretation of mill demands, with respect to work roll properties for roughing stands, may be summarized as follows:

• High roll bite based on high friction coefficient, allowing high reductions per pass without chattering or slippage, and consequently higher throughput with reduced heat loss of the product.
• High resistance of shell material against wear, thermal fatigue and oxidation/corrosion, resulting in low and homogeneous wear, allowing longer rolling campaigns and reduced downtime.
• High heat and fire crack resistance, which stands for a smooth, tiny fire crazing network, preventing high damage caused by mill stalls.
• Perfect roll surface quality over long runs, which means no peeling, no banding and no microspalling during one campaign.
• High safety against roll failures generated by any kind of operation conditions, including mill incidents, high thermal and mechanical loads, etc.

The different roll grades used in roughing mills are compared in Table 3 referring to these aspects.

High throughput for the HSM asks for a minimum number of passes in the roughing mill, which is of particular importance for semi-continuous HSMs. This means high reduction per pass, which is possible only

Figure 11
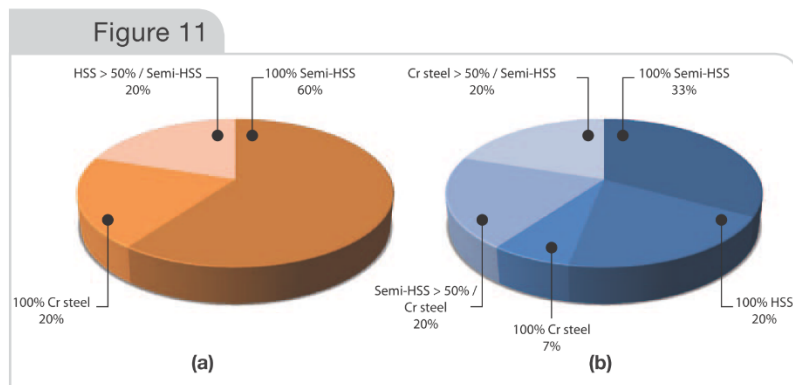
The 2010 situation in five full continuous HSMs in Europe (a); in 20 HSMs ($^1/_2$ – $^3/_4$ or DSP mills) in Europe (b).

with excellent roll biting behavior. It is well known that roll bite is improved with lower carbide content and lower hardness of the working surface. The semi-HSS grade and so far the new HSS grade for roughers have confirmed this basic rule.

Both semi-HSS and HSS for roughers offer improved mechanical properties at elevated temperatures compared to any other roll type so far used in roughing mills. High-temperature yield strength is mainly responsible for how far plastic deformation can be limited in the outer layer of the roll when the surface is heated to more than 600°C when it passes the roll gap in contact with the hot slab. Corresponding thermal compressive stresses are induced. The outstanding thermal resistance of these roll grades results in an extremely fine fire crazing network compared to other grades under similar conditions.

Normally, a low carbide content stands against high wear resistance. In case of the semi-HSS grade, the contradiction between low carbide content and high wear resistance has been eliminated by different factors.

The semi-HSS alloy results in a completely different microstructure containing primary and secondary carbides of MC-, M_6C- and some M_7C_3-compositions. All of these carbides have a higher hardness compared to normal high-chrome iron or high-chrome steel compositions. Even the M_7C_3 carbide, which is a typical chromium carbide, becomes harder whenever it contains alloying elements such as molybdenum and vanadium.

The very favorable roll bite behavior, based on low carbon content, allows for a strongly increased hardness and wear resistance of the homogeneous matrix for low and high temperature levels.

In addition, wear due to high-temperature oxidation is minimized by a matrix composition offering high-temperature corrosion resistance. The full benefit of these characteristics is obtained by a sophisticated heat-treatment process, which stands for a homogeneous distribution of micro-carbides and high temperature resistance. The improved mechanical properties at elevated temperatures and the absence of a closed primary carbide network guarantees a net improvement of shearing resistance and absence of micro-spallings.

The combination of better roll bite and wear resistance offers important advantages to mills. Examples from semi-continuous HSMs have proved that the standard seven-pass reversing operation in the roughing stand could be reduced to a standard five-pass practice. At the same time, the heat loss of the transfer bar is accordingly reduced. If the reversing rougher is the bottleneck of the whole hot mill process, the advantage of better roll bite improves the possible throughput by more than 20% compared to chrome steel work rolls. Pure wear performance of this new roll grade could be improved by 150–300% compared to chrome steel in either reversing or one-way roughing stands.

In many mills, campaign times could be doubled compared to chrome steel work rolls without exceeding the allowable tolerance of roll gap geometry. It has become standard to achieve 50,000–80,000 tons per run for reversing roughing stands and five-pass reductions. A further important behavior of this roll grade is the smooth, symmetric wear curve without any tendency for a dogbone profile. For one-way roughing stands, more than 200,000 tons per campaign could be realized even in the last roughing stand of a full-continuous mill. Regarding the roll cooling practice, no major modifications were necessary to adapt both semi-HSS and HSS work roll grades for normal rolling operation.

As far as semi-HSS is concerned, the semi-HSS 3 is confirmed as the optimum grade based on the investigations developed in this paper, which could be confirmed by numerous laboratory and industrial results.

Table 3

Comparison of Roll Behavior for Different Work Roll Grades in Roughing Stands

Roll grade	Bite	Wear resistance	Fire crack resistance	Surface quality	Campaign time	Safety in service
Chrome steel	4	4	3	4	4	4
Semi-HSS	5	5	5	5	5	4
HSS for roughers	4	5	4	5	5	4

5=Excellent 4=Good 3=Satisfactory 2=Sufficient 1=Poor

Feature Article

Regarding the HSS grade for roughing stands, industrial results in European HSMs with a high percentage of stainless steel rolling have shown that wear performance in terms of campaign time, as well as tonnage per millimeter wear, could be doubled compared to the traditional chrome steel grade. The consistency of roll gap geometry and roll surface quality has fulfilled all requirements. This grade has become a standard grade for stainless and special steels rolling.

Conclusions

Semi-high-speed steel grades for roughing stand work rolls of HSMs have been presented in this paper. Different roll properties of particular interest for mills have been discussed in comparison with other typical roll grades for roughing mills. The combination of equilibrium diagrams and DTA tests could be helpful for the actual solidification sequence prediction in the industrial conditions on working rolls, as the as-cast microstructure strongly influences subsequent mechanical properties.

Simulations of solidification in equilibrium conditions do not seem to be in good agreement with non-equilibrium conditions on the one hand, and with actual industrial conditions on the other hand. Differences between the results obtained from equilibrium and non-equilibrium conditions are probably due to the lack of acknowledgment of segregations in the equilibrium approach, as well as the heterogeneous germination phenomenon that is promoted by inclusions (sulfides promoting delta-ferrite formation, for example).

In addition, comparison of different semi-HSS grades with chromium steel done on roughing stands show that the new semi-HSS grade 3 exhibits better general behavior during the rolling process.

References

1. K.C. Hwang, et al., "Effects of Alloying Elements on Microstructure and Fracture Properties of Cast High-Speed Steel Rolls. Part I: Microstructural Analysis," *Materials Science and Engineering: A,* Vol. 254, 1998, pp. 282–295.

2. A. Molinari, et al., "Primary Carbides in Spincast HSS for Hot Rolls and Their Effect on Oxidation Behavior," *Proceedings of the 6th Tooling Conference,* Sweden, 2002, pp. 437–452.

3. X. Zhang, et al., "The Transformation of Carbides During Austenization and Its Effect on the Wear Resistance of High-Speed Steel Rolls," *Metallurgical and Materials Transactions A,* Vol. 38, March 2007, pp. 499–505.

4. H. Fu, et al., "Investigations on Heat Treatment of a High-Speed Steel Roll," *Journal of Materials Engineering and Performance,* Vol. 17, 2008, pp. 535–542.

5. L.A. Dobrzanski, et al., "Effect of Thermal Treatment on Structure of Newly Developed 47CrMoWVTiCeZr16-26-8 Hot-Work Tool Steel," *Journal of Materials Processing Technology,* Vols. 157–158, 2004, pp. 472–484.

6. F. Martiny, "The Roughing Work Roll for Hot Strip Mills," *Proceedings of Rolls 2000 + Conference,* Birmingham, U.K., March 1999, pp. 269–280.

7. J. Lecomte-Beckers, et al., "Metallurgical Assessment of Two HSS Rolls Grades for Hot Strip Mill," *AISTech Conference Proceedings,* 2007, AIST, Warrendale, Pa., pp. 427–436.

8. J. Lecomte-Beckers and J.T. Tchuindjang, "Structural Investigations of Solidification and Heat Treatment Influence on High-Alloyed Cast Irons Grades With Nb-Ti-V Additions," *Defect and Diffusion Forums,* Vols. 289–292, 2009, pp.77–86.

9. M. Durand-Charre, "La Microstructure des Aciers et des Fontes — Genèse et Interprétation (The Microstructure of Steels and Irons — Genesis and Interpretation)," SIRPE editions, Paris, 2003, pp. 122–124.

10. J.T. Tchuindjang and J. Lecomte-Beckers, "Melting and Crystallization Behavior of Multi-Component Fe-C-Cr-X Alloys: Microstructural Aspects," *Proceedings of the 13th European Microscopy Congress,* Antwerp, Belgium, 2004, pp. 651–652. ✦

Did You Know?

Engineers Week: 19–25 February 2012

Founded by the National Society of Professional Engineers (NSPE) in 1951, Engineers Week, or EWeek, is now organized by the National Engineers Week Foundation. The Foundation, a formal coalition of more than 100 professional societies, major corporations and government agencies, is dedicated to ensuring a diverse and well-educated future engineering workforce by increasing understanding of and interest in engineering and technology careers. Aimed at raising public awareness of engineers' positive contributions to quality of life, EWeek promotes recognition among parents, teachers and students of the importance of a technical education and a high level of math, science and technology literacy, and motivates youth to pursue engineering careers in order to provide a diverse and vigorous engineering workforce. EWeek includes such initiatives as "Introduce a Girl to Engineering Day," the Future City Competition and Discover E/K–12. Each year, EWeek reaches thousands of schools, businesses and community groups across the United States. For more information or to get involved, visit www.eweek.org.

.. **Article #5**

Phase Transformations and Crack Initiation in a High-Chromium Cast Steel Under Hot Compression Tests

Jérôme Tchoufang Tchuindjang, Ingrid Neira Torres, Paulo Flores, Anne Marie Habraken, and Jacqueline Lecomte-Beckers

The mechanical behavior of the fully austenitic matrix of high-chromium cast steel (HCCS) alloy is determined by external compression stress applied at 300 and 700 °C. The microstructure is roughly characterized toward both optical and scanning electron microscopy analyses. Dilatometry is used during heating from room temperature up to austenitization to study the solid-state phase transformations, precipitation, and dissolution reactions. Two various strengthening phenomena (precipitation hardening and stress-induced bainite transformation) and one softening mechanism (dynamic recovery) are highlighted from compression tests. The influence of the temperature and the carbide type on the mechanical behavior of the HCCS material is also enhanced. Cracks observed on grain boundary primary carbides allow establishing a rough damage model. The crack initiation within the HCCS alloy is strongly dependent on the temperature, the externally applied stress, and the matrix strength and composition.

Keywords	dilatometry, electron microscopy, internal damage, mechanical characterization, strengthening mechanism, tool steel

1. Introduction

High-chromium cast steels (HCCSs) are tool steels used in applications where sufficient wear resistance, high hot hardness, good oxidation behavior, and high fracture toughness are sought, these properties being also retained at elevated temperatures (Ref 1-3). A standard application for HCCS is the work roll of the roughing stand in the hot strip mill (HSM). In the case of cast work rolls, the initial chemical composition of the alloy, together with the solidification rate during the casting route, sets the grain size and the nature of the phases occurring in the solidification range, especially primary carbides often located at grain boundaries while forming a more or less continuous network (Ref 4, 5). These primary carbides represent the main parameter influencing the high hardness and the wear resistance of the alloy (Ref 4, 6).

The final properties of the material are promoted by the subsequent heat treatments following the casting route, which allow the formation of a martensitic matrix containing uniformly distributed secondary carbides that yield to enhanced

hardness (Ref 4, 7, 8). Though work rolls for the roughing mill are massive parts weighing up to 40 tons, the heat treatment that follows the casting route must be handled carefully, while considering moderated heating and cooling rates in order to avoid distortions or detrimental residual stresses (Ref 9). In addition, soaking times for both hardening treatment and tempering might be long enough to allow, respectively, sufficient homogenization within the as-cast (AC) microstructure and adequate incubation time for carbide precipitation. The final mechanical properties of the work roll strongly depend on both the casting route and the subsequent thermal treatment (Ref 4-8).

Numerous studies have been undertaken to understand the work roll behavior during hot rolling in order to prevent or to better control both surface and internal damage. These works are related to both experimental and modeling studies, and different damage phenomena are involved, such as banding failure, thermal fatigue, fire cracking, wear, etc. (Ref 10). In addition, residual stress distribution within the work roll in service is also taken into account in order to reach accurate simulations (Ref 11).

Nevertheless, internal damage within the work roll during its fabrication and prior to service has received little attention so far.

Actually, it is still difficult to predict the behavior of such heavy parts, either at the end of the casting route or later during the subsequent heat treatment, due to the complex three-level coupling between the mechanics, metallurgy, and thermal fields. Specifically, there is a need to know the mechanical behavior of every single phase involved in the composition of the studied alloy, such as retained austenite, bainite, or martensite for the HCCS grade. For the existing damage mechanisms, little data are available (Ref 12, 13).

Indeed, specific studies focusing on the hot forging of tool steels are related either to the higher temperature range between 900 and 1100 °C or to the intermediate temperature range slightly below 700 °C. The higher temperature range corresponds to hot forging processes where dynamic recrystalliza-

Jérôme Tchoufang Tchuindjang and **JacquelineLecomte-Beckers**, Division MMS, Department AME, Université de Liège, Liege, Belgium; **Ingrid Neira Torres**, Division MS2F, Department ArGEnCo, Université de Liège, Liege, Belgium and Department of Materials Engineering, Universidad de Concepción, Concepción, Chile; **Paulo Flores**, Department of Mechanical Engineering, Universidad de Concepción, Concepción, Chile; and **Anne Marie Habraken**, Division MS2F, Department ArGEnCo, Université de Liège, Liege, Belgium. Contact e-mails: j.tchuindjang@ulg.ac.be, inneira@udec.cl, pfloresv@udec.cl, anne.Habraken@ulg.ac.be, and jacqueline. Lecomte@ulg.ac.be.

tion, grain refinement, or decreasing primary carbide sizes are expected (Ref 14, 15). For the intermediate temperature range, a thermo-mechanical process also known as ausforming was developed which aims to plastically deform austenite at a constant temperature before its transformation (Ref 16). Such a process allows more or less dynamic recovery phenomenon, and at the same time, it has been reported to be very effective in refining the subsequent bainite/martensite structures which may later improve both strength and toughness (Ref 17, 18). Nevertheless, the two approaches previously quoted do not give the thermo-mechanical behavior of the austenite phase in tool steels. In fact, their main purpose is to achieve forging conditions that allow maximal strains under reduced stresses in order to produce a fine-grained structure at room temperature.

In addition, numerous works have been undertaken related both to the theoretical approach and to the simulation of the work hardening phenomenon in metals with a face-centered cubic (FCC) lattice, such as austenitic stainless steels, austenitic manganese steels, single crystals, and pure metals having low stacking fault energy (SFE). However, many of these studies focus on twinning, a phenomenon responsible for the subsequent enhanced ductility obtained on the material (Ref 19-21). Conversely, very few works have been undertaken on materials with a high SFE, such as HCCS grade material. The HCCS alloy studied in this paper is more like a high SFE material due to the high number of alloying elements, the precipitation inside the grains, and the micro-segregations at the grain boundaries.

The mechanical behavior of ultrahigh carbon steels at elevated temperatures is also investigated for various high strain rates to meet the requirements for developing dip die forging and other thermo-mechanical processing operations involving high deformations (Ref 22, 23). However, these studies deal with high SFE austenitic alloys. They mostly focus on the optimization of material formability through the construction of the deformation mechanism maps and the determination of the maximum ductility. Nevertheless, the main objectives of the above-mentioned works are quite far removed from the enhancement of the strengthening behavior of complex austenite phase with higher SFE, such as the HCCS involved in this work, in the intermediate and especially in the lower temperature ranges.

The current study forms a basis for the subsequent simulation of the thermo-mechanical behavior of the shell material of cast work rolls which contain different types of carbides (Ref 9).

The strengthening behavior of austenite in the studied HCCS alloy combines different hardening and softening phenomena. The current analysis enhances their specific contribution to the overall material behavior. This study chooses both an intermediate temperature and a low temperature for the compression tests performed together with two heating rates that allow obtaining more or less undissolved transition carbides within the matrix.

2. Material and Experimental Methods

2.1 Raw Material and Sampling

The studied alloy is an HCCS grade originating from the shell material of a work roll obtained from a vertical spin casting process and dedicated to the roughing stands of an HSM. The work roll has an outer diameter of 1200 mm and a shell depth of 80 mm. The average chemical composition of the

HCCS alloy as obtained from optical emission spectroscopy is given in Table 1.

Rough cylindrical samples with their axes parallel to that of the work roll are cut out within the first 20 mm over the entire 80-mm depth of the shell material. The samples are located close to the end of the barrel. The sizes of the cylindrical samples range between 5 and 10 mm for the diameter, and between 5 and 25 mm for the length, depending on the final test to be performed (Fig. 1).

The cylindrical specimens are obtained from an electro-discharge machining process. A preliminary metallographic preparation consisting of a hot mounting with epoxy resin followed by grinding and polishing down to 1 μm is performed prior to final super polishing down to 0.06 μm with colloidal silica, which is an active oxide polishing suspension (OPS). Elsewhere, classical nital etching is undertaken on stressed and polished samples in order to better reveal the phases within the matrix and to enhance transformation of parent austenite into hardened phases (bainite, martensite).

2.2 Experimental Methods

Heat treatment is undertaken on cylinders coming from HCCS blocks in the AC conditions, to allow both re-homogenization and hardening in the studied alloy. The so-called HT (heat-treated) samples are generated from this heat treatment as illustrated in the flow chart process given in Fig. 1. HT samples are the starting point for further experimental analyses, such as dilatometry or compression tests.

The compression tests are carried out with a SCHENCK Hydropuls 400 kN machine using a quad elliptical heater 4×2000 W, with a constant strain rate of 3×10^{-3} s^{-1}. Two heating rates are used on the HT samples when reheating them up to 950 °C: a high heating rate of 2 °C s^{-1} (A cycle) and a low heating rate of 1 °C s^{-1} (B cycle). Once the austenitizing temperature is reached, the cooling stage is obtained inside the furnace down to the temperature of the compression test, which is either set at 700 or at 300 °C. For a given heating rate A or B, each compression test is performed twice. In addition, in order to analyze the pure effect of the thermal cycle on the microstructure in the furnace used for compression tests, the thermal cycle B is run on a single additional sample without applying any compression stress.

Microstructure characterization is carried out at different stages of the work using various techniques such as optical microscopy (OM), scanning electron microscopy (SEM), and Vickers hardness measurements.

OM observations are made on an OLYMPUS BX60 microscope coupled with an OLYMPUS UC30 CCD digital camera and equipped with a motorized stage together with the OLYMPUS STREAM Motion® software. OM analyses are performed on longitudinal sections of cylindrical samples originated from AC, HT, and compression test (CT) conditions (Fig. 1).

SEM analyses are performed on a PHILLIPS XL 30 FEG-ESEM equipped with a 129 eV BRUKER energy dispersive x-ray spectrometer (EDS) with a silicon drift detector (SDD), the system being connected to ESPRIT® software for pre- and post-treatment of the data. The SEM allows identification of the matrix phases and carbides greater in size than one micron. Such a technique is not appropriate for thin precipitates as small as some nanometers.

The transmission electron microscopy (TEM) technique, often used for both dislocations and nanoscale precipitate

Table 1 Average chemical composition (weight %) of the HCCS alloy

Alloying elements								
	C	**Si**	**Mn**	**Ni**	**Cr**	**Mo**	**V**	**Fe**
Min	1.0	0.2	0.6	0.5	10.0	3.0	0.1	Base
Max	1.5	1.0	1.0	1.5	14.0	6.0	0.5	
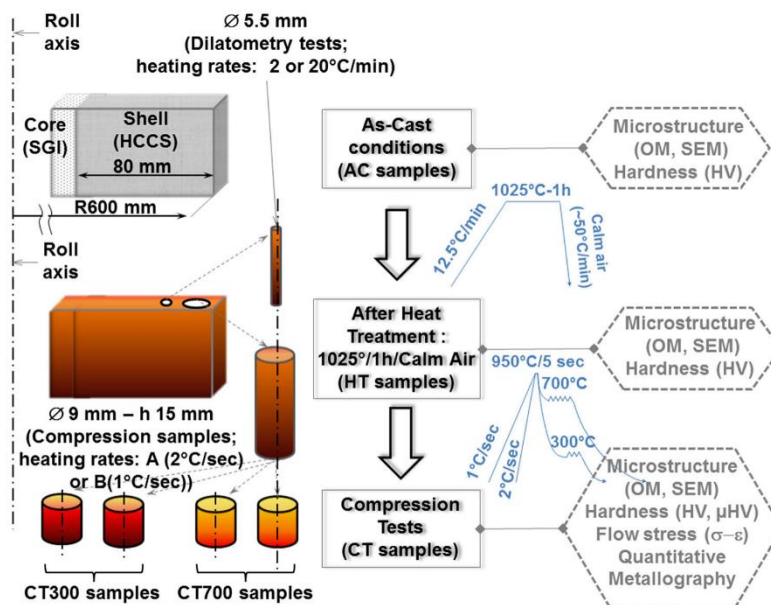
Fig. 1 Flow chart for the sampling and the experimental tests on HCCS alloy

studies, was discarded due to difficulties in preparing thin foil samples. With the available electro polishing device, carbides within the HCCS alloy remain undissolved during the preparation. Instead, dilatometry tests are carried out on HT samples, on a NETZSCH DIL 402C apparatus. Dilatometric tests consist of a reheating stage up to 960 °C prior to cooling down to room temperature. Two constant heating rates of 2 and 20 °C min^{-1} are used, while a single cooling rate of 20 °C min^{-1} is run. The dilatometry technique is used to detect tertiary carbides within the HT HCCS material, and to measure the critical temperatures for their precipitation and their subsequent dissolution. In addition, such a test helps to determine the coefficient of thermal expansion (CTE) of the phases existing in the studied sample.

Hardness measurements are done on a universal EMCO MC10 010 machine with an electronic cell force and closed loop regulation. Both micro-(HV$_1$ for 1 kg load) and macro-(HV$_{30}$ for 30 kg load) Vickers hardness are obtained in order to, respectively, assess the matrix hardness and the bulk hardness. For each sample, the average hardness value is obtained from 3 or 5 indentation points, respectively, for the micro-hardness (inside single grains) and for the macro-hardness (bulk hardness for about twenty grains including carbides located at grain boundaries).

Grain size measurements and primary carbide volume fractions are obtained using image processing software on compressed specimens. Grain size is obtained following the planimetric method (ASTM E112 chart). The carbide volume fraction is assessed while considering all the grain boundary carbides as a whole. The results of carbide quantification may represent the upper limit for their actual volume fraction within the studied samples. The main parameters for the setting of the quantitative metallography (grain size measurements and carbide quantification) are given in Table 2.

Sample designations with the related applied thermal cycle and heating rate are summarized in Table 3. Hereinafter, the following designations AC, HT, CT300, and CT700, will be used, respectively, for the as-cast sample, the heat-treated sample, the sample re-austenitized prior to the compression test at 300 °C, and the sample re-austenitized prior to the compression test at 700 °C. For the compressed samples, an additional letter, A or B that refers to the heating rate, can be used. The sample re-austenitized and cooled down to room temperature without applying any stress will be called the stress-free sample or SF300.

3. Results

In this work, the morphology, the distribution, and the chemical composition of the so-called primary and secondary

Table 2 Samples and setting used for grain size and primary carbide volume fraction assessment toward optical microscopy

Sample designation	Overall section size (mm)	Orientation of the section	Frame resolution (pixels)	Area/frame (mm^2)	Total number of frames	Ratio of the sampled region over the total area (%)
CT300-A CT300-B CT700	Height 5 Width 9	L (// roll axis)	2592 x 1944	5.8	3	12.9

Table 3 Summary of the thermal cycles applied during reheating up to 950 °C, and temperature of the subsequent compression tests performed during the subsequent cooling stage inside the furnace

Temperature for the compression tests	Sample designation	Number of samples	Heating rate achieved up to 950 °C, prior to compression test
300 °C	CT300-A	2	2 °C/s
	CT300-B	2	1 °C/s
Stress-free	SF300-B	1	1 °C/s
700 °C	CT700-A	2	2 °C/s
	CT700-B	2	1 °C/s

carbides are mentioned in section 3.1. In addition, the critical temperatures for both the primary and the secondary carbides are measured according to the specific nomenclature, determined in a previous study (Ref 24), reproduced hereafter:

- Primary carbides are eutectic types composed of Cr-rich M_7C_3 or Mo-rich M_2C that precipitate from the liquid at grain boundaries during the solidification process. They exhibit both lamellar and rod-like morphologies. Their main sizes range between 5 and 50 μm and they form at a single temperature for each, which is above 1100 °C.
- Secondary carbides precipitate around 1050 °C from the supersaturated austenite, in continuous cooling conditions during the casting route and just after the solidification process. These carbides are composed of Cr-rich $M_{23}C_6$ widespread inside grains, which define, at the same time around their cluster, a band strip also known as the "precipitate-free zone" (PFZ) that is close to the grain boundaries. They are mainly globular shaped, with sizes between 1 and 3 μm.

The mechanical results, microstructure characterization, and hardness and quantitative metallography are, respectively, given in sections 3.2, 3.3, and 3.4. Discussions involving various strengthening and softening mechanisms and the internal damage phenomena occurring within the compressed HCCS alloy are addressed in section 4, together with the development of a rough damage model. In particular, two extended studies based on the literature and the current results are proposed. Sections 4.2 and 4.3 provide, respectively, for the bainite transformation and for the carbides, the strengthening mechanism that occurs in the HCCS alloy.

3.1 Solid-State Transformations and Precipitation/Dissolution Reactions from the Dilatometry Study

Microstructures in the AC conditions, and after the re-homogenization and hardening heat treatment, are illustrated in Fig. 2.

The microstructures in both the AC (Fig. 2a) and HT (Fig. 2b) samples are quite similar, with a quasi-continuous network of carbides at grain boundaries and a mixed matrix composed of both fresh martensite (α') and retained austenite (γ). In addition, troostite is only present in the AC samples (Fig. 2a). The heat treatment undertaken on the AC samples allows full dissolution of the troostite phase into austenite prior to the subsequent martensitic transformation during air cooling. The final microstructure obtained on the HT samples exhibits enhanced bulk hardness as it is mainly composed of a martensitic matrix with a small amount of retained austenite (Table 4). Primary and secondary carbides are assumed to remain similar in the AC conditions and after re-homogenizing treatment because the austenitization temperature chosen is below the critical temperature at which the dissolution of secondary carbides begins.

The chemical distribution of elements within both the carbides and the matrix as obtained from the SEM-EDS analysis of the HT samples is illustrated in Fig. 3.

It appears that both primary Cr-rich M_7C_3 and Mo-rich M_2C carbides are mainly large eutectic carbides located at grain boundaries in a quasi-continuous network. These carbides exhibit constant chemical composition for each type. There are intragranular secondary Cr-rich $M_{23}C_6$ carbides that form clusters inside grains, with a chemical composition that changes depending on the carbide location. The Mo content in secondary carbides seems to be higher for precipitates located close to the grain boundaries than those in the center of the grain. In addition, the $M_{23}C_6$ carbide clusters leave around and close to the grain boundaries the so-called PFZs that describe annular strips without visible carbides inside.

Dilatometric curves obtained on the HT samples during the reheating stage up to 960 °C under two constant heating rates of 2 and 20 °C min^{-1} are given in Fig. 4, with the illustration of the CTE related to the phases that are present within the matrix.

Both HT samples exhibit a small expansion well below the Ac_1 point, which corresponds to fresh martensite (α') decomposition that also involves the formation of ferrite (α) and cementite (θ). This phase transformation occurs earlier under a low heating rate compared to the high heating rate. In addition,
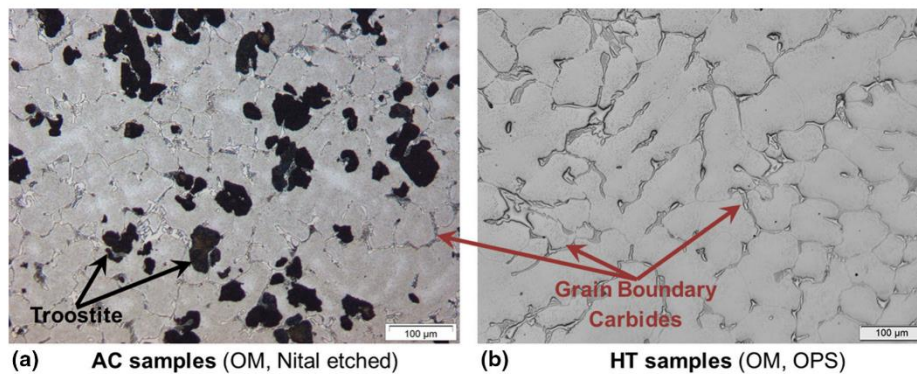
Fig. 2 Microstructure (optical micrographs) of the HCCS alloy in the as-cast conditions (AC samples) and after heat treatment (HT samples)

Table 4 Average Vickers hardness of the HCCS alloy after various thermo-mechanical treatments

Sample designation	Macro-hardness measurements (HV_{30}) in bulk material	Micro-hardness measurements (HV_1) with a single indentation inside each grain	
		Grains with bainite sheaf structure	Grains free of bainite sheaf structure
AC	582 ± 7	…	…
HT	805 ± 9	…	…
CT300-A	622 ± 4	599 ± 22	634 ± 0
CT300-B	664 ± 8	653 ± 4	685 ± 8
CT700-A	652 ± 6	635 ± 2	649 ± 3
CT700-B			
SF300-B	613 ± 10	603 ± 12	640 ± 16

the thermal expansion of the reheated HT samples seems to be higher with the low heating rate. Moreover, Ac_1 and Ac_3 corresponding, respectively, to the start point and to the end point of the austenite transformation are shifted to higher temperatures on increasing the heating rate.

Solid-state transformations with their related critical points, which are clearly identified on the dilatometric curves, may correspond to the following sequence: the α'-fresh martensite decomposition, the γ_0-austenite transformation, and the dissolution of θ-cementite into γ_0 to yield γ_1-austenite well above Ac_3. The later reaction is only observed on the HT sample with the low heating rate. The subscript ($i = 0$ or 1) used for austenite (γ_i) is intended to illustrate the difference within the chemical composition of the related phase. In fact, γ_1 that results from the dissolution of θ into γ_0 is more saturated in C than the parent γ_0 phase that comes from the transformation of α.

The increase in the heating rate seems to delay both the α'-martensite decomposition and the γ_0-austenitization range (Ac_1 and Ac_3), to higher temperatures.

Dilatometric curves exhibit three consecutive steady stages I, II, and III, which are represented by three constant slopes, each stage having a constant CTE that may be related to one or more "stable" phases (Fig. 4). The first stage is related to α'-martensite phase (a small amount of retained austenite can be present), the second to both α-ferrite and θ-cementite, and the third to γ_0-austenite. The first two stages are below the Ac_1

point, while the third is above the Ac_3 point. Any change in the slope of the curve corresponds either to a phase transformation or a precipitation/dissolution reaction. The corresponding CTE of α' ranges between the lowest one subsequently obtained on $\alpha + \theta$, and the highest one achieved on γ_1, at the end of the heating mode (Fig. 4). The decrease in the CTE of the newly formed α-ferrite compared to that of α'-martensite is expected as the tetragonal crystal lattice of the martensite is more saturated in interstitial atoms than the body-centered cubic lattice of the ferrite.

The decomposition of the α'-martensite into α-ferrite and the newly precipitated θ-cementite yields a small expansion in the dilatometric curve, while the allotropic transformation of α-ferrite into γ_0-austenite occurs under significant contraction (Fig. 4).

Moreover, the HT sample reheated under the low heating rate seems to exhibit a CTE slightly higher than that of the sample with a high heating rate, just above the Ac_3 point (Fig. 4). This phenomenon is well enhanced when cooling curves are considered for both samples due to the difference between the initial thermal expansion of the γ-austenite phase during the heating mode, and the corresponding contraction coefficient of the same phase during the subsequent cooling mode. Such a difference only exists for the HT sample with the low heating rate (Fig. 4), and it may correspond to θ-cementite dissolution into γ-austenite. This result is in good agreement with Chae et al. (Ref 25) who found that cementite dissolution
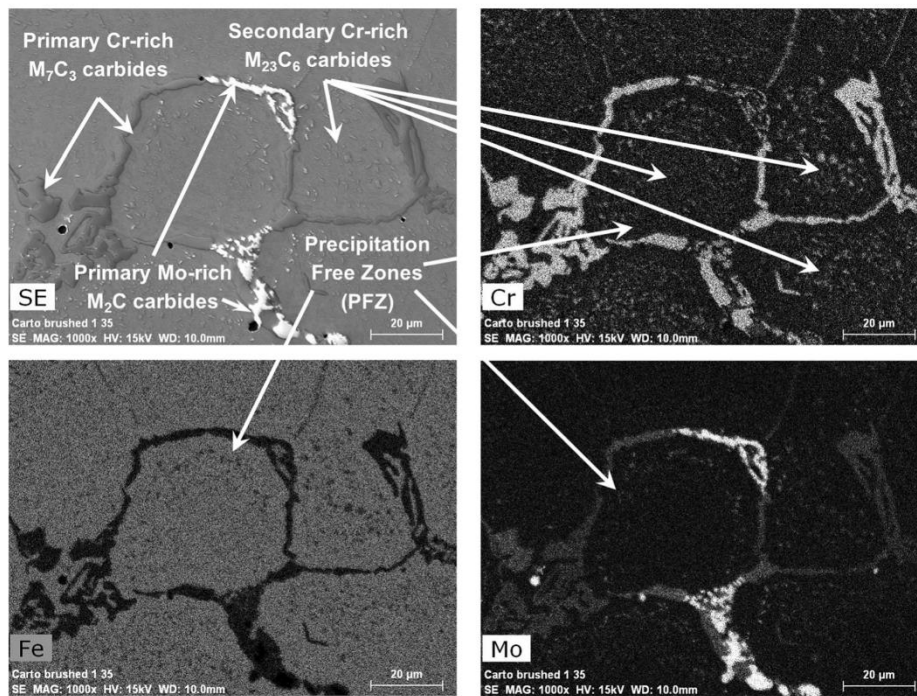
Fig. 3 EDS-map of HT samples enhancing carbide distribution and composition

in the austenite matrix under continuous heating conditions yields non-linear behavior on the dilatometry curve.

Therefore, it can be concluded that the matrix of HT samples at 960 °C is composed of γ_0 + undissolved θ-cementite when the reheating rate is as high as 20 °C min^{-1}. The same samples reheated at 2 °C min^{-1} may exhibit a matrix composed of a singe γ_1 phase, where θ-cementite precipitates are almost fully dissolved.

3.2 Flow Stress Curves and Work Hardening Rates of the HCCS Alloy

The thermal histories measured during the time spent by the samples in the furnace for the CTs are illustrated in Fig. 5(a) below. The related flow stress curves obtained from the CTs (logarithmic strain-true stress) are given in Fig. 5(b).

Flow stress curves show a hardening stage that increases with decreasing compression temperatures. All the samples subjected to the low heating rate of 1 °C s^{-1} prior to the CT, performed either at 700 or at 300 °C, exhibit similar flow stress curves. Therefore, the average between both curves is calculated and is considered hereinafter. In addition, flow stress curves obtained from the CT700-A samples are almost identical to the average of the CT700-B samples. This suggests similar hardening behavior for the batch of samples tested at 700 °C, regardless of the prior reheating rate up to the austenitizing temperature. The four samples tested at 700 °C will be referred to as CT700 hereinafter, irrespective of the heating rate used prior to the CTs.

Conversely, different mechanical behavior is observed between the two samples reheated at 2 °C s^{-1} (CT300-A)

and the two other samples reheated at 1 °C s^{-1} (CT300-B) prior to the CTs performed at 300 °C (Fig. 5b). The CT300-A samples exhibit the higher hardening effect, while maximum elongation has been achieved on the CT300-B samples.

The work hardening rate curves of all the tested samples are illustrated in Fig. 6. The work hardening rate curves present a decreasing trend below 0.02% logarithmic strain, before reaching the same asymptote above this limit. The decreasing trend in the work hardening rate is higher for the CT300-A samples, probably because the maximum strength reached is many times higher than that of the other samples.

3.3 Microstructures After the CTs

The microstructures obtained after the CTs performed at 300 °C are illustrated in Fig. 7 and 8, respectively, for the high (CT300-A) and for the low (CT300-B) heating rates.

The CT300-A samples contain bainite with preferential oriented sheaves, the rest of the matrix being composed of fresh martensite and possibly retained austenite (Fig. 7a). The bainite sheaf structure probably resulted from the compression stress applied to the sample. The crack path observed in the CT300-A samples is composed of single oriented cracks within the grain boundary carbides, these cracks being parallel to the externally applied stress (Fig. 7b). In addition, evidence of the secondary carbide's widespread inside grains is enhanced in the optical micrograph after OPS preparation (Fig. 7c).

The CT300-B samples exhibit bainite with oriented sheaves in their matrix, and either martensite or some retained austenite in addition (Fig. 8a). The crack path in the CT300-B clearly
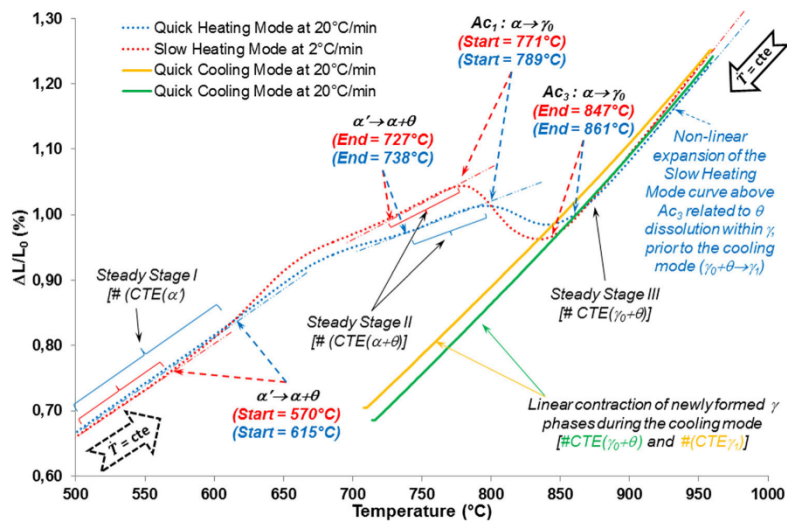
Fig. 4 Enhancement of the effect of heating rate on the phase transformations of HT samples during dilatometry tests
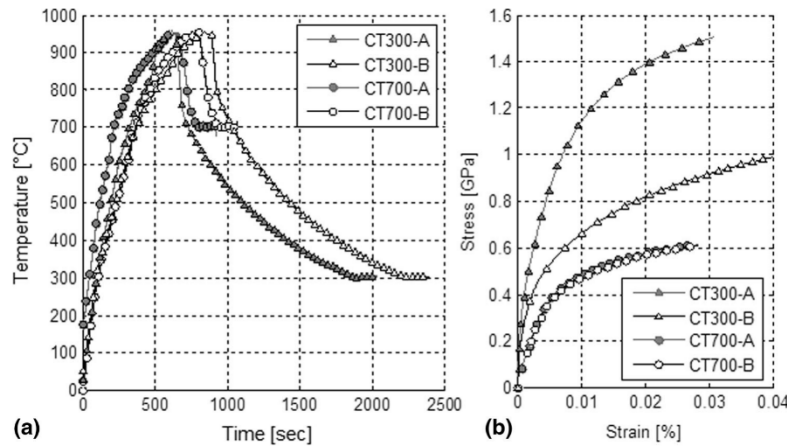

Fig. 5 (a) Thermal histories of the compression samples (b) Flow stress curves obtained after compression test performed during cooling stage either at 700 or at 300 °C

looks more complex and more extended than the previous one observed in CT300-A, due to the branching that occurs within the cracks (Fig. 8b). But the primary cracks remain parallel to the stress direction. Similar to CT300-A, evidence of numerous intragranular secondary carbides is enhanced in the optical micrograph after OPS preparation (Fig. 8c). In addition, the corrosion pits observed on the CT300-B are probably due to the infiltration of the nital etching into the large cracks that exist within the primary carbides (Fig. 8a). PFZs still exist on the CT300 samples (Fig. 7c and 8c).

For the CT700 samples (Fig. 9), very few large oriented bainitic sheaves are observed inside the grains, the rest of the matrix being composed of martensite and retained austenite

(Fig. 9a). This later phase is probably present in an amount higher than that of the previous CT300 samples. Such an assumption can be supported by two observations. First, the apparent volume fraction of the bainitic sheaves in the CT700 samples seems to be lower than that observed within the CT300 samples. Second, the low sensitivity of the etched sample to the nital reagent suggests that the austenite phase which remained un-etched is present in a significant amount.

While all the compressed samples seem to exhibit preferential oriented bainitic sheaves in various amounts and sizes, the stress-free SF300 sample contains large quantities of sheave-like bainite structures with haphazard oriented directions inside the grains (Fig. 10a). In addition, the grain
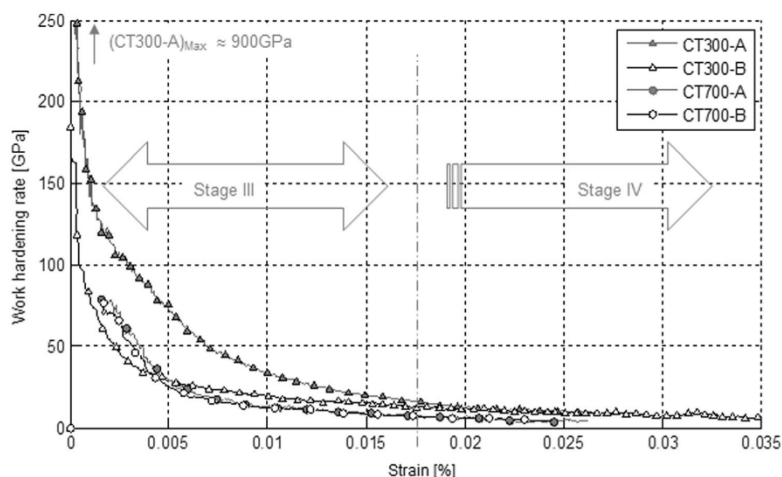
Fig. 6 Work hardening rate curves for HCCS material at 300 and 700 °C

boundary carbides do not exhibit cracks as no external stress was applied. Widespread secondary carbides are present inside the grains with PFZs around them (Fig. 10b), such an observation being similar to the previous ones made on the compressed samples.

3.4 Hardness Measurements, Grain Size, and Carbide Content

Hardness values are given in Table 4 with bulk hardness corresponding to macro-hardness, and micro-hardness corresponding to local hardness inside the grains. Hardness measurements are located in two different zones or grains, the first one containing bainite sheaf structure and the second one being free of bainite. This latter zone probably corresponds to the martensite phase with very low retained austenite. The average macro-hardness ranges between the two extreme values found for micro-hardness inside the grains, except for the CT700 samples where it is close to the higher micro-hardness values obtained.

The maximum macro-hardness is achieved on the HT samples, which contain a higher amount of martensite with a reduced quantity of retained austenite. In addition, no bainitic phase is found in these samples.

The lower bulk hardness value is obtained on the AC samples, probably due to the presence of the softer troostite phase (Fig. 2a).

Among the micro-hardness values, the lowest ones that correspond to 599 HV_1 and 634 HV_1 are obtained for the CT300-A samples, respectively, within grains containing bainitic sheaves and in grains without bainite phase. The CT700 samples exhibit hardness values that are inserted between those of the CT300-A and CT300-B for both macro- and micro-hardness. For the SF300-B sample, the minimum of the micro-hardness (603 HV_1) is observed inside the grains containing bainite sheaf structure, while the maximum of 640 HV_1 is obtained inside the bainite-free grains.

The maximum for the standard deviation has been measured within the CT300-A samples, probably due to very large discrepancies within the progress of the bainite-oriented transformation inside the grains.

The hardness measurements for the compressed samples confirm the strong differences within the HCCS behavior as observed in both the AC and HT samples. Section 4.5 will link these results to the microstructures generated during the heating, cooling, and, finally, the compressed states.

The results of the grain size and carbide content assessments are given in Table 5. Both the grain size and the volume fraction of the primary carbides are similar for all the compressed samples after the CTs.

4. Discussion

4.1 Work Hardening Rate in Compressed Samples

The work hardening rate curves of all the tested samples represent Stage III and Stage IV (Fig. 6) as described by Kalidindi for FCC polycrystals with high SFE, for which plastic deformation proceeds by slip alone, contrary to low SFE FCC metals (plastic deformation by both slip and twinning) (Ref 20). In addition, the first two stages (Stage I and Stage II) predicted by Kocks and Mecking (Ref 21), which are well defined for single crystal materials with low SFE, are reported to be hardly observed for FCC polycrystals with high SFE, which are similar to the HCCS alloy studied in this work.

In polycrystalline metals deforming by slip alone, the strain hardening response primarily comprises a dynamic recovery regime (Stage III) in which the strain hardening rate continuously decreases with increasing flow stress or imposed strain (Ref 20). At high strain rates, Stage III of such alloys may turn into Stage IV which corresponds to the region for low hardening rates where an asymptote for high strain is set (Ref 20, 21).
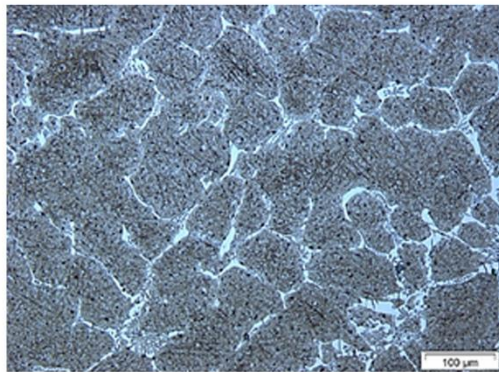
(a) Very few preferential oriented bainite sheaves in the matrix in association with martensite (OM, Nital etched)
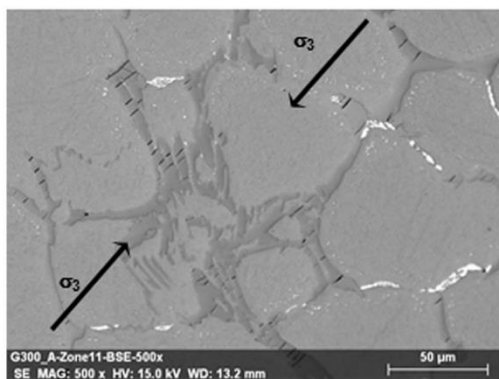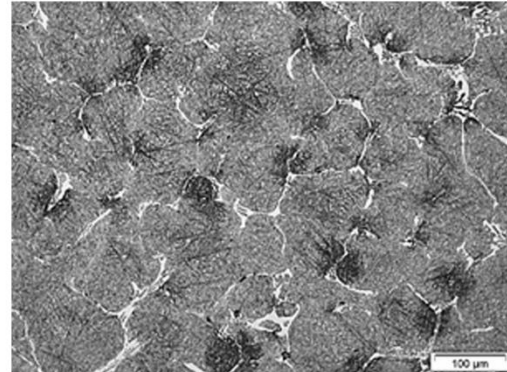

(b) Single orientation for the crack path inside primary carbides, in a direction similar to the external compression stress σ₃ (SEM-BSE, OPS)
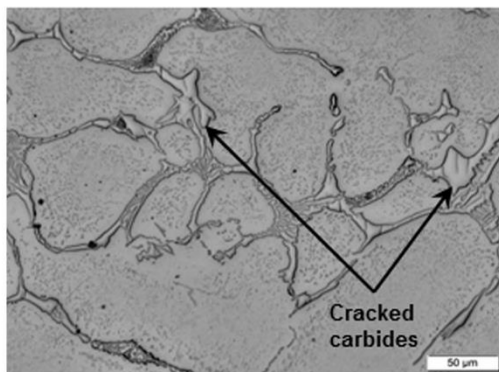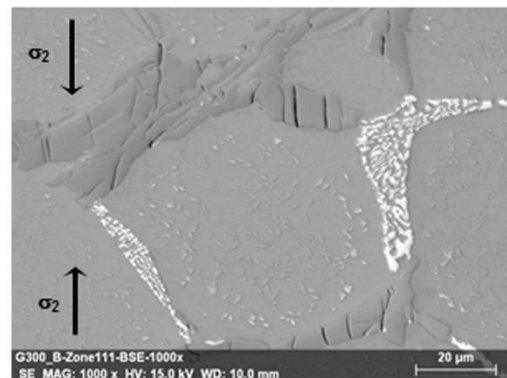

(c) Widespread secondary carbides inside grains, PFZ, and cracked grain boundary primary carbides (OM, OPS)

Fig. 7 Microstructures obtained after compression tests on CT300-A samples

(a) Numerous preferential oriented bainite sheaves in the matrix, and pitting corrosion around primary carbides (OM, Nital etched)

(b) Multiple orientation for the crack path on primary grain boundary carbides, large cracks being parallel to the stress σ₂ (SEM-BSE, OPS)
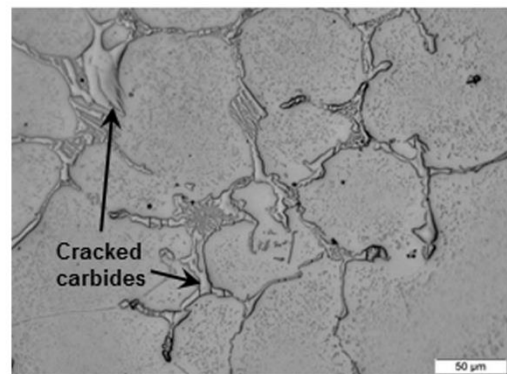
(c) Numerous intragranular secondary carbides, PFZ, and multiple cracked primary carbides at grain boundaries (OM, OPS)

Fig. 8 Microstructures obtained after compression tests on CT300-B samples

(a) Very few preferential oriented bainite sheaves in the matrix in association with martensite and retained austenite (OM, Nital etched)

(b) Cracks initiated on grain boundaries primary carbides parallel to the external applied stress σ_1; intragranular secondary carbides with PFZ around (OM, OPS)
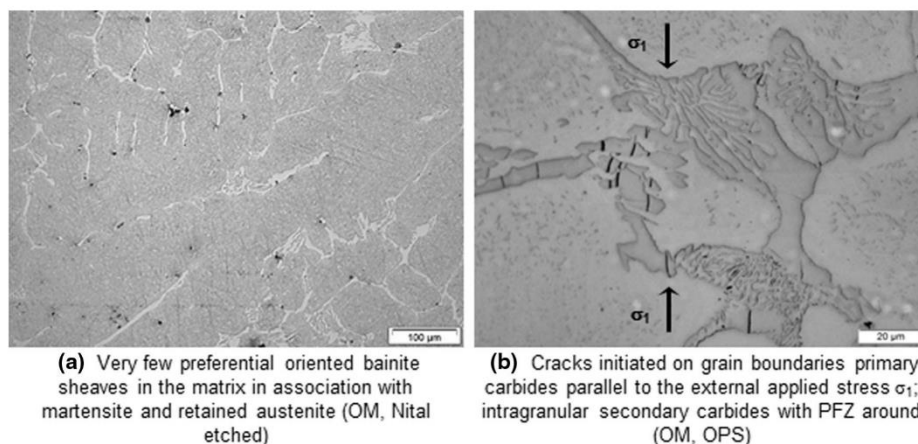
Fig. 9 Microstructures obtained after compression tests on CT700 samples

(a) Numerous bainitic sheaves haphazardly distributed inside grains (OM, Nital etched)

(b) Non-cracked carbides at grain boundaries, intragranular secondary carbides with PFZ around (OM, OPS)
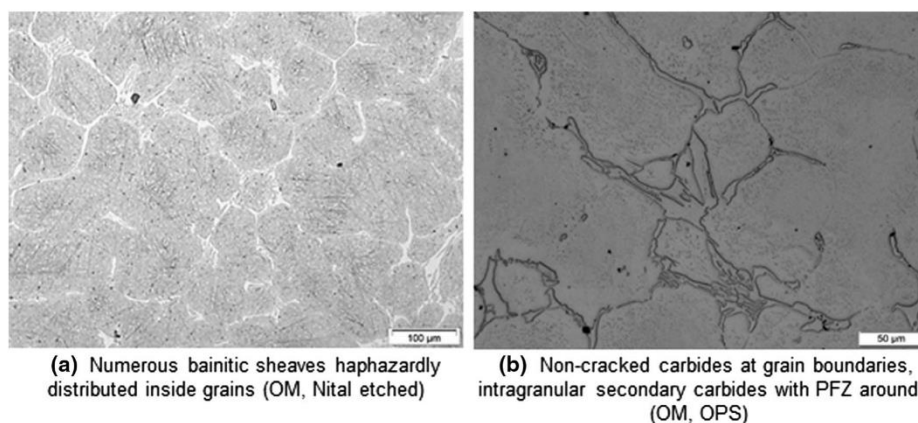
Fig. 10 Microstructures obtained on the stress-free sample (SF300)

Table 5 Grain size and carbide volume fractions obtained on various samples in the longitudinal direction, in different conditions

Sample designation	Grain size (G) according to ASTM E 112	Carbide volume fractions (%)$M_7C_3 + M_2C$
CT700	7.3 ± 0.1	18.6 ± 0.4
CT300-A	7.5 ± 0.1	17.4 ± 1.5
CT300-B	6.6 ± 0.5	19.3 ± 0.7

For the CT300-B samples which have a similar but more expanded Stage III than that of the CT700 samples, both the low heating rate up to the austenitizing temperature and the relatively longer holding time at this temperature promote θ-cementite dissolution into the fully γ_1 austenitic matrix. The composition of the parent γ_0 austenite phase is assumed to be modified at the same time, as all the elements previously contained in θ may enter into the composition of γ_1. Newly dissolved elements such as transition elements (Cr, Mo, and V), or interstitial elements such as C, respectively, act as substitution or insertion elements inside the FCC austenite lattice, which later promote the solution strengthening effect.

In a "sub-saturated" γ_0-austenite containing undissolved tertiary carbides (θ) such as that of the CT300-A samples, the work hardening behavior should be more influenced by the Orowan mechanism that involves dislocation-precipitate inter-
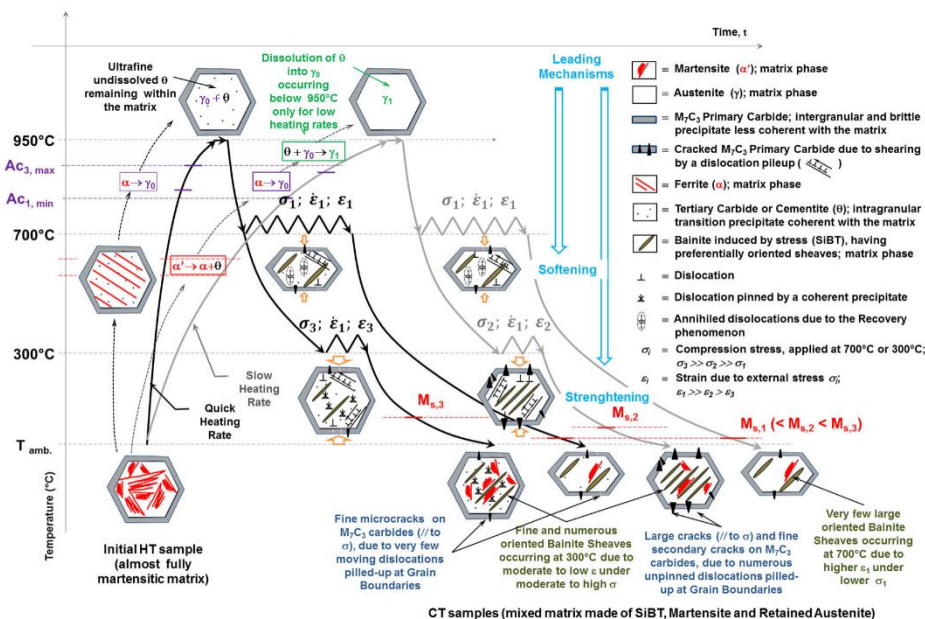
Fig. 11 Sketch of the strengthening and softening mechanisms and the internal damage process (crack initiation on grain boundary primary carbides) occurring on the HCCS alloy at different temperatures

actions in combination with either a phase transformation strengthening mechanism or a softening dynamic recovery phenomenon (Ref 21).

Finally, HCCS behavior at 700 and 300 °C fits the above definitions of Stages III and IV very well, except for the CT300-A samples, which exhibit Stage III well above that of the other samples. This difference can be explained through the microstructure itself (especially fine tertiary carbides, see section 4.3.1), as it is established that the preliminary reheating and cooling sequence prior to the CT can strongly influence the composition of the matrix.

4.2 Kinetics of Stress-Induced Bainite Transformation (SIBT)

4.2.1 Effect of Temperature and Stress on the Initiation of the SIBT. It is known that critical points for phase transformations strongly depend on the chemical composition of the parent austenite that may change the critical phase transformation temperatures. A former study (Ref 26) of a similar grade suggests that the bainitic nose in the continuous cooling transformation (CCT) diagram is far enough to prevent bainitic transformation for the applied cooling rate. However, this assumption is inaccurate according to the current microstructure observations (see section 3.3). In addition, the uniaxial applied stress can increase the start of the bainitic reaction while hindering the transformation of non-favorable oriented grains at the same time (Ref 27, 28).

Optical micrographs of samples that have undergone CTs either at 300 °C (Fig. 7a and 8a) or at 700 °C (Fig. 9a) show typical bainitic sheaves oriented following preferential direc-

tions, contrary to the stress-free samples (Fig. 10a), which exhibit haphazardly distributed sheaves of bainite. At the same time, the microstructure of the samples tested at 700 °C is different from that of the samples tested at 300 °C. In the former sample, bainitic sheaves are thicker but in relatively low quantity with a more limited number of orientations. These results are in good agreement with Hase et al. (Ref 27) who found that stress-assisted transformation results in large blocks of bainite in identical orientation, the sheaves growing under the influence of stress being thicker than those occurring without stress. In addition, the fact that bainitic sheaves look thicker in the CT700 samples than in the CT300 specimens also suggests a "coarsening" phenomenon that occurs on the sheaf-like microstructure due to the higher transformation temperature (Ref 27).

4.2.2 Effect of Temperature and Stress on the Growth of the SIBT (Amount of Retained Austenite). The retained austenite seems to be present in a higher amount in the CT700 samples than in the CT300. The fact that the apparent amount of bainitic sheaves seems to decrease with the increasing temperature of the CTs seems to be consistent with previous works (Ref 29-32), where it is shown that prior strain or prior stress of the parent austenite greatly influences the subsequent phase transformations during the cooling stage, especially the bainitic transformation.

Yang et al. (Ref 29) and Liu et al. (Ref 30) reinforce the fact that the prior deformation of austenite allows its mechanical stabilization in such a way that the subsequent bainitic transformation is significantly delayed, respectively, in isothermal and in continuous cooling conditions.

Jin et al. (Ref 31) found that the isothermal decomposition of deformed austenite into bainite is significantly promoted as

the incubation period is shortened with increasing strain rate. In the same study, it is noted that the start of isothermal bainite formation increases when the parent austenite phase is deformed. Most recently, Gong et al. (Ref 32) have found that the plastic deformation of the austenite phase accelerates the bainite transformation at a low temperature (300 °C, for a medium alloy steel), whereas the effect on the same transformation is reduced at a higher temperature (600 °C). They established that the difference between the two temperatures is ascribed to the dislocation structure introduced in the parent austenite phase, which remains on the active slip planes especially at the lower temperature. These dislocations later assist the bainite transformation under strong variant selection.

Nevertheless, the above findings may not be considered contradictory if additional information is taken into account. Bhadeshia et al. (Ref 27, 28, 33-35) found that the compressive uniaxial stress increases the bainite start temperature, accelerates the transformation rate, and causes microstructural alignment presented by typical sheaves in selected crystallographic variants of bainite preferentially formed on planes of maximum shear stress. In the meantime, the non-favorable directions are hindered by the same external stress because the shape deformation of a bainite plate does not comply with the external stress; therefore, they should remain austenitic.

Retained austenite that is weakly etched by nital reagent seems to be still present in the CT700 samples (Fig. 9a), in an amount which is lower than that of both the CT300-A (Fig. 7a) and CT300-B samples (Fig. 8a). In addition, the typically oriented bainitic sheaves observed in the final microstructure of the CT700 samples are larger than those found in the samples compressed at 300 °C, thus confirming their origin from the stressed material. Note that stress-free deformed austenite grains do not allow variant selections for bainite transformation and yield to haphazardly distributed sheaves of bainite (Ref 36) as observed in the SF300-B sample (Fig. 10a).

4.2.3 Conclusions on SIBT. It seems that the stress applied at both 300 and 700 °C allows bainitic transformation under variant selection. The retained and deformed austenite at 700 °C exhibits a mechanical stabilization that avoids further transformation into bainite, explaining why the volume fraction of bainite formed at 700 °C due to external stress is lower than the amount of bainite formed at 300 °C.

In addition, higher strains are observed on the samples compressed at 300 °C, especially when the specimens were previously submitted to a low reheating rate up to the austenitization temperature. Such large strains lead to a high amount of bainite that is issued both from the conventional phase transformation, which is linked to thermal history, and from the SIBT.

4.3 Carbide Influence on Hardening and Damage Mechanisms at 300 °C

4.3.1 Transition or Tertiary Carbides. It is important to specify why tertiary carbides are called either transition carbides or θ-cementite (M_3C) in the present work.

First, if isothermal conditions such as those achieved during the tempering heat treatment of high alloyed steels are considered, then we are dealing with a moderate heating rate up to a temperature well below Ac_1 with holding times from tens of hours. The long exposure times are needed both to allow an adequate incubation time for the so-called "secondary" carbide precipitation into the tempered martensitic matrix, and

to promote further destabilization of retained austenite during the subsequent cooling (Ref 2, 6-8, 37-39). For long aging times, "secondary carbides" may also undergo transformation into species that are more stable depending on both the temperature and the alloying elements. According to Durand-Charre (Ref 37), the first carbide to precipitate from the martensitic matrix in the range 500-600 C during the tempering of alloy steels is θ-cementite (M_3C), prior to a partial dissolution that allows carbon released and further combination with other elements whose carbides are more stable. The same result was obtained by Shtansky et al. (Ref 38), whose study focuses on the decomposition of fresh martensite just below Ac_1 on an Fe-17Cr-0.5C alloy. In almost all the previous studies, the initial precipitates are often strongly coherent with the matrix, with well-established orientation relationships and with their nuclei being only a few nanometers in size. The coherency with the matrix may be gradually lost with prolonged high temperature exposure due to a possible coarsening phenomenon, especially for carbides with complex crystal structures and low heat for formation (M_7C_3, M_6C, and $M_{23}C_6$). Therefore, θ-cementite (M_3C) precipitating during tempering under isothermal conditions can be considered as nuclei for more stable carbides which appear later within the martensite matrix, at the expense of the primary θ-cementite.

As a second step, if continuous heating conditions up to the completion of the austenite transformation are considered, then phase transformations within the matrix of the HCCS alloy will range between 570 and 860 °C (see the dilatometric curve in Fig. 4). Just below Ac_1 and prior to austenite transformation, the fresh martensitic matrix will decompose into ferrite and θ-cementite (M_3C) (Ref 37, 38). Between the points Ac_1 and Ac_3, the ferrite matrix will be transformed into austenite under an allotropic transformation, while θ-cementite will remain mostly undissolved or untransformed, due to the continuous heating conditions (Ref 25, 38, 39).

As the continuous heating conditions of the HCCS alloy are far away from the equilibrium, the complete transformation of metastable cementite into more stable Cr-rich carbides may occur neither below Ac_1 nor later during the austenite transformation. Therefore, it has been assumed that θ-cementite remains present and untransformed within the matrix either after its nucleation in the fresh martensite, or later when precipitating from the decomposed martensite, below Ac_1.

At the end of austenite transformation, the HCCS alloy is assumed to be composed of a fully austenite matrix containing ultrafine carbides mainly made of undissolved θ-cementite (M_3C), and possible "stable" carbides coming from the decomposition of partially dissolved θ-cementite. Above Ac_3, θ-cementite (M_3C) and other species will undergo dissolution within austenite in a temperature range whose width varies depending both on the chemical composition of the carbides, and on the heating rate. In fact, Cr is known to enhance cementite stability at high temperature, because retained carbide dissolution in austenite is not controlled by high diffusion rates of interstitial carbon, but by low diffusion rates of substitutional elements at the interfaces (Ref 25, 37-39). In addition, high heating rates may promote the so-called cementite remnants, which consist of undissolved particles within the austenite matrix up to 1000 °C (Ref 40).

From the above discussion, tertiary θ-cementite is referred to as transition carbide because it can be transformed into more stable species depending on the reheating route. In addition, θ-cementite (M_3C) that appears from fresh martensite decom-

position prior to austenite transformation is clearly different from the one which precipitated earlier within the tempered martensitic matrix, at a lower temperature. The cementite that precipitated later can remain undissolved within the austenite matrix above point Ac_3, due to both the high heating rates and the enhanced stability by substitutional elements partitioned into cementite.

As a consequence, transition carbides remained ultrafine and coherent with the γ_0-austenite matrix under a high heating rate up to 950 °C (A samples). Conversely, at least the coarsening of these tertiary carbides with a loss of their coherency with the austenite matrix is achieved under low heating rate conditions (B samples). Otherwise, partial to complete dissolution of these carbides might occur to yield supersaturated γ_1-austenite. Such an assumption of the increase of the dissolution temperature of the transition carbides with the heating rate was well established in a previous dilatometric study (Ref 41).

In conclusion, the reason for the higher strengthening effect observed at 300 °C for the CT300-A samples when compared to the CT300-B samples may be related to the presence of undissolved ultrafine and coherent transition carbides in the former samples that should heavily impede dislocation glide under the Orowan mechanism (Ref 21, 24). These undissolved carbides are assumed to be mainly composed of θ-cementite (M_3C) that precipitated first. They are also assumed to be stable due to both the presence of Cr and to the continuous heating conditions that delay transformations into other stable carbides. Similar transition carbides might have been more or less dissolved in the CT300-B samples due to their low reheating rate. Finally, the difference in total elongation between the CT300-A and CT300-B samples is linked to the fact that the grains of the former, which are full of undissolved tertiary carbides, are less deformable than those of the latter.

4.3.2 Secondary Carbides. Secondary carbides present in the HCCS alloy consist of $M_{23}C_6$ carbides that are widespread inside grains while leaving the PFZs away and close to the grain boundaries (Fig. 3, 7c, 8c, 9b, and 10b). These carbides are enriched in Cr but their Mo content increases close to the grain boundaries. The secondary carbides are assumed to enhance the overall hardness of the matrix (Ref 2). In addition, secondary carbides are also assumed to be present in a similar amount in all the compressed samples as they remain undissolved after the reheating stage up to 950 °C prior to compression, regardless of the reheating rate previously used. But contrary to tertiary carbides, the secondary carbides may have little influence on the strengthening effect due to the very few coherency relationships with the newly formed austenite.

4.3.3 Primary Carbides. Primary carbides are made of Cr-rich M_7C_3 carbides and Mo-rich M_2C carbides, which are located at grain boundaries. But only the M_7C_3 carbides, which represent the majority of the grain boundary carbides, contain more or less cracks that are related to the total elongation achieved under the external compression stress applied (Fig. 7b, 8b, 9b). In addition, the maximum elongation under compression at 300 °C seems to be related to the progress of the internal damage, as the CT300-A samples exhibit a total elongation lower than that achieved on the CT300-B samples.

Focusing on the crack path, it is made of primary carbides containing cracks parallel to the external compression stress, which correspond to the beginning of the internal damage process (CT300-A samples, Fig. 7b). With increasing strain, the crack path changes to a more complex oriented one

(CT300-B samples, Fig. 8b). Therefore, it could be assumed that the primary cracks parallel to the external stress correspond to the initiation of the internal failure mechanism, which is in good agreement with Dünckelmeyer et al. (Ref 42). They found that, for similar carbides, primary cracking is always parallel to the loading direction. The crack occurs when the normal stress of the carbide induced by the plastic deformation of the surrounding matrix is exceeded. This can be achieved either from dislocation pileups on the grain boundary carbides (Ref 43, 44), or due to micro-stresses resulting from differences between the thermal and the elastic properties of the matrix on the one hand, and of the eutectic carbides on the other (Ref 45).

In addition, Margolin et al. (Ref 46) in an earlier study that focuses on brittle fracture mechanisms set criteria for crack nucleation in the form of micro-discontinuities within the material under external stress. In most cases, the crack preferentially nucleates on a grain boundary carbide because the strength of such a phase is lower than the strength of the carbide/matrix interface. The micro-crack occurs in a carbide when the local stress at the head of the dislocation pileup exceeds the strength of the carbide, while remaining lower than the more resistant carbide/matrix bound at the same time. The same authors also found that the crack nuclei change from carbide micro-cracking to delamination at the carbide/matrix interface, only if higher stresses are reached for the same loading. Then a pore is formed at the carbide/matrix bound due to the existence of anti-parallel dislocation pileups within the interface, due to the higher local stresses. Moreover, Kroon and Faleskog (Ref 44) in a more recent work on ferritic steels established that the cleavage fracture is often initiated on brittle carbide as a result of a fiber loading mechanism in which the stress levels in the carbides are raised while the surrounding ferrite undergoes plastic deformation.

The other cracks especially observed on the CT300-B samples, which are oriented in directions different from that of the external stress, are probably ascribed to the progress of the internal damage process with the micro-plastic strain evolution, which allows the occurrence of other critical shear directions within the carbides.

In conclusion, the primary grain boundary M_7C_3 carbides serve as preferential crack initiation sites under external compression stress. The cracking of the carbides occurs due to their brittleness as they do not allow plastic deformation contrary to the surrounding matrix.

4.3.4 Conclusions on the Carbide Influence Strengthening Behavior of HCCS Alloy. Undissolved tertiary carbides significantly strengthen the HCCS alloy under compression stress at 300 °C, in such a way that the cracking that was initiated on grain boundary primary carbides is delayed. The secondary carbides probably increase the matrix hardness but have little influence on the strengthening mechanism itself, regardless of the test temperature. Primary carbides promote crack initiation under external stresses.

4.4 Enhancement of the Softening and the Damage Phenomena Occurring Under Compression at 700 °C

For the CT700-A samples subjected to a high heating rate, the assumption of a distinct prior austenite composition can be made together with the occurrence of a higher content of tertiary carbides when compared to CT700-B. At the end of the reheating stage, CT700-A may exhibit a microstructure similar to that of the CT300-A samples subjected to the same thermal

cycle. However, this difference within the prior austenite composition seems to have little influence on the strengthening behavior of the CT700-A samples as their flow curve is similar to that obtained on the CT700-B samples. In fact, all the samples tested at 700 °C exhibit a similar flow curve regardless of the heating rate used to reach the austenitization at 950 °C. Therefore, no strengthening effect can be expected from the presence (CT700-A samples) or the lack (CT700-B samples) of undissolved tertiary carbides within the matrix. Consequently, the leading mechanism occurring in the 700 °C samples during the CTs may correspond to the "softening dynamic recovery" phenomenon, which involves a reduction of dislocation density by mutual annihilation (Ref 47-49). In fact, only a small amount of dislocations may reach the grain boundaries where "brittle" primary carbides are located, prior to their cracking when their strength is exceed by the local stress. Therefore, the carbide micro-cracking observed at 700 °C may be similar to the mechanism which occurs at 300 °C, with narrow cracks for the higher compression temperature and large and branching cracks for the lower compression temperature.

In conclusion, although high plastic deformation occurs within the grains associated with significant total elongation, only a limited shearing phenomenon occurs on grain boundaries, leading to short cracks within primary carbides. The final result is a smaller fracture strain at 700 than at 300 °C.

4.5 Link Between the Hardness and the Microstructure of the Studied Samples

It can be seen that both primary and secondary carbides are present in all the sample batches. Although these carbides are known to enhance hardness, no mention will be made of their possible influence in what follows as it is assumed that they act in the same manner for all the samples.

4.5.1 AC and HT Samples. The minimum and the maximum of the bulk hardness are, respectively, obtained in the AC conditions (AC samples) and in the HT conditions (HT samples). All the other samples exhibit bulk hardness between the previous outer limits (Table 4).

The low hardness achieved in the AC samples is due to the presence of troostite within the matrix, such a phase being softer than bainite and martensite. Conversely, the HT samples that exhibit the maximum bulk hardness contain a matrix almost entirely composed of martensite, the rest being made of retained austenite. In addition, the martensite present in the HT samples is probably supersaturated as all the tertiary carbides have been dissolved during the reheating stage up to 1025 °C, prior to air quenching.

4.5.2 Samples Reheated and Isothermally Compressed During the Cooling Stage. As regards the specimens reheated up to 950 °C before being or not being submitted to an isothermal compression stress during the cooling stage, the CT300-B samples exhibit the highest values for both the bulk hardness and the hardness inside the grains.

For the compressed samples, the above results can be explained as follows. Due to the low reheating rate up to austenitization, tertiary carbides (θ-cementite) are almost dissolved leading to a supersaturated γ_1 matrix that has an austenitic composition with enhanced carbon and alloying element contents (CT300-B and CT700-B samples). Conversely, θ will remain undissolved in the matrix of the samples that have been submitted to a high reheating rate (CT300-A and

CT700-A samples) yielding a lower carbon-saturated γ_0 matrix. During the subsequent cooling, the application of compression stress may promote the bainitic transformation under the development of preferential oriented sheaves within certain grains, either at 700 or at 300 °C. The end of the cooling stage down to room temperature is later achieved following the withdrawal of the compression stress. During the final cooling stage of the pre-stressed samples, the austenitic grains that were not transformed into bainite under stress may undergo a martensitic transformation. But either the rate of the martensitic transformation or the hardness of the newly formed martensite will depend on the chemical composition of the parent austenite phase.

For samples compressed at 300 °C, the supersaturated γ_1-austenite present in the CT300-B samples will lead to a martensite with hardness higher than that of the lower carbon-saturated γ_0-austenite found in the CT300-A samples. In addition, the amount of SIBT previously formed at 300 °C will be higher in the CT300-B than in the CT300-A due to the higher strain achieved in the former specimen. In fact, the lack of tertiary carbides within the austenitic matrix of the CT300-B samples will allow more plastic deformation under stress compared to the CT300-A samples, which still contain undissolved θ that strengthens the material. In all, more bainite is formed in the CT300-B than in the CT300-A samples and also more martensite exists in the former specimens, thus justifying why both the bulk hardness and the hardness inside the grains, with or without bainite, are higher in the CT300-B than in the CT300-A samples.

For the samples compressed at 700 °C, a similar microstructure is obtained in the CT700-A and CT700-B samples, leading to similar hardness values both in the bulk and inside the grains. Very few oriented bainitic sheaves are isothermally formed under stress at 700 °C compared to 300 °C. After the withdrawal of the compression stress, a certain amount of martensite is formed from the parent deformed austenite, this amount being higher in grains free of bainite than in grains that already contain bainite. Nevertheless, the content of the untransformed austenite seems to be higher in the CT700 samples than in the CT300 samples, probably due to the relative stability of the former that arises from the higher plastic deformation which occurs at 700 °C compared to 300 °C. Finally, the hardness values achieved in the CT700 samples, which are between those obtained in the CT300-B and the CT300-A samples, are consistent with the microstructure present in the former samples.

4.5.3 Sample Reheated and Cooled Down Without Stress. For the SF300-B sample, the hardness values in the bulk and inside the grains are lower than those obtained in the CT300-B and CT700-B samples that have been subjected to the same reheating rate. This is because more bainite is formed within the SF300-B sample, this bainite exhibiting sheaves that are haphazardly oriented. Therefore, the bainite present in the SF300-B sample is formed without stress and under continuous cooling conditions, contrary to the SIBT observed in the compressed samples that have been formed isothermally.

In the SF300-B sample, the large amount of bainite that is formed consumes an equivalent proportion of the prior austenite phase, which in turn is no more involved in the subsequent martensitic transformation. Thus, the intrinsic hardening potential of the material, which is the maximum with martensite, is reduced when most of the parent austenite has been previously transformed into bainite.

4.5.4 Conclusions on the Hardness-Microstructure Relationship. Both the amount and the chemical composition of the phases present within the microstructures achieved at room temperature can justify the hardness values obtained following the various thermo-mechanical routes taken for the studied samples.

Higher amounts of martensite within the microstructure lead to higher hardness values both in the bulk and inside the grains. In addition, enhanced carbon content within the martensite, which comes from the supersaturation of the parent austenite phase, will increase the martensite hardness. Conversely, troostite, when present within the microstructure, yields a sharp drop in the hardness. This is due to the fact that troostite is a soft phase, when compared to retained austenite, bainite, or martensite.

4.6 Rough Damage Model for Internal Crack Initiation

Figure 11 shows a sketch of the internal damage mechanism occurring in samples submitted to CTs at 300 and 700 °C. This rough damage model can be described first depending on the temperature, and second depending on the type of austenitic matrix.

When the compression stress is applied at 300 °C on an austenitic matrix containing undissolved tertiary carbides, high work hardening rates can be expected, as these ultrafine and coherent carbides may pin the dislocations while at the same time impeding their glide toward the grain boundaries. Undissolved tertiary carbides strengthen the matrix in such a way that increased compression stresses are necessary to yield sufficient micro-plastic deformation and new dislocation generation within the grains. In addition, the SIBT which occurs will also account for the strengthening phenomenon. When dislocations are not pinned by intragranular carbides, then the dislocation glide may be possible in the direction of the grain boundaries where primary carbides are located. The presence of PFZs close to the grain boundaries may also promote dislocation gliding within these regions. Subsequent pileup of the dislocations on the primary carbides leads to a shearing process which in turn yields sharp micro-cracks as these species are known to be very brittle. The crack initiation within the grain boundary carbides will then follow the direction of the externally applied stress.

When the compression stress is applied at 300 °C on a supersaturated austenitic matrix where tertiary carbides have been dissolved, the matrix is softer and it can undergo significant plastic strain under limited externally applied stress. The increase in the compression stress leads to an increase in the dislocation density within the grains. Due to the weak presence of fine precipitates having high coherency with the matrix, such as undissolved tertiary carbides, most of the newly generated dislocations are free to move toward grain boundaries where they will pileup on primary carbides. The crack initiation process will then occur in the same manner as for the HCCS material containing undissolved tertiary carbides, with sharp micro-cracks parallel to the externally applied stress. Similarly, SIBT may also occur under stress. Nevertheless, the applied stress necessary to initiate cracks within the grain boundary carbides will be many times lower than that of the same material, which contains undissolved tertiary carbides. Moreover, the crack path inside the softer material will quickly change to a more complex and branched one. Such a complex crack path will contain, in addition to the large cracks parallel

to the direction of the external stress, other micro-cracks which are not parallel to the external stress.

For CTs performed at 700 °C, the leading phenomenon is softening dynamic recovery, which is little influenced by intragranular carbides, these precipitates being made either of the ultrafine tertiary coherent carbides or of the coarse secondary carbides. Very little oriented bainitic sheaves are formed at 700 °C, thus confirming the reduced strengthening phenomenon observed at this temperature. In addition, significant plastic deformation occurs under stress at 700 °C, compared to the samples compressed at 300 °C.

The quoted damage model (Fig. 11) mainly corresponds to the internal crack nucleation process on grain boundary primary carbides (M_7C_3) under the influence of tertiary carbides (θ) present or not within the austenite (γ) grains. Conversely, the secondary intragranular carbides ($M_{23}C_6$) hardly influence both the strengthening and the softening behaviors of HCCS, probably due to their low coherency relationships with the matrix. Therefore, these carbides are not illustrated on the rough damage model.

Note that the start of the martensitic transformation during cooling is affected both by the carbon content of the parent austenite and the level of the applied stress, thus explaining the different levels of the martensite start temperatures (M_{S1}, M_{S2}, and M_{S3} points) that are drawn in Fig. 11.

5. Conclusions

HCCS alloy after casting and subsequent hardening treatment is made of a mixed martensite and retained austenite matrix with both Cr-rich M_7C_3 and Mo-rich M_2C primary carbides located at the grain boundaries, and widespread Cr-rich $M_{23}C_6$ secondary carbides inside the grains.

When reheating the HCCS alloy up to austenitization, the tertiary carbides precipitate from the decomposition of the martensite before the beginning of the austenite transformation. These carbides may undergo subsequent dissolution in the newly formed austenite up to 950 °C, especially if low heating rates are used. High heating rates delay the tertiary carbide dissolution within the austenitic matrix.

Tertiary carbides strongly influence the strengthening behavior of the compressed austenite of the HCCS alloy when they remain undissolved. Their influence on the strengthening mechanism is significant at 300 °C where they pin dislocations, but more limited at 700 °C, due to the softening recovery phenomenon occurring within the material.

Secondary intergranular carbides remain undissolved when the HCCS alloy is reheated up to 950 °C. These carbides increase the hardness of the matrix inside the grains, but scarcely affect the strengthening behavior of the HCCS alloy.

Primary carbides that are located at grain boundaries represent the critical feature in damage mechanism initiation. This is particularly the case for M_7C_3 carbides that crack due to the external compression stress.

Compressed austenite, either at 700 or at 300 °C, yields bainite with preferentially oriented sheaves, this transformation accounting also for the strengthening mechanism of the HCCS alloy.

A rough damage model for internal crack initiation is proposed, which takes into account the composition of the parent austenite matrix and the related strengthening and

softening mechanisms occurring under an externally applied stress.

Acknowledgments

References

1. A.M. Bayer, B. Becherer, and T. Vasco, *High-Speed Tool Steels. ASM Handbook Vol. 16 Machining*, ASM International, Materials Park, 1989, p 51–59

2. Z. Zhang, D. Delagnes, and G. Bernhart, Microstructure Evolution of Hot-Work Tool Steels During Tempering and Definition of a Kinetic Law Based on Hardness Measurements, *Mater. Sci. Eng. A*, 2004, **380**(1), p 222–230

3. J. Lecomte-Beckers, M. Sinnaeve, and J. Tchoufang Tchuindjang, New Trends in Hot Strip Mill Roughing Mills: Characterization of High Chromium Steel and Semi-HSS Grades, Assoc. Iron & Steel Technol., Vol. 2, 2012, p 1–8

4. K.C. Hwang, S. Lee, and H.C. Lee, Effects of Alloying Elements on Microstructure and Fracture Properties of Cast High Speed Steel Rolls Part I: Microstructural Analysis, *Mater. Sci. Eng. A*, 1998, **254**(1), p 282–295

5. M. Boccalini and H. Goldstein, Solidification of High Speed Steels, *Inter. Mater. Rev.*, 2001, **46**(2), p 92–115

6. J.W. Park, H.C. Lee, and S. Lee, Composition, Microstructure, Hardness, and Wear Properties of High-Speed Steel Rolls, *Met. Mater. Trans. A*, 1999, **30**(2), p 399–409

7. H. Fu, Y. Qu, J. Xing, X. Zhi, Z. Jiang, M. Li, and Y. Zhang, Investigations on Heat Treatment of a High-Speed Roll, *Jrn. Mat. Eng. Perf.*, 2008, **17**(4), p 535–542

8. S.Z. Qamar, Effect of Heat Treatment on Mechanical Properties of H11 Tool Steel, *Jrn. Ach. Mater. Manuf. Eng.*, 2009, **35**(2), p 115–120

9. I. Neira Torres, G. Gilles, J. Tchoufang Tchuindjang, J. Lecomte-Beckers, M. Sinnaeve, and A.M. Habraken, Study of Residual Stresses in Bimetallic Work Rolls, *Adv. Mat. Res.*, 2014, **996**, p 580–585

10. H. Li, Z. Jiang, K.A. Tieu, and W. Sun, Analysis of Premature Failure of Work Rolls in a Cold Strip Plant, *Wear*, 2007, **263**(7), p 1442–1446

11. K.H. Ziehenberger and M. Windhager, Recent Developments in HSM Rougher Rolls: Risks and Chances, *Iron Steel Technol.*, 2006, **3**(9), p 38–41

12. R. Liang and A.S. Khan, A Critical Review of Experimental Results and Constitutive Models for BCC and FCC Metals Over a Wide Range of Strain Rates and Temperatures, *Int. Jrn. Plast.*, 1999, **15**(9), p 963–980

13. G.Z. Voyiadjis and F.H. Abed, Effect of Dislocation Density Evolution on the Thermomechanical Response of Metals with Different Crystal Structures at Low and High Strain Rates and Temperatures, *Arch. Mech.*, 2005, **57**(4), p 299–343

14. J. Liu, H. Chang, R. Wu, T.Y. Hsu, and X. Ruan, Investigation on Hot Deformation Behavior of AISI, T1 High-speed Steel, *Mater. Char.*, 2000, **45**(3), p 175–186

15. C.A.C. Imbert and H.J. McQueen, Dynamic Recrystallization of A2 and M2 Tool Steels, *Mater. Sci. Eng. A*, 2001, **313**(1), p 104–116

16. I. Tamura, M. Ibaraki, and H. Nozaki, Some Experiments on Ausforming of Tool Steels, *Trans. JIM.*, 1996, **7**(4), p 248–252

17. D. Jandova, L.W. Meyer, B. Masek, Z. Novy, D. Kesner, and P. Motycka, The Influence of Thermo-mechanical Processing on the Microstructure of Steel 20MoCrS4, *Mater. Sci. Eng. A*, 2003, **349**(1), p 36–47

18. T. Shigeta, A. Takada, H. Terasaki, and Y.-I. Komizo, The Effects of Ausforming on Variant Selection of Martensite in Cr-Mo Steel, *Qart. Jrn. Jpn. Weld. Soc.*, 2013, **31**(4), p 178s–182s

19. P.C.J. Gallagher, The Influence of Alloying, Temperature, and Related Effects on the Stacking Fault Energy, *Met. Trans.*, 1970, **1**(9), p 2429–2461

20. S.R. Kalidindi, Modeling The Strain Hardening Response of Low SFE FCC Alloys, *Int. Jrn. Plast.*, 1998, **14**(12), p 1265–1277

21. U.F. Kocks and H. Mecking, Physics and Phenomenology of Strain Hardening: The FCC Case, *Prog. Mater. Sci.*, 2003, **48**(3), p 171–273

22. K. Maruyama, K. Sawada, J. Koike, H. Sato, and K. Yagi, Examination of Deformation Mechanism Maps in 2.25Cr-1Mo Steel by Creep Tests at Strain Rates of 10^{-11} to 10^{-6} s^{-1}, *Mater. Sci. Eng. A*, 1997, **224**(1), p 166–172

23. P.J. Ferreira, J.B. VanderSande, M. AmaralFortes, and A. Kyrolainen, Microstructure Development During High-Velocity Deformation, *Met. Mater. Trans. A*, 2004, **35**(10), p 3091–3101

24. J. Tchoufang Tchuindjang, M. Sinnaeve, and J. Lecomte-Beckers, Influence of High Temperature Heat Treatment on in situ Transformation of Mo-rich Eutectic Carbides in HSS and Semi-HSS Grades, *Abrasion 2011, Conference Proceedings, Liege*, J. Lecomte-Beckers, J. Tchoufang Tchuindjang, Ed., 2011, p 61-75, ISBN 978-2-8052-0124-0

25. J.-Y. Chae, J.-H. Jang, G. Zhang, K.-H. Kim, J.S. Lee, H.K.D.H. Bhadeshia, and D.-W. Suh, Dilatometric Analysis of Cementite Dissolution in Hypereutectoid Steels Containing Cr, *Scripta Mater.*, 2011, **65**(3), p 245–248

26. I. Neira Torres, G. Gilles, J. Tchoufang Tchuindjang, J. Lecomte-Beckers, M. Sinnaeve, and A.M. Habraken, Prediction of Residual Stresses by FE Simulations on Bimetallic Work Rolls During Cooling, *Comp. Meth. Mater. Sci.*, 2013, **13**(2), p 84-91

27. K. Hase, C. Garcia-Mateo, and H.K.D.H. Bhadeshia, Bainite Formation Influenced by Large Stress, *Mater. Sci. Technol.*, 2004, **20**(12), p 1499–1505

28. H.K.D.H. Bhadeshia, Bainite in Steels: Transformations, Microstructures and Properties, 2nd ed., IOM Communication Ltd, London, 2001

29. J.R. Yang, C.Y. Huang, W.H. Hsieh, and C.S. Chiou, Mechanical Stabilization of Austenite Against Bainitic Reaction in Fe-Mn-Si-C Bainitic Steel, *Mater. Trans. JIM*, 1996, **37**(4), p 579–584

30. D.S. Liu, G.D. Wang, X.H. Liu, and G.Z. Cui, Mechanical Stabilization of Deformed Austenite During Continuous Cooling Transformation in a C-Mn-Cr-Ni-Mo Plastic Die Steel, *Acta Met. Sin.*, 2009, **11**(2), p 93–99

31. X.J. Jin, N. Min, K.Y. Zheng, and T.Y. Hsu, The Effect of Austenite Deformation on Bainite Formation in an Alloyed Eutectoid Steel, *Mater. Sci. Eng. A*, 2006, **438**, p 170–172

32. W. Gong, Y. Tomota, Y. Adachi, A.M. Paradowska, J.F. Kelleher, and S.Y. Zhang, Effects of Ausforming Temperature on Bainite Transformation, Microstructure and Variant Selection in Nanobainite Steel, *Acta Mater.*, 2013, **61**(11), p 4142–4154

33. H.K.D.H. Bhadeshia, S.A. David, J.M. Vitek, and R.W. Reed, Stress Induced Transformation to Bainite in Fe-Cr-Mo-C Pressure Vessel Steel, *Mater. Sci. Technol.*, 1991, **7**(8), p 686–698

34. H.K.D.H. Bhadeshia, Effect of Stress & Strain on Formation of Bainite Steels, *Hot Workability of Steels and Light Alloys-Composites, (Montreal, Canada)*, H.J. McQueen, E.V. Konpleva, N.D. Ryan, Ed., Can. Int. Min., 1996, p 543-556

35. S. Kundu, K. Hase, and H.K.D.H. Bhadeshia, Crystallographic Texture of Stress-affected Bainite, *Proc. R. Soc. A*, 2007, **463**(2085), p 2309–2328

36. A.A. Shirzadi, H. Abreu, L. Pocock, D. Klobcar, P.J. Withers, and H.K.D.H. Bhadeshia, Bainite Orientation in Plastically Deformed Austenite, *Int. Jrn. Mater. Res.*, 2009, **100**(1), p 40–45

37. M. Durand-Charre, Microstructure of Steels and Cast Irons, Chap. 11, Springer, New York, 2004, p 219–222, ISBN 3-540-20963-8

38. D.V. Shtansky, K. Nakai, and Y. Ohmori, Decomposition of Martensite by Discontinuous-like Precipitation Reaction in an Fe-17Cr-0.5C Alloy, *Acta Mater.*, 2000, **48**(4), p 969–983

39. G. Miyamoto, H. Usuki, Z.-D. Li, and T. Furuhara, Effects of Mn, Si and Cr Addition on Reverse Transformation at 1073 K from Spheroidized Cementite Structure in Fe-0.6 Mass% C Alloy, *Acta Mater.*, 2010, **58**(13), p 4492–4502

40. K.D. Clarke, C.J. Van Tyne, C.J. Vigil, and R.E. Hackenberg, Induction Hardening 5150 Steel: Effects of Initial Microstructure and Heating Rate, *Jrn. Mater. Eng. Perf.*, 2011, **20**(2), p 161–168

41. S.-J. Lee and K.D. Clarke, A Conversional Model for Austenite Formation in Hypereutectoid Steels, *Met. Mater. Trans. A*, 2010, **41**(12), p 3027–3031

42. M. Dünckelmeyer, C. Krempaszky, E. Werner, G. Hein, and K. Schörkhuber, On the Causes of Banding Failure, *Proc. of METEC InSteelCon 2011*, STEELSIM, 2011, p 1–9

43. P.W. Shelton and A.S. Wronski, Cracking in M2 High Speed Steel, *Mater. Sci. Technol.*, 1983, **17**(11), p 533–540

44. M. Kroon and J. Faleskog, Micromechanics of Cleavage Fracture Initiation in Ferritic Steels by Carbide Cracking, *Jrn. Mech. Phys. Sol.*, 2005, **53**(1), p 171–196

45. C.R.S. da Silva and M. Boccalini, Thermal Cracking of Multicomponent White Cast Iron, *Mater. Sci. Technol.*, 2005, **21**(5), p 565–573

46. B.Z. Margolin, V.A. Shvetsova, and A. Ya, Varovin, Preliminary Compression of a Material as a Factor in Changing the Brittle Fracture Mechanism for BCC Metals, *Str. Mater.*, 1996, **28**(4), p 251–261

47. V. Vodopivec, Dynamic Recovery of Austenite in Low Carbon Steels and its Relationship to the Precipitation of AlN, *Jrn. Mater. Sci.*, 1975, **10**(6), p 1082–1084

48. E. Nes, Recovery Revisited, *Acta Mater.*, 1995, **43**(6), p 2189–2207

49. L. Kubin, T. Hoc, and B. Devincre, Dynamic Recovery and its Orientation Dependence in Face-centered Cubic Crystals, *Acta Mater.*, 2009, **57**(8), p 2567–2575

..   Article #6

Laser cladding as repair technology for Ti–6Al–4V alloy: Influence of building strategy on microstructure and hardness

CrossMark

H. Paydas [a,*], A. Mertens [a], R. Carrus [b], J. Lecomte-Beckers [a], J. Tchoufang Tchuindjang [a]

[a] *University of Liege (ULg), Faculty of Applied Science, Department of Aerospace and Mechanics, Metallic Materials Science Unit, Chemin des Chevreuils, 1 B52/3, B 4000 Liège, Belgium*
[b] *Sirris Research Centre (Liège), Rue Bois St-Jean, 12, B 4102 Seraing, Belgium*

ABSTRACT

Laser cladding is a metal deposition technique used to fabricate or repair components made from high value metallic alloys. In the present work Ti–6Al–4V deposits with variable thickness are made to assess the use of laser cladding as a repair technology. Both the effect of the building strategy (BS) and the incident energy (IE) on the metallurgical characteristics of the deposits in relation to their complex thermal history have been studying. It is shown that for the configuration consisting in a decreasing track length (DTL) under high IE, a gradient of cooling rate exists that leads to the presence of different phases within the microstructure. Conversely homogeneous microstructures are present either for the configuration with a constant track length (CTL) under high IE, and for the strategy obtained from a DTL under low IE. Depending on the possible heat accumulation the nature of the phases are determined together with hardness maps within the deposits. Some qualification criteria are set prior to tensile tests to selected adequate candidate-deposit that does not weaken the cladded material when it is stressed. A thermo-metallurgical scheme is proposed that helps in understanding the effect of both the BS and the IE on the microstructure.

© 2015 Elsevier Ltd. All rights reserved.

1. Introduction

Laser cladding is an economic layer-by-layer near-net-shape process for the production of three-dimensional complex parts [1]. It also appears as a very interesting solution for the low-cost repair of damaged high-value components [2] and for coatings with improved surface properties [3,4]. In this technique, a metallic powder is projected through a nozzle onto a substrate and simultaneously melted with a laser to form a single track. With the movement of the laser or substrate, partial coverage tracks are made side by side to form a layer of dense material. By superposing layers, a 3D part is fabricated. The movement of the laser or substrate is guided by a CAD system that splits the 3D object into sets of tracks. The material studied in this work is titanium alloy Ti–6Al–4V, which is widely used in the aeronautic industry and laser metal deposition is used as a repair technology.

The thermo-metallurgical phenomena induced during deposition by laser cladding are complex. Solidification following melting and partial remelting of pre-existing layers is coupled with heat treatment of the

solidified material due to the repeated heating and cooling cycles during building [5,6]. As is well known, laser additive manufacturing (LAM) technologies induce very fast cooling during solidification, due to the high thermal gradient existing between the superheated melt pool and the cold substrate [7]. The solidification mode of Ti–6Al–4V, as well as the resulting grain morphology, is controlled mainly by thermal conditions that exist locally at the beginning of the solidification, while the fine-scale microstructure is controlled primarily by the post-solidification cooling rate [8]. Indeed, Ti–6Al–4V solidifies first in a β (BCC) structure that is susceptible to transformation into a Widmanstätten or martensitic structure upon further cooling [9]. The grain morphology of laser fabricated Ti–6Al–4V differs substantially from conventional metal-mold-casted Ti–6Al–4V due to the rapid solidification and the phenomenon of epitaxial growth, which leads to the formation of a columnar structure [8]. As a result, the deformation behavior depends strongly on the solicitation direction compared to the orientation of the columnar grain structure [10].

Many variables in LAM such as incident energy (power/scan speed), geometry of part (thickness, location), and scanning strategy can affect the post-solidification cooling rate and the microstructure of the resulting part, with the latter playing an essential role in controlling the mechanical properties. Numerous works have thus been carried out to establish the relationship between process parameters and the structure of deposits. However, these investigations often focused on the influence of the laser power [8,11] and of the scanning parameters [8,11,12] on the microstructure of deposits with a simple geometry (i.e. a constant thickness). There are only few studies related to the

use of laser metal deposition (LMD) as a repair technology, especially concerning Ti–6Al–4V. Graf et al. [2] investigated the feasibility of LMD for re-filling milled grooves of different shapes to repair parts made from stainless steel or titanium alloys, but the influence of the building strategy on the microstructure was not addressed. In fact, Ravi et al. [1] showed that the deposition strategy in relation with the thermal history strongly influence both the microstructure and the ductility of stainless steels alloys. Therefore it is worth enhancing the building strategy effect during laser cladding repair of Ti–6Al–4V alloys.

The microstructure in the deposit under as-built conditions may be different from the one that is present in the base material, which corresponds to a commercial Ti–6Al–4V alloy with its microstructure made of duplex α–β. Such a microstructure is usually obtained from a thermomechanical process (hot forging + annealing) which is carried out at a temperature high enough to allow dynamic recrystallization within the plastically deformed grains [13].

Nevertheless the repairing approach remains of concern if the main purpose is to restore or to extend the use of the repaired work piece until its normal lifetime, after the earlier break-up or the damage of one or more elements within the whole part. Repair and overhaul are inevitable choices as the replacement is far more expensive. In fact, laser processing as a near-net-shape technique may help producing component with a geometry that is close to the final dimensions, prior to possible subsequent heat treatment and machining processes that may allow fitting the sizes of the finished part.

In addition, although the actual microstructure of the base material is difficult to obtain from laser processing, it may be worthwhile to achieve from the repair process a microstructure in the deposit that is close to the original one in terms of metallurgical features and mechanical properties.

Therefore, the aforementioned issues lead to the definition of the two main objectives of the present work which are the assessment of laser cladding as a repair technology for Ti–6Al–4V on the one hand, and the mechanical qualification of the cladded material (deposit + base material) on the other hand. The first objective is achieved while studying the influence of BS and IE on the microstructure of the deposit. The second objective is reached towards the setting of criteria that allow selecting the adequate deposit in the as-built conditions before submitting the whole substrate + deposit composite material to tensile tests which ensure that the deposit itself is not the weakening part. In addition, a simplified thermo-metallurgical scheme is proposed that establishes a relationship between the processing parameters, the complex thermal history and the microstructure of the deposits.

2. Experimental methods

2.1. Processing

Ti–6Al–4V plasma-atomized powder with a chemical composition of 6.3 wt.% Al, 4.1 wt.% V, 0.09 wt.% O, 0.06 wt.% Fe, 0.0036 wt.% H, 0.01 wt.% C, and 0.01 wt.% N and a particle size range of 45–78 µm was used in this study.

Samples were produced using a 5-axis Irepa Laser cladding system. In order to enhance the flexibility of the laser cladding process, two different Nd-YAG laser sources were used with a maximum power of 2000 W and 300 W, respectively. The laser spot has a top-hat energy distribution with a diameter of 1400 µm for the higher power and 36 µm for the lower one. These two lasers were used separately for re-filling Ti–6Al–4V deposit on pre-machined substrate to simulate repair. Plates with sizes of $100 \times 20 \times 15$ mm, taken from Ti–6Al–4V standard roll bar, were used as substrate. A cup was machined in the plates to house the deposit, as shown in Fig. 1. With this geometry of substrate, it is possible to make a deposit with thickness varying (according to the Z axis) from 0 (extremity) to ≈ 5 mm (in the center). The microstructure of the substrate (base metal) is constituted of intergranular β dispersed in a dominating granular α matrix.

Building was carried out while using a hand-made protection cap filled which argon to avoid contamination of the melt pool by interstitial elements such as oxygen or nitrogen. The oxygen concentration within the protective atmosphere was below 10 ppm. The Ti–6Al–4V powder was dried before use in order to minimize indoor moisture during laser processing. The thick deposits were obtained by superimposing several layers following the OZ directions (Fig. 1), two consecutives layers being disposed staggered with an offset of 1/2ΔY (Table 1). Each layer was obtained from overlapping tracks that fit the same semi-circular shape as the one of the initial machined cup. The tracks were made by following a back and forth movement. The scanning parameters were selected in order to achieve fully dense deposits, the overlapping between adjacent tracks being set as 30% (Table 1). The substrate was kept in a fixed position, while the laser source was moving according to the three XYZ axes.

Three different configurations were defined that correspond to samples 1 to 3. Samples 1 and 2 were produced with the same high incident energy (HIE) while using the 2000 W laser source but two different building strategies (BS) were used corresponding respectively to the decreasing track length (DTL) and to the constant track length (CTL), (Table 1). Sample 3 was produced with a low incident energy (LIE) while using the 300 W laser source and a decreasing track length (DTL) with the aim of producing thinner tracks that allow a better dimensional accuracy. Such an approach was achieved at the expense of time (Table 1). The missing 4th configuration corresponding to LIE and CTL was discarded due to the assumption that no significant difference within the microstructure and the hardness can be expected compared to the configuration with LIE and DTL. The track length for each layer decreases continuously with building height for both samples 1 and 3 and it is kept constant for sample 2.

The table 1 below summarizes the parameters used for each of the three configurations. In what follows, designations sample i and deposit i will be respectively used for the substrate + the deposit of the configuration n°i, and the deposit n°i.

2.2. Metallographic characterization

Samples were machined by spark erosion, embedded in phenolic resin and then polished to a mirror finish. Analyses were performed on three sections following the three main directions in the as-polished condition to assess the metallurgical health within the deposit and in the bonding zone, and after etching with Kroll's reagent to reveal the details of the microstructure. Three complementary methods were used in order to study the microstructure: Optical Microscopy (OM), Stereo Microscopy (SM), and Scanning Electron Microscopy (SEM).

Vickers bulk hardness measurements (HV10) were carried out using a universal hardness device equipped with an electronic cell force. Measurements were carried out following a grid on the three sections (as-etched state) to locally characterize the deposit, the base metal and when possible the heat affected zone (HAZ). A distance of 1 mm was set between test points (horizontally and vertically) to avoid interactions between adjacent indentations and thus to determine the hardness field resulting from the complex thermal history. For a clearer graphic representation of the results, fictive intermediate points between the actual hardness points were generated in MATLAB using a "triangle-based cubic interpolation" in order to draw a map of iso-hardness contours.

2.3. Thermal measurements

Temperature measurements were made during the building of deposits 1 and 2 by means of a "type K" thermocouple (accuracy ± 1.5 °C). Temperature has been recorded on a permanent basis both inside the substrate (2 mm below the base of the cup in both the mid-length and the mid-width) and in the atmosphere within the protection
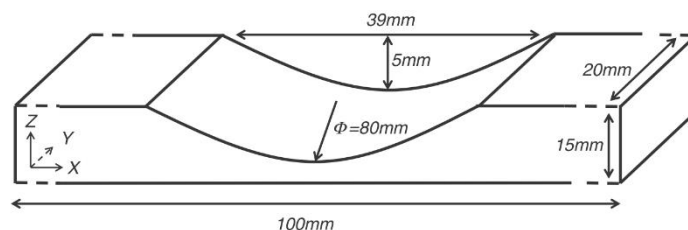
Fig. 1. Geometry of the substrate machined for laser cladding deposition.

cap (70 mm above the surface of the sample and 30 mm below the top of the cap, in an eccentric position).

In sample 3, the temperature evolution during building was recorded with an infrared thermal camera of type "VarioCAM® hr head 640" (accuracy 1%). The thermal image camera allows obtaining a relative evolution of the temperature that is different from the actual absolute values because no calibration was done. The calibration of a thermal camera requires knowledge of the emissivity coefficients that can change depending on surface finish (roughness, oxidation, etc.) as reported by Qian et al. [7]. Nevertheless such a thermal video recording may allow identifying the heat sources during the laser processing.

2.4. Tensile properties assessment

Standard dog-bone specimens were extracted from the as-built deposits (without stress relief) in order to assess the rough mechanical behavior, and especially to determine the fractured zone of the cladded material (Fig. 2). Tensile tests were carried out at room temperature according to standard NBN EN ISO 6892–1 (2009) using a ZWICK universal testing machine with a maximum load of 100 kN, at an initial strain rate of 0.00325 mm/s. Strains were measured with two different extensometers (ISO 9513). One extensometer with a gauge length of 65 mm was used to record the deformation in both the deposit and the substrate. Another extensometer with a reduced gauge length of 30 mm was used to record the deformation in the deposit. Each set of data reported was averaged from three samples.

Two main criteria were established in order to select the more appropriate configuration of the deposit to be used for subsequent tensile tests. The first criterion (C1) laid on the homogeneity of both the microstructure and the hardness within the deposit and the second one (C2) laid on the maximum ductility reserve (availability) for the microstructure present in the deposit. In addition, a third criterion (C3) based on the similarity of the deposit microstructure with that of the base material was also defined.

3. Results and discussions

3.1. Metallurgical health within the deposits

For all the samples obtained with the three configurations, no apparent defects between the substrate and the first layer of the deposit were observed indicating a sound metallurgical junction. However, very few gas porosities randomly distributed in the microstructure were observed in the volume of the deposit (Fig. 3) with a globular shape and

a diameter of $\approx 20\,\mu m$. The average area fraction of these porosities remains small and is well below 0.1%, which is considered acceptable [14]. These gas porosities are caused by entrapment of gas from the powder feed system [15].

3.2. Influence of BS and IE on the microstructure and the hardness of the deposits

3.2.1. Deposit 1 obtained with high incident energy (HIE) and a decreasing track length (DTL)

3.2.1.1. Macrostructure within sample 1. The macrostructure of the deposit 1 exhibits a columnar structure with primary β grains that are elongated and oriented more or less normal to the surface of the substrate as illustrated in Fig. 4a–b, d. Some of these grains extend over the whole thickness of the deposit. The development of an anisotropic coarse columnar primary β grains structure is a characteristic feature of additive manufacturing of titanium alloys [5,8,12,16]. These columnar grains grow epitaxially through multiple layers, producing textures aligned normal to the layers. Moreover, it can be noted that the grains present on the edges of deposit 1 (Fig. 4b) are not aligned following the normal to the substrate but are slightly tilted. This is because, near the edge, the heat is not evacuated only through the substrate but is also dissipated by convection and radiation through the walls of the deposit.

3.2.1.2. Microstructure within the heat affected zones of sample 1. Two types of HAZs were observed at different locations in the samples due to the different heating/cooling cycles experienced during building of the multiple layers, the first one (hereinafter referred to as HAZ1-1) being located at the substrate/deposit bonding or junction, and the second ones (hereinafter referred to as HAZ1-2) being present at various locations within the deposit.

As regards the HAZ1-1 located at the substrate/deposit junction, it can be said that during building of the first layer, a part of the substrate in contact with the melt pool was remelted. This is shown by the fact that the base of the columnar grains is located inside the substrate below the bottom of the initial cup (Fig. 4b). This dilution phenomenon is well marked, with an average dilution depth of $\approx 450\,\mu m$ (measured in the Z–Y plane, Fig. 4b). Below the dilution zone, a heat affected zone exists in the substrate with an average thickness of $\approx 1100\,\mu m$ as measured in the front section (Fig. 5). Moreover, this HAZ can be decomposed into two different subareas. The bottom area exhibits a very fine microstructure, while the top area is coarser. This observation is similar to a previous report by

Table 1
Details of the laser cladding processing parameters for the three configurations.

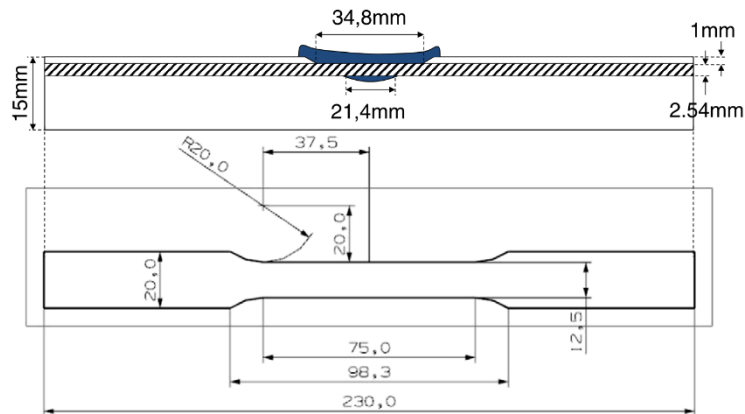|	Laser power [W]	Scan speed [mm/min]	Incident energy [W.min/mm]	Powder rate [mg/s]	ΔZ, ΔY increment [μm]	Number of layers	Number of passes by layer	Building strategy	Total building time [min]
Sample 1	1100	400	2.75	28	520, 2100	10	7	DTL	≈5.4
Sample 2	1100	400	2.75	28	520, 2100	10	7	CTL	≈8.1
Sample 3	210	600	0.33	5.14	170, 500	30	37	DTL	≈40

Fig. 2. Sampling zone within the cladded bar (top image) and sizes of the dog-bone specimen for tensile tests (bottom image).

Brandl et al. [17], who studied the microstructural features of Ti–6Al–4V single-weld laser wire deposition. They reported that the parts of the substrate heated to a subtransus temperature (T < T$_{\beta\text{-transus}}$) and to supertransus temperature (T > T$_{\beta\text{-transus}}$) correspond to two different HAZs: HAZ$_{\alpha\,+\,\beta}$, in which primary α grains may limit grain growth, and HAZ$_\beta$, which is more prone to grain coarsening. In the current case, the presence of these two types of HAZs (HAZ$_{\alpha\,+\,\beta}$ and HAZ$_\beta$) (Fig. 5) can be ascribed to the high heat input, which leads to a deep HAZ in the substrate.

Regarding the HAZ1-2 located almost everywhere within the deposit 1, it can be said that thermal phenomena similar to those observed in the junction (i.e. dilution and HAZs) occur during deposition of successive tracks. Indeed, the top of the pre-existing layer in contact with the melt pool from the new track was remelted and resolidified. At the same time, the solid part of the track located just below the remelted zone underwent a reheating due to the supply of heat during deposition of the subsequent layer. As a consequence, local microstructural modifications can occur depending on the temperature reached in the pre-existing layers, the thermal excursion time, and the cooling rate from this temperature. These phenomena are the origin of the presence of thermally affected zones in the deposit that are manifested by the presence of macroscopic bands. Kelly and Kampe [5,6] studied these bands in details in Ti–6Al–4V laser-deposited multilayers. They mentioned that the most probable origin of these bands is related to thermal cyclic effects incurred during the multiple passes.
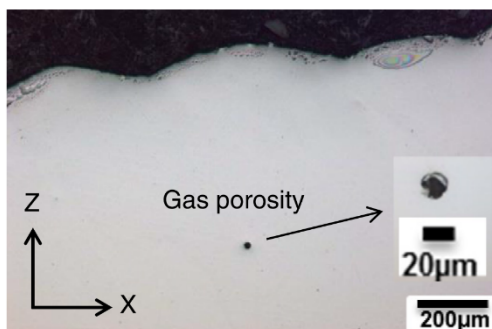
Fig. 3. Optical micrograph showing typical gas porosity (deposit 1).

3.2.1.3. Microstructure within the thinner and the thicker zones in the deposit 1. The thin zone (extremity of cup) and thick zone (center) of deposit 1 were also observed in detail. The microstructures of the thinner and thicker zones were very different. The microstructure of the thin areas was composed of orthogonal laths (Fig. 6a, b) with very few coarse nodular second phase present in some grain boundaries (Fig. 6c, d). In the thick areas, the microstructure was coarser and composed of α/β lamellae (Fig. 6e, f). Although optical microscopy allows the laths of martensite and α/β lamellae to be distinguished, these two structures are better highlighted by SEM due to its higher resolution.

The orthogonal laths observed in the thin areas of deposit 1 are typical of α′ martensite [18], produced by a displacive transformation without diffusion from β phase (BCC) to α′ phase (HCP) during rapid cooling from super-transus temperature (T > T$_{\beta\text{-transus}}$). Ahmed and Rack [9] demonstrated that a fully martensitic structure can be formed at a very high cooling rate (C.R. > 410 °Cs^{-1}). Indeed, the cooling rate during laser fabrication of Ti–6Al–4V thin-walled samples could be estimated as ≈ 7 × 10^4 Ks^{-1} based on a finite element model [7]. Attempts to determine experimentally the value of the cooling rate are much scarcer. Al-Bermani et al. [19] used an indirect method to estimate the cooling rate of electron-beam-melted Ti–6Al–4V from secondary dendrite arm spacing measurements of grains observed in a single melt track produced in a stainless steel base plate using their standard melting parameters. The cooling rate calculated under these conditions was between 10^3 and 10^5 Ks^{-1}. This might be somewhat overestimated since stainless steel exhibits a significantly higher thermal conductivity than Ti–6Al–4V [20]. However the difference between the thermal conductivity of the two alloys also decreases with increasing temperature, so that the cooling rate estimated by Al-Bermani et al. might be considered as a reasonable approximation. Besides, a metastable α′ martensitic microstructure was also observed by Squillace et al. [18] in Ti–6Al–4V laser-beam-welded butt joints processed with a low incident energy (i.e. between 0.23 and 1.18 W.min/mm).

At slightly lower cooling rates the coarse nodular second phase located at grain boundaries (Fig. 6c, d) was identified by Ahmed and Rack [9] under the so-called second α morphology (α$_m$). It is assumed that due to the slower cooling rate, some diffusion transformation can occur in some grain boundaries while elsewhere the prior β grains mainly transform under a diffusionless reaction to yield α′ martensite.

The α/β lamellae observed in the thick areas of deposit 1, on the other hand, correspond to a Widmanstätten equilibrium structure with a basketweave morphology which formed by diffusion from the β phase following a relatively slow cooling. This was also observed by
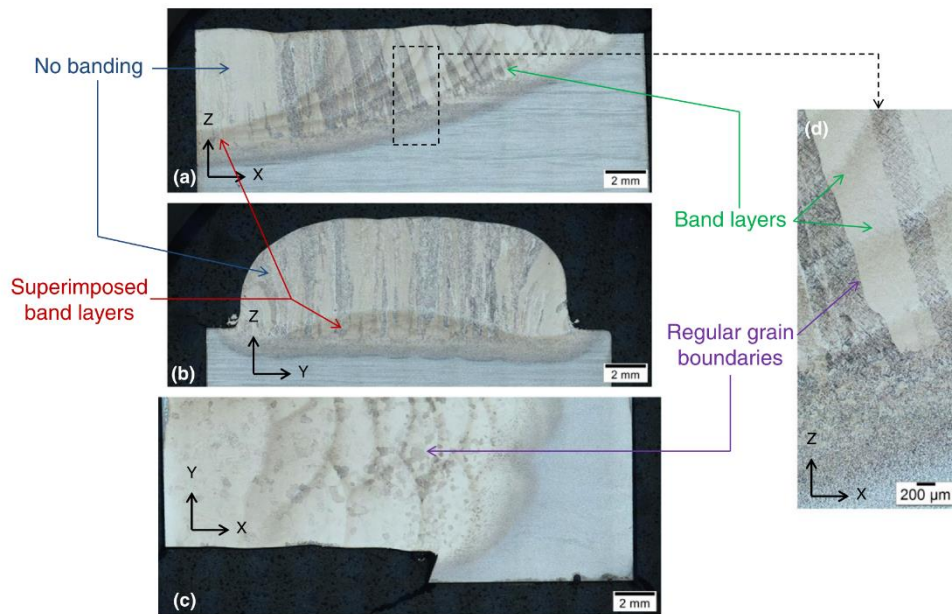
Fig. 4. Optical micrographs showing the macrostructure of sample 1: (a) front view (Z–X plane), (b) side view (Z–Y plane), (c) top view (Y–X plane) and (d) front view at higher magnification.

Baufeld et al. [10] in Ti–6Al–4V components fabricated by wire-based additive manufacturing with a high incident energy.

These differences in the cooling rates and in the resulting microstructures between the thicker and thinner areas of the deposit can be explained as follows. In the early stages, when the substrate is still cold, the deposit can be cooled very quickly through the substrate, leading to a martensitic structure. This fast cooling effect can diminish if the substrates (or pre-existing layers) warm up during building of successive layers [7]. When the temperature of the substrate becomes very high, the cooling rate in the deposit can become sufficiently low to lead to the formation of Widmanstätten structure. In the thicker zone of deposit 1, a high heat accumulation existed, which increased the temperature of the pre-existing layers and substrate. However, in the thinner zone, heat accumulation was lower because the laser moved away from this zone while building subsequent layers. This led to the gradient of cooling rates between these two zones and hence to the different microstructures. In addition some intermediate zones may exhibit cooling rates that ranges between the higher ones which led to the formation of martensite (thinner zones), and the lower ones which yield to the formation of Widmanstätten structure (thicker zones).
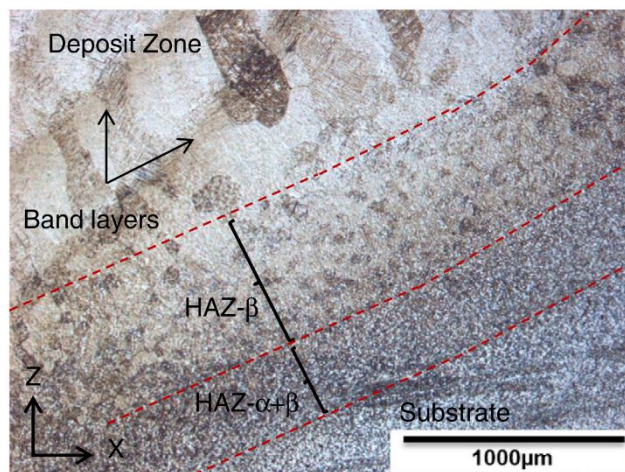
Fig. 5. Optical micrographs showing the heat affected zone (HAZ1-1) in the substrate of sample 1 (front view).
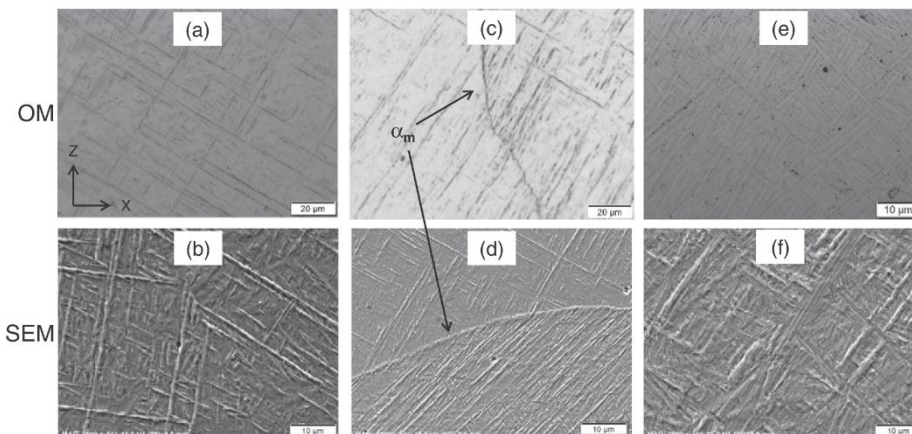
Fig. 6. Micrographs (OM and SEM) showing the microstructure at different locations in deposit 1. The thinner zones of deposit 1 (a and b) exhibit orthogonal α′ martensite microstructure and the thicker zones (e and f) are made of Widmanstätten structure with basketweave morphology; second α morphology (α_m) can be found in some grain boundaries closed to the thinner zones of deposit 1 (c and d).

3.2.1.4. Hardness assessment within sample 1. The two-dimensional hardness maps obtained on different sections of sample 1 are illustrated in Fig. 7.

In the front section (Z–X plane) of sample 1 (Fig. 7a, b), a high gradient of hardness exists between the thicker (softer) and thinner (harder) zones. Moreover, hardness in the thinner zone exhibits strong periodic variations as the standard deviations within these zones are high. In the side section (Z–Y plane) (Fig. 7c, d), the hardness field is relatively uniform. In the top section (Y–X plane) (Fig. 7e, f), the results are similar to those observed in the front section (Z–X plane): the thin zone is harder than the thick zone.

The hardness fields are related to the thermal history (temperature, cooling rate, heat accumulation, …), which depends on the process conditions and that in turn should affect the final microstructure. The harder zones of deposit 1 [≈ 350 to ≈ 370 HV] correspond to the martensitic microstructure formed after rapid cooling in the thinner zones of the deposit, while softer areas [≈ 315 to ≈ 350 HV] correspond to the Widmanstätten structure (basketweave) formed following a slower cooling as observed in thicker areas. These observations are in agreement with previous investigations on more simple geometries. In fact, according to Squillace et al. [18], the hardness of the α′ martensite obtained in the fusion zone of samples produced by laser-beam welding is between 355 and 390 HV0.5, and it increases with the cooling rate. Baufeld et al. [10], on the other hand, obtained a hardness of approximately ≈ 332 HV0.1 for a Widmanstätten microstructure in samples produced by wire-based laser beam deposition at a high incident energy that gave rise to a high heat accumulation. In addition [9] determined critical cooling rates that lead to different phases, the full α′ martensitic microstructure occurring for cooling rates above 410 °C/s, the mixed α′ + α_m structure occurring for cooling rates ranging between 410 and 20 °C/s, and the Widmanstätten structure forming below 20 °C/s. Therefore it can be assumed that for the overall hardness within the thin areas that range between 350 and 370 HV10 and which contain α′ martensite with very few α_m, the cooling rate achieved during the building was between 410 and 20 °C/s. Elsewhere, in the thicker zones containing Widmanstätten structure, the cooling rate was below 20 °C/s. Moreover, it can be assumed that the periodic variations observed on the hardness values within a single area, which corresponds either to a thicker or to a thinner zone, are related to the presence of macroscopic banding in the microstructure. Such a phenomenon may in turn be linked to the HAZ (type HAZ1-2) that have been previously observed within the deposit (see Section 3.2.1.2 above). These HAZ1-2

can be referred to as micro-HAZ (μ-HAZ) contrary to the macro-HAZ (type HAZ1-1) observed in the bounding zone between the deposit and the substrate. In addition it can also be assumed that the upper limit of the hardness set at 370 10 for the martensite, which remain lower than the maximum absolute value around 390–400 HV found elsewhere for the same structure cooled down above 410 °C, is due to the cooling rate that remains below the critical limit of 410 °C/s, but at the same time it should be higher than 20 °C/s. As a consequence, one can suggest that the lower cooling rates within this range may allow diffusionless transformation that lead to the formation of second α morphology α_m at grain boundaries. Conversely, higher cooling rates may yield to the freezing of the prior β grains and inhibit at the same time diffusionless transformation at the expense of full martensitic formation.

3.2.2. Deposit 2 obtained with a high incident energy (HIE) and constant track length (CTL)

3.2.2.1. Macrostructure and microstructure within sample 2. The macrostructure (grains morphology, macroscopic banding, HAZ, …) and microstructure observed in sample 2 are illustrated in Fig. 8. The macrostructure is similar to the previous one observed on the deposit 1.

The microstructure within the deposit is homogeneous and it is mainly composed of Widmanstätten structure with a basketweave morphology (Fig. 8d). This microstructure is similar to the one previously observed in the thicker zone of deposit 1 (Fig. 6e, f).

3.2.2.2. Hardness assessment within sample 2. The building strategy (BS) performed with a constant track length (sample 2) leads to a hardness field that is relatively homogeneous when the three sections are considered, with an average value around 330 HV10 (Fig. 9). This homogeneity observed both for the hardness and for the microstructure is linked to the relative uniform thermal conditions. Indeed, this BS promote small gradient within the heat input from one area to another in the deposit during building. Therefore, this leads to a low and uniform cooling rate over the whole deposit on sample 2, unlike deposit 1.

3.2.3. Deposit 3 obtained with a low incident energy (LIE) and decreasing track length (DTL)

3.2.3.1. Macrostructure and microstructure within sample 3. In sample 3, the macrostructure exhibits finer columnar grains which have a wavy
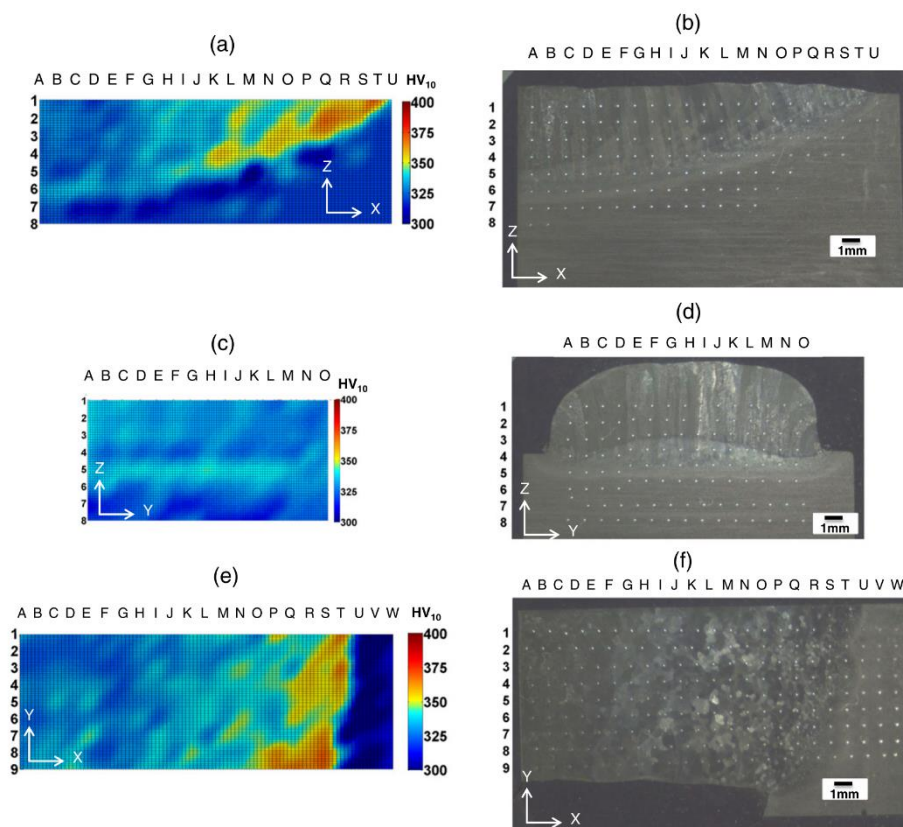
Fig. 7. Hardness maps (HV10, left images) and corresponding hardness indentation grids (right images) within sample 1, for: (a, b) the front section (Z–X plane); (c, d) the side section (Z–Y plane) and (e, f) the top section (Y–X plane).

appearance (Fig. 10) as observed by Kobryn and Semiatin [8]. The HAZ at the substrate/deposit junction with an average thickness of ≈250 μm, exhibits a very fine microstructure (Fig. 10), similar to the microstructure observed at the bottom of the HAZ in the substrate of deposit 1 (Fig. 5). As explained previously (Section 3.2.1.2), this very fine microstructure corresponds to a HAZ$_{\alpha + \beta}$ in which primary β grains may limit grain growth due to very short excursion time in the β domain. This is in turn related to the low incident energy that was insufficient to allow the thermal activation of grains coalescence in the substrate near the junction. The microstructure is relatively homogeneous over the whole deposit of sample 3 since the cooling conditions did not vary significantly from one area to another. This is due to the LIE which leads to a relatively low heat accumulation in the substrate or the pre-existing layers during building, even in regions where the heat input was concentrated (thicker zones). This allows obtaining a relatively uniform and rapid cooling throughout the deposit and substrate. This result is in good accordance with the assumption previously made to discard the configuration with LIE and CTL. The microstructure is mainly composed of α′ martensite (Fig. 11a, b) and neither α$_m$ structure nor Widmanstätten structure were observed within deposit 3, contrary to the deposit 1.

3.2.3.2. Hardness assessment within sample 3. Hardness measurements are illustrated in Fig. 12, and they are in good agreements with the previous results observed on deposit 1 (thinner zones), as martensite is

present almost everywhere in the deposit 3. In fact, the hardness field (Z–X plane) is relatively uniform (Fig. 12a, b) with hardness values ranging from 350 up to 400 HV10. The maxima for the hardness values are located on the top of the deposit, in the thicker zone (last layer to be built), where higher cooling rates are achieved compared to the rest of the deposit. Cyclic variations of the hardness that are observed in the bulk of the deposit (Fig. 12) are related to the μ-HAZ which exist between consecutive layers, a phenomenon which leads to the same macroscopic banding previously mentioned for deposits 1 and 2. The higher gap between the hardness in the μ-HAZ and the hardness inside "fusion" zones that are less affected by subsequent layers, suggest that the original martensitic microstructure within the deposit 3 is more likely to be influenced by thermal gradient than the Widmanstätten structure. This observation applies equally to the martensitic structure within the deposit 1 (thinner zones) compared to the Widmanstätten structure within the same deposit (thicker zones).

The microstructure present within deposit 3 exhibit hardness values higher than those previously observed within the thinner zones of the deposit 1 that contain a similar α′ martensitic microstructure, but with very few α$_m$ structure at grain boundaries.

Alike the deposit 1 in its thinner zones, the deposit 3 contains a martensitic structure which is present almost everywhere. But the interval for the hardness variation is higher for deposit 3 compared to deposit 1 (thin zones), the difference laying within the upper values that reach 400 HV10 in the former sample. The range for hardness variation
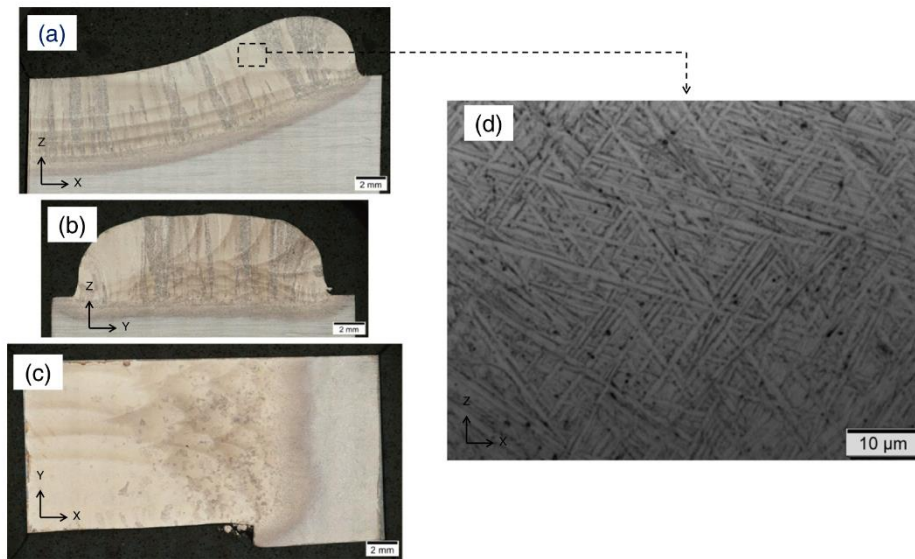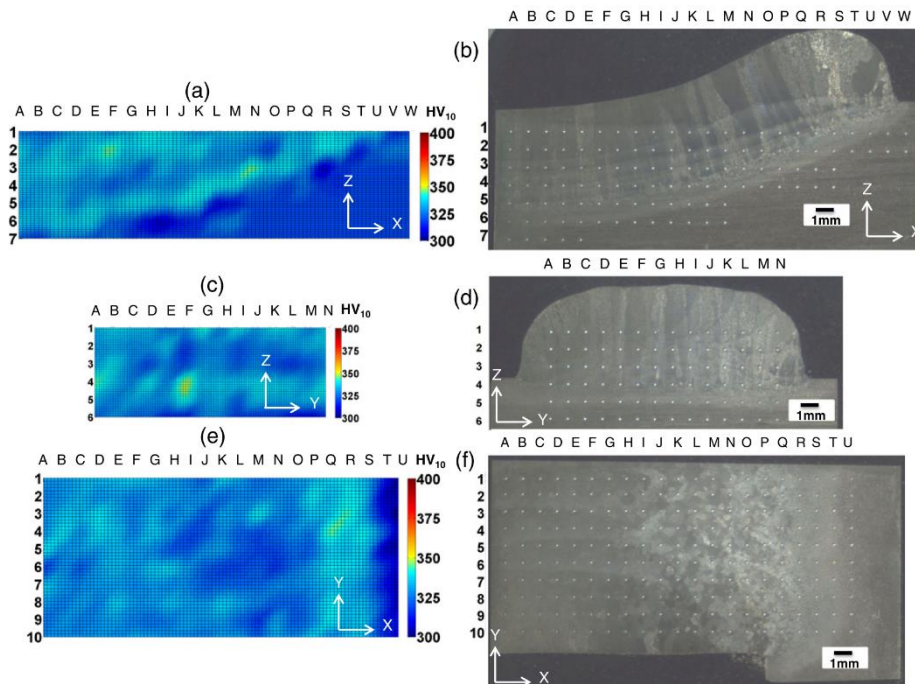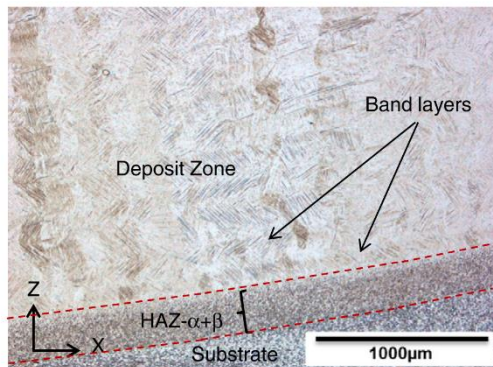
Fig. 8. (a–c) Optical micrographs showing the macrostructure of sample 2 in the three sections and (d) the microstructure within the deposit that consists in Widmanstätten structure with a basketweave morphology.

within deposit 3 is in good agreement with the values founded by Squillace et al. [18] (between 350 and 390 HV0.5), the latter values being also obtained under a LIE similarly to deposit 3. The lower limit

of the hardness range in deposit 3 is probably linked to µ-HAZ and the related macro banding phenomenon. When considering work from [9] and when taking into account the fact no α_m is present in deposit 3

Fig. 9. Hardness maps (HV10, left images) and corresponding hardness indentation grids (right images) within sample 2: (a, b) front section (Z–X plane); (c, d) side section (Z–Y plane); (e, f) top section (Y–X plane).

Fig. 10. Optical micrographs showing the heat affected zone (HAZ) in the substrate of sample 3 and the fine grains within the deposit (front view).

(contrary to deposit 1), it can be assumed that the cooling rates achieved under IE and DTL in sample 3 are higher or equal to the critical threshold of 410 °C/s. Such high cooling rates probably inhibit α_m formation while promoting at the same time only displacive transformation that yield α' martensite everywhere in the deposit. But due to both the very small amount of α_m and its location at grain boundaries in deposit 1, and taking into consideration the fact that macro hardness were performed (HV10 involved a 10 kg load), the overall hardness obtained even in areas containing α_m structure may be independent of this latter structure. Therefore, straight relationship between microstructure and hardness on the one hand, and IE level on the other hand, can be drawn.

3.2.4. Synthesis on the microstructure characterization and the average hardness obtained on the samples

Table 2 summarizes the average hardness values in different sections with the corresponding microstructure for the three samples 1 to 3, and for the substrate. In addition, when necessary, the local average hardness values of the thinner and thicker zones are mentioned due to the visible difference between these two zones (sample 1). It may be noticed that the hardness of the deposit is generally higher than that of the substrate regardless of the processing parameters used for the building.

In samples 1 and 2, the columnar prior-β grains boundaries are more regular, while those observed in sample 3 have a wavy appearance. In addition, the primary β grains are coarser in the two first samples.

In samples 1 and 2, two types of HAZs at the substrate/deposit junction were observed ($HAZ_{\alpha + \beta}$ and HAZ_β), while in sample 3, only the
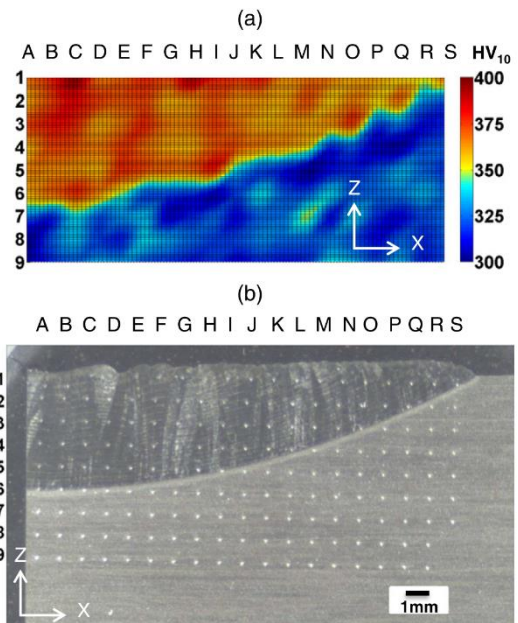

Fig. 12. Hardness maps (HV10) (a) and corresponding hardness indentation grids (b) within sample 3 (front section).

$HAZ_{\alpha + \beta}$ was present. The HAZ in sample 3 is four times thinner than the HAZ observed in both samples 1 and 2.

3.3. Influence of the BS and the IE on the thermal history of the deposits

3.3.1. Thermal history within samples submitted to a HIE and within the protective atmosphere

The evolution of temperature measured by means of a thermocouple inserted in the substrate (Fig. 13) illustrates how the substrate warms up during building with the two different strategies (with DTL and with CTL) with HIE. Each peak of temperature corresponds to the building of an individual track and each bundle of adjacent peaks corresponds to the building of the same layer (10 layers in total). During the deposition of each successive layer, peaks appear when the laser passes through the center of the cup (at mid-length in the X-direction) and the maximum peak is observed when the laser passes just above the thermocouple (at mid-width in the Y-direction).
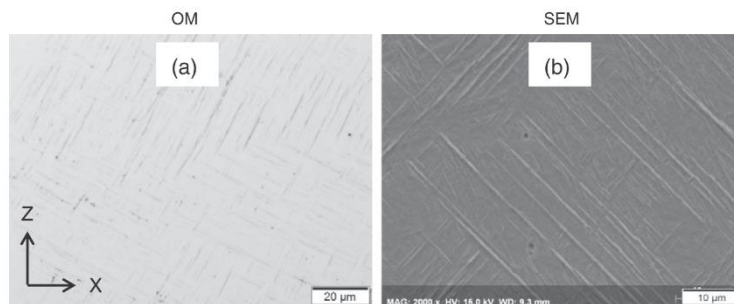

Fig. 11. (a) OM and (b) SEM micrographs showing the α' martensitic microstructure in the deposit 3 (front view).

Table 2
Average hardness value (HV10) with their locations and the corresponding microstructure for all the samples.

Sample 1 — High IE and DTL	Sample 2 — High IE and CTL	Sample 3 — Low IE and DTL
Z–X section: – thinner zone: 357 ± 7 HV (Martensite) – Thicker zone: 328 ± 5 HV (Widmanstätten) – Global: 338 ± 11 HV	Z–X section: 333 ± 5 HV (Widmanstätten)	Z–X section: 368 ± 8 HV (Martensite)
Z–Y section: 331 ± 4 HV (Widmanstätten)	Z–Y section: 331 ± 6 HV (Widmanstätten)	
Y–X section: − thinner zone: 356 ± 6 HV (Martensite) – Thicker zone: 332 ± 6 HV (Widmanstätten) – Global: 338 ± 11 HV	Y–X section: 329 ± 5 HV (Widmanstätten)	

Substrate (structure α–β)
Z–X section: 320 ± 7 HV
Z–Y section: 320 ± 6 HV
Y–X section: 310 ± 7 HV

During building with a DTL strategy (sample 1), the mean temperature of the substrate increases continuously (Fig. 13a) up to a maximum that is reached at the end of the process ($T_{MAX} = T_{END} = 738$ °C). Conversely, the strategy with a CTL (sample 2) yields a higher increase in the heating rate within the substrate up to an absolute maximum of 780 °C that is reached during the building of the third layer (Fig. 13b). From the third layer up to the last tenth layer, the temperature within the substrate fluctuated around the mean value of 700 °C with decreasing amplitudes. The same lowering phenomenon occurring within the amplitude of the average temperature values is observed for sample 1. It is worth noting that the temperature reached in the substrate of sample 2 at the end of the process ($T_{END} = 700$ °C) is lower than that achieved in sample 1 ($T_{END} = 738$ °C).

The evolution of the temperature under the protection cap follows a cyclic variation with less oscillations compared to the substrate. The maxima for both strategies (sample 1 and sample 2) are achieved on "double" peaks that respectively correspond to switch-on switch-off positions of the laser (Fig. 13)

In addition, the baseline that corresponds to the minimum of the temperature which is recorded under the protection cap is almost constant with lower value for the DTL configuration (around 100 °C) compared to the CTL one (around 150 °C).

The maximum temperature is achieved at half the duration of the building process for both configurations. This maximum is set as 380 °C for the DTL strategy and it is significantly higher for the CTL strategy (600 °C). Relative maxima seems to always occur at the same point located in the corner where the building process starts for both strategies.

Moreover, the total time duration which is lower for DTL strategy compared to the CTL configuration is consistent with decreasing switch-on periods observed for the laser used on sample 1, compared to the constant periods achieved on sample 2.

Nevertheless, none of the thermal histories above mentioned could help determining the heat sources involved during the building process. But more extensive information should be expected from the results of the thermal imaging camera that are illustrated in the following subsection.

3.3.2. Thermal evolutions within sample 3 submitted to a LIE (with DTL strategy) and within the laser nozzle

The infrared thermal camera that is used to record the temperature evolution under configuration 3 (LIE and DTL strategy) allows highlighting the heat sources which exist during the laser processing. It was found from the video that the surface of the deposit is the main heat
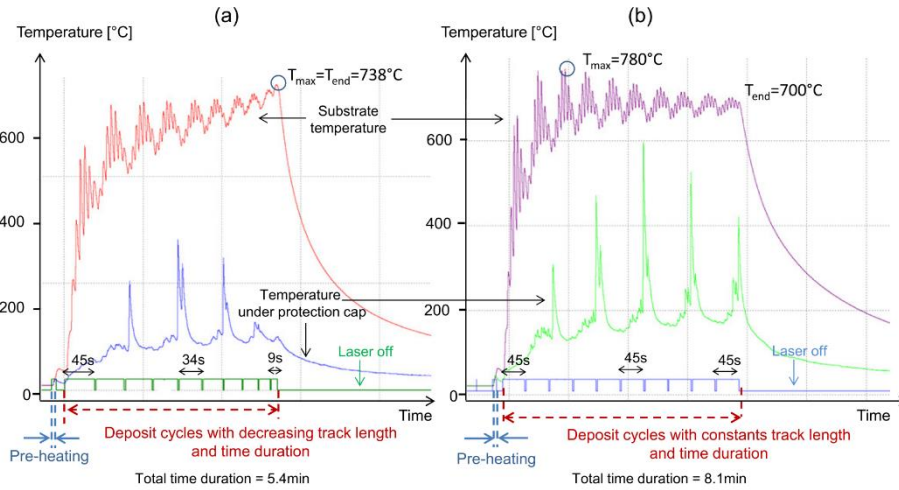

Fig. 13. Temperature histories within the substrate (2 mm below the bottom of the cup, at mid-length in the X-direction and at half-width in the Y-direction) and within atmosphere under the protection cap for sample 1 with DTL strategy (a) and sample 2 with CTL strategy (b).

source that yield both radiant heat flux and convection heat transfer. The heat accumulation within both the substrate and the pre-existing layers was low during the building process including the center of the cup. This is due to the low incident energy (0.33 W.min/mm) involved for sample 3 compared to the higher one used for both samples 1 and 2 (2.75 W.min/mm).

Conversely, there is a progressive heating of the laser nozzle walls from the outside, probably due to the thermal radiation from the deposit surface. This phenomenon can be combined later with conduction heating (from the inner walls of the laser nozzle) yielded by the increase in the temperature of the flowing powder, prior to their fusion onto the" surface of the deposit which is under building. The temperature of the flowing powder can increase due to the permanent location of the melt pool below the laser nozzle during the building or due to the laser beam itself.

Extrapolating the above observations on the laser source with higher power that was used for both samples 1 and 2, it can be assumed that similar heat sources such as those found within the LIE building strategy are also present for the HIE strategies. In addition to the laser nozzle walls, the flowing powder, the bigger melt pool and to the surface of the deposit under building, the bulk of the deposit may also account for the heat source due to the heat accumulation that is more significant under HIE conditions than in the LIE ones. All these heat sources when combined to each other makes it possible to justify the temperature peaks observed on a single corner for the deposits built on samples 1 and 2. Theses peaks occurred when all the heat sources including the laser nozzle are close to the thermocouple which is located in an eccentric position inside the protection cap. Otherwise the temperature within the protection cap, especially near the thermocouple, is set to the minimal level (baseline), notably due to the screen effect of the laser nozzle itself. Nevertheless, the temperature elsewhere in the protection cap, especially close to or inside the deposit under building, may be many times higher than the values that are recorded by the thermocouple and at the same time, their definite values remain an issue that can be solved thanks to an accurate thermal simulation.

Finally, it can be concluded that the increase of the temperature within the protection cap is mainly due to the deposit itself (surface and bulk, melt pool), to the laser nozzle, to the flowing powder, etc. Heat sources may yield almost all the heat transfer modes including radiation, convection and conduction.

3.4. Tensile behavior

3.4.1. Selection of the adequate deposit (sample 2) for tensile specimen's elaboration

The three custom criteria (C1 to C3) set to find the adequate candidate deposit among the different configurations are as follows:

– C1; for the homogeneity within both the microstructure and the hardness;
– C2; for the maximal ductility; and
– C3; for similarity with the microstructure of the base material.

The deposit 1 has been rejected because it failed to fulfill at least 2 criteria (C1 and C3) among the 3 proposed ones. In fact, this deposit is heterogeneous and made of phases that are quite different from the base material (Table 2). Regarding the martensite in Ti–6A–l4V alloy, it is made of the hexagonal close-packed crystal and it has definite ductility. But, such ductility remains many times lower than the one achievable in the BM, the tensile strength of the martensite being higher than that of the latter [21]. The martensite is also quite different from the duplex α–β structure and it is also less stable as it can undergo decomposition under the influence of temperature [22]. Furthermore, if martensite is the main phase obtained in a thick deposit with a complex shape regarding a repair process, significant distortions may already

arise from the stress relief treatment. Nevertheless, martensite can be the adequate phase for application where wear resistance is sought. The work of [23] show interesting results on a Ti6Al4V hip prosthesis that has been surface hardened with a laser, leading to the formation of a thin and hard martensitic layer on the surface, the base material beneath remaining untransformed and made of a duplex α–β structure. However, in applications where good biocompatibility, high temperature oxidation resistance and improved wear resistances are sought, thicker deposits are required and advanced composite materials are preferred over Ti–6Al–4V alloy, the latter material still representing the substrate [3,4]. Weng et al. [3] make a review on the functional coatings cladded on Ti–6Al–4V substrate. In this study, principles for selecting cladding materials are given leading to four categories of cladding material systems from ceramics to composite alloys. Adebiyi et al. [4] investigates the abrasive wear damage of intermetallic composites formed on the surface of Ti–6Al–4V by laser alloying in order to yield a thin coating with an enhanced abrasive wear resistance over twenty times that of the native alloy. The coating was obtained by using a Nd: YAG laser to incorporate different premixed compositions of Mo, Zr and stellite powders.

Similarly, the deposit 3 was rejected due to its fully martensitic structure that is however far away from that of the base material (Table 2), which may exhibits a higher ductility. In fact, the assumption of a lower ductility in the rejected deposit 3 is supported either by the nature of the matrix that is almost fully martensitic, and by the fact very low (or little) heat accumulation is achieved under this configuration. In addition Ravi et al. in their study [1] show that more ductility can be expected from stainless steel cladded materials that undergo ageing during laser processing due to the building strategy which allows heat accumulation.

The deposit 2 was selected for tensile tests due to the fulfillment of almost all the three criteria.

3.4.2. Observations and discussion on the tensile tests performed on specimens obtained from the configuration 2

As a reminder, the tensile tests were carried out not for the mechanical characterization of the deposit alone, but to determine the behavior of the whole represented by the base material associated with the cladded deposit. Such a qualification of the rough laser cladding process may be considered successful if the weakening part of the composite material under tensile stress is neither located in the deposit itself nor in the HAZ between the deposit and the base material.

The Fig. 14 shows the engineering tensile stress–strain curves obtained and the corresponding broken specimens.

From the results of the tensile tests, it appears that both the deposit and its HAZ do not mechanically weaken the repaired part. The selected deposit (configuration 2) has higher tensile strength than the substrate.

Typical stress–strain curves obtained either with the long extensometer that gave the overall behavior of the composite or on the short extensometer restricted to the deposit allow obtaining young modulus and yield strength similar to date found in the literature respectively for duplex and for Widmanstätten structure [21].

Examination of the fractured composite specimens showed that the failure always occurred in the base material under a ductile mode, with evidence of necking in a way similar to data found in the literature [21, 22]. At the same time, it is shown that the deposit itself undergo plastic deformation after exceeding the yield strength that is higher than the one of the base material. The transition to the plastic field for the deposit did not yield failure within the corresponding zone (Fig. 14a).

Nevertheless, the ultimate elongation obtained on the composite (~9%, Fig. 14a) was almost two times lower than the expected values achieved on Ti–6Al–4V commercial duplex alloys [24]. The low ductility is probably due to the remaining residual stresses that were not release from the as-built specimens. Such internal stresses are known to enhance the consolidation within the material while increasing the density of dislocations that may later impair the ductility. The consolidation
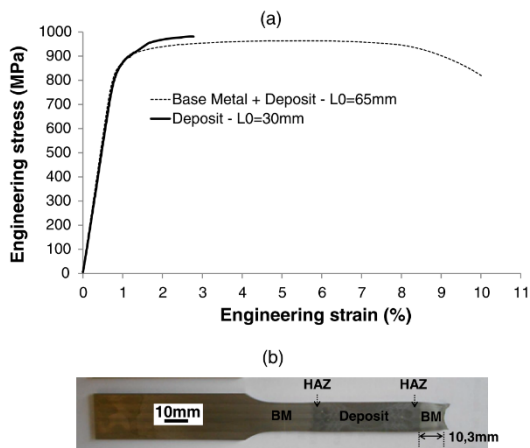
Fig. 14. (a) Engineering tensile stress–strain curves of composite Ti–6Al–4V (base material + cladded deposit) obtained under a HIE with a DTL building strategy (sample 2) (b) failed specimen exhibiting the safe deposit and the failure that occurs in the base material with evidence of necking.

phenomenon may thus correspond to dislocation hardening that can slightly improve the tensile strength [10]. The initial ductility within the base material can be retrieved if a stress relief treatment if performed.

The assessment of the protection cap used during processing can be assessed from the comparison of the mechanical behavior of the actual samples with those of other specimens obtained with a laser processing method performed without preventing contamination [24]. In their study, Brandl et al. [24] show that when unexpected interstitial elements such as O, N or even C, which are present within the normal atmosphere go into solid solution inside the microstructure, both the tensile strength and the ductility collapse. Even if we did not evaluate the content in impurities within the cladded samples, and taking into account the results previously quoted on samples that were contaminated with interstitials elements on the one hand, and also the tensile strength and UTS that are similar to conventional annealed Ti–6Al–4V, it can be assumed that no significant contamination exist in the cladded samples.

The selected deposit (configuration 2) has higher tensile strength than the substrate. In addition, the deposit exhibits a definite ductility. Moreover, the deposit is not the weak link of the cladded material under external tensile stress. Therefore, laser cladding can be considered as an adequate repair technology for Ti–6Al–4V alloy.

4. Summary and simplified thermo-metallurgical scheme

From the comparison drawn in the previous sections regarding the microstructures and the thermal history of the three deposits built with different building strategies and incident energies, a simplified thermo-metallurgical scheme is proposed (Fig. 15). This qualitative scheme set the microstructure nature and hardness ranges at different locations of the deposit, both features being linked to the cooling rates achieved during laser processing.

Noted that in Fig. 15, T_2 is considered lower than T_1 due to the lower IE that leads to a superheating of the melt which is less significant compared to the one obtained with a HIE. This is in good agreement with the work of Yu et al. [25] who found that the temperature of the melt pool increase with the input energy.

In sample 1 (HIE and DTL), a gradient of cooling rate exists between the thin areas of the deposit, where the microstructure consists of martensite, and the thick areas, where the microstructure consists of a
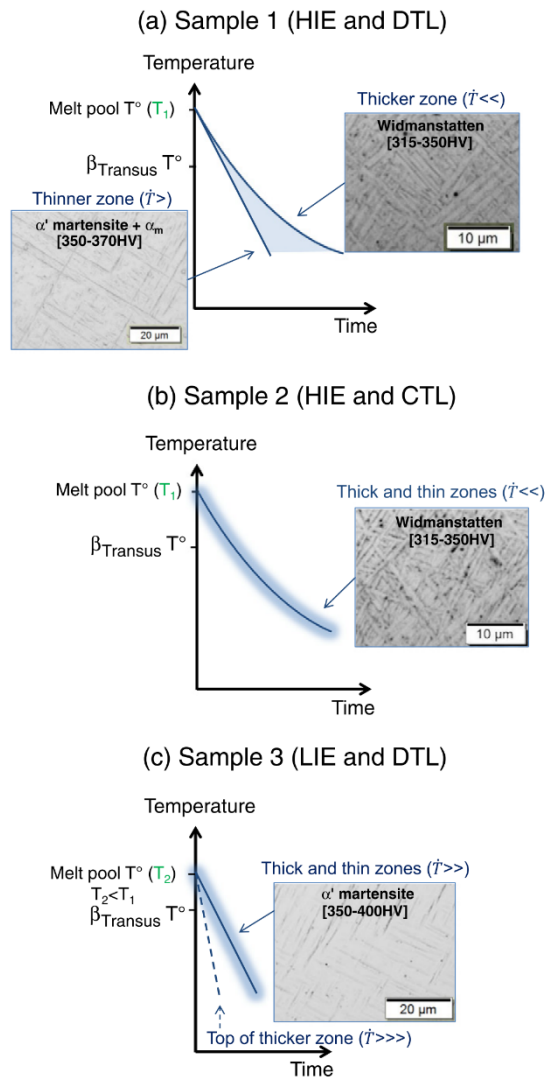

Fig. 15. Sketch of the influence of both the IE and the BS on the cooling rate and the metallographical features at different locations of a cladded deposit; illustration of the corresponding microstructure and hardness ranges for (a) sample 1 built with HIE and DTL (b) sample 2 built with HIE and CTLand (c) sample 3 built with LIE and DTL.

Widmanstätten structure with a basketweave morphology. This is due to the higher heat accumulation in the thicker areas (in the center of the cup), which leads to a lower cooling rates compared to thinner areas, where cooling happens faster. The martensitic microstructure present in the thinner zones may gradually be modified to yield the Widmanstätten structure when moving towards the thicker zones of the deposit. Mixed microstructures may be found between these two ones depending on the thermal gradient.

In sample 2 (HIE and CTL), the heat accumulation is high and approximately uniform over the whole volume of the deposit, leading to a uniform low cooling rate. The microstructure in this case is composed

of a Widmanstätten structure with a basketweave morphology over the entire deposit.

In sample 3 (LIE and DTL), the low incident energy does not lead to a significant heat accumulation in the substrate or the pre-existing layers. This allows obtaining a relatively uniform and rapid cooling throughout the deposit and substrate. The microstructure was composed predominantly of fine martensite.

The width of the grains depend on the IE, and thus explaining why finer grains are obtained within deposit 3 while coarser grains are observed in both deposits 1 and 2. These findings are in good agreement with work from Kobryn and Semiatin [8].

The thermal gradient depends on both the melt pool and the heat accumulation. Higher thermal gradients within the solidification range will promote faster nucleation and related finer prior β grain size. The microstructure achieved at room temperature should be influenced by the thermal gradient that exists within the solid state transformation range as it was suggested by Ahmed and Rack [9].

As mentioned by Qian et al. [7], given the complex thermal history (i.e. the multiple heating and cooling cycles) of parts built by laser cladding, it is difficult to establish a quantitative relationship between a location inside the deposit and the exact amount of martensite or Widmanstätten structure. Nevertheless, the present diagram makes it possible to understand the effect of the building strategy and the incident energy on the microstructure at different locations in deposits of variable thicknesses, in relation to the thermal history. Moreover, this scheme facilitates a quick identification of the nature of phases based on the hardness values and on simple metallographic observations. Furthermore this simplified scheme fits the Continuous Cooling Diagram established by Ahmed and Rack [9] while supplementing it with the addition of corresponding hardness ranges for the main phase fields.

It can be noted that the incident energy strongly influences the productivity during laser cladding. Indeed, for a given geometry of the deposit, the building time depends on the size of individual tracks and the total number of tracks to be deposited. These factors mainly depend on the incident energy. The building strategy, on the other hand, has little influence on the building time. Finally, these two parameters play an essential role in controlling the microstructure and the mechanical properties of the repaired part processed by laser cladding.

5. Conclusions

1. Ti–6Al–4V has been deposited by laser cladding on a machined substrate to simulate repair under different conditions. In particular, the effects of the building strategy on the macrostructure, microstructure, and hardness were studied.
2. A healthy metallurgical junction between substrate and deposit is obtained under all of the investigated processing conditions. The volume fraction of gas porosities remained small under all building conditions.
3. With a decreasing track length building strategy, the microstructure can be more or less homogeneous depending on incident energy:
   – for low incident energy, the microstructure is homogeneous and mainly composed of martensite; and
   – for high incident energy, the microstructure is more heterogeneous, the thicker zone being composed of Widmanstätten structure and the thinner zone being made of martensite.

4. Constant track length building strategy with a high incident energy leads to a relatively homogeneous microstructure mainly composed of a Widmanstätten structure. This configuration was chosen for mechanical qualification.
5. The deposit within the cladded material has a higher tensile strength than the substrate, which is the weakening zone under external stress. The deposit exhibits a definite ductility.

6. A simplified thermo-metallurgical scheme is proposed that enhances the influence of the building strategy and the incident energy on both the microstructure and the hardness.
7. This scheme set the microstructure nature and the hardness ranges, both features being linked to the cooling rates during laser processing.
8. Laser cladding can be considered as an adequate repair technology for Ti–6Al–4V alloy.

Appendix A. Supplementary data

Supplementary data to this article can be found online at http://dx.doi.org/10.1016/j.matdes.2015.07.035.

References

[1] G.A. Ravi, X. Hao, N. Wain, X. Wu, M.M. Attallah, Direct laser fabrication of three dimensional components using SC420 stainless steel, Mater. Des. 47 (2013) 731–736, http://dx.doi.org/10.1016/j.matdes.2012.12.062.

[2] L. Thijs, F. Verhaeghe, T. Craeghs, J. Van Humbeeck, J.P. Kruth, A study of the microstructural evolution during selective laser melting of Ti6Al4V, Acta Mater. 58 (2010) 3303–3312, http://dx.doi.org/10.1016/j.actamat.2010.02.004.

[3] F. Weng, C. Chen, H. Yu, Research status of laser cladding on titanium and its alloys: a review, Mater. Des. 58 (2014) 412–425, http://dx.doi.org/10.1016/j.matdes.2014.01.077.

[4] D.I. Adebiyi, A.P.I. Popoola, Mitigation of abrasive wear damage of Ti–6Al–4V by laser surface alloying, Mater. Des. 74 (2015) 67–75, http://dx.doi.org/10.1016/j.matdes.2015.02.010.

[5] S.M. Kelly, S.L. Kampe, Microstructural evolution in laser-deposited multilayer Ti–6Al–4V builds: part 1. Microstructural characterization, Metall. Mater. Trans. A 35A (2004) 1861–1867, http://dx.doi.org/10.1007/s11661-004-0094-8.

[6] S.M. Kelly, S.L. Kampe, Microstructural evolution in laser-deposited multilayer Ti–6Al–4V builds: part 2. Thermal Modeling, Metall. Mater. Trans. A 35A (2004) 1869–1879, http://dx.doi.org/10.1007/s11661-004-0095-7.

[7] L. Qian, J. Mei, J. Liang, X. Wu, Influence of position and laser power on thermal history and microstructure of direct laser fabricated Ti–6Al–4V samples, Mater. Sci. Technol. 21 (5) (2005) 597–605, http://dx.doi.org/10.1179/174328405X21003.

[8] P.A. Kobryn, S.L. Semiatin, Microstructure and texture evolution during solidification processing of Ti–6Al–4V, J. Mater. Process. Technol. 135 (2003) 330–339, http://dx.doi.org/10.1016/S0924-0136(02)00865-8.

[9] T. Ahmed, H.J. Rack, Phase transformations during cooling in α + β titanium alloys, Mater. Sci. Eng. A 243 (1998) 206–211, http://dx.doi.org/10.1016/S0921-5093(97)00802-2.

[10] B. Baufeld, E. Brandl, O. Van der Biest, Wire based additive layer manufacturing: Comparison of microstructure and mechanical properties of Ti6Al4V components fabricated by laser-beam deposition and shaped metal deposition, J. Mater. Process. Technol. 211 (2011) 1146–1158, http://dx.doi.org/10.1016/j.jmatprotec.2011.01.018.

[11] X. Wu, J. Liang, J. Mei, C. Mitchell, P.S. Goodwin, W. Voice, Microstructures of laser-deposited Ti–6Al–4V, Mater. Des. 25 (2004) 137–144, http://dx.doi.org/10.1016/j.matdes.2003.09.009.

[12] B. Graf, A. Gumenyuk, M. Rethmeier, Laser metal deposition as repair technology for stainless steel and titanium alloys, Phys. Procedia 39 (2012) 376–381, http://dx.doi.org/10.1016/j.phpro.2012.10.051.

[13] Lütjering G, Williams JC. Titanium, 2003. vol. 2. Berlin: Springer.

[14] T. Vilaro, C. Colin, J.D. Bartout, As-fabricated and heat-treated microstructures of the Ti–6Al–4V alloy processed by selective laser melting, Metall. Mater. Trans. A 42A (2011) 3190–3199, http://dx.doi.org/10.1007/s11661-011-0731-y.

[15] P.A. Kobryn, E.H. Moore, S.L. Semiatin, The effect of laser power and traverse speed on microstructure, porosity, and build height in laser-deposited Ti–6Al–4V, Scr. Mater. 43 (4) (2000) 299–305, http://dx.doi.org/10.1016/S1359-6462(00)00408-5.

[16] A.A. Antonysamy, J. Meyer, P.B. Prangnell, Effect of build geometry on the β-grain structure and texture in additive manufacture of Ti–6Al–4V by selective electron beam melting, Mater. Charact. 84 (2013) 153–168, http://dx.doi.org/10.1016/j.matchar.2013.07.012.

[17] E. Brandl, V. Michailov, B. Viehweger, C. Leyens, Deposition of Ti–6Al–4V using laser and wire, part I: microstructural properties of single beads, Surf. Coat. Technol. 206 (2011) 1120–1129, http://dx.doi.org/10.1016/j.surfcoat.2011.07.095.

[18] A. Squillace, U. Prisco, S. Ciliberto, A. Astarita, Effect of welding parameters on morphology and mechanical properties of Ti–6Al–4V laser beam welded butt joints, J. Mater.

510   *H. Paydas et al. / Materials and Design 85 (2015) 497–510*

Process. Technol. 212 (2) (2012) 427–436, http://dx.doi.org/10.1016/j.jmatprotec.
2011.10.005.

[19] S.S. Al-Bermani, M.L. Blackmore, W. Zhang, I. Todd, The origin of microstructural di-
versity, texture, and mechanical properties in electron beam melted Ti–6Al–4V,
Metall. Mater. Trans. A 41A (2010) 3422–3434, http://dx.doi.org/10.1007/s11661-
010-0397-x.

[20] A. Mertens, S. Reginster, H. Paydas, Q. Contrepois, T. Dormal, O. Lemaire, J. Lecomte-
Beckers, Mechanical properties of alloy Ti–6Al–4V and of stainless steel 316 L proc-
essed by selective laser melting: influence of out-of-equilibrium microstructures,
Powder Metall. 57 (3) (2014) 184–189, http://dx.doi.org/10.1179/1743290114Y.
0000000092.

[21] L. Facchini, E. Magalini, P. Robotti, A. Molinari, S. Höges, K. Wissenbach, Ductility of a
Ti–6Al–4V alloy produced by selective laser melting of prealloyed powders, Rapid
Prototyp. J. 16 (6) (2010) 450–459, http://dx.doi.org/10.1108/13552541011083371.

[22] W. Xu, M. Brandt, S. Sun, J. Elambasseril, Q. Liu, K. Latham, M. Qian, Additive
manufacturing of strong and ductile Ti–6Al–4V by selective laser melting via in
situ martensite decomposition, Acta Mater. 85 (2015) 74–84, http://dx.doi.org/10.
1016/j.actamat.2014.11.028.

[23] V.K. Balla, J. Soderlind, S. Bose, A. Bandyopadhyay, Microstructure, mechanical and
wear properties of laser surface melted Ti6Al4V alloy, J. Mech. Behav. Biomed.
Mater. 32 (2014) 335–344, http://dx.doi.org/10.1016/j.jmbbm.2013.12.001.

[24] E. Brandl, F. Palm, V. Michailov, B. Viehweger, C. Leyens, Mechanical properties of
additive manufactured titanium (Ti–6Al–4V) blocks deposited by a solid-state
laser and wire, Mater. Des. 32 (10) (2011) 4665–4675, http://dx.doi.org/10.1016/j.
matdes.2011.06.062.

[25] J. Yu, X. Lin, J. Wang, J. Chen, W. Huang, Mechanics and energy analysis on molten
pool spreading during laser solid forming, Appl. Surf. Sci. 256 (14) (2010)
4612–4620, http://dx.doi.org/10.1016/j.apsusc.2010.02.060.

.. Article #7

3D thermal finite element analysis of laser cladding processed Ti-6Al-4V part with microstructural correlations

H.-S. Tran[a], J.T. Tchuindjang[b], H. Paydas[b], A. Mertens[b], R.T. Jardin[a], L. Duchêne[a], R. Carrus[c], J. Lecomte-Beckers[b], A.M. Habraken[a],[*]

[a] *Dpt ArGEnCo, MS2F-MSM, University of Liège, Allée de la Découverte 9, B4000 Liège, Belgium*
[b] *Dpt A & M, MMS, University of Liège, Allée de la Découverte 9, B4000 Liège, Belgium*
[c] *Sirris Research Centre (Liege), Rue Bois St-Jean, 12, B 4102 Seraing, Belgium*

A R T I C L E   I N F O

A B S T R A C T

In this study, a 3D thermal model of laser cladding by powder injection applied to Ti-6Al-4V is developed. The manufactured part is made of a Ti-6Al-4V substrate on which successive layers of laser melted powder are added, leading to a thick deposit. The computed temperature field and its time evolution are compared to experimental measurements. The temperature distribution in the substrate allows the prediction of the depths of the melt pool and the heat affected zone. Correlations between simulated thermal histories and the final microstructure in the thick deposit are established, leading to the enhancement of a dynamic shift of the critical transformation points due to high thermal rates during laser processing. The nature of the phases present within the deposit is discussed.

1. Introduction

Ti-6Al-4V alloy is widely used in various industrial sectors including the aerospace, automotive and petrochemical fields [1]. Its main advantages are the high strength-to-weight ratio, good corrosion resistance and good fatigue behavior. It is also a superplastic material, undergoing large strains before failure [2].

The laser cladding process is able to form a large variety of alloys and can be used on uneven substrates [3]. However, industries applying this technology face various problems, including the appearance of cracks and difficulties in producing net shapes [4]. Modeling is an efficient means to optimize this process. In recent years, several finite element (FE) models dealing with laser cladding have been developed, focused on specific topics (melt pool, heat affected zone, grain morphology, residual stresses, etc.). They can also be classified according to different types of simulation (thermal, thermo-mechanical, thermo-metallurgical, etc.).

Toyserkani et al. [5] and Alimardani et al. [6] focus on the prediction of the clad geometry of a multi-layer solid free form generated by this fabrication process. These authors considered only elastic strain and neglected plasticity effects. Yang et al. [7] developed 3D thermal FE simulations to predict the heat affected zone (HAZ). However, they did not study the melt pool in this way, while other works have been done using FE thermal simulations to analyze the melt pool [8–13] without extension to the HAZ. In addition, a specific coupled finite element approach also known as the cellular automata method has been used by Zinoviev et al. [14] to simulate the evolution of grain structure within a stainless steel processed by selective laser melting (SLM). The quality of deposition greatly depends on process parameters such as scanning speed, laser power, powder quality, and preheating temperature. Therefore, some authors [15–17] have tried to define the influence of different processing parameters on the thermal evolution, size of the melt pool and HAZ. Among all the thermal models of laser cladding previously quoted, none focused on the evolution of the microstructure in the deposit. The model developed in the present paper is validated by both thermal and metallurgical measurements.

The presence of a high temperature gradient within the laser process induces an important mechanical effect on the manufactured parts: this effect is investigated using thermo-mechanical models [12,18–23], where residual stresses can be used as a means of validation. However, such simulations, even if they give good indications about the residual stress state within the as-fabricated component, are not focused on information on the thermal history or the microstructural evolution of the deposit.

Thermo-metallurgical models applied to additive manufactured or welded Ti-6Al-4V have also been developed, such as the work by Kelly et al. [24] and the study by Murgau et al. [25], who established correlation with the microstructure evolution in the deposit after

---

simulating the Laser Metal Deposition (LMD) and Tungsten Inert Gas (TIG) arc welding processes respectively. In addition, Crespo et al. [26] described a thermo-kinetic model that allows the calculation of the distribution of phases and properties of Ti-6Al-4V parts manufactured by laser metal deposition. All these studies were developed for a "thin-wall" type deposit. In addition, even if these models account for both diffusion and diffusionless transformations, they assume fixed transformation points that are close or similar to the equilibrium conditions. Recently, Ahn et al. [27] predicted and measured residual stresses and distortions by taking into account the phase transformations in a laser-welded Ti-6Al-4V alloy. However, the critical melting points as well as those for solid phase transformations during heating are considered constants.

From a general point of view, two studies presenting the state-of-the-art of laser cladding of titanium and its alloys on the one hand, and on in-situ control during production by additive manufacturing (AM) on the other hand, can be mentioned. In the first case, the work by Weng et al. [28] is mainly based on functional coatings on a titanium substrate. These authors list problems and propose the related practical solutions that already exist. Thus, they clearly establish that modeling is a key issue to achieve optimal parameters of laser cladding processes. According to them, a combination of numerical simulation and experimental testing should be imperative. This is the approach followed in the present research work.

The review by Everton et al. [29] is rather a macroscopic approach focused on dimensional control and internal health (soundness) during production. Adding various accessories to an existing device, such as a pyrometer and infrared camera, allows monitoring of the process. In some cases, the monitoring methods can be linked to process inputs, allowing a closed-loop control of the process by simultaneous control of the melt pool temperature and track morphology. Many manufacturers offer additional modules that can be added to the basic AM machine; however, the data generated are stored but not analyzed in real-time for closed-loop feedback due to their huge volume. While in-situ monitoring helps to adapt the process parameters to achieve an accurate size and shape of a component during fabrication, it fails to simultaneously predict the microstructure of the workpiece. The model developed here is based on simple measurements by thermocouples associated with a good knowledge of the microstructure for validation.

In this study, a 3D thermal FE model of laser cladding by powder injection applied to Ti-6Al-4V for multi-layer deposition is developed. It is based on the non-linear finite element code Lagamine, which is an academic FE code that has been developed since 1984 to model metal-forming processes, for instance deep drawing [30], rolling [31], continuous casting [32], and single point incremental forming [33]. This thermo-mechanical-metallurgical code accounts for all the interactions between the different fields; however, within this study, only the thermal module is activated. The material properties are defined as a function of the temperature.

In order to implement the movement of the heat source within the model and the addition of material, the "switch" approach was tailored for this application. It permits the progressive activation of finite elements representing the clad. Transition refinement elements within the mesh are used to reduce the number of degrees of freedom and to provide a local refined or coarse mesh according to simulation requirements. The model is validated by the thermal history experimentally recorded within the substrate. The temperature distribution and its history are computed to predict the melt pool and HAZ depths and the microstructure evolution within the thick deposit.

The achievement of the thermal history simulation within both the melt pool and the deposit thanks to the 3D thermal model is just a first step developed. The article's innovation is the fact that the simulated thermal histories are used to establish correlation with the microstructure in the deposit, thus allowing a better understanding of the phenomena which occur during laser metal deposition, which have received little attention so far. The main outcomes emerging from the cross-analysis between the simulated thermal histories and the microstructure are recalled below, thus highlighting the major contributions of this work. A dynamic shift of the phase transformation points during (re)heating stages is enhanced, due to the influence of the high thermal rates achieved during laser processing.

High cooling rates achieved during laser cladding processing also lead to martensitic transformation. Therefore, an in-depth discussion is developed about the most relevant position of the M_s point, which stands for the start of the martensite transformation, based on the simulated thermal histories within the thick deposit. Furthermore, when it is formed, martensite phase does not undergo a reverted transformation into β, which makes it possible to introduce the concept of pseudo-isothermal annealing (PIA), during which the untransformed martensite is more or less decomposed.

Due to the thermal history, the thick deposit is a mixed microstructure that is made of α′ martensite, α/β Widmanstätten structure, possible retained β inside grains, and the α_m phase at grain boundaries. The variations observed at the microscale within the microstructure also represent a novelty compared to the previous result that shows a homogeneous macrostructure having an almost constant macro-hardness within the thick deposit.

The experimental setup and main experimental results are presented in Section 2. The numerical model analysis and its validation are reported in Section 3, while the focus of Section 4 lies on the correlation between the simulated thermal histories, the melt pool depth and the heat affected zone depth on the one hand, and the measured thermal history, the macrostructure and the microstructure within the deposit on the other hand.

2. Experimental setup and measurements

The "reference specimen" for this study comes from a batch of samples that were fabricated by laser cladding while changing the building strategy and fabrication details. The main results of this experimental study related to the influence of processing parameters on the microstructure have already been published [3]. This so-called reference specimen presents a Ti-6Al-4V substrate originating from a commercial duplex alpha/beta material. The substrate contains a machined cup (see Fig. 1) for further laser cladding deposition in the same Ti-6Al-4V material. This case is illustrated in Fig. 1a, together with the laser path achieved for each of the 10 layers making up this thick deposit. For each layer, seven tracks (Fig. 1b) are performed following a defined sequence.

The raw material for the thick deposit corresponds to a Ti-6Al-4V plasma-atomized powder with a chemical composition of 6.3 wt% Al, 4.1 wt% V, 0.09 wt% O, 0.06 wt% Fe, 0.0036 wt% H, 0.01 wt% C, 0.01 wt% N, balance Ti and a particle size ranging from 45 to 78 μm. The thick deposit is fabricated using a 5-axis Irepa Laser cladding system. An Nd-YAG laser source is used with a maximum power of 2000 W. The laser spot has a top-hat energy distribution with a diameter of 1400 μm. Plates with sizes of $100 \times 20 \times 15$ mm, extracted from a Ti-6Al-4V standard roll bar, are used as substrate.

Deposit building was carried out using a hand-made protection cap filled with argon to avoid contamination of the melt pool by interstitial elements such as oxygen or nitrogen. The oxygen concentration within the protective atmosphere is below 10 ppm. The Ti-6Al-4V powder is dried before use in order to minimize indoor moisture during laser processing. The substrate was kept in a fixed position, while the laser source moved along the three axes X, Y and Z, remaining vertical (always aligned parallel to the axis Z). The thick deposit was obtained by superimposing 10 layers along the OZ direction, each layer being obtained with 7 adjacent tracks in the OX-OY plane (Fig. 1b). The scanning parameters were selected in order to achieve fully dense deposits (Table 1). A type-K thermocouple located 3 mm below the base of the cup in both the mid-length and the mid-width position (see Fig. 1c) was introduced inside the substrate to record temperature
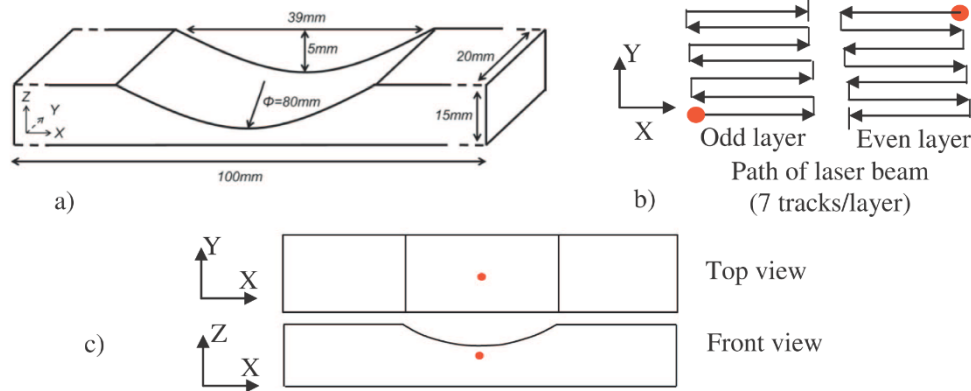
Fig. 1. (a) Geometry of the machined substrate for laser cladding deposition, (b) trajectory of the laser beam, (c) location of thermocouple within the substrate.

versus time. As demonstrated by the recorded thermal history, this position is optimal as, for each layer, it is sensitive to each track of the laser displacement. Of course, it could not be located in the fusion zone. The top of the thermocouple hole is 2 mm below the bottom of the cup, the hole diameter is also 2 mm as well as the size of the thermocouple (⌀ 2 mm). The recorded thermal curve (Fig. 2) will serve as a reference for the validations presented hereafter.

3. Modeling of laser deposition

3.1. Heat transfer finite element analysis

Two types of thermal laws are required in the modeling approach: (i) bulk heat transfer by conduction, including the heat accumulation in the solid, and (ii) surface heat transfer by convection and radiation. The classical non-linear equation of conduction is:

$$\frac{\partial}{\partial x}\left(k\frac{\partial T}{\partial x}\right) + \frac{\partial}{\partial y}\left(k\frac{\partial T}{\partial y}\right) + \frac{\partial}{\partial z}\left(k\frac{\partial T}{\partial z}\right) + Q_{int} = \rho c_p \frac{\partial T}{\partial t} \quad (1)$$

with $T(x,y,z,t)$ the transient temperature, k the thermal conductivity, c_p the apparent heat capacity, ρ the density, Q_{int} the power generated per volume in the work-piece, and t the time. Heat exchange by convection and radiation is defined by:

$$-k(\nabla T.\,n) = -h(T - T_0) - \varepsilon\sigma(T^4 - T_0^4) \quad (2)$$

where h is the convection coefficient [W·m^{-2}·K^{-1}], σ is the Stefan–Boltzmann constant (5.67×10^{-8} W·m^{-2}·K^{-4}), ε is the emissivity coefficient, T_0 is the initial temperature. The effects of the latent heat of fusion L_f and vaporization L_e are integrated in the definition of c_p, defining an apparent heat capacity. The effect of fluid motion due to the thermo-capillary phenomenon (i.e. Marangoni flow) is not considered, in order to reduce the complexity of the problem, as in many FE studies focused on a global approach.

3.2. Finite element code for numerical model

The thermal field is computed by the FE code Lagamine developed at the University of Liège. This implicit FE code is validated by benchmarks [34] or measurements [35]. Using this FE code, the Lagamine developers, i.e. the authors of the present paper, have a total control of constitutive models, type of element or element birth and death technique. Within this study, the BLZ3T thermo-mechanical solid finite element [36] is selected; only its thermal degrees of freedom are activated. It is an 8-node 3D brick element with a mixed formulation adapted to large strains and large displacements. This element is based on the non-linear three-field (stress, strain and displacement) Hu–Washizu variational principle [37–39].

The substrate and filler materials are simulated as solid bodies in the FE model. To model the 3D solid in an efficient way, a non-uniform mesh refinement was used. The parts subjected to the laser source are refined in order to accurately model heat fluxes, while the bottom of the substrate is coarsely meshed to reduce the computation time (see Fig. 3). To generate an optimal mesh, transition refinement element groups are used. An element mesh size of 0.5 mm is selected for the refined zone to have a total of nine elements describing the heat flux loading under the laser beam (see Fig. 4). Convection and radiation elements are also placed on the boundaries of the substrate and the deposit. They are used to model the heat escape to the environment.

Within the model, the initial temperature field $T_0(X,Y,Z,0)$ = 325.89 K is defined from experimental conditions where a preheating phase was applied. Convection and radiation are considered with the environment where the ambient temperature is 298.15 K and is assumed constant.

The laser heat input is applied through a heat flux at a group of nodes. The thermal balance equation of heat flux density (2) is modified under the laser beam:

$$-k(\nabla T\cdot n) = q_{laser} - h(T - T_0) - \varepsilon\sigma(T^4 - T_0^4) \quad (3)$$

where q_{laser} [W·m^{-2}] is the laser heat flux density given by:

$$q_{laser} = \beta \cdot I(X,Y,Z,U,t) \quad (4)$$

where β is the absorption factor, I [W·m^{-2}] is the laser heat flux density distribution and U [m/s] is the velocity vector of the laser in the X, Y, Z directions respectively. In this study, U is accurately evaluated in a similar way as experimentally, taking into account the fact that the laser is moving on a curved surface. The thermal history of the first

Table 1
Details of the laser cladding processing parameters.

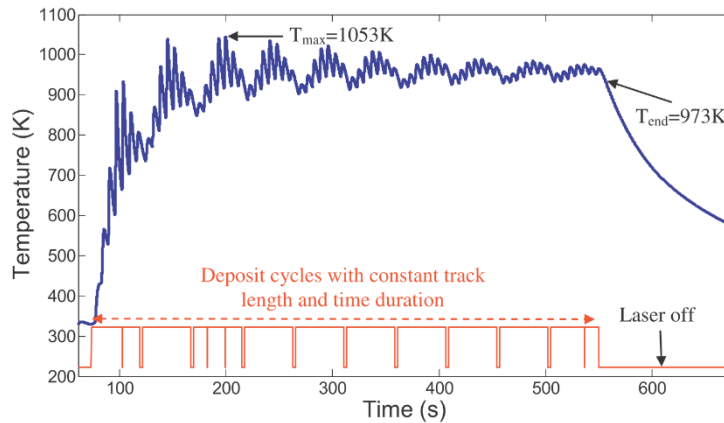| Laser power [W]	Scan speed [mm/min]	Incident energy [W·min/mm]	Powder rate [mg/s]	ΔY increment [μm]	Number of tracks/layer	Number of layers	Building time/layer [s]
1074	400	2.75	28	2100	7	10	≈ 42.5

132

Fig. 2. Thermal history recorded by the thermocouple located within the substrate for the complete deposition of 10 layers, with illustration of the stop and go sequences of the laser beam, including the initial preheating stage and cooling.

three tracks is not sensitive to accurate values of h and ε (see Fig. 6). Therefore, the absorption factor is calibrated until obtaining the same temperature at the thermocouple for the cladding of the first three tracks. A laser absorptivity coefficient of $\beta = 0.35$ is numerically identified. This value is close to the values given in the literature, ranging from 0.30 to 0.40 [7].

Within state-of-the-art researches, the accurate model developed by Goldak [40] consisting of a double ellipsoidal flux density distribution is sometimes used to model laser heat flux density. However, a simple circular Gaussian is also considered [7,41], while Contuzzi et al. [42] assume a constant flux density to model the laser beam heat input. These authors claim that this fact has only a minor effect on the simulation results. Within the present work, different flux density assumptions (rectangular or trapezoidal shapes) have been tested, confirming no significant effect on the results. These selected "top-hat" profiles are related to information provided by the laser manufacturer. The effect of the moving laser beam is taken into account by updating the position of the nodes under the laser, based on the velocity and the trajectory of the laser processing head.

In this powder injection technique, the continuous addition of material on the substrate is often modeled by the element birth technique [18,20,43,44]. In this research, all the elements of the deposit are switched off at the beginning of the fabrication. A group of six elements (three bulk elements and three interface convection radiation elements under the laser beam of diameter 1.6 mm with a top-hat profile) is switched on, and the group of three convective elements covered by bulk elements is simultaneously switched off as new material is added, following the travel of the heat source (Fig. 4). The numerical laser beam velocity and idle time between tracks and layers are obtained from experimental conditions.

3.3. Parameter sensitivity analysis

3.3.1. Material properties

Fig. 5 presents the heat conductivity of the Ti-6Al-4V alloy measured by Mertens et al. [45]. The measurement precision is about 7%. A significant peak of conductivity appears at the α to β transition temperature. The heat capacity values are chosen to be similar to those used by Mills [46]. The heat loss due to radiation is described by a single value of emissivity which is common practice in laser cladding
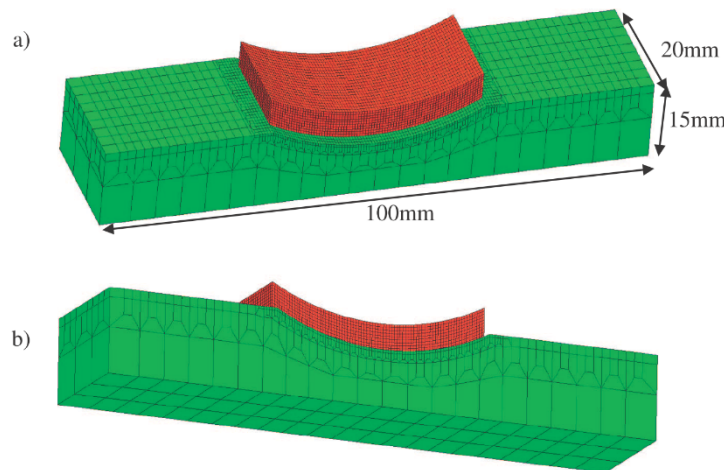

Fig. 3. 3D finite element mesh used for the numerical simulation of the laser cladding process: a) top view, b) bottom view.
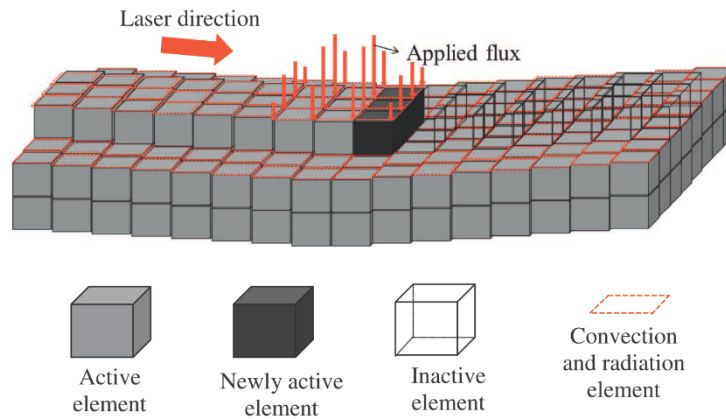
133

Fig. 4. Schematic view of element birth and death technique along the curved surface, in an updated state when the laser has moved (elements are indeed continuous as shown by the mesh of Fig. 3).
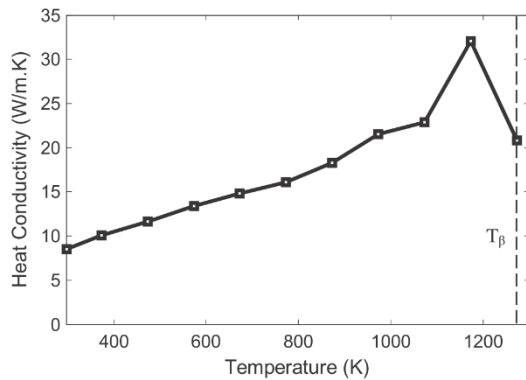

Fig. 5. Heat conductivity of the Ti-6Al-4V.

Table 2
Constant transformation temperatures used here for Ti-6Al-4V as in [24,26].

T_{VAP}	Vaporization temperature	3560 K
T_L	Liquidus temperature	1933 K
T_β	$\beta_{transus}$ temperature	1253 K
T_{DISS}	Temperature where α begins to dissolve into β	981 K

modeling [47,48]. Here, the emissivity used is $\varepsilon = 0.8$. The sensitivity analysis of the air convection coefficient is presented in the next section. The assumed constant transformation temperatures of Ti-6Al-4V are given in Table 2, and are based on values already published [24,26].

3.3.2. Sensitivity analysis

In this section, the influence of the convection parameter on the predicted temperature within the substrate and deposited part is investigated. As only natural convection was involved (free convection in this process), a constant heat transfer coefficient h was used [48]. Numerical simulations were run with the three different convection parameters from Table 3. One finds that the thermal history at the thermocouple and within the first layer of the deposit reaches a plateau after deposition of the fifth layer (see Fig. 7b). Therefore, the sensitivity of the parameters can be analyzed with the first half of the deposition.

Table 3
Input heat transfer coefficients and difference in temperature between experimental value and prediction at thermocouple after five layers of deposition.

	Set 1	Set 2	Set 3
h (W/m^{2}K)	5	52	100
ε	0.8	0.8	0.8
$\Delta T_{5\ end}$ (K)	169	4	-184

The obtained results show a high sensitivity to the convection parameter (Fig. 6a). At the thermocouple in the substrate, the difference between the experimental values and simulation results is rather low after the deposition of the first layer, but it increases with time and the number of layers (Fig. 6a). The third parameter set presents the highest difference between predicted and measured temperatures. The simulation results within the deposit show that variations of predictions due to the input parameters have the same order of magnitude (Fig. 6b). The predictions of the second parameter in Fig. 6a match the thermocouple measurement well. This shows that to accurately capture the thermal behavior of laser cladding by FE simulations, the convection coefficient must be correctly applied to the evolving surface. Hereafter, this second set of parameters will be used to predict the thermal field within the substrate and deposit during the whole laser cladding process.

3.3.3. Model validation

The local temperature history recorded by the thermocouple measurement within the substrate is compared with the thermal predictions (Fig. 7a and b) to validate the simulation results. The experimental curve shows an oscillating aspect corresponding to the alternating displacement of the laser. The complex thermal history can only be predicted if the numerical model is relying on a correct set of input material parameters and accurate boundary conditions. One can see the close agreement between the simulation of the seven tracks within the first layer and the experimental measurement in Fig. 7a, and for the whole cladding experiment (10 layers) in Fig. 7b, confirming the validation of the proposed thermal numerical model.

4. Results and discussion

4.1. Melt pool and HAZ depths within the substrate

In this subsection, the thermal model is used to evaluate the depth of the melt pool and the HAZ within the substrate. Transformation
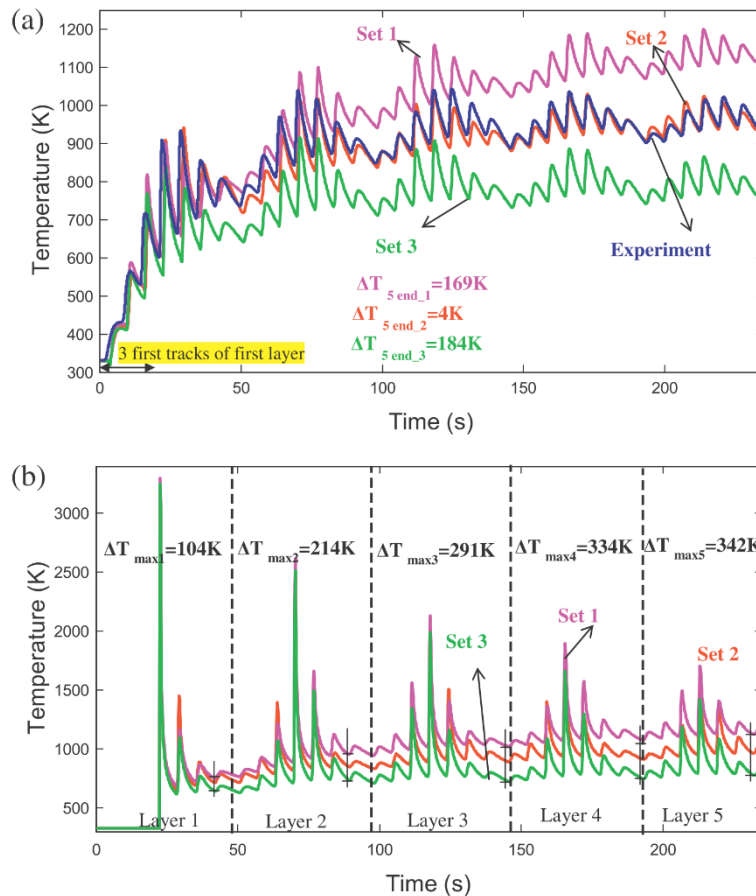
134

Fig. 6. (a) Sensitivity of temperature history due to convection parameter at the location of the thermocouple. $\Delta T_{5\ end}$ is the difference in temperature between prediction and experimental values at the end of the 5th layer ($t = 235$ s); (b) within the deposit, $\Delta T_{max\ i}$ is the maximum difference in temperature during the deposition of each layer i between results generated by the three values of the convection parameter.

temperatures are assumed constant. They are equal to the values achieved under equilibrium conditions. These transformation temperatures are referred to T_{DISS}, which corresponds to the start of the $\alpha \rightarrow \beta$ solid state phase transformation and T_L (liquidus temperature). These temperatures are given in Table 2. The computed depth profiles for both the melt pool and the HAZ are compared with the experimental observations.

Fig. 8a shows the temperature profile at $t = 40.6$ s at the deposit surface as well as at the substrate surface associated with the final track (the seventh) of the first layer when the laser was processing the top of the Ti-6Al-4V material of the substrate. Coupled with Fig. 9 and Fig. 10, these results indicate that the temperature gradients along the three directions are very large. One can see that the maximum temperature at the top of the deposit (i.e. 3500 K) is significantly higher than the melting temperature of Ti-6Al-4V. For that reason, part of the substrate under the laser beam is melted (Fig. 8b). A stable thermal contour under the laser beam during the different tracks was observed. These thermal distributions enable a comparison of the melting depth predicted by the model with the experimental data.

The 3D thermal FE model allows the volume of the melt pool to be defined at each time step by 3D thermal contour lines over 1933 K (T_L) corresponding to the fusion temperature (Fig. 9). The simulation predicts that the melting depth (h_{DL}) is 508 μm within the substrate. It also enables the determination of the HAZ by the FE model. The temperature contours higher than 981 K correspond to the HAZ zone (see Fig. 10), where α within the substrate begins to dissolve into β, i.e. above the T_{DISS} temperature.

The simulation predicts a deeper dilution (h_{DL}) of 508 μm than the estimated value of 450 μm from previous experimental results identified with an optical microscope [3]. It predicts a slightly deeper h_{HAZ} (1618 μm for the simulation, 1501 μm for the experiment [3]). The difference of 8–13% between the prediction and measurement shows that we are still in qualitative validation. It is important to mention that the characteristic temperatures for the Ti-6Al-4V alloy are not indeed constant values, but vary in more or less extended ranges, with an upward offset with an increase in heating rates [49]. This point may explain the discrepancy between the thermal contours. The use of higher values for critical phase transformation temperatures to post-process the numerical thermal field would lead to reductions in the prediction of the depths of both the melt pool and the HAZ. Such an assumption of the right shift of transformation points would generate a closer agreement with the previous metallographic inspections [3]. Therefore, the influence of the heating rate on the shift of the critical transformation temperatures is considered in the next sections, in order
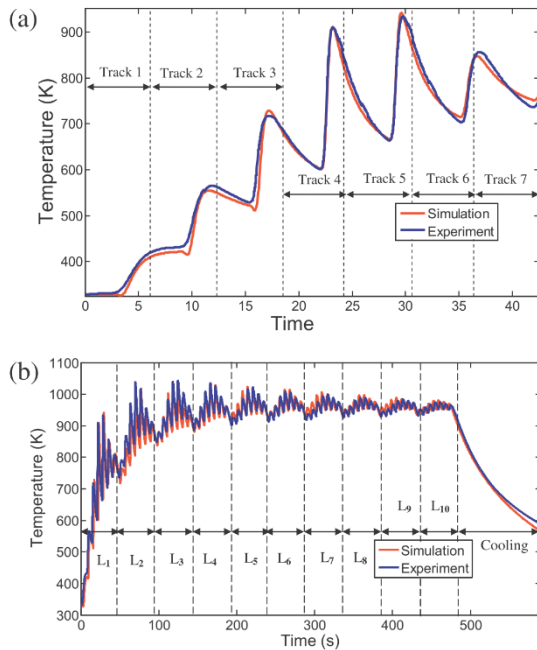
135

Fig. 7. Comparison between the simulated and the experimental thermal history as obtained from the thermocouple located within the substrate: (a) for the first layer made of seven tracks of the laser, (b) for the 10 layers of the laser deposit.

to establish the correlations between the simulated thermal histories and the observed microstructure within the deposit.

4.2. Correlation between the observed microstructure and the simulated thermal histories within the deposit

Three points of interest (POIs), referred to as POI1, POI2 and POI3,

are chosen in the longitudinal section A-A (see Fig. 11a). The choice of these points is based on simulated thermal histories obtained from the computed 3D thermal field. It takes into account the heat accumulation effect during manufacturing on the one hand, and the progress within the building of the multi-layer thick deposit on the other hand. For that reason, POI1 and POI2 are located 1 mm beyond the top surface of the substrate and belong to the first layer, while POI3 located is 1 mm under the final surface of the deposit. The macroscopic characterization of this section in terms of Vickers hardness and macrostructure has been carried out and published in a previous study [3]. In the present work, the microstructure of the three POIs at a smaller scale was revealed by a scanning electron microscope (SEM) and an optical microscope (OM) (Fig. 12). The correlation between the observed microstructure and the calculated thermal history is presented hereafter.

4.2.1. Simulated thermal histories and macrostructure at the POIs

Fig. 11b illustrates the thermal histories of the three POIs obtained from the simulation. Both POI1 and POI2 are activated during the deposition of the first layer while POI3 is activated during the deposition of the 8th layer. The simulated thermal history of a single point shows series of peaks depending on the laser path. The higher thermal peaks occur when the laser beam is close to the point under investigation. The rapid increase and the subsequent temperature drop correspond to the laser beam getting closer to or moving away from the related point, respectively. The remelting of a single material point will depend on the local incident energy of the laser beam and the accumulated energy achieved during the deposition.

Table 4 gives the maxima temperatures and the related heating and cooling rates for the first 6 peaks obtained for each point. Table 5 establishes a synthesis of the thermal parameters which characterize the thermal histories at these three points, and in particular the extreme temperature during the last solidification, as well as the average cooling rates (during the last solidification). The average temperature and duration of the equivalent annealing are also indicated. These values are estimated by considering that the structure generated by the identified last solidification is no longer remelted. Explanations of this approach are outlined in the following discussion.

For the three studied zones, the macrostructure observed under OM is made of typical orthogonal laths corresponding to α′ martensite (Fig. 12a, d, g). Martensite is indeed often observed in Ti-6Al-4V
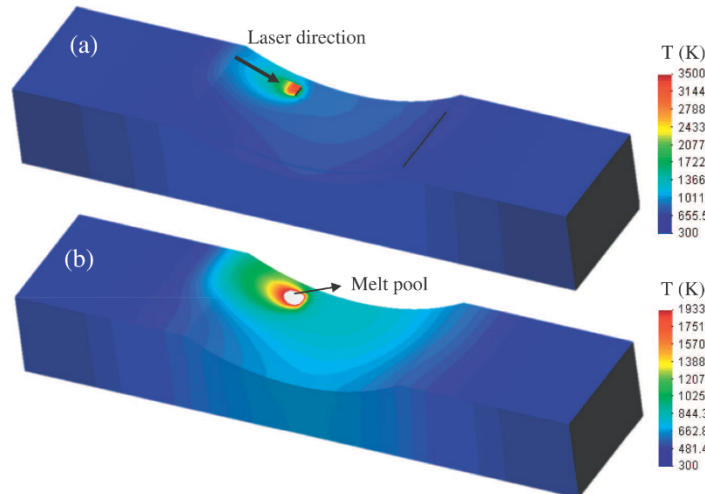

Fig. 8. 3D temperature distribution during deposition of the final (seventh) track of the first layer at *t* = 40.6 s (a) in the deposit, (b) in the substrate. White color corresponds to a temperature higher than 1933 K for (b).
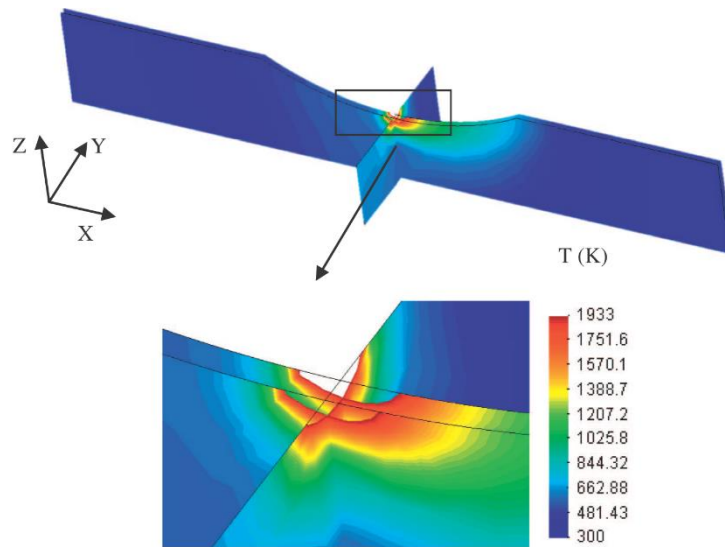
136

Fig. 9. 3D view of the thermal gradient around the melt pool (first layer, middle of track 4), where material at a higher temperature than 1933 K has white color.

processed by additive manufacturing techniques [3,45,50].

Concerning the microstructure observed at a micro-scale using SEM, a substructure located between martensite laths is found (see Fig. 12b, c, e, f, h, i). Such a substructure corresponds to lamellas arranged in triangles, which is typical of the so-called α/β Widmanstätten structure that has basketweave morphology. The Widmanstätten structure is denser at POI3 than at POI1 and at POI2. SEM micrographs also enhance the morphology of martensite laths, which varies from the thick shape at POI1 and POI2 to a finer shape at POI3.

4.2.2. Influence of the thermal histories on the solidification structures within the thick deposit

A specific study of POI2 is proposed hereinafter in order to establish the correlation between the simulated thermal history (Fig. 13) and the observed microstructure at this point. The same analysis could also be applied to POI1 and POI3.

The activation of POI2 takes place at the moment when the molten powder is deposited during the laser cladding process. This first melting is achieved at 3226 K with a high heating rate of 11,772 K/s (see Table 4). Then, the temperature drops, leading to a fast solidification with an average cooling rate around 464 K/s down to a minimum temperature of 602 K. However, the first peak is followed by a second peak having a maximum temperature above 2300 K, which is achieved under a high heating rate around 1739 K/s. In total, there are four peaks exceeding the "equilibrium" liquidus temperature set as

1923 K ± 15 (according to [50]). Therefore, POI2 may undergo several remelting sequences after being solidified for the first time, and the last melting phenomenon should occur during the deposition of the 4th layer (see Fig. 13). Afterwards, in the additional layers between the 5th up to the last and 10th layer, the peak temperature no longer allows the point to be remelted. However, according to the work of Basak et al. [49], high heating rates lead to a right shift of the melting temperatures, especially the solidus point, which ends up coinciding with the liquidus in a way similar to an eutectic alloy. Thus the solidification range is reduced when the heating rate increases. The same authors have also mentioned that melting at very high heating rates requires a certain incubation time before the reaction occurs, assuming the final temperature to be equal to the liquidus temperature. This time was estimated to be around 5 s for a Ti-20Nb alloy heated up at 5000 K/s. In the present study, the holding time under the maximum temperature for a given peak is very short (less than 2 s for all the POIs). Thus, it can be considered that only temperatures above the theoretical liquidus (1933 K) lead to complete melting at a point of the deposit. For temperatures lower than or equal to the theoretical liquidus, and taking into account the fact that such temperatures are reached under high heating rates around thousands of K/s, the total remelting sequence may not be achieved due to a short holding time (less than 1 s at the maximum for POI2). POI2 is therefore remelted 3 times after being solidified for the first time, the last remelting sequence occurring at 2047 K (peak 4 in Table 4).

Fig. 10. Temperature distribution within the fusion zone and the HAZ in a longitudinal section located in the middle of the substrate at $t = 22.7$ s (i.e. half of the first layer deposition), showing the asymmetrical thermal gradient.
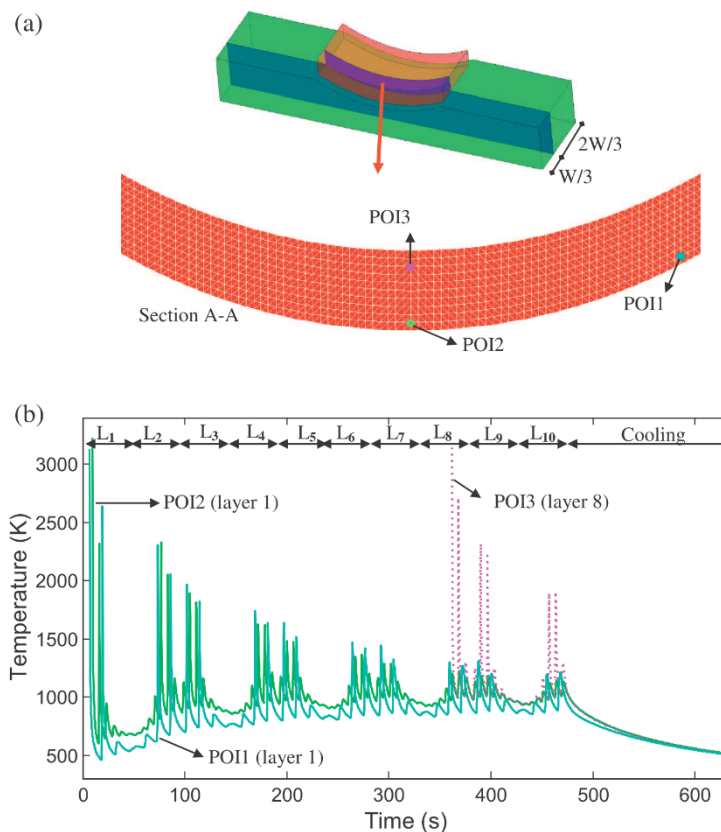
137

Fig. 11. (a) Location of the three points of interest (POIs) within the deposit and (b) simulated thermal evolution of the POIs as obtained from the 3D thermal model.

4.2.3. Influence of the thermal history on the solid state phase transformations within the thick deposit

After the last solidification, the parent β phase will undergo a transformation whose products will depend on the cooling rates [51]. Cooling rates below 20 K/s may promote diffusive transformation leading to an α/β basketweave morphology phase that nucleates at grain boundaries before expanding inside. This phase is also known as Widmanstätten structure. Cooling rates between 20 K/s and 410 K/s allow diffusionless transformations. The generated phases are made of α′ martensite inside grains and α_m at grain boundaries. Cooling rates higher than 410 K/s lead to a full α′ martensite with no additional phase within the grain boundaries of the parent β phase.

A starting point also known as the M_s temperature has to be chosen for the martensitic transformation. Based on both the simulated thermal histories (see Fig. 11 and Fig. 13) and the macrostructure with typical orthogonal laths that are present within the deposit (Fig. 12), and also the work by Tan et al. [52], it is decided to consider an M_s point as high as 1073 K, instead of the lower values such as 848 K, 898 K and 923 K that can also be found in the literature [24–26]. Such an assumption on a high M_s point seems to be more relevant for the Ti-6Al-4V alloy, and this statement is consistent with the results of various studies which are referred to hereafter.

The first research was carried out by Boyer et al. [1], who linked the variation of the M_s point with the chemical composition of titanium alloys by using a pseudo-binary Ti-6Al-V diagram. The temperature of the M_s point decreases with the vanadium content, with a value of

1073 K for the Ti-6Al-4V. The second study completed the previous one by establishing, in a similar way to steel alloys, an equation for the determination of the M_s point, which takes into account the weighted influence of the main alloying elements [53]. The M_s point is computed at 1098 K from this empirical equation.

Although the actual M_s temperature used within the studies of laser processed deposits of Ti-6Al-4V is not often mentioned [3,45,50,52,54], it is clear that the M_s temperature value used in these studies is set above 873 K during the process. At the same time, the macrostructure often achieved in the laser and electron beam processed Ti-6Al-4V deposits exhibits typical orthogonal laths corresponding to martensite that is assumed to be more or less decomposed.

The completion of the martensitic reaction is almost achieved when the temperature reaches the end point of the transformation temperature (M_f). But very few values are mentioned in the literature concerning this M_f point, and these values are very disparate. This is particularly the case with Crespo et al. [26], who set M_f at 673 K, while Jovanovic et al. [55] suggested a temperature below 298 K. In the present study, M_f is set equal to 673 K without further investigation because this is not relevant for the qualitative analysis that has been currently developed. When the minimum temperature reached on a single material point during the last solidification stage is below M_s and above M_f, and given the fact that the cooling rate is well above the threshold value of 20 K/s, the initial β phase should be transformed into α′ martensite and α_m, with a possible retained and untransformed β if the M_f point is not reached.
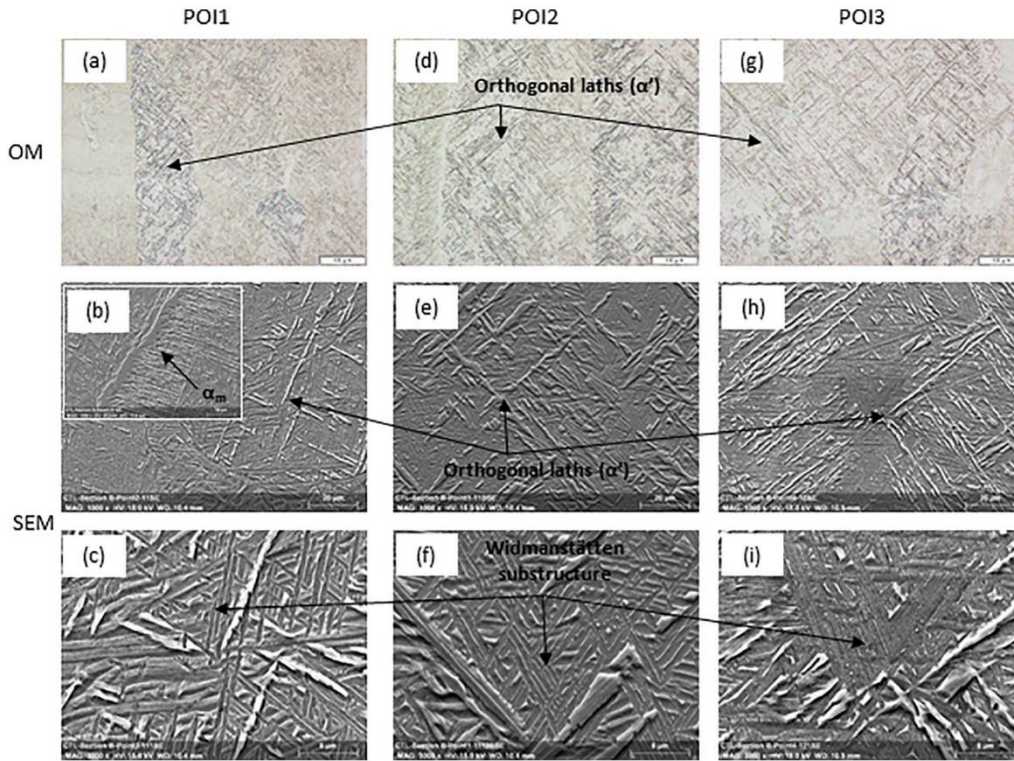
Fig. 12. Micrographs (OM and SEM) showing both the macrostructure and the microstructure for POI1 (a, b, c), POI2 (d, e, f) and POI3 (g, h, i) within the deposit. Orthogonal laths of α′ martensite are clearly highlighted on the macrostructure, as obtained from OM micrographs (a, d and g), whereas Widmanstätten structure with a basketweave morphology located between α′ laths represents the substructure that is better enhanced under SEM micrographs (b, c, e, f, h, i). Second α morphology (α_m) can be found at grain boundaries, mainly within the POI1 (see insertion in b).

Table 4
Main peak temperatures, heating rates (HR) and cooling rates (CR) reached during deposition at the three points of interest (POIs) from simulated thermal history.

Point of interest	Calculated thermal parameters	Peak 1	Peak 2	Peak 3	Peak 4	Peak 5	Peak 6
POI1	$T°$ (K)	3133	2637	2307	2057	1967	1821[a]
	HR (K/s)	11,388	2950	1147	1407	859	1099
	CR (K/s)	226	170	141	96	108	87
POI2	$T°$ (K)	3226	2315	2326	2047	1893[a]	1816[a]
	HR (K/s)	11,772	1739	1538	1619	1005	1212
	CR (K/s)	464	265	261	197	172	158
POI3	$T°$ (K)	3364	2708	2319	2212	1891[a]	1903[a]
	HR (K/s)	12,337	2321	1332	1615	919	909
	CR (K/s)	419	301	230	212	163	156

[a] Assumed not to be remelted.

Table 5
Thermal characteristic features (see Fig. 13) calculated from the simulated thermal histories of the three POIs and related local hardness values as extracted from the hardness mapping [3].

Computed characteristic thermal features and hardness	POI1	POI2	POI3
Last solidification stage			
T_{max} (K)	1967	2047	2212
T_{min} (K)	739	882	1011
Average cooling rate achieved during the last solidification stage (K/s)	108	197	212
Pseudo-isothermal annealing (PIA)			
T_{mean} (K)	927 ± 144	1013 ± 116	1041 ± 147
Equivalent holding time (s)	355	382	68
Final continuous cooling stage			
T_{end} (K)	1211	1132	1299
Average cooling rate during the final cooling stage (K/s)	4	4	5
Hardness (HV_{10})			
Local hardness value (HV10)	346	331	331

The temperature increase following the end of a cooling phase is very sharp, with heating rates of the order of thousands of degrees per second (see Table 4). Several studies where rapid heating rates have been carried out on Ti alloys, especially while using pulsed current [56], observe a shift toward high temperatures for the critical transformation points including β$_{transus}$. A heating rate of 400 K/s causes a shift of β$_{transus}$ to 1393 K, which could be extrapolated to 1473 K if a heating rate around 2000 K/s is considered according to [56]. This range of heating rate is similar to the corresponding peaks obtained from the simulated thermal histories (Table 4). In addition, the peaks

that follow the final solidification within a single point exhibit a similar shape (high sharpness) to the previous ones occurring during the remelting stages, reflecting very short holding times of less than 2 s. The experimental work carried out with high heating rates also showed that sufficiently long holding times (order of minutes) are required to
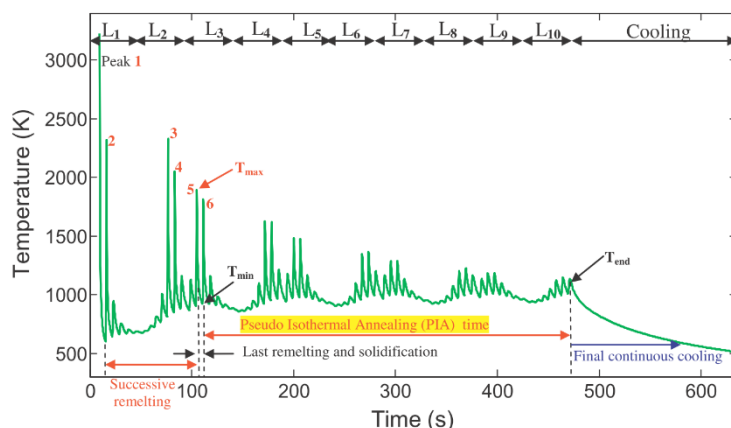
Fig. 13. Simulated thermal history of POI2, showing the specific thermal events such as the last solidification stage and the subsequent PIA (pseudo-isothermal annealing); characteristic thermal features (Peak, T_{max}, $T_{average}$).

initiate diffusional phase transformation [57]. This observation results from the fact that the phase transformation is thermally activated and diffusionally controlled (see JMAK model [26]). Therefore, it is assumed that newly formed martensite does not reversely transform into β phase during quick heating stages. However, the fresh martensite may undergo a thermal cycle that can be approximated to a pseudo-isothermal annealing (PIA) whose characteristic features are set as the average temperature and the total holding time until the end of the deposition process. They are summarized in Table 5.

At the end of the deposition process, the laser beam is switched off, leading to a low cooling rate down to room temperature, within both the deposit and the substrate. The maximum of the cooling rate is estimated at 4 K/s, thus explaining the formation of the Widmanstätten structure, which is presented as a substructure between the martensite laths (Fig. 12c, f, i). The occurrence of such an α/β Widmanstätten structure probably results from a diffusive-like solid state phase transformation of the residual β phase that still exists due to the non-completion of the previous martensitic transformation. Therefore the subsequent formation of Widmanstätten structure close to pre-existing martensite laths suggests that the M_f point is not reached during successive and rapid cooling stages in the solid state, prior to the final and slow cooling stage that follows the deposition process.

4.2.4. Qualitative analysis on the nature of different phases contained in the matrix of the deposit

The martensitic transformation occurs for the three POIs. The amount of martensite within each POI increases with the decrease of the minimal temperature achieved during the fast cooling following the final solidification stage. An identical M_s point for the three POIs is assumed. Thus POI1, which is rapidly cooled down to 739 K, should contain more martensite than the POI2 (cooled down to 882 K) and the POI3 (cooled down to 1011 K).

The newly formed α′ martensite does not later revert into β for all the three POIs, but it can undergo a decomposition phenomenon during the so-called PIA heat treatment. Such a decomposition, which has been widely documented in the literature [50,52,54], is also clearly highlighted within POI2 where the longest PIA occurred (382 s at 1013 K), leading to the coarsening of certain laths (Fig. 12e, f). Conversely, martensite decomposition is markedly less pronounced within POI3, where the PIA is very short (about 68 s), leading to thin martensitic laths similar to those of the fresh martensite (Fig. 12h, i). Although the cooling rates after the last solidification of the three POIs are high enough to allow the martensitic transformation, the lower cooling rate achieved within POI1 may explain the presence of a greater amount of

$α_m$ phase at grain boundaries compared to the two other POIs, where such phase is not observed. The Widmanstätten structure is formed from the retained β during the final and slow cooling stage down to room temperature.

Ultimately, the three POIs contain the same phases that account for a mixed microstructure. It is made of fresh and/or decomposed α′ martensite, $α_m$, α/β Widmanstätten structure, and very few retained β. α′ martensite, α/β and retained β are located inside grains, whereas $α_m$ is located within the grain boundaries. The amount of each phase within the entire microstructure depends on the local thermal history of the related zone within the deposit.

The differences in the type and the nature of the phases, together with the occurrence of sub-structures within the microstructure, are clearly highlighted under SEM analyses carried out at a microscale. However, OM observations at a mesoscale show a homogeneous macrostructure having a constant hardness almost everywhere in the deposit, which exhibits orthogonal laths, as has already been published [3]. In this previous study based on a macroscopic characterization by hardness measurements and OM analysis, the structure in the deposit was assumed to be homogeneous, mostly made of the Widmanstätten type. The present 3D thermal model makes it possible to bring more precision especially at the microscale. SEM analyses highlight the mixed microstructure within the thick deposit, which looks homogeneous under a macroscale. This research can be used as a mandatory preliminary step for the optimization of the microstructure. Through adequate setting of the parameters of the additive manufacturing process, it is possible to promote a defined microstructure with one or more phases in order to achieve the desired mechanical properties.

5. Conclusions

This article describes a numerical model of the laser cladding process applied to Ti-6Al-4V alloy. 3D thermal FE simulation reproduced an experiment representative of the use of laser cladding as a repair technology. The 3D thermal FE model allows correlation of the evolution of the microstructure within every single point of the thick deposit with the thermal history simulated at the same point. The main outcomes are outlined below:

- The model is able to predict the thermal history within the substrate and in different locations inside the thick deposit when the additive manufacturing process took place. It is validated by thermal measurements and by a direct correlation between the observed microstructure and the microstructures associated with the thermal

history.

- Morphological features (i.e. shape, size) of the melt pool and the HAZ within the substrate can be computed from the simulation. A validation is provided by the optical microscopic inspections.
- A point within the deposit undergoes successive remelting stages before a final solidification which is followed by a PIA with a variable duration. High heating rates during laser processing lead to the right shift of transformation points including $\beta_{transus}$ and solidus.
- High cooling rates that are also achieved during laser processing promote martensitic transformation, with an M_s. point set around 1073 K. A certain amount of the parent β phase can be retained during the martensitic transformation, because the transformation end point (M_f) is not reached.
- The martensitic α′ phase, which undergoes a rapid increase in temperature during the process, should not be reverted into β but will be subjected to an annealing corresponding to a decomposition phenomenon.
- At room temperature, a mixed matrix composed of several phases is formed, which exhibit a homogeneous macroscopic hardness.

Knowledge of the thermal history in different areas of the deposit can help to better understand the observed final microstructure. At the same time, it becomes possible to predict the microstructure and its evolution (i.e. the nature and grain size of the phases). The present qualitative approach was a mandatory step before the ongoing extension that will provide quantitative results by using the thermo-metallurgical model. Furthermore, once extended to the thermo-mechanical analysis, the model will offer interesting perspectives in different areas, including the improvement of manufacturing process parameters, the prediction of deformation and the determination of residual stresses within the final part.

Acknowledgments

References

[1] G.W. Rodney Boyer, Materials Properties Handbook: Titanium Alloys, Materials Park, OH, ASM International, 1994.
[2] M. Vanderhasten, L. Rabet, B. Verlinden, Ti-6Al-4V: deformation map and modelisation of tensile behaviour, Mater. Des. 29 (6) (2008) 1090–1098, http://dx.doi.org/10.1016/j.matdes.2007.06.005.
[3] H. Paydas, A. Mertens, R. Carrus, J. Lecomte-Beckers, Tchuindjang J. Tchoufang, Laser cladding as repair technology for Ti-6Al-4V alloy: influence of building strategy on microstructure and hardness, Mater. Des. 85 (2015 Nov 15) 497–510, http://dx.doi.org/10.1016/j.matdes.2015.07.035.
[4] M. Alimardani, E. Toyserkani, J.P. Huissoon, C.P. Paul, On the delamination and crack formation in a thin wall fabricated using laser solid freeform fabrication process: an experimental-numerical investigation, Opt. Lasers Eng. 47 (11) (2009 Nov) 1160–1168, http://dx.doi.org/10.1016/j.optlaseng.2009.06.010.
[5] E. Toyserkani, A. Khajepour, S. Corbin, 3-D finite element modeling of laser cladding by powder injection: effects of laser pulse shaping on the process, Opt. Lasers Eng. 41 (6) (2004 Jun) 849–867, http://dx.doi.org/10.1016/S0143-8166(03)00063-0.
[6] M. Alimardani, E. Toyserkani, J.P. Huissoon, A 3D dynamic numerical approach for temperature and thermal stress distributions in multilayer laser solid freeform fabrication process, Opt. Lasers Eng. 45 (12) (2007 Dec) 1115–1130, http://dx.doi.org/10.1016/j.optlaseng.2007.06.010.
[7] J. Yang, S. Sun, M. Brandt, W. Yan, Experimental investigation and 3D finite element prediction of the heat affected zone during laser assisted machining of Ti6Al4V alloy, J. Mater. Process. Technol. 210 (15) (2010 Nov 19) 2215–2222, http://dx.doi.org/10.1016/j.jmatprotec.2010.08.007.
[8] P. Peyre, P. Aubry, R. Fabbro, R. Neveu, A. Longuet, Analytical and numerical modelling of the direct metal deposition laser process, J. Phys. D. Appl. Phys. 41 (2) (2008) 025403, , http://dx.doi.org/10.1088/0022-3727/41/2/025403.
[9] J. Gockel, J. Beuth, K. Taminger, Integrated control of solidification microstructure and melt pool dimensions in electron beam wire feed additive manufacturing of Ti-6Al-4V, Addit. Manuf. 1–4 (2014 Oct) 119–126, http://dx.doi.org/10.1016/j.addma.2014.09.004.
[10] V.D. Fachinotti, A. Cardona, B. Baufeld, O. Van der Biest, Finite-element modelling of heat transfer in shaped metal deposition and experimental validation, Acta Mater. 60 (19) (2012 Nov) 6621–6630, http://dx.doi.org/10.1016/j.actamat.2012.08.031.
[11] J. Romano, L. Ladani, J. Razmi, M. Sadowski, Temperature distribution and melt geometry in laser and electron-beam melting processes — a comparison among common materials, Additive Manufacturing 8 (2015 Oct) 1–11, http://dx.doi.org/10.1016/j.addma.2015.07.003.
[12] M. Labudovic, D. Hu, R. Kovacevic, A three dimensional model for direct laser metal powder deposition and rapid prototyping, J. Mater. Sci. 38 (1) (2003) 35–49, http://dx.doi.org/10.1023/A:1021153513925.
[13] L. Wang, S. Felicelli, Y. Gooroochurn, P.T. Wang, M.F. Horstemeyer, Optimization of the LENS® process for steady molten pool size, Mater. Sci. Eng. A, 474 (1) (2008) 148–156, http://dx.doi.org/10.1016/j.msea.2007.04.119.
[14] A. Zinoviev, O. Zinovieva, V. Ploshikhin, V. Romanova, R. Balokhonov, Evolution of grain structure during laser additive manufacturing. Simulation by a cellular automata method, Mater. Des. 106 (2016 Sep 15) 321–329, http://dx.doi.org/10.1016/j.matdes.2016.05.125.
[15] R.B. Patil, V. Yadava, Finite element analysis of temperature distribution in single metallic powder layer during metal laser sintering, Int. J. Mach. Tools Manuf. 47 (7) (2007) 1069–1080, http://dx.doi.org/10.1016/j.ijmachtools.2006.09.025.
[16] T.H.C. Childs, C. Hauser, M. Badrossamay, Mapping and modelling single scan track formation in direct metal selective laser melting, CIRP Ann. Manuf. Technol. 53 (1) (2004) 191–194, http://dx.doi.org/10.1016/S0007-8506(07)60676-3.
[17] J. Yin, H. Zhu, L. Ke, W. Lei, C. Dai, D. Zuo, Simulation of temperature distribution in single metallic powder layer for laser micro-sintering, Comput. Mater. Sci. 53 (1) (2012 Feb) 333–339, http://dx.doi.org/10.1016/j.commatsci.2011.09.012.
[18] M. Chiumenti, M. Cervera, A. Salmi, C. Agelet de Saracibar, N. Dialami, K. Matsui, Finite element modeling of multi-pass welding and shaped metal deposition processes, Comput. Methods Appl. Mech. Eng. 199 (37–40) (2010 Aug 1) 2343–2359, http://dx.doi.org/10.1016/j.cma.2010.02.018.
[19] J. Ding, P. Colegrove, J. Mehnen, S. Ganguly, P.M. Sequeira Almeida, F. Wang, et al., Thermo-mechanical analysis of wire and arc additive layer manufacturing process on large multi-layer parts, Comput. Mater. Sci. 50 (12) (2011 Dec) 3315–3322, http://dx.doi.org/10.1016/j.commatsci.2011.06.023.
[20] A. Lundback, L.E. Lindgren, Modelling of metal deposition, Finite Elem. Anal. Des. 47 (10) (2011 Oct) 1169–1177, http://dx.doi.org/10.1016/j.finel.2011.05.005.
[21] A. Hussein, L. Hao, C. Yan, R. Everson, Finite element simulation of the temperature and stress fields in single layers built without-support in selective laser melting, Mater. Des. 52 (2013 Dec) 638–647, http://dx.doi.org/10.1016/j.matdes.2013.05.070.
[22] L. Wang, S.D. Felicelli, P. Pratt, Residual stresses in LENS-deposited AISI 410 stainless steel plates, Mater. Sci. Eng. A 496 (1) (Nov 25 2008) 234–241, http://dx.doi.org/10.1016/j.msea.2008.05.044.
[23] C. Li, Y. Wang, H. Zhan, T. Han, B. Han, W. Zhao, Three-dimensional finite element analysis of temperatures and stresses in wide-band laser surface melting processing, Mater. Des. 31 (7) (2010 Aug) 3366–3373, http://dx.doi.org/10.1016/j.matdes.2010.01.054.
[24] S.M. Kelly, Thermal and Microstructure Modeling of Metal Deposition Processes With Application to Ti-6Al-4V, Virginia Tech., 2004 Doctoral dissertation https://theses.lib.vt.edu/theses/available/etd-11242004-211009/.
[25] C. Charles Murgau, R. Pederson, L.E. Lindgren, A model for Ti-6Al-4V microstructure evolution for arbitrary temperatures changes, Model. Simul. Mater. Sci. Eng. 20 (2012) 1–23, http://dx.doi.org/10.1088/0965-0393/20/5/055006.
[26] A. Crespo, R. Vilar, Finite element analysis of the rapid manufacturing of Ti-6Al-4V parts by laser powder deposition, Scr. Mater. 63 (1) (2010 Jul) 140–143, http://dx.doi.org/10.1016/j.scriptamat.2010.03.036.
[27] J. Ahn, E. He, L. Chen, R.C. Wimpory, J.P. Dear, C.M. Davies, Prediction and measurement of residual stresses and distortions in fibre laser welded Ti-6Al-4V considering phase transformation, Mater. Des. 115 (2017) 441–457, http://dx.doi.org/10.1016/j.matdes.2016.11.078.
[28] F. Weng, C. Chen, H. Yu, Research status of laser cladding on titanium and its alloys: a review, Mater. Des. 58 (2014 Jun) 412–425, http://dx.doi.org/10.1016/j.matdes.2014.01.077.
[29] S.K. Everton, M. Hirsch, P. Stravroulakis, R.K. Leach, A.T. Clare, Review of in-situ process monitoring and in-situ metrology for metal additive manufacturing, Mater. Des. 95 (2016 Apr 5) 431–445, http://dx.doi.org/10.1016/j.matdes.2016.01.099.
[30] L. Kaiping, A.M. Habraken, H. Bruneel, 2nd international conference on numerical simulation of 3-D sheet metal forming processes. Simulation of square-cup deep-drawing with different finite elements, J. Mater. Process. Technol. 50 (1) (1995) 81–91, http://dx.doi.org/10.1016/0924-0136(94)01371-7.
[31] S. Casotto, F. Pascon, A.M. Habraken, S. Bruschi, Thermo-mechanical-metallurgical model to predict geometrical distortions of rings during cooling phase after ring rolling operations, Int. J. Mach. Tools Manuf. 45 (6) (2005 May) 657–664, http://dx.doi.org/10.1016/j.ijmachtools.2004.10.007.
[32] F. Pascon, A.M. Habraken, Finite element study of the effect of some local defects on the risk of transverse cracking in continuous casting of steel slabs, Comput. Methods Appl. Mech. Eng. 196 (21–24) (2007 Apr 1) 2285–2299, http://dx.doi.org/10.1016/j.cma.2006.07.017.
[33] C.F. Guzman, J. Gu, J. Duflou, H. Vanhove, P. Flores, A.M. Habraken, Study of the geometrical inaccuracy on a SPIF two-slope pyramid by finite element simulations, Int. J. Solids Struct. 49 (25) (2012 Dec 1) 3594–3604, http://dx.doi.org/10.1016/j.

141

ijsolstr.2012.07.016.

[34] J.I.V. de Sena, C.F. Guzman, L. Duchene, A.M. Habraken, R.A.F. Valente, R.J. Alves de Sousa, Numerical simulation of a conical shape made by single point incremental, in: J.W. Yoon, T.B. Stoughton, B. Rolfe, J.H. Beynon, P. Hodgson (Eds.), AIP Conference Proceedings, 1567 (1) 2013 December, pp. 852–855. AIP http://dx.doi.org/10.1063/1.4850104.

[35] V. Tuninetti, G. Gilles, O. Milis, T. Pardoen, A.M. Habraken, Anisotropy and tension-compression asymmetry modeling of the room temperature plastic response of Ti-6Al-4V, Int. J. Plast. 67 (2015 Apr) 53–68, http://dx.doi.org/10.1016/j.ijplas.2014.10.003.

[36] Y.Y. Zhu, S. Cescotto, Unified and mixed formulation of the 8-node hexahedral elements by assumed strain method, Comput. Methods Appl. Mech. Eng. 129 (1) (1996) 177–209, http://dx.doi.org/10.1016/0045-7825(95)00835-7.

[37] T. Belytschko, L.P. Bindeman, Assumed strain stabilization of the 4-node quadrilateral with 1-point quadrature for nonlinear problems, Comput. Methods Appl. Mech. Eng. 88 (3) (1991) 311–340, http://dx.doi.org/10.1016/0045-7825(91)90093-L.

[38] L. Duchene, F. El Houdaigui, A.M. Habraken, Length changes and texture prediction during free end torsion test of copper bars with FEM and remeshing techniques, Int. J. Plast. 23 (8) (2007 Aug) 1417–1438, http://dx.doi.org/10.1016/j.ijplas.2007.01.008.

[39] J.C. Simo, T.J.R. Hughes, On the variational foundations of assumed strain methods, J. Appl. Mech. 53 (1) (1986 Mar 1) 51–54, http://dx.doi.org/10.1115/1.3171737.

[40] J. Goldak, A. Chakravarti, M. Bibby, A new finite element model for welding heat sources, Metallurgical Transactions B15 (2) (1984) 299–305, http://dx.doi.org/10.1007/BF02667333.

[41] V. Neela, A. De, Three-dimensional heat transfer analysis of LENSTM process using finite element method, Int. J. Adv. Manuf. Technol. 45 (9) (2009) 935–943, http://dx.doi.org/10.1007/s00170-009-2024-9.

[42] N. Contuzzi, S.L. Campanelli, A.D. Ludovico, 3D finite element analysis of selective laser melting process, International Journal of Simulation Modelling (IJSIMM) 10 (3) (2011 Sep) 113–121, http://dx.doi.org/10.2507/IJSIMM10(3)1.169.

[43] P. Michaleris, Modeling metal deposition in heat transfer analyses of additive manufacturing processes, Finite Elem. Anal. Des. 86 (2014 Sep 1) 51–60, http://dx.doi.org/10.1016/j.finel.2014.04.003.

[44] C.A. de Saracibar, A. Lundback, M. Chiumenti, M. Cervera, Shaped metal deposition processes, Encyclopedia of Thermal Stresses, Springer Netherlands, 2014, pp. 4346–4355, , http://dx.doi.org/10.1007/978-94-007-2739-7_808.

[45] A. Mertens, S. Reginster, H. Paydas, Q. Contrepois, T. Dormal, O. Lemaire, et al., Mechanical properties of alloy Ti-6Al-4V and of stainless steel 316L processed by selective laser melting: influence of out-of-equilibrium microstructures, Powder Metall. 57 (3) (2014 Jul 1) 184–189, http://dx.doi.org/10.1179/1743290114Y.

0000000092.

[46] K.C. Mills, Ti: Ti-6 Al-4 V (IMI 318). Recommended Values of Thermophysical Properties for Selected Commercial Alloys, Woodhead Publishing Series in Metals and Surface Engineering, Woodhead Publishing, 978-1-85573-569-9, 2002, pp. 211–217.

[47] L. Wang, S. Felicelli, Analysis of thermal phenomena in LENS deposition, Mater. Sci. Eng. A 435–436 (2006 Nov 5) 625–631, http://dx.doi.org/10.1016/j.msea.2006.07.087.

[48] M.F. Gouge, J.C. Heigel, P. Michaleris, T.A. Palmer, Modeling forced convection in the thermal simulation of laser cladding processes, Int. J. Adv. Manuf. Technol. 79 (1) (2015) 307–320, http://dx.doi.org/10.1007/s00170-015-6831-x.

[49] D. Basak, W.J. Boettinger, D. Josell, S.R. Coriell, J.L. McClure, S. Krishnan, A. Cezairliyan, Effect of heating rate and grain size on the melting behavior of the alloy Nb-47 mass% Ti in pulse-heating experiments, Acta Mater. 47 (11) (1999) 3147–3158, http://dx.doi.org/10.1016/S1359-6454(99)00191-3.

[50] M. Qian, W. Xu, M. Brandt, H.P. Tang, Additive manufacturing and postprocessing of Ti-5Al-4V for superior mechanical properties, Materials Research Society 41 (2016) 775–783, http://dx.doi.org/10.1557/mrs.2016.215.

[51] T. Ahmed, H.J. Rack, Phase transformations during cooling in alpha and beta titanium alloys, Mater. Sci. Eng. A 243 (1–2) (1998 Mar 15) 206–211, http://dx.doi.org/10.1016/S0921-5093(97)00802-2.

[52] X. Tan, Y. Kok, Y.J. Tan, G. Vastola, Q.X. Pei, G. Zhang, Y.W. Zhang, S.B. Tor, K.F. Leong, C.K. Chua, An experimental and simulation study on build thickness dependent microstructure for electron beam melted Ti-6Al-4V, J. Alloys Compd. 646 (2015) 303–309, http://dx.doi.org/10.1016/j.jallcom.2015.05.178.

[53] S. Neelakantan, P.E.J. Rivera-Díaz-del-Castillo, S. van der Zwaag, Prediction of the martensite start temperature for β titanium alloys as a function of composition, Scr. Mater. 60 (8) (2009) 611–614, http://dx.doi.org/10.1016/j.scriptamat.2008.12.034.

[54] W. Xu, M. Brandt, S. Sun, J. Elambasseril, Q. Liu, K. Latham, ... M. Qian, Additive manufacturing of strong and ductile Ti-6Al-4V by selective laser melting via in situ martensite decomposition, Acta Mater. 85 (2015) 74–84, http://dx.doi.org/10.1016/j.actamat.2014.11.028.

[55] M.T. Jovanović, S. Tadić, S. Zec, Z. Mišković, I. Bobić, The effect of annealing temperatures and cooling rates on microstructure and mechanical properties of investment cast Ti-6Al-4V alloy, Mater. Des. 27 (3) (2006) 192–199, http://dx.doi.org/10.1016/j.matdes.2004.10.017.

[56] P.E. Markovsky, S.L. Semiatin, Tailoring of microstructure and mechanical properties of Ti-6Al-4V with local rapid (induction) heat treatment, Mater. Sci. Eng. A 528 (7) (2011) 3079–3089, http://dx.doi.org/10.1016/j.msea.2010.12.002.

[57] R. Pederson, Microstructure and Phase Transformation of Ti-6Al-4V, Licentiate Thesis, 30 Luleå University of Technology, 2002 ISSN 1402-1757 http://epubl.ltu.se/1402-1757/2002/30/.

.. Article #8

Table of contents

Nomenclature

Phase types

α	Alpha phase
α-case	Oxygen enriched layer within Alpha phase
α'	Martensite
β	Beta phase
$\alpha + \beta$	Complex dual structure made of Alpha and Beta phases
$\alpha\beta_C$	Alpha/Beta with colony morphology
$\alpha\beta_W$	Alpha/Beta Widmanstätten, having a basket-weave morphology
α_{GB}	Alpha grain boundary formed prior to intragranular α or $\alpha\beta_W$
α_m	Alpha massive formed at grain boundaries, prior to intragranular martensite.
α_P	Primary Alpha phase present in the bimodal structure
$\beta_{retained}$, β_{ret}	Fraction of untransformed parent β phase

Transition points

Liquidus	1660°C, end of the melting for the solid (heating), or onset of solidification for the melt (cooling)
Solidus	1590°C in equilibrium conditions, onset of the melting for the solid (heating) or the end of solidification for the melt (cooling)
$\alpha_{transus}$, α_{tr} or $T_{Dissolution}$ T_{Diss}	708°C, onset of $\alpha \rightarrow \beta$ or end of $\beta \rightarrow \alpha$ reactions under quasi equilibrium conditions. α phase starts to dissolve from this point during heating stage
$\alpha'_{transus}$, α'_{tr}	Onset of $\alpha \rightarrow \beta$ and $\alpha' \rightarrow \beta$ transformation for quick heating rate
$\beta_{transus}$, β_{tr}	980°C, end of $\alpha \rightarrow \beta$ or onset of $\beta \rightarrow \alpha$ transformations under quasi equilibrium conditions
$\beta'_{transus}$, β'_{tr}	$> \beta_{tr}$, onset of $\alpha \rightarrow \beta$ transformation during quick heating, the same point is also considered for $\alpha' \rightarrow \beta$.
$M_{s,\alpha m}$	893°C onset of $\beta \rightarrow \alpha_m$ transformation for cooling rate ranging between 410 and 20°C/s
$M_{f,\alpha m}$	End of $\beta \rightarrow \alpha_m$ transformation (very close to $M_{s,\alpha m}$)
$M_{s,\alpha'}$	800°C onset of $\beta \rightarrow \alpha'$ transformation for rapid cooling >20°C/s
$M_{f,\alpha'}$	612°C end of $\beta \rightarrow \alpha'$ transformation for rapid cooling >20°C/s
β_s	Onset of $\alpha' \rightarrow \beta$ transformation during a steep heating
β_f	End of the displacive $\alpha' \rightarrow \beta$ transformation during steep heating.

Key temperatures, temperature rates and times

$\dot{T}$	Average heating rate between T_{min} and T_{max} on the rising section of the heating curve, for the first peak of TTB3. (°C/s)
$\|\dot{T}\|$	Average cooling rate between T_{max} and T_{min} on the decreasing section of the cooling curve, for the single peak of TTB1 or for the second peak of TTB3 (°C/s)
$\|\dot{T}\|_{inst,4}$	Instantaneous cooling rate calculated during final slow down cooling stage within TTB4 (°C/s)
$T_{start,\ 4}$	Starting or maximum peak temperature for the slow down cooling stage related to TTB4 (°C)
$T_{crit,\ 4}$	First temperature at which $\|\dot{T}\|_{inst,4}$ falls below the critical cooling rate of 20°C/s (°C)

2/

T_{max}	Maximum temperature at the starting point for the fast cooling stage within TTB1 (single peak), or the maximum temperature achieved during the fast heating stage within TTB3 among the two existing peaks (°C)
T_{min}	Minimum temperature corresponding to the end point for the fast cooling stage within TTB1 (single peak), or minimum temperature achieved during the fast cooling stage within TTB3for the second of the two existing peaks (°C)
T_{mean}	Average temperature over the total length of pseudo-isothermal cycle (only for TTB2) (°C)
T_{peak}	Maximum temperature achieved for any steep heating occurring during TTB0, TTB2 and TTB3 (°C)
t_0	Time at which the deposition within a given POI begins (s)
$t_{1\%}$, $t_{50\%}$	Respectively the incubation and half the progress reaction times to achieve isothermal transformation $\beta \rightarrow \alpha\beta_W$ within TTB2
t_{start}, t_{end}	Respectively the start and the end times for average temperature (T_{mean}) used on the pseudo isothermal plateau within TTB2

Other features

POI1, 2 or 3	Points of interest 1, 2 or 3
TTB1 to TTB4	Time-phase-Transformation-Block 1, 2, 3 or 4
^{a,b,c}TTBi	a, b and c identifies the more relevant peak within TTBi as its related phase transformations remain in the final stage
α_i, $\alpha_{m,i}$, α'_i, $\alpha\beta_{W,i}$, β_i, $\beta_{ret,i}$	Index i identifies the related TTBi when the phase is formed

Glossary

AM	Additive manufacturing
CCR	Critical cooling rate
CCT	Continuous cooling transformations
CHR	Critical heating rate
CHT	Continuous heating transformations
CTL	Constant track length
DDfT	Direct diffusive transformation
DDsT	Direct displacive transformation
DED	Directed energy deposition
DTL	Decreasing track length
EBDT	Element birth and death technique
FE	Finite element
HAZ	Heat affected zone
IE	Incident energy
IT	Isothermal transformation
JMAK	Johnson-Mehl-Avrami & Kolmogorov
KM	Koistinen-Marburger
LM	Light microscopy
PBF	Powder bed fusion
RDfT	Reverse diffusive transformation
RDsT	Reverse displacive transformation
SEM	Scanning electron microscopy
STH	Simulated thermal history
TTB	Time-phase-Transformation-Block
TTT	Time-Temperature-Transformations
VH	Vickers Hardness

4/

A New Concept for Modeling Phase Transformations in Ti6Al4V alloy manufactured by Directed Energy Deposition

J. T. Tchuindjang[a]*, H. Paydas[a], H-S. Tran[b], R. Carrus[c], L. Duchêne[b], A. Mertens[a], A.-M. Habraken[b,d]

[a]A&M, MMS, University of Liège, Quartier Polytech 1, Allée de la Découverte 9 (B52), B-4000 Liège, Belgium
[b]UEE, MSM, University of Liège, Quartier Polytech 1, Allée de la Découverte 9 (B52), B-4000 Liège, Belgium
[c]Sirris Research Centre (Liège), Rue Bois Saint-Jean 12, B-4102 Seraing, Belgium
[d]F.R.S-FNRS Fund for Scientific Research, rue d'Egmont 5, B-1000 Bruxelles, Belgium

*Corresponding author: J.Tchuindjang@uliege.be

Abstract

The new concept of Time-phase-Transformation-Block (TTB) aims to correlate the thermal histories computed by a Finite Element model and the final microstructure of a multilayered Ti6Al4V alloy obtained from Directed Energy Deposition (DED). This approach adapts Continuous Heating Transformations (CHT), Continuous Cooling Transformations (CCT) and Time-Temperature-Transformations (TTT) diagrams to better account for the ultra-fast heating and cooling rates and the local variations of thermal histories typical of DED. Based on experiments and a state-of-the-art review, a flowchart summarizes the conditions for the occurrence of solid-state phase transformations, whether they occur by displacive or diffusive mechanisms. This approach represents a necessary prerequisite towards the accurate numerical prediction of microstructural evolution during DED based on computed thermal histories.

Keywords

Directed Energy deposition; Microscopy and microanalysis techniques; Titanium alloys; Phase transformation kinetics; Experimental validation

1. Introduction

Understanding the mechanisms that trigger phase transformations during Additive Manufacturing (AM) remains a major issue, as the final microstructure strongly influences the mechanical properties. Numerous studies have investigated the influence of processing parameters on the melt pool temperature and geometry [1–6], the solidification modes [1,2,6–10], the grain size and texture [3,5,7–9,11–13], as well as internal defects and distortions [1,6,10–12,14,15]. On another level, few studies have focused on the in-situ monitoring of AM processing parameters to control the temperature of the melt pool or to prevent internal defects as porosities or cracks [16–18]. However, these approaches centered on macroscopic properties of AM parts neglect the understanding of the microstructure genesis during manufacturing. Attempts have also been made to optimize the microstructure of as-built AM parts, by heat treatments, changes in chemical composition, or by combining rolling deformation with the chosen AM process. However the improvements of the final properties remain questionable [2,3,8,12,19–22]. In fact, each AM process produces different phases in type, morphology and volume fraction [1,7,8,13,20,23–26]. Those microstructures lead to distinct mechanical properties that can be potentially improved by post heat treatments [1,5,7,8,10,14,20,23–25,27–

5/

29]. Nevertheless, none of these approaches focuses on the accurate prediction and control of microstructural evolution during AM.

Analytical approaches and Finite Element (FE) simulations, on the other hand, can predict macroscopic features, internal flaws, residual stresses and microstructures [4,11,14,15,29–33]. FE macroscopic models used on their own or associated with Cellular Automaton (CA) model can predict the thermal history, the melt pool geometry and the grain size and morphology during AM. CA is for instance used for 3D β-grain solidification simulation [34–36]. However, for subsequent solid phase transformations, this approach remains irrelevant. Existing kinetic models consider fixed transition points and ignore the effect of thermal gradient strongly influencing both the mechanism and the kinetics of transformations (see literature review **section 2**). Several works based on the partial exploitation of simulated thermal histories during the solidification or the final cooling stages can be found, but almost none of them are dealing with the evolution of the microstructure during AM [9,11,14,24,30,32,33,37].

In Ti6Al4V alloy, the process parameters, the temperature and the microstructure evolution have already been correlated for welding and laser hardening processes [4,15,32,33,38–42]. However these cases are characterized by single cycle and high incident energies (IE) leading to low thermal gradients [19,24,33,38,39,41,43] while AM processes face complex cycles with lower IE and higher thermal gradients [11,30,31,44–46]. A macroscopic model to determining the influence of processing parameters on both density and mechanical properties, was established for instance by [47], however it is not suitable for the prediction of microstructure evolution during AM.

The first trials of "replicated" thermal histories of AM were obtained by resistive heating and air cooling, thus leading to relatively slow heating and cooling rates [9,48,49] which is still far away from the steep thermal gradients achieved in AM [4,5,7,39,40,44,45]. Besides, there is currently no consensus on the values of the critical cooling rates, or on the transition points for the displacive martensite transformation and the diffusion-like $\beta \rightarrow \alpha$ transformation upon cooling [4,11,33,39,45,50–53]. Similarly, a fixed value of $\beta_{transus}$ is often used for the completion of reverse transformation during heating regardless of the heating rate $\dot{T}$ [1,11,15,32,33,37,39,40,43,45,49–51,54]. The recent work by Liu and Shin [36] combines multi-physics models to predict grain size and orientation, and phase distributions in single layer DED deposit. In this study, macro and microstructures in the fusion zone and Heat affected zone (HAZ) are compared, but not the evolution of the microstructure. The phase amount is validated based on the rules of mixtures yielding the overall hardness. However, hardness prediction seems of poor accuracy as shown in **subsection 2.4**. To the author's knowledge, there is currently no model taking into account the effect of $\dot{T}$ on either the mechanism or the kinetics of reverse transformations $\alpha/\alpha' \rightarrow \beta$. In many studies, martensitic transformation is simply ignored during simulations [30,31,42,45], and when the final microstructure appears complex, an accurate validation based on precise microstructural characterization is often lacking [15,31,33,36,37,40,41,45,49–53].

Experimental studies and numerical simulations of AM processes remain too often separated, preventing a correct understanding of the microstructural evolution during manufacturing [46]. Relying on extensive experimental work and a careful literature review on the mechanisms that trigger solid phase transformations in Ti6Al4V alloy, this study defines a clear flowchart and quantitative threshold values to improve phase predictions by FE simulations. The state-of-the-art is reviewed in **section 2. Section 3** describes the experiments reminds the used FE thermal model [5,44]. **Section 4** is devoted to new results, i.e. simulated thermal curves within three points of interest (POI). The paper novelty is introduced in **section 5** where the new tool for microstructure prediction, the **T**ime-phase-**T**ransformation-**B**lock (TTB) concept is described and applied on three Points Of Interest (POIs) of the experiment sample. A graphical synthesis

6/

allowing any interested reader to exploit the concept of TTB is provided at the end of **section 5** prior to drawing the main conclusions (**section 6**).

2. Solid phase transformation mechanisms and kinetics – state of the art

Hereafter, the specific metallurgical phenomena associated to the steep thermal gradients experienced during AM are highlighted. The focus is on the phase transformations in the solid state more than on the solidification and remelting sequences. A distinction is made between non-isothermal and isothermal transformations. For the former ones, both heating and cooling modes are considered, while for the isothermal transformations, the focus is on the holding temperature and duration.

In addition, the hardness values reported on Ti6Al4V in different metallurgical states are reminded, to highlight the limits in the interpretation of this parameter for characterizing the microstructure. Moreover, current kinetic models are reviewed showing that to apply them as such to AM is inappropriate.

2.1 Continuous heating transformations

If the starting phase is α, the beginning and end points of the reverse transformation into β, referred to as $\alpha_{transus}$ and $\beta_{transus}$, will increase with $\dot{T}$ [33,42,48,55]. For instance shifts of 169°C and 190°C above the "equilibrium $\beta_{transus}$" have been found for $\dot{T}$ of 43°C/s and 100°C/s respectively, to achieve complete transformation into β upon heating [22,42]. Diffusion of V from α into β is reported to control the kinetics of this phase transformation, inducing changes in the lattice parameters of the two phases [22,23,27,40,55]. In addition, any β retained at low temperature will remain untransformed upon heating.

If the starting phase is α', a steep increase of the temperature leads to a **R**everse **Dis**placive **T**ransformation (RDsT) α'$\rightarrow \beta$ before the remelting of β above the liquidus [2,56]. No diffusion occurs, the parent phase remains supersaturated up to complete transformation into β. This statement fits with the observation by Kenel et al. [56] that ultra-high heating rates result in the highest rate of expansion of the lattice parameter in the α' phase (left-hand side of Fig. 1). However at lower heating rates, a high mobility of substitutional alloying elements promotes **R**everse **Dif**fusive **T**ransformation (RDfT) in Ti6Al4V [22]. It is thus assumed that α'$\rightarrow \beta$ reverse transformation is displacive (RDsT) above a critical heating rate (CHR) $\dot{T}$ of 20°C/s and diffusive (RDfT) below this CHR. For RDfT the following sequence is achieved: α'$\rightarrow \alpha$ (+β) $\rightarrow \beta$. Note that the beginning and the end of the RDsT, called β_s [57] and β_f (Fig. 1), are distinct from $\beta_{transus}$. The driving force for the RDfT of α' is controlled by V diffusion [3,23,27], which also depends on $\dot{T}$. Both the onset and the endset of diffusional α'/$\alpha \rightarrow \beta$ transformation, referred to as α'$_{transus}$ and β'$_{transus}$ respectively, will increase with $\dot{T}$. Note that β'$_{transus}$ is higher than the equilibrium $\beta_{transus}$. The decrease in the expansion rate of the α' lattice at lower heating rates (bottom of Fig. 1) is assumed to correspond to the desaturation of the martensite lattice [3,56].
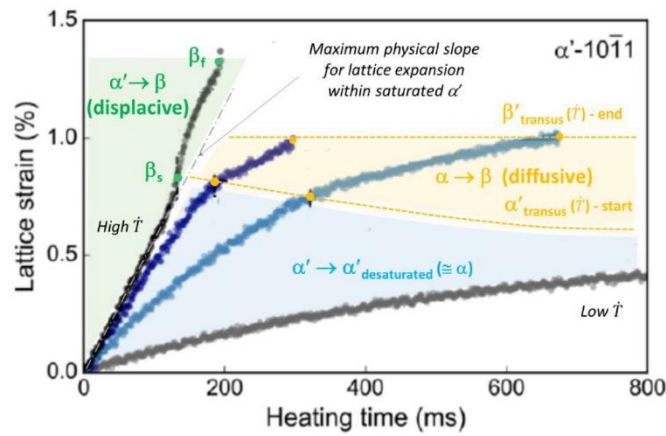
Figure 1: Influence of heating rate ($\dot{T}$) on the mechanism and transition points of the reverse transformations of α', as given by the lattice parameter evolution (adapted from [56]).

2.2 Continuous cooling transformations

Phase transformations under continuous cooling conditions are usually represented by CCT diagrams that depend on the specific alloy and the applied solution treatment. In this regard, there are very few CCT diagrams for Ti6Al4V [1,29,32,49,52,58], and most of them are linked to one among the following two examples.

In 1998, the CCT diagram (Fig. 2) established by [58] corresponds to a simple sketch, for which extended experimental validations are still missing. The fields for the various phases are incompletely defined: only the starting points of the phase transformations are illustrated, while the end points are not shown. Moreover, the clear separation between the fields related to α_m and α' suggests that these two phases may be distinctly formed [49]. The $M_{s,\alpha'}$ temperature associated with the martensitic transformation of the β phase seems too low, according to later publications as reported hereafter.
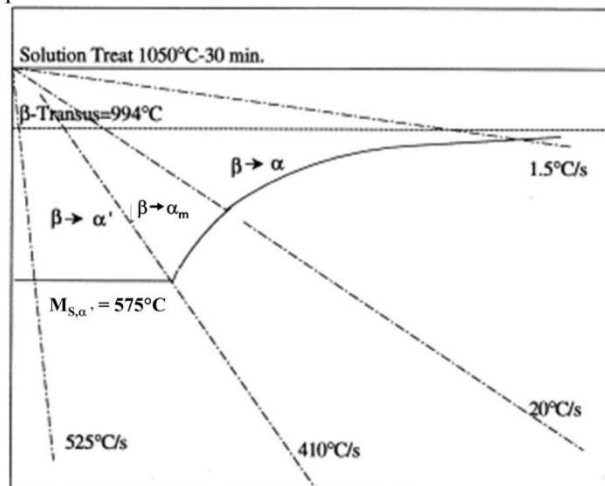

Figure 2: Schematic CCT diagram with only the starting points of the transformations of parent β phase and their related critical cooling rates $|\dot{T}|$. The apparent variation of starting temperatures for both α_m and α phases with $|\dot{T}|$, and the non-dependence of this same point for α' with $|\dot{T}|$, suggest a DDfT and DDsT respectively, for the related transformation products (adapted from [58]).

8/

Thanks to an extended experimental validation, in 2011, the CCT diagram in Fig. 3 [52] presents both the starting and end points of the transformation for the different phases. The values related to martensitic transformation appear relevant as explained hereafter and the location of phase fields is consistent with the transformation mechanisms. When $|\dot{T}|$ increases, the $\beta_{transus}$ corresponding to the start of diffusive transformation decreases and the transformation range becomes narrower. No mention is made about $\alpha_{m.}$.
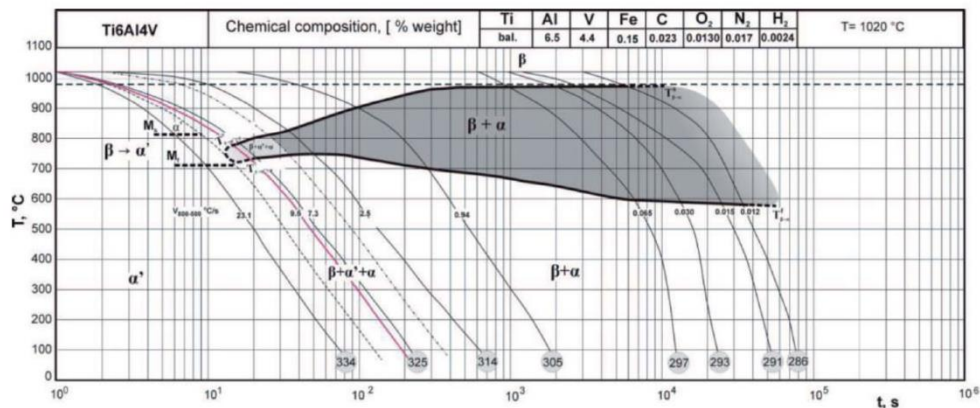

Figure 3: Experimental CCT diagram for Ti6Al4V, with both $M_{s,\alpha'}$ and $M_{f,\alpha'}$ values (from [52]).

When the starting phase is β, either **D**irect **D**iffusion **T**ransformation (DDfT) or **D**irect **D**isplacive **T**ransformation (DDsT) occurs according to $\dot{T}$ [1,29,32,36,49,52,58,59]. For $|\dot{T}|$ lower than 20°C/sec, DDfT yields an $\alpha\beta$ structure, with a basket-weave (α/β_W) or a colony morphology (α/β_C), for higher or lower $|\dot{T}|$ respectively [3,11,24,44,45,52,58,60]. The starting point of the DDfT is given by $\beta_{transus}$, which decreases from its equilibrium value with increasing $|\dot{T}|$ [48]. When the end point of the DDfT is reached, the transformation stops and a retained fraction of β remains (β_{ret}) [27,33,36,44,45,50,52]. For $|\dot{T}|$ higher than 20°C/s, the mechanism changes to DDsT generating α_m at grain boundaries, and/or α' inside β grains. The coexistence of α_m and α' occurs for 20< $|\dot{T}|$<410°C/s [1,9,32,36,39,46,49,58,61], whereas only α' is present for $|\dot{T}|$>410°C/s [2,7,19,24,32,36,39,49,58]. The start point for α_m formation (called $M_{s,\alpha m}$) is 893°C [62]. No mention exists for the end point of α_m formation. Clearly no consensus exists for the starting point $M_{s,\alpha'}$ and the end point $M_{f,\alpha'}$ of the $\beta \rightarrow \alpha'$ transformation. Their values are shown hereafter:

i) $M_{s,\alpha'}$, 575°C [15,20,32,45,58], 650°C [7,15,40,41,53,56], 780 to 851°C [1,44,52,63,64] or 915°C [11,61,65];

ii) $M_{f,\alpha'}$, 800°C [66], 710°C [52], 690°C [65], 650°C [1,64] or 400°C [53]; $M_{f,\alpha'}$ is also often assumed to be close to or lower than room temperature.

According to [67], the temperature gap between $M_{s,\alpha'}$ and $M_{f,\alpha'}$ should be small. Some amount of untransformed β_{ret} (with strongly distorted grains) remains after rapid cooling, due to high solute concentration and large undercooling [29,33,64,67–70].

2.3 Isothermal transformations

Isothermal transformation after cooling assumes a starting temperature higher than the soaking temperature and is usually linked to the parent phase β in AM of Ti6Al4V. Isothermal

9/

transformation after heating stage assumes heating up to a temperature where the sample is maintained and should be related to either α or α' as starting phases, the latter being more relevant in AM.

Usually, isothermal transformations involve an incubation time before the start of any reaction. The different stages related to both activation energies and diffusion of species are illustrated in TTT diagrams (Fig. 4a). Then starting with β, the transformation products correspond to $α_{GB}$ or $α/β_W$, both resulting from a DDfT. A DDsT yielding $α_m$ or α' should however be expected as the quenching temperature falls into the thermal range for martensitic transformation (Fig. 4b). Such a case is very often ignored [23,24,28,39,48,50,58,68], as confirmed by both simulated and experimental TTT diagrams [11,15,39,40]. To authors' knowledge, the only TTT diagram which combines DDfT and DDsT, is a sketch where no value is defined for the beginning nor the end of the transformations (see Fig. 4c) [61]. Otherwise one can find the pseudo-binary diagram, where equilibrium phases coexist with unexpected metastable phases (Fig. 4d),
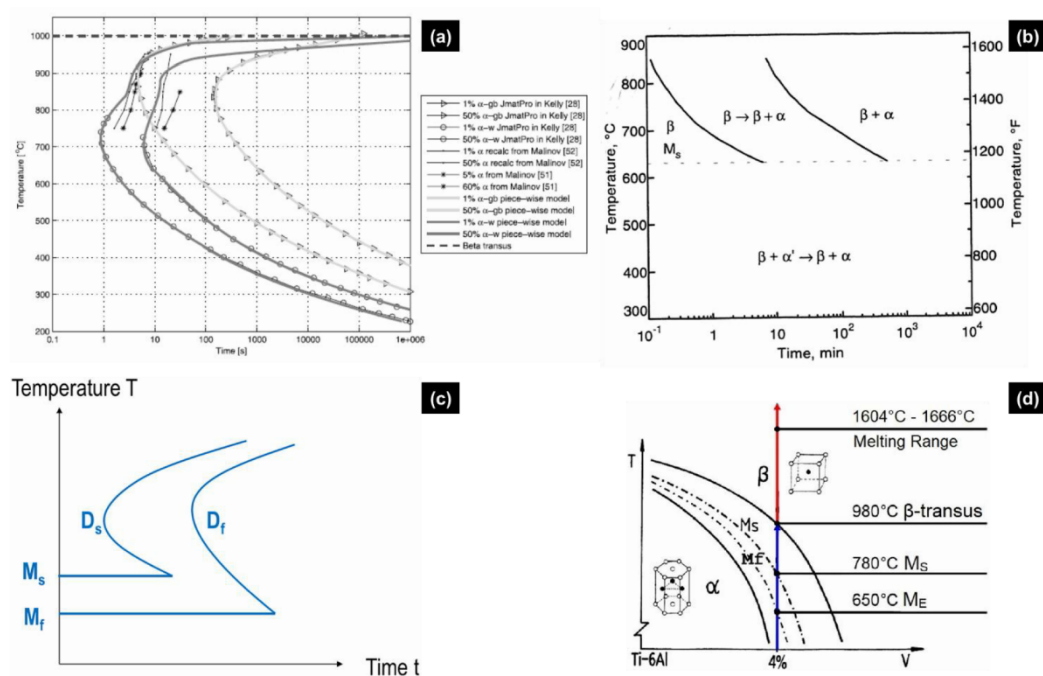

Figure 4: Examples of TTT diagrams; (a) Compilation of sparse experimental data and simulated TTT diagrams for $α_{GB}$ or $α/β_W$ resulting from the transformation of β (from [39]); (b) TTT diagram of Ti6Al4V after solution annealed at 1020°C and direct quenching to reaction temperatures showing DDfT and DDsT and Ms at 625°C (from [71]); (c) Sketch of a TTT diagram plotting both a diffusional transformation (D) and a martensitic transformation (M), with their related starting curves D_s and M_s, and the finishing curves D_f and M_f (from [61]); (d) Schematic pseudo-binary diagram of Ti6Al4V showing equilibrium metastable phase fields, with their related crystal structure and transition points (from [64]).

With α' martensite as starting phase, a decomposition that is ascribed to a diffusion controlled phenomenon occurs, which has mainly been investigated experimentally [3,7,11,20,23,27,39,44,50,58,66]. The only existing model for the decomposition of martensite is the one established by Mur et al. [66]. However, this model has several limitations discussed in **subsection 2.5**.

10/

The case relating to a mixed α+β as starting phases will not be considered here, because it is rather specific to thermomechanical treatments carried out on the conventional alloy.

2.4 Microstructures and hardness in Ti6Al4V

To see how considering only hardness measurement can be misleading to identify the phase distribution within a Ti6Al4V microstructure, a literature review is presented in Table 1 and 2. Bimodal structure seems to exhibits the lower hardness. A small increase in hardness can be achieved under stress-relief treatment when starting from martensite, provided the tempering temperature is not too high (Table 1). Conversely a decrease of both the strength and hardness is often expected from subsequent heat treatments carried out on martensite under high temperature.

Nevertheless, other features can also influence Ti6Al4V hardness processed by AM, such as the amount of interstitial elements (O, C and N) within the raw material, or contamination that is due either to inadequate storage conditions, to the reuse of powders or to poor atmospheric protection conditions during processing (Table2). These phenomena lead to a significant increase of the hardness regardless of the nature of the phases within the polluted material.

As a conclusion, different phases within Ti6Al4V may exhibit overlapping hardness values. The use of overall hardness based on rules of mixtures to validate phase amount may be inadequate, in particular if the hardness values are modified by the physicochemical and metallurgical effects mentioned above [36]. Therefore, Vickers hardness alone is not relevant for microstructure characterization of Ti6Al4V.

11/

Table 1: Literature summarizing correlations between structure hardness of Ti6Al4V, for classical manufacturing processes

Processes	Thermomechanical treatment	Macrostructure	Microstructure	Hardness range (HV)	Comments related to mechanical properties	References
Castings	Slow cooling from the melt	Coarse structure	Coarse α/β_W with large α lamellae α_P along prior β grain boundaries with α/β_W inside grains	[320 – 345]	Lower mechanical and fatigue properties Porosities	[70,72–74]
Wrought	Extensive mechanical working within (α +β) field + mill-annealed, prior to furnace cooling	Equiaxed structure	Equiaxed α grains with intergranular short-rod β Large α/β_C	[330 – 370]	Hardness scattering related to both the forging temperature and the grain size	[59,73,74]
		Bimodal structure	Granular α_P and thin intergranular α/β_W lamellae	[265 – 295]	Hardness decreases with increasing amount of α_P (HV max at 10% of α_P)	[75]
Solution Treated Quenching (STQ)	Up to 1h above $\beta_{transus}$ prior to water quenching	Needle-like	Lath and twinned α' + ($\beta_{retained}$)	[345 – 420]	Hardness increases with decreasing lath size	[59,70,72]
Ageing after STQ	Several hours between 480°C and 750°C, prior to furnace cooling	-	-	[345 – 380]		[69,70]

12/

Table 2: Literature summarizing correlations between structure hardness of Ti6Al4V, for AM processes

Processes	Incident energies (J/mm)	Macrostructure	Microstructure	Hardness range (HV)	References
DED	≤ 60		Needle-like α' + ($\beta_{retained}$)	[310 – 400]	[5,13,76]
	[165 – 480]	Columnar structure with epitaxial β grains	α' + α/β_W $\alpha/\beta_W + \alpha_{GB}$	[315 – 370]	[5,13,76]
L-PBF	[0.20 – 1.05]		α' Fine α' with acicular laths α/β_W	[320 – 400]*	[13,64,76,77]
EB-PBF	≤ 0.1		Prominent acicular α plates and β $\alpha/\beta_W + \alpha_{GB}$	[330 – 450]*	[13,24,73]

*Oxygen content increases the hardness

13/

2.5 A brief review on kinetic models and their limitations with regard to AM

Several kinetic models applied to AM processes can be found in the literature. For diffusion transformations, JMAK (Johnson-Mehl-Avrami-Kolmogorov) equation determines the amount of α lamellae within α/β_W or α/β_C structures obtained from β transformation, including incomplete reactions [39,49–51,54,78,79]. This approach has been successfully extended to the prediction of mechanical properties through the size of α lamellae [23,24,27,43].

For the martensitic transformation, the empirical KM (Koistinen-Marburger) equation is often used to predict the amount of α' resulting from very quick cooling down from the β field [4,49,53,61,79]. However, the setting of the parameters for this model is strongly dependent on the transition points $M_{s,\alpha'}$ and $M_{f,\alpha'}$, or on the critical cooling rates considered for the activation of this transformation. As already mentioned, there is no consensus on these data. In addition, Fig. 2 clearly suggests threshold functions depending on $\dot{T}$ contrarily to the threshold points for diffusion transformations that are usually constant and independent of $\dot{T}$. It is probably because of the above assumptions that the recent model developed by Baykasoglu and coworkers [49] cannot predict higher values and abrupt variations within the hardness of a thin-walled DED deposit. Furthermore, several authors decide not to integrate the martensitic transformations in their microstructural model, either because these transformations are poorly understood, or due to the discrepancy within the cooling rates that allow displacive reactions, or because of the challenge of distinguishing and quantifying α' in the presence of the α phase [43,54]. Moreover, even the very recent study by Liu & Shin [36], presents several limitations concerning the kinetic model. Firstly, the model assumes only a diffusive mechanism for the reverse transformation α → β during heating, and the related critical points are set as fixed values. Then only the CCT approach is considered for β → α/α' transformation without taking into account the possible isothermal reactions that involve either β or α' as parent phases. To the authors' knowledge, no model integrates the case of the RDsT for the heating transformation from α' phase, in the same way that no model combines both CCT and TTT approaches for solid phase reactions during cooling.

Gil & Mur [66] established a model for the decomposition of martensite upon annealing, i.e. heating up to a temperature below $\beta_{transus}$ followed by a holding time. For this model, the parameters were based on the evolution of hardness with annealing time, between a quenched martensitic and subsequent annealed states. Assuming the martensite decomposition to be similar to recrystallization, the precipitation fraction of β by-product is obtained using an Avrami-like equation.

However, the hardness of 330 HV taken as a reference for the quenched conditions seems low compared to that of the fresh martensite. In addition, for the annealed states, hardness values were not measured at the tempering temperature, but after cooling down to room temperature. As a result, an increasing trend up to 410 HV for the hardness was found with increasing annealing temperatures, thus suggesting a possible α-case [80]. Moreover, Gil & Mur [66] mention a critical $M_{f,\alpha'}$ of 800°C as a ceiling value for the tempering, which is rather known as the start point of martensitic transformation [1,44,52,63] during cooling. Therefore, this kinetic model for martensite decomposition [66] based on hardness measurements does not seem reliable.

In summary, different phases can be observed in the final microstructure of as-built Ti6Al4V AM parts, as a result of the complex thermal history achieved during manufacturing. However, only few attempts have been made to use or combine existing kinetic models to predict and validate, the presence of α, α' and possible β_{ret} at the same time. The main challenge appears to be how to simultaneously take into account the specific mechanisms governing all the phase transformations, and to simplify the thermal history to offer an efficient model coupled with FE

14/

simulations. The present paper introduces a novel concept, namely the Time-phase – Transformation – Block (see **subsection 3.4.**), referred to as TTB that will help numerical teams to select only parts of the thermal history and still keep the key thermal features governing the final microstructure.

3. Manufacturing, characterization and simulation of the samples

3.1 Material origin and processing

A 5-axis Irepa Laser cladding system equipped with a Nd-YAG laser source of maximum power 2000W was used for the sample production. The laser spot has a top-hat energy distribution with a diameter of 1400 µm. The laser power was set at 1100W, the scan speed at 400 mm/min, and the powder feed rate at 28 mg/s. A type-K thermocouple was inserted 3 mm below the base of the notch at a position corresponding to the mid-length and mid-width (Fig. 5a), in order to record the temperature as a function of time. As described in [44] the recorded thermal history is used as reference to validate the thermal model presented in **subsection 3.3**. More details on the feedstock materials and fabrication process can be found in [5,44].
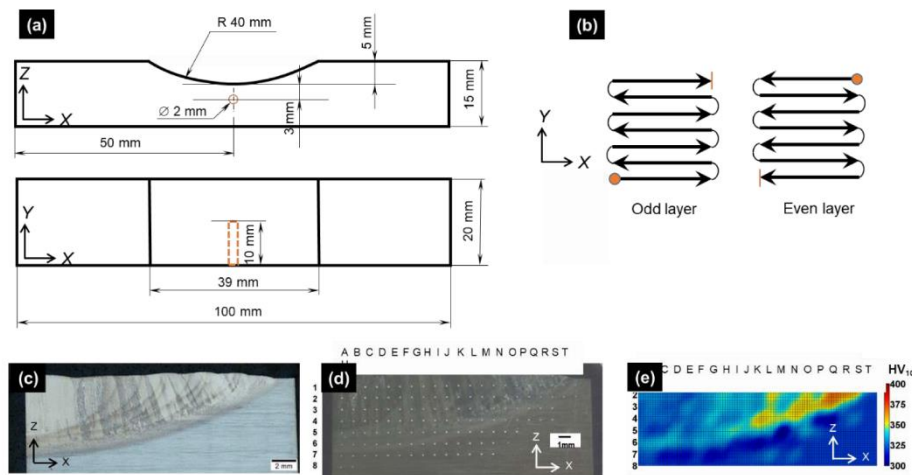

Figure 5: (a) Sample geometry and type-k thermocouple location within the substrate; (b) Path of laser beam for the decreasing track length deposition strategy (7 tracks/layer, and 10 layers); (c) view of half deposit in as-built conditions with columnar macrostructure and enhancement of HAZ (dark curved areas) and large nugget in the center (light area); (d) indentations grid within the cladded deposit (HV_{10}); (e) Vickers hardness map

3.2 Experimental methods

Samples for metallographic observations were machined by spark erosion, embedded in phenolic resin and polished to a mirror finish. Samples were etched using Kroll's reagent in order to reveal the details of the microstructure. Observations were carried out using both optical microscopy (OM) and scanning electron microscopy (SEM). Vickers hardness measurements (HV10) were performed following a grid (Fig. 5d), by means of universal hardness EMCO MC10 010 device equipped with an electronic cell force. In order to avoid interactions between adjacent indentations, a distance of 1 mm was set between test points. To draw a map of iso-hardness contours (Fig. 5e), fictive intermediate points between actual hardness measurements were generated using a "triangle-based cubic interpolation" in MATLAB. Additional details on experimental characterization procedures may be found in [5]

15/

3.3 Microstructure characterization focusing on three points of interests (POIs)

The microstructures of three points of interest, POI1, POI2 and POI3 corresponding respectively to the maximum, the medium and the minimum of Vickers hardness are given in Fig. 6a

- For POI1 (Fig. 6b), the matrix is made of orthogonal thin laths of martensite with acicular morphology. α massive (α_m) is also present at prior β columnar grain boundaries.

- The microstructure in POI2 (Fig. 6c) presents fewer thick α' laths, and typical α lamella not aligned with α' orthogonal laths. α represents the main phase corresponding to the Widmanstätten Structure with Basket-weave morphology (α/β_W).

- POI3 exhibits both α' and α_m alike POI1, with very few α/β_W between α' laths (Fig. 6d).

Compared with the constant track length case analyzed in [5], the decreasing track length strategy enhances the clad heterogeneity and results in a graded microstructure [2,5,40,41,53] as proved by Vickers hardness (Fig. 5e), OM and SEM observations (Fig. 6).
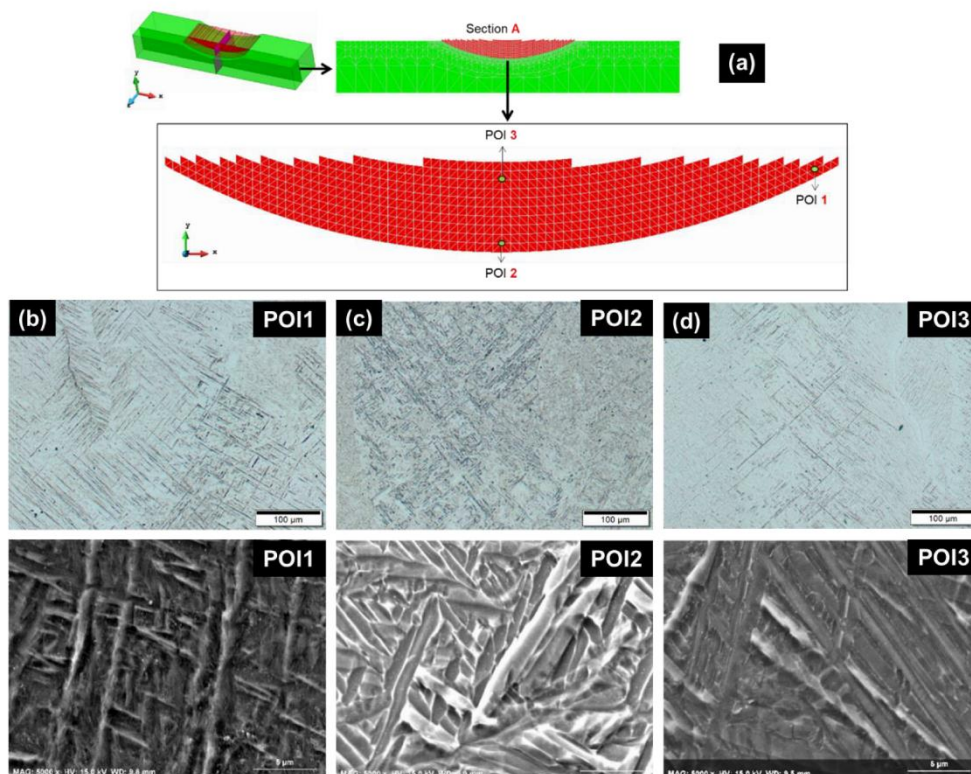

Figure 6: Microstructure in the as-built conditions; (a) location of the three points of interest (POIs), and FE mesh; (b) to (d) Light microscope (top) and zoom under SEM (bottom) for POIi – (b) POI1: α' martensite matrix made of thin orthogonal laths, with α_m at prior β grain boundary; (c) POI2: α/β_W basket-weave structure, with few coarsened discontinuous laths of "decomposed" α'; (d) POI3: α' with some neighboring α/β_W structure, and α_m at prior β grain boundary.

16/

3.4 Thermal modeling

The updated Lagrangian FE software called Lagamine developed by the University of Liège to model forming processes [81] was applied here. An 8-node 3D thermo-mechanical element with a reduced integration scheme and an hourglass control technique [82] was used, however only the thermal degrees of freedom was activated. The 3D-mesh was refined in the deposit and at the top of the substrate while a coarser mesh was chosen at the bottom of the substrate (see Fig. 7). The material addition was simulated by the element birth technique while interface elements modeled the evolution of the boundary conditions of convection and radiation. Here , the decreasing track length strategy to fill the notch was applied while previous study [44]was focused on a constant track length strategy. The distance between the bottom of the groove and the type-K thermocouple location within the substrate was 3 mm here instead of 2 mm in the previous works [44].
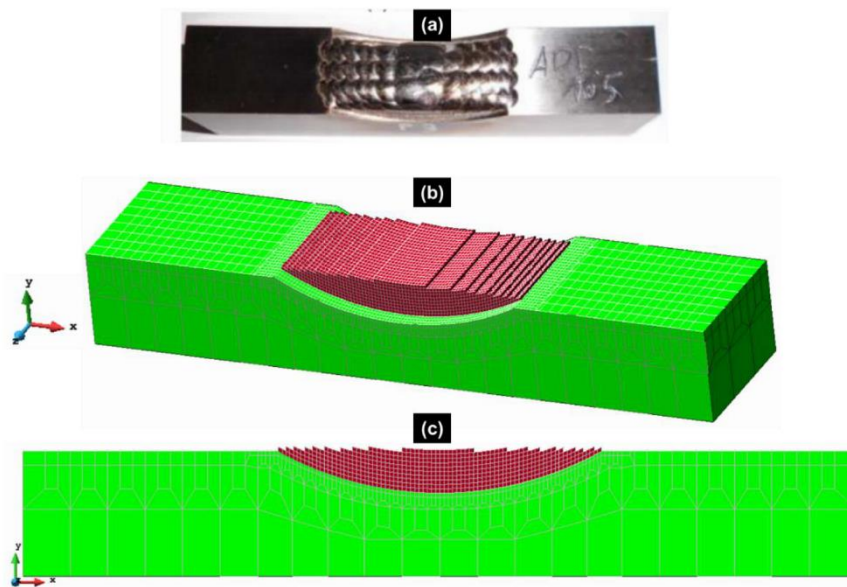

Figure 7: (a) Deposit in the as-built conditions, and 3D finite element mesh used for the numerical simulation of the laser cladding process; (b) 3D view; (c) front view.

The effects of the latent heat of fusion and vaporization was integrated in the definition of an apparent heat capacity and the fluid motion (i.e. Marangoni flow) was not considered, in order to reduce the complexity of the problem.

The initial constant temperature field was defined based on the preheating conditions. The convection and radiation phenomena were considered with the ambient temperature 298.15 K. An element mesh size of 0.5 mm was selected for the deposit, which means a total of nine elements describing the heat flux q_{laser} loading under the laser beam (see Fig. 8):

$$q_{laser} = \beta.I(x,y,z,U,t) \tag{4}$$

where β is the absorption factor, I the laser heat flux density distribution and U the experimental velocity of the laser in the x, y, z directions respectively. By inverse modeling, a laser absorptivity coefficient of 0.35 was numerically identified based on the experimental temperature curve of the first layers while both convection and radiation coefficients were

17/

calibrated with the next layers. β value is close to the values given in literature, ranging from [0.30 - 0.40] [83]. The laser beam velocity and the idle time between tracks and layers were obtained from the experimental conditions.

The predicted thermal field was validated by the comparison of the measured and predicted thermal histories (Fig. 9) as well as the sizes of the dilution zone and the HAZ within the substrate measured under metallographic inspection. Both checks were important to identify a single set of input parameters. A difference around 10% was found. Such a discrepancy can be due to the variable shift within the transformation points of Ti6Al4V alloy with high heating rates under AM processing, while the current simulations use constant temperature value.
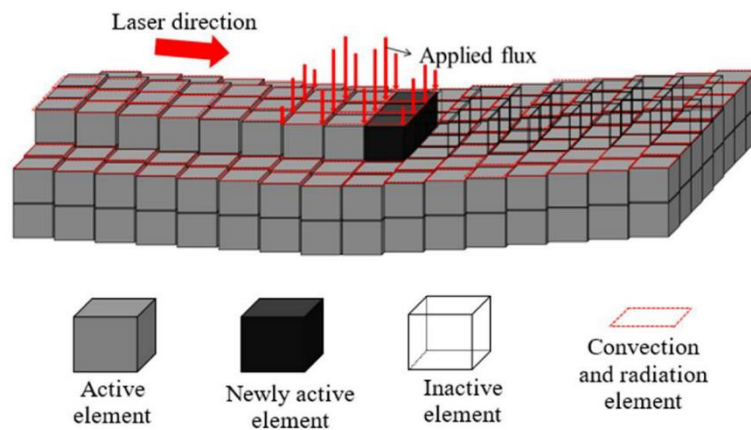

Figure 8: Scheme of element birth and death technique along the curved surface, updated state when the laser has moved (from [44]).
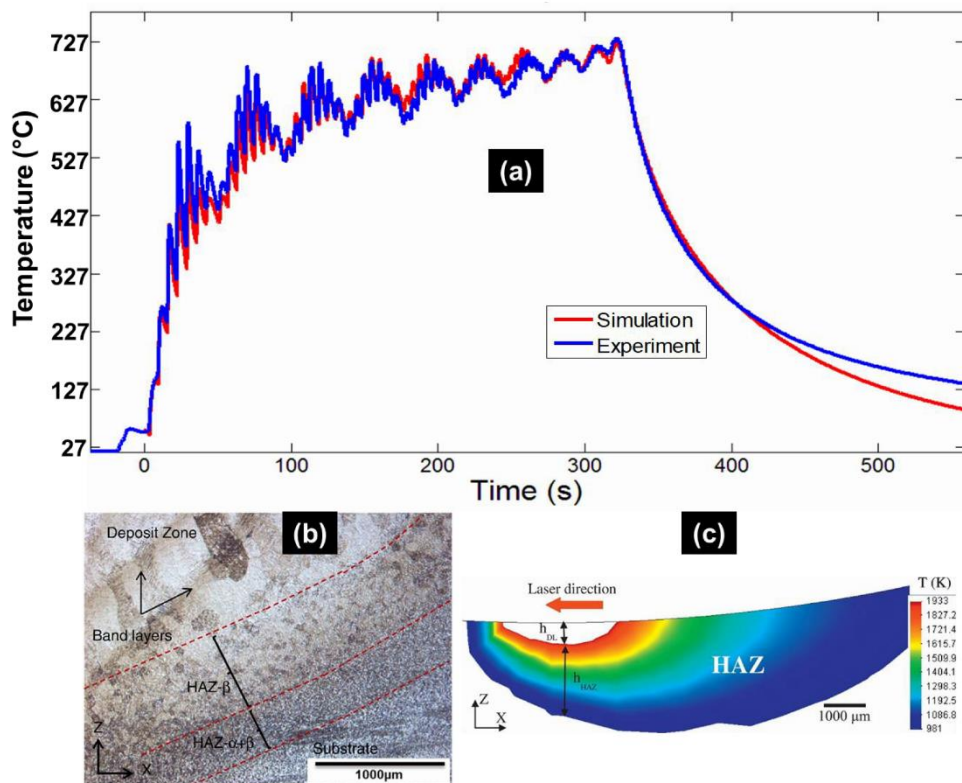
Figure 9: (a) Predicted and measured temperature-time curves at the thermocouple inside the substrate for 10 layers (b) Estimation of deposition features (dilution zone, HAZ) at the first layer and the mid-width of the substrate beneath the thick Ti6Al4V deposit obtained by DED, with parameters measured by metallographic inspection (from [5]); (c) parameters predicted using the validated thermal model (from [44]).

4. Results

Based on the validated 3D FE thermal model, the simulated thermal histories for the three POIs were obtained and analyzed hereafter.

4.1 Simulated thermal history on POI1

This point is located on the edge of the cup and corresponds to the beginning of the deposition (first track). In the thermal history (Fig. 10) the first peak, also the highest one, sets the element activation in the simulation. The peaks above the liquidus are paired off. Each pair corresponds to the two adjacent tracks belonging to the same layer, located close to the related POI. The closer the laser beam is to the POI, the higher the peak temperature. If there is a marked difference between two paired peaks, the one with the highest temperature will be that for which the laser beam was closest.

Complete melting is assumed for each peak higher than the liquidus, prior to the rapid cooling to a temperature much lower than $\beta_{transus}$, thus allowing the solidification to locally occur. New remelting is achieved again if local temperature increases above liquidus. The maximum amplitude of the complete remelting peaks decreases with time (Fig. 10 and Table 3).

For POI1, melting is achieved four times before solidifying for the last time, starting from a peak temperature of 1675°C (Fig. 10 and Table 3). The last solidification is achieved with an

19/

average cooling rate of 93°C/s, determined between the maximum and the minimum peaks (Table 3). The method for calculating these cooling rates is explained in **subsection 5.2.2**.

After the last solidification, POI1 experiences a thermal cycling with peak temperatures ranging well below $\beta_{transus}$ until the deposition stops. The amplitude of the thermal cycling quickly decreases over time because of the building strategy. Indeed, the heat source becomes more and more remote as deposition proceeds, moving from the edge of the cup where POI1 is located, to the center of the cup. Simultaneously, the minimum temperature slightly increases with time, up to a plateau around 450°C as the result of a moderate heat accumulation.

At the end of the deposition process, when the laser beam is turned off, there is a continuous cooling down to the room temperature that follows a typical exponential decay.
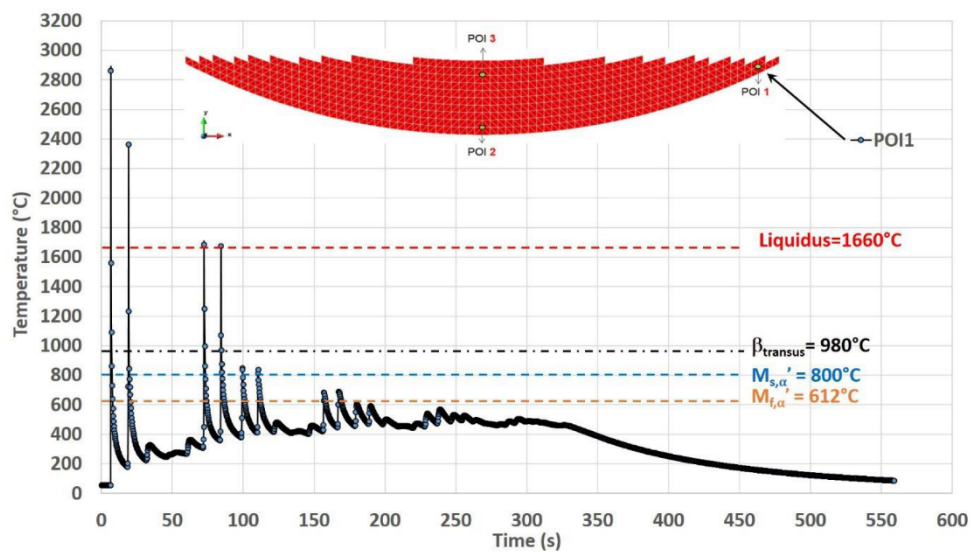

Figure 10: Simulated thermal history of POI1, starting from the material deposition, up to the final cooling at the end of deposition.

4.2   Simulated thermal history on POI2

This point, located on the bottom center of the cup, is filled out after POI1 within the same first layer and is re-melted 3 times (corresponding to the first two layers). The last solidification is achieved starting from a temperature of 1804°C, under an average cooling rate of 228°C/s (Fig.11, and Table 3). Alike POI1, the remelting peaks within POI2 follow a decreasing trend with time, their values being well above the liquidus. However, the thermal cycles following the last solidification of POI2 present a series of paired peaks whose temperatures are significantly higher than $\beta_{transus}$, contrarily to what occurs within POI1. These peaks are relative to layers 3 to 7. The last three pairs of peaks (layers 8 to 10) have a maximum either close to $\beta_{transus}$, or slightly below. Similarly to POI1, turning off the laser beam at the end of deposition process leads to a final continuous cooling down to room temperature.

Thermal cycles of lower amplitude are present between paired peaks characterized by values higher than $\beta_{transus}$. The maximum of these intermediate peaks remains below $\beta_{transus}$ and their minimum falls sometimes below $M_{f,\alpha'}$ however their cooling rate $|\dot{T}|$ is always lower than the Critical Cooling Rate (CCR) of 20°C/s (Table 4).

20/

There are more temperature fluctuations within POI2 thermal history than POI1 one. While the minimum temperature is still increasing gradually up to a plateau, the average temperature exhibits an even more pronounced increasing trend, a phenomenon probably due to the heat accumulation as the result of the building strategy.
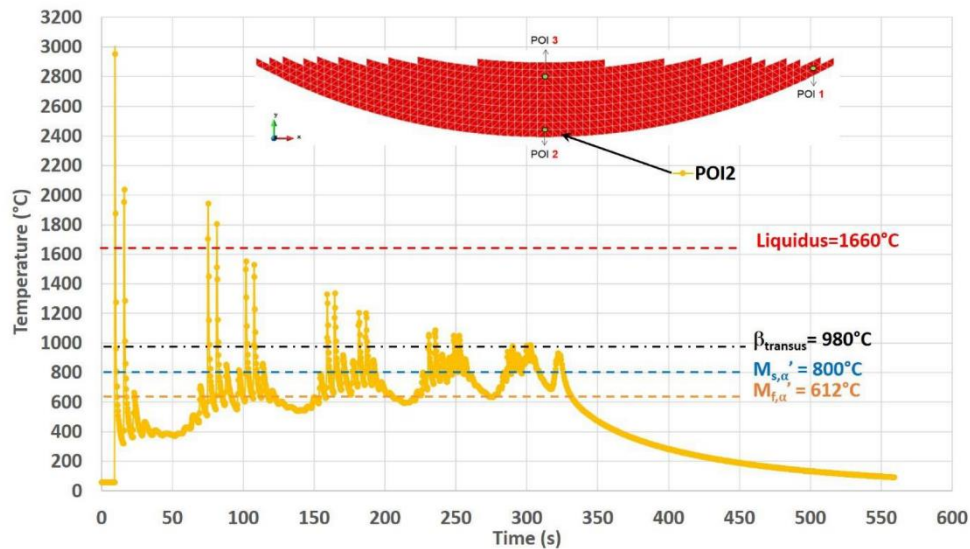

Figure. 11: Simulated thermal history of POI2, starting from the material deposition up to the final cooling.

4.3   Simulated thermal history on POI3

POI3 is re-melted 5 times as the maximum of the temperature peak passes 6 times over the liquidus upon heating. This is usually achieved under high heating rates (Fig. 12 and Table 3). The maximum temperature of 3083°C for the molten liquid is reached when melting the powder for the first time. Nevertheless, this temperature remains below the evaporating temperature of Ti6Al4V (3287°C, [44]), thus avoiding changes within the composition of the alloy. The corresponding $\dot{T}$ is also at its highest value (12316°C/s). Therefore, both the peak temperature and the heating rate achieved for the first melting within POI3, represent the highest values among all the equivalent data obtained within the three POIs. This fact is related to the effect of heat accumulation, more pronounced in POI3 due to the building strategy. A similar result was established in a previous work ([44]) for a point of interest also located in the top center of the cup, but with a constant track length building strategy.
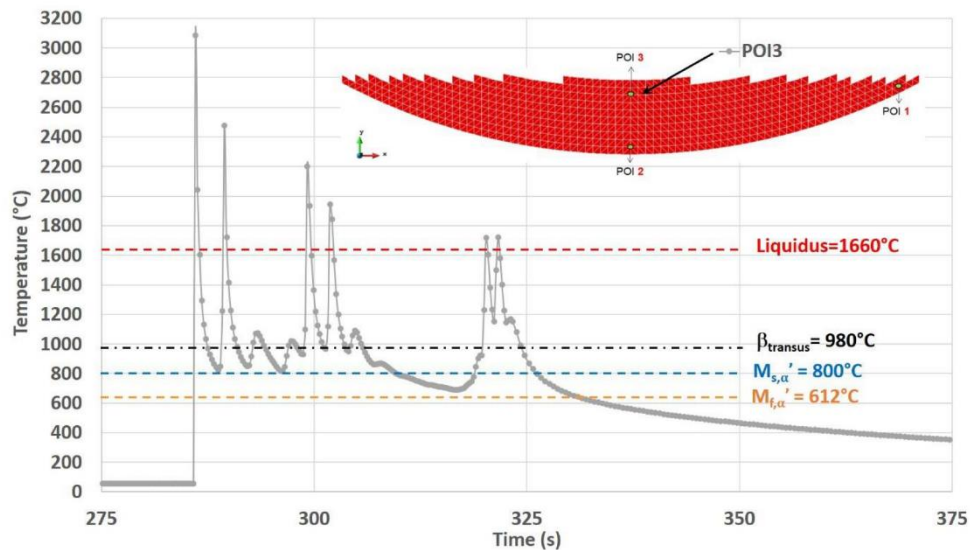
21/

Figure 12: Simulated thermal history of POI3, starting from the material deposition up to the final cooling.

The last melting peak in POI3 has its maximum at 1722°C. The consecutive $|\dot{T}|$ upon cooling reaches a value of 612°C/s, leading to a relative minimum of 1145°C at the end of the cooling stage. This minimum temperature is well above all critical transition points for solid phase transformations, which means that the parent β phase should remain untransformed. Then there is an almost instantaneous increase in temperature up to 1170°C, followed by a slow cooling stage as already observed on both POI1 and POI2.

5. Discussion

5.1 Introduction of the TTB concept

As demonstrated in the literature survey of **section 2**, predicting an accurate microstructural evolution during AM remains a major challenge. The authors propose the new concept of Time-phase–Transformation–Block (TTB) to tackle this issue. More specifically, the TTB approach consists in simplifying the complex thermal histories of the AM process as obtained from a validated thermal model simulation, by cutting them into successive blocks of time. Each block represents a thermal sequence that can be distinguished according to the single phase transformation mechanism that occurs. The by-products of the previous block of the TTBs are used as new parent phases upon the transition from one TTB to the following one.

For the definition of each TTB, one must focus on a specific thermal sequence. Upon heating, the TTB should highlight CHT (Continuous heating transformations), while CCT (Continuous cooling transformations) should be considered during cooling stages. Under quasi isothermal conditions, TTT (Time-Temperature-Transformations) are considered together with the mechanism related to phase transformation kinetics. In the latter case, it is possible to start from a higher temperature to cool down to a lower and fixed temperature, or to heat up to a plateau and hold for a definite time. Hereafter, the implementation of the TTB concept on the case presented in **section 3** is described.

22/

5.2   Application of TTB concept to the microstructure evolution within the POIs

5.2.1 Setting of TTBs

The TTB concept is intended to cut the complex thermal histories observed in AM into simple segments. This sectioning eases the transposition of existing predictive models, with some improvement as they do not currently take into account most of the phenomena involved either by high thermal gradients or short dwell times. To guide numerical model without excessive simplification, the new concept – Time-phase Transformation Block (TTB) – is developed hereafter.

The threshold values defined in **section 2** (β'$_{transus}$, α'$_{transus}$, β_s, β_f, $M_{s,\alpha m}$, $M_{s,\alpha'}$, $M_{f,\alpha'}$) for phase transformations have to be determined and reported for each POI case (**subsection 5.2.2**). Upon heating, a temperature range for β'$_{transus}$ above $\beta_{transus}$ is considered for defining the end of the RDfT yielding β phase regardless of the starting α or α' phase. Although the onset of the RDfT (α'$_{transus}$) increases with $\dot{T}$, it will not be taken into account here. Indeed hereafter, the focus is only on specific cases for which the transformations are complete, thus assuming a peak temperature higher than β'$_{transus}$. In addition, displacive limits β_s and β_f well above β'$_{transus}$ are considered for RDsT of α'.

For DDsT occurring upon cooling, $M_{s,\alpha m}$ and $M_{s,\alpha'}$ are set at 893°C and 800°C respectively, the latter value being chosen in view of its good agreement with thermodynamic approach and because it is composition dependent [8,52,63]. $M_{f,\alpha'}$ is set at 612°C as the average of the four empirical values previously mentioned in **subsection 2.2**.

5.2.2 Application of TTB to simulated thermal histories

The new TTB concept is applied on simulated thermal histories of **section 3** to highlight metallurgical phenomena.
It is worth nothing that heating rates $\dot{T}$ of the first peaks calculated by the FE simulation have not the real physical meaning (Peak 1 in Table 3). In fact, the element birth technique used during simulation activates a new element only when it is heated by the laser beam and does not accurately models all the phenomena related to powder grains. The methods for calculating the average cooling rates $|\dot{T}|$ used within both TTB1 and TTB3 are explained in Fig.13. In this case, $|\dot{T}|$ are computed between $M_{s,\alpha'}$, $M_{f,\alpha'}$ or from $M_{s,\alpha'}$ to the minimum of temperature reached (Table 3).
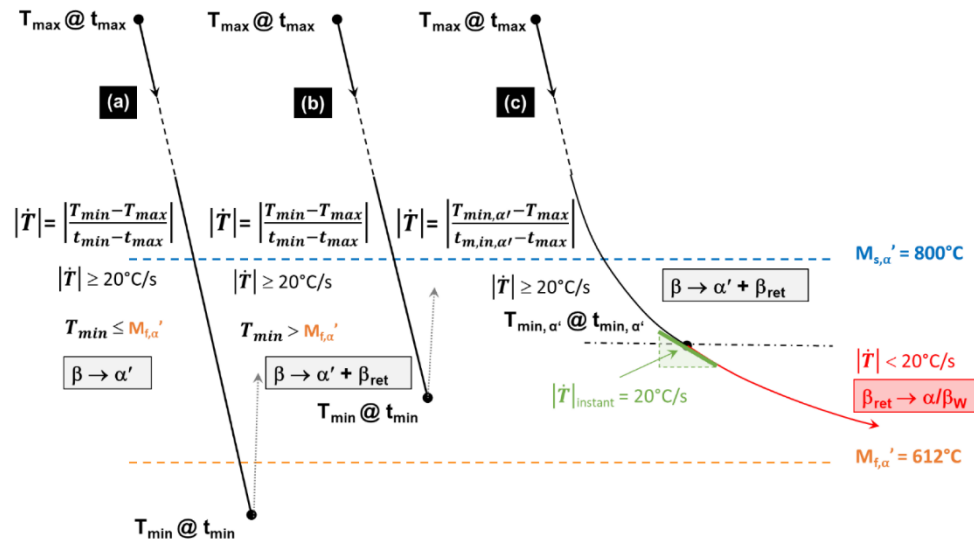
23/

Figure 13: Methods determining the average cooling rates $|\dot{T}|$ in TTB1 and TTB3. Case (a) allows a complete martensite transformation, (b) a partial one , and (c) a combined transformation starting with a displacive mechanism before switching to a diffusive mode, when $|\dot{T}|$ is lower than the CCR of 20°C/s .

Tables 3 and 4 summarize the parameters characterizing each TTBs for the three POIs. They are key input data for the application of the TTB methodology. These values help enhancing the transformation mechanism, which can change from displacive to diffusive when $|\dot{T}|$ rapidly decreases during cooling. In this case, the switching time is set when the instant $|\dot{T}|$ becomes lower than the CCR of 20°C/s.

Table 3: FE predicted main peak temperatures, heating ($\dot{T}$) and cooling rates ($|\dot{T}|$) within TTB0 and TTB1 for the three points of interest (POIs)

Points of interest	Computed thermal parameters	Peak 1	Peak 2	Peak 3	Peak 4	Peak 5	Peak 6
POI1	T (°C)	2860	2362	1685	1675	847*	
	$\dot{T}$ (°C/s)	11390	2956	1157	1396	495	
	$|\dot{T}|$ (°C/s)	228	171	120	93	42	
POI2	T (°C)	2952	2038	1944	1804	1552*	1529*
	$\dot{T}$ (°C/s)	11763	2325	1457	1272	961	1225
	$|\dot{T}|$ (°C/s)	448	299	271	228	190	184
POI3	T (°C)	3089	2477	2201	1944	1719	1722
	$\dot{T}$ (°C/s)	12316	2235	2582	1990	1619	1155
	$|\dot{T}|$ (°C/s)	848	611	569	457	600	612

*assumed not to be remelted

24/

Table 4: Thermal characteristic and time-based features related to TTB1 to TTB4 as calculated by simulated thermal histories of the three POIs and related local Vickers hardness (VH) values

Computed thermal features and hardness	POI2	POI1	POI3
Last solidification stage during TTB1			
T_{max} (°C) @ time (s)	1804°C @ 82 s	1675°C @ 84 s	1722°C @ 322s
T_{min} (°C) @ time (s)	579°C @ 87 s	380°C @ 98 s	1145°C @ 323 s
Average cooling rate ($\lvert\dot{T}\rvert$ °C/s) achieved during the last solidification stage	228°C/s	93°C/s	612°C/s
Isothermal Transformation for β during TTB2*			
T_{mean} (°C) @ Equivalent holding time (s)	[a]669°C ± 67 @ 39 s [b]829°C ± 56 @ 09 s [c]777°C ± 97 @ 66 s	487°C ± 56 @ 228 s	-
Incubation time (s) for β → α/β_W transformation under TTT ($t_{1\%}$) @ T_{mean} (°C) [39]	[a]1 sec @ 669°C [b]5 sec @ 829°C [c]1 sec @ 777°C	30 sec @ 487°C	-
Time (s) for progress transformation β → α/β_W under TTT ($t_{50\%}$) @ T_{mean} (°C) [39]	[a]7 sec @ 669°C [b]10 sec @ 829°C [c]9 sec @ 777°C	700 sec @ 487°C	-
Fast reheating peak above β_transus and related steep cooling during TTB3*			
T_{max} (°C) and related $\dot{T}$ (°C/s) achieved on the first of the two peaks during heating	[a]1203°C @ 868°C/s [b]1057°C @ 660°C/s [c]1049°C @ 462°C/s	-	-
T_{min} (°C) and related $\lvert\dot{T}\rvert$ (°C/s) achieved on the second of the two peaks during cooling	[a]718°C @ 219°C/s [b]746°C @ 173°C/s [c]804°C @ 160°C/s	-	-
Final continuous cooling stage during TTB4			
Starting peak temperature T_{end} (°C) @ time (s)	930°C @ 322 s	461°C @ 326 s	1170°C @ 323 s
First temperature (°C) at which instant $\lvert\dot{T}\rvert$ cooling rate falls below 20°C/s @ time (s)	661°C @ 330 s	$\lvert\dot{T}\rvert$ always under 20°C/s	642°C @ 331 s
Vickers Hardness (HV_10)			
Local VH on POIs (HV_{10})	327	370	331

* Indices [a], [b] and [c] are related to the successive relevant TTB2 (4th, 5th, 6th) and TTB3 (3rd, 4th, 5th) occurring on POI2 and during which all or some of the solid phases already formed remain within the subsequent thermal cycles (see Fig. 14).

The first focus is on POI2 (Fig. 14) that exhibits the most complex thermal history before transposition to other POIs (Fig. 15 and 16). Five distinct types of TTBs are defined as follows:

- TTB0 corresponds to the initial stage comprising a series of superheating peaks with their maximum above the liquidus, and during which the material previously solidified, is systematically remelted.
- TTB1 identifies a single peak corresponding to the last solidification event. Its maximum temperature T_{max} is higher than the liquidus. T_{min} value reached after the peak

25/

and the cooling rate $\dot{T}_{mean}$ between these extrema determine the new parent phase "1" (α', α_m, α/β_W or β_{ret}).

- TTB2 covers the time periods where a succession of peaks have their maximum lower than $\beta_{transus}$. The average of this saw-tooth thermal profile provides a representative isothermal value.
- TTB3 corresponds to the paired peaks with both steep temperature increases and decreases. Their maxima, well above $\beta_{transus}$, generate partial or complete reverse transformation into β, depending on the highest temperature achieved during heating. The minimum temperature and the cooling rate achieved during the cooling stage of the last peak set the provisional microstructure at the end of TTB3.
- TTB4 is the last continuous cooling down to room temperature, at the end of AM process. Solid state transformations can still occur during this period, if the thermodynamic conditions allow it.

5.2.2.1   POI2 analysis

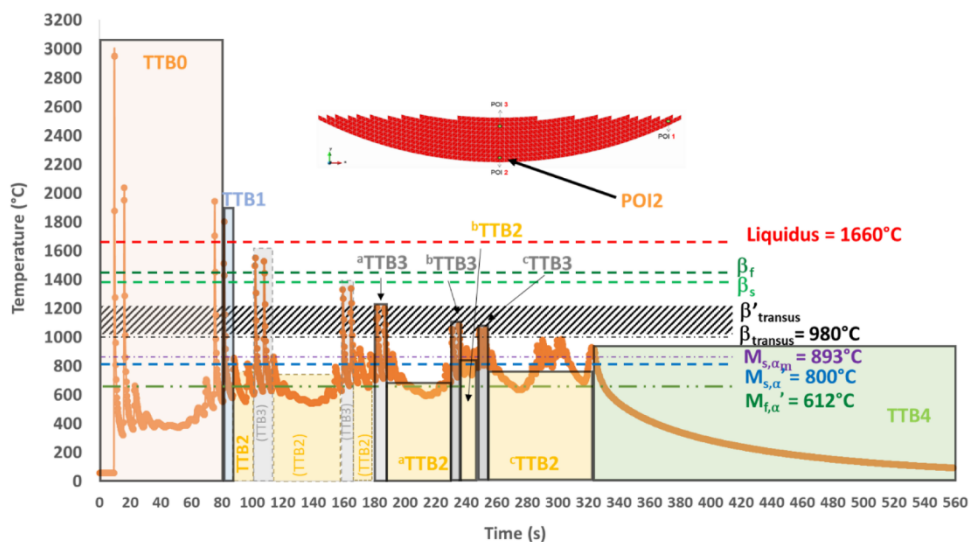All the TTBs applied to POI2 are illustrated in Fig. 14.

Figure 14: TTB sequence within the simulated thermal history in POI2 ; dashed line boxes for phase transformations wiped out during processing, and solid line boxes for phase transformations products remaining in the final state (three relevant TTB3s and three relevant TTB2s are underlined).

Within TTB0, POI2 is consecutively melted 3 times. The 3rd melting peak occurs about 75s after the element activation. The first peak is the highest, probably because it is the one for which the laser beam is just right in the POI during the deposition of the first layer. It can be noted that both $\dot{T}$ and $|\dot{T}|$ related to those remelting peaks are very high (Table 3). The cooling stage during the first peak occurs under a $|\dot{T}|$ of 488°C/s down to a temperature that is well below $M_{f,\alpha'}$. Martensite is necessarily formed after this peak, but it disappears by a diffusionless transformation into β, a phase which itself is almost immediately re-melted when the laser beam approaches POI2 again, for the deposition of an adjacent track within the same first layer. In the same way, martensite is again directly formed during the cooling associated with the second melting, as a result of a displacive transformation of the parent β formed earlier during

26/

solidification. Such a statement is in good agreement with [56], where mechanisms for quick heating transformations up to remelting, have been evidenced by SXRD. This second martensite will in turn undergo a thermal cycling that can lead to further modifications. However they are neglected here, as another complete remelting will be achieved later on. Indeed the 3rd and 4th peaks correspond to the laser beam passing over POI2 and melting this material point again, when building two adjacent tracks belonging to the 2nd layer. In addition, it can also be observed in Table 3 that $\dot{T}$ does not necessarily follow a monotonic evolution. Solid phase transformations occurring within TTB0 are not considered because the complete remelting achieved later wipes out the solid phases. However, such a thermal cycling up to complete remelting may be interesting for studies related to melt pool geometries, and primary β grain size and morphology, including epitaxial growth.

After TTB0, a single TTB1 follows. It identifies the single peak corresponding to the last remelting of POI2 (see its characteristics in Table 4). It may be noted that a $|\dot{T}|$ of 228°C/s is achieved during cooling, down to a minimum temperature of 579°C that is lower than $M_{f,\alpha'}$. Therefore, the martensitic transformation is complete at the end of TTB1.

Following TTB1, there are 6 TTB2s intercalated by 5 TTB3s. The three first TTB2s are followed by TTB3s, where a complete transformation of the existing α' phase into β without recrystallization is assumed (see Supplementary Material for details). This hypothesis seems reliable as the peak temperatures within these TTB3s are higher than $β'_{transus}$. One can thus forget these three first TTB2s (see Fig 14 and Table 4). In addition, the temperature peaks corresponding to the tracks closest to POI2 for the last three layers (8 to 10) have their maximum lower than $β_{transus}$. As previously established (**subsection 2.1**), the transition point such as $β'_{transus}$ is higher than equilibrium reference point $β_{transus}$ due to $\dot{T}$ effect. In addition, the minimum residence time for an isothermal transformation is not achieved under a single peak (see Supplementary Material for details).

One can identify the first relevant TTB3, noted as [a]TTB3, whose product phases will remain afterwards. In particular, during the second cooling, the minimum temperature reached is lower than $M_{s,\alpha'}$ and still higher than $M_{f,\alpha'}$, thus leading to an incomplete martensitic transformation (Table 4, [a]TTB3). Both α' and $β_{ret}$ are then submitted to an isothermal annealing ([a]TTB2). α' undergoes a decomposition while $β_{ret}$ leads to $α/β_W$ by a diffusional transformation (see TTT diagram [4,15,39,50]). During [b]TTB3, an incomplete reverse transformation of parent α and α' phases into β happens because the maximum peak is lower than $β'_{transus}$. Then, the newly formed β undergoes a martensitic transformation upon cooling. The progression of this martensitic transformation is less marked than for [a]TTB3 since the minimum temperature achieved (746°C) is higher than the previous one (718°C) (Fig. 14 and Table 4). The phases present at the end of [b]TTB3 then undergo an isothermal sequence [b]TTB2. This cyclic approach alternating TTB3 and TTB2 decreases the amount of martensite since its decomposition takes place within [a,b,c]TTB2s while new α' is expected only in [a,b]TTB3s. Indeed, T_{min} for [c]TTB3 is higher than M_s. In the meantime, a complete transformation of $β_{ret}$ into $α/β_W$ during [c]TTB2 is achieved at 777°C (Table 4). During the final cooling (TTB4), no transformation occurs because there is no β phase left, and there is no phase decomposition during cooling. POI2 exhibits the lowest hardness among the three POIs due to the relatively high amount of $α/β_W$ that is obtained under quasi isothermal conditions (Fig. 5e and Table 4).

In conclusion, the thermal history of POI2 with peak temperatures higher than $β_{transus}$ and subsequent high temperature isothermal annealing enhances the conditions for recrystallization.

27/

5.2.2.2   POI1 analysis

POI1 is melted 4 times, and the maximum temperature of the melt follows a decreasing trend (Table 3). Among the melting events, the first three ones occur within TTB0, and the last is related to TTB1 (Fig. 15). Both α_m and α' martensite are formed at the end of TTB1 (Table 4) due to an average cooling rate of 93°C/s down to 380°C, which is well below $M_{f,\alpha'}$. During TTB2, martensite is submitted to an annealing at a low average temperature (487°C) during 228s, which is too short to allow its decomposition [11,20,23,27,50,66]. POI1 ends its cooling stage with TTB4 during which no phase transformation is expected. The hardness in POI1 is among the highest values achieved within the deposit (Fig. 5e and Table 4) .

In conclusion, the thermal history of POI1 with peak temperatures lower than $\beta_{transus}$ and subsequent low temperature isothermal annealing enhances the conditions for martensite decomposition.
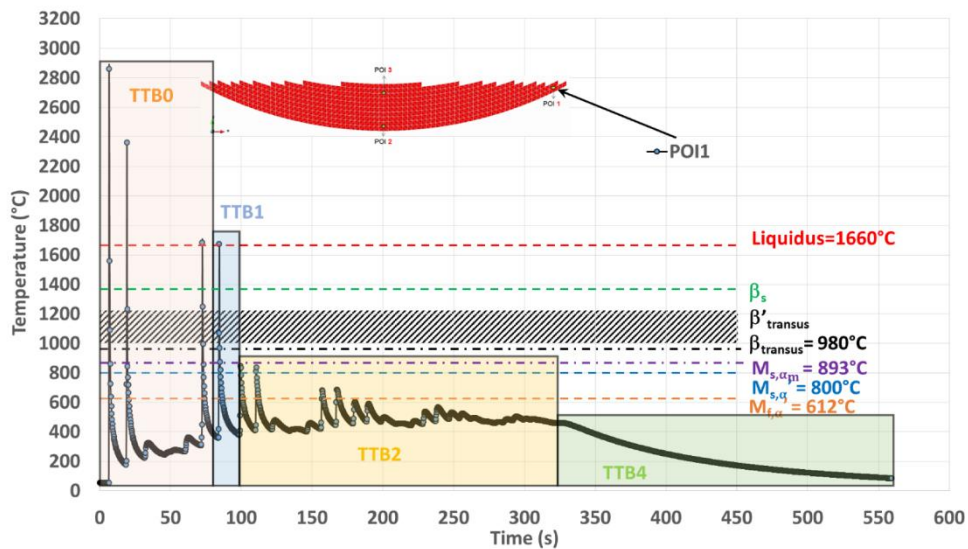

Figure 15: TTB sequence within the simulated thermal history on POI1 where TTB3 is missing due to peak temperature well below transition points after TTB1 and TTB2.

5.2.2.3   POI3 analysis

For POI3, TTB1 does not allow the transformation of β because the minimum temperature levels reached under the high $|\dot{T}|$ remain higher than the transition points. Phase transformations take place during TTB4 that follows TTB1, as both the isothermal-like TTB2 and the reheating TTB3 are missing (Fig. 16).
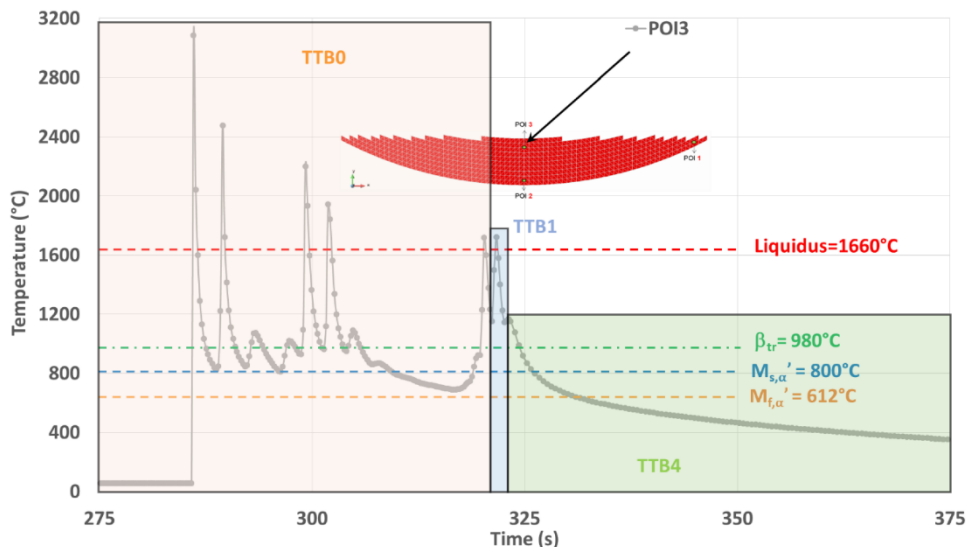
Figure 16: TTBs sequence within the simulated thermal history on POI3 where both TTB2 and TTB3 are missing due to quasi continuous cooling straight from the last remelting, down to room temperature.

The final cooling rate (CR) continuously decreases, starting with a value higher than the CCR of 20°C/s that allows martensitic transformation. However, CR falls down below this CCR value stopping the martensitic transformation before its completion, i.e. for $T>M_{f,\alpha'}$. As a result, the final microstructure within POI3 originates from two distinct successive mechanisms. First, a DDsT that allows the parent β phase to transform into α'. This martensitic transformation continues as long as $|\dot{T}|$ remains higher than 20°C/s. Second, a DDfT that allows β_{ret} to transform into α/β_W. This two-stage phase transformation is in good agreement with the mixed (or dual) matrix observed within POI3 (Fig. 6d), where a hardness between that of POI1 and POI2 is achieved (Fig. 5e and Table 4).

The following continuous cooling stage down to room temperature occurring within POI3, differs from thermal cycling made of several successive heating and cooling sequences observed on both POI1 and POI2. Therefore, the microstructure associated with POI3 is likely to lead to reduced dislocation densities, which explains why a relatively low hardness is achieved within this point.

In conclusion, the thermal history of POI3 with complex CCT achieved due to the suppression of subsequent reheating and isothermal annealing enhances the conditions for change within the transformation mechanism.

## 5.3 Flowchart describing the evolution of microstructure during DED based on TTBs

In summary, the thermal history obtained by FE simulation is analyzed through TTB concept. It selects the relevant thermal features required to identify the solid phase transformations occurring during the process. An accurate prediction of the microstructural evolution at any point of a multilayered Ti6Al4V thick deposit manufactured by DED should be developed based on this concept.

29/

For each block of the TTB concept, the type of transformations according to their critical temperatures, critical thermal rates ($|\dot{T}|$ or $\dot{T}$) is summarized in the flowchart of Fig. 17.

Key data for displacive transformations occurring under continuous cooling conditions have been set, such as critical points ($M_{s,\alpha m}$, $M_{s,\alpha'}$, $M_{f,\alpha'}$) and related critical cooling rates $|\dot{T}|$. The most relevant values for the transition points, or the range of values for $|\dot{T}|$, have also been identified. These values (key input for any transformation model) have been achieved thanks to a critical review of the literature followed by an experimental validation on a manufactured part.

For the diffusive transformations, critical cooling rates remain to be determined. The influence of the heating rate $\dot{T}$ on both the mechanism for reverse transformations $\alpha/\alpha' \rightarrow \beta$ and the critical transition points are also highlighted. These parameters still require additional experimental works.   A function of the heating rate for the critical transition temperature of RDfT, as well as constant values for RDsT when $\dot{T}$ reaches a threshold value, have still to be identified.

However the flowchart of Fig. 17 allows numerical teams to easily implement a set of phenomenological equations based on physic roots. Indeed a set of unknown material parameters are still to be determined. However carefully validated thermal histories associated to microstructure characterizations will allow their identification by inverse modeling.
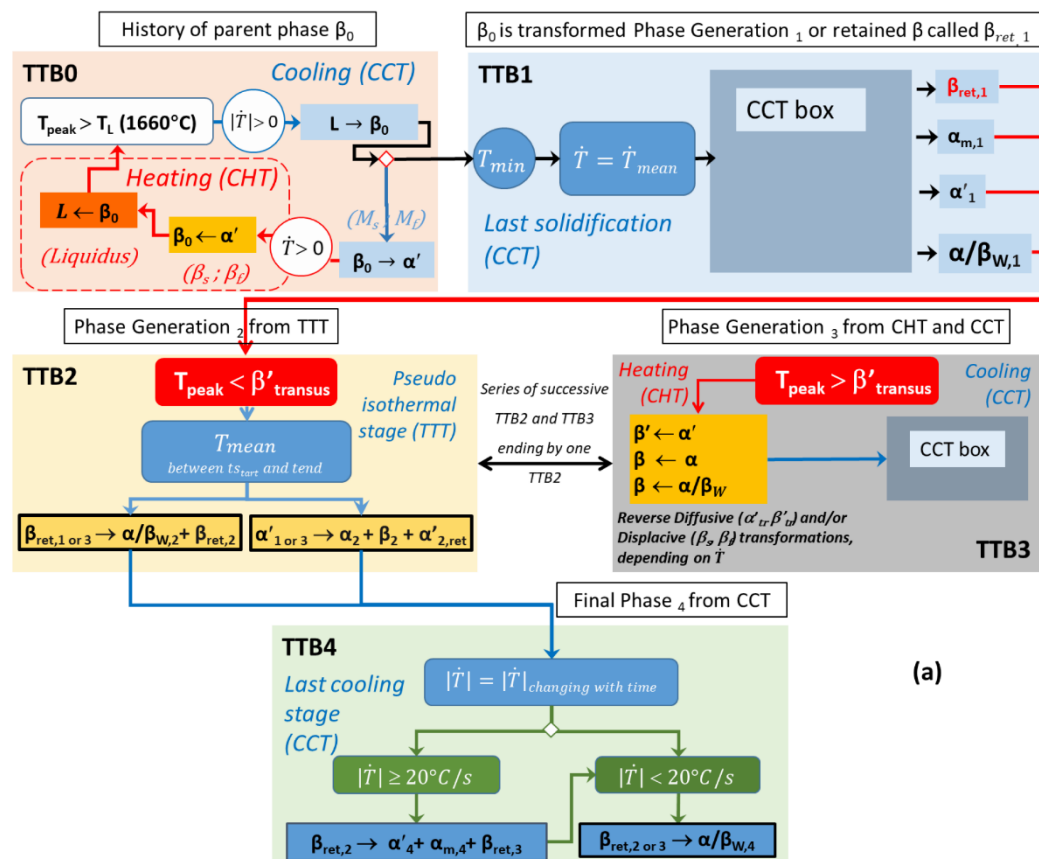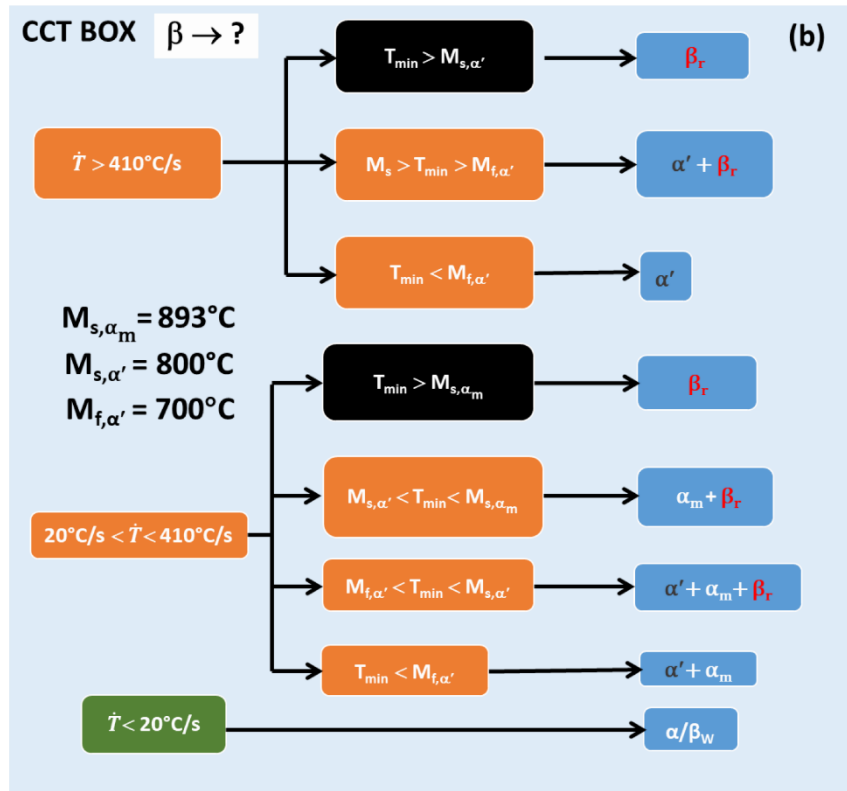
Figure 17: (a) General Time-transformation-blocks (TTBs) based on thermal histories with related phase transformations occurring during DED; (b) Highlighting of CCT Box transformations occurring within TTB1 and TTB3.

Finally, the TTB approach provides an easy way to understand the transformation mechanisms and facilitates an efficient implementation of the phenomenological models such as JMAK and KM with a single data set adapted to the AM of Ti6Al4V. Indeed, in literature, one difficulty of these models is the identification of a single set of material parameters as the parent phases have different compositions. Here the TTB approach and the good understanding of the transformation mechanisms will help the definition of functions for the input parameters which will enhance the accuracy of the prediction. Such models correctly validated can generate the large amount of data required to train the new machine learning approaches and to reduce the heavy characterizations and experimental campaigns.

6. Conclusions

The following conclusions can be drawn:
- A thick multilayer deposit was fabricated by DED using a decrease track length strategy which allows to obtain a heterogeneous microstructure. This case can be representative of a repair method.
- The use of a validated thermal model provides simulated thermal histories at different POIs, each corresponding to a specific microstructure within the DED deposit.

31/

- The critical analysis of thermal histories using the new TTB concept highlights the mechanisms that drive phase transformations, either during solidification and possible remelting sequences, or later in the solid state.
- In this article, the identification of the transformation mechanisms allows a qualitative explanation of the presence of any phase within the deposit, using the concept of TTB.
- The TTB concept will help numerical teams to adapt simple models like JMAK and KM to predict the amount of phases during AM. The flowchart of Fig. 17 identifies critical data and sequences that should be taken into account in these models.

Acknowledgments

References

[1]   S. Liu, Y.C. Shin, Additive manufacturing of Ti6Al4V alloy: A review, Materials & Design. 164 (2019) 107552. https://doi.org/10.1016/j.matdes.2018.107552.

[2]   J. Yang, H. Yang, H. Yu, Z. Wang, H. Wang, X. Zeng, A novel approach to in-situ fabricate Ti-6Al-4V alloy with graded microstructure and property by selective laser melting, Materials Letters. 215 (2018) 246–249. https://doi.org/10.1016/j.matlet.2017.12.098.

[3]   P. Barriobero-Vila, J. Gussone, J. Haubrich, S. Sandlöbes, J. Da Silva, P. Cloetens, N. Schell, G. Requena, Inducing stable α+ β microstructures during selective laser melting of Ti-6Al-4V using intensified intrinsic heat treatments, Materials. 10 (2017) 268. https://doi.org/10.3390/ma10030268.

[4]   L.-E. Lindgren, A. Lundbäck, M. Fisk, R. Pederson, J. Andersson, Simulation of additive manufacturing using coupled constitutive and microstructure models, Additive Manufacturing. 12 (2016) 144–158. https://doi.org/10.1016/j.addma.2016.05.005.

[5]   H. Paydas, A. Mertens, R. Carrus, J. Lecomte-Beckers, J. Tchoufang Tchuindjang, Laser cladding as repair technology for Ti–6Al–4V alloy: Influence of building strategy on microstructure and hardness, Materials & Design. 85 (2015) 497–510. https://doi.org/10.1016/j.matdes.2015.07.035.

[6]   L. Thijs, F. Verhaeghe, T. Craeghs, J.V. Humbeeck, J.-P. Kruth, A study of the microstructural evolution during selective laser melting of Ti–6Al–4V, Acta Materialia. 58 (2010) 3303–3312. https://doi.org/10.1016/j.actamat.2010.02.004.

[7]   M.J. Bermingham, D. Kent, H. Zhan, D.H. StJohn, M.S. Dargusch, Controlling the microstructure and properties of wire arc additive manufactured Ti–6Al–4V with trace boron additions, Acta Materialia. 91 (2015) 289–303. https://doi.org/10.1016/j.actamat.2015.03.035.

[8]   L. Qian, J. Mei, J. Liang, X. Wu, Influence of position and laser power on thermal history and microstructure of direct laser fabricated Ti–6Al–4V samples, Materials Science and Technology. 21 (2005) 597–605. https://doi.org/10.1179/174328405X21003.

[9]   X. Wu, J. Liang, J. Mei, C. Mitchell, P.S. Goodwin, W. Voice, Microstructures of laser-deposited Ti–6Al–4V, Materials & Design. 25 (2004) 137–144. https://doi.org/10.1016/j.matdes.2003.09.009.

[10] S. Gorsse, C. Hutchinson, M. Gouné, R. Banerjee, Additive manufacturing of metals: a brief review of the characteristic microstructures and properties of steels, Ti-6Al-4V and high-entropy alloys, Science and Technology of Advanced Materials. 18 (2017) 584–610. https://doi.org/10.1080/14686996.2017.1361305.

[11] X. Tan, Y. Kok, Y.J. Tan, G. Vastola, Q.X. Pei, G. Zhang, Y.-W. Zhang, S.B. Tor, K.F. Leong, C.K. Chua, An experimental and simulation study on build thickness dependent microstructure for electron beam melted Ti–6Al–4V, Journal of Alloys and Compounds. 646 (2015) 303–309. https://doi.org/10.1016/j.jallcom.2015.05.178.

[12] N. Sridharan, A. Chaudhary, P. Nandwana, S.S. Babu, Texture Evolution During Laser Direct Metal Deposition of Ti-6Al-4V, JOM. 68 (2016) 772–777. https://doi.org/10.1007/s11837-015-1797-6.

[13] M. Neikter, P. Åkerfeldt, R. Pederson, M.-L. Antti, V. Sandell, Microstructural characterization and comparison of Ti-6Al-4V manufactured with different additive manufacturing processes, Materials Characterization. 143 (2018) 68–75. https://doi.org/10.1016/j.matchar.2018.02.003.

[14] S.J. Wolff, S. Lin, E.J. Faierson, W.K. Liu, G.J. Wagner, J. Cao, A framework to link localized cooling and properties of directed energy deposition (DED)-processed Ti-6Al-4V, Acta Materialia. 132 (2017) 106–117. https://doi.org/10.1016/j.actamat.2017.04.027.

32/

[15] J. Ahn, E. He, L. Chen, R.C. Wimpory, J.P. Dear, C.M. Davies, Prediction and measurement of residual stresses and distortions in fibre laser welded Ti-6Al-4V considering phase transformation, Materials & Design. 115 (2017) 441–457. https://doi.org/10.1016/j.matdes.2016.11.078.

[16] S.K. Everton, M. Hirsch, P. Stravroulakis, R.K. Leach, A.T. Clare, Review of in-situ process monitoring and in-situ metrology for metal additive manufacturing, Materials & Design. 95 (2016) 431–445. https://doi.org/10.1016/j.matdes.2016.01.099.

[17] M. Khanzadeh, W. Tian, A. Yadollahi, H.R. Doude, M.A. Tschopp, L. Bian, Dual process monitoring of metal-based additive manufacturing using tensor decomposition of thermal image streams, Additive Manufacturing. 23 (2018) 443–456. https://doi.org/10.1016/j.addma.2018.08.014.

[18] S.J. Wolff, H. Wu, N. Parab, C. Zhao, K.F. Ehmann, T. Sun, J. Cao, In - situ high-speed X-ray imaging of piezo-driven directed energy deposition additive manufacturing, Sci Rep. 9 (2019) 1–14. https://doi.org/10.1038/s41598-018-36678-5.

[19] J. Yang, H. Yu, J. Yin, M. Gao, Z. Wang, X. Zeng, Formation and control of martensite in Ti-6Al-4V alloy produced by selective laser melting, Materials & Design. 108 (2016) 308–318. https://doi.org/10.1016/j.matdes.2016.06.117.

[20] W. Xu, M. Brandt, S. Sun, J. Elambasseril, Q. Liu, K. Latham, K. Xia, M. Qian, Additive manufacturing of strong and ductile Ti–6Al–4V by selective laser melting via in situ martensite decomposition, Acta Materialia. 85 (2015) 74–84. https://doi.org/10.1016/j.actamat.2014.11.028.

[21] J. Donoghue, A.A. Antonysamy, F. Martina, P.A. Colegrove, S.W. Williams, P.B. Prangnell, The effectiveness of combining rolling deformation with Wire–Arc Additive Manufacture on β-grain refinement and texture modification in Ti–6Al–4V, Materials Characterization. 114 (2016) 103–114. https://doi.org/10.1016/j.matchar.2016.02.001.

[22] O.M. Ivasishin, R.V. Teliovich, Potential of rapid heat treatment of titanium alloys and steels, Materials Science and Engineering: A. 263 (1999) 142–154. https://doi.org/10.1016/S0921-5093 (98) 01173-3.

[23] X.-Y. Zhang, G. Fang, S. Leeflang, A.J. Böttger, A. A. Zadpoor, J. Zhou, Effect of subtransus heat treatment on the microstructure and mechanical properties of additively manufactured Ti-6Al-4V alloy, Journal of Alloys and Compounds. 735 (2018) 1562–1575. https://doi.org/10.1016/j.jallcom.2017.11.263.

[24] H. Galarraga, R.J. Warren, D.A. Lados, R.R. Dehoff, M.M. Kirka, P. Nandwana, Effects of heat treatments on microstructure and properties of Ti-6Al-4V ELI alloy fabricated by electron beam melting (EBM), Materials Science and Engineering: A. 685 (2017) 417–428. https://doi.org/10.1016/j.msea.2017.01.019.

[25] H.K. Rafi, N.V. Karthik, H. Gong, T.L. Starr, B.E. Stucker, Microstructures and Mechanical Properties of Ti6Al4V Parts Fabricated by Selective Laser Melting and Electron Beam Melting, Journal of Materials Engineering and Performance. 22 (2013) 3872–3883. https://doi.org/10.1007/s11665-013-0658-0.

[26] S. Reginster, A. Mertens, H. Paydas, J. Tchoufang Tchuindjang, Q. Contrepois, T. Dormal, O. Lemaire, J. Lecomte-Beckers, Processing of Ti Alloys by Additive Manufacturing: A Comparison of the Microstructures Obtained by Laser Cladding, Selective Laser Melting and Electron Beam Melting, Materials Science Forum. 765 (2013) 413–417. https://doi.org/10.4028/www.scientific.net/MSF.765.413.

[27] W. Xu, E.W. Lui, A. Pateras, M. Qian, M. Brandt, In situ tailoring microstructure in additively manufactured Ti-6Al-4V for superior mechanical performance, Acta Materialia. 125 (2017) 390–400. https://doi.org/10.1016/j.actamat.2016.12.027.

[28] E. Brandl, A. Schoberth, C. Leyens, Morphology, microstructure, and hardness of titanium (Ti-6Al-4V) blocks deposited by wire-feed additive layer manufacturing (ALM), Materials Science and Engineering: A. 532 (2012) 295–307. https://doi.org/10.1016/j.msea.2011.10.095.

[29] J. He, D. Li, W. Jiang, L. Ke, G. Qin, Y. Ye, Q. Qin, D. Qiu, The Martensitic Transformation and Mechanical Properties of Ti6Al4V Prepared via Selective Laser Melting, Materials. 12 (2019) 321. https://doi.org/10.3390/ma12020321.

[30] P. Peyre, P. Aubry, R. Fabbro, R. Neveu, A. Longuet, Analytical and numerical modelling of the direct metal deposition laser process, Journal of Physics D: Applied Physics. 41 (2008) 025403. https://doi.org/10.1088/0022-3727/41/2/025403.

[31] P. Peyre, M. Dal, S. Pouzet, O. Castelnau, Simplified numerical model for the laser metal deposition additive manufacturing process, Journal of Laser Applications. 29 (2017). https://doi.org/10.2351/1.4983251.

[32] K.-M. Hong, Y.C. Shin, Analysis of microstructure and mechanical properties change in laser welding of Ti6Al4V with a multiphysics prediction model, Journal of Materials Processing Technology. 237 (2016) 420–429. https://doi.org/10.1016/j.jmatprotec.2016.06.034.

[33] Y. Fan, P. Cheng, Y.L. Yao, Z. Yang, K. Egland, Effect of phase transformations on laser forming of Ti–6Al–4V alloy, Journal of Applied Physics. 98 (2005) 013518. https://doi.org/10.1063/1.1944202.

[34] J. Yang, H. Yu, H. Yang, F. Li, Z. Wang, X. Zeng, Prediction of microstructure in selective laser melted Ti6Al4V alloy by cellular automaton, Journal of Alloys and Compounds. 748 (2018) 281–290. https://doi.org/10.1016/j.jallcom.2018.03.116.

[35] S. Chen, Y. Xu, Y. Jiao, A hybrid finite-element and cellular-automaton framework for modeling 3D microstructure of Ti–6Al–4V alloy during solid–solid phase transformation in additive manufacturing, Modelling Simul. Mater. Sci. Eng. 26 (2018) 045011. https://doi.org/10.1088/1361-651X/aabcad.

33/

[36] S. Liu, Y.C. Shin, Prediction of 3D microstructure and phase distributions of Ti6Al4V built by the directed energy deposition process via combined multi-physics models, Additive Manufacturing. 34 (2020) 101234. https://doi.org/10.1016/j.addma.2020.101234.

[37] G. Vastola, G. Zhang, Q.X. Pei, Y.-W. Zhang, Modeling the Microstructure Evolution During Additive Manufacturing of Ti6Al4V: A Comparison Between Electron Beam Melting and Selective Laser Melting, JOM. 68 (2016) 1370–1375. https://doi.org/10.1007/s11837-016-1890-5.

[38] M. Akbari, S. Saedodin, D. Toghraie, R. Shoja-Razavi, F. Kowsari, Experimental and numerical investigation of temperature distribution and melt pool geometry during pulsed laser welding of Ti6Al4V alloy, Optics & Laser Technology. 59 (2014) 52–59. https://doi.org/10.1016/j.optlastec.2013.12.009.

[39] C.C. Murgau, R. Pederson, L.-E. Lindgren, A model for Ti–6Al–4V microstructure evolution for arbitrary temperature changes, Modelling and Simulation in Materials Science and Engineering. 20 (2012) 055006. https://doi.org/10.1088/0965-0393/20/5/055006.

[40] J.D. Hahn, Y.C. Shin, M.J.M. Krane, Laser transformation hardening of Ti–6Al–4V in solid state with accompanying kinetic model, Surface Engineering. 23 (2007) 78–82. https://doi.org/10.1179/174329407X169467.

[41] J.W. Elmer, T.A. Palmer, S.S. Babu, W. Zhang, T. DebRoy, Phase transformation dynamics during welding of Ti–6Al–4V, Journal of Applied Physics. 95 (2004) 8327–8339. https://doi.org/10.1063/1.1737476.

[42] J.W. Elmer, T.A. Palmer, J. Wong, In situ observations of phase transitions in Ti–6Al–4V alloy welds using spatially resolved x-ray diffraction, Journal of Applied Physics. 93 (2003) 1941–1947. https://doi.org/10.1063/1.1537464.

[43] J. Irwin, E.W. Reutzel, P. Michaleris, J. Keist, A.R. Nassar, Predicting microstructure from thermal history during additive manufacturing for Ti-6Al-4V, Journal of Manufacturing Science and Engineering. 138 (2016) 111007. https://doi.org/10.1115/1.4033525.

[44] H.-S. Tran, J.T. Tchuindjang, H. Paydas, A. Mertens, R.T. Jardin, L. Duchêne, R. Carrus, J. Lecomte-Beckers, A.M. Habraken, 3D thermal finite element analysis of laser cladding processed Ti-6Al-4V part with microstructural correlations, Materials & Design. 128 (2017) 130–142. https://doi.org/10.1016/j.matdes.2017.04.092.

[45] S.M. Kelly, S.L. Kampe, Microstructural evolution in laser-deposited multilayer Ti-6Al-4V builds: Part II. Thermal modeling, Metallurgical and Materials Transactions A. 35 (2004) 1869–1879. https://doi.org/10.1007/s11661-004-0095-7.

[46] M.M. Kirka, P. Nandwana, Y. Lee, R.R. Dehoff, Solidification and solid-state transformation sciences in metals additive manufacturing, Scripta Materialia. 135 (2017) 130–134. https://doi.org/10.1016/j.scriptamat.2017.01.005.

[47] F. Bartolomeu, S. Faria, O. Carvalho, E. Pinto, N. Alves, F.S. Silva, G. Miranda, Predictive models for physical and mechanical properties of Ti6Al4V produced by Selective Laser Melting, Materials Science and Engineering: A. 663 (2016) 181–192. https://doi.org/10.1016/j.msea.2016.03.113.

[48] S.S. Babu, S.M. Kelly, E.D. Specht, T.A. Palmer, J.W. Elmer, Measurement of phase transformation kinetics during repeated thermal cycling of Ti-6Al-4V using time-resolved X-ray diffraction, in: International Conference on Solid-Solid Phase Transformations in Inorganic Materials 2005, 2005: pp. 503–508.

[49] C. Baykasoğlu, O. Akyildiz, M. Tunay, A.C. To, A Process-Microstructure Finite Element Simulation Framework for Predicting Phase Transformations and Microhardness for Directed Energy Deposition of Ti6Al4V, Additive Manufacturing. (2020) 101252. https://doi.org/10.1016/j.addma.2020.101252.

[50] E. Salsi, M. Chiumenti, M. Cervera, Modeling of Microstructure Evolution of Ti6Al4V for Additive Manufacturing, Metals. 8 (2018) 633. https://doi.org/10.3390/met8080633.

[51] A. Suárez, M.J. Tobar, A. Yáñez, I. Pérez, J. Sampedro, V. Amigó, J.J. Candel, Modeling of phase transformations of Ti6Al4V during laser metal deposition, Physics Procedia. 12 (2011) 666–673. https://doi.org/10.1016/j.phpro.2011.03.083.

[52] R. Dąbrowski, The kinetics of phase transformations during continuous cooling of the Ti6Al4V alloy from the single-phase β range, Archives of Metallurgy and Materials. 56 (2011) 703–707. https://doi.org/10.2478/v10172-011-0077-x.

[53] A. Crespo, R. Vilar, Finite element analysis of the rapid manufacturing of Ti–6Al–4V parts by laser powder deposition, Scripta Materialia. 63 (2010) 140–143. https://doi.org/10.1016/j.scriptamat.2010.03.036.

[54] C. Baykasoglu, O. Akyildiz, D. Candemir, Q. Yang, A.C. To, Predicting Microstructure Evolution During Directed Energy Deposition Additive Manufacturing of Ti-6Al-4V, J. Manuf. Sci. Eng. 140 (2018). https://doi.org/10.1115/1.4038894.

[55] J.W. Elmer, T.A. Palmer, S.S. Babu, E.D. Specht, In situ observations of lattice expansion and transformation rates of α and β phases in Ti–6Al–4V, Materials Science and Engineering: A. 391 (2005) 104–113. https://doi.org/10.1016/j.msea.2004.08.084.

[56] C. Kenel, D. Grolimund, X. Li, E. Panepucci, V.A. Samson, D.F. Sanchez, F. Marone, C. Leinenbach, In situ investigation of phase transformations in Ti-6Al-4V under additive manufacturing conditions combining laser melting and high-speed micro-X-ray diffraction, Scientific Reports. 7 (2017) 16358. https://doi.org/10.1038/s41598-017-16760-0.

34/

[57] S. Banerjee, P. Mukhopadhyay, eds., Chapter 1 - Phases and Crystal Structures, in: Pergamon Materials Series, Pergamon, 2007: pp. 1–86. https://doi.org/10.1016/S1470-1804 (07) 80054-X.

[58] T. Ahmed, H.J. Rack, Phase transformations during cooling in α+ β titanium alloys, Materials Science and Engineering: A. 243 (1998) 206–211. https://doi.org/10.1016/S0921-5093 (97) 00802-2.

[59] J. Dai, J. Xia, L. Chai, K.L. Murty, N. Guo, M.R. Daymond, Correlation of microstructural, textural characteristics and hardness of Ti–6Al–4V sheet β-cooled at different rates, Journal of Materials Science. 19 (2020) 8346–8362. https://doi.org/10.1007/s10853-020-04603-9.

[60] E. Brandl, D. Greitemeier, Microstructure of additive layer manufactured Ti–6Al–4V after exceptional post heat treatments, Materials Letters. 81 (2012) 84–87. https://doi.org/10.1016/j.matlet.2012.04.116.

[61] Q. Zhang, J. Xie, Z. Gao, T. London, D. Griffiths, V. Oancea, A metallurgical phase transformation framework applied to SLM additive manufacturing processes, Materials & Design. 166 (2019) 107618. https://doi.org/10.1016/j.matdes.2019.107618.

[62] S.L. Lu, M. Qian, H.P. Tang, M. Yan, J. Wang, D.H. StJohn, Massive transformation in Ti–6Al–4V additively manufactured by selective electron beam melting, Acta Materialia. 104 (2016) 303–311. https://doi.org/10.1016/j.actamat.2015.11.011.

[63] S. Neelakantan, P.E.J. Rivera-Díaz-del-Castillo, S. van der Zwaag, Prediction of the martensite start temperature for β titanium alloys as a function of composition, Scripta Materialia. 60 (2009) 611–614. https://doi.org/10.1016/j.scriptamat.2008.12.034.

[64] K. Dietrich, J. Diller, S. Dubiez-Le Goff, D. Bauer, P. Forêt, G. Witt, The influence of oxygen on the chemical composition and mechanical properties of Ti-6Al-4V during laser powder bed fusion (L-PBF), Additive Manufacturing. 32 (2020) 100980. https://doi.org/10.1016/j.addma.2019.100980.

[65] H.H. Weigand, Zur Umwandlung von α+ β - Titanlegierungen mit Aluminium, Z. Metallkde. 54 (1963) 43–49.

[66] F.X. Gil Mur, D. Rodríguez, J.A. Planell, Influence of tempering temperature and time on the α′-Ti-6Al-4V martensite, Journal of Alloys and Compounds. 234 (1996) 287–289. https://doi.org/10.1016/0925-8388 (95) 02057-8.

[67] S. Banerjee, P. Mukhopadhyay, eds., Chapter 4 - Martensitic Transformations, in: Pergamon Materials Series, Pergamon, 2007: pp. 257–376. https://doi.org/10.1016/S1470-1804 (07) 80057-5.

[68] H. Matsumoto, L. Bin, S.-H. Lee, Y. Li, Y. Ono, A. Chiba, Frequent Occurrence of Discontinuous Dynamic Recrystallization in Ti-6Al-4V Alloy with α′ Martensite Starting Microstructure, Metallurgical and Materials Transactions A. 44 (2013) 3245–3260. https://doi.org/10.1007/s11661-013-1655-5.

[69] T. Morita, K. Hatsuoka, T. Iizuka, K. Kawasaki, Strengthening of Ti–6Al–4V Alloy by Short-Time Duplex Heat Treatment, Materials Transactions. 46 (2005) 1681–1686. https://doi.org/10.2320/matertrans.46.1681.

[70] S.-T. Oh, K.-D. Woo, J.-H. Kim, S.-M. Kwak, The Effect of Al and V on Microstructure and Transformation of β Phase during Solution Treatments of Cast Ti-6Al-4V Alloy, Korean Journal of Metals and Materials. 55 (2017) 150–155. https://doi.org/2017.55.3.150.

[71] G. Welsch, R. Boyer, E.W. Collings, Section IV: Alpha-Beta Alloys. Ti-6Al-4V, in: Materials Properties Handbook: Titanium Alloys, ASM international, 1993: pp. 483–636.

[72] M.T. Jovanović, S. Tadić, S. Zec, Z. Mišković, I. Bobić, The effect of annealing temperatures and cooling rates on microstructure and mechanical properties of investment cast Ti–6Al–4V alloy, Materials & Design. 27 (2006) 192–199. https://doi.org/10.1016/j.matdes.2004.10.017.

[73] M. Koike, P. Greer, K. Owen, G. Lilly, L.E. Murr, S.M. Gaytan, E. Martinez, T. Okabe, Evaluation of Titanium Alloys Fabricated Using Rapid Prototyping Technologies—Electron Beam Melting and Laser Beam Melting, Materials. 4 (2011) 1776–1792. https://doi.org/10.3390/ma4101776.

[74] K. Beyl, K. Mutombo, C.P. Kloppers, Tensile properties and microstructural characterization of additive manufactured, investment cast and wrought Ti6Al4V alloy, IOP Conf. Ser.: Mater. Sci. Eng. 655 (2019) 012023. https://doi.org/10.1088/1757-899X/655/1/012023.

[75] R. Sahoo, B.B. Jha, T.K. Sahoo, Effect of primary alpha phase variation on mechanical behaviour of Ti–6Al–4V alloy, Materials Science and Technology. 31 (2015) 1486–1494. https://doi.org/10.1179/1743284714Y.0000000736.

[76] J.S. Zuback, T. DebRoy, The Hardness of Additively Manufactured Alloys, Materials. 11 (2018) 2070. https://doi.org/10.3390/ma11112070.

[77] B. Vandenbroucke, J. Kruth, Selective laser melting of biocompatible metals for rapid manufacturing of medical parts, Rapid Prototyping Journal. 13 (2007) 196–203. https://doi.org/10.1108/13552540710776142.

[78] H. Fujii, Continuous cooling transformation characteristics of alpha+ beta titanium alloys, Nippon Steel Tech. Rep. (Japan). 62 (1994) 74–79.

[79] P. Tan, F. Shen, B. Li, K. Zhou, A thermo-metallurgical-mechanical model for selective laser melting of Ti6Al4V, Materials & Design. 168 (2019) 107642. https://doi.org/10.1016/j.matdes.2019.107642.

[80] A. Montelione, S. Ghods, R. Schur, C. Wisdom, D. Arola, M. Ramulu, Powder Reuse in Electron Beam Melting Additive Manufacturing of Ti6Al4V: Particle Microstructure, Oxygen Content and Mechanical Properties, Additive Manufacturing. 35 (2020) 101216. https://doi.org/10.1016/j.addma.2020.101216.

35/

[81]   F. Pascon, A.M. Habraken, Finite element study of the effect of some local defects on the risk of transverse cracking in continuous casting of steel slabs, Computer Methods in Applied Mechanics and Engineering. 196 (2007) 2285–2299. https://doi.org/10.1016/j.cma.2006.07.017.

[82]   Y.Y. Zhu, S. Cescotto, Unified and mixed formulation of the 8-node hexahedral elements by assumed strain method, Computer Methods in Applied Mechanics and Engineering. 129 (1996) 177–209. https://doi.org/10.1016/0045-7825 (95) 00835-7.

[83]   J. Yang, S. Sun, M. Brandt, W. Yan, Experimental investigation and 3D finite element prediction of the heat affected zone during laser assisted machining of Ti6Al4V alloy, Journal of Materials Processing Technology. 210 (2010) 2215–2222. https://doi.org/10.1016/j.jmatprotec.2010.08.007.

36/

Supplementary Material: Conditions for recrystallization occurrence during reheating
A conventional heat treatment has been performed to better understand the mechanism of the reverse phase transformation occurring upon heating when martensite is already present in a part of the deposit during DED. For this purpose, a solution heat treatment has been carried out under Argon, on a small sample extracted from the as-built deposit of Fig. S1a. After heating up to 1000°C for 30 minutes and water quenching, the original columnar grains (Fig. S1b) present in the as built part, become martensitic with equiaxed grains (Fig. S1c) smaller in size than the prior β columnar grains.
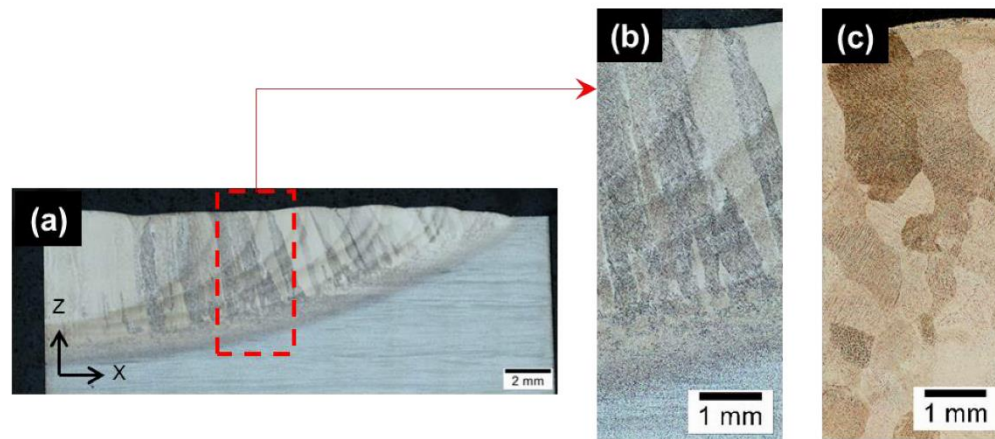

Figure S1: (a) Overview of half deposit in as-built conditions with enhancement of HAZ (dark curved areas) and large nugget in the center (light area) (from [1]); (b) Close-up view of the inset within (a), showing the prior columnar β grains in the as-built deposit; (c) β columnar grains turned into equiaxed due to recrystallization after furnace reheating to 1000°C/30'and later transformed into α' due to subsequent water quenching.

An average hardness of 377± 4 HV$_{10}$ was measured, which is either due to grain refinement, or to high dislocation densities, twins or stacking faults [2–8]. Recovery usually takes place prior to recrystallization whose rate increases with the dislocations density [9–11]. Both recovery and recrystallization kinetics are thermally activated [9,12,13]. After a sufficient residence time at high temperature, the quenched sample (Fig. S1c) undergoes nucleation and growth of newly formed β grains [6,14,15]. Additional strengthening/hardening is achieved due to rapid water cooling from β field that suppresses diffusion, leading to supersaturated α' that contains twins. The nanotwin boundaries are more effective obstacle to slip than ordinary high angle boundaries between prior β grains.

However, it must be concluded that the steep thermal cycles with short residence times achieved during DED do not induce any recrystallization within the prior β-grains that grew epitaxially, leading to a coarse columnar macrostructure (Fig. S1b) observed in the as-built samples.

References
[1]   H. Paydas, A. Mertens, R. Carrus, J. Lecomte-Beckers, J. Tchoufang Tchuindjang, Laser cladding as repair technology for Ti–6Al–4V alloy: Influence of building strategy on microstructure and hardness, Materials & Design. 85 (2015) 497–510. https://doi.org/10.1016/j.matdes.2015.07.035.

[2]   J. Yang, H. Yu, J. Yin, M. Gao, Z. Wang, X. Zeng, Formation and control of martensite in Ti-6Al-4V alloy produced by selective laser melting, Materials & Design. 108 (2016) 308–318. https://doi.org/10.1016/j.matdes.2016.06.117.

[3]   J. He, D. Li, W. Jiang, L. Ke, G. Qin, Y. Ye, Q. Qin, D. Qiu, The Martensitic Transformation and Mechanical Properties of Ti6Al4V Prepared via Selective Laser Melting, Materials. 12 (2019) 321. https://doi.org/10.3390/ma12020321.

[4]   S. Banerjee, P. Mukhopadhyay, eds., Chapter 4 - Martensitic Transformations, in: Pergamon Materials Series, Pergamon, 2007: pp. 257–376. https://doi.org/10.1016/S1470-1804 (07) 80057-5.

[5]   L.E. Murr, S.A. Quinones, S.M. Gaytan, M.I. Lopez, A. Rodela, E.Y. Martinez, D.H. Hernandez, E. Martinez, F. Medina, R.B. Wicker, Microstructure and mechanical behavior of Ti–6Al–4V produced by rapid-layer manufacturing,

37/

for biomedical applications, Journal of the Mechanical Behavior of Biomedical Materials. 2 (2009) 20–32. https://doi.org/10.1016/j.jmbbm.2008.05.004.

[6] J. Dai, J. Xia, L. Chai, K.L. Murty, N. Guo, M.R. Daymond, Correlation of microstructural, textural characteristics and hardness of Ti–6Al–4V sheet β-cooled at different rates, Journal of Materials Science. 19 (2020) 8346–8362. https://doi.org/10.1007/s10853-020-04603-9.

[7] B. Vandenbroucke, J. Kruth, Selective laser melting of biocompatible metals for rapid manufacturing of medical parts, Rapid Prototyping Journal. 13 (2007) 196–203. https://doi.org/10.1108/13552540710776142.

[8] S.-T. Oh, K.-D. Woo, J.-H. Kim, S.-M. Kwak, The Effect of Al and V on Microstructure and Transformation of β Phase during Solution Treatments of Cast Ti-6Al-4V Alloy, Korean Journal of Metals and Materials. 55 (2017) 150–155. https://doi.org/2017.55.3.150.

[9] H. Matsumoto, L. Bin, S.-H. Lee, Y. Li, Y. Ono, A. Chiba, Frequent Occurrence of Discontinuous Dynamic Recrystallization in Ti-6Al-4V Alloy with α′ Martensite Starting Microstructure, Metallurgical and Materials Transactions A. 44 (2013) 3245–3260. https://doi.org/10.1007/s11661-013-1655-5.

[10] E. Brandl, A. Schoberth, C. Leyens, Morphology, microstructure, and hardness of titanium (Ti-6Al-4V) blocks deposited by wire-feed additive layer manufacturing (ALM), Materials Science and Engineering: A. 532 (2012) 295–307. https://doi.org/10.1016/j.msea.2011.10.095.

[11] J.S. Zuback, T. DebRoy, The Hardness of Additively Manufactured Alloys, Materials. 11 (2018) 2070. https://doi.org/10.3390/ma11112070.

[12] J. Donoghue, A.A. Antonysamy, F. Martina, P.A. Colegrove, S.W. Williams, P.B. Prangnell, The effectiveness of combining rolling deformation with Wire–Arc Additive Manufacture on β-grain refinement and texture modification in Ti–6Al–4V, Materials Characterization. 114 (2016) 103–114. https://doi.org/10.1016/j.matchar.2016.02.001.

[13] O.M. Ivasishin, R.V. Teliovich, Potential of rapid heat treatment of titanium alloys and steels, Materials Science and Engineering: A. 263 (1999) 142–154. https://doi.org/10.1016/S0921-5093 (98)01173-3.

[14] E. Brandl, D. Greitemeier, Microstructure of additive layer manufactured Ti–6Al–4V after exceptional post heat treatments, Materials Letters. 81 (2012) 84–87. https://doi.org/10.1016/j.matlet.2012.04.116.

[15] J.D. Hahn, Y.C. Shin, M.J.M. Krane, Laser transformation hardening of Ti–6Al–4V in solid state with accompanying kinetic model, Surface Engineering. 23 (2007) 78–82. https://doi.org/10.1179/174329407X169467.

38/

• ANNEXE 2 : LISTE DE PUBLICATIONS SCIENTIFIQUES DE L'AUTEUR – ARTICLES DE JOURNAUX

•

Publications et ouvrages de Jérôme Tchoufang Tchuindjang [u182995]

Légende 📕, 📄, etc: texte intégral du document disponible en Open Access 🔒📕, 🔒📄, etc: texte intégral du document disponible en accès restreint. **(Article #X et *Chapitre Y*, utilisés dans la thèse)**

• **Thèses et mémoires**

• Mémoire de DEA

Effet des inclusions et des carbures sur les propriétés mécaniques dans des alliages Fe-Cr-C-X : application à la rupture en fatigue. (2004) https://explore.lib.uliege.be/permalink/32ULG_INST/1iujq0/alma990016313940502321

• **Articles dans des revues scientifiques avec peer reviewing**

• À portée internationale

En tant que premier ou dernier auteur

🔒📕

Maurizi-Enrici, T., Mertens, A., Sinnaeve, M., & Tchuindjang, J. T. (2019). Elucidation of the solidification sequence of a complex graphitic HSS alloy under a combined approach of DTA and EBSD analyses. *Journal of Thermal Analysis and Calorimetry, 1*(15). *(Chapitres I, II, III et X)*
http://hdl.handle.net/2268/241632

🔒📕

Paydas, H., Mertens, A., Carrus, R., Lecomte-Beckers, J., & Tchuindjang, J. T. (2015). Laser cladding as repair technology for Ti6Al4V alloy: Influence of building strategy on microstructure and hardness. *Materials and Design, 85*, 497-510. **(Article #6)**
http://hdl.handle.net/2268/183796

🔒📕

Tchuindjang, J. T., Neira Torres, I., Fores, P., Habraken, A., & Lecomte-Beckers, J. (2015). Phase Transformations and Crack Initiation in a High-Chromium Cast Steel Under Hot Compression Tests. *Journal of Materials Engineering and Performance, 24*(5), 2025-2041. **(Article #5)**
http://hdl.handle.net/2268/179263

📕

Lecomte-Beckers, J., Sinnaeve, M., & Tchuindjang, J. T. (2012, February). Current Developments of Alloyed Steels for Hot Strip Roughing Mills : Characterization of High-Chromium Steel and Semi-High Speed Steel. *Iron and Steel Technology*, 33-40. **(Article #4)**
http://hdl.handle.net/2268/121453

📕

Lecomte-Beckers, J., & Tchuindjang, J. T. (2011). Study of the origin of the unexpected pearlite during the cooling stage of two cast high-speed steels. *Solid State Phenomana, 172-174*, 803-808. **(Article #3)**
http://hdl.handle.net/2268/95529

📕

Lecomte-Beckers, J., & Tchuindjang, J. T. (2009). Structural investigation of solidification and heat treatments influence on High Alloyed Cast Irons Grades with Nb-V-Ti Additions. *Defects and diffusion forum, 289-292*, 77-86. **(Article #2)**

http://hdl.handle.net/2268/18896

Tchuindjang, J. T., & Lecomte-Beckers, J. (2007). Fractography survey on high cycle fatigue failure: Crack origin characterisation and correlations between mechanical tests and microstructure in Fe-C-Cr-Mo-X alloys. *International Journal of Fatigue, 29*(4), 713-728. **(Article #1)**
http://hdl.handle.net/2268/24845

Lecomte-Beckers, J., & Tchuindjang, J. T. (2005). Use of Microscopy for identification of complex MC, M2C, M6C, M7C3 and M23C6 carbides in high speed-steels. *Imaging and Microscopy, 2*, 48-49.
http://hdl.handle.net/2268/24887

En tant que co-auteur

Ganou Koungang, B. M., Ndapeu, D., Tchuindjang, J. T., Wenga Ntcheping, B., Tchemou, G., Bistac, S., Njeugna, E., & Courard, L. (2020). Influence of temperature on the creep behaviour by macroindentation of Cocos nucifera shells and Canarium schweinfurthii cores (bio-shellnut wastes in Cameroon). *Materials Research Express, 7*(10), 14.
http://hdl.handle.net/2268/251570

Mertens, A., Delahaye, J., Dedry, O., Vertruyen, B., Tchuindjang, J. T., & Habraken, A. (2020). Microstructure and Properties of SLM AlSi10Mg: Understanding the Influence of the Local Thermal History. *Procedia Manufacturing, 47*, 1089-1095. *(Chapitre X)*
http://hdl.handle.net/2268/245024

Maurizi-Enrici, T., Dedry, O., Boschini, F., Tchuindjang, J. T., & Mertens, A. (2020, May 28). Microstructural and Thermal Characterization of 316L+WC Composite Coatings obtained by Laser Cladding. *Advanced Engineering Materials*. *(Chapitre X)*
http://hdl.handle.net/2268/247752

Delahaye, J., Tchuindjang, J. T., Lecomte-Beckers, J., Rigo, O., Habraken, A., & Mertens, A. (2019). Influence of Si precipitates on fracture mechanisms of AlSi10Mg parts processed by Selective Laser Melting. *Acta Materialia, 175*, 160-170. *(Chapitre X)*
http://hdl.handle.net/2268/236982

Tomé Jardin, R. A., Tchuindjang, J. T., Duchene, L., Tran, H. S., Hashemi, S. N., Carrus, R., Mertens, A., & Habraken, A. (2019). Thermal histories and microstructures in Direct Energy Deposition of a High Speed Steel thick deposit. *Materials Letters, 236*, 42-45. *(Chapitre X)*
http://hdl.handle.net/2268/229743

Tran, H. S., Tchuindjang, J. T., Paydas, H., Mertens, A., Tomé Jardin, R. A., Duchene, L., Carrus, R., Lecomte-Beckers, J., & Habraken, A. (2017). 3D thermal finite element analysis of laser cladding processed Ti-6Al-4V part with microstructural correlations. *Materials and Design, 128*, 130-142. **(Article #7)**
http://hdl.handle.net/2268/210584

Neira Torres, I., Gilles, G., Tchuindjang, J. T., Flores, P., Lecomte-Beckers, J., & Habraken, A. (2017). FE modeling of the cooling and tempering steps of bimetallic rolling mill rolls. *International Journal of Material Forming, Volume 10*(Issue 3), 287–305. *(Chapitre V)*
http://hdl.handle.net/2268/194318

Hashemi, S. N., Mertens, A., Montrieux, H.-M., Tchuindjang, J. T., Dedry, O., Carrus, R., & Lecomte-Beckers, J. (2017). Oxidative wear behaviour of laser clad high speed steel thick deposits: influence of sliding speed, carbide type and morphology. *Surface and Coatings Technology, 315*, 519-529. ***(Chapitre X)***
http://hdl.handle.net/2268/207848

De Baere, K., Verstraelen, H., Willemen, R., Smet, J.-P., Tchuindjang, J. T., Lecomte-Beckers, J., Lenaerts, S., Meskens, R., Jung, H. G., & Potters, G. (2017). Assessment of corrosion resistance, material properties, and weldability of alloyed steel for ballast tanks. *Journal of Marine Science and Technology, 22*(1), 176-199.
http://hdl.handle.net/2268/203103

Neira Torres, I., Gilles, G., Tchuindjang, J. T., Lecomte-Beckers, J., sinnaeve, M., & Habraken, A. (2014). Study of residual stresses in bimetallic work rolls. *Advanced Materials Research, 996*, 580-585.
http://hdl.handle.net/2268/171571

Lecomte-Beckers, J., Tchuindjang, J. T., Pirard, E., & Breyer, J.-P. (2003). Development of a new high-speed steel with optimized carbide composition for mill rolls. *Stal', 2*, 88-92.
http://hdl.handle.net/2268/20389

- ## Ouvrages

3.b. En tant qu'éditeur scientifique ou directeur de publication

Lecomte-Beckers, J., & Tchuindjang, J. T. (Eds.). (2011). *Proceedings of the international conference Abrasion 2011 (Abrasion Wear Resistant Alloyed White Cast Irons For Rolling and Pulverizing Mills), 4th Edition*. Liège, Belgium: ULg-Service MMS.
http://hdl.handle.net/2268/112806

. ANNEXE 3 : COURT CV SCIENTIFIQUE (EXPERTISES)

Ingénieur de recherches sur conventions et projets (1998 à présent)

- Chercheur métallurgiste chargé de la caractérisation des microstructures en lien avec les procédés d'élaboration et les propriétés. Etablissement de corrélations et rédactions de rapports techniques.
- Participations à des conférences scientifiques (plus d'une trentaine)
- Quinzaine de projets divers (RW, FEDER, FWB, PAI, etc.) avec collaboration universitaire et parrainage industriel, souvent en parallèle. Durée variable (6 mois à 3 ans)
- Thématiques variées, en métallurgie et en mécanique (Liste non exhaustive)

📁 ARC - Macro-mousses - Conception machine d'impact - 2004 à 2006

📁 BLUM - Soudure par friction Ti6Al4V - TechspaceAero - 2012 à 2014

📁 CENCYLAM - Modeling the vertical Spin Casting Process - Appui DEA Studer - 2007 à 2010

📁 Characterization of various work hardened steels - Appui PhD ROSSI - 2011 à 2012

📁 Convention RW 3937_MK - Développpement de nouveaux alliages et leur technologie pour cylindres de laminoir à chaud - 1999 à 2000

📁 Convention RW 4844_MK - Traces sur ICDP - 2005 à 2007

📁 Convention RW 5359_MK - Dégradation Thermochimique des cylindres - 2007 à 2009

📁 Convention RW 6148_MK - Développement technologies et matériaux innovants pour fabrication de cylindres à chaud - MK- 2010 à 2012

📁 Convention RW 6418 - Ultra CB - Faisabilité développement revêtement protection anti-corrosion sur substrat métallique - 2008 à 2012

📁 Convention RW 6929_MK - Endefinu - Endommagement de cylindres dernières cages finisseuses pour mise au point nouvelle nuance - 2013 à 2015

📁 Convention RW 7522_MK - Nerorolls - Développement nouvelles nuances semi-HSS pour cages dégrossisage - 2017 à 2019

📁 Coopération CGRI Bulgarie-Liège_MK - Etude et caractérisation de singuarités dans le brut de coulée de cylindres - 2009-2011

📁 DRI, Bulgarie, CF, RW_MK - Mesure austénite résiduelle dans enveloppes de cylindres par diverses techniques - 2006 à 2007

📁 GEMMAG - Etude d'un générateur magnétothermique - 2006 à 2007

📁 IAWATHA - FEDER - Innovation en Wallonie par les Technologies Additives - 2016_présent

📁 PHAKIR_MK - Cinétique des changements de phases et application à la précipitation dans des alliages à Haut Cr - Appui First Entreprise -2004 à 2006

📁 QUALAM - Quality in Additive Manufacturing - 2016 à 2019

📁 QUAPERIN - Optimal conditions to cast in peritectic alloys without crakcs in Continuous Casting - Appui PhD SCHWARTZ - 2006 à 2008

📁 RECYCLAD - RW 11-1-7335 - Fabrication de Cylindres Bimétalliques par Rechargement Laser - 2011 à 2015

📁 RW114877_INCA - Effet des inclusions et carbures dans aciers et fontes fortement alliés soumis à des sollicitation sévères - 2002 à 2004

📁 RW9713651_COST517 - Relation entre schéma inclusionnaire_nature et distribution de carbures et propriétés mécaniques - 1998 à 2001

📁 SOUBIRO - Modelling of the Cooling and the Thermal Treatment of Bimetallic Rolls - Appui PhD NeirA - 2010 à 2014

Collaborateur scientifique (2003 à présent)

- Encadrement de stages et TFEs en lien avec projets de recherches
- Participation à des travaux dans le cadre de PhD (appui en Sciences de matériaux)

Expert scientifique pour diagnostic de rupture ou de corrosion (1999 à présent)

- Laboratoire MMS est actif depuis environ 25 ans, dans le conseil et les analyses de pièces métalliques et/ou de composants mécaniques sinistrés avant ou au cours leur mise en service. L'auteur a démarré les expertises en 1999 (un an après l'intégration à l'unité).
- Travail réalisé à la demande d'un client externe (entreprise ou particulier, utilisateur final ou fournisseur), à la demande d'un autre laboratoire universitaire (complément d'études), ou via un expert judiciaire auprès d'un tribunal (cas de litige entre plusieurs intervenants).
- Délivrable de type rapport d'analyses (fixant le scénario de l'endommagement ou posant son hypothèse la plus probable) ou avis scientifique (étude bibliographique ou état de l'art)
- Plus de deux cents (200) études réalisées, sur les vingt dernières années, à destination de tous les types d'entreprises (multinationales, GE, PME, TPE, etc.), des particuliers, ou de médias

- 2VALORISE - Fuites sur échangeurs cuivre - T WILLEM - Octobre 2018
- 3B - Analyse sur 2e oreille cassée prématurément - P SIMON - Novembre 2013
- 3B - Binani - Fibreglass - Crack at ear n bushings - F LEMOINE - Feb 2020
- 3B - Corrosion sur acier support filière + Spécifications Matières - D LAURENT, Nov 2017
- 3B - Dégradation Ring enfourneuse - J M GERON - Oct 2017
- 3B - Fiberglass - Tôles Pt-Rh fissurées - D Laurent - Avril 2012
- 3B - FibreGlass - Binani - Rupture vis Felxible Busbar - D LAURENT - Septembre 2018
- 3B - Rupture Ring enfourneuse - P LECRENIER - Nov 2015
- 3B FibreGlass - Binami - Ruptures sur Oreilles de Filières - D. LAURENT - Février 2020
- A & EBA - Tôles corrodées d'une verrière - Expert Didier GOFFAUX - Avril 2011
- A & EBA - Tuyauteries Acier Galva Corrodées - Expert Didier GOFFAUX - Mai 2006
- ABB Belgium - Masques Mo et recouvrement Zn - Christophe GALLOY - Novembre 2005
- ACTE - Corrosion sur collecteur pour thermo-échangeur en Inox 321 - S DUBOIS - Avril 2013
- ACV Manufacturing - Contrôle qualité sur soudure inox fissurée - P Forret - Juillet 2012
- AF COMPRESSORS - Thermal Treatment and QC on Ductile Cast Iron for Cranshafts - V d'OULTREMONT - March 2014
- AIB Vinçotte - ITER - L STEFANSKI - Sept 2013
- AIDE - Corrosion sur tuyauterie inox - Jean-Pierre SILAN, Février 2010
- AIDE - Couvercle pompe en fonte corrodé - O MATHONET, Oct 2017
- Aigremont - Pigon rompu - P-A Mottart, Janvier 2012
- AKERS - Micros HV
- AKERS Rolls - Caractérisation et quantification de carbures - Mars 2014 - C GASPARD
- ALD-TP - Tubé étiré - David MATHUS, Décembre 2008
- ALSTOM Transport - Rupture sur détendeurs thermostatiques - F GARNICHE - Décembre 2008

- AMA - Corrosion in Al-bearing steel - Prof. K De BAERE, Jan 2013
- AMOS - CTE St37
- AMOS - Taches sur AA6061 anodisé - M DORTHU, Janv 2016
- Analyses Chimiques CRM
- APRUZZESE - CQ sur garde-corps en Alu 6060 - B RENETTE - Février 2017
- ARSA - Rides oscillation sur brame de coulée continue - Nicolas TRIOLET
- ARSOC SA - Contrôle passivation sur vis inox - F V MAES, Mars 2001
- ASTRON Buildings - Biblio et Avis scientifique utilisation SJ355 - J L LECOMTE - Avril 2019
- ASTRON Buildings SA - Assessment of a metallurgical model tool for mechanical validation of flat-rolls products - WEINQUEIN - March 2006
- Atelier SAUVAGE - Avis sur effet Pb dans Bronze pour coussinet - Janvier 2008
- Ateliers SAUVAGE - Calculs en Mécanique de la rupture sur arbre fretté
- Ateliers SAUVAGE - Contrôle Qualité sur moyeu et patin pour enrobeuse - M SAUVAGE, Avril 2006
- Atlantis International Services - Christian COLLEE - Maillon de chaîne rompu, Octobre 2010 et Mai 2011
- AXIMA Services - Dépôts oxides sur axe en inox - Raperie Longchamps-Inox recouvert - Mars 2006
- BC&M - Contrôle-Qualité sur Vis Inox - Stas de RICHELLE, Décembre 2012
- BE E-BEx - Rupture sur collecteur laiton - D Fleury - Mars 2017
- BE Ghyselen - Analyses sur tuyaux oxydés - M GHYSELEN, Mai 2001
- BE J DARGENT - Rupture attache remorque - Octobre 2018
- BE Pol Louis - Marteaux Broyeur rompus - M MARECHAL pour LHONNEUX - Juillet 2005
- BE Pol Louis - Rupture sur tuyaux échangeurs à chaleur DELHEZ Bois SPRL - Janvier 2010
- BE Pol Louis- Contrôle-Quaité sur Boulons Inox pour Four de fonderie - M MARECHAL - Mai 2004
- BE RIGO - Août 2016 - Pièce en laiton usée - POYSAT
- BE RIGO - Corrosion paroi métallique piscine - Août 2020
- BOMBARDIER Transportation - Usure prématurée sur des bandages de roues de tram - Mrs CHAVEE & ZANUTTI, Février 2003
- BOSAL International - Anayses chimiques sur plaques inox - T BECO, Mai 2007
- Bureau GHAYE sprl - Expertise sur fissuration citerne à mazout - P. GHAYE, Juin 2011

- CEB Arbis - Vannes laitons rompues en service - M MARCHAL - Juillet 2014
- CEB Arbis ancien BE Pol Louis - Tuyauteries galvanisées corrodées - Novembre 2011 - Juillet 2013
- CED - Rupture Axe LAND KITE - C. COMEIN, Fév 2018
- CED International - Corrosion sur trappillon fonte - C COMEIN - Oct 2017
- CEWAC - Mesures Austenite résiduelle par UAR sur soudures Inox - Jonathan De SIMONE, Février 2005
- CFR - Métallos sur Bandages Tram - Marc TRAVERSIN, Novembre 2006
- CIEX - Aile de voiture froissée - Expert P LEGRAND, Février 2011
- CIEX - Rupture sur chapeau de vanne - Expert P LEGRAND, Octobre 2009
- CIEX - Vannes ZR 3e série et Soupapes IVECO - Expert P LEGRAND, Novembre 2012
- CLOSE - Rupture de raccords en laiton pour flexibles circuit plafonds froids - C de FROIDMONT, Février 2014
- CMI - Goupille Inconel 601 fluée - Joseph PRIAROLLO
- CMI - Rupture Butée de sécurité AA5xxx - Aurore GEORGES - Juin 2014
- CMI Defence - Avis scientifique sur traitement de surface sur Alu 6082 - M ROURE - Mars 2017
- CMI Defence - Clavette frein de bouche canon rompue - V NIHOUL & E BOUHY - Janvier 2016
- CMI Defence - Fissuration Boîte à fumée - P NACHTERGAELE - Juillet 2018
- CMI Defence - Fissures après impacts sur plaque convoyeur AA 5083 - V NIHOUL, Avril 2012
- CMI Defence - Rupture sur vis M24 en service - P DELVAUX, Novembre 2014

- CPL Industries - Axe de chaîne d'élévateur rompu - R DOSSERAY - Avril 2012
- CPL Industries - Maillon de chaîne rompu - Rafael CORTES, Cimenterie , Mars 2007
- CPL Industries - Rupture axe - R DOSSERAY - Juin 2019
- CPL Industries, Maillon et Axe pour CQ - R CORTES, Novembre 2007
- CPL-Axes de chaîne d'étirage - Rafael CORTES, Décembre 2004
- CPL-Industrie - Rupture axe ventilateur - R DOSSERAY, Juin 2019
- DELTA - Duretés comparées de plaquettes de carbures - Marc LIENART pour PRECIMECA, Juin 2003

- DOA Luxembourg - Barre de précontrainte rompue - Expert DUBOIS - Remise Avril 2005
- Dr RATY - Composition chimique pipe Bamun - Mars 2017
- DREVER Group - Dépôt sur tige de fixation de brique réfractaire dans four de galvanisation - Mme DUBOIS, Décembre 2000
- DSITRIGAZ - Analyses soudures et étanchéité sur conduite de gaz - Litige Pont de Vivegnis - TPI Liège, Octobre 2002
- DUCHENE - Corrosion sur conduites Inox pressurisées - J-M DUBOIS, Mars 2012
- DUCHENE-EIFFAGE - Corrosion connecteurs en Cu par H2S - J-M DUBOIS, Sept 2014
- DUFERCO - Duretés sur Blocs bruts oxycoupés - Stefaan MENTEN - 301109

- ENSIVAL MORET - CQ et Rupture sur tuyauterie Inox pour pompe - U GULSU - Juin 2016
- Euro Metal Service - Tâches en surface de tôles acier avec revêtement Zincalume - A DEBAHY - Mars 2017
- EURO-DIESEL - Cavitation sur arbre transmission DAI - P VOIGT, Décembre 2017
- EURO-DIESEL - Coefficients de dilatation thermique - K-E. VOIGT, Avril 2019
- EURO-DIESEL - Contrôle-validation traitement thermique sur arbre 42CrMo4 - L. SPRONCK - Mars 2018
- EURO-DIESEL - Corrosion sur bandages de roulements à rouleaux cylindriues - P VOIGT, Mai 2018
- EURO-DIESEL - Degradation sur roulements à billes - P. VOIGT - Sept 2018
- EURO-DIESEL - WRTC Bearings - P FALZONI - March 2019

- Expert DENIS - Arbre Essieu rompu - Mai 2000
- Expert Ed RADOUX - Rupture différentiel VW Golf - Octobre 2016
- Expert HOUCHARD - Filament Ampoule W, Affaire Gaertner - Juin 2008
- Expert HOUCHARD - Filament d'ampoule W rompu, M HOUCHARD, Mars 2001
- Expert PIGNEUR - Ruptures multiples sur chaîne de transmission pour bétonneuse
- Expert RADOUX - Rupture rivet fixation couronne différentiel, 150908
- Expert SOMJA - Filament d'ampoule W rompu - Aout 2000
- Experts-Partners - Vis rompue - J-P Octave - Juin 2020
- EXPLORAID - Serre-câbles corrodés - A SOUBRY, Octobre 2014
- Factures intermédiaires
- Failure and bubbling in Fe-Ni reed switches coated with Cu-Ag - Confidentiel, Sept 2015
- Forges de Zeebrugge SA - Corrosion sur moteur_tube Alu-brin acier zingué - C DEFISE - Oct 2016
- Forges de Zeebrugge SA - Rupture précoce sur tube en Alu 7075T - Christian EHX - Mars 2014
- FREYSSINET - Diagnostic Rupture et CQ sur tiges filetées - L GOFFART - Avril 2017
- GANTREX - FAilure of a composite rail - R JARDIN, Feb 2020
- GANTREX - Failure of a mono rail - R JARDIN, July 2020
- GANTREX - Rupture rails guidage grue - J VIS, Nov 2019
- GDK - Mesure d'épaisseur de cuivre électrolytique - G Dekoninck - Janvier 2010
- GE - Mesure défauts par profilomtérie optique - A BLANCHY, Février 2019

- GEBR LUNGES - Fissure et cavitation sur piston motheur diesel 12kW - F VLEIGEN, Juin 2015
- GEC ALSTHOM - Aanlyses SEM sur matériaux frittés avec substrat résiduel, Juillet 2001
- GeoMar - Vannes laiton rompues - Expert MARECHAL
- Gerard DEBRASSINE & FILS- Vannes laiton rompues - G DEBRASSINE, Janvier 2006
- GERKEN sa - Rupture rondelles et vis flasque - A CRIMINISI - Septembre 2016
- GEXA - Rupture sur boulons nacelle - V MARCHAL - Nov 2017
- GIGA - Inox 316L pour siphon corrodé - M WINANDY
- HALLIBURTON - Usure abrasive sur trépans aciers pour forage roches - O MAGEREN, Janvier 2014
- HAMON THERMAL - Avis scientifique sur tenue AA3003 à la corrosion - F BOUTON, Février 2015
- HAMON THERMAL - Tubes en acier revêtus en Al, avec ailettes - Intmd F MICEL et A DARIMONT, Mars 2012
- HAMON THERMAL EUROPE - Essais de corrosion sur Inox dans environnement chlorés - Mars 2008
- HAMON THERMAL EUROPE - Etude Théorique sur tenue de matériaux divers à un environnement chloré - Ludovic SIRJACQ - Août 2009
- HAMON THERMAL GbmH - Corrosion Inox 304 sous eau chlorée, Avis scientifique - Mrs EXNER, F BOUTON & V GANZITTI - Juillet 2006
- HP Linden - Tenue calamine sur aciers de construction, Avis scientifique - U LINDEN, Septembre 2018
- Hydro Aluminium - Analyse chimique XRF de renforts en Alu - F BARTHOLOME - Septembre 2007
- Hydro Aluminium - CQ sur filières X37CrMoV5-1 - DOSSIN - Mars 2013

📁 INOWAI - KUBIK - Analyse perforation battéries échangeurs thermiques - G Bauer - Novembre 2016

📁 IRENO - Corrosion boulons galvanisés - SCHWIND et FRANSOLET - Octobre 2015

📁 IRENO - Provisoire

📁 ISS - Pivot d'excavateur rompu - DOSSERAY pour HOLCIM Granulats (Mme COETSIER) - Octobre 2003

📁 ISSEP - Déformation sur polymères

📁 JAC Machines - Evaluation système freinage motoréducteur - G Thomas, Novembre 2017

📁 JAC-MACHINES - HV sur lames couteaux - A HUMBLET - Septembre 2006

📁 JOSKIN SA - Anneaux d'attelage rompus - LENARTZ et JAEGHERS - Juillet 2009

📁 KEYVEST - Analyse morphologique poudres Si - R STASSEN - Juin 2017

📁 KINOLT - Ex-EURO-DIESEL - KS7 BBC - Briers - September 2019

📁 KINOLT - Roulement KS7-II Marseille - Briers - Février 2020

📁 KnaufInsulation - Déformation de chaînon d'un convoyeur de four de cuisson - C MEDINA, Novembre 2013

📁 KnaufInsulation - Surchauffe sur chainons de convoyeur de four de cuisson - C MEDINA, Septembre 2014

📁 KONE - Tube en inox avec taches de corrosion - STRIJMEERSCH, Oct 2011

📁 LABORELLEC - ENGIE - Identification of failure mechanism on SS HAZ - M LOT, May 2016

📁 LHOIST Western Europe - CQ sur poinçon en acier Z100CDV5 - B FISSON, Avril 2016

📁 LOUISE Belgique - Rupture arbre élévatuer à godets - A DELWAIDE - Janvier 2009

📁 MATERNE Confilux - Corrosion sur fourreau de remplissage HEAM - J-P BLOOM, Février 2015

📁 McLarens Young Belgium pour GSK Bio - fissuration conduites centrales de cogénération - Mai 2012

📁 Me s'SERSTEVENS - Avis scientifique sur rupture différée panneau alu - Novembre 2019

📁 Mecanique Ressort Belgique - CQ sur fil en 17-7 PH - S BAIMONTE

📁 MECATECH SPRL - Contrôle d'amagéntisme - Sylvia VANDERBYSE-PAPALIA

📁 MEISTER CC - Mesures UAR sur pièces cémentées - Salvatore FALZONE - Janvier 2005

📁 MICHELIN - Propriétés thermophysiques Acier Maraging 18Ni300 - A Treilhes, Décembre 2015

📁 MK - Duretés sur blocs de contrôle pour cylindres coulés - M SINNAEVE, Juin 2018

📁 MS²F - Fatigue properties for AISI 4140, DIN 42CrMo4 - Bouffioux, July 2018

📁 MTS Benelux - Soudures rompues sur enveloppes Chauffes-eau - Thibault BOULANGER, Février 2004

📁 MUSTAD - Effet plomb sur propriétés acier type C15Pb pour compresseur - Jean-Sebastien DENOEL

📁 N & B KNAUF et Cie - Analyses chimiques sur cornières Alu - Jules HERMANT - Octobre 2006

📁 Ney & Partners - Contrôle qualité et soudabilité sur poutrelle en acier - Van BOUCHOUT, Mars 2004

📁 NLMK Europe - Boursouflures sur revêtement galvanique feuillards cerclage fûts - C VERGNE - Janv 2018

📁 NLMK Europe - Boursouflures sur revêtement galvanique renforts automobiles - C VERGNE - Nov 2017

📁 NLMK EUrope - Boursouflures sur revêtement galvanisé renforts automobiles - C VERGNE - Nov 2017

📁 NLMK Europe - Défauts sur plaques galvanisées - C VERGNE, Février 2019

📁 NLMK Europe -Identification de défauts sur tôles galvanisées et embouties - C VERGNE - Mars 2017

📁 NLMK Europe -Métallographies sur tôles laminées et galvanisées - C VERGNE - Nov 2016

- ORES - Rupture sur vis couronne giratoire nacelle - D GERARD, Décembre 2017
- OXYBEL - Rupture sur boulons - A MARION, Mai 2005
- Paul CALLENS - Etude de soudabilité sur poutrelle - 09062011
- PCH Luxembourg - Rupture sur barre de béton précontraint - Expert PMD et Guy TOUSSIN de PCH Lux, Décembre 09
- PHARMA TECHNOLOGY - Perte ductilité Inox martensitique - Y FERAUX - Janv 2017
- PRAYON - Duretés sur Phosphate de Sodium - Février 2020
- Prof DARIMONT - Fissure sur câble précontraint - Mai 2003
- Prof E BECHET - Usure et CQ sur roulement à rouleaux - Décembre 2015
- Prof Luc COURAD - Duretés sur tôles - Janvier 2010
- Prof Luc COURAD - Epaisseur de galvanisation sur tôles - Janvier 2010
- Raffinerie Tirlemontoise - Analyse chimique sur limailles - MAGGI, BOCKIAU - Mars 2018
- Raffinerie Tirlemontoise - Corrosion sur tube échangeur acier au carbone - J WARNANT - Mars 2020
- Raffinerie Tirlemontoise SA - Bride inox corrodée - J Warnant, Nov 2012
- Raffinerie Tirlemontoise SA - Rupture roue à aubes inox - L Detroux, Oct 2013
- Raffinerie Tirlemontoise SA - Tuyères inox fissurées - J Warnant, Février 2013
- RTBF - Mini-cocottes en fonte émaillée -CQ - T Mahy, Mai 2014
- SA GEORGE & Cie - Teneur en P des fontes - B. GOFFINET - Mars 2013
- SANSEN & GANGI - Argent noir - Févier 2013
- SECOLUX - Analyse chimiques et soudabilité sur acier et fonte - Ir Dumbruck, Octobre 2009
- Shur-Lok International - CQ sur boulons rivetés Alu - Benoit COLAUX
- Sirris - SLM Titane, porosités et µstr - Février 2013
- SOLVAY - Coude en Ti rompu et corrodé - VANDEWATTYNE- Avril 2011
- SOLVAY - Fuite sur tuyauterie en Inox 304L - VANDEWATTYNE, Octobre 2011
- SOLVAY - Manchette perforée - VANDEWATTYNE- Janvier 2012
- SOLVAY - Corrosion sur soudure paroi citerne en acier - VANDEWATTYNE, Juin 2011

- SONACA - Inserts de copeaux dans des tôles inox pour moteur primaire centre d'usinage - Prof DEBONGNIE - Avril 2004
- SWDE - CQ sur Revêtement Zn15Al sur tuyau en fonte - B THIBERT, Octobre 2014
- SWDE - Sinistre sur chantier Grue # Prise d'eau - Me Thierry CORDIER, Avril 2008
- TAC - Alu 7075 - Gérard NOEL, Novembre 2005
- TAC - CQ sur acier 4130 - P VANISEGHEM, Février 2011
- TECHSPACE AERO - Analyse tâches sur surface rotor - Mars 2012
- TECHSPACE AERO - Analyses diverses au MEB-EDX - A LENAIN, CATµ
- Techspace Aero - Caractérisation Alu tube soudéà embase - E GERIN - Avril 2013
- TECHSPACE AREO - Surchauffe sur aubages rotor superalliage Ni - A LENAIN, Janvier 2007
- TECHSPACEAERO - Fractos sur éprouvettes Ti
- THALES - Materials Selection for leaf springs - BECHET, Juin 2019
- Truflo Rona - Corrosion vanne conduite hydrocarbures - F LEMBREE - Mai 2013
- Wellpumps SA - Rupture sur axes de pompes en Inox 316 et 304 - E DUBOIS, Octobre 2014
- WOW COMPANY sa - Usure prématurée sur anneaux - D Horion, Oct 2011